ADVANCED TECHNOLOGIES IN EARTH SCIENCES

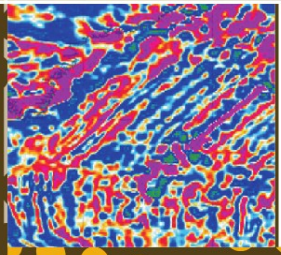

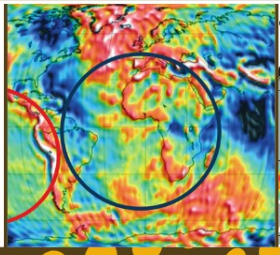
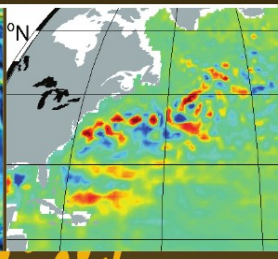

F. Flechtner · Th. Gruber · A. Güntner · M. Mandea
M. Rothacher · T. Schöne · J. Wickert (Eds.)

System Earth via Geodetic-Geophysical Space Techniques

Springer

Advanced Technologies in Earth Sciences

Frank Flechtner · Thomas Gruber ·
Andreas Güntner · Mioara Mandea ·
Markus Rothacher · Tilo Schöne · Jens Wickert
Editors

System Earth via Geodetic-Geophysical Space Techniques

Springer

Editors
Dr. Frank Flechtner
Helmholtz Centre Potsdam
GFZ German Research
Centre for Geosciences
Telegrafenberg
14473 Potsdam
Germany
frank.flechtner@gfz-potsdam.de

Dr. Thomas Gruber
TU München
Arcisstr. 21
80333 München
Germany
thomas.gruber@bv.tum.de

Dr. Andreas Güntner
Helmholtz Centre Potsdam
GFZ German Research
Centre for Geosciences
Telegrafenberg
14473 Potsdam
Germany
guentner@gfz-potsdam.de

Prof. Dr. Mioara Mandea
Université Paris Diderot -
Institut de Physique du
Globe de Paris
Géophysique spatiale et
planétaire - Bâtiment
Lamarck
Case 7011, 5 rue Thomas Mann
75205 Paris Cedex 13, France
mioara@ipgp.fr

Prof. Dr. Markus Rothacher
ETH Zürich
Photogrammetrie
HPV G 52
Schafmattstr. 34
8093 Zürich
markus.rothacher@ethz.ch

Dr. Tilo Schöne
Helmholtz Centre Potsdam
GFZ German Research
Centre for Geosciences
Telegrafenberg
14473 Potsdam
Germany
tschoene@gfz-potsdam.de

Dr. Jens Wickert
Helmholtz Centre Potsdam
GFZ German Research
Centre for Geosciences
Telegrafenberg
14473 Potsdam
Germany
wickert@gfz-potsdam.de

ISSN 2190-1635 e-ISSN 2190-1643
ISBN 978-3-642-10227-1 e-ISBN 978-3-642-10228-8
DOI 10.1007/978-3-642-10228-8
Springer Heidelberg Dordrecht London New York

Library of Congress Control Number: 2010924887

Cover design: Bauer, Thomas

Printed on acid-free paper

Springer is part of Springer Science+Business Media (www.springer.com)

Preface

Our planet is currently experiencing substantial changes due to natural phenomena and direct or indirect human interactions. Observations from space are the only means to monitor and quantify these changes on a global and long-term perspective. Continuous time series of a large set of Earth system parameters are needed in order to better understand the processes causing these changes, as well as their interactions. This knowledge is needed to build comprehensive Earth system models used for analysis and prediction of the changing Earth. Geodesy and geophysics contribute to the understanding of system Earth through the observation of global parameter sets in space and time, such as tectonic motion, Earth surface deformation, sea level changes and gravity, magnetic and atmospheric fields.

In the framework of the German geoscience research and development programme GEOTECHNOLOGIEN, research projects related to the theme "Observing the Earth System from Space" have been funded within two consecutive phases since 2002, both covering 3 years. The projects address data analysis and model development using the satellite missions CHAMP, GRACE, GOCE and complementary ground or airborne observations. The results of the first phase projects have been published in the Springer book, titled "Observation of the Earth System from Space", edited by Flury, Rummel, Reigber, Rothacher, Boedecker and Schreiber in 2006. The present book, titled "System Earth via Geodetic-Geophysical Space Techniques" summarizes in 40 scientific papers the results of eight coordinated research projects funded in the second phase of this programme (2005–2008). These projects partly represent a continuation of the first phase, while some new projects have been initiated. The book provides an overview of the main outcomes of this research. At the same time it should inspire future work in this field. The programme was funded by the German Federal Ministry of Education and Research (BMBF). The support of the GEOTECHNOLOGIEN programme by BMBF is gratefully acknowledged. All projects were carried out in close cooperation between universities and research institutes.

A total of eight coordinated projects have been carried out. Three of them address the processing of static and time variable gravity field models from CHAMP, GRACE and GOCE data including methods for validation ("Improved GRACE Level-1 and Level-2 Products and their Validation by Ocean Bottom Pressure", "More accurate and faster available CHAMP and GRACE Gravity Fields for

the User Community" and "Gravity and steady-state Ocean Circulation Explorer GOCE"). The papers related to CHAMP and GRACE provide deeper insight into the sensors, the processing methods and the applied algorithms. Results of orbit and gravity field determination including validation are presented as well. As GOCE was not yet in orbit during the project period, the rationale of GOCE gravity gradient processing to static geoid solutions and their validation are described in several papers. Two out of the eight coordinated projects are related to applications of GRACE results, altimeter, GPS and other data for geophysical analyses ("Time-Variable Gravity and Surface Mass Processes: Validation, Processing and First Application of New Satellite Gravity Data"; "Sea Level Variations – Prospects from the Past to the Present"). The papers in these chapters focus on the use of geodetic observations for assessing variations in the global water cycle and the analysis of sea level variations derived from satellite altimetry and observations taken at GPS and tides gauge stations. The remaining three chapters address contributions to the Global Geodetic-Geodynamic Observing System (GGOS), the atmospheric sounding by the geodetic based GPS radio occultation technique with CHAMP and GRACE and the observation of the Earth's magnetic field with CHAMP ("Integration of Space Geodetic Techniques as the Basis for a Global Geodetic-Geophysical Observing System – GGOS-D", "Near-Real-Time Provision and Usage of Global Atmospheric Data from GRACE and CHAMP" and "The Earth's Magnetic Field: At the CHAMP Satellite Epoch"). The articles in the GGOS section address the consistent processing of space-geodetic data, combination techniques and solutions for a global terrestrial reference frame. Results of atmospheric sounding using GPS radio occultation with CHAMP and GRACE are summarized in the subsequent chapter. Special focus is hereby given to the near-real time satellite data analysis, fundamental precondition for the application of the innovative GPS occultation data to improve global weather forecast. Finally, a review paper describes the progress made in magnetic field modelling during the CHAMP era.

In order to ensure high quality of the papers included in this book a review process was conducted before publication. The editors would like to thank all internal and external reviewers for their valuable contributions, which significantly helped to improve the quality of the book. The editors are indebted to all authors and to the publisher for the excellent cooperation when preparing this book. Sabine Lange and Anja Schlicht of the German GOCE project office at the Technische Universität München coordinated the editing process and the compilation of the book. The editors gratefully acknowledge their valuable support.

Potsdam, Germany
October 2009

Frank Flechtner
Thomas Gruber
Andreas Güntner
Mioara Mandea
Markus Rothacher
Tilo Schöne
Jens Wickert

Contents

Contributors

Oleg Abrikosov Helmholtz Centre Potsdam, GFZ German Research Centre for Geosciences, Department 1: Geodesy and Remote Sensing, Telegrafenberg, 14473 Potsdam, Germany, abrik@gfz-potsdam.de

Detlef Angermann Deutsches Geodätisches Forschungsinstitut, D-80539 München, Germany, angerman@dgfi.badw.de

Thomas Artz Institut für Geodäsie und Geoinformation, Universität Bonn, D-53115 Bonn, Germany, thomas.artz@uni-bonn.de

Franz Barthelmes Helmholtz Centre Potsdam, GFZ German Research Centre for Geosciences, Department 1: Geodesy and Remote Sensing, Telegrafenberg, 14473 Potsdam, Germany, bar@gfz-potsdam.de

Oliver Baur Institute of Geodesy, University of Stuttgart, 70174 Stuttgart, Germany, oliver.baur@gis.uni-stuttgart.de

Georg Beyerle Helmholtz Centre Potsdam, GFZ German Research Centre for Geosciences, Department 1: Geodesy and Remote Sensing, Telegrafenberg, 14473 Potsdam, Germany, gbeyerle@gfz-potsdam.de

Sarah Böckmann Institut für Geodäsie und Geoinformation, Universität Bonn, D-53115 Bonn, Germany, boeckmann@uni-bonn.de

Olaf Boebel Alfred Wegener Institute for Polar and Marine Research, D-27570 Bremerhaven, Germany, Olaf.Boebel@awi.de

Carmen Böning Alfred Wegener Institute for Polar and Marine Research, D-27570 Bremerhaven, Germany, carmen.boening@jpl.nasa.gov

Roland Braun Department of 1 'Geodesy and Remote Sensing', Helmholtz Centre Potsdam, GFZ German Research Centre for Geosciences, 14473 Potsdam, Germany, Roland.Braun@astrium.eads.net

Phillip Brieden Institut für Erdmessung, Leibniz Universität Hannover, 30167 Hannover, Germany, brieden@ife.uni-hannover.de

Jan Martin Brockmann Institute of Geodesy and Geoinformation, University of Bonn, Bonn, Germany, brockmann@geod.uni-bonn.de

Jianqing Cai Institute of Geodesy, University of Stuttgart, 70174 Stuttgart, Germany, cai@gis.uni-stuttgart.de

Christoph Dahle Helmholtz Centre Potsdam, GFZ German Research Centre for Geosciences, Department 1: Geodesy and Remote Sensing, Telegrafenberg, 14473 Potsdam, Germany, dahle@gfz-potsdam.de

Michael Dähnn Helmholtz Centre Potsdam, GFZ German Research Centre for Geosciences, Department 1: Geodesy and Remote Sensing, Telegrafenberg, 14473 Potsdam, Germany; Current affiliation: Norwegian Mapping Authority, N-3507 Hønefoss, Norway, michael.daehnn@statkart.no

Sergey Danilov Alfred-Wegener-Institute for Polar- and Marine Research, D-27570 Bremerhaven, Germany, sergey.danilov@awi.de

Heiner Denker Institut für Erdmessung (IfE), Leibniz Universität Hannover, D-30167 Hannover, Germany, denker@ife.uni-hannover.de

Reinhard Dietrich Institut für Planetare Geodäsie, Technische Universität Dresden, 01219 Dresden, Germany, dietrich@ipg.geo.tu-dresden.de

Henryk Dobslaw Helmholtz Centre Potsdam, GFZ German Research Centre for Geosciences, Department 1: Geodesy and Remote Sensing, Telegrafenberg, 14473 Potsdam, Germany, henryk.dobslaw@gfz-potsdam.de

Petra Döll Institute of Physical Geography, Goethe University Frankfurt am Main, 60438 Frankfurt am Main, Germany, p.doell@em.uni-frankfurt.de

Hermann Drewes Deutsches Geodätisches Forschungsinstitut, D-80539 München, Germany, drewes@dgfi.badw.de

Annette Eicker Institute of Geodesy and Geoinformation, University of Bonn, 53115 Bonn, Germany, annette@geod.uni-bonn.de

Saskia Esselborn Helmholtz Centre Potsdam, GFZ German Research Centre for Geosciences, Department 1: Geodesy and Remote Sensing, Telegrafenberg, 14473 Potsdam, Germany, saskia.esselborn@gfz-potsdam.de

Carsten Falck Helmholtz Centre Potsdam, GFZ German Research Centre for Geosciences, Department 1: Geodesy and Remote Sensing, Telegrafenberg, 14473 Potsdam, Germany, falck@gfz-potsdam.de

Kristina Fiedler Institute of Physical Geography, Goethe University Frankfurt am Main, 60438 Frankfurt am Main, Germany, fiedler@em.uni-frankfurt.de

Frank Flechtner Helmholtz Centre Potsdam, GFZ German Research Centre for Geosciences, Department 1: Geodesy and Remote Sensing, Telegrafenberg, 14473 Potsdam, Germany, frank.flechtner@gfz-potsdam.de

Christoph Förste Helmholtz Centre Potsdam, GFZ German Research Centre for Geosciences, Department 1: Geodesy and Remote Sensing, Telegrafenberg, 14473 Potsdam, Germany, foer@gfz-potsdam.de

Willi Freeden Geomathematics Group, Department of Mathematics, TU Kaiserslautern, 67653 Kaiserslautern, Germany, freeden@mathematik.uni-kl.de

Mathias Fritsche Institut für Planetare Geodäsie, Technische Universität Dresden, 01219 Dresden, Germany, fritsche@ipg.geo.tu-dresden.de

Björn Frommknecht RHEA S.A., Louvain La Neuve, Belgium; ESA/ESRIN, 00040 Frascati, Italy, Institut für Astronomische und Physikalische Geodäsie (IAPG), Technische Universität München, 80333 München, Germany, bjorn.frommknecht@esa.int

Gerd Gendt Helmholtz Centre Potsdam, GFZ German Research Centre for Geosciences, Department 1: Geodesy and Remote Sensing, Telegrafenberg, 14473 Potsdam, Germany, gendt@gfz-potsdam.de

Lutz Gericke Helmholtz Centre Potsdam, GFZ German Research Centre for Geosciences, Centre for GeoInformation Technology, Telegrafenberg, 14473 Potsdam, Germany, lg@gfz-potsdam.de

Michael Gerstl Deutsches Geodätisches Forschungsinstitut, D-80539 München, Germany, gerstl@dgfi.badw.de

Michael Gorbunov Obukhov Institute for Atmospheric Physics, Moscow, Russia, gorbunov@dkrz.de; m_e_gorbunov@mail.ru

Thomas Gruber Institute of Astronomical and Physical Geodesy, Technische Universiät München, Munich, Germany, Thomas.Gruber@bv.tu-muenchen.de

Andreas Güntner Helmholtz Centre Potsdam, GFZ German Research Centre for Geosciences, Department 5: Earth Surface Processes, Telegrafenberg, 14473 Potsdam, Germany, guentner@gfz-potsdam.de

Sean B. Healy European Centre for Medium-Range Forecasts, ECMWF, Reading, UK, sean.healy@ecmwf.int

Stefan Heise Helmholtz Centre Potsdam, GFZ German Research Centre for Geosciences, Department 1: Geodesy and Remote Sensing, Telegrafenberg, 14473 Potsdam, Germany, heise@gfz-potsdam.de

Rico Hengst Department 1 'Geodesy and Remote Sensing', Helmholtz Centre Potsdam, GFZ German Research Centre for Geosciences, 14473 Potsdam, Germany, rico.hengst@tropos.de

Matthias Holschneider Institut für Mathematik, Universität Potsdam, 14469 Potsdam, Germany, hols@math.uni-potsdam.de

Martin Horwath Institut für Planetare Geodäsie, Technische Universität Dresden, 01219 Dresden, Germany, martin.horwath@legos.obs-mip.fr

Michael Hosse Institut für Astronomische und Physikalische Geodäsie (IAPG), Technische Universität München, D-80333 München, Germany, michael.hosse@bv.tu-muenchen.de

Johannes Ihde Bundesamt für Kartographie und Geodäsie (BKG), D-60598 Frankfurt am Main, Germany, johannes.ihde@bkg.bund.de

Karl-Heinz Ilk Institute of Geodesy and Geoinformation, University of Bonn, 53115 Bonn, Germany, ilk@geod.uni-bonn.de

Focke Jarecki Institut für Erdmessung, Leibniz Universität Hannover, 30167 Hannover, Germany, jarecki@ife.uni-hannover.de

Boris Kargoll Institute of Geodesy and Geoinformation, University of Bonn, Bonn, Germany, bkargoll@uni-bonn.de

Rainer Kelm Deutsches Geodätisches Forschungsinstitut, D-80539 München, Germany, kelm@dgfi.badw.de

Armin Köhl Institut für Meereskunde, KlimaCampus, Universität Hamburg, Hamburg, Germany, koehl@ifm.uni-hamburg.de

Wolfgang Köhler Helmholtz Centre Potsdam, GFZ German Research Centre for Geosciences, Department 1: Geodesy and Remote Sensing, Telegrafenberg, 14473 Potsdam, Germany, wolfk@gfz-potsdam.de

Rolf König Helmholtz Centre Potsdam, GFZ German Research Centre for Geosciences, Department 1: Geodesy and Remote Sensing, Telegrafenberg, 14473 Potsdam, Germany, koenigr@gfz-potsdam.de

Daniel König Helmholtz Centre Potsdam, GFZ German Research Centre for Geosciences, Department 1: Geodesy and Remote Sensing, Telegrafenberg, 14473 Potsdam, Germany, dkoenig@gfz-potsdam.de

Ronny Kopischke Helmholtz Centre Potsdam, GFZ German Research Centre for Geosciences, Centre for GeoInformation Technology, Telegrafenberg, 14473 Potsdam, Germany, roko@gfz-potsdam.de

Ina Krasbutter Institute of Geodesy and Geoinformation, University of Bonn, Bonn, Germany, ina.krasbutter@geod.uni-bonn.de

Enrico Kurtenbach Institute of Geodesy and Geoinformation, University of Bonn, 53115 Bonn, Germany, enrico@geod.uni-bonn.de

Jürgen Kusche University of Bonn, Institute of Geodesy and Geoinformation, 53115 Bonn, Germany, kusche@uni-bonn.de

Vincent Lesur Helmholtz Centre Potsdam, GFZ German Research Centre for Geosciences, Department 2: Physics of the Earth, Telegrafenberg, 14473 Potsdam, Germany, lesur@gfz-potsdam.de

Hermann Lühr Helmholtz Centre Potsdam, GFZ German Research Centre for Geosciences, Department 2: Physics of the Earth, Telegrafenberg, 14473 Potsdam, Germany, luehr@gfz-potsdam.de

Andreas Macrander Alfred Wegener Institute for Polar and Marine Research, D-27570 Bremerhaven, Germany, Andreas.Macrander@awi.de

Mioara Mandea Helmholtz Centre Potsdam, GFZ German Research Centre for Geosciences, Department 2: Physics of the Earth, Telegrafenberg, 14473 Potsdam, Germany; Now at Universitee Paris Diderot, Institut de Physique du Globe de Paris, France, mioara@gfz-potsdam.de

Torsten Mayer-Gürr Institute of Geodesy and Geoinformation, University of Bonn, 53115 Bonn, Germany, mayer-guerr@geod.uni-bonn.de

Barbara Meisel Deutsches Geodätisches Forschungsinstitut, D-80539 München, Germany, meisel@dgfi.badw.de

Vivien Mende Helmholtz Centre Potsdam, GFZ German Research Centre for Geosciences, Centre for GeoInformation Technology, Telegrafenberg, 14473 Potsdam, Germany, Vivien.Mende@gfz-potsdam.de

Ulrich Meyer Helmholtz-Zentrum Potsdam, Deutsches GeoForschungsZentrum (GFZ), D-82234 Weβling, Germany; Astronomical Institute, University of Bern, 3012 Bern, Switzerland, ulrich.meyer@aiub.unibe.ch

Grzegorz Michalak Helmholtz Centre Potsdam, GFZ German Research Centre for Geosciences, Department 1: Geodesy and Remote Sensing, Telegrafenberg, 14473 Potsdam, Germany, michalak@gfz-potsdam.de

Jürgen Müller Institut für Erdmessung, Leibniz Universität Hannover, 30167 Hannover, Germany, mueller@ife.uni-hannover.de

Jan Müller Bundesamt für Kartographie und Geodäsie (BKG), D-60598 Frankfurt am Main, Germany, jan.mueller@bkg.bund.de

Horst Müller Deutsches Geodätisches Forschungsinstitut, D-80539 München, Germany, mueller@dgfi.badw.de

Karl Hans Neumayer Helmholtz Centre Potsdam, GFZ German Research Centre for Geosciences, Department 1: Geodesy and Remote Sensing, Telegrafenberg, 14473 Potsdam, Germany, hneum@gfz-potsdam.de

Axel Nothnagel Institut für Geodäsie und Geoinformation, Universität Bonn, D-53115 Bonn, Germany, nothnagel@uni-bonn.de

Helga Nutz Geomathematics Group, Department of Mathematics, TU Kaiserslautern, 67653 Kaiserslautern, Germany, hnutz@rhrk.uni-kl.de

Dave Offiler Met Office, Exeter, UK, dave.offiler@metoffice.gov.uk

Natasha Panafidina ETH Zürich, Institute of Geodesy and Photogrammetry, Zurich Switzerland, panatali@ethz.ch

Svetozar Petrovic Helmholtz Centre Potsdam, GFZ German Research Centre for Geosciences, Department 1: Geodesy and Remote Sensing, Telegrafenberg, 14473 Potsdam, Germany, sp@gfz-potsdam.de

Detlef Pingel Deutscher Wetterdienst, DWD, Offenbach, Germany, detlef.pingel@dwd.de

Jean-Claude Raimondo Helmholtz Centre Potsdam, GFZ German Research Centre for Geosciences, Department 1: Geodesy and Remote Sensing, Telegrafenberg, 14473 Potsdam, Germany, raimondo@gfz-potsdam.de

Markus Ramatschi Helmholtz Centre Potsdam, GFZ German Research Centre for Geosciences, Department 1: Geodesy and Remote Sensing, Telegrafenberg, 14473 Potsdam, Germany, maram@gfz-potsdam.de

Heiko Reinhardt Stiftung Alfred Wegener Institut für Polar und Meeresforschung, 27570 Bremerhaven, Germany, heiko.reinhardt@awi.de

Andreas Rhodin Deutscher Wetterdienst, Offenbach, Germany, andreas.rhodin@dwd.de

Falk Richter Alfred-Wegener-Institute for Polar- and Marine Research, D-27570 Bremerhaven, Germany, Falk.Richter@awi.de

Bernd Richter Bundesamt für Kartographie und Geodäsie, 60598 Frankfurt am Main, Germany, bernd.richter@bkg.bund.de

Bernd Ritschel Helmholtz Centre Potsdam, GFZ German Research Centre for Geosciences, Centre for GeoInformation Technology, Telegrafenberg, 14473 Potsdam, Germany, bernd.ritschel@gfz-potsdam.de

Vanya Romanova Institut für Meereskunde, KlimaCampus, Universität Hamburg, Hamburg, Germany, romanova@ifm.uni-hamburg.de

Markus Rothacher ETH Zürich, Photogrammetrie, HPV G 52, Schafmattstr. 34, 8093 Zürich markus.rothacher@ethz.ch

Sergei Rudenko Helmholtz Centre Potsdam, GFZ German Research Centre for Geosciences, Department 1: Geodesy and Remote Sensing, Telegrafenberg, 14473 Potsdam, Germany, sergei.rudenko@gfz-potsdam.de

Axel Rülke Institut für Planetare Geodäsie, Technische Universität Dresden, 01219 Dresden, Germany, ruelke@ipg.geo.tu-dresden.de

Reiner Rummel Institute of Astronomical and Physical Geodesy, Technische Universiät München, Munich, Germany, rummel@bv.tum.de

Anja Schlicht Institute for Astronomical and Physical Geodesy, 80333 München, Germany, schlicht@bv.tum.de

Torsten Schmidt Helmholtz Centre Potsdam, GFZ German Research Centre for Geosciences, Department 1: Geodesy and Remote Sensing, Telegrafenberg, 14473 Potsdam, Germany, tschmidt@gfz-potsdam.de

Nana Schön Helmholtz Centre Potsdam, GFZ German Research Centre for Geosciences, Department 1: Geodesy and Remote Sensing, Telegrafenberg, 14473 Potsdam, Germany, nana.schoen@gfz-potsdam.de

Tilo Schöne Helmholtz Centre Potsdam, GFZ German Research Centre for Geosciences, Department 1: Geodesy and Remote Sensing, Telegrafenberg, 14473 Potsdam, Germany, t.schoene@gfz-potsdam.de

Jens Schröter Alfred Wegener Institute for Polar and Marine Research, D-27570 Bremerhaven, Germany, Jens.Schroeter@awi.de

Wolf-Dieter Schuh Institute of Geodesy and Geoinformation, University of Bonn, Bonn, Germany, schuh@uni-bonn.de

Wolfgang Schwegmann Bundesamt für Kartographie und Geodäsie, 60598 Frankfurt am Main, Germany, wolfgang.schwegmann@bkg.bund.de

Manuela Seitz Deutsches Geodätisches Forschungsinstitut, D-80539 München, Germany, seitz@dgfi.badw.de

Richard Shako Helmholtz Centre Potsdam, GFZ German Research Centre for Geosciences, Department 1: Geodesy and Remote Sensing, Telegrafenberg, 14473 Potsdam, Germany, rst@gfz-potsdam.de

Dimitry Sidorenko Alfred-Wegener-Institute for Polar- and Marine Research, D-27570 Bremerhaven, Germany, Dmitry.Sidorenko@awi.de

Frank Siegismund Institut für Meereskunde, KlimaCampus, Universität Hamburg, Hamburg, Germany, frank.siegismund@zmaw.de

Nico Sneeuw Institute of Geodesy, University of Stuttgart, 70174 Stuttgart, Germany, sneeuw@gis.uni-stuttgart.de

Krzysztof Snopek Helmholtz Centre Potsdam, GFZ German Research Centre for Geosciences, Department 1: Geodesy and Remote Sensing, Telegrafenberg, 14473 Potsdam, Germany, krzysztof.snopek@gfz-potsdam.de

Detlef Stammer Institut für Meereskunde, KlimaCampus, Universität Hamburg, Hamburg, Germany, detlef.stammer@zmaw.de

Peter Steigenberger Institute of Astronomical and Physical Geodesy, Technische Universität München, D-80333 München, Germany, steigenberger@bv.tum.de

Volker Tesmer Deutsches Geodätisches Forschungsinstitut, D-80539 München, Germany, tesmer@dgfi.badw.de

Daniela Thaller Department of 1 ‘Geodesy and Remote Sensing’, Helmholtz-Zentrum Potsdam, Deutsches GeoForschungsZentrum (GFZ), D-14473

Potsdam, Germany; University of Bern, Astronomical Institute, CH-3012 Bern, Switzerland, daniela.thaller@aiub.unibe.ch

Maik Thomas Helmholtz Centre Potsdam, GFZ German Research Centre for Geosciences, Department 1: Geodesy and Remote Sensing, Telegrafenberg, 14473 Potsdam, Germany, maik.thomas@gfz-potsdam.de

Ralph Timmermann Alfred Wegener Institute for Polar and Marine Research, Bremerhaven, Germany, Ralph.Timmermann@awi.de

Mariella Tomassini Deutscher Wetterdienst, Offenbach, Germany, maria.tomassini@dwd.de

Christian Voigt Institut für Erdmessung (IfE), Leibniz Universität Hannover, D-30167 Hannover, Germany, voigt@ife.uni-hannover.de

Manfred Wenzel Alfred Wegener Institute for Polar and Marine Research, 27570 Bremerhaven, Germany, manfred.wenzel@awi.de

Werner Wergen Deutscher Wetterdienst, Offenbach, Germany, werner.wergen@dwd.de

Martin Wermuth Institute for Astronomical and Physical Geodesy, TU Munich, now at Deutsches Zentrum für Luft und Raumfahrt (DLR), Oberpfaffenhofen, Germany, martin.wermuth@dlr.de

Susanna Werth Helmholtz Centre Potsdam GFZ German Research Centre for Geosciences, 14473 Potsdam, Germany, swerth@gfz-potsdam.de

Jens Wickert Helmholtz Centre Potsdam, GFZ German Research Centre for Geosciences, Department 1: Geodesy and Remote Sensing, Telegrafenberg, 14473 Potsdam, Germany, wickert@gfz-potsdam.de

Herbert Wilmes Bundesamt für Kartographie und Geodäsie (BKG), D-60598 Frankfurt am Main, Germany, herbert.wilmes@bkg.bund.de

Insa Wolf Institut für Erdmessung, Leibniz Universität Hannover, 30167 Hannover, Germany, kiwolf@gmx.de

Kerstin Wolf Geomathematics Group, Department of Mathematics, TU Kaiserslautern, 67653 Kaiserslautern, Germany, Kerstin-wlf@gmx.de

Johann Wünsch Helmholtz Centre Potsdam, GFZ German Research Centre for Geosciences, Department 1: Geodesy and Remote Sensing, Telegrafenberg, 14473 Potsdam, Germany, wuen@gfz-potsdam.de

Part I
CHAMP and GRACE

More Accurate and Faster Available CHAMP and GRACE Gravity Fields for the User Community

Frank Flechtner

1 Introduction

The German Research Centre for Geosciences (GFZ) is strongly involved in the realization and operation of the German CHAllenging Mini-satellite Payload (CHAMP, Reigber et al., 1999) and the US/German Gravity Recovery and Climate Experiment (GRACE, Tapley and Reigber, 2001) missions launched in 2000 and 2002, respectively. The GRACE mission configuration, key instrumentation, the gravity field products and the coarse data flow within the GRACE Science Data System is already described in this chapter. While the GRACE mission is primarily focusing on the determination of the time-variable gravity field of the Earth and – with reduced priority – on atmospheric limb sounding CHAMP has three equivalent science objectives:

- Generation of highly precise global long to mid wavelength features of the static Earth gravity field and the temporal low frequency variation of this field.
- Determination of the main and crustal magnetic field of the Earth and the space/time variability of these field components.
- Collection of globally distributed GPS refraction data caused by the atmospheric and ionospheric signal delay and transformation into temperature, water vapor and electron content profiles.

To derive these mission goals CHAMP has the following key instrumentation onboard (see Fig. 1):

The *GPS Receiver TRSR-2* onboard CHAMP was provided by NASA and manufactured at NASA's Jet Propulsion Laboratories (JPL). In combination with the STAR accelerometer (see below) it serves as the main tool for CHAMP high-precision orbit and gravity field determination. Additional features are implemented for atmospheric limb sounding and the experimental use of specular reflections

F. Flechtner (✉)
Helmholtz Centre Potsdam, GFZ German Research Centre for Geosciences,
Department 1: Geodesy and Remote Sensing, Telegrafenberg, 14473 Potsdam, Germany
e-mail: frank.flechtner@gfz-potsdam.de

F. Flechtner et al. (eds.), *System Earth via Geodetic-Geophysical Space Techniques*,
Advanced Technologies in Earth Sciences, DOI 10.1007/978-3-642-10228-8_1,

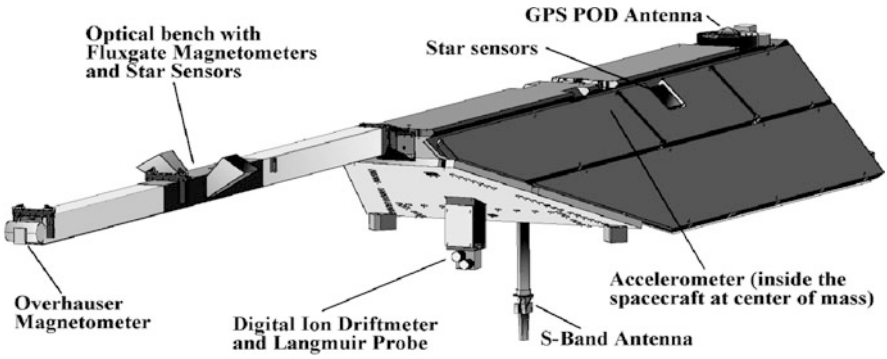

Fig. 1 CHAMP key instrumentation. Not shown is the LRR and the reflectometry antenna on the nadir side and the GPS limb sounding antenna array on the back side. The S-band antenna is used for communication purposes only

of GPS signals from ocean surfaces for GPS-altimetry. Unfortunately this experiment could never been performed due non provided software. A synchronization pulse delivered every second is used for precise onboard timing purposes, and the autonomously generated navigation information is used by both the CHAMP AOCS (Attitude and Orbit Control System) and the star sensors (see below) to update their orbital position.

The *STAR accelerometer* sensor was provided by the Centre National d'Etudes Spatiales (CNES) and manufactured by the Office National d'Etudes et de Recherches Aerospatials (ONERA). It serves for measuring the non-gravitational accelerations such as air drag, Earth albedo and solar radiation acting on the CHAMP satellite. The STAR accelerometer uses the basic principle of an electrostatic micro-accelerometer: a proof-mass is floating freely inside a cage supported by an electrostatic suspension. The cavity walls are equipped with electrodes thus controlling the motion (both translation and rotation) of the test body by electrostatic forces and thus supports the recovery of the orbit from GPS data and by this the gravity field estimation. By applying a closed loop-control inside the sensor unit it is intended to keep the proof-mass motionless in the center of the cage. The detected acceleration is proportional to the forces needed to fulfill this task. Unfortunately, there seems to be a hyper-sensitivity to both temperature variations in the accelerometer cage and external noise signals by the X3 electrode pair likely caused by a malfunctioning drive-voltage amplifier. This requires a slightly different post-processing strategy of the accelerometer data (see Grunwaldt and Meehan, 2003).

The *Laser Retro Reflector* (LRR) is a passive payload instrument consisting of 4 cube corner prisms intended to reflect short laser pulses back to the transmitting ground station. This enables to measure the direct two-way range between ground station and satellite with a single-shot accuracy of 1–2 cm without any ambiguities. These data will be used for precise orbit determination in connection with GPS for gravity field recovery, calibration of the on-board microwave orbit determination

system (GPS) and two-colour ranging experiments to verify existing atmospheric correction models. The Laser Retro Reflector was developed and manufactured inhouse at GFZ.

The *Advanced Stellar Compass* (ASC) has been developed and fabricated under contract by the DTU (Technical University of Denmark, Lyngby). The design of this star imager is based on a new development already flown on the Ørsted satellite. On CHAMP there are two ASC systems each consisting of two Camera Head Units (CHU) and a common Data Processing Unit (DPU). One ASC is part of the magnetometry optical bench unit on the boom (see below) and the other provides high precision attitude information for the instruments fixed to the spacecraft body. Additionally the ASCs serve as sensors for the satellite attitude control system.

The *Fluxgate Magnetometer* (FGM) was developed and manufactured under contract by the DTU (Technical University of Denmark) Lyngby. The design is based on the CSC (Compact Spherical Coil) sensor which was newly developed for the Ørsted mission. The FGM is probing the vector components of the Earth magnetic field and is regarded as the prime instrument for the magnetic field investigations of the CHAMP mission. The interpretation of the vector readings requires the knowledge of the sensor attitude at the time of measurement. For that reason the FGM is mounted rigidly together with star cameras (cf. Advanced Stellar Compass) on an optical bench. For redundancy reasons a second FGM is accommodated on the optical bench, 60 cm inward from the primary sensor.

The *Overhauser Magnetometer* (OVM) was developed and manufactured under contract by LETI (Laboratoire d'Electronique de Technologie et d'Instrumentation) at Grenoble. It serves as the magnetic field standard for the CHAMP mission. The purpose of this scalar magnetometer is to provide an absolute in-flight calibration capability for the FGM vector magnetic field measurements. A dedicated program ensuring the magnetic cleanliness of the spacecraft allows for an absolute accuracy of the readings of <0.5 nT.

The *Digital Ion Drift Meter* (DIDM) is provided by the AFRL (Air Force Research Laboratory, Hanscom). The DIDM is an improved version of an analogue ion drift-meter type flown successfully on many upper atmospheric satellites. The purpose of this instrument is to make in-situ measurements of the ion distribution and its moments within the ionosphere. A number of key parameters can be determined from the readings, such as the ion density and temperature, the drift velocity and the electric field by applying the ($v \times B$)-relation. Together with the magnetic field measurements these quantities can be used to estimate the ionospheric current distribution. Knowing these currents will help significantly to separate internal from external magnetic field contributions. All components and functions of DIDM are performing nominally except of two problems: the intermediate loss after launch of one of the two nearly redundant sensors, and an uneven gain evolution of the microchannel-plate used for ion detection that has required development of an in-space calibration procedure (Cooke et al., 2003). In combination with the DIDM a Planar Langmuir Probe (PLP) is operated. This device provides auxiliary data needed to

interpret the ion drift measurements. Quantities that can be derived from the PLP sweeps are spacecraft potential, electron temperature and density.

For details on the CHAMP magnetic field and limb sounding measurement principle, experiments and results please refer to the contributions of the "MAGFIELD" (Magnetic Field Determination) and "NRT-RO" (Near real-time Provision and Usage of Global Atmospheric Data from GRACE and CHAMP) projects in this issue.

2 Gravity Field Determination from Analysis of High-Low SST Data

With the launch of CHAMP on 15 July 2000, a new era in Earth gravity field recovery from space began. High-low satellite-to-satellite (hlSST) using the American Global Positioning System (GPS) and on-board accelerometry combined with a low altitude and almost polar orbit (87.3° inclination) made CHAMP the first satellite being especially designed for long to medium wavelength global gravity field mapping. The mean flight altitude of CHAMP, being initially 454 km, decreased with an average rate of approximately 2–3 km/month over the first years of the mission. To increase the mission life time above the design mission duration of 5 years 4 orbit raise manoeuvres have been performed in 2002, 2006 and 2009. Due to the expected increase of the solar activity and the meanwhile very low orbital height of about 325 km the mission will end likely early 2010 (Fig. 2).

Compared to all former geodetic satellite missions used for global gravity field recovery, CHAMP has the following principal advantages (Reigber et al., 2003,

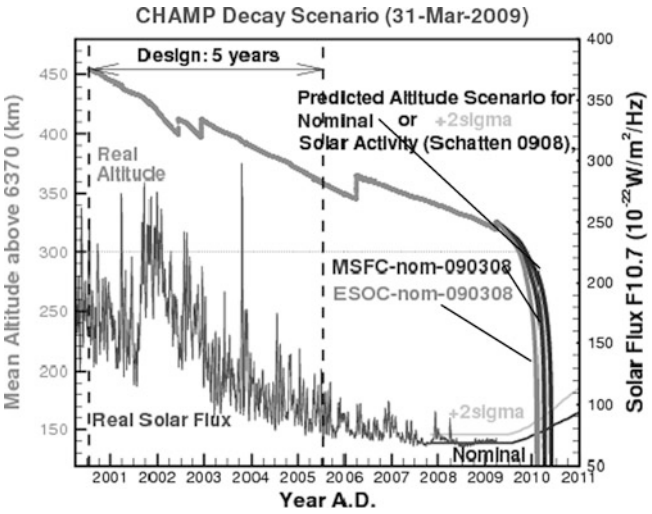

Fig. 2 CHAMP decay scenario in terms of mean altitude above 6,370 km as a function of various solar activity predictions (status 31 March 2009)

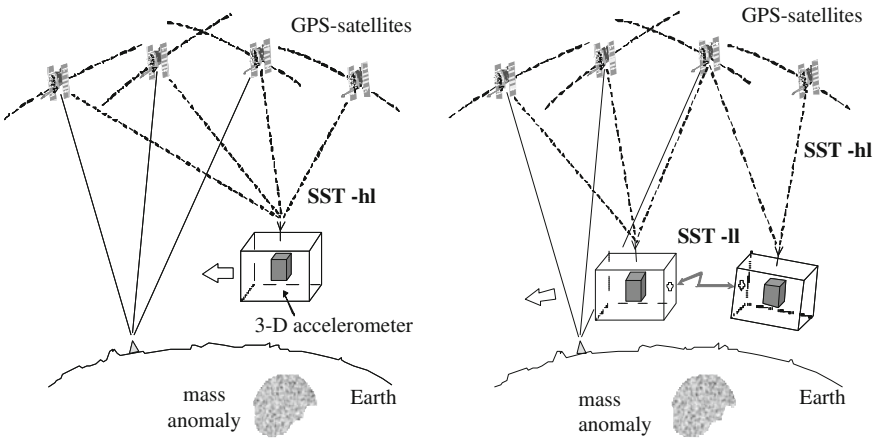

Fig. 3 Schematic view of the concept of satellite-to-satellite tracking in high-low (SST-hl, CHAMP, *left*) and low-low (SST-ll, GRACE, *right*) mode (courtesy of Prof. Dr. R. Rummel, Institute of Astronomical and Physical Geodesy of the Technical University Munich)

Fig. 3): GPS high-low SST yields a continuous multi-directional monitoring of the orbit compared to only one-dimensional sparse ground based tracking during station overflights, and, being important for a very low flying satellite, the onboard accelerometer measurements replace insufficient air drag modelling. By this, the purely gravitational orbit perturbation spectrum can be exploited for gravity field recovery along the orbit (Fig. 3) limited only by the instrument's performance. In addition, the almost polar orbit provides a complete coverage of the Earth with observations. Therefore, it could be shown for the first time that with CHAMP it was possible to derive a global gravity field model based upon only one satellite and from only a few months' worth of tracking data. Moreover the resulting gravity fields have been proven to be superior in long wavelength geoid and gravity field approximation as any pre-CHAMP satellite-only precursor models (e.g. Reigber et al. 2002, 2003 or 2005; chapter "The Release 04 CHAMP and GRACE EIGEN Gravity Field Models" by Flechtner et al., this issue) such as EGM96S (Lemoine et al., 1998) or GRIM-5S1 (Biancale et al. 2000).

Global gravity field recovery from satellite orbit perturbations relies on a precise numerical orbit integration taking into account all reference system and force model related quantities. The integrated orbit is fitted to the tracking observations (here GPS-CHAMP code and carrier phase ranges) in a least squares adjustment process solving iteratively for the satellite's state vector at the beginning of the arc and for other observation and configuration specific parameters, in particular GPS receiver clock offsets, phase ambiguities and calibration parameters (bias and scales) for the accelerometer. The arc length has to be chosen to be long enough to retain longer-period gravitational orbit perturbations and short enough to avoid an accumulation of systematic force model' errors such as those linked to accelerometer data. For CHAMP gravity field determination the arc length is e.g. 36 h for EIGEN-2 (Reigber

et al., 2003) and 24 h for EIGEN-CHAMP05S (chapter "The Release 04 CHAMP and GRACE EIGEN Gravity Field Models" by Flechtner et al., this issue).

After convergence of the initial orbit adjustment with the a-priori force field model, the observation equations are extended by partial derivatives for the looked-for global parameters, i.e. the unknown spherical harmonic coefficients describing the static gravitational potential. The arc-by-arc derived normal equation systems are then accumulated over the whole time period (which should be as long as possible) to one overall system which is then solved by matrix inversion. When processing GPS-LEO satellite-to-satellite tracking data, the precise ephemerides and clock parameters of the GPS satellite constellation have to be known. These are determined before-hand using GPS tracking data from a globally distributed ground station network and the held fixed in the subsequent CHAMP (or GRACE) orbit adjustment process.

3 Main Results of the BMBF/DFG Project "CHAMP/GRACE"

As mentioned above, the CHAMP and GRACE static gravity field models up to mid 2005 already showed a very large increase of accuracy compared to the gravity field solutions existing before CHAMP and GRACE, such as e.g. EGM96S or GRIM-5S1. Also, seasonal changes in the global continental hydrological water budget computed from monthly GRACE gravity field time series already exhibit a high degree of agreement with corresponding predictions of hydrological models. But, the GRACE gravity fields did not yet reach the accuracy predicted before the launch ("baseline accuracy", Kim, 2000) and the long-wavelength gravity field time series derived from CHAMP data analysis did not show significant correlations with GRACE and/or hydrological models (chapter "The Release 04 CHAMP and GRACE EIGEN Gravity Field Models" by Flechtner et al., this issue).

Besides possible reasons investigated in the parallel project "Improved GRACE Level-1 and Level-2 Products and their Validation by Ocean Bottom Pressure" (Flechtner, this issue) such as insufficient accuracy of the instrument data, the background models or wrong or insufficient instrument parameterization, also weak algorithms (e.g. the numerical integration of the CHAMP and GRACE satellites or the ambiguity fixing of the GPS ground and LEO (Low Earth Orbiter) observables) and/or weak methods (e.g. the two-step approach to solve the GPS satellite orbits and clocks first which then serve as a fixed reference frame in the following gravity field adjustment process) could be a possible reason.

Additionally, the transformation of CHAMP and GRACE observations into continuous, high quality gravity field products for the user community requires a number of subsystems that must be operated in a continuous manner. First to name are here the GFZ processor for orbit and gravity field computation (Earth Parameter and Orbit System, EPOS) and the ISDC (Integrated System and Data Centre) for a long term archiving and distribution of products to the users. Apart from that, there are a couple of additional tasks essential for product generation and quality control within gravity field processing. There are furthermore intermediary products

vital to keep other subsystems running outside the gravity field complex, but nevertheless necessary to attain the mission goals of CHAMP and GRACE. This "base processing" includes, for example, GPS satellite and clock parameters for the establishment of a consistent reference frame for LEO orbit adjustment. Also necessary are the uninterrupted computation and provision of orbit predictions for the international SLR ground stations, which in turn provide SLR measurements that serve as an independent quality control tool for CHAMP and GRACE orbit products exclusively based on GPS observations. Last but not least, there is the need of computation of fast orbit products (Rapid Science Orbits) for magnetic field data analysis (project "MAGFIELD") as well as for probing the ionosphere and the atmosphere (project "NRT-RO").

These tasks have been investigated in the GFZ project "More Accurate and Faster Available CHAMP and GRACE Gravity Fields for the User Community" funded within the programme "Geotechnologien" of BMBF (Ministry for Education and Research) and DFG (German Research Community) under grant 03F0436. Two main work packages have been defined: (a) the improvement of the CHAMP and GRACE base processing, in order to be able to provide the products to the user faster and more accurate and (b) optimization of the algorithms and procedures used for orbit and gravity field determination which is an essential requirement to attain the goal "faster and more accurate". The most important results are described in the following articles and can be summarized as follows:

The Information System and Data Center (ISDC) portal of the Helmholtz Centre Potsdam GFZ German Research Centre for Geosciences (http://isdc.gfz-potsdam.de) is the online service access point for all manner of geoscientific geodata, its corresponding metadata, scientific documentation and software tools. Initially, there have been different project driven and independent parallel operating ISDCs, such as the CHAMP, GRACE or GNSS ISDCs. As a consequence, users who were interested in e.g. orbit products from different satellite missions, had to enter sequentially different access points to find the required data and meta information. To overcome this unfavorable situation, to improve the Graphical User Interface (GUI) of the ISDC and to reduce double work and costs related to the operation and maintenance, the different portals were integrated under one roof. After the launch of the first release of the new ISDC portal in March 2006, the number of users increased from around 800 to almost 2000 in February 2009. Especially within the first year after the start there was an exponential increase of users, which also demonstrates the great user acceptance and successful development of the new portal system. Also the grown international importance of geosciences data and information provided by the ISDC portal is clearly visible. Today, more than 80% of the registered users are from foreign countries, such as from China and the USA, both with almost 300 users, followed by India, Japan, Canada, UK, France, Italy and others. The daily data input/output rate has reached a value of about 5,000 data files. By now, the registered and authorized users have access to more than 20 million geosciences data products, always consisting of data and metadata files of almost 300 different product types. Further information on the GFZ ISDC can be found in Ritschel et al. (this issue).

In order to obtain highly accurate and reliable orbit products for a wide range of applications (gravity field modelling, radio occultation analysis or TerraSAR-/TanDEM-X baseline determination) GFZ continuously works on improvements of its data processing systems. In Michalak and König details of the GPS phase wind-up correction and the GPS attitude model, as well as its implementation are given and initial validation results for both GPS and LEOs (CHAMP, GRACE and TerraSAR-X) are presented. Phase windup is an effect of the relative orientation between sending and transmitting antennas on the observed phase measurements, and, if neglected, introduces range errors of the phase observations at the decimeter level. It has been shown that the application of the phase wind-up corrections improves the GPS orbit accuracy by 1–2 cm (15–25%); the LEO orbit improvement measured by SLR is also significant and amounts to 3 mm (6%).

It was also demonstrated, that reversing the block IIR X-axis direction to match the convention for block II/IIA has no influence on the orbit and clocks in case when integer ambiguity fixing is applied. Half of the phase cycle difference is absorbed by the ambiguities. Correct application of the phase wind-up requires additionally correct modelling of the GPS satellite attitude (in particular yaw rotation) as it influences the orientation of the transmitting antenna. A test version of the attitude model including midnight/noon, shadow and post-shadow turns is already built and will be implemented in the operational data processing software after successful testing. It was shown that neglecting the attitude model and assuming geometric attitude as the nominal one can lead to large yaw differences exceeding even one full rotation of the satellite. This can have non-negligible impacts on the estimated orbits and clocks, which are intended to be used for high precision applications.

A reliable Rapid Science Orbit (RSO) processing system for the daily generation of precise GPS and LEO orbits with latencies of 1 day to support radio occultation and magnetic field studies has been developed. Currently the system regularly generates orbits of five LEO satellites: CHAMP, GRACE-A/B, SAC-C and TerraSAR-X. The system is flexible and allows easy extensions to new LEO missions. This was demonstrated by the inclusion of a test phase for the six COSMIC satellites. The 3D position accuracy of the GPS RSOs obtained from comparisons to the IGR orbits provided by the International GNSS Service (IGS) is 14 cm and was recently improved to 7–8 cm as a result of the introduction of integer ambiguity fixing into the processing. It can be concluded, that the GPS RSO accuracy in any direction (radial, along- and cross-track) is now close to 4–5 cm. The radial accuracy can be confirmed independently also by SLR, e.g. the laser ranging residuals to GPS PRN05 and PRN06 shows a scatter of about 5 cm. Position accuracy of the LEO orbits, obtained also from SLR, is uniform for all LEOs and in the range of 4–5 cm. Orbits of both GPS and most LEOs show centimeter-level negative bias in the SLR residuals of rather unclear nature. In spite of this, the accuracy of the orbits fulfil the radio occultation and magnetic field project requirements, and the availability of the orbit products is guaranteed to almost 100% due to operator interaction in case of failures of the automatic processing. The RSO orbits are publicly available

in GFZ's Information System and Data Center (ISDC). Further details on RSOs can be found in Michalak and König. It should also be noted that beside these RSOs with a latency of 1 day also near real-time (NRT) orbits with a latency of about 15–30 min after data dump are routinely produced. These ultra-fast orbits are an indispensable prerequisite for the provision of radio occultation analysis results (e.g. temperature and humidity profiles) to the weather services (see Michalak et al. in the NRT-RO section).

Precise orbit predictions are service products to support ILRS (International Laser Ranging Service), pre-processing of mission data and mission operations. In all cases it is necessary to know the position of the satellite at some time in the future with a dedicated accuracy depending on the application. Currently, GFZ delivers a suite of orbit prediction products for these purposes for the LEOs CHAMP, GRACE-A/B, and, since June 2007 also for TerraSAR-X. These products highly contribute to the success of these missions as SLR observations play an important role for Precise Orbit Determination (POD) validation. The orbit prediction system is running fully automated and is robust against various critical situations, e.g. hardware problems. A very high percentage of the distributed orbit prediction products meet the requirements of the users, and a constant effort is put to improve the quality which is monitored regularly by a Quality Control (QC) subsystem. The most demanding application of the orbit predictions is the laser tracking of the above-mentioned LEO satellite missions carried out by the ILRS ground stations. For the acquisition of SLR data the required accuracy is about 70 m in along-track direction which is equivalent to a 10 ms time bias when the satellite becomes visible over a station (i.e. the satellite is too early or too late). This quality criterion governs the QC and consequently the frequency of the generation of orbit predictions. Currently it is twice a day for GRACE-A/B and four times per day for CHAMP. Further information is provided in Snopek et al. (this issue).

In preparation of the reprocessing of GRACE and CHAMP gravity field data (see below), a thorough re-work of software and processing chains was performed, with a special emphasis on storage management and computation speed (Neumayer). First, significant improvements were already obtained by simply migration of the processing software from large shared-memory SunOS workstations to a cluster of high performance Linux PCs. A more efficient treatment of GPS clock parameters allowed to increase the processing speed by a factor of up to two. Crucial here was the exploitation of certain structures in the normal equation matrix. As a side effect, the treatment of GPS measurements is now more or less similar to the treatment of non-GPS data such as K-band SST or SLR data. An already existing column-block parallel computation method to obtain normal equation matrices from design matrices has been augmented with a corresponding row-block parallel computation scheme. If those new features are fully exploited on the high-performance Linux cluster of GFZ within the next months, the gain in processing speed may reach a factor of 5–10. A prerequisite is the need of large intermediary storage space and a large number of computation nodes.

The updated background models, processing standards and strategies, which have been investigated in this and in the parallel project "Improved GRACE Level-1 and Level-2 Products and their Validation by Ocean Bottom Pressure", have been used for a homogeneous reprocessing of the nearly complete CHAMP and GRACE data base (for details refer to chapter "The Release 04 CHAMP and GRACE EIGEN Gravity Field Models" by Flechtner et al.). As a result a new GFZ release 04 (RL04) EIGEN (European Improved Gravity field of the Earth by New techniques) time series of monthly CHAMP and GRACE gravity model have been produced complete to degree and order 120 and 60, respectively. Both, the monthly and static EIGEN-GRACE05S gravity fields could be improved by about 15 and 25% w.r.t. it's RL03 precursor models. Also, the EIGEN-CHAMP05S monthly solutions now show a very high correlation for the long wavelength structures of the gravity field when compared with GRACE.

For the first time, GRACE gravity fields are provided with weekly resolution (up to degree and order 30 and aligned to GPS calendar week) which may provide further insight into mass variations which take place at ten-daily or even shorter time scales such as barotropic Rossby waves, continental water storage changes or solid Earth and ocean tides.

The new static satellite-only and combined gravity models EIGEN-5S and EIGEN-5C are complete to degree and order 150 and 360, respectively. Independent comparisons with geoid heights, determined point-wise by GPS positioning and GPS levelling, show notable improvements. Also, the unrealistic meridional striping patterns over the oceans in the precursor EIGEN models could be much reduced. Therefore, ESA has decided to use both models as the standard for ESA's official data processing of the upcoming gradiometer satellite mission GOCE. Additionally the monthly EIGEN-CHAMP05S models have been used to derive a new mean CHAMP-model. Orbit adjustment tests with CHAMP and GRACE arcs show a significant improvement of this model with respect to its precursor EIGEN-CHAMP03S and also no degradation when compared to state of the art combined gravity models.

These new RL04 EIGEN models provide an important data base to monitor mass transport and mass distribution phenomena in the system Earth, such as the continental hydrological cycle, ice mass loss in Antarctica and Greenland, ocean mass changes or the ocean surface topography. Nevertheless, the GRACE baseline mission accuracy has still not been reached by a factor of 7.5 (static field) and 15 (monthly solutions), respectively. Therefore plans already exist for a further consistent reprocessing of the complete CHAMP and GRACE time series.

RL04 EIGEN models along with their calibrated errors and ancillary products such as the corresponding mean atmospheric and oceanic non-tidal mass variations as well as supporting documentation are or will be shortly available at the CHAMP and GRACE Integrated System and Data Center (ISDC, http://isdc.gfz-potsdam.de) at GFZ. Additionally the models can be downloaded from the ICGEM (International Centre for Global Earth Models) data base at GFZ Potsdam (http://icgem.gfz-potsdam.de).

References

Biancale R, Balmino G, Lemoine JM, Marty JC, Moynot B, Barlier F, Exertier P, Laurain P, Gegout P, Schwintzer P, et al. (2000) A new global earth's gravity field model from satellite orbit perturbations: GRIM5-S1. Geophys. Res. Lett. 27, 3611–3614.

Cooke D, Turnbull CW, Roth Ch, Morgan A, Redus R (2003) Ion drift-meter status and calibration. In: Reigber Ch, Lühr H, Schwintzer P (eds.), First CHAMP Mission Results for Gravity, Magnetic and Atmospheric Studies, Springer, Berlin, pp. 212–219.

Grunwaldt L, Meehan T (2003) CHAMP orbit and gravity instrument status. In: Reigber Ch, Lühr H, Schwintzer P (eds.), First CHAMP Mission Results for Gravity, Magnetic and Atmospheric Studies, Springer, Berlin, pp. 3–10.

Kim J (2000) Simulation Study of a Low-Low Satellite-to-Satellite Tracking Mission. Technical Report, University of Texas at Austin, Austin, TX.

Lemoine FG, Kenyon SC, Factor JK, Trimmer RG, Pavlis NK, Chinn DS, Cox CM, Klosko SM, Luthke SB, Torrence MH, et al. (1998) The Development of the Joint NASA GSFC and the National Imagery and Mapping Agency (NIMA) Geopotential Model EGM96. NASA Technical Paper, Goddard Space Flight Center, Greenbelt, NASA/TP-1998-206861, 509 pp.

Reigber Ch, Schwintzer P, Lühr H (1999) The CHAMP geopotential mission. Boll. Geof. Teor. Appl. 40, 285–289.

Reigber Ch, Balmino G, Schwintzer P, Biancale R, Bode A, Lemoine JM, König R, Loyer S, Neumayer KH, Marty JC, et al. (2002) A high-quality global gravity field model from CHAMP GPS tracking data and accelerometry (EIGEN-1S). Geophys. Res. Lett. 29(14), doi: 10.1029/2002GL015064.

Reigber Ch, Balmino G, Schwintzer P, Biancale R, Bode A, Lemoine JM, König R, Loyer S, Neumayer KH, Marty JC, et al. (2003) Global gravity recovery using solely GPS tracking and accelerometer data from CHAMP. Space Sci. Rev. 00, 1–12.

Reigber Ch, Jochmann H, Wünsch J, Petrovic S, Schwintzer P, Barthelmes F, Neumayer KH, König R, Förste Ch, Balmino G, et al. (2005) Earth gravity field and seasonal variability from CHAMP. In: Reigber Ch, Lühr H, Schwintzer P, Wickert J. (eds.), Earth Observation with CHAMP – Results from Three Years in Orbit, Springer, Berlin, pp. 25–30.

Tapley BD, Reigber Ch (2001) The GRACE mission: Status and future plans. EOS Trans. AGU 82(47), Fall Meet. Suppl. G41, C-02.

The CHAMP/GRACE User Portal ISDC

Bernd Ritschel, Lutz Gericke, Ronny Kopischke, and Vivien Mende

1 Introduction

The Information System and Data Center (ISDC) portal of the Helmholtz Centre Potsdam GFZ German Research Centre for Geosciences (http://isdc.gfz-potsdam.de) is the online service access point for all manner of geoscientific geodata, its corresponding metadata, scientific documentation and software tools. The majority of the data and information, the portal currently offers to the public, are global geomonitoring products such as satellite orbits and Earth gravity field data as well as geomagnetic and atmospheric data for the exploration. These products for Earths changing system are provided via state-of-the art retrieval techniques. The portal's design and the operation is a project of the ISDC team within the GFZ's Data Center. Before the start of the first release of the portal in March 2006, there have been different project driven and independent operating ISDCs, such as the GGP ISDC for the handling of local gravity and appropriate meteorological data of the international Global Geodetic Project (GGP) or the CHAMP ISDC, the GRACE ISDC and the GNSS ISDC for the management of geodetic, geophysical and atmospheric and ionospheric geomonitoring data and information derived from the CHAMP, GRACE and GPS satellites and GPS ground stations. Because of the existence of unique and independent ISDCs, users, who were interested in e.g. orbit products from different satellite missions, had to go into the appropriate ISDC, such as CHAMP ISDC, GRACE ISDC or GNSS ISDC in order to find required orbit data and information. To overcome the just described complicated situation, for the improvement of the Graphical User Interface (GUI) of the ISDC and for the reduction of double work and costs related to the operation and maintenance of different ISDC, the idea of the integration of the ISDC systems under one portal roof was born. In conclusion, the requirements and constraints for the development of an ISDC portal were:

B. Ritschel (✉)
Helmholtz Centre Potsdam, GFZ German Research Centre for Geosciences,
Centre for GeoInformation Technology, Telegrafenberg, 14473 Potsdam, Germany
e-mail: bernd.ritschel@gfz-potsdam.de

F. Flechtner et al. (eds.), *System Earth via Geodetic-Geophysical Space Techniques*,
Advanced Technologies in Earth Sciences, DOI 10.1007/978-3-642-10228-8_2,

- the integration of new product types related to new collaboration projects, such as e.g. the GNSS monitoring project which deals with Global Navigation Satellite System data and the Galileo Geodetic Service Provider (GGSP) project,
- the management of a constant increasing number of users and user groups,
- the improvement of the system usability and the request for a single sign on,
- the realization of a multi-domain geoscience information and data retrieval,
- the optimization of system and service operation and maintenance.

Figure 1 illustrates that after the launch of the first release of the GFZ ISDC portal in March 2006, the number of users increased from around 800 to almost 2,000 in February 2009. Especially within the first year after the start there was an exponential increase of users, which also demonstrates the great user acceptance and successful development of the new portal system.

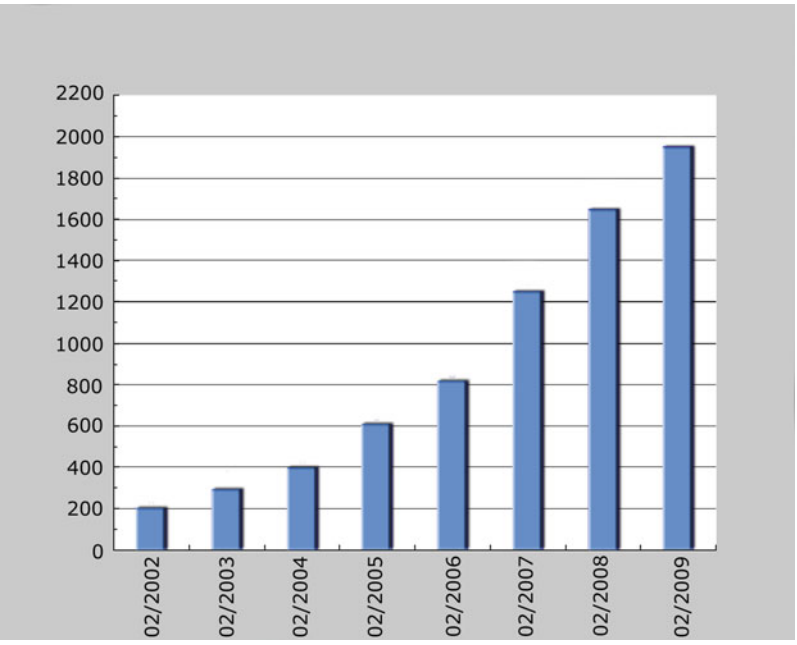

Fig. 1 User development graph (2009-02-11)

The grown international importance of the geosciences data and information (Klump et al., 2008), provided by the portal is shown in Fig. 2. Now, more than four fifth of the registered portal users are from foreign countries, such as from China and the USA, both with almost 300 users, followed by India, Japan, Canada, UK, France, Italy and others. The daily data input/output rate has reached a value of about 5,000 data files. By now, the registered and authorized users have access to more than 20 million geosciences data products, always consisting of data and metadata

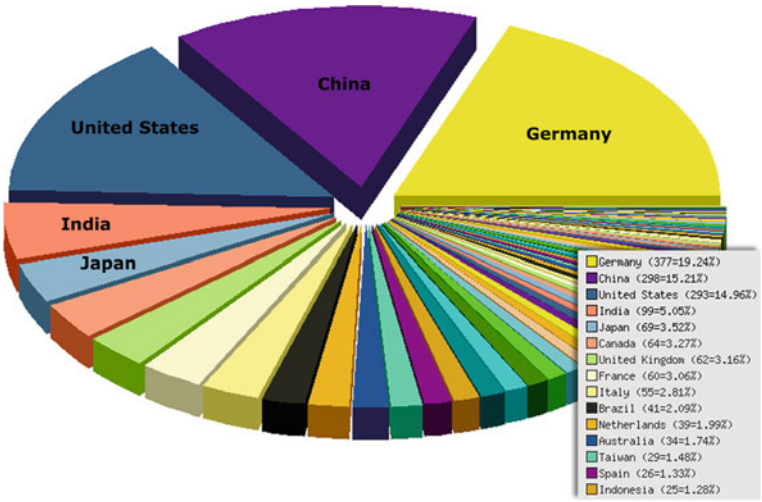

Fig. 2 User country statistics (2009-02-11)

files structured in almost 300 different product types related to main geosciences domains, such as:

- geodesy, e.g. GPS data, satellite orbits, local gravity data, Earth gravity models, and Earth rotation parameter,
- geophysics, e.g. Earth magnetic field data, both vector and scalar data,
- atmosphere and ionosphere, e.g. tropospheric temperature profiles and ionospheric electron density profiles.

The objectives of the data lifecycle management, the ISDC metadata classification model and used metadata standards, the portal design and the data retrieval and data access interfaces as well as the description of the backend functionality are subjects of the next chapters.

2 Data Lifecycle Management

The challenge of the exponential growing number and volume of and the increasing danger of data waste and data loss data (Gantz et al., 2008) only can be solved by the introduction of a framework which guides the process of data management from the birth of data to the transformation process into knowledge or the death of the data.

In a framework of a complete data life cycle (Lyopn, 2007), as shown in (Fig. 3), the portal system is responsible for the geoscience data and information handling from the ingestion of geoscience data products, provided by scientists, until the provision of geoscience knowledge in form of e.g. publications or model visualizations, which are based on the ISDC data. Even in the project elaboration phase the ISDC expertise attends the process for the definition, description and classification of data

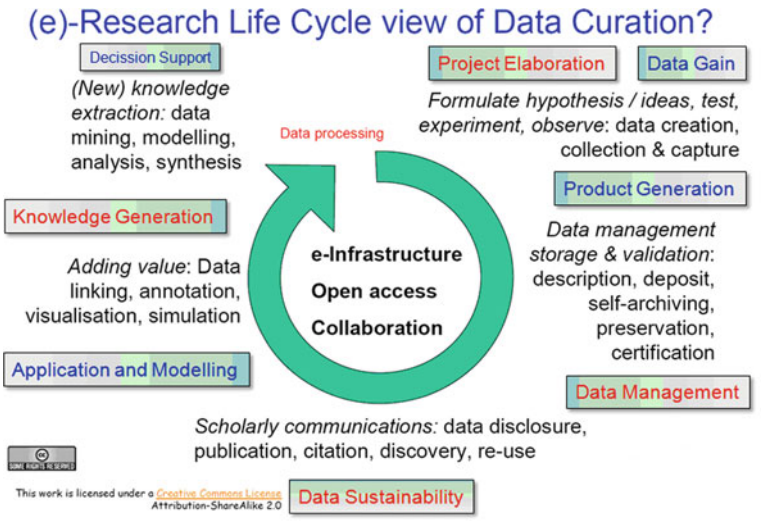

Fig. 3 e-Research life cycle, data curation and related processes* Lyopn (2007) (*edited by Ritschel, B.)

products. In the data product generation phase the portal is both, data drain and data source. Half-formed or low-level processed data products are ingested and stored at the ISDC as well as later provided to user or user groups for further processing. Finalized data products are stored in a sustainable way at long-term and online archive systems. Data sets are imported, if the appropriate metadata documents are complete, consistent and valid. Thus at least a minimum of a formal data file validation process is realized. Because of almost 300 different product types, there is no real check of the content of the data files at the ISDC ingestion process possible. But the standardized data product and product type metadata documents are used for the creation of a complete and consistent ISDC data product catalog. Complete data sustainability is realized, if the disclosure, the discovery and the reuse of data is guaranteed for everybody, for a long time. Publication and citation of data are important activities which support the sustainable data management idea. The disclosure of new data products in the portal is realized by special features of the portal, such as e.g. the publication of newsletters or the provision of RSS feeds. The ISDC data product catalog system enables a detailed search for data, which are accessible, downloadable and finally reusable. Knowledge generation starts with adding value to the data, such as data integration, annotation, visualization or simulation. Both, for the data integration and the annotation of data products, the portal provides the appropriate features. Knowledge extraction processes are data mining, modeling, analysis and synthesis. Another process which is important, but not part of the "Research Life Cycle view of Data Curation" in Fig. 3, is the science driven data review process, which should be done on a cyclical basis. This review process contains such activities, as the harmonization and aggregation of data, the tailoring of data and the removal of data. Reviewing is necessary for the enhancement of data

interoperability, the re-usage of data at other scientific domains and finally for the maintenance of the operational status of the ISDC portal.

3 Metadata Model

The ISDC portal backend software manages almost 300 geoscience product types from different projects. In order to handle such a big variety of product types, a special ISDC product philosophy and metadata handling mechanism has been developed and introduced (Ritschel et al., 2006). The key for the solution of this challenge is the compulsory usage of a standardized metadata format for the description of the product types and the appropriate data products.

The relation of project-related product types at ISDC is shown in Fig. 4. Each product type consists of a set of products. A product is composed of a data file(s) and metadata that is created by using DIF XML.

As explained in detail in Mende et al. (2008) and Ritschel et al. (2007b), each product type that results from a geoscience project consists of a set of data products. A data product is composed of a data file or a data set and a standardized metadata document. In order to describe and manage the data products, the ISDC system uses NASA's Directory Interchange Format (http://gcmd.gsfc.nasa.gov/User/difguide/difman.html) metadata standard DIF. Currently, the ISDC backend accepts both, ASCII DIF version 6, e.g. for CHAMP satellite data products, and an enhanced XML DIF version 9.x, e.g. for TerraSAR-X satellite data products. First, the DIF standard was developed for the Global Change Master Directory (http://gcmd.nasa.gov/Aboutus) and is used for the semantical description of all kinds of Earth science data sets, which are categorized in domain specific product types. The metadata standard uses general metadata attributes, which are defined as required attributes, such as e.g. Entry_ID (unique identifier), Entry_Title (title of the product type), Parameters (science keywords that are representative of the product type being described), Summary (brief description of the product type that

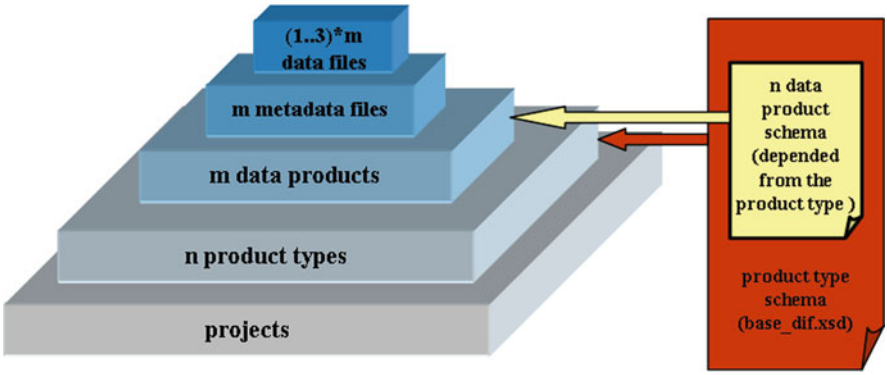

Fig. 4 Project – product type – data product schema, which especially illustrates the relations between product types and data products and appropriate XML schemata

allows users to determine if the data set is useful for their requirements) and others. In addition to the required elements there is a set of metadata attributes, which describe the product type in a much more detailed way. Such attributes are e.g. Start_Date and Stop_Date describing the temporal coverage of the data collection, or Latitude, Longitude and Attitude or Depth, which determine the spatial coverage of the data. The DIF metadata standard has the potential to provide the right structure for the description of all kinds of geosciences data sets. Counting all GCMD DIF files, almost 40,000 different data sets or product types from A as agriculture to T as terrestrial hydrosphere are semantically described by DIF compliant metadata documents. Even more, DIF metadata is transferable to the Federal Geographic Data Committee (FGDC) standard (http://www.fgdc.gov), and there are XSL transformation specifications, as shown in Fig. 5 for the creation of ISO 19115 (http://www.iso.org/iso/search.htm?qt=ISO+19115&published=on) compliant metadata documents. The listed features of the DIF standard proof the right choice of the DIF standard for the management of ISDC product types (Ritschel et al., 2006; Ritschel et al., 2007a). The ISDC base schema of the product type DIF XML documents is defined in the "base-dif.xsd" file (Mende et al., 2008). The ISDC XML Schema Definition (XSD) has been defined on the basis of the GCMD XSD and is available at http://isdc.gfz-potsdam.de/xsd/base_dif.xsd. Because the ISDC portal manages both – product types and data products – it was necessary to extend the DIF standard. For the management of data products, the ISDC deals with a combination of product type and data product DIF documents. The metadata of product types is stored in associated data product type DIF files according to the "base-dif.xsd" schema. The data file specific metadata is documented in data product DIF XML files. The combination of a data file or a set of data files (currently max. 3 data files) and the appropriate metadata file define

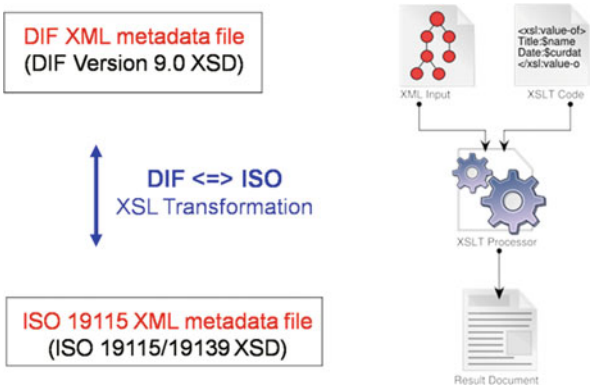

Fig. 5 Mapping of metadata standards[1]

[1]Dreftymac (2007) diagram of the basic elements and processing flow of XSL Transformations retrieved February 2009 from http://en.wikipedia.org/ (edited by Ritschel, B.).

the ISDC data product, as seen in Fig. 4. Each product type has its own schema for the data product DIF XML files. Data product DIF documents are necessary for the description of the data file specific properties. The complex XML type <Data_Parameters> in the data product DIF XML document provides the specific extension of the product type DIF XML structures, which are used for semantic information of the data file, such as e.g. temporal and spatial information about the data in the data file and technical information such as e.g. data file name or data file size and other information. The connection between the data product DIF XML files and the product type DIF XML document is given by the equality of the main parts of the <Entry_ID> element in both the product type and the related product metadata documents. Additionally, the content of the <Parent_DIF> element in the data product DIF XML document refers to the appropriate product-type DIF document. Figure 4 illustrates the relation between the XML schemata for the definition of product types and the definition of data products. The addition of mandatory elements to the schemata of data products keeps the usefulness of data product metadata DIF documents without the appropriate product type DIF documents.

The ISDC ontology class model based on the semantic Web approach (Daconta et al., 2003) contains the metadata classes project, platform, instrument, product type and institution. Keywords from controlled and free vocabularies are used for the description of the different metadata classes. The new ISDC metadata concept is an extension to the ISDC product type and metadata philosophy (Ritschel et al., 2008) and is based on the extended metadata classification model of the GCMD. Figure 6 illustrates the new metadata classes and its relations as well as the use of controlled and free vocabularies. The ISDC metadata class model defines the appropriate classes, relations and the input of different vocabularies. The relation between project and instrument (dashed line) is an implicit one only, realized via the project – platform – instrument relation. The science domain, used for semantic description of the product type is defined by the project objectives and extended by the physical features of the instrument.

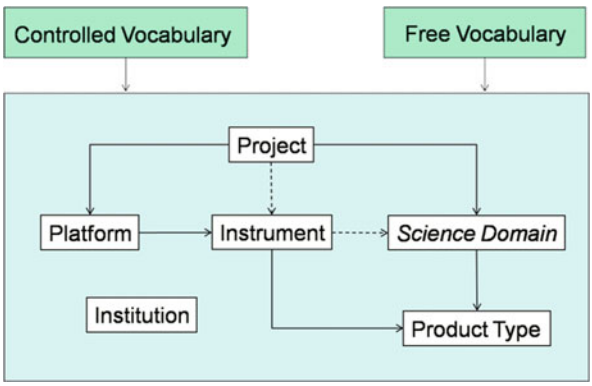

Fig. 6 The ISDC metadata class model

Table 1 ISDC metadata classes and semantical relations

Metadata classes	Product type	Instrument	Platform	Project	Institution
Semantical occurrences					
<project>	Attributes			Attributes	
<platform>	Attributes	References	Attributes	References	
<instrument>	Attributes	Attributes	References		
<institution>	Attributes	References	References	References	Attributes

The introduction of the new metadata classes project, platform and instrument are a result of the necessity both to describe the semantics of the appropriate classes in a deeper, more detailed and standardized manner (Pfeiffer, 2008). The concept model of the ISDC metadata classes also contains the independent class institution, because data and information about institutions, organisations and persons are always part of the other classes in the model.

The relations between ISDC metadata classes and attributes are shown in Table 1. Because of historical reasons, the class product type always contains real attributes, whereas the other classes have attributes for the description of own properties and use references for the crosslink to the appropriate classes. Detailed information about the ISDC metadata concept model is available at (Ritschel et al., 2008a).

As done for the semantic description of product type metadata, keywords from controlled and free vocabulary is used for the metadata content of documents related to projects, platforms and instruments. The implementation of the new ISDC concept model will provide advanced and new ISDC portal retrieval features. A classified keyword search over the complete stock of metadata documents offers a total new view about the relations between and in projects, platforms, instruments and product types.

4 Portal Architecture

The current solution uses PostNuke[2] as a portal framework. The decision for using this platform was based on the detailed analysis of different portal systems in 2004. The main selection criteria were costs and simplicity. Because of PostNuke's open architecture and the large community around this open-source software, there are many free components that became part of the current portal implementation. One main component for backend services is a Sybase database (http://www.sybase.com), where data flow information, rights management and user statistics is stored and periodically updated. This big challenge that had to be solved: managing metadata and fine-granular rights for tens of millions of data files. As mentioned already, there are currently around 20 million products, and each product has its own set of access rights.

[2]Now known as Zikula (http://zikula.de/)

4.1 Application Framework

The PHP Application Framework PostNuke, stands is a PHP-based portal and Content Management System (CMS). The implementation details are not specific for this platform. The independence from a specific framework was a central point for the software development because PostNuke was meant to be a solution to consolidate the existing systems and prepare the way towards the planed GFZ-wide portal system solution. The PostNuke framework runs on a typical LAMP[3]-Environment. We use Solaris (http://www.sun.com/software/solaris/) as operating system, an Apache Webserver with a MySQL database and PHP as web scripting language. This configuration provides flexibility and basic functionality for specific functions, such as e.g. user management. Another standard component is the CMS in PostNuke for managing news postings or article editing and the storage and handling of such accessible documents as e.g. descriptions of product types, project related information or documentations and publications of the portal. The PostNuke Application Program Interface (API) provides the possibility for the implementation of encapsulating functionality into ISDC-specific plug-ins. There are four big areas:

- Data product retrieval
- User account management
- User collaboration
- System monitoring

The use of an application-wide theme for a standardized layout for all components makes it easy to separate the data model from the portal GUI.

4.2 Data Flow

As already mentioned, there is a main database interface between user portal and backend services. This design decision was done because of evolutional-based development reasons, which result in both, positive and negative aspects. The main system limit is the time delay between the ingestion and the provision of data. Every backend process runs as operating system cronjob in time intervals between 1 and 15 min. Some jobs (e.g. aggregation of statistics) even only run on a daily or weekly basis. The advantage of that asynchronous process handling approach is the work independence or loose coupling of system modules. If a new file is imported, delivered or archived, not all systems have to work synchronal or on-request, which avoids mutual process blocking within and between system modules and components. For example, data providers often upload their files just from time to time into appropriate FTP-directories, but the services for the import of data run independently and periodically and process these files sequentially. Therefore performance

[3]Linux/Unix + Apache + MySQL + PHP.

issues can be controlled efficiently and transactions are safely. The FTP based services are a central aspect of data ingestion, data storage and data delivery. Users do not have direct access to the data, instead of the system sends a qualified user requests to the archive system in order to transfer the requested files to the appropriate user FTP-directories, where the files are cached for the download. This approach is used because of security reasons and the necessity for the system to operate with different archive systems at the same time. Background processes collect the data files from these different services and transfer them to the user directories. The user is notified when the transfer process was completed and the files are ready for download.

4.3 Interfaces

Internally all inter-system communication is controlled by database transactions. All functional needs are covered by this approach. As an example, here is the workflow of the user registration process:

- new user registers at the portal website
- user data is saved to the database
- a cronjob checks newly registered users
- new users are added to the FTP user accounts and appropriate user home directories are created
- system clears specific portal area for input of required data for system usage
- users now choose projects and interests and define favorite product types
- administrator checks users data in order to apply grants for certain internal product types (grants for public product types are assigned automatically).

Only a part of the presented work flow is human-centric. Lots of activities are done in an automatic mode. Only the triggering of some process and the approval tasks are realized be user interaction. The Graphical User Interface (GUI) of the ISDC homepage is presented in Fig. 7.

The portal frame of the GUI contains navigation and monitoring elements on the right and left side of the portal. The central area is used for the report of news, and after clicking a navigation link, for the display of appropriate content, such as information about projects and product types or tools for the retrieval and access to data products. In order to provide a project-centric access to data and information every project has its own homepage within the portal framework, such as e.g. the CHAMP ISDC homepage (http://isdc.gfz-potsdam.de/champ) or the GRACE ISDC homepage (http://isdc.gfz-potsdam.de/grace).

The Data Product Browser, which can be seen as virtual FTP directory browser, shown in Fig. 8, is an excellent example for the realization of a user request driven interface for an easy access to the different data product files. The files are categorized into projects, such as e.g. CHAMP and GRACE, processing levels (1–4), the product types and temporal units (year, month, day). Also the visibility of product types and data products is granted according to the user access rights only, which

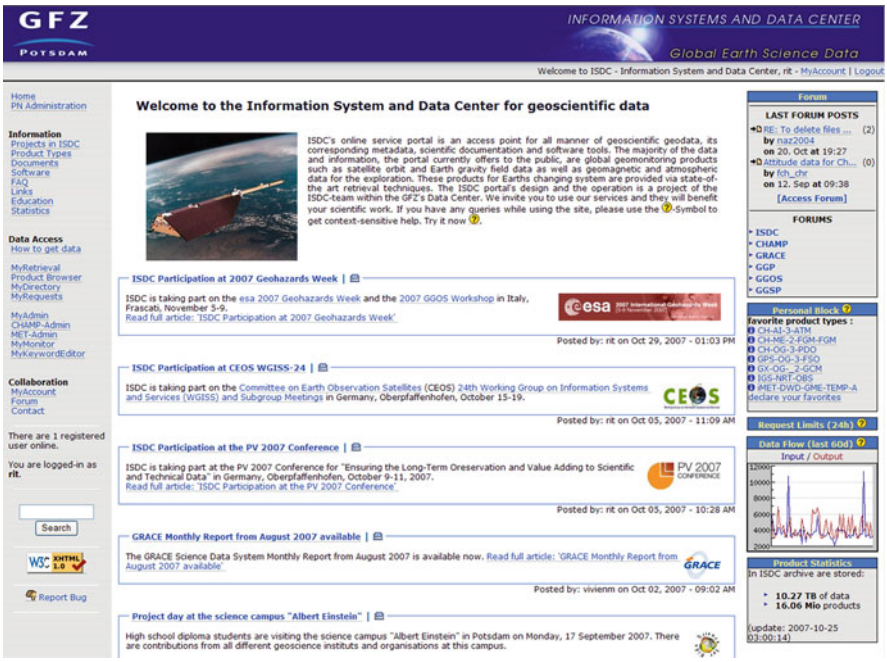

Fig. 7 Graphical user interface of the GFZ ISDC portal (ISDC portal homepage)

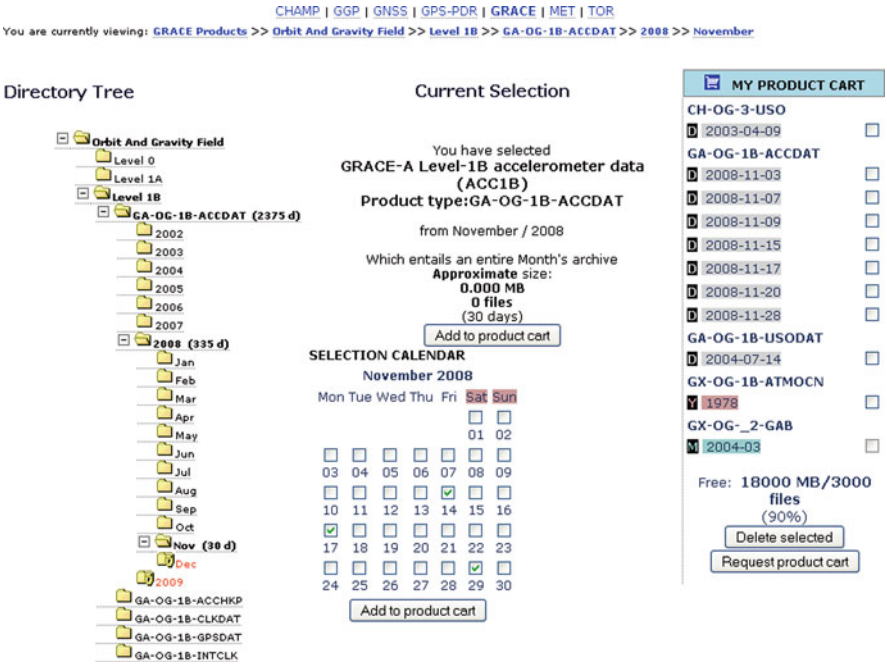

Fig. 8 Data product browser

was an essential data policy constraint. The calendar function of the Data Product Browser provides data products of a specific product type on a daily basis which are put into MY PRODUCT CART on user request. The user can repeat this action for different product types until the user-dependent limit (standard: 1,000 files, 1 giga byte per day) is reached. After clicking the "Request product card"-button, the required files are transferred to the user FTP directory.

5 Backend for Operational Services

As explained in Chap. 4 already, there are several cronjobs, which run on the different backend servers and zones (Fig. 9). There are data transfer processes, such as the data import or export, metadata extraction processes, and actions, which are necessary for data mining and aggregation purposes. Most of appropriate jobs are driven by database transactions. An example for a background aggregation process is the computation of user grant dependent time-line information for the creation of an occurrence chart, which displays the availability of data products in a certain period of time. This process is too complex for an on-the-fly computation.

5.1 Component Deployment

Whereas the former ISDC system components were installed on SUN Servers, Fibre Channel RAID Systems and the Solaris 9 Operating System in 2003, as described and illustrated at (Ritschel et al., 2006), the new ISDC portal is based

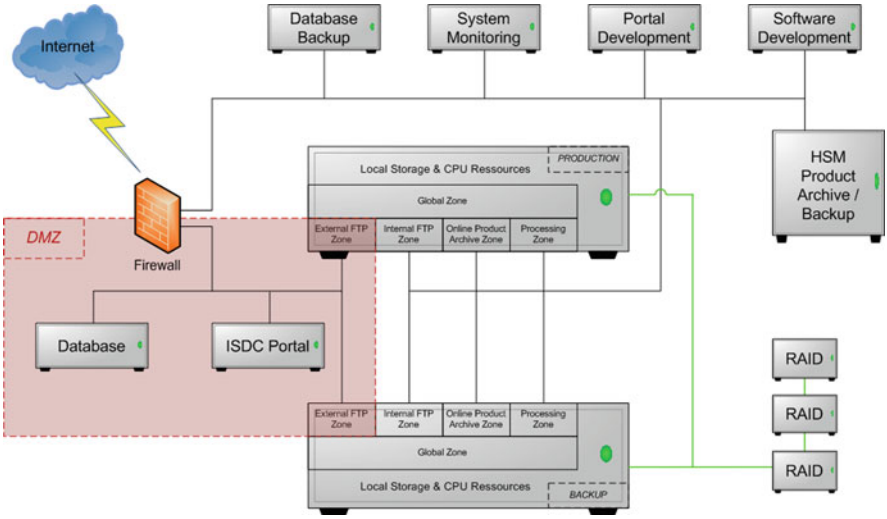

Fig. 9 Deployment diagram

on a new system architecture using innovate features of Solaris 10 operating system, such as a new virtualization technology (http://www.sun.com/software/solaris/virtualization.jsp) called Solaris Container and the Zettabyte File System (ZFS) (http://www.sun.com/software/solaris/data_management.jsp). Now it was possible to decrease the number of required workstation based servers, to reduce system administration tasks and to fulfill increasing requirements related to higher performance and system availability. A Solaris Container is the combination of resource control and partition technology provided by zones. Zones are lightweight Virtual Machines with an isolated process tree. That means active processes in a zone cannot affect processes outside in another zone. Each Zone is an isolated virtual server with an own node name, virtual network interface, and storage assigned to it. Zones do not require a dedicated CPU, storage or physical network interface. Any of these resources can be assigned specifically to one zone. (http://www.softpanorama.org/Solaris/Virtualization/zones.shtml) Solaris ZFS is a 128-bit file system and therefore memory management should not be a problem in the foreseeable future. The ZFS protects data from corruption, with integrated error detection and correction, and provides virtual unlimited scalability by using virtual storage pools. Another advantage is the snapshot feature for the preservation of the current state of the file system. File systems can be expanded by simply adding more drives. Building up virtual storage pools with integrated mirroring, Solaris ZFS RAIDZ or Solaris ZFS RAIDZ2 mechanisms increase redundancy and availability. Solaris Container technology provides the advantage of storage sharing via different Zones. Because of security constrains, network connections between hosts in the demilitarized zone (DMZ) are not allowed at the Helmholtz Centre Potsdam German Research Centre for Geosciences (GFZ). Using Zones, former four separate operating workstations could be integrated on one new workstation (PRODUCTION), each deployed into a single zone, as shown in Fig. 9. One of these zones, the external FTP-server has an own network interface into the DMZ, the other three zones using network interfaces into the LAN. Now the disc storage based on ZSF can be shared with different zones. A part of the storage is used for the internal and external FTP-server. The same storage is used simultaneously at the processing zone and the Online Product Archive (OPA). Another part of the storage is mapped only into the OPA, invisibly by all other zones. This prevents FTP users for the compromise of the data archive. A second machine, called BACKUP is setup with the same configuration as the PRODUCTIVE machine and is used as production host in case of hardware failures.

6 Outlook

The step-by-step implementation of the ISDC ontology metadata concept is important for the realization of a semantic-driven information system (Daconta et al., 2003) for the multi-domain retrieval of geosciences data, information and knowledge. The planned integration of Web 2.0 technologies and the

implementation of appropriate user interfaces are necessary for user feedback and communication processes in order to ingest the often uninvested knowledge of the user community. A new release of the ISDC portal will be based on JAVA technology and will provide new user interfaces as well as standardized interfaces and services to other information systems, such as e.g. GCMD and GEOSS.

References

Daconta MC, Oberst JO, Smith TK, Fensel D (2003) The Semantic Web: A Guide to the Future of XML, Web Services, and Knowledge Management: A Guide to the Future of XML, Web Services and Knowledge Management, Wiley & Sons; Auflage, p. 1

Gantz JF, et al. (2008) An Updated Forecast of Worldwide Information Growth Through 2011, IDC White Paper

Klump J, Allison L, Asch K, Fox P, Gundersen L, Jackson I , Loewe P, Snyder WS, Ritschel B (2008) Enabling global collaboration in the geosciences. EOS Trans. AGU 89(49), doi:10.1029/2008EO490007.

Lyopn L (2007) Dealing with Data: Roles, Rights, Responsibilities and Relationships Consultancy Report, UKOLN, University of Bath, p. 48, Retrieved January 2009 from http://www.ukoln.ac.uk/ukoln/staff/e.j.lyon/reports/dealing_with_data_report-final.pdf

Mende V, Ritschel B, Freiberg S, Palm H, Gericke L (2008) Geoinformatics 2008—Data to Knowledge, Proceedings: U.S. Geological Survey Scientific Investigations Report 2008-5172, p. 76, Retrieved January 2009 from http://pubs.usgs.gov/sir/2008/5172/. Directory Interchange Format (DIF) Metadata and Handling at the German Research Center for Geosciences' Information System and Data Center, pp. 43–46, edited by Brady, S.R., Sinha, A.K., and Gundersen, L.C.

Pfeiffer S (2008) Verknüpfung von geowissenschaftlichen ISDC-Produkten mit Semantic-Web-Techniken zur Erschließung inhaltlicher Zusammenhänge, Retrieved February 2009 from http://digibib.hs-nb.de/metadata/dbhsnb_thesis_0000000037

Ritschel B, Bendig A, Palm H, Kopischke R, Freiberg S, Flechnter F, Meyer U (2006) Observation of the Earth System from Space, p. 494, Design and Operation of the GRACE ISDC, pp. 71–82, edited by Flury, J., Rummel, R., Reigber, Ch., Rothacher, M., Boedecker, G., Schreiber, U.

Ritschel B, Bruhns Ch, Freiberg S, Gericke L, Kopischke R, Mende V (2007a). ISDC Services: Data Management, Catalog Interoperability and International Cooperation, Geotechnologien Science Report No. 11, München, 22–23 November 2007, Koordinierungsbüro Geotechnologien; Potsdam, S.18–S.22.

Ritschel B, Bruhns Ch, Kopischke R, Mende V, Palm H, Freiberg S, Gericke L (2007b). The ISDC Concept for Long-Term Sustainability of Geoscience Data and Information, PV 2007 – Ensuring the Long-Term Preservation and Value Adding to Scientific and Technical Data, Conference Proceedings, German Aerospace Center (DLR), A Member of the Helmholtz Association, 9–11 October 2007, S.1–S.8.

Ritschel B, Mende V, Palm H, Gericke. L, Freiberg S, Kopischke R, Bruhns Ch (2008) Geoinformatics 2008—Data to Knowledge, Proceedings: U.S. Geological Survey Scientific Investigations Report 2008-5172, p. 76, Retrieved January 2009 from http://pubs.usgs.gov/sir/2008/5172/. The German Research Center for Geosicences' Information System and Data Center – Portal to Geoscientific Data, pp. 33–35, edited by Brady, S.R., Sinha, A.K., and Gundersen, L.C.

Improvements for the CHAMP and GRACE Observation Model

Grzegorz Michalak and Rolf König

1 Introduction

Highly precise GPS orbits and clock estimates are the basis for many navigation applications and for this reason special attention for the proper modelling of many small dynamical and geometrical effects is required. In this chapter we present initial results of recent improvements in modelling of GPS-based orbits in GFZ's Precise Orbit Determination (POD) software system called EPOS (Earth Parameter and Orbit System). In particular, this concerns the so-called GPS carrier phase wind-up and the attitude model for GPS satellites. Phase windup is an effect of the relative orientation between the sending and transmitting antennas on the observed phase measurements. If neglected, phase windup causes range errors in the phase observations at the decimetre level (Wu et al., 1993). The GPS attitude model defines the nominal attitude of the GPS satellites as well as their attitude behaviour during shadow crossing or orbit noon/midnight periods. An accurate attitude model is the pre-requisite for the precise computation of the phase wind-up correction. Additionally, since the antennas on the Block IIA satellites have an offset of 27 cm in X-direction, the correct attitude allows to properly relate the measurements to the centre of mass of the satellite. The GPS attitude model as presented in this chapter is based on the model developed by Bar-Sever (1996).

2 GPS Carrier Phase Wind-Up

2.1 General

The relative orientation between the sending and the receiving GPS antennas influences the observed carrier phase measurements; the change of the phase due to this orientation is called phase wind-up (Wu et al., 1993). The relative orientation

G. Michalak (✉)
Helmholtz Centre Potsdam, GFZ German Research Centre for Geosciences,
Department 1: Geodesy and Remote Sensing, Telegrafenberg, 14473 Potsdam, Germany
e-mail: michalak@gfz-potsdam.de

F. Flechtner et al. (eds.), *System Earth via Geodetic-Geophysical Space Techniques*,
Advanced Technologies in Earth Sciences, DOI 10.1007/978-3-642-10228-8_3,

between the GPS satellites and the receiving antennas near the Earth surface or onboard Low Earth Orbiting satellites (LEOs) undergoes continuous changes. The phase range increases or decreases depending on the direction of the relative rotation. One full rotation translates into one cycle phase change. The GPS satellites perform a continuous attitude yaw rotation in order to keep the solar panels perpendicular to the direction to the Sun. In addition, the orbital motion of the GPS satellites and the motion of the receivers (for ground stations due to Earth rotation, for space-borne receivers due to LEO satellite dynamics) change the sending-receiving geometry which is sensed by the receiver also as a relative rotation. Neglecting the phase wind-up causes significant differences in GPS clock solutions. It influences also the orbits, in particular when integer ambiguity fixing is applied.

The phase wind-up correction (in units of degrees), according to (Wu et al., 1993), is given by:

$$\Delta\phi = \mathrm{SIGN}(\zeta) \cdot \arccos\left(\frac{\vec{D}_T \cdot \vec{D}_R}{|\vec{D}_T||\vec{D}_R|}\right) \tag{1}$$

where $\vec{D}_T$ and $\vec{D}_R$ are effective dipole vectors for the transmitter and the receiver respectively, ζ is the angle between the satellite-station vector $\vec{T}_R$ and the vector perpendicular to the plane of the two effective dipoles:

$$\zeta = \vec{T}_R \cdot (\vec{D}_T \times \vec{D}_R) \tag{2}$$

$$\vec{D}_R = \vec{X}_R - \vec{T}_R \cdot (\vec{T}_R \cdot \vec{X}_R) + (\vec{T}_R \times \vec{Y}_R) \tag{3}$$

$$\vec{D}_T = \vec{X}_T - \vec{T}_R \cdot (\vec{T}_R \cdot \vec{X}_T) - (\vec{T}_R \times \vec{Y}_T) \tag{4}$$

where $\vec{X}_T$, $\vec{Y}_T$, $\vec{X}_R$ and $\vec{Y}_R$ are unit vectors in the direction of two dipole elements of transmitter and receiver. For a ground station the local right hand system consists of the triad North-West-Up, so $\vec{X}_R$ = North, $\vec{Y}_R$ = West. For LEO satellites, the antenna local system is composed of the azimuth origin vector ($\vec{X}_R$), antenna boresight vector ($\vec{Z}_R$) and third axis ($\vec{Y}_R$) completing the right hand system. In most cases the LEO local antenna system is close to orbital transversal-normal-radial system, the deviation from this system is given by satellite attitude. For GPS satellite antenna the $\vec{X}_T$ and $\vec{Y}_T$ match the satellite body fixed system unit vectors X and Y. For the GPS Block II/IIA satellites the Z axis points to the Earth center, Y is in the solar panel beam direction and X is towards the Sun direction completing the right hand system. For the Block IIR satellites the sense of the X and Y axis is reversed by 180°. All vectors must be transformed into a common reference frame.

A positive rotation of the transmitter (right hand screw) around the receiving antenna boresight vector +Z increases the phase range. In order to correct for this, the wind-up correction $\Delta\phi$ (converted to cycles), which is also positive in this case, has to be subtracted from the phase measurements. The $\Delta\phi$ given by Eq. (1) is in the range (–180, +180) degrees; to assure continuity the integer number of full

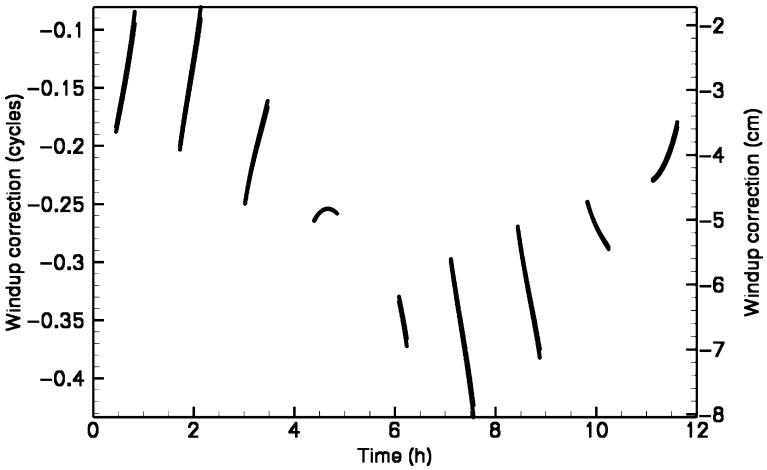

Fig. 1 Typical CHAMP windup corrections to L1 phase observations of PRN 18 on April 02, 2008

rotations is added in case of transition of $\Delta\phi$ between +180° and –180° within the observation time window.

For the proper computation of the wind-up correction, the accuracies of GPS and LEO orbits are not needed to be very high. A test computation shows, that for elevations above 0° an orbit error of 100 km produces differences of the wind-up corrections in the order of ∼0.6°, what is less then the 1° of the GPS attitude error due to mispointing of the satellite (Bar-Sever, 1996). An example of wind-up corrections between PRN18 and CHAMP on April 02, 2008, is given in Fig. 1.

2.2 Carrier Phase Wind-Up Validation

The influence of the application of the carrier phase wind-up correction was tested for both, GPS and LEO orbits. The parameterization of the orbits is the same as for the so-called Rapid Science Orbits (RSOs, see chapter "Rapid Science Orbits for CHAMP and GRACE Radio Occultation Data Analysis" by Michalak and König, 2010, this issue). For the GPS orbits, when no integer ambiguity fixing is applied, an improvement of the orbit accuracy was not found in comparison to IGS orbits. The orbit improvement becomes clearly visible when integer ambiguity fixing is applied. The integer ambiguity fixing is applied here by estimating floating L3 ambiguities and imposing side constraints on the double-difference integer ambiguities (Ge et al., 2005). In Table 1 the results of the tests for four GPS 1-day long arcs in January 2009 are presented. The orbits are estimated by applying the ambiguity fixing both with and without phase wind-up and compared to IGS Rapid Orbits (IGR). The values in the table are the RMS values of 3-D position differences before and after an applied Helmert transformation. In the last

Table 1 Comparison of the GPS orbits to IGR orbits without and with phase wind-up corrections. The RMS of the 3-D position differences are given before/after a Helmert transformation. In the last column the windup was computed assuming the satellite Block IIR body fixed axes to be the same as for Block IIA (+X towards the Sun)

GPS Orbits (yy/mm/dd)	Without wind-up (cm)	With wind-up (cm)	Axes IIR = IIA (cm)
09/01/28	7.2/6.2	5.8/5.7	6.3/5.7
09/01/29	7.6/6.9	6.6/6.2	6.6/6.2
09/01/30	8.7/7.1	6.6/5.8	6.6/5.7
09/01/31	7.8/6.8	6.9/6.5	6.9/6.5
Mean	7.8/6.8	6.5/6.1	6.6/6.0

column the phase wind-up correction is computed for the case when the X and Y axes of the satellite body fixed system of Block IIR and IIA satellites are chosen to be the identical (as practiced by some IGS analysis centers, for example CODE) instead of being reversed (according to the Block IIR definition) to see the influence of such a convention. It is obviously from Table 1 that the mean improvement due to the application of the phase wind-up correction is quite significant (1.3 cm without Helmert transformation). There is almost no influence of changing the axes convention for block IIR satellites on the orbits. A closer analysis of one of the orbits showed that the half cycle bias (180°) resulting from the Block IIR axes reversal is absorbed by the estimated floating ambiguities, the orbits, clock values and other parameters remained almost unchanged. Just a small degradation of 0.1% of the standard deviations of the parameters was observed in this case.

For testing of the influence of the phase wind-up corrections on LEO orbits, a one week period (July 15–21, 2008) was selected. The GPS RSO-type orbits (1-d arcs), without application of integer ambiguity fixing, are estimated with and without wind-up correction. The resulting GPS orbits and clocks are next used as fixed for 1-d long LEO RSO-type orbits (two-step method), estimated with and without

Table 2 Statistics of orbital fits for CHAMP. GRACE-A and TerraSAR-X RSO-type orbits obtained with and without applying the phase wind-up correction. For this test, seven orbits of 1-d arc length were used in the period April 15–21, 2008

	Code RMS (cm)	Phase RMS (cm)	SLR RMS (cm)
Without wind-up			
CHAMP	61.84	0.980	4.85
GRACE-A	118.23	1.286	4.09
TerraSAR-X	63.93	0.940	3.85
With wind-up			
CHAMP	61.70	0.953	4.62
GRACE-A	117.95	1.245	3.68
TerraSAR-X	63.83	0.930	3.66

wind-up correction. Although the application of the wind-up correction for GPS orbits without integer ambiguity fixing shows no effect as mentioned above, for LEO satellites there is a noticeable impact. The results for CHAMP, GRACE-A and TerraSAR-X orbits (code, phase and SLR RMS values) are summarized in Table 2. It can be seen that the application of the phase wind-up correction improves the overall fit to code and phase data. The average SLR RMS, used for external validation, improves also by about 3 mm.

3 GPS Attitude Model

The description of the GPS attitude model is given in details in Bar-Sever (1996) or Kouba (2008). Below, for the purpose of clearness, we summarize shortly the attitude regimes and formulas used.

Geometric (Nominal) Yaw Regime: Normally the GPS satellites keep their nominal attitude which is defined by the condition, that the Y-axis (along solar panels) must always be perpendicular to the Sun direction, the Z-axis points always towards the Earth centre and the X-axis points either towards the Sun (in case of the Block II and IIA satellites) or into the opposite direction (Block IIR). These conditions force the satellites to rotate continuously around its Z-axis, producing a changing yaw angle which is defined as the angle between the orbit transversal vector and the X-axis of the satellite. The yaw angle defined this way can be called geometric yaw angle, sometimes it is called nominal yaw angle when neglecting the so-called *B*-yaw bias (see below).

Noon/Midnight Turn Regime: When the elevation of the Sun over the orbital plane (the "Sun β angle") is small, the maintenance of the nominal (geometric) yaw model would require a very fast rotation (even becoming infinitely large if β becomes zero) around the orbit noon and midnight points respectively. A hardware limit restricts the rotation in such a way, that the actual yaw angle always lags the nominal yaw angle. This attitude behaviour is called noon/midnight turn. It starts when the nominal yaw rate exceeds the maximum rate allowed and ends when the satellite resumes the nominal attitude. The noon turn is performed by all satellites, the midnight turn by satellites of Block IIR only. The satellites of Block II/IIA perform shadow turns instead of midnight turns.

Shadow Crossing Regime: A further attitude regime is when a satellite enters the Earth's shadow. The signal from the satellite's Sun sensor is no longer available to determine the nominal attitude. The satellite starts to rotate in one direction, first with maximum rotation acceleration and next with maximum rotation rate. This attitude behaviour is called shadow turn. This turn is performed by satellites of Block II/IIA only. The IIR satellites perform midnight turns in the shadow as if they saw the Sun. To make the direction of the rotation in the shadow determinable, a constant hardware yaw bias (typically +0.5°) is imposed on the Sun sensor of the Block II/IIA satellites. Outside the shadow this has a side effect on the nominal yaw attitude, i.e. the actual yaw angle error due to this bias is larger than 0.5° and can reach more than 10° in extreme cases.

Post-shadow Manoeuvre: After emerging from the shadow, the satellite tries to recover the nominal attitude in the fastest possible way. This attitude regime is called post-shadow manoeuvre. In this regime the satellite can continue its rotation in the same direction as it was in shadow or it can reverse the rotation direction. Both actions intend to regain the nominal attitude. The decision is dependent on the difference between the actual yaw angle when exiting the shadow and the nominal yaw angle. The yaw angle when leaving the shadow is very uncertain as it depends on uncertain shadow entry and exit times and on uncertain maximum rotation rates. For this reason the modelling of the post-shadow manoeuvre is the most uncertain. A common approach for the data processing is to remove all observations up to 30 min after leaving the shadow. In the following we eliminate data only up to the estimated end time of the post-shadow manoeuvre and in the case of large deviations from some conditions (see below for more details).

3.1 Nominal Yaw Regime

Mostly the satellites remain in the nominal attitude regime. For the Block II/IIA satellites, the nominal yaw attitude is given by

$$\Psi_n = \arctan(-\tan\beta, \sin\mu) + B(b,\beta,\mu) \tag{5}$$

where β is the sun beta angle, μ is the "orbit angle" (the angle between the satellite position vector and the vector in the orbital plane that points furthest from then sun, i.e. orbit midnight), b is the hardware yaw bias (typically +0.5°). The first term in the Eq. (5) is the geometric yaw angle; the second one is the contribution of the hardware bias b to the yaw angle and will be given below. For Block IIR there is no hardware bias b and the +X axis is reversed in comparison to Block IIA, the nominal yaw attitude is therefore given by

$$\Psi_n = \arctan(tan\beta, -\sin\mu) \tag{6}$$

The nominal yaw rate is computed from formula

$$\dot{\Psi}_n = \dot{\mu}\tan\beta\cos\mu/(\sin^2\mu + \tan^2\beta) + \dot{B}(b,\beta,\mu) \tag{7}$$

The constant $\dot{\mu} = 0.00836°/s$. For Block IIR the yaw bias is $B = 0$. For Block II/IIA the yaw B bias and its rate is given by

$$B(b,\beta,\mu) = B(b,E) = \arcsin(0.0175b/\sin E) \tag{8}$$

$$\dot{B}(b,\beta,\mu) = -0.0175b\dot{\mu}\cos E\cos\beta\sin\mu/(\cos B\sin^3 E) \tag{9}$$

where E is the "Earth-Spacecraft-Sun" angle. The yaw error B is singular for E satisfying the condition $0.0175|b| < \sin(E)$. The $|b|$ should be taken here

because E>0 and the b bias can be negative, f.i. $b = -3.5°$ for PRN23 in the past (see http://ftp://sideshow.jpl.nasa.gov/pub/GPS_yaw_attitude/yaw_bias_table). It should be noted here, that the B-yaw bias is generally in the range 0.5–0.8° for large β angles. At the beginning of the noon turn, when β is close to zero, the bias can be as large as 7–8°, in extreme cases (f.i. PRN 29 on September 28, 2007, $\beta = 0.06$) the B-yaw bias reaches even 15–20° before starting noon turns. Neglecting this bias (like f.i. in Kouba, 2008) can lead to non-negligible differences in the yaw angle during the noon turn. The rate of the bias (Eq. 9) contributes additionally to the nominal yaw rate (Eq. 7) what has significant impact on the proper time of the beginning of the noon turn and finally for the actual yaw angle during the turn.

3.2 Noon/Midnight Turn Regime

The noon/midnight turn regime starts when the nominal yaw rate reaches the hardware threshold for the yaw rate. This happens around orbit noon, and for the satellites of Block IIR additionally at orbit midnight. The begin epoch t_s for the noon and midnight turn is obtained from the condition that the nominal yaw rate $\dot{\Psi}_n$ (Eq. 7) is equal to the maximum allowed hardware yaw rate R, e.g.

$$\dot{\Psi}_n(t) = R \tag{10}$$

To find this epoch, Eq. (10) is solved numerically. The hardware yaw rates R are satellite dependent (we use here the values estimated by JPL or specified by the satellite producers). For all epochs after the begin of the turn, the satellite rotates with constant maximum rotation rate R. The turn ends when the actual yaw approaches the nominal one. The duration of the turns depend on the values of R, which is satellite block dependent. For Block IIR R is 0.2°/s, the turn can last up to 15 min, for the other blocks for which R is in the range of 0.08–0.14°/s, the noon turn can last up to approximately 30 min. If the begin of the arc lies in the singularity region of E or is already within the turn regime where the condition (Eq. 10) is not fulfilled, the approximate begin of the turn t_s is search up to 45 min back in time. The β angle needed in Eq. (7) is assumed to be constant, the quantities μ and E are computed as

$$\mu_t = \mu_0 + \dot{\mu}(t - t_0) \tag{11}$$

$$E_t = \arccos(\cos\beta \cos\mu_t) \tag{12}$$

where t_0 and μ_0 are the current epoch and orbit angle for the current epoch. Once the start time of the manoeuvre is known, for all epochs $t > t_s$ the yaw angle is modeled as rotation with maximum yaw rate R in the same direction as at the beginning of the turn according to the formula:

$$\Psi(t) = \Psi_n(t_s) + \text{SIGN}(R, \dot{\Psi}_n(t_s)) \cdot (t - t_s) \tag{13}$$

The SIGN(x,y) is a Fortran function returning ABS(x)SGN(y).

3.3 Shadow Crossing Regime

The satellites undergo Earth's shadow crossing events when the Sun β angle is less then approximately 13.5°. It is commonly assumed, that a shadow crossing starts if the Earth-Spacecraft-Sun angle E reaches 13.5°. The start time t_s and end time t_e of the shadow turn is computed from the following analytical formulas (Kouba, 2008):

$$t_s = t + t_m - \sqrt{E_{Sh}^2 - \beta^2}/\dot{\mu} \tag{14}$$

$$t_e = t + t_m + \sqrt{E_{Sh}^2 - \beta^2}/\dot{\mu} \tag{15}$$

$$t_m = \pm\sqrt{E^2(t) - \beta^2}/\dot{\mu} \tag{16}$$

where t is the current epoch, t_m is the mid epoch of the shadow turn, it is positive (+) if the current epoch t is before the mid epoch, and negative (–) if t is after the mid epoch. $E_{Sh} = 13.5°$ and $E(t)$ are the Earth-Spacecraft-Sun angles at the shadow crossing and at the current epoch, respectively. Together with Eqs. (11) and (12) these analytical formulas allow the computation of the shadow crossing time and finally the correct yaw angle, even if the start of the arc is already within the shadow or post-shadow regime.

After the shadow entry, the satellite starts to spin-up with the yaw acceleration RR (yaw rate) to reach the maximum rotation rate R and then it rotates with this constant rate in the direction determined by the hardware b yaw bias until the shadow exit. The spin-up time t_1 is given by

$$t_1 = [\text{SIGN}(R,b) - \dot{\Psi}_n(t_s)]/\text{SIGN}(RR,b) \tag{17}$$

The yaw acceleration RR is assumed to be 0.00165°/s^2 for block IIA and 0.0018°/s^2 for block II. For $t_s < t \leq (t_s + t_1)$ the yaw angle in the shadow is given by:

$$\Psi(t) = \Psi_n(t_s) + \dot{\Psi}_n(t_s) \cdot (t - t_s) + 0.5 \cdot \text{SIGN}(RR,b) \cdot (t - t_s)^2 \tag{18}$$

and for $(t_s + t_1) < t < t_e$ by

$$\Psi(t) = \Psi_n(t_s) + \dot{\Psi}_n(t_s) \cdot t_1 + 0.5 \cdot \text{SIGN}(RR,b) \cdot t_1^2 + \text{SIGN}(R,b)(t - t_s - t_1) \tag{19}$$

3.4 Post-shadow Regime

After leaving the shadow, a GPS satellite tries to resume the nominal attitude as quickly as possible. Upon the shadow exit, the satellites attitude control system has two options to reach the nominal attitude. One is to continue the rotation in the same direction and with the same rotation rate. The second option is to reverse the yaw rate and to rotate with full rate until the nominal attitude is reached. In this model this decision is based on the difference D between the nominal and the actual yaw angle at the shadow exit time t_e:

$$D = \Psi_n(t_e) - \Psi(t_e) - \mathrm{NINT}\left(\frac{\Psi_n(t_e) - \Psi(t_e)}{360}\right) \cdot 360 \tag{20}$$

The difference D is in the range (–180, +180) degrees, the sign of the yaw rate during the post-shadow manoeuvre is dependent on the sign of D and will be SIGN(R,D). Given the yaw angle $\Psi(t_e)$ and the yaw rate SIGN(R,b) at the shadow exit, the spin-down time is given by:

$$t_1 = [\mathrm{SIGN}(R,D) - \mathrm{SIGN}(R,b)]/\mathrm{SIGN}(RR,D) \tag{21}$$

The t_1 is 0 if the sign of D is the same as the sign of the yaw bias b; there is no reversal of the yaw rate in such a case and the satellite continues its rotation in the same direction until the nominal yaw angle is reached. For $t < (t_e + t_1)$ the yaw angle is given by:

$$\Psi(t) = \Psi(t_e) + SIGN(R,b) \cdot (t - t_1) + 0.5 \cdot \mathrm{SIGN}(RR,D) \cdot (t - t_e)^2 \tag{22}$$

and for $t \geq (t_e + t_1)$:

$$\Psi(t) = \Psi_n(t_s) + \mathrm{SIGN}(R,b) \cdot t_1 + 0.5 \cdot \mathrm{SIGN}(RR,D) \cdot t_1^2 + \mathrm{SIGN}(R,D)(t - t_e - t_1) \tag{23}$$

The time of reaching the nominal yaw angle is computed just after the satellite leaves the shadow by finding the root of the equation $\Psi(t) = \Psi_n(t)$. The yaw angle during the post-shadow manoeuvre is largely uncertain because of yaw errors caused by the uncertain shadow entry, shadow exit time and maximum yaw rate during the shadow. For this reason most of the analysis centres eliminate all data up to 30 min after leaving the shadow.

To avoid unnecessary elimination of data, we have implemented three possible options for the post-shadow data elimination. The first option is the unconditional elimination of all data up to the computed end time of the post-shadow manoeuvre. The second option is the conditional elimination of data when $|D|$ differs less than 10° from 180°. In such a case, due to the actual yaw angle uncertainty, the model could reverse the rotation direction; therefore the probability of getting incorrect yaw angles is high. The third option is to accept all post-shadow data.

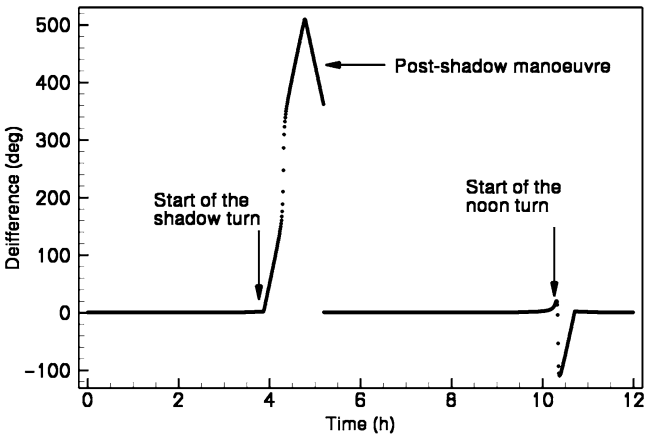

Fig. 2 Difference between the actual yaw angle (including modeling of shadow and noon turn) and the geometric one for PRN29 on September 28, 2007. During the post-shadow manoeuvre the satellite reversed the yaw rate and reached the nominal attitude which differs by 1 cycle from the geometric one. The maximum difference is larger then one full rotation of the satellite

As an example of the performance of the model, the difference between the modelled yaw angle (nominal + shadow turn + post-shadow manoeuvre + noon turn) and the geometric yaw (no B-yaw bias and turns) for the Block IIA satellite PRN 29 on September 28, 2007 ($\beta = \sim 0°$) is given in Fig. 2. It can be clearly seen that assuming the nominal (geometric) attitude in the processing can lead to yaw errors larger than one full rotation (360°) in the shadow and tens of degrees yaw angle errors during noon/midnight turns.

The here presented GPS attitude model is not yet fully validated. First tests are already performed and indicate orbit improvements on the level of centimeters for satellites performing the turns. For testing purposes the model was developed outside the operational software. For the final validation it is planned to integrate the model into the operational software.

4 Summary

GFZ is continuously working on improvements of its data processing systems to guarantee high accurate and reliable orbit products for a wide range of applications (radio occultations, baseline determination, gravity field estimation). In this chapter the details of the carrier phase wind-up correction and the GPS attitude model, as well as its implementation are given and initial validation results for both GPS and LEOs (CHAMP, GRACE and TerraSAR-X) are presented. It has been shown that the application of the phase wind-up corrections improves the GPS orbit accuracy by 1–2 cm (15–25%). The LEO orbit improvement measured by SLR is also significant and amounts to 3 mm (6%). It was also demonstrated, that reversing the

GPS Block IIR X-axis direction to match the convention for the Block II/IIA has no influence on the orbit and clocks in case when integer ambiguity fixing is applied. In that case half of the phase cycle differences is absorbed by the ambiguities. The correct application of the phase wind-up additionally requires the correct modelling of the GPS satellite attitude (in particular the yaw rotation), since this affects the orientation of the transmitter antenna. A test version of the attitude model including the modelling of midnight/noon, shadow and post-shadow turns is built and will be also implemented in the main data processing software at GFZ after further tests. It was shown that neglecting the attitude model and assuming an ideal geometric attitude as the nominal one can raise large yaw angle differences exceeding even one full rotation of the satellite. This can have non-negligible impact on the estimated orbits and clocks, which are intended to be used for high precision applications.

Acknowledgments We would like to thank IGS for providing GPS data, ILRS for providing SLR data and IERS for providing Earth Orientation Parameters. This study was carried out in the Geotechnologien programme under the grant of the German Federal Ministry of Education and Research.

References

Bar-Sever YE (1996) A new model for GPS yaw attitude. JoG 70, 714–723.

Ge M, Gendt G, Dick G, Zhang FP (2005) Improving carrier-phase ambiguity resolution in global GPS network solution. J. Geod., doi: 10.1007/s00190-005-0447–0.

Kouba J (2008) A simplified yaw-attitude model for eclipsing GPS satellites. GPS Solut., doi: 10.1007/s10291-008-0092-1.

Wu JT, Wu SC, Hajj GA, Bertiger WI, Lichten SM (1993) Effect of antenna orientation on GPS carier phase. Manuscripta Geodaetica 18, 91–98.

The Release 04 CHAMP and GRACE EIGEN Gravity Field Models

Frank Flechtner, Christoph Dahle, Karl Hans Neumayer, Rolf König, and Christoph Förste

1 Introduction

At the beginning of 2005 GFZ had produced a release 02 (RL02) time series of 17 monthly gravity field models for the period February 2003 until July 2004 and a corresponding static satellite-only gravity field model based on 376 days of GRACE mission data. These models were called EIGEN-GRACE03S and are complete to degree and order 120 and 150, respectively. Additionally, a high resolution static model up to degree and order 360 had been derived from combination of CHAMP, GRACE and terrestrial gravity data (EIGEN-CG03C, Förste et al., 2005). The evaluation of these static models showed that both models benefit in their long-to-medium wavelength part from an extended data base of GRACE, an improved processing of GRACE data as well as a meanwhile more complete and homogeneous compilation of surface data (Schmidt et al., 2006).

At about the same time the latest CHAMP-only model called EIGEN-CHAMP03S (Reigber et al., 2004) was derived from CHAMP GPS satellite-to-satellite and accelerometer data covering the period October 2000 through June 2003. EIGEN-CHAMP03S is the final version of the preliminary model EIGEN-CHAMP03Sp (Reigber et al., 2004) and resulted from a homogeneous reprocessing of all normal equations including an improved parameterization of the accelerometer calibration parameters. EIGEN-CHAMP03S is complete up to degree and order 120 plus selected terms for CHAMP sensitive and resonant orders up to degree 140. A regularisation was applied starting at degree 60. The processing standards were similar, but not identical to GRACE RL02. The monthly EIGEN-GRACE03S time series already allowed monitoring and quantifying present-day mass redistributions near the Earth surface which are related to mass changes in the continental water cycle, the oceans or ice melting in Greenland and Antarctica. The high-resolution combination model EIGEN-CG03C had been successfully applied

F. Flechtner (✉)
Helmholtz Centre Potsdam, GFZ German Research Centre for Geosciences,
Department 1: Geodesy and Remote Sensing, Telegrafenberg, 14473 Potsdam, Germany
e-mail: frank.flechtner@gfz-potsdam.de

F. Flechtner et al. (eds.), *System Earth via Geodetic-Geophysical Space Techniques*,
Advanced Technologies in Earth Sciences, DOI 10.1007/978-3-642-10228-8_4,

for various oceanic and geophysical applications including the determination of ocean surface topography as well as the interpretation of the Earth's interior and geodynamic processes in the Earth's mantle and lithosphere.

Although the GRACE RL02 gravity fields were already of unprecedented accuracy, the expected GRACE baseline mission accuracy, as simulated before launch (Kim, 2000) has not been reached by a factor of 12.5 (static field) and 25 (monthly solutions), respectively. Besides imperfect algorithms and methods applied in the gravity field determination process itself, also the processing strategy to derive calibrated instrument data from raw data, deficiencies in the background models such as the non-tidal atmosphere and ocean de-aliasing product or a wrong or insufficient parameterization of the K-band range-rate and accelerometer instrument data have been identified as potential reasons. To investigate these topics two projects have been initiated within the German ministry for education and research (BMBF) GEOTECHNOLOGIEN program "Observation System Earth from Space": "Improved GRACE Level-1 and Level-2 products and their validation by ocean bottom pressure" and "Better and faster CHAMP and GRACE gravity fields for the user community". Most of the findings of these two projects have been used to derive firstly an improved intermediate RL03 and further on, the present RL04 CHAMP and GRACE gravity models. The latest time-variable models are called EIGEN-GRACE05S (now available as monthly and weekly solutions) and EIGEN-CHAMP05S (monthly solutions). The corresponding static satellite-only and high-resolution combination fields are named EIGEN-5S and EIGEN-5C. In the following sections background information and improvements related to all these new RL04 models are described.

2 Monthly EIGEN-GRACE05S Time Series

As all precursor CHAMP and GRACE gravity field models, EIGEN-GRACE05S has been derived by the so called "dynamic approach". This method is based on the Newtonian formulation of the satellites' equation of motion in an inertial frame centered at the Earth's center of mass using a dedicated modeling of gravitational and non-conservative forces acting on the spacecraft. In order to solve the non-linear problem for the orbit determination and gravity recovery a numerical integration method is combined with an adjustment procedure. This allows for the determination of unknown orbital, instrumental, geometric, kinematic and dynamical parameters including the spherical harmonic coefficients of the gravity field from the observation data. These comprise the GPS high-low SST (satellite to satellite tracking), K-Band low-low SST, star camera and accelerometer instrument data. Starting from best-guess (e.g. from a previous release) initial values the gravity field parameters are estimated by minimizing the observational residuals according to the Gaussian least-squares principle. The critical issue is the elimination of non-gravitational systematic effects (e.g. caused by instrumental errors) in the observational residuals by means of an adequate parameterization which retains the systematic distortions in the residuals caused by the unknown gravity signal to

actually improve the initial values for the gravity field parameters. Further details are given in e.g. Reigber et al. (2005).

At the time of writing, the RL04 EIGEN-GRACE05S time series consists of 72 monthly gravity field models complete up to degree and order 120 covering the period between August 2002 and December 2008. The most important changes in the applied processing methods, standards and background models compared to RL02 EIGEN-GRACE03S are as follows (further details can be found in the corresponding RL02, RL03 and RL04 GRACE Level-2 Processing Standards Documents; Flechtner, 2005a, b, 2007a):

Arc Length: CHAMP and GRACE RL02 data were processed in batches of 36 h. As mentioned above, the optimum arc length within the dynamic approach is always a compromise between "short" to avoid the accumulation of data and modeling errors during numerical integration and "long" to retain resonant longer-period gravitational perturbations. Since the accelerometer data are treated as "true" non-gravitational forces in the observation equations, the accelerometer errors and noise are accumulated over time. Dedicated experiments for the intermediate RL03 time series EIGEN-GRACE04S have shown that the processing of daily batches gives slightly decreased observation residuals as well as slightly improved gravity fields.

GPS Data Processing: High-low GPS data are essential to observe the long-wavelength part of the gravity field and to geo-locate the GRACE K-band measurements. This is done in a two step approach: First the orbits and clock parameters of the GPS satellites are adjusted from ground-based GPS tracking data. Then, in the second step, the orbit determination and computation of observation equations of the LEO (Low Earth Orbiter) is performed with fixed GPS spacecraft positions and clocks derived from step one. The quality of this approach depends strongly on the correct modeling of the GPS ambiguities or the phase center corrections. The ambiguity fixing of the GPS spacecraft constellation could be much improved within RL03 by implementation of an integer ambiguity fixing algorithm to our EPOS (Earth Parameter and Orbit System) software. The comparisons of our orbits with those delivered by the IGS (International GNSS Service) for the period June 2002 to December 2004 show a significant improvement (see Fig. 1), as the orbit differences decrease from 4.1 to 2.6 cm (radial direction), from 6.8 to 5.0 cm (along-track direction) and from 7.0 to 4.2 cm (cross-track direction). The GPS ambiguities for the LEO satellites are still estimated as floating point numbers because the integer ambiguity fixing algorithm has not yet been implemented within the LEO subroutines of EPOS. This indicates further room for improvements. Azimuth/elevation-dependent phase center patterns, e.g. provided by JPL for GRACE, have been implemented for RL04 and led to slight improvements for the GPS residuals. As an example, for August 2003 the GPS code residuals of more than 1 million observations decreased from 36.3 to 35.7 cm and the phase residuals improved from 0.62 to 0.57 cm.

Static Background Gravity Field: The static background gravity field up to degree and order 150 has been changed from EIGEN-CG01C (Reigber et al., 2006) to EIGEN-CG03C (Förste et al., 2005) for RL03 and to EIGEN-GL04C for RL04. EIGEN-GL04C is an update of EIGEN-CG03C based e.g. on the RL03 EIGEN-GRACE04S satellite-only model (Förste et al., 2008a). In both cases the improved

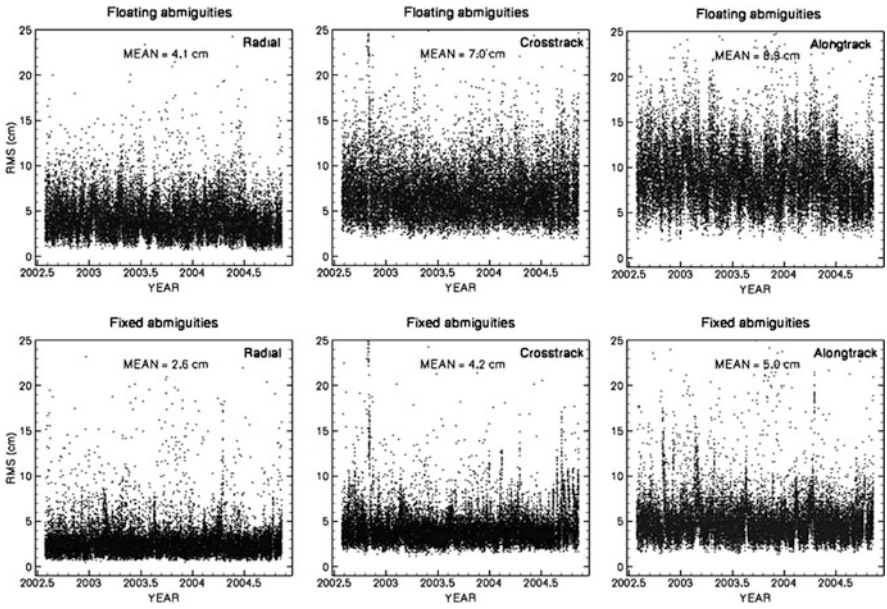

Fig. 1 Radial (*left*), along-track (*middle*) and cross-track (*right*) orbit differences w.r.t. IGS orbits in case of floating (*top*) and integer (*bottom*) fixed GPS ambiguities between June 2002 and December 2004

static background model gave slightly decreased omission errors ("the impact of an imperfect mean reference gravity model on the solution").

Secular Rates: The secular rates for low degree harmonics have been completed. While for RL02 and RL03 only the rates for C_{20}, C_{30} and C_{40} with respect to the reference epoch January 1, 1997 were a-priori reduced, the rates for C_{21} and S_{21} have been added and the reference epoch has been shifted to January 1, 2000. The values of the C_{20}, C_{21} and S_{21} rates are applied according to the IERS2003 conventions (McCarthy and Petit, 2003); the C_{30} and C_{40} rates are taken from to Cheng et al. (1997).

Ocean Tide Model: The FES2004 model (Lyard et al., 2006) is applied since RL02. For RL04 the K_2 tide has been corrected to the FES2000 model values as proposed in Lyard et al. (2006) and the non-linear tide M_4 has been added.

Non-tidal Mass Variations: Until RL02 the atmospheric and oceanic non-tidal mass variations have been calculated with the barotropic ocean model PPHA (developed by Pacanowski, Ponte, Hirose, and Ali; Hirose et al., 2001). But tests performed in 2004 (Flechtner et al., 2006) indicated that this model has certain deficiencies, e.g. the exclusion of the Arctic Ocean requires a pure inverse barometric response assumption of the sea surface north of 65° or a reduced energy when compared to in-situ ocean bottom pressure. As a consequence, since RL03 the baroclinic model OMCT (Ocean Model for Circulation and Tides, Thomas et al., 2001) with global (including the Arctic ocean) output is used. For the latest RL04 atmosphere and ocean de-aliasing level-1B product (AOD1B) OMCT is mass conserving, its

bathymetry is adjusted to the AOD1B land-ocean mask and it uses an updated thermodynamic sea ice model and a new data set for surface salinity relaxation. Further details on the OMCT model and the de-aliasing product can be found in Dobslaw and Thomas and Flechtner et al. (both in this issue).

Ocean Pole Tide Model: The model (Desai, 2002) describes the long-wavelength component of the geocentric pole tide deformations at the Chandler wobble period and is applied since RL03. A software bug in the implementation was corrected with RL04.

Relativity: The general relativistic contributions to the satellite accelerations are computed as specified in the IERS2003 conventions (McCarthy and Petit, 2003). For RL04 the Lense-Thirring and de Sitter effects have been added as proposed by IERS2003.

Reference Frame: For RL04 the IERS2003 nutation and precession model has been implemented and the numerical integration of the orbits and variational equations is now performed in the Conventional Inertial System (CIS). Until RL03 it was performed in the quasi-inertial True of Date System (TDS).

Statistical Constraints: GRACE experienced a 4d repeat cycle orbit between July and October 2004. The resulting sparse ground track pattern (Fig. 2) caused instabilities in the quality of the corresponding 4 monthly GRACE gravity field products. To overcome this problem, also constrained solutions (using a-priori information from the background gravity model EIGEN-GL04C) have been generated for this period. In December 2006 there was a GPS anomaly on GRACE-B causing a 4 day data gap between December 24 and December 27 which degraded the corresponding standard monthly field. Consequently, the same methodology as for 2004 has been applied. At higher degrees users will observe that all monthly coefficient values of the constrained solutions tend towards the coefficient values from the background mean field EIGEN-GL04C. The lower degree harmonics are variable from month to month, and still represent the monthly average mass variability. Also, the formal errors of these constrained solutions appear to be too optimistic. Therefore,

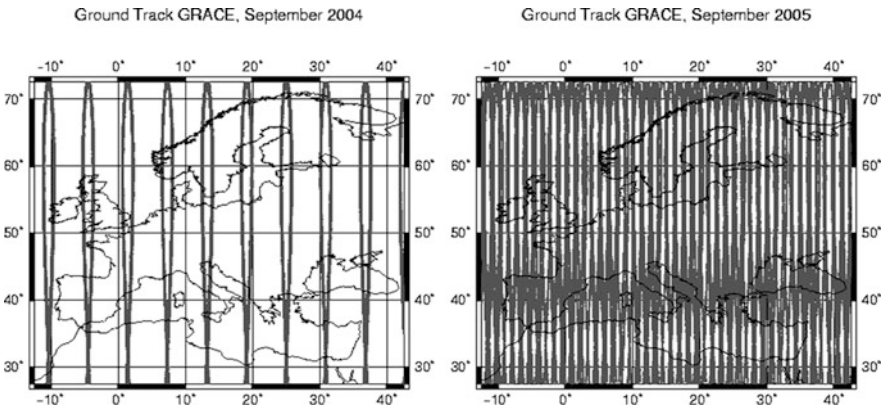

Fig. 2 GRACE ground track pattern over Europe for September 2004 (*left*) and September 2005 (*right*)

calibrated errors have not been derived and therefore identical as for the corresponding unconstrained products. Caution is advised for these reasons in the use of the 5 months in conjunction with the unconstrained solutions. For example, they should not be used in an equally weighted time-series analysis.

Figure 3 and Table 1 show the improvements of the calibrated errors of the static and monthly EIGEN gravity field time series from the very first model EIGEN-GRACE01S (RL00) to the recent solution EIGEN-GRACE05S (RL04).

It becomes obvious that (a) every new release results in an improved error level (decreased degree variances towards the pre-launch simulated GRACE baseline accuracy (Kim, 2000) and smaller accumulated errors) and (b) the relative improvements of RL04 mentioned above with respect to the precursor models RL03 and RL02 is relatively large (25 and 40% for the static field, 14.3 and 40% for the monthly solutions, respectively). Nevertheless, EIGEN-GRACE05S is still a factor of 7.5 (static field) and 15 (monthly solutions) above the baseline. Consequently, the current background models and processing standards should be further investigated and improved.

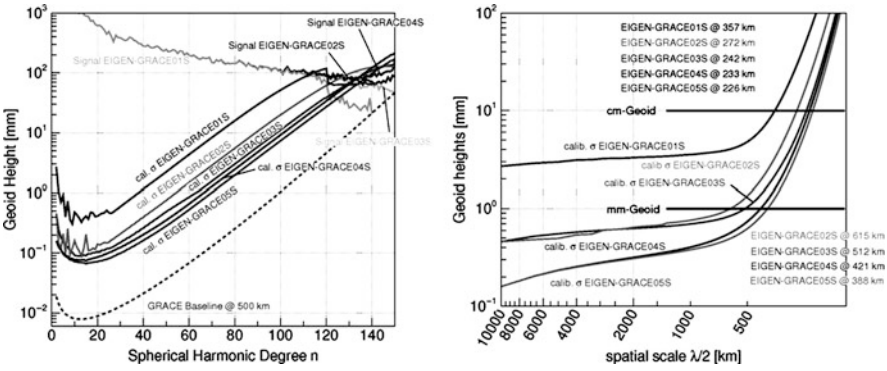

Fig. 3 Improvement of the static EIGEN gravity field time series in terms of degree variances (*left*) and accumulated errors (*right*) from the very first model EIGEN-GRACE01S (RL00) to the recent solution EIGEN-GRACE05S (RL04)

Table 1 Error level of the static and monthly GRACE-only EIGEN models in terms of "factor above the pre-launch simulated baseline error" and "improvement with respect to precursor solution in percent"

Model EIGEN-	Static field		Monthly fields	
	Factor (–)	Improvement (%)	Factor (–)	Improvement (%)
GRACE01S	∼50.0		No monthly fields processed	
GRACE02S	∼20.0	60.0	∼40.0	
GRACE03S	∼12.5	37.5	∼25.0	37.5
GRACE04S	∼10.0	20.0	∼17.5	30.0
GRACE05S	∼7.5	25.0	∼15.0	14.3

EIGEN-GRACE05S monthly models are available in the GRACE ISDC at GFZ (http://isdc.gfz-potsdam.de/grace) along with their calibrated errors and monthly mean non-tidal mass variation products (GAA-GAD; Flechtner, 2007b).

3 Weekly EIGEN-GRACE05S Time Series

Parallel to the monthly EIGEN-GRACE05S time series GFZ has processed weekly gravity field solutions in the framework of the German Research Foundation (DFG) Special Priority Program SPP1257 "Mass Transports and Mass Distribution in the Earth System" (Ilk et al., 2005) within the JIGOG project (surface mass redistribution from Joint Inversion of GPS site displacements, Ocean bottom pressure (OBP) models, and GRACE gravity models, Rietbroek et al., 2009).

These models have the highest temporal resolution compared to all other processing centres and will provide insight into mass variations which take place at ten-daily or even shorter time scales such as barotropic Rossby waves, continental water storage changes or solid Earth and ocean tides (Ilk et al., 2005). The models are aligned to the GPS calendar week and complete to degree and order 30. These maximum values are a result of a dedicated ground track analysis based on orbit configuration (see also Fig. 2) and GRACE instrument data availability. The RL04 weekly solutions have been derived from 7-day batches of daily GRACE normal equation systems using the same processing standards and background models as applied for the monthly solutions. No further constraints have been applied.

Time series of pure and pseudo-weekly (smoothed version from combination with two down-weighted preceding and succeeding weekly products) solutions have been compared to the corresponding results of the monthly RL04 GRACE gravity models (see Fig. 4). Although the pure weekly solutions show a larger variability,

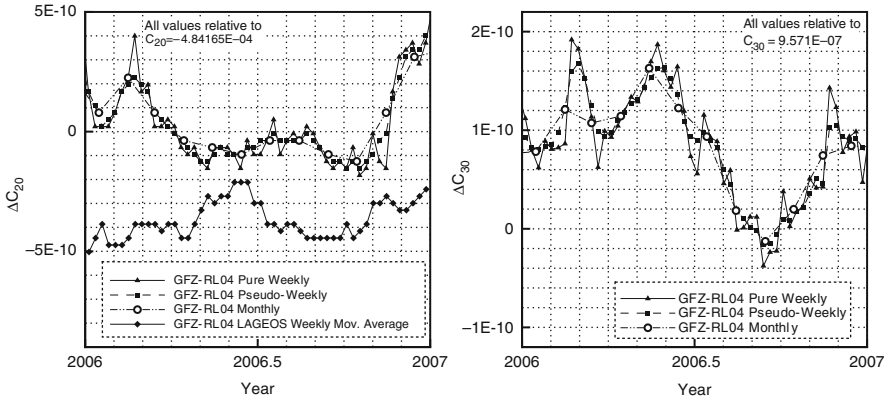

Fig. 4 C_{20} (*left*) and C_{30} (*right*) spherical harmonic coefficients of EIGEN-GRACE05S monthly and weekly gravity field products

they generally agree well with the monthly solutions. For some weeks, larger deviations ("outliers") are visible which do not necessarily correlate with the results of the ground track analysis. Therefore, it seems to be plausible that some of these outliers rather represent physically induced signal than noise. The well-known "GRACE C_{20} bias" e.g. when compared to the latest version of GFZ's RL04 LAGEOS time series is obvious and has still to be investigated.

Presently 306 pure weekly EIGEN-GRACE05S products for the period August 2002 till July 2008 are available. Only 7 weeks could not be derived due to sparse GRACE L1B data. These models are available in the GRACE ISDC at GFZ (http://isdc.gfz-potsdam.de/grace) along with their weekly mean non-tidal mass variation products (GAA-GAD; Flechtner, 2007b). The calibrated errors will be provided soon. Further information on the processing method and validation of the weekly products can be found in Schmidt et al. (2007) and Dahle et al. (2008).

4 Monthly EIGEN-CHAMP05S Time Series

All CHAMP data between October 2002 and September 2008 have been reprocessed using the EIGEN-GRACE05S background models, processing standards and strategy described above. While the pure GRACE monthly gravity field solutions can be estimated up to degree and order 120, the CHAMP monthly gravity fields - due to the missing low-low SST link – are limited to degree and order 60 and based on a moving average of three month of data. As for GRACE and in contrast to previous CHAMP solutions, no regularization is applied.

Figure 5 shows the correlation between the spherical harmonic coefficients of the EIGEN-GRACE05S and EIGEN-CHAMP05S time series up to degree and order 9. Figure 6 depicts selected results for the time series of four selected harmonics. The GRACE error bars are the calibrated errors while for CHAMP still the formal

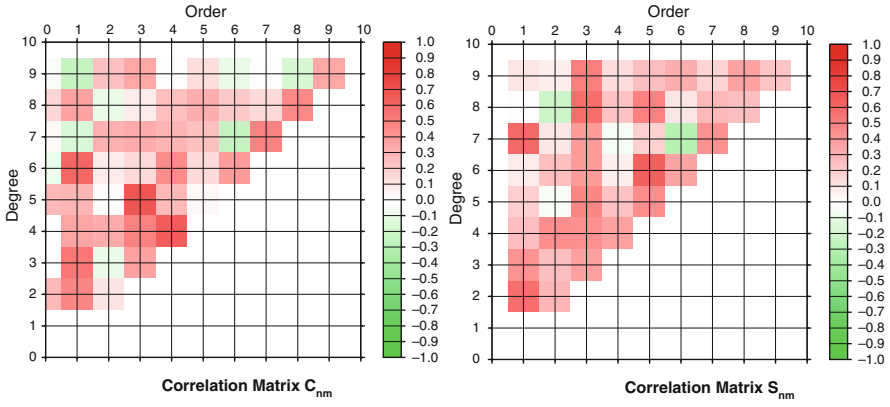

Fig. 5 Correlations between the spherical harmonic coefficients C_{nm} (*left*) and S_{nm} (*right*) of the EIGEN-GRACE05S and EIGEN-CHAMP05S time series up to degree and order 9

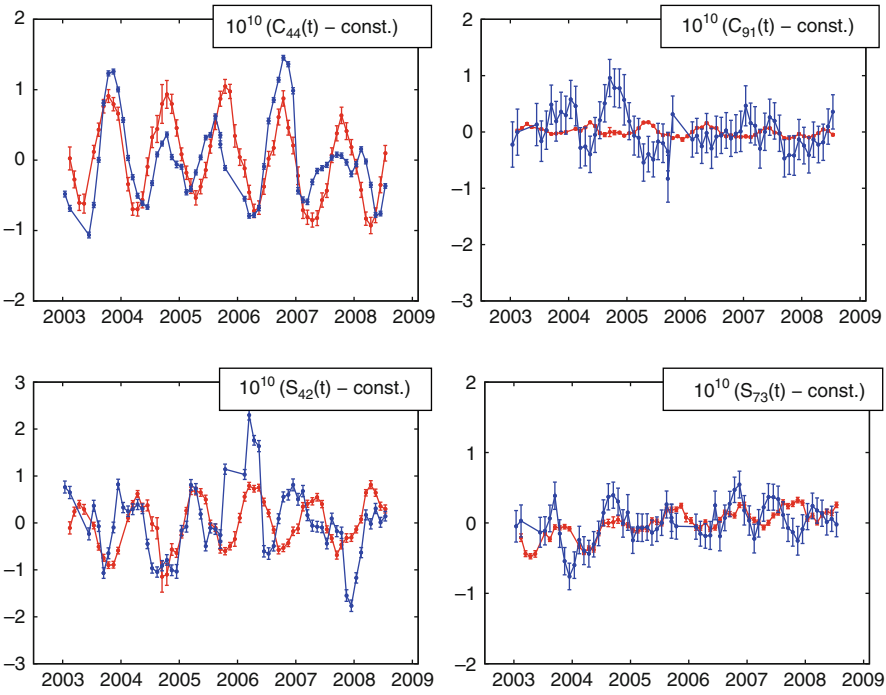

Fig. 6 Time series of spherical harmonic coefficients C_{44} (*top left*), C_{91} (*top right*), S_{42} (*bottom left*) and S_{73} (*bottom right*) from the EIGEN-GRACE05S and EIGEN-CHAMP05S monthly gravity fields

errors from the gravity field solution are given. It is obvious that the majority of the coefficients are highly correlated and the smaller the a-posteriori sigmas are for both GRACE and CHAMP the higher the correlations are.

The EIGEN-CHAMP05S monthly models are available at the CHAMP ISDC at GFZ (http://isdc.gfz-potsdam.de/champ). The still missing monthly models from the beginning and end of the mission, the corresponding mean field, calibrated errors and monthly mean non-tidal mass variation products (GAA-GAD; Flechtner, 2007b) will be provided soon.

5 Satellite-Only and Combined EIGEN-5S and EIGEN-5C Solutions

The combined gravity field model EIGEN-5C is an upgrade of EIGEN-GL04C (Förste et al., 2008a). The model represents a combination of GRACE and LAGEOS mission data plus $0.5° \times 0.5°$ gravimetric and altimetry surface data. The combination of the satellite and surface data has been done by the combination of normal equations, which are obtained from observation equations for the spherical harmonic coefficients.

The satellite data have been provided by GFZ (EIGEN-GRACE05S static field derived from monthly solutions between February 2003 and January 2007) and GRGS (Groupe de Recherches Geodesie Spatiale) Toulouse (static field derived from 10-daily GRACE solutions for the period August 2002 till January 2007 and 10-daily LAGEOS solutions for the period January 2002 till December 2006). The GRGS processing standards and background models are, with minor differences (e.g. the ocean model to correct short-term non-tidal mass variations is MOG2D; Carrère and Lyard, 2003), nearly identical to EIGEN-GRACE05S.

The used surface data are identical to EIGEN-GL04C except of new gravity anomaly data sets for Europe (H. Denker, IfE Hannover, 2007, personal communication), the Arctic Gravity Project gravity anomaly data (Forsberg and Kenyon, 2004) as updated in 2006 and newer Australian gravity anomalies (W. Featherstone, Curtin University of Technology, 2008, personal communication). As the precursor joint GFZ/GRGS combined gravity field models, EIGEN5-C is complete to degree and order 360 in terms of spherical harmonic coefficients which corresponds to a spatial resolution of 55 km on the Earth's surface. Also, a special band-limited normal equation combination method (Förste et al., 2008a) has been applied in order to preserve the high accuracy from the satellite data in the lower frequency band of the geopotential and to form a smooth transition to the high frequency information coming from the surface data.

Independent comparisons with geoid heights determined point-wise by GPS positioning and GPS levelling show notable improvements (Table 2). The results given in this table have been derived for GPS/leveling points of the USA (Milbert, 1998), Canada (M. Véronneau, Natural Resources Canada, 2003, personal communication), Germany (Ihde et al., 2002), Europe (Ihde, 2008, personal communication) and Australia (G. Johnston, Geoscience Australia and W. Featherstone, Curtin University of Technology, 2007, personal communication). For this comparison, height anomalies were calculated from the spherical harmonic coefficient data sets and reduced to geoid heights (c.f. Rapp, 1997). The topographic correction was done by using the DTM2006.0 model, which is available in spherical harmonic coefficients (Pavlis et al., 2007).

Also, the unrealistic meridional striping patterns over the oceans in the precursor EIGEN models could be much reduced (Fig. 7). Therefore, EIGEN-5C and its associated satellite-only model EIGEN-5S have been selected as standard for ESA's official data processing of the upcoming gradiometer satellite mission GOCE.

Table 2 Root mean square (rms) about mean of GPS-levelling minus gravity field model derived geoid heights (cm) (number of points in brackets)

Gravity Model	USA (6169)	Canada (1930)	Australia (201)	Europe (1234)	Germany (675)
EIGEN5C	34	25	24	30	15
EIGEN-GL04C	34	25	24	34	18
EIGEN-CG03C	35	31	26	36	20
EIGEN-CG01C	35	27	26	37	22

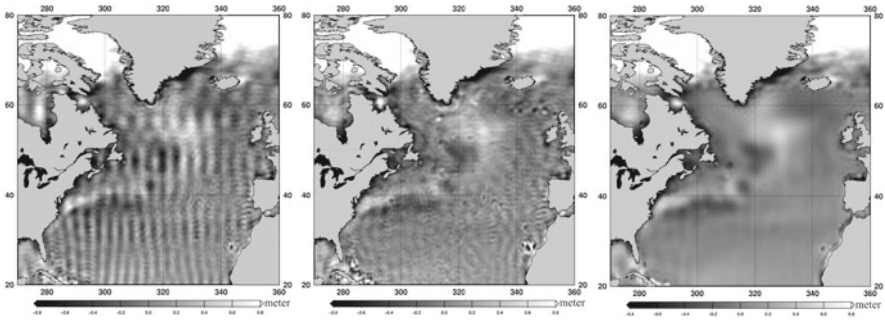

Fig. 7 North Atlantic geoid heights (scale ±0.8 m) of EIGEN-CG03C (*left*), EIGEN-GL04C (*middle*) and EIGEN5C (*right*) after subtraction of a surface gravity data based geoid

The EIGEN-5C as well as the EIGEN-5S spherical harmonic coefficients are available for download at the ICGEM (International Centre for Global Earth Models) data base at GFZ Potsdam (http://icgem.gfz-potsdam.de). Further details about these gravity field models as well as the coefficients can be found at http://www-app2.gfz-potsdam.de/pb1/op/grace/results and in Förste et al. (2009).

6 A New Mean, Static EIGEN-CHAMP05S Gravity Field Model and Its Evaluation

The reprocessed CHAMP data have been used to compute a new mean, static CHAMP-only gravity field model. This has been done by accumulating the mentioned monthly CHAMP normal equations from the time span between October 2002 and September 2008. The obtained mean EIGEN-CHAMP05S gravity field model is of a maximum degree/order 150. Before solving the accumulated normal equation system, the system has been stabilized by stochastic a-priori information for all spherical harmonic coefficients with a degree $l \geq 70$, because the gravitational signal fades out for these higher degree terms. The stabilization, following Kaula's degree variance model (Kaula, 1966), constraints the resulting coefficients towards a value of zero if there is no information at all in there observation data.

Figure 8 shows a global gravity anomaly plot of EIGEN-CHAMP05S in comparison with its precursor CHAMP-only model EIGEN-CHAMP03S. The resolution of the plotted grid is $1° \times 1°$. It can be seen from the comparison of these two plots, that the unrealistic meridional stripes in EIGEN-CHAMP03S are significantly reduced in the new EIGEN-CHAMP05S, in particular in the south pacific and south atlantic regions as marked by the red and blue circles. This enhanced quality of our new mean CHAMP-only model is assumed to be achieved by the mentioned application of the improved RL04 background modelling, processing standards and strategies.

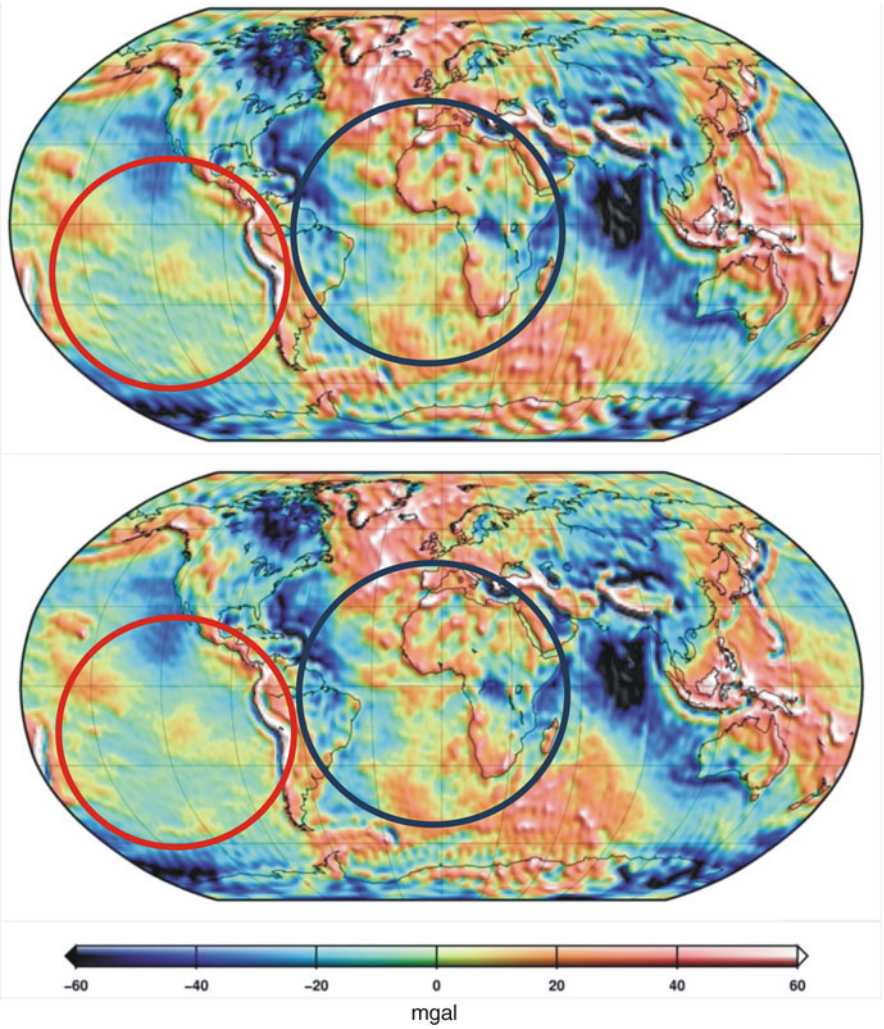

Fig. 8 Gravity anomaly plot (spatial resolution 1° × 1°) for the new mean EIGEN-CHAMP05S (*bottom*) in comparison with EIGEN-CHAMP03S (*top*). The *blue* and *red circles* mark regions, where the meridional stripes in EIGEN-CHAMP05S are obviously reduced w.r.t. EIGEN-CHAMP03S

One measure of the long-to-medium wavelength accuracy of a gravity field model is the fit of observations to the adjusted satellite orbit. Here we present satellite laser ranging (SLR) residuals for CHAMP and GRACE arcs after an orbit determination by using GPS-SST and accelerometer data (CHAMP and GRACE) and K-Band Range-Rate data (GRACE), where the SLR measurements were not included into the orbit adjustment. Table 3 gives the number of the included SLR observations and the measurement time periods:

Table 3 SLR data and test arcs of the orbit computation tests

Satellite	Number of included SLR observations/data period/tested arcs: number and lengths
CHAMP	358/October 2001/4 × 1.5 days
GRACE	592/September 2002/4 × 1.5 days

Table 4 SLR residuals (cm) after an orbit determination based on GPS-SST and accelerometer data (CHAMP, GRACE) and K-band range-rate data (GRACE). The SLR data were not included in the orbit adjustment

Satellite	Max. degree used	GGM03C	EGM2008	EIGEN-5C	EIGEN-CHAMP03S	EIGEN-CHAMP05S
CHAMP	80	9.51	9.34	9.69	10.77	9.40
	90	6.10	6.02	6.14	7.11	5.91
	100	5.96	5.97	6.03	6.36	5.59
	110	5.53	5.57	5.59	6.23	5.43
	120	5.45	5.51	5.51	6.28	5.31
	150	5.44	5.46	5.49	6.19	5.52
GRACE	80	6.54	7.27	6.44	11.54	6.92
	90	5.05	5.57	4.93	11.34	5.48
	100	5.20	5.54	5.09	11.03	5.42
	110	5.31	5.45	5.19	11.45	5.56
	120	5.28	5.46	5.15	11.51	5.48
	150	5.27	5.43	5.14	11.51	5.45

The orbit fits for CHAMP and GRACE were performed with the adjustment of one scaling factor and one bias parameter per arc for each of the three acceleration components in addition to the orbital elements, GPS ambiguities and clocks. Additionally for CHAMP one thruster parameter per arc and thruster pair and one scaling factor per component and arc for the Lorentz force on the accelerometer proof mass have been adjusted. In the case of GRACE one Range bias 1/rev per arc, range acceleration and range-rate bias per revolution were adjusted for the K-Band.

Table 4 gives the orbit fit residuals for the mean CHAMP models EIGEN-CHAMP03S (blue column) and EIGEN-CHAMP05S (red column) in comparison to the most recent global combined gravity field models GGM03C (Tapley et al., 2007), EGM2008 (Pavlis et al., 2008) and EIGEN-5C (Förste et al., 2008b). We carried out our orbit computations for these two satellites with different maximum degrees of the spherical harmonic coefficients to investigate possible degree-related differences between the tested gravity field models.

For both satellites the obtained orbit fit residuals for EIGEN-CHAMP05S are significantly smaller i.e. better than for EIGEN-CHAMP03S. In particular the obtained residuals of GRACE (∼11 cm for EIGEN-CHAMP03S vs. ∼5.5 cm for EIGEN-CHAMP05S above maximum used degree 80) are an impressive indication for the strong improvement of EIGEN-CHAMP05S vs. EIGEN-CHAMP03S. Furthermore

it is noticeable, that the obtained numbers for GRACE with the new EIGEN-CHAMP05S as well as with the GRACE-based combined models are of the same order of magnitude of about 5 cm. This finding indicates that our new CHAMP-only model features no major performance difference with the compared GRACE-based models for the investigated degree range up to 150 when using for LEO orbit computations. Lastly, EIGEN-CHAMP05S show no significantly different behaviour compared to the combined models, when inspecting the dependency of the orbit fits on the maximum used degree.

To investigate the error of the mean EIGEN-CHAMP05S model we compared the variability of partial solutions. For this purpose we computed two partial solutions, namely from the accumulation of the odd as well as of the even months for the included time span from October 2002 till September 2008. Figure 9 shows the difference degree amplitudes between these partial solutions (black line) in comparison with the formal errors of EIGEN-CHAMP05S (red line). The values of the difference degree amplitudes have been divided by 2 to take into account the double number of observation in the EIGEN-CHAMP05S models with respect to the partial solutions. When taking the variability of partial solutions as measure for the error of the obtained spherical harmonic coefficients, it is remarkable that the formal errors for EIGEN-CHAMP05S (red) till about degree 70 (wherefrom the regularization starts) are almost of the same order of magnitude as the computed variability

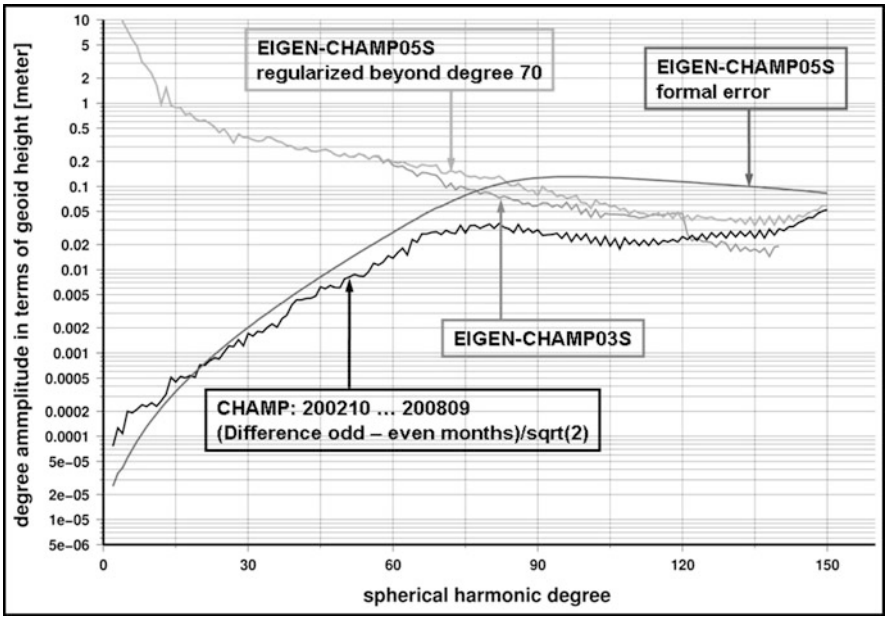

Fig. 9 Difference degree amplitudes between CHAMP partial solutions (i.e. the difference between the accumulated odd and evens months between October 2002 and September 2008) in comparison to the formal errors of EIGEN-CHAMP05S. Additionally the degree amplitudes for EIGEN-CHAMP05S and EIGEN-CHAMP03S are given

values. This indicates an optimum parameterization and a good internal consistency of our CHAMP gravity field processing.

Additionally the degree amplitudes of EIGEN-CHAMP05S and EIGEN-CHAMP03S are given in Fig. 9 for comparison. It can bee seen, that the spectrum of EIGEN-CHAMP05S contains more power beyond degree 60 compared to the older EIGEN-CHAMP03S. This should be mainly caused by the increased number of included measurement years (6 years for EIGEN-CHAMP05S vs. ∼3.5 years for EIGEN-CHAMP03S) and by an increased sensitivity due to the meanwhile decreased altitude of the CHAMP satellite (∼350 km end of 2008 vs. ∼400 km end of 2003, which was the end of the EIGEN-CHAMP03S measurement time span).

7 Summary and Conclusions

At GFZ release 04 (RL04) EIGEN (European Improved Gravity field of the Earth by New techniques) time series of monthly CHAMP and GRACE gravity models, pure weekly GRACE solutions and satellite-only and terrestrial data combined static gravity fields of the Earth have been derived by homogeneous reprocessing for nearly the whole CHAMP and GRACE mission periods. The updated background models, processing standards and strategies led to significant improvements of the reprocessed gravity field models. Both the monthly and static EIGEN-GRACE05S gravity fields could be improved by about 60% (in terms of "factor above the pre-launch simulated baseline error; Kim, 2000"). For the first time, GRACE gravity fields are provided with weekly resolution (up to degree and order 30 and aligned to GPS calendar week) which may provide further insight into mass variations which take place at ten-daily or even shorter time scales such as barotropic Rossby waves, continental water storage changes or solid Earth and ocean tides. The monthly EIGEN-CHAMP05S models show a high correlation to EIGEN-GRACE05S for the long-wavelength components. The new static satellite-only and combined gravity models EIGEN-5S and EIGEN-5C are complete to degree and order 150 and 360, respectively. Independent comparisons with geoid heights determined point-wise by GPS positioning and GPS levelling show notable improvements. Also, the unrealistic meridional striping patterns over the oceans in the precursor EIGEN models could be much reduced. Therefore, ESA has decided to use both models as the standard for ESA's official data processing of the upcoming gradiometer satellite mission GOCE.

In addition to the monthly EIGEN-CHAMP05S models a new 6-years mean CHAMP-model has been computed. In particular orbit adjustment tests with CHAMP and GRACE show a significant improvement of this model with respect to its precursor EIGEN-CHAMP03S.

These new RL04 EIGEN models provide an important data base to monitor mass transport and mass distribution phenomena in the system Earth, such as the continental hydrological cycle, ice mass loss in Antarctica and Greenland, ocean mass changes or the ocean surface topography. Nevertheless, the GRACE baseline mission accuracy has still not been reached by a factor of 7.5 (static field)

and 15 (monthly solutions), respectively. Therefore plans already exist for a further consistent reprocessing of the complete CHAMP and GRACE time series. This includes (a) refinements in the observation models, (b) improvements of the background models and (c) upgrade of the applied processing strategy and standards.

The first topic comprises the treatment of the accelerometer data after filtering, outlier removal and calibration as direct observations instead of measured surface forces. Additionally, the accelerometer data shall be improved by analysis of various satellite induced effects such as heater and magnet torquer spikes, twangs or penumbra-transitions. Finally, for GPS data processing the still missing integer ambiguity fixing for LEO satellites and phase wind-up and absolute phase center corrections for ground and LEO GPS observations will be implemented. The background models will be completed by seasonal variations derived from the RL04 time series as well as by improved tidal and non-tidal oceanic and atmospheric models. As the integrated one-step approach turned out to give more reliable and precise low degree harmonics (geocenter motion, Earth flattening) compared to the "standard" two-step approach (Zhu et al., 2004), also the processing strategy to derive GRACE gravity fields has still room for improvements.

RL04 EIGEN models along with their calibrated errors and ancillary products such as the corresponding mean atmospheric and oceanic non-tidal mass variations as well as supporting documentation are or will be shortly available at the CHAMP and GRACE Integrated System and Data Center (ISDC, http://isdc.gfz-potsdam.de) at GFZ. Additionally the models can be downloaded from the ICGEM (International Centre for Global Earth Models) data base at GFZ Potsdam (http://icgem.gfz-potsdam.de).

Acknowledgment This is publication no. GEOTECH-1276 of the programme GEOTECHNOLOGIEN of BMBF and DFG, grant 03F0436A.

References

Carrère L, Lyard F (2003) Modeling the barotropic response of the global ocean to atmospheric wind and pressure forcing – comparisons with observations. Geophys. Res. Lett. 30(6), 1275, doi:10.1029/2002GL016473.

Cheng MK, Shum CK, Tapley BD (1997) Determination of the long-term changes in earth's gravity field from satellite ranging observations. J. Geophys. Res. 102, B10.

Desai SD (2002) Observing the pole tide with satellite altimetry. J. Geophys. Res. 107, C11, doi:10.1029/2001JC001224.

Dahle Ch, Flechtner F, Kusche J, Rietbroek R (2008) GFZ EIGEN-GRACE05S (RL04) Weekly Gravity Field Time Series. Proceedings of the 2008 GRACE Science Team Meeting, San Francisco, CA, December 12/13 2008, http://www.csr.utexas.edu/grace/GSTM

Flechtner F (2005a) GFZ Level-2 Processing Standards Document for Product Release 0002. Rev. 1.0, GRACE project documentation, pp. 327–743.

Flechtner F (2005b) GFZ Level-2 Processing Standards Document for Product Release 0003. Rev. 1.1, GRACE project documentation, pp. 327–743.

Flechtner F, Schmidt R, Meyer U (2006) Dealiasing of short-term atmospheric and oceanic mass variations for GRACE. In: Flury J, Rummel R, Reigber Ch, Rothacher M, Boedecker G,

Schreiber U (eds.), Observation of the Earth System from Space, Springer, Berlin, pp. 83–97, ISBN 3-540-29520-8.

Flechtner F (2007a) GFZ Level-2 Processing Standards Document for Product Release 0004. Rev. 1.0, GRACE project documentation, pp. 327–743.

Flechtner F (2007b) AOD1B Product Description Document for Product Releases 01 to 04. Rev. 3.0, GRACE project documentation, pp. 327–750.

Förste C, Flechtner F, Schmidt R, Meyer U, Stubenvoll R, Barthelmes F, König R, Neumayer KH, Rothacher M, Reigber C, et al. (2005) A New High Resolution Global Gravity Field Model Derived from Combination of GRACE and CHAMP Mission and Altimetry/Gravimetry Surface Gravity Data. Poster presented at EGU General Assembly 2005, Vienna, Austria, 24–29, April 2005.

Förste C, Schmidt R, Stubenvoll R, Flechtner F, Meyer U, König R, Neumayer KH, Biancale R, Lemoine JM, Bruinsma S, et al. (2008a) The GeoForschungsZentrum Potsdam/Groupe de Recherche de Gèodésie Spatiale satellite-only and combined gravity field models: EIGEN-GL04S1 and EIGEN-GL04C. J. Geod. 82, 331–346, doi:10.1007/s00190-007-0183-8.

Förste C, Flechtner F, Schmidt R, Stubenvoll R, Rothacher M, Kusche J, Neumayer K.-H, Biancale R, Lemoine J.-M, Barthelmes F, et al. (2008b), EIGEN-GL05C – A new global combined high-resolution GRACE-based gravity field model of the GFZ-GRGS cooperation, General Assembly European Geosciences Union (Vienna, Austria, 2008). Geophysical Research Abstracts, Vol. 10, Abstract No. EGU2008-A-06944.

Förste Ch, Stubenvoll R, Barthelmes R, König R, Raimondo JC, Flechtner F, Kusche J, Dahle Ch, Biancale R, Lemoine JM, et al. (2009) Evaluation of EGM2008 by comparison with other recent global gravity field models. Newton's Bull. 4, accepted and in press, ISSN 1810–8555.

Forsberg R, Kenyon S (2004) Gravity and geoid in the Arctic region – The Northern gap now filled. Proceedings of the 2nd GOCE User Workshop, ESA SP-569, ESA Publication Division, Noordwijk, The Netherlands.

Hirose N, Fukumori I, Zlotnicki V, Ponte R (2001) High-frequency barotropic response to atmospheric disturbances: Sensitivity to forcing, topography, and friction. J. Geophys. Res. 106, 30987.

Ihde J, Adam J, Gurtner W, Harsson B. G, Sacher M, Schlüter W, Wöppelmann G (2002) The Height Solution of the European Vertical Reference Network (EUVN). Mitteilungen des BKG, Bd. 25, EUREF Publication No. 11/I, Frankfurt a. M, pp. 53–79.

Ilk KH, Flury J, Rummel R, Schwintzer P, Bosch W, Haas C, Schröter J, Stammer D, Zahel W, Miller H, et al. (2005) Mass Transport and Mass Distribution in the Earth System – Contribution of the New Generation of Satellite Gravity and Altimetry Missions to Geosciences, 2nd ed., Proposal for a German Priority Research Program, GOCE Project Office Germany, Technical University Munich, GeoForschungsZentrum, Potsdam.

Kaula W (1966) Theory of Satellite Geodesy. W. H. Freemann, San Francisco, CA, 1967, reprint by Dover Publications Inc., Mineola, New York, 2000, ISBN 0-486-41465–5.

Kim J (2000) Simulation Study of a Low-Low Satellite-to-Satellite Tracking Mission. Technical Report, University of Texas at Austin, Austin, TX.

Lyard F, Lefevre F, Letellier T, Francis O (2006) Modelling the global ocean tides: Modern insights from FES2004. J. Ocean Dyn. doi:10.1007/s10236-006-0086-x.

McCarthy D, Petit G (2003) IERS Conventions (2003). IERS Technical Note 32, Verlag des Bundesamts für Kartographie und Geodäsie, Frankfurt am Main, 2004, 127 pp, paperback, ISBN 3-89888-884-3.

Milbert D G (1998) Documentation for the GPS benchmark data set of 23-July-1998. IGeS Int. Geoid Serv. Bull. 8, 29–42.

Pavlis NK, Factor JK, Holmes SA (2007) Terrain-related gravimetric quantities computed for the next EGM. Proceedings of the 1st International Symposium of the International Gravity Field Service "Gravity field of the Earth" (Istanbul 2006), Harita Dergisi, year 73, special issue 18, pp. 318–323, General Command of Mapping, Ankara/Turkey, ISSN 1300-5790.

Pavlis NK, Holmes SA, Kenyon SC, Factor JK (2008) An Earth Gravitational Model to Degree 2160: EGM2008. Presented at the 2008 General Assembly of the European Geosciences Union, Vienna, Austria, April 13–18, 2008.

Rapp RH (1997) Use of potential coefficient models for geoid undulation determinations using a spherical harmonic representation of the height anomaly/geoid undulation difference. J. Geod. 71, 282–289.

Reigber C, Jochmann H, Wünsch J, Petrovic S, Schwintzer P, Barthelmes F, Neumayer KH, König R, Förste C, Balmino G, et al. (2004) Earth gravity field and seasonal variability from CHAMP. In: Reigber C, Lühr H, Schwintzer P, Wickert J (eds.), Earth Observation with CHAMP – Results from the Three Years in Orbit, Springer, Berlin, pp. 25–30.

Reigber C, Schmidt R, Flechtner F, König R, Meyer U, Neumayer KH, Schwintzer P, Zhu SY (2005) An earth gravity field model complete to degree and order 150 from GRACE: EIGEN-GRACE02S. J. Geodyn. doi:10.1016/j.jog.2004.07.001.

Reigber C, Schwintzer P, Stubenvoll R, Schmidt R, Flechtner F, Meyer U, König R, Neumayer KH, Förste C, Barthelmes F, et al. (2006) A High Resolution Global Gravity Field Model Combining CHAMP and GRACE Satellite Mission and Surface Data: EIGEN-CG01C. Scientific Technical Report STR06/07, GeoForschungsZentrum, Potsdam.

Rietbroek R, Brunnabend S, Dahle Ch, Flechtner F, Kusche J, Schröter J, Timmermann R (2009) Changes in total ocean mass derived with GRACE, GPS, and ocean modelling with weekly resolution. J. Geophys. Res., 114, C11004, doi:10.1029/2009JC005449.

Schmidt R, Flechtner F, Meyer U, Reigber Ch, Barthelmes F, Förste Ch, Stubenvoll R, König R, Neumayer KH, Zhu S (2006) Static and time-variable gravity from GRACE mission data. In: Flury J, Rummel R, Reigber Ch, Rothacher M, Boedecker G, Schreiber U (eds.), Observation of the Earth System from Space, Springer, Berlin, pp. 115–129, ISBN 3-540-29520-8.

Schmidt R, Meyer U, Dahle Ch, Flechtner F, Kusche J (2007) Monthly and weekly EIGEN-GRACE05S gravity field solutions for monitoring of mass variations in the earth system. Proceedings of the Second Space for Hydrology Workshop "Surface Water Storage and Runoff: Modeling, In-Situ Data and Remote Sensing", 12–14 November 2007, Geneva, Switzerland, Benveniste J., et al. (eds.), ESA Publication WPP-280.

Tapley B, Ries J, Bettadpur S, Chambers D, Cheng M, Condi F, Poole S (2007) The GGM03 Mean Earth Gravity Model from GRACE. Eos Trans. AGU 88(52), Fall Meet. Suppl. Abstract G42A-03.

Thomas M, Sündermann J, Maier-Greiner E (2001) Consideration of ocean tides in an OGCM and impacts on subseasonal to decadal polar motion excitation. Geophys. Res. Lett. 12, 2457.

Zhu S, Reigber Ch, Koenig R (2004) Integrated adjustment of CHAMP, GRACE, and GPS data. J. Geod. 78(1–2), 103–108.

Orbit Predictions for CHAMP and GRACE

Krzysztof Snopek, Daniel König, and Rolf König

1 Introduction

Precise orbit predictions are service products to support SLR, pre-processing of mission data and mission operations. In all cases it is necessary to know the position of the satellite at some time in the future with a dedicated accuracy depending on the application. Currently, GFZ delivers a suite of orbit prediction products for these purposes for the Low Earth Orbiters (LEOs) CHAMP, GRACE-A and -B, and, since June 2007 also for TerraSAR-X. These applications highly contribute to the success of these missions as, e.g. in the end, SLR observations play an important role for validation in Precise Orbit Determination (POD).

The orbit prediction system is running fully automated and it is robust against various critical situations, e.g. hardware problems. Though a high percentage of the distributed orbit prediction products meet the requirements of the users, as will be shown later in this article, a constant effort is put to improve the quality which is monitored regularly by a Quality Control (QC) subsystem.

The most demanding application of the orbit predictions is the laser tracking of the above-mentioned satellite missions carried out by the International Laser Ranging Service (ILRS; Pearlman et al., 2002) ground stations. For the acquisition of SLR data the required accuracy for these LEOs is about 70 m in along-track direction that is equivalent to a 10-ms bias of the time the satellite becomes visible over a station (i.e. the satellite is too early or too late), shortly the time bias. With view on this quality criterion the QC is carried out. Based on the actual QC, the frequency of the generation of orbit predictions is chosen; currently it is twice a day for GRACE-A/-B and four times per day for CHAMP.

K. Snopek (✉)
Helmholtz Centre Potsdam, GFZ German Research Centre for Geosciences,
Department 1: Geodesy and Remote Sensing, Telegrafenberg, 14473 Potsdam, Germany
e-mail: krzysztof.snopek@gfz-potsdam.de

F. Flechtner et al. (eds.), *System Earth via Geodetic-Geophysical Space Techniques*,
Advanced Technologies in Earth Sciences, DOI 10.1007/978-3-642-10228-8_5,

2 Orbit Prediction System

The orbit prediction software system consists of a set of UNIX shell scripts and binary programs. The kernel of the whole system is the GFZ-own EPOS-OC (Earth Parameter and Orbit System – Orbit Computation) software that carries out the proper POD from recent tracking data and predicts the orbit by numerical orbit integration with an optimized dynamical model. All software components are regularly upgraded. In general the orbit prediction algorithm comprises the preprocessing of tracking and auxiliary data, the orbit adjustment and prediction, the generation of the orbit prediction products, and the dissemination of the products, see also (Schmidt et al., 2003).

2.1 Preprocessing

In the preprocessing part the observational data as well as some auxiliary data are assembled and provided in EPOS-OC-readable format. On the basis of the assembled data an EPOS-OC control file is created defining as well the parameterisation of the respective POD problem.

The main observational data used are orbit ephemerides available as on-board navigation solution (NAV) or as near real-time orbits (NRT) from the mission ground segment parts run in-house (chapter "Near-Real Time Satellite Orbit Determination for GPS Radio Occultation with CHAMP and GRACE" by Michalak et al., this issue). Originally, NAV solutions have been used for both CHAMP and GRACE. Since the year 2007 NRT orbits are used as the primary source of orbit ephemeris for CHAMP. The advantages of using NRT orbits instead of NAV solutions is that they do not have to be downloaded from a remote place and that they

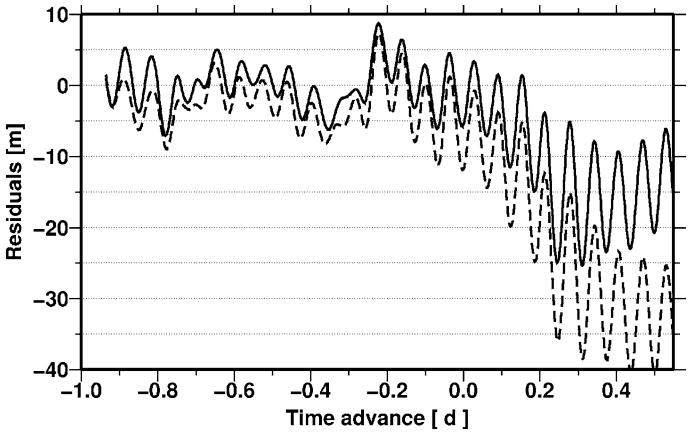

Fig. 1 Differences between a reference orbit (RSO) and a predicted orbit (*solid line*: NRT based, *dashed line*: NAV based). Time advance 0.0 refers to the epoch of the last available observation

lead to smaller positional residuals in the observed part of the orbit prediction process as revealed by Fig. 1. In addition to orbit ephemerides also SLR normal points are used as observations.

The auxiliary data used comprise gravity fields of Earth, Sun, and Moon, Earth orientation parameters, an atmospheric density and solar radiation pressure model driven by solar and geomagnetic activity indices, an atmospheric gravity variation model, ocean tides and solid Earth tides models, and a macro model of the respective satellite for modelling the atmospheric density and the solar radiation pressure forces acting on its surface.

2.2 Orbit Determination

The proper calculation of the predicted orbit consists of two steps. In the first step the POD for that part of the orbit covered by observations (the "observed part") is carried out. The length of the observed part depends on the availability of observation data; in general 1 day is used.

The accuracy of the predicted orbits of CHAMP is influenced by the observational data. In Fig. 1 the differences between a reference Rapid Science Orbit (RSO; see chapter "Rapid Science Orbits for CHAMP and GRACE Radio Occultation Data Analysis" by Michalak and König, this issue) and a predicted orbit, based one time on NRT data and the other time based on NAV data, is plotted. As a RSO is a highly accurate reference orbit with an accuracy of orbit positions on the level of a few centimetres Fig. 1 clearly reveals that the predicted part is more accurate if the whole predicted orbit is based on NRT data.

In the POD step, various model parameters are estimated allowing the adjustment of the modelled perturbing forces acting on the satellite from the tracking data. Among the parameterised orbit forces the atmospheric drag is the most critical one in case of LEOs, it mainly influences the along-track error of the adjusted orbit. Atmospheric drag parameters are set up every 6 h in the observed part resulting in four values to be estimated.

Once the orbit adjustment of the observed part has converged the critical estimated parameters as well as the RMS values of the residuals are checked for certain thresholds. In case all requirements are met the second step of the orbit prediction process is carried out by extrapolating the orbit of the observed part by pure numerical forward integration using the estimated parameters stemming from the first step. The resulting orbit is called the "predicted part". For the modelling of the atmospheric drag the mean of the last three drag parameters of the observed part is introduced into the predicted part as starting value of a linear function leading to 1.0 approximately 30 days later. The aim of this averaging is to make the predicted part more stable. The histograms in Fig. 2 show a comparison of residuals for a time advance of 12 h in along-track direction. The left histogram refers to predictions without averaging of the atmospheric drag parameters; the right plot refers to the case where the drag parameters are averaged as explained before. A significant

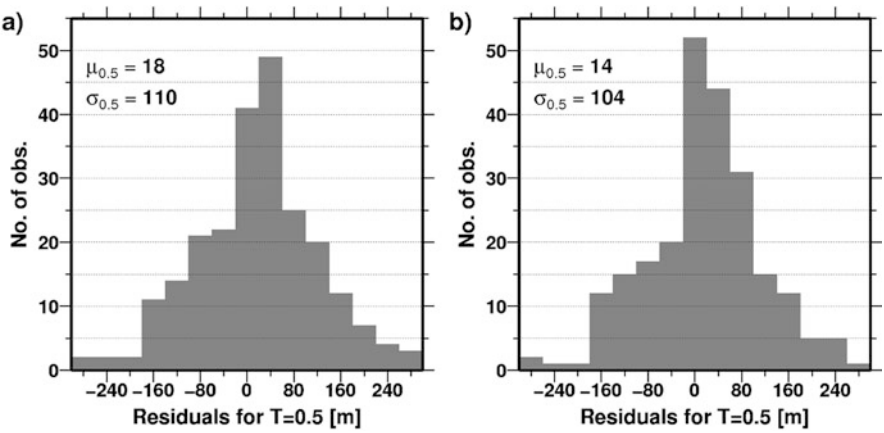

Fig. 2 Comparison of residuals of predicted orbits in along-track direction 12 h (i.e. 0.5 d) after the last available observation as compared to a reference orbit. *Left histogram*: residuals of predicted orbits without extrapolation of atmospheric drag parameters; *Right histogram*: residuals in case of extrapolation of atmospheric drag parameters

improvement in bias and standard deviation can be detected justifying the averaging of the atmospheric drag parameters.

2.3 Products

The prediction products to be derived from the predicted orbits depend on their application. Table 1 summarizes the prediction products generated by GFZ as well as the corresponding archive used and the application intended. The main recipients of GFZ orbit prediction products are the ILRS community and the telemetry stations of GFZ and DLR (German Aerospace Centre, Cologne, Germany).

Prior to June 2008, beside Smithsonian Astronomical Observatory (SAO; Pearlman et al. 1979) elements and Two-line elements (TLEs, 2009) the ILRS required predictions as well in the standard "Tuned Inter-Range Vector" (TIRV,

Table 1 GFZ prediction products for CHAMP, GRACE, and TerraSAR-X

Product	Application	Archive	Comment
IRV + DRAG function	SLR tracking	CDDIS, EDC, ISDC	Ceased after 2008
SAO	Scheduling of satellite passes	CDDIS, EDC, ISDC	Ceased after 2008
CPF	SLR tracking	CDDIS, EDC, ISDC	Since 2006
TLE	Scheduling of satellite passes	CDDIS, EDC, ISDC	Ongoing
PDO	CHAMP science data system	ISDC	Since 2000 Only for CHAMP

2009) format accompanied by DRAG functions (2009) for additionally modelling the atmospheric drag. As the ILRS decided in 2005 to migrate to the Consolidated Prediction Format (CPF; Ricklefs, 2006) in order to replace the TIRVs from February 2006 on, the ILRS also required predictions in this new format. Thus, for a transition period from 2006 to 2008 both TIRVs with DRAG functions and CPFs were generated and disseminated accordingly. Since the official ILRS prediction format is CPF as of June 2008 GFZ ceased the generation and distribution of TIRVs, DRAG functions, and SAO elements.

The TLEs are used by SLR stations (formerly mainly SAO) and telemetry stations for scheduling the contacts with the satellites, the CPFs serve for steering the laser beam to hit the satellites to be tracked. All orbit prediction products mentioned so far are immediately disseminated after generation and stored to various data centres comprising the Crustal Dynamics Data Information System (CDDIS, 2009), the EUROLAS Data Center (EDC, 2007), and GFZ's Information System and Data Center (ISDC, 2009). Additionally, CPFs are directly sent to some SLR stations by email.

Other orbit prediction products generated only for CHAMP are the Predicted Science Orbits (PDOs). They are available at the ISDC in the CHORB format (Koenig et al., 2001).

3 Accuracy of Predicted Orbits

The accuracy of the predicted orbits is continuously monitored at GFZ by means of a QC subsystem. The predicted orbits are compared to RSOs that act as highly accurate reference orbits. Analysis of cross-track and radial components shows that the residuals with respect to the reference orbits have a sinusoidal characteristic with amplitude of up to five metres in cross-track and eight metres in radial. The most critical factor of the quality of the predicted orbits is their accuracy in along-track direction or time bias. It is important to note that the time bias grows exponentially with time as revealed by Fig. 1. The most demanding requirement on orbit prediction accuracy is posed by tracking a satellite by SLR during daylight. There, the absolute value of the time bias has to remain below 10 ms.

In order to monitor the accuracy, two kinds of statistics are computed. The first one is a success rate of time biases below 10 ms at a given time advance, i.e. at a given time after the last observation. This 10-ms rate is defined as a percentage of orbits for which the time bias is less than 10 ms. For CHAMP, the rate is computed at a time advance of 9 h and for GRACE at a time advance of 12 h. Figure 3 shows monthly 10-ms rates for CHAMP opposed to solar flux and the orbit height of CHAMP. A strong correlation between the solar activity and the quality of the predicted orbits is visible. The quality improvement in 2005 is on the one hand caused by lower solar activity, and on the other hand due to updates of various background models used. For instance, as of June 2005 the newer EIGEN-CG01C-2 which is a derivative of EIGEN-CG01C-1 (Reigber et al., 2006). Earth gravity field is used replacing the old GRIM5-C1 (Gruber et al., 2000) model. The 10-ms rate plots for

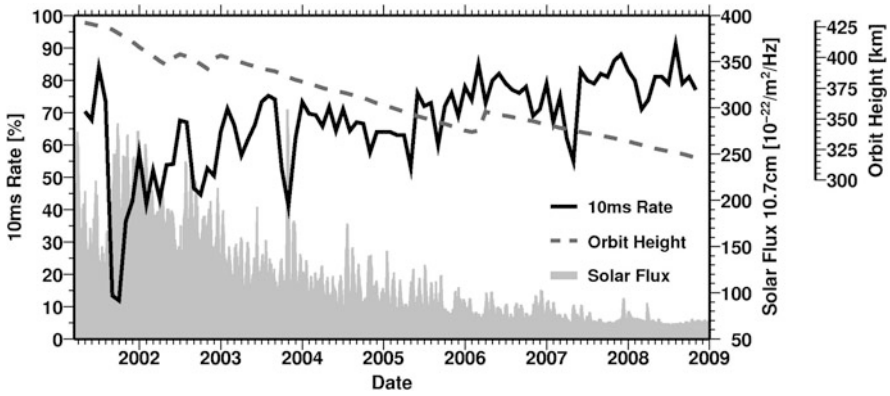

Fig. 3 10 ms success rate for CHAMP (*solid line*) for time advance 9 h, plotted with solar flux (*gray peaks*) and orbit height (*dashed line*)

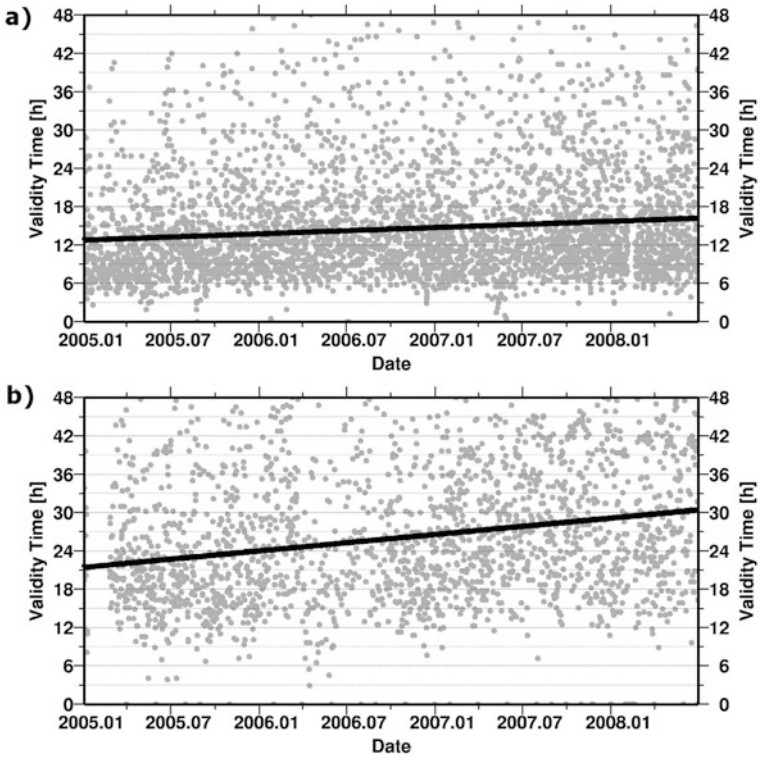

Fig. 4 Orbit prediction validity time plotted for each predicted orbit since 2005 for CHAMP (a) and GRACE-A (b)

the GRACE satellites are similar to those for CHAMP, but due to the higher orbit height (about 470 km in 2005), the rates are higher than for CHAMP and on a level of 80–100% at a time advance of 12 h.

In order to check the accuracy of the predicted orbits, a second statistic is computed. The prediction validity time is defined as the time after the last observation in which the time bias is less than 10 ms. In other words, the validity time determines how long a given prediction can be used at SLR stations, before it has to be replaced by a newer one. The validity time is computed for each orbit prediction for CHAMP and GRACE generated in the period January 2005 to November 2008. The results of this analysis are plotted in Fig. 4. The upper plot shows the validity time for CHAMP and the lower one for GRACE-A. The plot for GRACE-B is almost identical to the GRACE-A plot. The thick solid lines mark the linear trend. The increasing trend for both satellites can be again attributed to the lowering solar activity and to the upgrading of the prediction procedures. Remarkable is the trend for CHAMP for which it was expected that the decreasing orbit altitude would eliminate the positive effect of the low solar activity. The analysis of the validity time for CHAMP and GRACE shows also that the majority of predictions are valid more than 6 h for CHAMP and more than 12 h for GRACE. These results justify the update frequency of the predictions which are: four per day for CHAMP and twice per day for GRACE.

4 Conclusions

Orbit predictions for the CHAMP and GRACE satellite missions are computed and distributed regularly and automatically at GFZ. The QC of the generated products focuses particularly on monitoring the time biases of the predicted orbits. Thanks to the decreasing solar activity and a constantly upgraded processing the quality of orbit predictions produced at GFZ has increased in the last years. For CHAMP, the 10-ms success rate at 9 h after the last observation is usually higher than 66%. For GRACE the rate computed 12 h after the last observations exceeds regularly 80%. The prediction validity time analysis justifies the present prediction frequency for CHAMP: four times a day, and for GRACE: twice a day.

References

Crustal Dynamics Data Information System internet site, http://cddisa.gsfc.nasa.gov/, modified 2009-03-13.

DRAG function format: http://ilrs.gsfc.nasa.gov/products_formats_procedures/predictions/drag_function/index.html modified: 2009-03-13.

EUROLAS Data Center internet site: http://www.dgfi.badw-muenchen.de/edc/, modified 2007-08-30.

Gruber T, Bode A, Reigber Ch, Schwintzer P, Balmino G, Biancale R, Lemoine JM (2000) GRIM5-C1: Combination solution of the global gravity field to degree and order 120. Geophys. Res. Lett., 27(24), 4005–4008.

Information System and Data Center internet site: http://isdc.gfz-potsdam.de/index.php, modified 2009-03-13.

Koenig R, Schwintzer P, Reigber Ch (2001) Format Description: The CHAMP Orbit Format CHORB, http://op.gfz-potsdam.de/champ/docs_CHAMP/CH-GFZ-FD-002.pdf

Pearlman MR, Degnan JJ, Bosworth JM (2002) The international laser ranging service. Adv. Space Res. 30(2), 135–143, doi: 10.1016/S0273–1177(02)00277-6.

Pearlman MR, Romaine S, Latimer JH (1979) Updating Ephemerides Software for Laser Tracking, Memorandum, June 1st 1979, Non-singular Variables for Ephemerides, May 22nd 1979, Checkword for Transmission of Orbital Elements, Memorandum C-248, August 15th 1979. Smithonian Institution Astrophysical Observatory, Cambridge.

Reigber Ch, Schwintzer P, Stubenvoll R, Schmidt R, Flechtner F, Meyer U, Koenig R, Neumayer H, Foerste Ch, Barthelmes F, et al. (2006) A High Resolution Global Gravity Field Model Combining CHAMP and GRACE Satellite Mission and Surface Gravity Data: EIGEN-CG01C. Scientific Technical Report, GeoForschungsZentrum, Potsdam, 2006.

Ricklefs RL (2006) Consolidated Laser Ranging Prediction Format Version 1.01, February 2006, http://ilrs.gsfc.nasa.gov/docs/cpf_1.01.pdf

Schmidt R, Baustert G, Koenig R, Reigber C (2003) Orbit predictions for CHAMP – Development and status. In: First CHAMP Mission Results for Gravity, Magnetic and Atmospheric Studies. Springer, Berlin, pp. 104–111, ISBN 3-540-00206-5.

Tuned Inter-Range Vector format: ftp://cddis.gsfc.nasa.gov/pub/reports/formats/tirv.format, modified2009-03-13.

Two-Line Elements format: http://ghrc.msfc.nasa.gov/orbit/tleformat.html, modified: 2009-03-13.

Rapid Science Orbits for CHAMP and GRACE Radio Occultation Data Analysis

Grzegorz Michalak and Rolf König

1 Introduction

One of the important objectives of the CHAMP and GRACE satellite missions (Reigber et al., 2003; Wickert et al., 2005) is to measure the GPS signal propagating through the Earth's atmosphere during occultation events. The characteristics of the signal enable the computation of important atmospheric parameters as humidity and temperature on a global scale. These parameters are used in atmospheric studies and weather forecast systems (Wickert et al., 2009; Healy et al., 2007). To enable processing of the GPS occultation data, precise and rapidly available orbits for the GPS constellation and for the Low Earth Orbiters (LEOs) are needed. For this reason the Helmholtz Centre Potsdam GFZ German Research Centre for Geosciences (shortly GFZ hereafter) has set up a Precise Orbit Determination (POD) system for the generation of Rapid Science Orbits (RSOs) for the GPS constellation and for CHAMP in March, 2001, after the enabling of the occultation measurements on-board CHAMP (Michalak et al., 2003). The system delivers satellite orbits and clock biases on a daily basis to GFZ's Information System and Data Center (ISDC) making them available for evaluation of radio occultations (Wickert et al., 2001). The orbits are used also to support the magnetic/electric field studies. Over the years the system has constantly been subject to improvements and developments to enable multi satellite processing. Currently, the RSOs are generated besides for GPS, CHAMP and GRACE-A also for GRACE-B, SAC-C and TerraSAR-X. In addition, the applicability of the RSO system for the six FORMOSAT-3/COSMIC satellites (Anthes et al., 2008) was also demonstrated. The rapid orbits are generated with approximately 1 day latency. In case of data or processing problems, the RSOs are always generated manually. The core of the system was also applied in a Near-Real Time (NRT) orbit processing system (chapter "Near-Real Time Satellite Orbit Determination for GPS Radio Occultation with CHAMP and GRACE" by Michalak

G. Michalak (✉)
Helmholtz Centre Potsdam, GFZ German Research Centre for Geosciences,
Department 1: Geodesy and Remote Sensing, Telegrafenberg, 14473 Potsdam, Germany
e-mail: michalak@gfz-potsdam.de

F. Flechtner et al. (eds.), *System Earth via Geodetic-Geophysical Space Techniques*,
Advanced Technologies in Earth Sciences, DOI 10.1007/978-3-642-10228-8_6,

et al., 2009, this issue) which generates less precise orbits with latency below 2.5 h required to use the occultation data products for weather predictions (Wickert et al., 2009). The NRT system is, however, affected by data gaps and delays as well as network outages and can not guarantee 100% orbit accessibility. For this reason precise RSOs are necessary for off-line validations and climate studies based on occultation products.

In the LEO orbit determination, the so-called two-step approach is used in which firstly estimated GPS orbits and clocks are fixed for the subsequent estimation of the LEO orbits. For this reason, the RSO processing consists of chains generating GPS orbits and separate chains generating the orbits of the LEOs. Details of the chains and processing strategies are given in the following sections.

2 GPS Rapid Science Orbits

The dynamic RSOs for the GPS satellites are generated on a daily basis using the ionosphere free L3 combination of GPS code and phase data from the GFZ/JPL low latency ground station network (Galas et al., 2001) as well as from IGS sites (hourly and daily data). To reduce the computation time and assure high precision of the orbits, a ground station optimization procedure is applied that selects approximately 60 stations with preferably uniform distribution on the globe. The orbits cover 1 day, the spacing was initially 5 min and since October 2007 decreased to 30 s, thus matching the spacing of the LEO data. The dynamic model for POD of the GPS satellites consists of

- the gravity field and Earth tides model GRIM5-C1 (12×12) (Gruber et al., 2000)
- perturbations from Sun, Moon and the planets (JPL ephemerides DE 403)
- solar radiation pressure model ROCK 4 (Fliegel et al., 1992)
- periodic empirical forces in orbit transversal and normal directions.

For each arc the following parameters are estimated:

- initial states for all GPS satellites,
- global scaling factor and y-bias for the solar radiation model,
- periodic empirical coefficients in cross- and along-track direction, four for each satellite,
- tropospheric corrections, six for each station,
- station coordinates,
- station clock biases,
- floating ambiguities, since February 2009 constrained by fixed double difference integer ambiguities.

The processing time of a 1 day arc with 30 s spacing and ambiguity fixing amounts to almost 6 h on an UltraSparc III 900 MHz machine. The orbits are

generated in SP3 format and delivered to GFZ's Information System and Data Center (ISDC) with a latency of approximately 12 h. We define here the latency as the difference between the time of the orbit generation and the last epoch in the data used in the processing. Currently, for the GPS RSO the relative phase centres for ground antennas are used (see [IGSMAIL-5189] for more details). It should also be noted, that some components of the dynamic model (especially the solar radiation pressure model) are out of date, but they are not critical to meet the orbit accuracy requirements for LEO satellites ($\sim$0.05 mm/s for velocity corresponding to $\sim$1 dm for position at LEO orbit altitudes; see, e.g., Wickert, 2002). For the future, however, for applications requiring high orbit accuracy (f.e. gravity field determination, precise inter-satellite baseline determination, precise kinematic positioning) a number of improvements are required. Some of them, like the phase wind-up correction (Wu et al., 1993) and ambiguity fixing (Ge et al., 2005) were already implemented. Another important improvement which is planned for implementation is the introducing of the solar radiation pressure model COD9801 (Springer et al., 1999) and the GPS attitude model (Bar-Sever, 1996), and the change from relative to absolute antenna phase centre corrections both for the ground stations and for the GPS satellites. The GPS orbit accuracy is constantly monitored by comparison with IGS Rapid Orbits (IGR). The resulting differences computed after Helmert transformation can be seen in Fig. 1. The typical 3-D difference is in the range of 13–14 cm. The recent implementation of integer ambiguity fixing significantly improved the RSO accuracy, mainly in along-track and cross-track directions, reducing the 3-D difference to IGR orbits to 7–8 cm, as can be seen also in Fig. 1. The obvious oscillations with yearly period can be attributed to cumulative, multi-satellite dynamical effects of mismodelling of the solar radiation pressure.

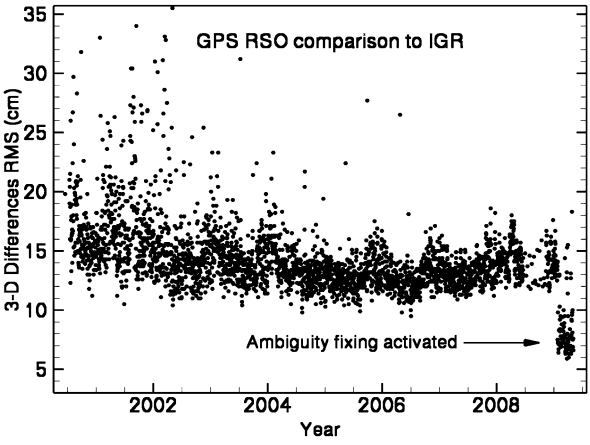

Fig. 1 Comparison of the daily GPS RSOs to the IGR

Two of the GPS satellites, PRN05 and PRN06, are equipped with laser retro-reflectors, what enables validation of the orbits by means of Satellite Laser Ranging (SLR). The SLR residuals for both satellites are given in Figs. 2 and 3. The SLR residuals exhibit a negative bias of 3–4 cm, this bias was found earlier also by others (see, e.g., Urschl et al., 2007) and the reason for it is still unclear. The standard deviation of the SLR residuals is around 5 cm what allows to conclude that the radial accuracy, most important for positioning applications, is also close to 5 cm. The generation of the GPS RSOs runs fully automatic, in case of data or software problems, manual interaction is performed to assure 100% availability of the orbit products.

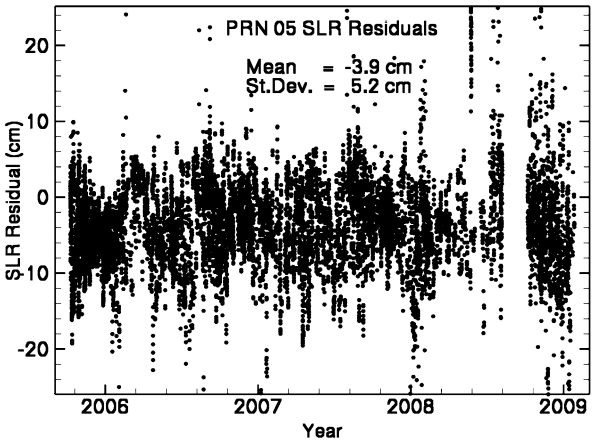

Fig. 2 Validation of the RSOs of PRN 05 by SLR

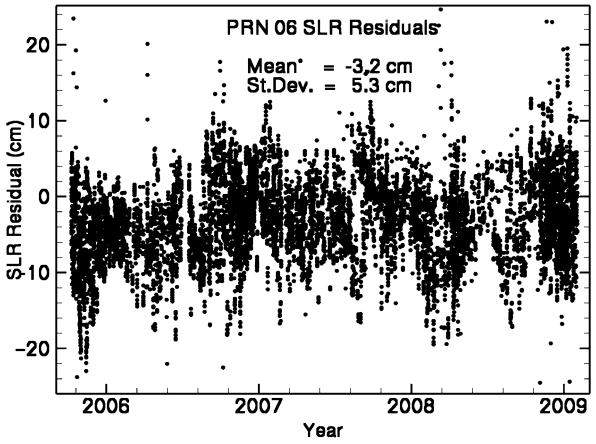

Fig. 3 Validation of the RSOs of PRN 06 by SLR

3 Low Earth Orbiters Rapid Science Orbits

The RSO system for LEO satellites uses the GPS RSO orbits and clocks as fixed reference (two-step approach) and generates on a daily basis two 14 h long dynamic orbits with 30 s spacing from space-borne GPS Satellite-to-Satellite Tracking data. As in the GPS RSO chain, ionospheric free L3 combinations of both code and phase data are used in the processing. The 14 h long LEO orbits begin always at 22:00 and at 10:00, with 2 h overlaps for 22:00–24:00 and 10:00–12:00 respectively. The overlaps serve for internal quality checks. More details on LEO POD can be found in (Michalak et al., 2003; König et al., 2005). The LEO orbits are generated with a latency of 1 day. Currently for the LEO orbit adjustment the force model consists of:

- Earth gravity model EIGEN-CG01C-2 (120 × 120) (Reigber et al., 2004),
- third body attraction by Sun, Mercury, Venus, Mars, Jupiter, Saturn (DE 403),
- lunar gravity field Ferrari (4 × 4),
- Earth and ocean tides GRIM5-C1 (Gruber et al., 2000),
- atmosphere drag based on density model DTM94 (Berger et al., 1997),
- solar radiation pressure model,
- apparent forces, relativistic effects,
- empirical periodic accelerations in along- and cross-track direction, 1/rev and 2/rev.

For each 14 h LEO arc the following parameters are estimated:

- initial state vector,
- scaling factor for solar radiation pressure model,
- scaling factors for air drag model (linear, continuous, every 4 h),
- periodic empirical coefficients (every 45 min),
- floating ambiguities (∼300 parameters),
- 30-s clock biases (∼1,700 parameters).

The RSO system was initially designed to support radio occultations and magnetic field studies for the CHAMP satellite launched on July 15, 2000. Over the years the system was successfully extended by more LEOs. In March 2002 the Argentinian/US satellite SAC-C, carrying the same GPS receiver as CHAMP (BlackJack) and performing occultation measurements as well, was included. GRACE-A and GRACE-B RSOs started to be generated in October 2004, the TerraSAR-X satellite was included in September 2007, 3 months after its launch. The RSO system was also used to generate some days of orbits of the six COSMIC satellites (Michalak et al., 2007) increasing the total number of LEOs we use in the RSO system temporarily to 11.

The quality of the data and orbits is monitored internally by checking the post-fit code and phase residuals, the overlap comparisons, the total number and the percentage of eliminated observation and the data coverage. For external, independent orbit

quality check the SLR residuals are used. An example of the post-fit RMS values for the L3 code and phase residuals for CHAMP RSOs are given in Fig. 4. The average code RMS value is around 60–70 cm, the periodic oscillations present in the code RMS values could be probably caused by longer periods with large multi-path effects due to tracking of the satellites at low elevations. Similar regular oscillations of the code RMS values, but with quite different frequencies are visible for other LEOs as well. The definite explanation of the oscillations requires more detailed investigations. The average CHAMP phase RMS value, 2.8 cm, was recently significantly reduced to below 1 cm after changing the spacing for GPS RSOs clocks from 5 min to 30 s in October 2007. The reason being that there is no need anymore to interpolate the 5 min GPS clocks to match the 30 s LEO spacing. The SLR residuals, which serve as independent accuracy assessment for CHAMP, for both GRACE and for the TerraSAR-X satellites can be seen in Figs. 5, 6, 7, and 8. The overall LEO RSO accuracy is here around 5 cm. It has to be noted, that the RSO processor does not perform SLR outlier elimination, therefore the mean and RMS values given in the plots can be affected by poor quality or systematic biases in the data of some of the laser stations. Surprisingly, a negative bias of 0.6–1.2 cm could be detected for all but the GRACE-A satellite. The origin of the bias is unclear, probable reasons are deficiencies in the dynamic modelling of the orbits or incorrect values of the retro-reflector locations. The differences in the biases for GRACE-A and GRACE-B could result from missing attitude data, which are not available during the RSO processing; but this requires independent confirmation. The SAC-C

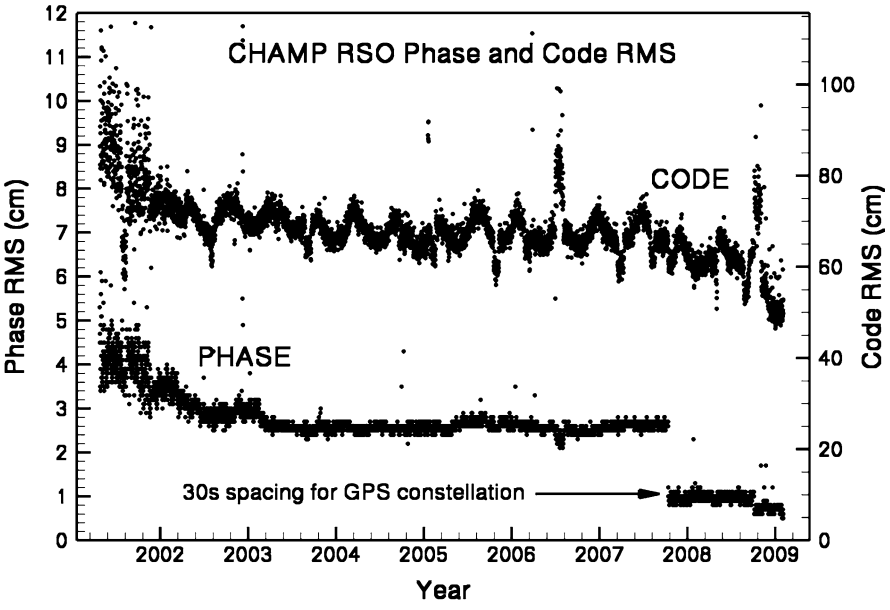

Fig. 4 CHAMP phase (*left axis*) and code (*right axis*) RMS values in the course of the mission

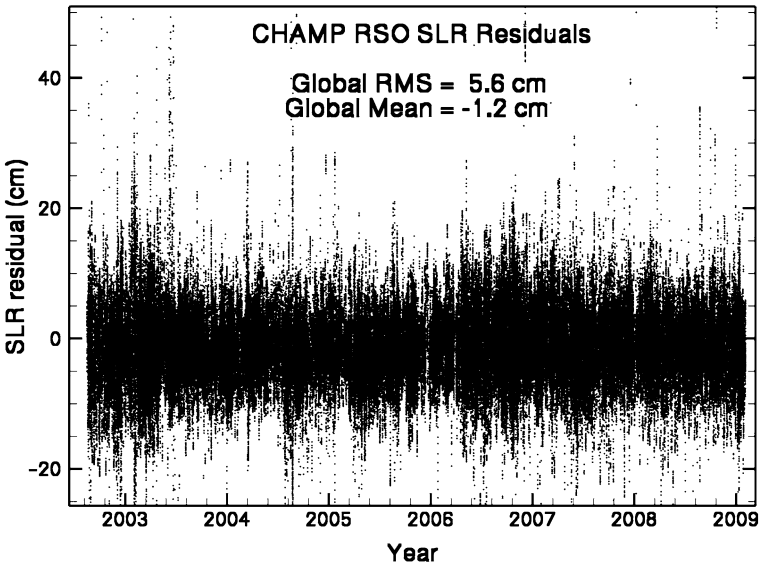

Fig. 5 SLR residuals for the CHAMP RSOs

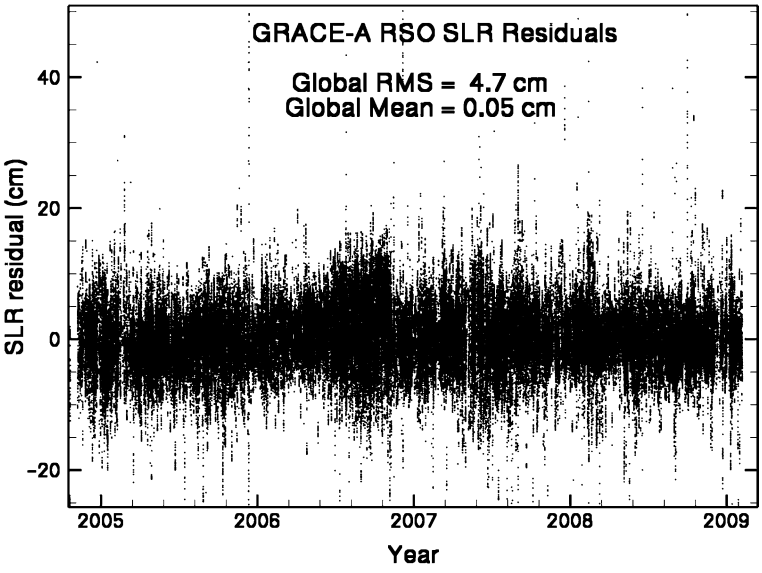

Fig. 6 GRACE-A RSO SLR residuals

satellite has no retro-reflector and for this reason an independent orbit validation using SLR can not be done. For this satellite, solely overlap values from the internal quality checks can be used; they are displayed in Fig. 9, the consistency of the orbits is 7–8 cm.

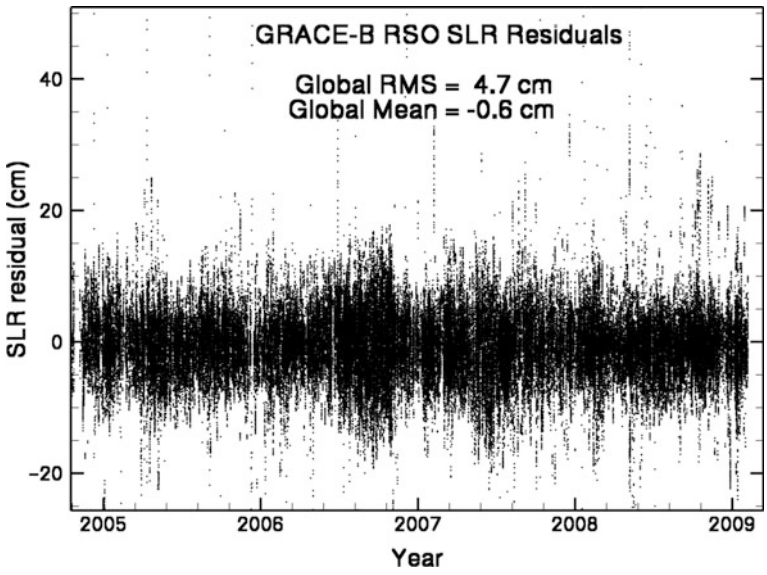

Fig. 7 GRACE-B SLR residuals

The RSO orbits, besides being pre-requisite for radio occultation and magnetic field applications, are also used for the quality assurance of the orbit predictions (chapter "Orbit Predictions for CHAMP and GRACE" by Snopek et al., 2009, this issue). Due to their public accessibility, a variety of applications outside of GFZ are reported e.g. in (Reigber et al., 2005).

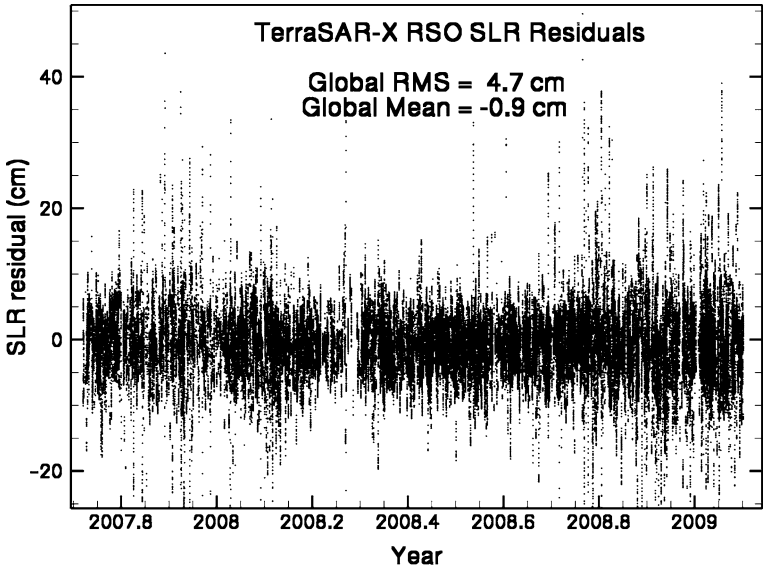

Fig. 8 SLR residuals for TerraSAR-X residuals

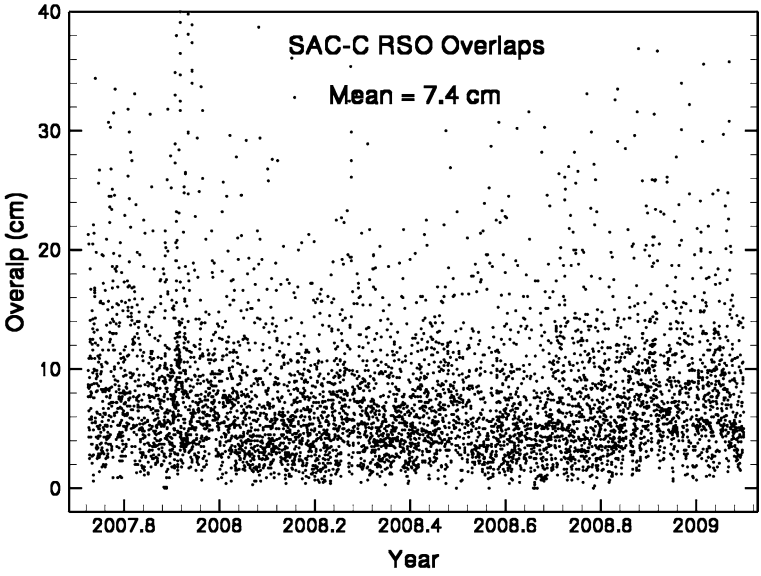

Fig. 9 SAC-C satellite overlap values for the last 2 h of each orbit

4 Summary

Within the German "Geotechnologien" research programme a reliable RSO processing system was developed for the daily generation of precise GPS and LEO orbits with latencies of 1 day to support radio occultation and magnetic field studies. Currently the system generates regularly orbits of five LEO satellites: CHAMP, GRACE A/B, SAC-C and TerraSAR-X. The system is flexible and allows easy extensions to new LEO missions, what was demonstrated by the inclusion of the six COSMIC satellites for a test phase. The 3-D position accuracy of the GPS RSOs obtained from comparisons to IGR orbits is 14 cm and was recently improved to 7–8 cm as a result of the introduction of integer ambiguity fixing into the processing. It can be concluded, that the GPS RSO accuracy in any direction (radial, along- and cross-track) is now close to 4–5 cm. The radial accuracy can be confirmed independently also by SLR. The laser ranging to PRN05 and PRN06 shows a scatter of the residuals of around 5 cm. Position accuracy of the LEO orbits, obtained also from SLR, is nearly uniform for all LEOs and in the range of 4–5 cm. Orbits of both GPS and most LEOs show centimetre-level negative biases in the SLR residuals. The origin of the biases requires more detailed investigation. In spite of this, the accuracy of the orbits fulfil the radio occultation accuracy requirements, the availability of the orbit products is guaranteed to almost 100% due to operator interaction in case of failures of the automatic processing. The RSO orbits are publicly available at GFZ's Information System and Data Center (ISDC) also for other scientific applications.

Acknowledgments We would like to thank IGS for providing GPS data and ILRS for providing SLR data. We also thank J. Wickert for his useful comments. This study was carried out in the Geotechnologien programme under the grant of the German Federal Ministry of Education and Research.

References

Anthes RA, et al. (2008) The COSMIC/FORMOSAT-3 mission: Early results. Bull. Am. Meteor. Soc., doi: 10.1175/BAMS-89-3-313.

Bar-Sever YE (1996) A new model for GPS yaw attitude. J. Geod. 70, 714–723.

Berger C, Biancale R, Barlier F, Ill M (1997) Improvement of the empirical thermospheric model DTM: DTM94 – A comparative review of various temporal variations and prospects in space geodesy applications. J. Geod. 72(3), 161–178.

Galas R, Wickert J, Burghardt W (2001) High rate low latency GPS ground tracking network for CHAMP. Phys. Chem. Earth (A) 26, 649–652.

Ge M, Gendt G, Dick G, Zhang FP (2005) Improving carrier-phase ambiguity resolution in global GPS network solution. J. Geod. 82(7), doi: 10.1007/s00190-005-0447-0.

Gruber T, et al. (2000) GRIM5-C1: Combination solution of the global gravity field to degree and order 120. Geophys. Res. Lett. 27(24), 4005–4008.

Fliegel HF, Gallini TE and Swift ER (1992) Global positioning system radiation force model for geodetic application. Geophys. Res. Lett. 97(B1), 559–568.

Healy SB, Wickert J, Michalak G, Schmidt T, Beyerle G (2007) Combined forecast impact of GRACE-A and CHAMP GPS radio occultation bending angle profiles. Atmos. Sci. Lett. 8, 43–50, doi: 10.1002/asl.149.

König R, Michalak G, Neumayer KH, Schmidt R, Zhu SY, Meixner H, Reigber C (2005) Recent developments in CHAMP orbit determination at GFZ. In: Reigber C, Lühr H, Schwintzer P, Wickert J (eds.), Earth Observation with CHAMP. Results from Three Years in Orbit, Springer, Berlin Heidelberg, pp. 65–70.

Michalak G, Baustert G, König R, Reigber C (2003) CHAMP rapid science orbit determination – Status and future prospects. In: Reigber C, Lühr H, Schwintzer P (eds.), First CHAMP Mission Results for Gravity, Magnetic and Atmospheric Studies. Springer, Berlin Heidelberg, pp. 98–103.

Michalak G, Wickert J, König R, Rothacher M (2007) Precise orbit determination of COSMIC/Formosat-3 satellites for radio occultations. European Geosciences Union General Assembly 2007 Vienna, Austria, 15–20 April 2007, Poster EGU2007-A-08402.

Reigber C, Lühr H, Schwintzer P (eds.) (2003) First CHAMP Mission Results for Gravity, Magnetic and Atmospheric Studies, Springer, Berlin Heidelberg, ISBN 3-540-00206-5.

Reigber C, Schwintzer P, Stubenvoll R, Schmidt R, Flechtner F, Meyer U, König R, Neumayer H, Förste C, Barthelmes F, et al. (2004) A high resolution global gravity field model combining CHAMP and GRACE satellite mission and surface gravity data: EIGEN-CG01C. Solid Earth Abstr. 24, 16.

Reigber C, Lühr H, Schwintzer P, Wickert J (eds.) (2005) Earth Observation with CHAMP. Results from Three Years in Orbit. Springer, Berlin Heidelberg, ISBN 3-540-22804-7.

Springer TA, Beutler G, Rothacher M (1999) A new solar radiation pressure model for GPS. Adv. Space Res. 23(4), 673–676.

Urschl C, Beutler G, Gurtner W, Hugentobler U, Schaer S (2007) Contribution of SLR tracking data to GNSS orbit determination. Adv. Space Res. 39(10), 1515–1523.

Wickert J, Galas R, Beyerle G, König R, Marquardt C, Schmidt T, Grunwaldt L, Galas R, Meehan TK, Melbourne WG, et al. (2001) Atmospheric sounding by GPS radio occultation: First results from CHAMP. Geophys. Res. Lett. 28, 3263–3266.

Wickert J (2002) The CHAMP radio occultation experiment: Algorithms, processing system, and first results. PhD Thesis (in German), University of Graz, Scientific Technical Report 02/07 GFZ Potsdam, Germany.

Wickert J, Beyerle G, König R, Heise S, Grunwaldt L, Michalak G, Reigber C, Schmidt T (2005) GPS radio occultation with CHAMP and GRACE: A first look at a new and promising satellite configuration for global atmospheric sounding. Ann. Geophysicae 23(3), 653–658.

Wickert J, et al. (2009) GPS radio occultation: Results from CHAMP, GRACE and FORMOSAT-3/COSMIC. Terr. Atmos. Ocean. Sci. 20(1), 35–50, doi: 10.3319/TAO.2007.12.26.01(F3C).

Wu JT, Wu SC, Hajj GA, Bertiger WI, Lichten SM (1993) Effect of antenna orientation on GPS carrier phase. Manuscripta Geodaetica 18, 91–98.

Parallelization and High Performance Computation for Accelerated CHAMP and GRACE Data Analysis

Karl Hans Neumayer

1 Introduction

At the Helmholtz Centre Potsdam GFZ German Research Center for Geosciences, CHAMP (König et al., 2006) and GRACE (chapter "The Release 04 CHAMP and GRACE EIGEN Gravity Field Models" by Flechtner et al., this issue) base products are provided in a broad variety and on a regular schedule. Among others, there are Rapid Science Orbits (RSO) for Radio Occultation (RO) data analysis (König et al., 2002; Healy et al., 2007), orbit predictions distributed to laser tracking stations to facilitate satellite laser ranging (SLR) data acquisition (chapter "Orbit Prediction for CHAMP and GRACE" by Snopek et al., this issue), and, most important, there is the obligation to produce monthly gravity fields (Flechtner et al., 2008) within the GRACE mission as well as static fields from GRACE (Förste et al., 2008) and suites of satellite missions including CHAMP, GRACE and other useful geodetic missions. Mid of 2005, at the beginning of a thorough and consistent reprocessing of the complete CHAMP and GRACE missions, with more extensive background modeling involved, and a steadily growing amount of all types of data, it became obvious that something had to be done with respect to computation efficiency and processing speed. Out of these needs emerged the work package *Parallelization and High-Performance Computing*. The task was two-fold: to make the vector of solve-for parameters as large as possible, and to make computations faster at the same time.

In a preliminary step, a significant part of the processing chains was migrated from available (and still existing) SUN workstations to network clusters of high-performance, low-cost Linux PCs. Most items of the Linux world are public domain, this helped to save costs for software, consulting and service. CPU performance is growing on a breathtaking scale year by year, thus the PCs were already faster as the workstations simply because they were purchased more recently. As Linux is

K.H. Neumayer (✉)
Helmholtz Centre Potsdam, GFZ German Research Centre for Geosciences,
Department 1: Geodesy and Remote Sensing, Telegrafenberg, 14473 Potsdam, Germany
e-mail: hneum@gfz-potsdam.de

F. Flechtner et al. (eds.), *System Earth via Geodetic-Geophysical Space Techniques*,
Advanced Technologies in Earth Sciences, DOI 10.1007/978-3-642-10228-8_7,

almost similar to UNIX, all of the shell and perl scripts of the CHAMP and GRACE processing environment could be easily adapted to run on both operating systems.

A more serious problem posed the substantially different memory architectures. The SUN workstations feature a large number of CPUs, typically 16–20 that use one large random access memory – again, typical values would be 64–128 GB – in common. This is a so-called *shared memory architecture*. On the other side, the individual nodes of the PC cluster have generally 2–8 CPUs sharing 4–8 GB only, but those nodes are connected via a network of a dedicated topology. We have a *distributed memory* scenario. This peculiarity had to be taken into account when implementing parallelization. A combination of shared memory applications already realized so far in the UNIX environment had to be combined with algorithms using the *Message-Passing Interface* (MPI), which is typical for computational work on high-performance clusters.

With the exception of the raw GPS and GRACE K-band ranging data preprocessing, the GFZ automatic software chains that produce CHAMP and GRACE gravity field models are essentially made up of three Fortran95 packages with suitable interfaces controlled and combined by shell and perl scripts. These three packages (see Fig. 1) are named EPOS-OC, VERBGL_2_NGL and TOTSOL. The functionality may briefly be described as follows: EPOS-OC (EPOS – Orbit Computation module) is primarily used for precise orbit determination, and it can adjust from ground and satellite observations of various data types (GPS, SLR, Precise Range and Range Rate Equipment (PRARE), Doppler Orbitography and Radiopositioning Integrated by Satellite tracking system receiver (DORIS), spaceborne GPS satellite-to-satellite tracking data (SST) etc.) any parameters involved including the gravity field coefficients. It features (a) the generation of normal equations and their solution (in case of GPS the clock parameters are reduced beforehand and substituted back after inversion), (b) the generation of normal equations and their storage (in case of GPS the clock parameters are reduced) and (c) the generation of observation equations and their storage. VERBGL_2_NGL generates in a highly parallel mode large normal equations (e.g. for gravity field, ocean and atmospheric tides) from the observation equations produced by EPOS-OC. In case of GPS, the clock parameters are reduced. TOTSOL provides a collection of linear

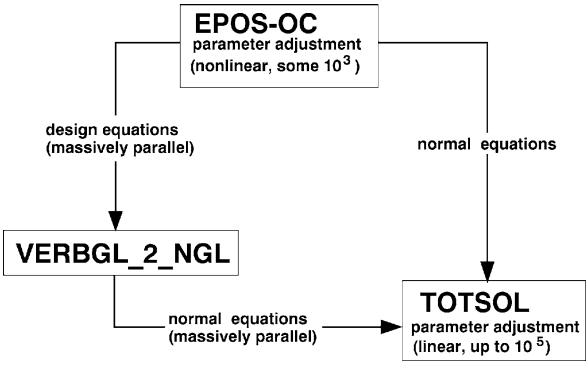

Fig. 1 Essential modules for gravity field determination and their state of parallelization mid of 2005

algebra functionalities to manipulate those normal equations: adding, parameter reduction, parameter mapping, parameter solution and post-processing.

In principle EPOS-OC can carry out the adjustment on its own, without the help of the other software packages. Mild non-linearities are admissible, as the solution is achieved in an iterative manner. However, the number of estimable parameters is limited to a few thousands and the satellite arc lengths to some days. In contrast, TOTSOL can solve for some ten thousands of parameters at the same time, but the problem must be strictly linear.

Several work packages have been defined to achieve the goals mentioned, and three of those we will enlarge upon in the following. It should be noted that, for all changes applied to the software, its original convenient modularity was maintained.

2 Removal of GPS Clock Parameters from the Observation Equations Using Dedicated Projections

As the implemented reduction of GPS clock parameters and their back-substitution is hard to handle from the viewpoint of parallelization, an alternative was planned by adding an off-projection of the clock parameters from the observation equations. This offers excellent possibilities for parallelization in both memory architectures, shared and distributed.

The general structure of the observation equations for un-differenced GPS measurements is

$$\begin{aligned} A_1 \cdot x_1 + \qquad\qquad B \cdot u &= r_{\text{code}} + v_{\text{code}}, \quad v_{\text{code}} \sim N\left(0, \frac{1}{p_{\text{code}}} \cdot I\right) \\ A_1 \cdot x_1 + A_2 \cdot x_2 + B \cdot u &= r_{\text{phase}} + v_{\text{phase}}, \; v_{\text{phase}} \sim N\left(0, \frac{1}{p_{\text{phase}}} \cdot I\right) \end{aligned} \tag{1}$$

The vector x_2 comprehends the float ambiguities, the vector x_1 the non-ambiguity parameters, as e.g. station coordinates, tropospherical scaling factors, spacecraft dynamical parameters etc.

Both the matrices A_1 and A_2 have as many rows as there are code/phase measurement pairs in the GPS campaign. The rows of the matrix A_1 are the partial derivatives of the pure code observation with respect to those parameters that are not ambiguities. The rows of the matrix A_2 are the partial derivatives of the phase observations with respect to the ambiguities.

The column vectors r_{code} and r_{phase} contain the observed-minus-computed values for code and phase measurements. We always suppose that code and phase observations occur in pairs, i.e. r_{code} and r_{phase} have the same dimension, and for a given index j, $r_{\text{code}}(j)$ and $r_{\text{phase}}(j)$ are the code and the phase part of one and the same measurement.

The measurement errors v_{code} and v_{phase} are assumed to be Gaussian and uncorrelated with measurement variances that give rise to the weights p_{code} and p_{phase}, respectively.

The common row number of the matrices A_1 and A_2 is the total number of observations (in a low earth orbiter (LEO) satellite arc or for a ground network campaign or for an integrated solution, Zhu et al., 2004). The sender and the receiver clock parameters are contained in the vector u. The corresponding part B of the design matrix has a block structure, we have

$$B = \begin{pmatrix} B_1 & & & \\ & B_2 & & \\ & & \ddots & \\ & & & B_N \end{pmatrix} \tag{2}$$

where N is the number of measurement epochs. For a given measurement epoch number m, the number of rows of B_m equals the number of paired code/phase measurements in that epoch, and the number of columns equals the number of sender and receiver clocks that were involved at the given epoch. As every observation is the signal travel time between a GPS sender and a ground station or a LEO GPS receiver, the corresponding row in the matrix B_m has exactly two nonzero entries at most: 1 (plus one) for the receiver clock and –1 (minus one) for the GPS satellite sender clock. If one clock is fixed a-priori, such as e.g. in the context of the LEO two-step method, we have only one nonzero entry.

The normal equation system originating from the design equations (1) is given by

$$\begin{pmatrix} (p_{\text{code}} + p_{\text{phase}}) \cdot C_{11} & p_{\text{phase}} \cdot C_{12} & (p_{\text{code}} + p_{\text{phase}}) \cdot C_{13} \\ p_{\text{phase}} \cdot C_{12}^T & p_{\text{phase}} \cdot C_{22} & p_{\text{phase}} \cdot C_{23} \\ (p_{\text{code}} + p_{\text{phase}}) \cdot C_{13}^T & p_{\text{phase}} \cdot C_{23}^T & (p_{\text{phase}} + p_{\text{code}}) \cdot C_{33} \end{pmatrix} \cdot \begin{pmatrix} x_1 \\ x_2 \\ u \end{pmatrix} = \begin{pmatrix} d_1 \\ d_2 \\ d_3 \end{pmatrix} \tag{3}$$

where

$$\begin{aligned} C_{jk} &= A_j^T \cdot A_k \\ C_{j3} &= A_j^T \cdot B \quad \text{for } 1 \le j \le k \le 2 \\ C_{33} &= B^T \cdot B \end{aligned} \tag{4}$$

and

$$\begin{aligned} d_1 &= A_1^T \cdot z_{\text{mean}} \\ d_2 &= A_2^T \cdot z_{\text{phase}} \\ d_3 &= B^T \cdot z_{\text{mean}} \end{aligned} \tag{5}$$

with

$$\begin{aligned} z\_{\text{mean}} &= p_{\text{code}} \cdot r_{\text{code}} + p_{\text{phase}} \cdot r_{\text{phase}}, \\ z_{\text{phase}} &= p_{\text{phase}} \cdot r_{\text{phase}} \end{aligned} \tag{6}$$

The matrix B of Eq. (2) and, therefore, also C_{33} of Eq. (4), have a very sparse block structure. To get an impression of that sparseness cf. Fig. 2.

Up to now, it has therefore been the policy in EPOS-OC and its auxiliary programs to reduce the clock parameters epoch-wise.

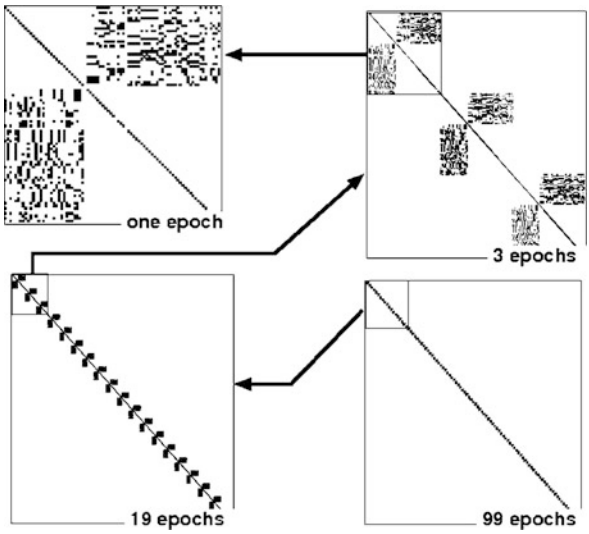

Fig. 2 The structure of the matrix B^TB of Eq. (4) for a realistic example, the combined adjustment of satellite orbits, clock parameters and ground station coordinates for April 26th 2009. Sub-matrices of B^TB are shown for the first epoch, for the three first epochs, the first 19 epochs and the first 99 epochs. As the GPS data spacing is 30 s, we have 2,880 (!) epochs for the whole day

This leads to a normal equation matrix of the form

$$\begin{pmatrix} (p_{\text{code}} + p_{\text{phase}}) \cdot \tilde{C}_{11} & p_{\text{phase}} \cdot \tilde{C}_{12} \\ p_{\text{phase}} \cdot \tilde{C}_{12}^T & p_{\text{phase}} \cdot \tilde{C}_{22} \end{pmatrix} \cdot \begin{pmatrix} x_1 \\ x_2 \end{pmatrix} = \begin{pmatrix} \tilde{d}_1 \\ \tilde{d}_2 \end{pmatrix} \tag{7}$$

with

$$\begin{aligned} \tilde{C}_{11} &= A_1^T \cdot (I - P) \cdot A_1 \\ \tilde{C}_{12} &= A_1^T \cdot (I - P) \cdot A_2 \\ \tilde{C}_{22} &= A_2^T \cdot (I - zP) \cdot A_2 \end{aligned} \tag{8}$$

and

$$\begin{aligned} \tilde{d}_1 &= A_1^T \cdot (I - P) \cdot z_{\text{mean}} \\ \tilde{d}_2 &= A_2^T \cdot z_{\text{phase}} - z \cdot A_2^T \cdot P \cdot z_{\text{mean}} \end{aligned} \tag{9}$$

where P is the projection matrix

$$P = B \cdot (B^TB)^{-1} B^T \tag{10}$$

and z equals the ratio

$$z = \frac{p_{\text{phase}}}{p_{\text{phase}} + p_{\text{code}}} \tag{11}$$

That reduced normal equation is then solved for x_1 and x_2.

Due to the pairing of code and phase measurements, and because of the presence of clock parameters, the computation of normal equations from observation equations in the case of GPS observation processing is rather involved. If we had non-GPS measurements with an observation equation of the form

$$A \cdot x = b + v \quad v \sim N(0,I), \tag{12}$$

where we assume, for the sake of simplicity, that the measurement noise has unit variance (which can always be achieved with a proper scaling of the lines of the observation equations), then the normal equations

$$C \cdot x = d \tag{13}$$

with

$$\begin{aligned} C &= A^T A \\ d &= A^T b \end{aligned} \tag{14}$$

can be established with a trivial matrix–matrix and a matrix–vector multiplication, for which there are very efficient subroutine libraries, e.g. LAPACK or NAG. In the case of GPS, things are much more complicated, as the epoch parameters (clocks) have to be taken care of via parameter reduction.

The idea for the simplification which will be sketched here has been inspired by the observation that it is possible to re-write the sub-matrices $\tilde{C}_{ij}$ on the left hand side of the normal equation system of Eq. (7) in the form

$$\tilde{C}_{ij} = \tilde{A}_i^T \cdot \tilde{A}_j \tag{15}$$

with

$$\begin{aligned} \tilde{A}_1 &= (I - P) \cdot A_1 \\ \tilde{A}_2 &= (I - \gamma P) \cdot A_2 \end{aligned} \tag{16}$$

where P is the highly sparse, block-diagonal projection matrix of Eq. (10) and γ is any one of the two roots of the quadratic polynom

$$\gamma \mapsto \gamma^2 - 2\gamma + \frac{p_{\text{phase}}}{p_{\text{phase}} + p_{\text{code}}}. \tag{17}$$

When the pre-multiplication of A_1 and A_2 have been performed according to Eq. (16), the normal equation matrix of Eq. (7) can be obtained by first computing the matrix

$$\tilde{A}^T \tilde{A} \tag{18}$$

with

$$\tilde{A} = (\, \tilde{A}_1 \;\; \tilde{A}_2 \,) \tag{19}$$

as in the first part of Eq. (14), and then by scaling dedicated sub-matrices of the result with the weighting factors p_{phase} and $p_{\text{phase}} + p_{\text{code}}$, respectively.

More or less the same trick is applied to the sub-vectors $\tilde{d}_1$ and $\tilde{d}_2$ on the right hand side of Eq. (7). We have

$$\begin{aligned} \tilde{d}_1 &= \tilde{A}_1^T \cdot \tilde{b}_1, \\ \tilde{d}_2 &= \tilde{A}_2^T \cdot \tilde{b}_2 \end{aligned} \tag{20}$$

with

$$\begin{aligned} \tilde{b}_1 &= p_{\text{code}} r_{\text{code}} + p_{\text{phase}} r_{\text{phase}}, \\ \tilde{b}_2 &= p_{\text{phase}}((I - (1+\tau)P) r_{\text{phase}} + \tau P r_{\text{code}}) \end{aligned} \tag{21}$$

where τ is the square root of $\frac{p_{\text{code}}}{p_{\text{code}}+p_{\text{phase}}}$ with either the positive or the negative sign.

Abbreviating

$$\tilde{d} = \begin{pmatrix} \tilde{d}_1 \\ \tilde{d}_2 \end{pmatrix} \quad \text{and} \quad \tilde{b} = \begin{pmatrix} \tilde{b}_1 \\ \tilde{b}_2 \end{pmatrix} \tag{22}$$

we have

$$\tilde{d} = \tilde{A}^T \tilde{b} \tag{23}$$

just as in the second part of Eq. (14).

Thus the complicated GPS case has been essentially reduced to the much simpler processing method for non-GPS measurements.

The clock parameter reduction in the normal equation has been replaced with the pre-multiplication of the design equations with dedicated projection matrices according to Eq. (16). Crucial for an overall performance gain is the speed of that latter operation. The following remarks are in order:

- The projection matrix P of Eq. (10), and, therefore, also the matrix I–tP with any real number t, are block diagonal where every diagonal block corresponds to a dedicated measurement epoch. The pre-multiplications of Eq. (16) are epoch-wise independent, and the multiplication may therefore be performed for all epochs in parallel at the same time.
- As the said pre-multiplication of a matrix amounts to pre-multiplying every column vector independently, it may be done for all columns independently in parallel.
- The pre-multiplications according to Eq. (16) amounts to replacing a vector y with y–tPy where either $t = 1$ or $t = \gamma$ with γ of Eq. (17). The latter operation becomes extremely simple if all sender clocks are fixed and all receiver clocks are solved for. This is the case for the adjustment method for LEOs with GPS receivers, where GPS sender satellite arcs and their clock parameters are determined and fixed in a preceding step. If we have only one receiver in the

epoch, then the clock parameter design matrices B_m of Eq. (2) are column vectors $\left(1\ 1\ \cdots\ 1\right)^T$ with unit entries, and a dimension N that is equal to the number of observations made by the given receiver. The projection reduces to replacing every entry y_j of the vector $y = (y_1 \cdots y_N)^T$ with $y_j - t\bar{y}$ where $\bar{y} = \frac{1}{N}\sum_{\rho=1}^{N} y_\rho$ is the mean of all elements referring to that receiver. In the case of several receivers, this applies for every receiver independently.

So henceforward, the processing chains of GPS and K-band processing for GRACE are more or less similar, which simplifies process management and, due to the efficient bypass of the clock parameters, increases processing speed up to a factor of two.

3 Accelerated Computation of Normal Equations from Observation Equations via Additional Row-Block Parallelization

The already realized distributed memory parallelization for the determination of observation equations with EPOS-OC by column-wise distribution of processes has been augmented in TOTSOL by a line-wise distribution. The creation of normal equations from observation equations amounts to performing a matrix multiplication with a re-scaled version of the design matrix. Before the advent of Geotechnologien II, that procedure was parallelized in such a manner that the normal equation matrix was computed block-wise as sketched in Fig. 3, just like the tiles at a bathroom wall. This was, and is still achieved by a Fortran95 program called verbgl_2_ngl_mpi_multi-input that distributes the computation of the individual sub-matrices over the nodes of a computer network with the help of MPI, see the right half of Fig. 4.

In a preceding step, the design equation files for the individual parameter subblocks are created by EPOS-OC runs started in parallel; and there are as many individual runs as there are parameters subsets. This is shown on the left half of Fig. 4. Contrary to the above-mentioned matrix product, an inter-process communication environment like MPI is unnecessary, as the individual EPOS-OC runs are mutually independent.

In gravity field processing, the overwhelming part of the parameter vector is made up of gravity field expansion coefficients. It is therefore appropriate to distribute those coefficients in the first place, and to leave the rest of the parameters alone.

This method is sketched in Fig. 5. where the original set of solve-for Stokes coefficients, up to degree and order 150 of an example gravity field, are evenly distributed over 40 individual gravity fields that have some 280 free coefficients each.

For each one of those fields, one EPOS-OC job is started. The original, undistributed job would have had almost 23,000 solve-for parameters from the gravity field alone. It is clear that, by employing more and more processing nodes of the

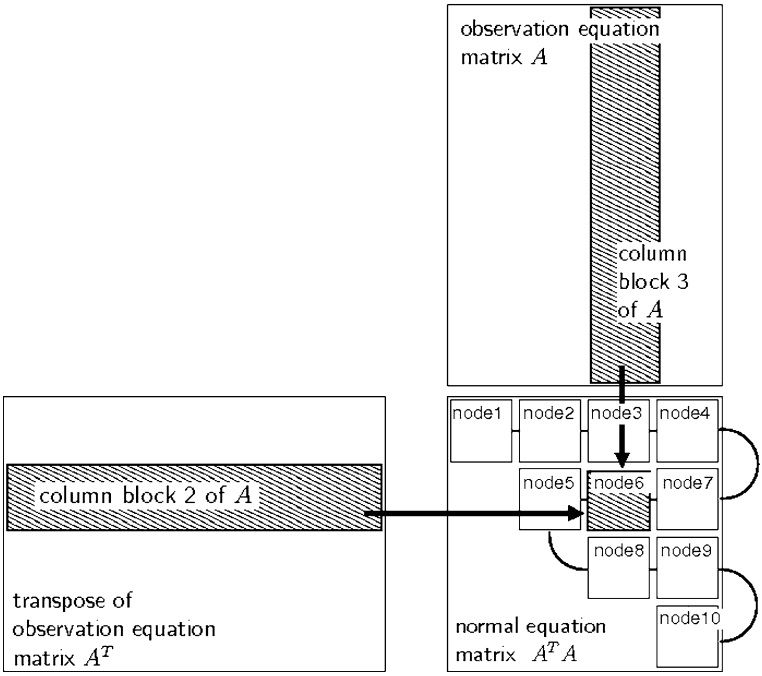

Fig. 3 Computation of the normal equation matrix on a distributed memory computer cluster (node1, node2, node3, . . .). The design matrix is broken down into column blocks, and the normal equation matrix is created block-wise in parallel

computer network, the processing time may be brought down to the time EPOS-OC takes for an adjustment without any gravity field coefficients at all.

The method implemented here for further acceleration is to employ that block-wise distribution not only with respect to the columns of the overall design matrix, i.e. the parameter vector, but also with respect to its rows, which means to bundle the set of observations into appropriate subsets.

How this is achieved is sketched in Fig. 6 for an example with 100,000 observations that are broken down into groups of 10,000. The number of EPOS-OC jobs started at the same time to create the design matrices is still equal to the number of parameter groups, i.e. column blocks, however every individual EPOS-OC run does not create one design equation file, but as many as there are observation subsets.

For the second step, the block matrix multiplication programverbgl_2_ngl_ mpi_multi-input is not invoked once, but as many times in parallel as there are row blocks, and the same number of intermediary normal equation files are created. The latter ones are added up using the Fortran95 program ad_hoc_add_neq.272 to the target normal equation, and then removed in the end.

It is obvious that thus the processing time is reduced further by a factor that is equal to the number of observation subgroups: where, up to now, 1 day was necessary to accumulate a GRACE normal equation of 1 month worth of GPS and K-band

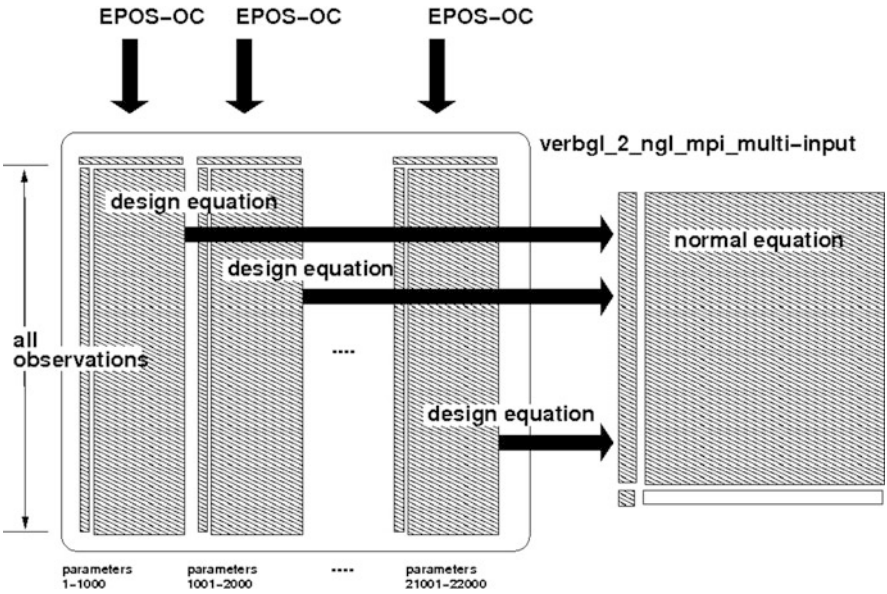

Fig. 4 Traditional way to compute a normal equation in a column block-wise manner. In a first step, several EPOS-OC jobs create design equation files. Subsequently, a program parallelized with MPI multiplies them block-wise, thereby establishing the normal equation matrix

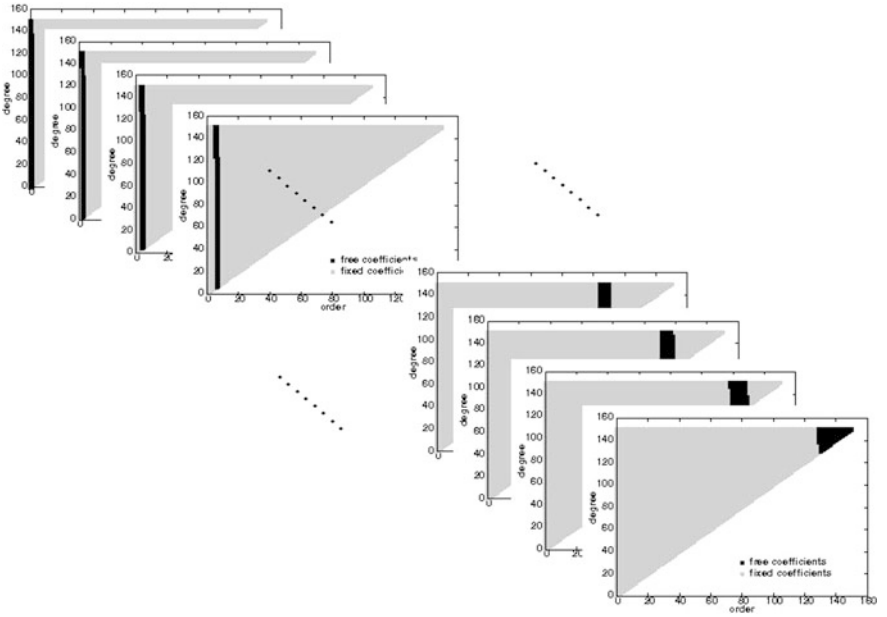

Fig. 5 Distribution of the solve-for parameters of a gravity field (degree and order 150) over 40 individual gravity fields, to establish design equations block-column-wises. Orders and degrees are indicated on the vertical and the horizontal axis. The solve-for stokes coefficients are marked up in *black*

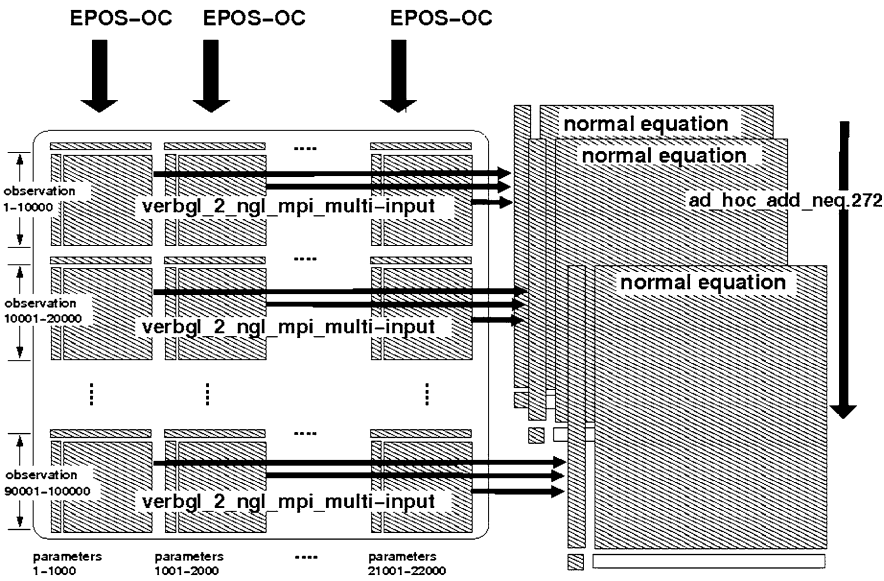

Fig. 6 Improved way to compute a normal equation, in a manner that is at the same time column block-wise and row block-wise

ranging data, we can finish the job in 4–5 h if the observations of every individual day of that month are cut into 5-h batches, and in some 2–3 h if the whole day of observations is cut into 10 slices. The optimal way of distributing computational work depends on the individual case and has to be found empirically.

However, it shall not be denied that this gain of processing speed does not come entirely for free: not only one, but several normal equation files have to be kept on the storage disks, with a typical size of 4 GB per observation subgroup and every observation type. Thus, if we have GPS as well as K-band ranging measurements, and the observations are distributed into 5 subgroups, we need at least 40 GB of intermediary normal equations at the intermediate stage, just to produce a 4 GB normal equation matrix in the end.

If the intermediate normal equation matrices are produced in parallel, then as many verbgl_2_ngl_mpi_multi-input processes have to be started as there are measurement subgroups. One verbgl_2_ngl_mpi_multi-input process needs $n \cdot (n+1)/2$ computation nodes, where n is the number of row/column blocks the normal equation matrix is made up for processing, so if we cut the parameter vector into $n = 5$ sub-vectors of roughly the same size, we need 15 free processing nodes per individual normal equation matrix. If the whole set of measurements is divided into 5 subgroups, we need 75 processing nodes alone for the computation of the normal equation from the observation equations, and if we divide into 10 groups, we need 150. On the 202 node computation grid at GFZ this is basically possible only at times of low ambient computation load.

4 Adjustment of Satellite Arcs of Arbitrary Length

GRACE and CHAMP data are typically analyzed in batches of 1 month and 3 months (in the sense of a moving average of 1 month), respectively. From the viewpoint of consistency, the parameter adjustment (primarily 22,500 spherical harmonic gravity field coefficients in case of an upper bound for degree and order of 150) should be performed in one step taking into account all available instrument data (approximately 1,100,000 GPS and 500,000 K-Band range-rate observations per month). As this would require an enormous amount of memory, in practice the data are processed in daily batches and the corresponding normal equations are accumulated and solved.

This straightforward method has the drawback to produce daily initial states, namely positions and velocities of the satellites at the beginning of each day, as auxiliary parameters. Thus for 1 month, and for every satellite, we have some 30 positions and 30 velocities, both somewhat artificial, in addition to the original pool of parameters that enter the overall adjustment and, in the worst case, may distort it.

The remedy implemented is to eliminate those additional states in the final phase, when the daily normal equations are added up to the whole month, with the help of dedicated side constraints that emerge in a quite natural manner, as the position and the velocity of a given satellite at the end of a given day must coincide with the position and the velocity of that satellite at the beginning of the following day. The linear map that connects both is the solution of the homogenous variational equation, which is produced anyway as a by-product of the observation equations.

The basic idea of the method is sketched in Fig. 7. For the day number m, we have a 1-day normal equation of the form

$$C_m \xi_m = d_m.$$

Here ξ_m is the parameter vector of the given day, C_m is the normal equation matrix and d_m is its right hand side.

The solution vector may be interpreted as the minimum of the quadratic polynom in several variables

$$\xi \mapsto \xi^T C_m \xi - 2 d_m^T \xi + q_m$$

where q_m is the weighted mean square of the observation residuals. The connection between day number m and day number m+1 is established with an equation of the form

$$E_m \xi_{m+1} = F_m \xi_m + h_m$$

where E_m is that fragment of a unit matrix that picks out satellite positions and velocities from the overall parameter vector, and F_m contains the matrix of the partial derivatives of satellite positions and velocities at the end of day m with respect to the positions and velocities at the begin of day m. Figure 7 shows how the individual

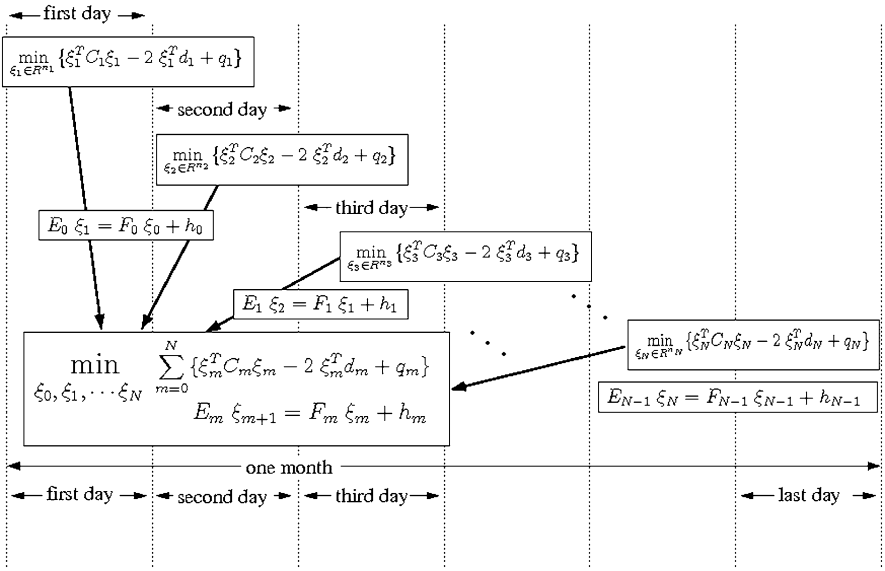

Fig. 7 Daily normal equations for 1 month of data are combined to a linear-quadratic optimization problem via suitable side constraints connecting adjacent days

adjustment problems for the sequence of the days in the month, together with the side constraints connecting adjacent days, are combined into one linear-quadratic optimization problem with a side constraint sequence in form of a linear dynamical system.

EPOS-OC and TOTSOL have been connected via suitable interfaces so that arcs of any length (up to approximately 1 month) with any number of non-linear parameters become feasible. The adjustment of such long arcs is based on a preliminary adjustment of short arcs with EPOS-OC, and then the parameters are corrected via linear relations between the arc-wise normal equations. These parameter corrections can be achieved by linear-quadratic optimization process outside of EPOS-OC. As the short a-priori arcs are independent, a massive parallel processing becomes feasible without having to change the source code of EPOS-OC (e.g. insertion of MPI instructions).

It is therefore now possible to process 1 giant arc of 1 month length or more, together with all non-linearities, in the disguise of a batch of daily satellite arcs for 1 month worth of data.

5 Conclusion

In the context of the recent re-processing of GRACE and CHAMP gravity field data, a thorough re-work of software and processing chains was performed, with a special stress on storage management and computation speed. First significant

improvements were already obtained by simply migrating the processing software from large shared-memory SunOS workstations to a cluster of high performance Linux PCs. A more efficient treatment of clock parameters that emerge in GPS processing allowed to increase the processing speed by a factor of up to two. Crucial here was the exploitation of certain structures in the normal equation matrix. As a side effect, the treatment of GPS measurements is now more or less similar to the treatment of non-GPS data. An already existing column-block parallel computation method to obtain normal equation matrices from design matrices has been augmented with a corresponding row-block parallel computation scheme. If those new features are fully exploited on the high-performance Linux cluster of GFZ, the gain in processing speed may reach a factor five to ten. A drawback is the need to have large intermediary storage space, to use a large number of computation nodes. The adopted method of choice to generate monthly gravity fields by stacking daily normal equations has been transformed, by adding appropriate side constraints, to a method to process satellite arcs of arbitrary lengths in a consistent manner.

Acknowledgment This is publication no. GEOTECH-1279 of the programme GEOTECHNOLOGIEN of BMBF and DFG, grant 03F0436A.

References

Flechtner F, Dahle Ch, Neumayer KH, König R, Kusche J (2008) Towards GFZ EIGEN-GRACE06S Gravity Field Time Series, AGU2008 Fall Meeting, San Francisco.

Förste C, Schmidt R, Stubenvoll R, Flechtner F, Meyer U, König R, Neumayer H, Biancale R, Lemoine JM, Bruinsma S, et al. (2008) The GeoForschungsZentrum Potsdam/Groupe de Recherche de Geodesie Spatiale satellite-only and combined gravity field models: EIGEN-GL04S1 and EIGEN-GL04C. J. Geod. 82(6), 331–346.

Healy SB, Wickert J, Michalak G, Schmidt T, Beyerle G (2007) Combined forecast impact of GRACE-A and CHAMP GPS radio occultation bending angle profiles. Atmos. Sci. Lett. 8(2), 43–50.

König R, Michalak G, Neumayer KH, Zhu S (2006) Remarks on CHAMP orbit products. In: Flury J, Rummel R, Reigber Ch, Rothacher M, Boedecker G, Schreiber U (eds.), Observation of the Earth System from Space, Springer, Berlin Heidelberg, pp. 17–26.

König R, Zhu S, Reigber Ch, Neumayer KH, Meixner H, Galas R, Baustert G, Schwintzer P (2002) CHAMP rapid orbit determination of GPS atmospheric limb sounding. Adv. Space Res. 30(2), 289–293.

Zhu S, Reigber Ch, König R (2004) Integrated adjustment of CHAMP, GRACE and GPS data. J. Geod. 78(1–2), 103–108.

Part II
GRACE

Improved GRACE Level-1 and Level-2 Products and Their Validation by Ocean Bottom Pressure

Frank Flechtner

1 Introduction

At the end of last century tracking data from some tens of satellites at different altitudes and orbit inclinations with various observation techniques (e.g. Doppler, SLR, PRARE or Doris) covering almost about three decades had to be used to improve our knowledge on Earth's gravity field. While this "conventional" strategy has provided useful information on the static and long wavelength field, these models have insufficient accuracy and spatial and temporal resolution to support a wide range of geophysical applications. The limitations are due to the attenuation of the gravitational signal with altitude, the inhomogeneous and sparse tracking data quality and global coverage as well as the difficulties in modeling the non-gravitational forces for most of the satellites.

With the German CHAMP (CHAllenging Mini-satellite Payload) mission, launched in 2000, for the first time a dedicated configuration has been realized to solve the afore mentioned problems: a satellite flying on a low and near-polar orbit carrying an on-board accelerometer and a GPS receiver for continuous, simultaneous precise tracking of up to 10 high-orbiting GPS satellites. These characteristics led to a break-through in the determination of the long-wavelength gravitational field already from a limited amount of mission data (Reigber et al., 2002).

It was noted already decades ago by Wolff (1969) that the intersatellite signal between a pair of satellites orbiting the Earth in the same orbit plane has significant information on the medium to shorter wavelength components of the Earth's gravitational field and, if this relative motion can be measured with sufficient accuracy, this approach will provide significant improvement in the gravity field modeling. This mission concept was proposed for the early GRAVSAT experiment by US scientists (Fischell and Pisacane, 1978) and the SLALOM mission in Europe (Reigber, 1978). Both of these experiment proposals as well as the follow-on US Geopotential

F. Flechtner (✉)
Helmholtz Centre Potsdam, GFZ German Research Centre for Geosciences,
Department 1: Geodesy and Remote Sensing, Telegrafenberg, 14473 Potsdam, Germany
e-mail: frank.flechtner@gfz-potsdam.de

F. Flechtner et al. (eds.), *System Earth via Geodetic-Geophysical Space Techniques*,
Advanced Technologies in Earth Sciences, DOI 10.1007/978-3-642-10228-8_8,

Research Mission GRM and the European POPSAT and BRIDGE mission proposals were not successful in being accepted for funding. The break-through came with the acceptance of the Gravity Recovery and Climate Experiment (GRACE) mission, proposed as a joint US–German partnership mission (Tapley and Reigber, 2001) within NASA's Earth System Science Pathfinder (ESSP) program.

2 The GRACE Mission Configuration and Key Instrumentation

The GRACE mission is a first realization of the so-called Satellite-to-Satellite Tracking concept in the low-low mode (low-low SST). The basic idea is to trace the spatio-temporal gravity field with an increased sensitivity by means of micrometer-precise inter-satellite range respectively range-rate observations of two co-planar orbiting satellites. As the two satellites move along their common orbit separated by a mean inter-satellite distance of approximately 220 km the relative motion of the spacecrafts, visible as continuous variations in the measured range and range-rate, respectively, is proportional to the differences of the gravity accelerations felt by each satellite at its individual position. Exploiting these differential observations, corrected for contributions from non-conservative forces, the underlying gravity field can be derived with high resolution and accuracy. Onboard the GRACE satellites such low-low SST measurements are realized by means of a microwave radio link using two frequencies in the K/Ka-band (therefore labeled K-Band-Instrument) providing dual one-way range observations. To allow for a detection of the gravity signals in the inter-satellite data well below the micron level the GRACE satellites are placed into a low orbit (initial altitude $\approx$ 500 km, no ground track control respectively natural orbit decay due to drag forces) and to yield a global coverage an almost polar inclination of 89.5° has been selected.

The absolute positioning of the spacecrafts, required for a precise referencing of the inter-satellite observations with respect to an Earth fixed frame, is provided by a space-proofed multi-channel, two-frequency GPS receiver onboard each GRACE satellite as well as by two star camera assemblies for the determination of the absolute and relative orientation of the observations in space. For the consideration of non-conservative components in the inter-satellite data each GRACE satellite is equipped with a capacitive SuperSTAR accelerometer with ten times better accuracy than the CHAMP STAR instrument. Located precisely in the center of mass of each satellite (offset better than 100 μm) the accelerometer measures the three dimensional vectors of the non-conservative forces (originating from air drag and solar and Earth radiation pressure acting on the individual satellite) which can be used to remove the non-gravitational signal components from the observed range and range-rate data. Finally, a laser retro-reflector (LRR) is placed at the nadir-looking panel of each GRACE spacecraft. The independent mm-cm precise laser ranging data from the ground station network of the International Laser Ranging Service (ILRS) is used for the verification respectively calibration of the prime microwave-based

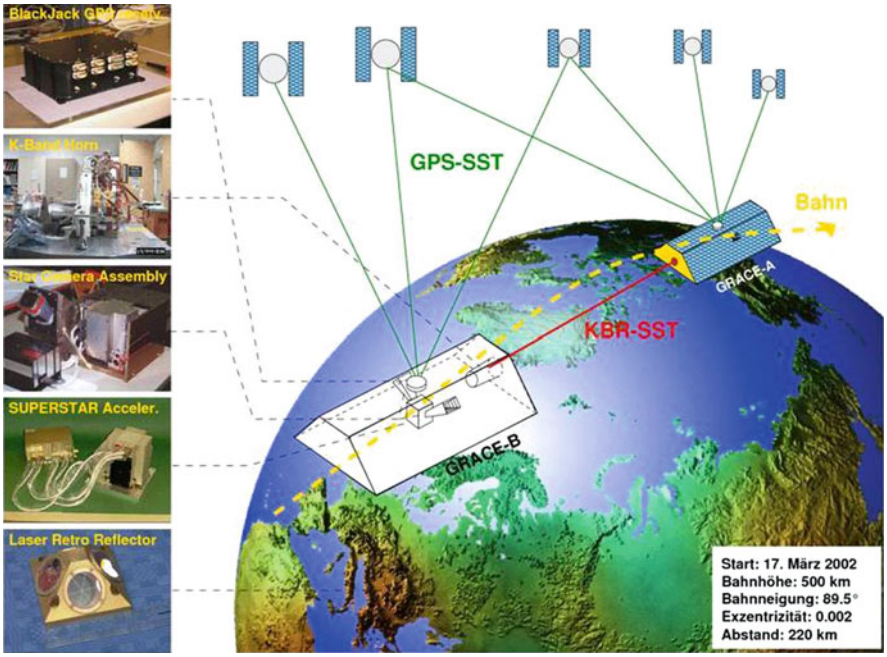

Fig. 1 GRACE mission configuration and key instrumentation. GPS-SST = satellite-to-satellite tracking based on GPS observations between the onboard GPS receivers and the GPS sender satellites, KBR-SST = K-band range and range-rate satellite-to-satellite tracking between the two GRACE satellites orbiting in a low (500 km), almost polar (89.5°) co-planar orbit. Until mid of December 2005 the leading satellite was the spacecraft labeled GRACE-A and the trailing one was GRACE-B. Then, the order has been changed in order to avoid any possible loss of thermal control over the K-band horns which would affect the ranging signal quality, making GRACE-B the leading and GRACE-A the trailing satellite. The orbit altitude is not kept fixed and therefore decreases due to air drag with an average rate of about 2.7 km/year (from Schmidt et al., 2007)

tracking instruments, i.e. the GPS receivers and the K-band instrument. Figure 1 displays a sketch of the GRACE mission configuration and key instrumentation.

3 The GRACE Level-1 and Level-2 Products

The Jet Propulsion Laboratory (JPL) in Pasadena is responsible for the GRACE Level-1A and Level-1B instrument data processing. Level-1A data products are the result of a non-destructive processing applied to the raw Level-0 data which are routinely downloaded from the two satellites to the ground stations in Neustrelitz and Weilheim in Germany as well as to Ny Alesund on Spitsbergen. In this initial step the binary encoded measurements are converted to engineering units and time tagged to the respective satellite receiver clock time. Quality control flags are added and the data is reformatted for further processing. The Level-1B data products are the result of an irreversible processing applied to the Level-1A data.

Here, the data are correctly time-tagged to GPS time and the data sample rate is reduced by appropriate filtering from e.g. 10 to 0.2 Hz. The German Research Centre for Geosciences in Potsdam (GFZ) is responsible for the routine provision of the AOD Level-1B product to take into account short-term non-tidal atmospheric and oceanic mass variations in the monthly gravity field determination process. This process is called "de-aliasing" and is necessary to avoid the mapping of signal from higher frequencies onto the lower frequencies due to undersampling. Further information on the GRACE gravity sensor system and Level-1 instrument data processing is given in chapter "The GRACE Gravity Sensor System" by Frommknecht and Schlicht, this issue. The chapters of Flechtner et al. and Dobslaw and Thomas provide further insight in the de-aliasing process.

The Level-1B instrument data are then used by the GRACE Science Data System (SDS) teams at the Center for Space Research at the University of Austin (CSR), GFZ and JPL or at other processing centers such as the Institute for Geodesy and Geoinformation (IGG) of the University in Bonn or the Group de Recherches de Geodesie Spatial (GRGS) in Toulouse to derive GRACE Level-2 gravity field products. These products comprise time-series of monthly or even sub-monthly sets of spherical harmonic coefficients and a corresponding long-term mean field and are provided to the user community by the GRACE archives ISDC (Integrated System and Data Center) and PODACC (Physical Oceanography Distributed Active Archive Center) at GFZ and JPL, respectively (see Fig. 2).

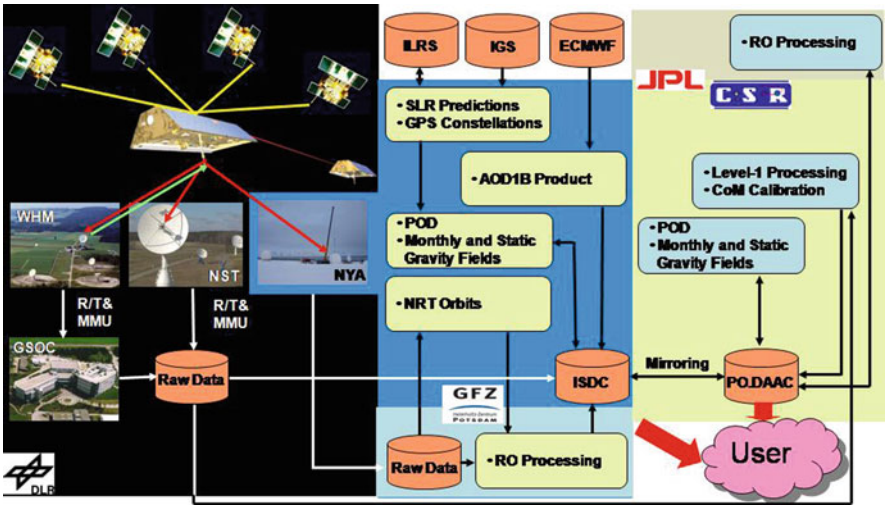

Fig. 2 Coarse GRACE SDS data flow

Since mission launch several model releases have been made public while the length of the time series has been extended and the quality of these models has been significantly improved from release to release through several complete iterations and reprocessing of the steadily increasing GRACE data set. At GFZ and IGG nearly the complete GRACE mission data have recently been reprocessed based

on updated background models and processing standards. These time series are called EIGEN-GRACE05S (chapter "The Release 04 CHAMP and GRACE EIGEN Gravity Field Models" by Flechtner et al., this issue) and ITG-GRACE03S (chapter "ITG-GRACE: Global Static and Temporal Gravity Field Models from GRACE Data" by Mayer-Gürr et al., this issue), respectively.

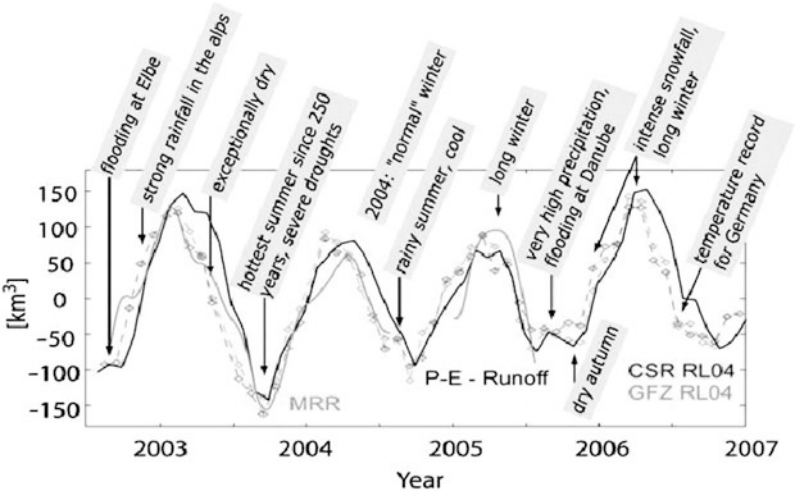

Fig. 3 Inter-annual water mass variations and extremes in Central Europe from GRACE, based on global spherical harmonics from GFZ (*grey dots*), CSR (*black dots*) and a regional multi-resolution representation (*grey line*), and independent data from a combined atmospheric-terrestrial water balance (*black line*) (from Seitz et al., 2008)

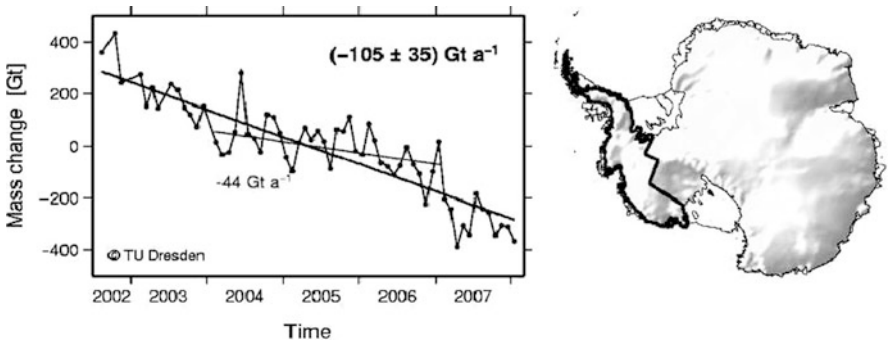

Fig. 4 GRACE-based estimate of ice mass changes in a part of the Antarctic Ice Sheet (from Horwath and Dietrich, 2009). The considered region (see boundary in the map on the *right*) is responsible for the bulk of present Antarctic ice mass changes. Monthly changes (*dotted curve*) are derived from GFZ Release 04 monthly solutions for the period of 08/2002 to 01/2008. A model of glacial isostatic adjustment (GIA) (Ivins and James, 2005) is reduced. The overall trend of –105 Gt/a corresponds to a +0.30 mm/a eustatic seal level contribution. The given uncertainty of 35 Gt/a results from a comprehensive error assessment including the GIA correction uncertainty. To illustrate the need for a long-term mass monitoring the trend over a selected 3-year section is shown as well

In principle, GRACE observes the integrated effect of the total gravity field (static and time-varying), which is composed by many sources in the Earth system. For the interpretation of the residual (monthly minus long-term mean) signal various known time-variable gravity effects are already reduced from the GRACE data in the course of the adjustment process in order to reduce the signal size of the gravity observations. These comprise e.g. the gravity signals induced by the third-body accelerations on the satellites and the Earth due to the gravitational pull from the Sun, the Moon and planets, gravity variations from short-term (non-tidal) mass redistributions in the atmosphere and the oceans (the AOD1B product), secular gravity changes in selected long-wavelength gravity coefficients due to the global isostatic adjustment as well as the pole tide effect on the solid Earth and the oceans caused by the variations in the Earth's rotation. Finally the luni-solar tides of the solid Earth, the oceans and the atmosphere (inclusive the indirect effects from loading and deformation due to the change in the mass distribution) are corrected by appropriate models. Consequently, the residual gravity signal derived from the GRACE monthly models should mainly represent unmodeled seasonal to secular time-varying geophysical and climatologically driven phenomena in the system Earth such as the continental hydrological cycle (see Fig. 3), post glacial rebound or ice mass loss of the polar and Greenland ice caps (see Fig. 4) and inland glaciers. Until now, the mission's sensitivity to trace such mass motion signals has been widely demonstrated. A list of (non-exhaustive) GRACE-related publications covering at the time of writing about 450 papers is collected at http://www.gfz-potsdam.de/pb1/op/grace (follow link "Publications").

4 Main Results of the BMBF/DFG Project "GRACE"

In 2005 the available GRACE-only gravity field models already showed a substantial improvement in consistency and accuracy when compared to the existing pre-GRACE satellite-only solutions such as GRIM-5S1 (Biancale et al., 2000) or EIGEN-CHAMP03S (Reigber et al., 2005). For example, time series of gravity changes induced by the global seasonal hydrological cycle derived from EIGEN-GRACE02S showed a high correlation compared to predictions derived from hydrological models (see contributions from project TIVAGAM, this issue). Nevertheless, as shown in chapter "The Release 04 CHAMP and GRACE EIGEN Gravity Field Models" by Flechtner et al. (this issue), the 2005 performance was still significantly below (approximately a factor of 18) that projected by simulation studies before launch (Kim, 2000). Additionally the GRACE solutions show typical meridional-oriented spurious distortions ("stripes"). This geographically correlated systematic effects are most likely due to the non-isotropic data sampling due to the GRACE North-South oriented orbital ground tracks and the subsequent pure along-track sampling of the K-band SST instrument data. This degradation and the not yet reached baseline accuracy has a significant effect on all higher-level scientific products derived (separated) from GRACE gravity field solutions such as ice melting in

the Polar Regions, derivation of surface and deep ocean currents or estimation of ocean mass for sea level rise analysis.

Besides weak algorithms (e.g. the numerical integration of the GRACE satellite orbits or the ambiguity fixing of the GPS ground and LEO observables) and methods (such as the two-step approach to solve the GPS satellite orbits and clocks first which then serve as a fixed reference frame in the following gravity field adjustment process) applied in the gravity field determination process, three principal causes have been identified. First, the accuracy of the GRACE instruments could be below its specification or the processing strategy to derive calibrated instrument from raw data could not be optimal. Second, deficiencies in the background models, such as the short-term non-tidal atmosphere and ocean mass variations or the ocean tides, could alias into the solutions (Wünsch et al., 2005). Third, a wrong or insufficient parameterization of the GRACE K-band range-rate or accelerometer observations could have an influence on the quality of the derived gravity field models.

Additionally, the global gravity field solutions based on the adjustment of globally defined spherical harmonic coefficients could show deficiencies which may be reduced by dedicated regional modeling derived by alternative mathematical representations. Finally, the validation of these global and regional GRACE gravity models and the benefit of the applied improvements is not trivial as no global data sets with comparable resolution and accuracy are available. Therefore, beside standard methods such as the comparison with an oceanic geoid (derived from a mean sea level model and a dynamic ocean topography) or gravity anomalies over land a validation with globally distributed in-situ ocean bottom pressure (OBP) data was suggested.

To answer the above questions and to develop improvements for the GRACE Level-1 instrument data and Level-2 gravity model products a consortium build by GFZ, IGG, the Institute for Astronomical and Physical Geodesy of the Technical University of Munich (IAPG), the Institute for Planetary Geodesy of the University of Dresden (IPG), and the Alfred-Wegener-Institute in Bremerhaven (AWI) has been formed. The tasks and results of the project "Improved GRACE Level-1 and Level-2 products and their validation by ocean bottom pressure" funded within the programme "Geotechnologien" of BMBF (Ministry for Education and Research) and DFG (German Research Community) under grant 03F0423 are described in detail in the following chapters and can be summarized as follows.

The GRACE gravity sensor system, comprised by the low-low SST K-band tracking system, the 3-axis accelerometer, the star camera system and the GPS receiver has been investigated and realistic error measures for the Level-1B instrument data have been derived by analysis of real Level-1A and Level-1B data. It turned out that the GRACE instrument performance generally agrees within its specification and that all suggested data processing model enhancements currently do not yield to improvements in the corresponding alternative gravity field models (see chapter "The GRACE Gravity Sensor System" by Frommknecht and Schlicht, this issue).

The background model to correct for short-term atmospheric and oceanic mass variations (AOD1B) has been analyzed in detail. As the barotropic model PPHA

(developed by Pacanowski, Ponte, Hirose, and Ali) used for release (RL) 01 and 02 showed some deficiencies such as the exclusion of the Arctic ocean or less variance in ocean bottom pressure than other comparable models the latest AOD1B versions RL03 and RL04 are based on the baroclinic Ocean Model for Circulation and Tides (OMCT). For the operational RL04 processing the model configuration is based on an improved bathymetry and the total ocean mass has been held artificially constant at each time step as investigations have shown that the impact of freshwater fluxes is generally small on time scales less than 1 month. The increase of the temporal resolution from 6 to 3 h using European Center for Medium-range Weather Forecast (ECMWF) forecast instead of analysis data has shown no improvements implying that the S_2 air tide is corrected for properly. Even the error caused by complete neglecting of the S_2 air tide is below the current GRACE error level which was confirmed by a simulation study (see below). For a consistent combination of SLR derived low degree harmonics with GRACE gravity models the AOD1B model time series has been reprocessed back to 1976 (see chapter "The Release 04 CHAMP and GRACE EIGEN Gravity Field Models" by Flechtner et al., this issue).

A simulation study taking into account real GRACE instrument data errors from the GRACE gravity sensor system and various background model uncertainties has been performed. The results (chapter "Global Gravity Fields from Simulated Level-1 GRACE Data" by Meyer et al., this issue) point to inaccuracies in the applied FES2004 ocean tide model which may be partly accounted for in the future by parallel estimation of ocean tide constituents (Bosch et al., 2009). Additionally it was found that the accelerometer noise is not treated sufficiently by the current instrument parameterization. A solution could be a more dense parameterization or to shorten the arc length (currently 24 h at the GRACE Science Data System centers) for GRACE data analysis to avoid noise accumulation over time.

In an alternative approach – compared to the standard GRACE Science Data System (SDS) spherical harmonic representation – the model ITG-GRACE03S is parameterized by continuous base functions in the time domain (chapter "ITG-GRACE: Global Static and Temporal Gravity Field Models from GRACE Data" by Mayer-Gürr et al., this issue). The physical model of the gravity field is based on Newton's equation of motion, formulated as a boundary value problem in the form of a Fredholm type integral equation. The principle characteristic of this method is the use of short arcs of the satellite orbits in order to avoid accumulation of instrument noise (as suggested by the simulation study) and a rigorous consideration of correlations between the range observations in the subsequent adjustment process.

In-situ ocean bottom pressure (OBP) data time series have been collected from various institutes and fed into an OBP data base at AWI. As of February 2009 the data base comprises 168 data sets from 152 deployments at 100 different locations. These time series have been compared by means of a correlation analysis with various SDS and non-SDS GRACE gravity field time series showing that the – compared to hydrological mass variations – much smaller OBP signal is generally captured quite well by all latest GRACE gravity models especially at high latitude sites with comparatively large OBP signals (up to 5 cm equivalent water height,

EQWH) and dense satellite ground track pattern. In contrast, some other regions such as the tropical Atlantic, the coastal Northern Pacific or the Drake Passage show remarkably large differences between the GRACE solutions and the in-situ data. Here, the in-situ OBP variability is close to the current GRACE accuracy limit of about 1 cm EQWH at spatial scales of some 100 km. Possible reasons for this may be due to differences in the captured spatial scales of the point-wise in-situ and the area-averaged GRACE data, deficiencies in the tidal and non-tidal background models or measurement and processing errors in the in-situ and GRACE OBP data. Details are given in chapter "Validation of GRACE Gravity Fields by In-Situ Data of Ocean Bottom Pressure" by Macrander et al., this issue.

Finally, the representation of the transport variability of the Antarctic Circumpolar Current (ACC) as derived from GRACE gravity field models and the Finite Element Sea Ice-Ocean (FESOM) model has been investigated to gain further insight into the capability of GRACE to derive real ocean mass phenomena (see chapter "Antarctic Circumpolar Current Transport Variability in GRACE Gravity Solutions and Numerical Ocean Model Simulations" by Böning et al., this issue). Simulations with FESOM have shown that a part (more than 50%) of the ACC transport variability can be explained by OBP anomalies. A major outcome of the study was that the GRACE gravity models, which can be connected to OBP fluctuations (see above) and thus also to geostrophic transport variations, show a high correlation (>0.75) for the annual and semi-annual components as derived with FESOM.

This and other related results give trust in the consistency and accuracy of the current GRACE gravity field models. Also the "factor above the GRACE baseline accuracy" could be reduced within this project by about 15% from 18 to 15. Nevertheless, as mentioned before, there is still room for improvement. Especially the background models could be further enhanced by adding seasonal variations derived from GRACE or hydrological models, by updated ocean tide models or by inclusion of uncertainties of meteorological data used to derive the AOD1B product. Also an integrated adjustment of ground, LEO and GPS satellite observation data seems to be promising.

References

Biancale R, Balmino G, Lemoine JM, Marty JC, Moynot B, Barlier F, Exertier P, Laurain P, Gegout P, Schwintzer P, et al. (2000) A new global earth's gravity field model from satellite orbit perturbations: GRIM5-S1. Geophys. Res. Lett. 27, 3611–3614.

Bosch W, Savcenko R, Flechtner F, Dahle Ch, Mayer-Gürr T, Stammer D, Taguchi E, Ilk H (2009) Residual ocean tide signals from satellite altimetry, GRACE gravity fields, and hydrodynamic modeling. Geophys. J. Int. 178(3), 1185–1192, doi: 10.1111/j.1365-246X.2009.04281.x.

Fischell RE, Pisacane VL (1978) A drag-free low-low satellite system for improved gravity field measurements. Proceedings of the 9th GEOP conference, Department of Geod. Sci. Rep. 280, Ohio State University, Columbus, USA, pp. 213–220.

Horwath M, Dietrich R (2009) Signal and error in mass change inferences from GRACE: The case of Antarctica. Geophys. J. Int., doi:10.1111/j.1365-246X.2009.04139.x.

Ivins ER, James TS (2005) Antarctic glacial isostatic adjustment: A new assessment. Antarctic Sci. 17(4), 541–553.

Reigber Ch (1978) Improvements of the gravity field from satellite techniques as proposed to the European Space Agency. Proceedings of the 9th GEOP conference, Department of Geod. Sci. Rep. 280, Ohio State University, Columbus, USA, pp. 221–232.

Reigber Ch, Balmino G, Schwintzer P, Biancale R, Bode A, Lemoine JM, König R, Loyer S, Neumayer KH, Marty JC, et al. (2002) A high-quality global gravity field model from CHAMP GPS tracking data and accelerometry (EIGEN-1S). Geophys. Res. Lett. 29(14), doi: 10.1029/2002GL015064.

Reigber Ch, Jochmann H, Wünsch J, Petrovic S, Schwintzer P, Barthelmes F, Neumayer KH, König R, Förste Ch, Balmino G, et al. (2005) Earth gravity field and seasonal variability from CHAMP. In: Reigber Ch, Lühr H, Schwintzer P, Wickert J. (eds.), Earth Observation with CHAMP – Results from Three Years in Orbit, Springer, Berlin, pp. 25–30.

Schmidt R, Meyer U, Dahle Ch, Flechtner F, Kusche J (2007) Monthly and weekly EIGEN-GRACE05S gravity field solutions for monitoring of mass variations in the earth system. In: Benveniste J, et al. (eds.), Proceedings of the Second Space for Hydrology Workshop "Surface Water Storage and Runoff: Modeling, In-Situ data and Remote Sensing", 12–14 November 2007, ESA Publication WPP-280, Geneva, Switzerland.

Seitz F, Schmidt M, Shum CK (2008) Signals of extreme weather conditions in Central Europe in GRACE 4-D hydrological mass variations. Earth Planet. Sci. Lett. 268(1–2), 165–170.

Tapley BD, Reigber Ch (2001) The GRACE mission: Status and future plans. EOS Trans. AGU 82(47), Fall Meet. Suppl. G41, C-02.

Wolff M (1969) Direct measurements of the earth's gravitational potential using a satellite pair. J. Geophys. Res. 74(22), 5295–5300.

Wünsch J, Schwintzer P, Petrovic S (2005) Comparison of Two Different Ocean Tide Models Especially with Respect to the GRACE Satellite Mission. Scientific Technical Report STR05/08, GeoForschungsZentrum, Potsdam.

The GRACE Gravity Sensor System

Björn Frommknecht and Anja Schlicht

1 GRACE Sensor System

Since the gravity field modelling by orbit distortion of a proof mass is limited today to around 1 cm by GPS tracking, a better insight in the variations of the gravity field in time and space can be achieved by taking two proof masses following each other in the same orbit and measuring the differences in the orbit distortion via a tracking link. In the case of GRACE it is a dual one way microwave link working with two frequencies in the K/Ka band. So both satellites carry a K-band ranging equipment consisting of an ultra stable oscillator (USO), a K-band horn, and a phase sensitive electronic device (KBR assembly). As the orbiters do not compensate for atmospheric friction they have an accelerometer on board. The centre of mass (CoM) of the spacecraft can be regulated with a trim assembly (MTM) and corresponding electronics (MTE) to ensure that the accelerometer is always exactly in the centre of mass. The GPS navigation antenna is essential for exact orbit determination and the star cameras (SCA) measure the orientation of the satellite, which is regulated by magnetic torquers (MTQ) as well as cold gas thrusters.

Figure 1 shows the sensor location within one GRACE satellite. The accelerometer is in the CoM and the star sensor heads and GPS antenna are near by. The gas tanks for the cold gas thrusters are placed symmetrically around and at the front of the satellite, the equipment for the K-band ranging system can be found. The back of the satellite holds the on-board data handling unit, the radio frequency and electronics assembly and the GPS occultation antenna.

In the following, we give a short overview of the sensors that are relevant for the gravity field determination.

B. Frommknecht (✉)
RHEA S.A., Louvain La Neuve, Belgium; ESA/ESRIN, 00040 Frascati, Italy,
Institut für Astronomische und Physikalische Geodäsie (IAPG), Technische Universität München, 80333 München, Germany
e-mail: bjorn.frommknecht@esa.int

F. Flechtner et al. (eds.), *System Earth via Geodetic-Geophysical Space Techniques*, Advanced Technologies in Earth Sciences, DOI 10.1007/978-3-642-10228-8_9,

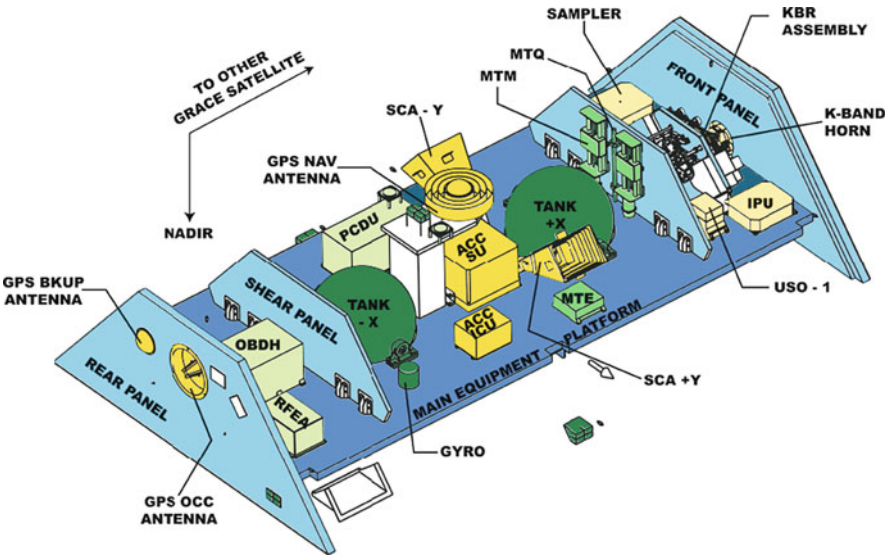

Fig. 1 Detailed view of the different sensor systems and their location inside the satellites, figure from www.gfz-potsdam.de

1.1 The Accelerometer

In a satellite in free fall there is one point where gravity is exactly compensated by centrifugal force; this is the centre of mass (CoM). A levitating proof mass put in this point does not move from its position. But mostly a satellite is not really in free fall as frictional forces like air drag, solar wind and earth albedo tend to slowdown the orbiter, In this case, the levitating proof mass will leave the CoM. Measuring the force needed to keep the proof mass in the centre shows up for the non-gravitational forces acting on the satellite.

The SuperSTAR accelerometer is a three-axis capacitive accelerometer. There are two high-sensitive axes and one less-sensitive axis for testing the instrument on Earth. The accelerometer is orientated in the way that the less-sensitive axis goes insight with cross track direction. The proof mass is a gold-coated titan cube, its size is about $40 \times 40 \times 10$ mm^3, its mass is 70 g. In principle the accelerometer consists of two parts: a position detector, that detects the position of the proof mass inside the cage and the servo mechanism that keeps the proof mass at its nominal position. The electrodes are arranged in a way that the rotation of the proof mass can be detected as well (see Fig. 2).

The accelerometer specifications are summarized in Table 1.

1.1.1 Logical Model

Figure 3 shows the schematic design for one axis. The proof mass is located between two electrodes, charged with voltage $+V$ and $-V$, respectively. The proof mass is

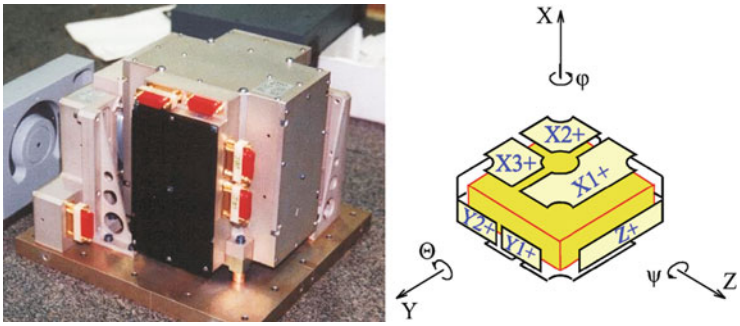

Fig. 2 GRACE accelerometer

Table 1 SuperSTAR accelerometer specifications

Axis (SRF)	Range	Accuracy
x	$\pm 5 \cdot 10^{-5}$ m/s^2	$1 \cdot 10^{-10}$ m/s^2/$\sqrt{\text{Hz}}$
y	$\pm 5 \cdot 10^{-4}$ m/s^2	$1 \cdot 10^{-9}$ m/s^2/$\sqrt{\text{Hz}}$
z	$\pm 5 \cdot 10^{-5}$ m/s^2	$1 \cdot 10^{-10}$ m/s^2/$\sqrt{\text{Hz}}$
$\dot{\omega}_x$	$\pm 1 \cdot 10^{-2}$ rad/s^2	$5 \cdot 10^{-6}$ rad/s^2/$\sqrt{\text{Hz}}$
$\dot{\omega}_y$	$\pm 1 \cdot 10^{-3}$ rad/s^2	$2 \cdot 10^{-7}$ rad/s^2/$\sqrt{\text{Hz}}$
$\dot{\omega}_z$	$\pm 1 \cdot 10^{-2}$ rad/s^2	$5 \cdot 10^{-6}$ rad/s^2/$\sqrt{\text{Hz}}$

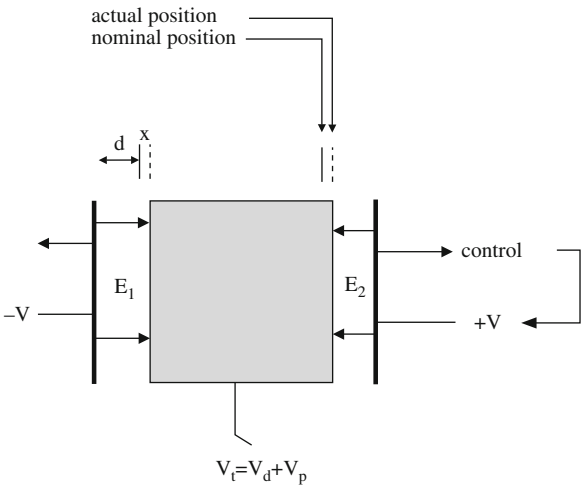

Fig. 3 Logical concept of the accelerometer

charged with a voltage V_t consisting of the polarization voltage V_p and an alternating current, the detection voltage V_d:

$$V_t = V_p + V_d(t). \tag{1}$$

The frequency of the detection voltage is about 100 kHz, too high to affect the motion of the proof mass. The nominal position of the proof mass is in the middle between the electrodes, with no offset, i.e. $x = 0$. Between the walls of the proof mass and the electrodes, there are two electric fields E_1 and E_2 are forming. If V and V_t are assumed to be positive and constant, the proof mass will start to move towards the electrode charged with $-V$. The gap between proof mass and electrode reduces, increasing the capacitance, the electric field and the attraction. In this configuration the accelerometer system is inherently unstable and servo control of the proof mass motion is mandatory. A capacitive detector measures the position of the proof mass by comparing the capacitances. A feedback loop including a PID (*P*roportional *I*ntegrative *D*erivative) controller determines the control voltage V and keeps the proof mass motionless at its nominal position. This voltage V is the measure for the acceleration of the satellite due to non-conservative forces.

1.1.2 Accelerometer Noise Model

A detailed derivation of the noise model can be found in Frommknecht (2009) and Josselin et al. (1999). The accelerometer instrument noise rises at low frequencies with a rate of $1/\sqrt{f}$ in the root PSD. At high frequencies, the noise is white at a level of $1{\cdot}10^{-9}$ m/s^2/$\sqrt{\text{Hz}}$ for the less-sensitive axis and $1{\cdot}10^{-10}$ m/s^2/$\sqrt{\text{Hz}}$ for the sensitive axes, cf. Fig. 4.

1.2 The Star Sensor

The purpose of the star tracker is to determine the absolute orientation of the satellite with respect to an inertial system. In order to accomplish this task, digital star images taken by each of the two sensor heads are processed. The observed stellar constellations are compared to stellar maps and catalogues (e.g. the HIPPARCOS catalogue) inside the processing unit by means of image processing. The derived orientation is the orientation with respect to the reference frame of the used star catalogue (Fig. 5). The star sensor or Advanced Stellar Compass (ASC) used on the GRACE satellites is identical to the star sensor used for the CHAMP mission. It is manufactured by the department of automation of the Technical University of Denmark (DTU). It was used and tested for the missions Teamsat, ASTRID 2 und ørsted, see Jørgenson (1999). The database contains 13,000 of the brightest stars from the HIPPARCOS catalogue. An orientation based on star positions deviating more than 10 arcs from the star catalogue data is rejected. The typical duration of an attitude acquisition is about 200 ms. Attitude is given as a set of quaternions.

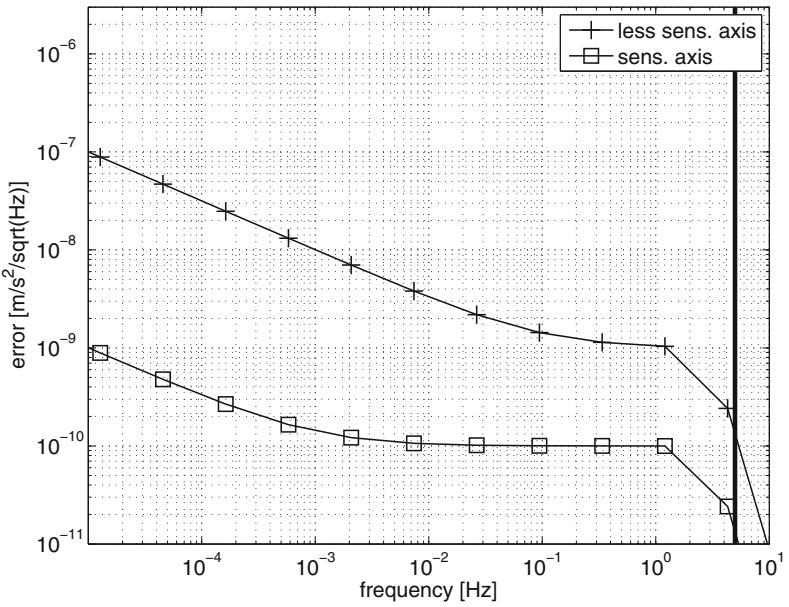

Fig. 4 Accelerometer noise model showing the root PSD of the error

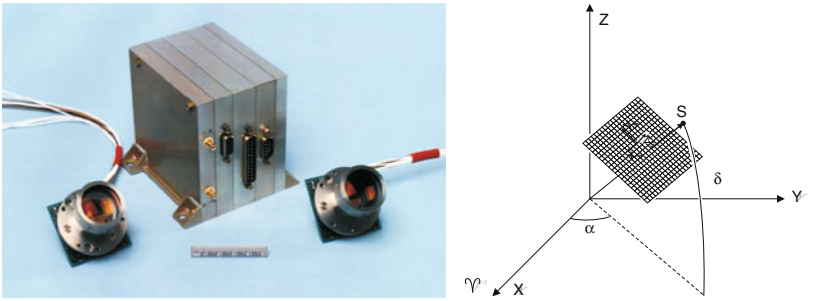

Fig. 5 Star sensor and its inertial system (X,Y,Z) oriented to the vernal equinox. The position of a star S is given in right ascension α and declination δ

1.2.1 Star Sensor Noise Model

A detailed description and derivation can be found in Wertz (1991) and Frommknecht (2009).

The star sensor measurement error contributors are:

- The position errors of the stars positions in the star catalogue,
- the error caused by the optical system,
- the error caused by the image digitalization.

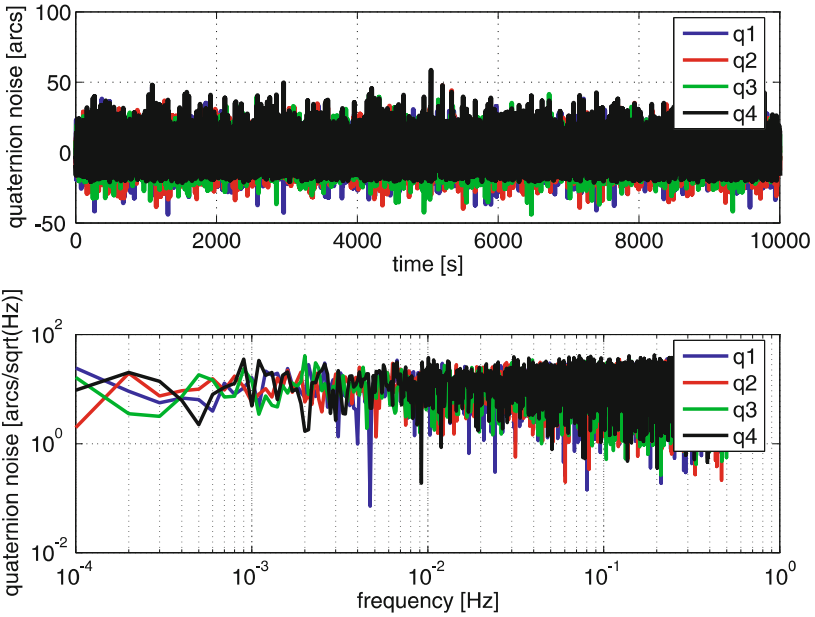

Fig. 6 Star sensor noise in the time (*upper*) and spectral (*lower*) domain

Table 2 Standard deviation of quaternion components

Component	s (arcs)
q4	11
q1	9
q2	9
q3	9

The star sensor quaternion noise is assumed to be white; it is about 11 arcs for the rotation angle and about 9 arcs for the rotation axis vector components, see Fig. 6 and Table 2.

1.3 The GPS Receiver

On both GRACE satellites a space approved Black-Jack *G*lobal *P*ositioning *S*ystem (GPS) receiver is installed, see Fig. 7. In contrast to the K-band ranging system, the GPS receiver is a passive ranging system, i.e. it does no emit electromagnetic signals, it only receives them via the GPS antenna. The signal source are the GPS satellites. We will not give a detailed description of the GPS, the interested reader may consult (Rothacher, 2001), also for additional literature. We will not give a measurement model here, a detailed description is given in Rothacher (2001).

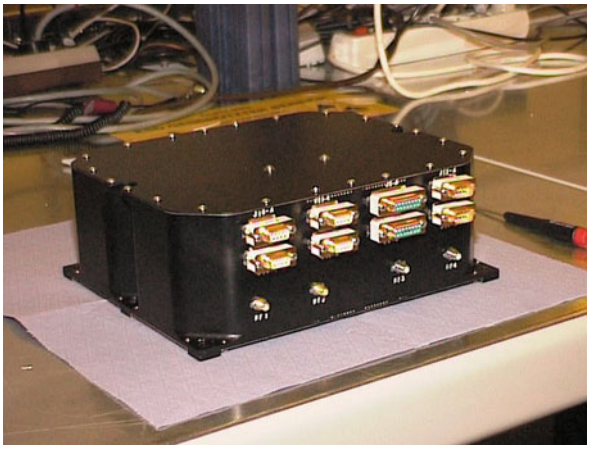

Fig. 7 GPS receiver

1.3.1 Error Model

The error model we will use for the data analysis is simple; we model the phase measurement error and the code measurement error as white noise of a certain power. The other error sources are neglected as they are not random but systematic, at least over short time intervals. During the real data analysis, only consecutive epochs, where the same satellite has been tracked, are used. The noise specifications are given in Table 3, cf. Stanton et al. (1998).

Table 3 GPS receiver measurement noise specification, from Stanton et al. (1998)

Observation type	Noise level 1σ (cm) 10 s sampling	Error ($\sqrt{\text{PSD}}$cm/s$^{2/}\sqrt{\text{Hz}}$)
Code measurements	100	400
Phase measurements	1	4

1.4 The K-Band Ranging System

The K-band ranging system (KBR) is the key instrument of the GRACE mission. A schematic overview is shown in Fig. 8. Each satellite is equipped with a horn used for transmission and reception of the intersatellite dual-band μ-wave signals at 24 GHz for K-band and 32 GHz for Ka-band. The horns are based on the type of feed horns used in JPL's Deep Space Network. The transmitted signals on the K- and Ka-band are sinusoidal. On each band there is a frequency offset between the two satellites signals of 0.5 MHz. The signals are generated by an ultra stable oscillator (USO). Upon reception the signals of each band are down-converted to 0.5 MHz using the transmitted signal of the same band as a reference. In the instrument processing unit (IPU) the phase is extracted and delivered to the on-board data handling (OBDH) computer at a nominal sample rate of 10 S/s.

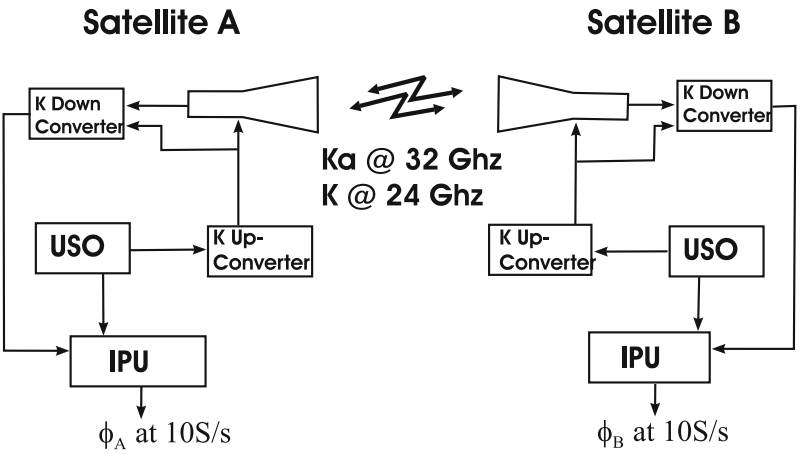

Fig. 8 K-Band microlink

1.4.1 Error Model

A detailed derivation of the KBR measurement error model can be found in Kim (2000), Thomas (1999), and Frommknecht (2009).

Figure 9 shows the KBR total noise expressed in m/$\sqrt{\text{Hz}}$. At low frequencies, the measurement error is determined by the error of the USO that generates the K-Band

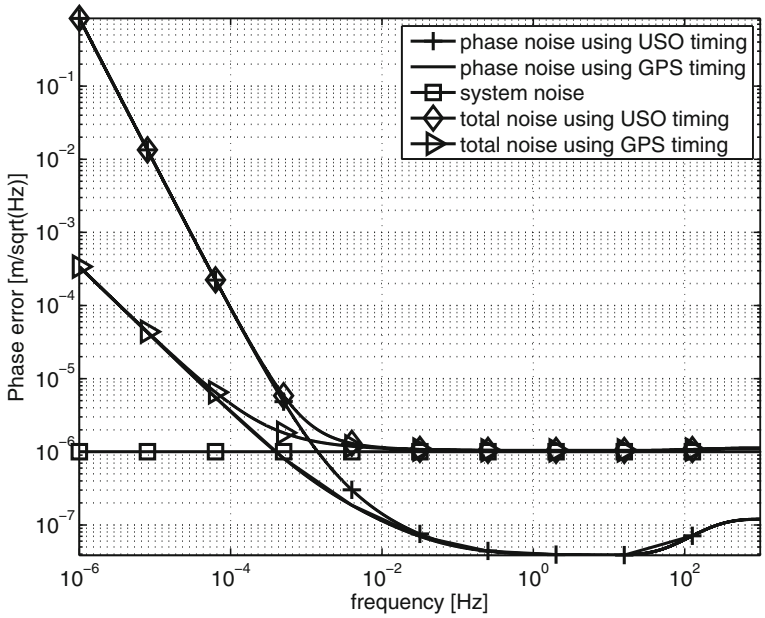

Fig. 9 KBR range total noise

measurement signal and rises at a rate of $1/f^2$. If the measurements on both satellites are synchronized using GPS timing, this error can be reduced. At high frequencies the measurement error is white at a level of about 1 $\mu m/\sqrt{Hz}$.

2 Sensor System Interaction

In Fig. 10 the interaction of the sensor system components among themselves and the environment of the GRACE satellites are shown. We start from the top. There are two kinds of forces that act on the satellite: the gravitational force G_A and then frictional forces F_A. G_A act on the centre of mass (CoM) of the satellite causing mostly linear accelerations (only small torques are caused by the gravity gradient). F_A acts on the centre of pressure (CoP) and can cause linear accelerations as well as rotational torques (M), if the CoP goes not insight with the CoM. The torques result in angular velocities (Ω) and angular accelerations ($\dot{\Omega}$), their magnitude depends on the inertia tensor (I_{ij}). Angular velocity and angular acceleration lead to a change in the orientation of the satellite, which is measured by the star sensors. The star sensor measurements are input to the attitude control system. It applies control torques via the cold gas thrusters and the magnetic torque rods.

The linear accelerations measured by the accelerometer are the sum of two components: linear accelerations acting on the satellite and the part due rotational accelerations and velocities influencing the measurements as the accelerometer is not exactly in the centre of mass. The measurements are downsampled as their

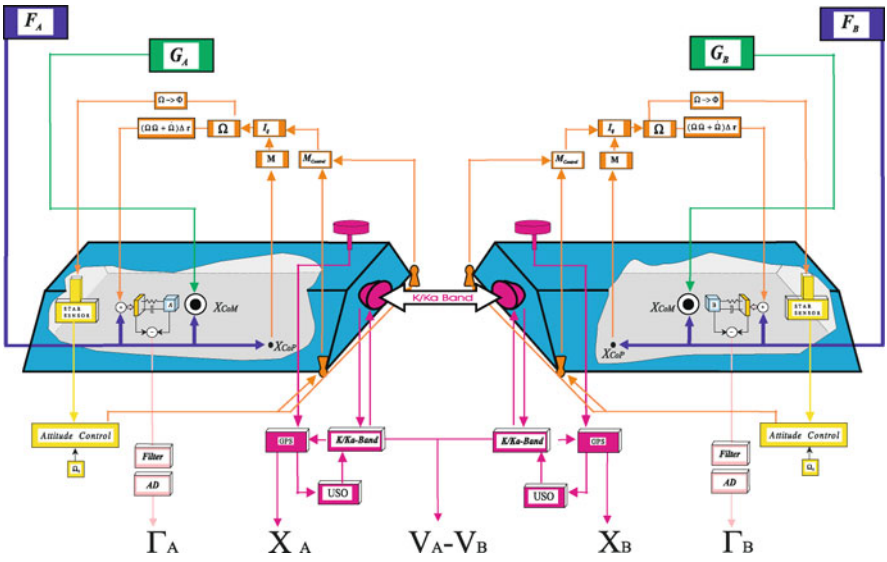

Fig. 10 Overview of the GRACE sensor system

bandwidth is limited, corresponding to a sampling rate of 10 Hz by the application of a low-pass filter and are converted from analogue to digital (Γ).

The position of the satellite (X) is measured by the GPS receiver with cm precession. Last but not least, the K-band system measures the differential range between the two GRACE satellites with μm precession. GPS and K-band measurements together provide differential range and range rates between the two GRACE satellites, caused by the difference in the geopotential ($V_A - V_B$).

3 Force Models

The motion of the GRACE satellites is determined by two kinds of forces acting on them: Gravitational forces and non-gravitational forces. In the following sections we give a brief overview of them.

3.1 Gravitational Forces

Concerning the acceleration of the satellites caused by gravitational forces, the acceleration caused by the Earth is strongest, followed by the acceleration caused by the Moon, the Sun, the indirect tides by the Sun and the Moon, the Ocean and Pole tides and the Frequency-dependent corrections to the solid Earth tides. An analysis in the frequency domain shows that the main power is at twice per revolution, as the satellites pass through the tidal ellipse. Only for the gravitational acceleration caused by the Earth, the main power is on once per revolution. Table 4 shows a comparison of the magnitude of the different effects.

3.2 Non-gravitational Forces

The non-gravitational forces acting on the satellites, directly affect the K-band measurement as differential accelerations. As for gravity field determination only the

Table 4 Gravitational forces

Source	Mean (m/s^2)	Power on twice per rev ($m/s^2/\sqrt{Hz}$)	σ (m/s^2)
Earth	8.4	$3 \cdot 10^{-2}$ (on 1 cpr)	$2 \cdot 10^{-2}$
Direct sun	$4.5 \cdot 10^{-7}$	$1 \cdot 10^{-5}$	$1 \cdot 10^{-8}$
Direct moon	$5.5 \cdot 10^{-7}$	$4 \cdot 10^{-6}$	$2 \cdot 10^{-7}$
Indirect sun	$1.3 \cdot 10^{-7}$	$5 \cdot 10^{-6}$	$2 \cdot 10^{-9}$
Indirect moon	$1.6 \cdot 10^{-7}$	$8 \cdot 10^{-5}$	$6 \cdot 10^{-8}$
Ocean	$5 \cdot 10^{-8}$	$2 \cdot 10^{-6}$	$2 \cdot 10^{-8}$
Pole	$1 \cdot 10^{-8}$	$6 \cdot 10^{-7}$	$5 \cdot 10^{-9}$
Freq. dep. corr.	$1 \cdot 10^{-8}$	$5 \cdot 10^{-9}$	$2 \cdot 10^{-9}$

Table 5 Comparison of gravitational forces

Source	Along (m/s^2)	Cross-track (m/s^2)	Radial (m/s^2)
Air drag	$(-1.5 \pm 1)\cdot 10^{-7}$	$(0 \pm 1)\cdot 10^{-8}$	$(0.25 \pm 1)\cdot 10^{-8}$
Solar drag	$(0 \pm 2)\cdot 10^{-8}$	$(0 \pm 3)\cdot 10^{-8}$	$(0 + 7)\cdot 10^{-8}$
Albedo	$(0 \pm 1)\cdot 10^{-9}$	$(0 \pm 1)\cdot 10^{-9}$	$-(1.5 + 1)\cdot 10^{-8}$

gravitational forces by the Earth are the desired quantity, the non-gravitational forces are measured by the accelerometers in order to correct the K-band observations. We restrict our analysis to the forces caused by air drag, solar radiation pressure and Earth albedo. A detailed analysis can be found in Frommknecht (2009). The analysis in the spectral domain shows that, apart from a mean value, the main power is at once per revolution. Table 5 shows a comparison of the different effects in the satellite fixed reference frame.

4 Real Data Analysis

The gravity sensor system consists of all the different sensors described before. The logic is the following: The basic measurement is the intersatellite range, derived from the K-Band measurements (for details see Josselin et al., 1999). The measured range is the distance between the phase centres of the K-Band measurement systems of both GRACE satellites. This range has to be reduced to the line connecting the mass centers of the satellites, using the star sensor measurement. In order to correct the range, that is not only affected by gravitational forces, but also by non-gravitational forces like air drag, solar radiation pressure and earth albedo, the accelerometer measurements have to be projected on the same line as the range measurement. Therefore also the star sensor accuracy has an impact on the quality of the derived pure gravitational range measurement.

In this section however we restrict the real data analysis to 10 Hz Level 1A data of the accelerometer. The accelerometer is chosen as its measurements are affected by a series of interesting phenomena:

1. peaks,
2. thruster effects and
3. twangs.

Detailed analyses can be found in Flury et al. (2007), Frommknecht (2009), Hudson (2003), and Flury (2004). All other instruments agree well with its specification.

The most frequent acceleration spikes are due to switching in about 30 of the 64 heaters onboard of the satellites. These events occur in average nearly once per second being the major signal contribution at high frequencies. The duration of these peaks is about 1 s. Thruster effects are accelerations due to the activation of the cold gas thrusters. Twangs are damped oscillations in the acceleration signal.

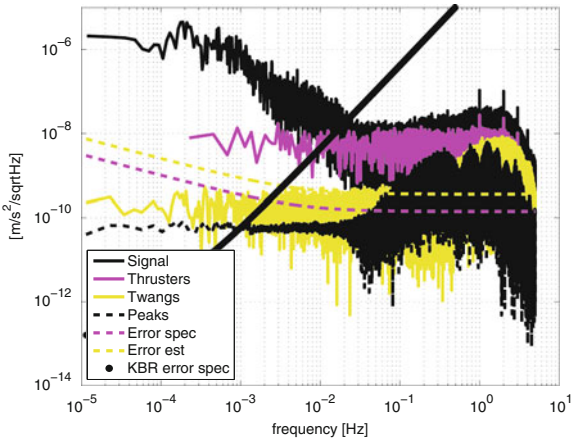

Fig. 11 Accelerometer measurement signal and its constituents as root PSD

Figure 11 shows the accelerometer measurement signal and the contributions caused by thruster events, twangs and peaks in the spectral domain. We notice a peak at once per revolution that is less prominent as for the linear accelerations themselves. The signal then decreases to about $2–3 \cdot 10^{-2}$ Hz, where the signal seems to level out into white noise. Looking at the root PSD of the thruster events of the same day, one realizes that the thruster events seem to be responsible for the flat spectrum. The characteristic peak at 1 Hz and multiples is also caused by the thruster events. The peak effects mainly cause an effect at frequencies higher than $2–3 \cdot 10^{-2}$ Hz and rise to a level of about $1 \cdot 10^{-8}$ m/s^2/$\sqrt{\text{Hz}}$. At frequencies lower than $2–3 \cdot 10^{-2}$ Hz the peak effect is below the specified measurement accuracy. The twangs seem to affect high frequencies mainly as well. The magnitude of their effect rises to a level of about $1 \cdot 10^{-8}$ m/s^2/$\sqrt{\text{Hz}}$. At frequencies lower than $2 \cdot 10^{-1}$ Hz, the twang effect is below the specified measurement accuracy. One should also keep in mind that during the next step in the data processing the bandwidth of the accelerometer measurement is reduced to about 0.1 (5 s sampling) resp. 0.5 Hz (1 s sampling). The effects visible in the differential acceleration measurement caused by the thruster events represent real accelerations, assuming the K-band measurements contain them as well, they do not contribute to the error budget of the measurement. The peak and twang effects contribute to the error budget of the measurement, as they are supposedly no real accelerations. As their influence for a 5 s sampling is below the measurement error specification, it seems that they can be neglected. For a 1 s sampling however, it seems that they would rise the measurement error to a level of about $1 \cdot 10^{-9}$ m/s^2/$\sqrt{\text{Hz}}$, so it may be worthwhile to think about a way of correcting these effects. As conclusion, we can state that the performance of the linear acceleration measurement is about $6 \cdot 10^{-10}$ m/s^2/$\sqrt{\text{Hz}}$, i.e. about 2 times higher than the performance specification, if 5 s data is used. If 1 s data is used and the effects of the twangs and peaks are not corrected for, the performance is estimated to be about $1 \cdot 10^{-9}$ m/s^2/$\sqrt{\text{Hz}}$ or about 3 times the specified performance. Flury et al. (2007) state that during a time span, without heater activity the accelerometers indeed achieve the expected sensitivity with a noise level just below 10^{-10} m/s^2/$\sqrt{\text{Hz}}$ in the sensitive axis.

5 Data Processing

The raw instrument data of all sensors has to be processed before it can be used for the gravity field determination. The basic processing steps are described in Wu et al. (2006). A key processing step is the application of an anti-aliasing low-pass filter. In Frommknecht (2009) alternatives to the approach described in Wu et al. (2006) were investigated. The resulting filter performance is shown in Fig. 12, for the K-Band measurement, as there the performance requirements for the filter are strictest. The Kaiser filter performs significantly better that the convoluted rectangle filter, but also the convoluted rectangle filter error is below the K-Band error specification. Therefore only a slight improvement of the measurement quality is expected around the orbit frequency of the measurement spectrum.

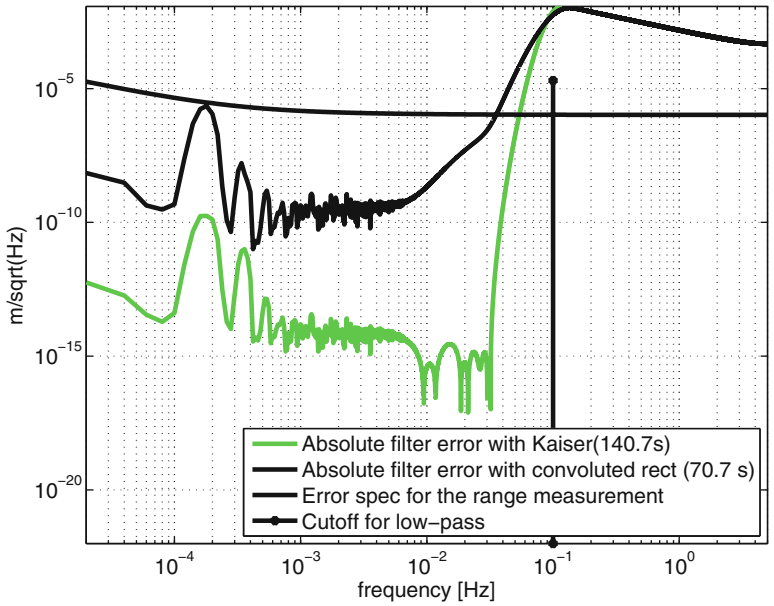

Fig. 12 Comparison of the Kaiser filter with the convoluted rectangle filter

6 Conclusions and Outlook

Concerning the accelerometer measurement performance, it can be stated that the twangs and peaks seem to have limited influence if a 5 s sampling rate is used, if a 1 s sampling rate is envisaged, it may be worthwhile to investigate adequate correction methods. But as the physical mechanism for the various effects are not understood yet, a final conclusion can not be drawn and further investigations have to be made. Concerning the star sensor and the K-Band measurement system performance estimation, it can be stated that they are nominal, cf. Frommknecht (2009).

The alternative low-pass filter seems to yield only slight improvements in data quality for the K-Band measurement around the orbit frequency, at least for the orbit height of the time span under investigation. In later stages of the mission, when the orbit height decreases and thus the signal to noise ration increases, a more significant improvement may be achieved. Further investigations on the data processing methods may e.g. focus on the combination of the star tracker and the accelerometer data.

Acknowledgment This is publication no. GEOTECH-1266 of the GEOTECHNOLOGIEN program of the BMBF, grant 03F0423B.

References

Flury J (2004) Beiträge zur Signalanalyse der GRACE L1a Akzelerometerdaten.

Flury J, Bettadpur S, Tapley B (2008) Precise accelerometry onboard the GRACE gravity field satellite mission. Adv. Space Res., 42, 1414–1423.

Frommknecht B (2009) Integrated Sensor Analysis of the GRACE Mission, SVH Publishing, Saarbrücken.

Hudson D (2003) In-Flight Characterization and Calibration of the SuperSTAR Accelerometer. Thesis, University of Texas, Austin.

Josselin V, Touboul P, Kielbasa R (1999) Capacitive detection scheme for space accelerometers. Appl. Sens. Actuators, Elsevier Science Ltd., 78, 92–98.

Jørgenson J (1999) In-Orbit Performance of a Fully Autonomous Star Tracker. Technical Report University of Denmark.

Kim J (2000) Simulation Study of a Low-Low Satellite-to-Satellite Tracking Mission. Technical Report University of Texas at Austin.

Rothacher M (2001) Vorlesungsskript Messmethoden der Physikalischen Geodäsie.

Stanton R, Bettadpur S, Dunn C, Renner K-P, Watkins M (1998) GRACE Science \& Mission Requirements Document. Technical Report 327-200 Jet Propulsion Laboratory.

Thomas J (1999) An Analysis of the Gravity Field Estimation Based on Dual-1-Way Intersatellite Biased Ranging. Technical Report Jet Propulsion Laboratory Pasadena.

Wertz J-R (1991) Spacecraft Attitude Determination and Control, Kluwer Academic Publishers, Dordrecht/Boston/London.

Wu S-C, Kruizinga G, Bertinger W (2006) Algorithm Theoretical Basis Document for GRACE Level-1B Data Processing. V1.2 Technical Report JPL D-27672 Jet Propulsion Laboratory.

Numerical Simulations of Short-Term Non-tidal Ocean Mass Anomalies

Henryk Dobslaw and Maik Thomas

1 Introduction

The Earth's gravity field undergoes changes due to mass exchanges between and mass re-distribution within its sub-systems. A significant contribution to the Earth's time-variable gravity field is caused by atmosphere and ocean dynamics. As these variable masses influence the gravity field estimation from satellite missions like the Gravity Recovery and Climate Experiment (GRACE), such signals have to be removed from the data in order to calculate a monthly mean gravity field.

By means of simulated gravity data, Wahr et al. (1998) showed that GRACE is expected to be sensitive to large scale ocean mass variations on annual timescales up to degree 37. Wünsch et al. (2001) additionally analysed high-frequency ocean mass variations, finding significant variability even on daily timescales which is well above the sensitivity threshold of GRACE. In order to reduce aliasing effects due to such short-term mass variations, atmosphere and ocean mass anomalies are reduced in standard GRACE gravity field processing using European Centre for Medium-Range Weather Forecasts (ECMWF) analysis data and corresponding oceanic data obtained from the baroclinic Ocean Model for Circulation and Tides (OMCT; Thomas, 2002).

Here, sensitivity experiments performed with OMCT are described in order to define the most appropriate model configuration for operationally calculating the ocean mass anomaly fields for the GRACE atmosphere-ocean de-aliasing (AOD) product. After a brief description of the OMCT model physics (Sect. 2), different atmospheric forcing fields from the ECMWF are evaluated (Sect. 3). In the following, atmospheric and continental freshwater fluxes and their impact on short-term ocean mass anomalies are presented (Sect. 4), together with their impacts on the time-variable total ocean mass. These total ocean mass variations are in particular discussed in view of the requirements for operationally running a numerical ocean model (Sect. 5).

H. Dobslaw (✉)
Helmholtz Centre Potsdam, GFZ German Research Centre for Geosciences,
Department 1: Geodesy and Remote Sensing, Telegrafenberg, 14473 Potsdam, Germany
e-mail: henryk.dobslaw@gfz-potsdam.de

F. Flechtner et al. (eds.), *System Earth via Geodetic-Geophysical Space Techniques*,
Advanced Technologies in Earth Sciences, DOI 10.1007/978-3-642-10228-8_10,

2 Ocean Model for Circulation and Tides (OMCT)

The OMCT was developed by adjusting the originally climatological Hamburg Ocean Primitive Equation Model (HOPE) (Wolff et al., 1997; Drijfhout et al., 1996) to synoptic time-scales of the atmosphere and coupling with an ephemeral tidal model. The model is based on the nonlinear balance equations for momentum, the continuity equation for an incompressible fluid and conservation equations for heat and salt. The hydrostatic as well as the Boussinesq approximations are applied. Implemented is a prognostic thermodynamic sea-ice model (Hibler, 1979) that predicts ice-thickness, compactness and drift. Prognostic variables are horizontal velocities, surface elevation, three-dimensional temperature and salinity fields, sea ice thickness and compactness. Higher order effects such as nonlinearities are accounted for as well as the secondary potential due to loading and self-attraction (LSA) of the water masses (see Thomas et al., 2001). To maintain sufficient long-term stability of the thermohaline circulation, surface salinity has been coupled to a mean climatology obtained from the World Ocean Atlas (Conkright et al., 2002) with a relaxation time-scale of 38 days. In its present configuration, the model uses a time step of 30 min, a horizontal resolution of 1.875° and 13 layers in the vertical.

Since baroclinic ocean models using the Boussinesq approximation conserve volume rather than mass, and artificial mass and consequently bottom pressure changes are introduced due to applied heat and freshwater fluxes, following Greatbatch (1994) a spatially uniform layer of mass is added to the sea-surface to enforce mass conservation (see, e.g., Ponte and Stammer, 2000; Gross et al., 2003). The implications of freshwater fluxes altering the total oceanic mass will be discussed in Sect. 5.

In order to allow the reproduction of tidal dynamics, the OMCT takes into account effects from the complete luni-solar tidal potential computed from the ephemerides of the tide-generating bodies. Ephemerides are derived from a simplified version of the VSOP87 theory (Bretagnon and Francou, 1988) following suggestions by Meeus (1991). Thus, the model is now capable of generating precise ephemerides from knowledge of the actual date alone (Thomas and Dobslaw, 2010). Although the chosen numerical approach allows to study the interactions among circulation and tides, tidal dynamics have not been considered throughout this study and throughout all other OMCT simulations related to GRACE. Within the GRACE processing, ocean tides are corrected by means of the FES2004 tide model (Flechtner, 2007).

To produce a quasi steady-state thermohaline and wind-driven circulation, the OMCT was initially spun up for 265 years with cyclic boundary conditions, i.e., climatological wind stresses according to Hellerman and Rosenstein (1983) and annual mean surface temperatures and salinities according to Levitus (1982). The climatological initial model run was followed by real-time simulations for the period 1958–2000 driven by wind stress components, 2m-temperatures, freshwater fluxes, and atmospheric surface pressure from the ECMWF reanalysis project ERA-40 covering the period from September 1957 to August 2002. Starting 2001, OMCT model runs have been forced by different operational ECMWF data-sets in order

to separate individual effects of various physical processes and forcing conditions. Mass anomalies from all these runs have been stored every 6 h concurrent with the applied atmospheric forcing fields.

3 ECMWF Analyses and Forecasts

The ECMWF provides atmospheric data from its weather prediction model on an operational basis. The numerical model currently in use has a spectral resolution of wave number 511 (which corresponds to ∼25 km grid spacing along the equator) and 60 vertical layers. Every day, four global analyses are disseminated describing the state of the atmosphere at 00, 06, 12 and 18 UTC. These analyses are obtained from two 4D-VAR minimisation cycles (Klinker et al., 2000, and references therein) running from 03 to 15 UTC and from 15 to 03 UTC. By assimilating observational data for this time period, an optimal transient state of the model atmosphere is determined. Instantaneous fields from these optimal fits, containing the best estimate of the atmospheric state at a certain time step, are provided as analysis fields. These analyses are applied in the standard GRACE de-aliasing procedure.

Additionally, medium range forecast runs are performed following each 4D-VAR minimisation cycle. Forecasts with a temporal resolution of up to 3 h are disseminated up to 10 days ahead the main synoptic hours at 00 and 12 UTC. These forecast fields contain information on instantaneous state quantities of the atmosphere like three-dimensional distributions of temperature, pressure, and wind speeds for the end of each forecast interval. In addition to instantaneous fields, forecasts provide accumulated information on evolving properties of the atmosphere, e.g., the amount of precipitation and evaporation as well as wind stresses accumulated over the forecast interval (Persson, 2003), which lead to representative mean values of these quantities for the considered time interval.

Although forecasts are not constrained by data and consequently may contain forecast errors, the accumulated wind stress information and the doubled temporal resolution make forecasts potentially valuable also for post processing tasks. As updated forecast sets become available every 12 h, the first four forecast steps at +3, +6, +9 and +12 h have to be used. While instantaneous fields provided in each forecast are referenced to the end of the forecast interval, accumulated fields contain information from the last analysis until the end of the forecast interval. Therefore, the ultimate preceding forecast field has to be subtracted in order to assess the information for the considered 3 h interval only, which is subsequently used to calculate a representative mean.

To analyse the impact of atmospheric forecasts on numerical simulations of short-term ocean mass variations, different OMCT model runs are compared in order to separate the impact of accumulated winds and forecast induced errors. In particular, the effects of accumulated wind stresses are assessed by means of instantaneous wind speed information provided with each forecast. Further, this dataset is comparable to standard analysis and is therefore applied to estimate the impact of a transition from analysis to forecast alone. For simplicity, analyses serve as reference

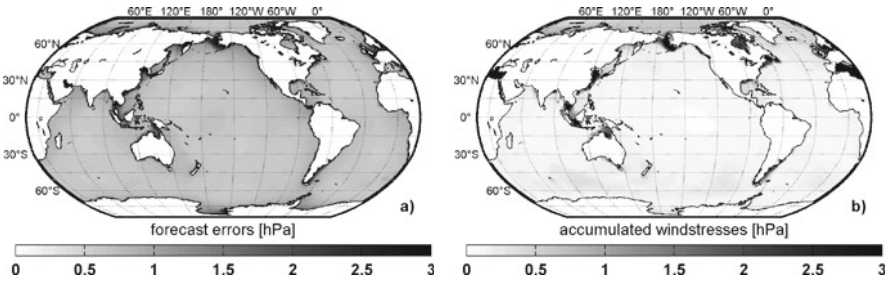

Fig. 1 Rms variability of simulated global ocean mass anomalies due to forecast errors as deduced from differences among ECMWF analyses and short-term forecasts (**a**), as well as differences among wind stresses accumulated over the 6 hourly intervals and instantaneous wind estimates (**b**)

fields and, thus, are assumed to be error-free in this study and all deviations from these reference states are considered as forecast errors.

The impact of increased temporal resolution is not further considered in this chapter, since the benefit of 3 hourly forecasts in resolving the semidiurnal atmospheric tide has been already discussed by Dobslaw and Thomas (2005). Moreover, the additional synoptic variability contained in 3 hourly forecasts has been evaluated with respect to the GRACE gravity field processing by Dobslaw and Thomas (2007b).

Based on the numerical experiments performed with OMCT, the impact of forecast errors on simulated ocean mass anomalies (Fig. 1a) is typically around 1 hPa (which corresponds to a 1 cm change in sea-level) in large parts of the ocean, with generally higher values along the coasts. Highest impacts can be found in shallow water areas as, e.g., the Bering Strait, where rms values of more than 3 hPa are simulated. In turn, the potential benefits of using accumulated rather than instantaneous wind stresses (Fig. 1b) are significantly smaller with values below 0.5 hPa in most open ocean areas, while higher values exceeding 3 hPa are only predicted in shallow enclosed areas as the Yellow Sea or the Mediterranean Sea. Although the application of accumulated wind stresses is expected to be of great benefit for coastal applications, it is not expected to outweigh the drawback due to the forecast errors, leading to, consequently, disregarding of ECMWF forecast fields for the GRACE standard gravity field processing.

4 Continental and Atmospheric Freshwater Fluxes

In order to analyse freshwater fluxes among atmosphere, oceans and continental hydrology, the representation of the hydrological cycle in ECMWF short-term forecast data is primarily important, since freshwater fluxes are not available from the analyses. The accuracy of the modelled hydrological cycle in ERA-40 has been validated by Hagemann et al. (2005), while the current representation in the operational model has been reviewed by Andersson et al. (2005). According to their findings,

significant changes in precipitation trends occur within ERA-40, which are connected with the advent of new observing systems rather than with real changes of mass transports in the hydrological cycle. Moreover, due to significant overestimations of precipitation over tropical oceans within the atmospheric model, precipitation exceeds evaporation over oceans as well as over land. As indicated by Andersson et al. (2005), improvements of clouds and rain assimilation in the ECMWF forecasting system will take place in the near future, which will probably result in more realistic net freshwater fluxes from ECMWF operational data. Despite these errors, data from weather prediction models currently provide the only opportunity to examine the transient impact of freshwater fluxes on ocean circulation in an operational model set-up.

To ensure consistent water mass fluxes among the major sub-systems of the Earth, river discharges used in this study are based on the same atmospheric data, which are also used to force the ocean model OMCT. Geographically distributed river discharge data have been obtained from numerical simulations with the Hydrological Discharge Model (HDM; Hagemann and Dümenil, 1998). This model is part of the coupled atmosphere-ocean global circulation model ECHAM5/MPI-OM (Latif et al., 2003) and has been used in several studies, e.g., to validate the hydrological cycle of ERA-40 (Hagemann et al., 2005) and to analyse the impact of hydrological mass variations on the Earth's rotation (Walter, 2007). HDM is a linear cascade model with a constant horizontal resolution of 0.5° in longitude and latitude and uses a time step of 1 day. The model is capable of simulating lateral discharge in 3 layers: overland flow, river flow and ground water flow. Applied forcing fields are daily estimates of run-off and drainage, which have been obtained from 2m-temperatures and precipitation provided by ERA-40 and ECMWF's operational data sets using a land-surface scheme (Hagemann and Dümenil, 1998). The quality of simulated river flow has been validated by means of gauge data provided by the Global Run-off Data Centre (Koblenz, Germany). According to Walter (2007), annual mean discharges as well as seasonal variations are reproduced realistically by HDM.

Based on OMCT simulations covering the period 1958–2005, the impact of time-variable freshwater fluxes on ocean mass variability has been evaluated. Mass varability due to changes in total ocean mass have been corrected for, since they will be considered separately in the following section. Generally, the direct effects of freshwater fluxes on ocean mass transports are small (Fig. 2a), since freshwater anomalies primarily cause variations in the density structure and therefore in steric sea-level (see, e.g., Dobslaw, 2007). Thus, there are consequences on ocean bottom pressure only in the rare case of density changes throughout the whole water column down to the bottom, or indirectly due to changes in the thermohaline circulation. Significant mass variability due to freshwater fluxes is therefore confined to shallow coastal areas, while mass re-distributions of most parts of the oceans are not affected, provided that the long-term stability of the thermohaline circulation is maintained by, e.g., relaxation of the sea surface salinity towards an observational climatology (Conkright et al., 2002). For this particular analysis, the relaxation timescale has been extended to 180 days in order to avoid influences of the relaxation

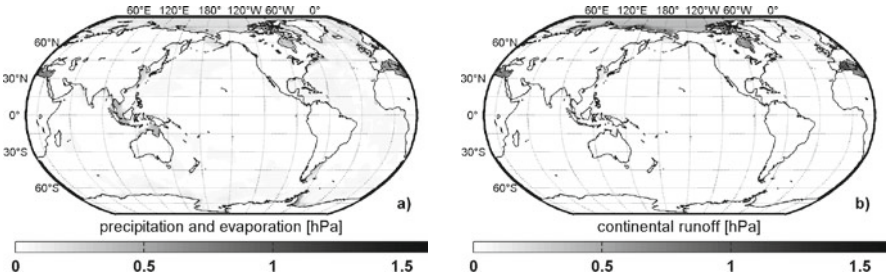

Fig. 2 Rms variability of simulated global ocean mass anomalies due to precipitation and evaporation (**a**), as well as continental runoff (**b**)

on subseasonal mass redistributions (see Dobslaw and Thomas, 2007a for further details).

According to Fig. 2b, the impact of river runoff is even more local, except for a significant mass anomaly in the Arctic Ocean. Further analysis of the signal's temporal pattern reveals a strong effect of the large river transports during the snow-melt season of the northern hemisphere (Dobslaw and Thomas, 2007a), which contains almost no sub-monthly mass variability. Therefore, river discharges are not affecting the generation of monthly mean gravity fields from the GRACE observations and have therefore not to be corrected for during the GRACE de-aliasing process, allowing to safely neglect river runoff within the operational simulations for GRACE.

5 Variations in Total Ocean Mass

Besides the impact of freshwater fluxes on altering the ocean's density structure and, consequently, the ocean's mass re-distribution through changes in the thermohaline circulation, net-freshwater fluxes additionally alter the total ocean mass. ECMWF analyses indicate a seasonal variation of the total atmospheric mass. Expressed in hPa of a homogeneous layer of mass extended over the surface of the world's oceans, the total atmospheric mass varies annually about 0.7 hPa peak-to-peak due to the changing moisture content (Fig. 3). In comparison, variations in total continental water masses as derived from HDM reach amplitudes up to 2 hPa on annual scales, with additional interannual variations super-imposed, since the storage capacities of soil layers and groundwater aquifers are much larger compared to the atmosphere's ability to absorb precipitable water. Assuming that mass is not lost but re-distributed among the sub-systems atmosphere, ocean, continental hydrosphere and cryosphere, with the latter being disregarded in this study, a seasonal variation of $\sim$1.5 hPa of the total ocean mass is expected.

However, changes of total ocean mass are difficult to derive from freshwater fluxes provided by numerical models. Daily atmospheric freshwater fluxes into the ocean reveal that net-transports are significantly overestimated (Fig. 4). Instead of confirming a continuous mass-loss of the oceans due to excess of evaporation, global

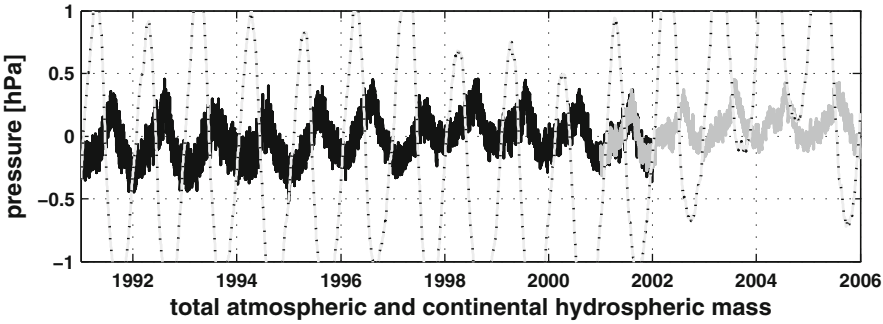

Fig. 3 Variations of total atmospheric mass from ERA-40 reanalysis data (*solid black*) and from operational ECMWF data (*solid grey*), as well as of the continental water masses as simulated with HDM (*dotted*)

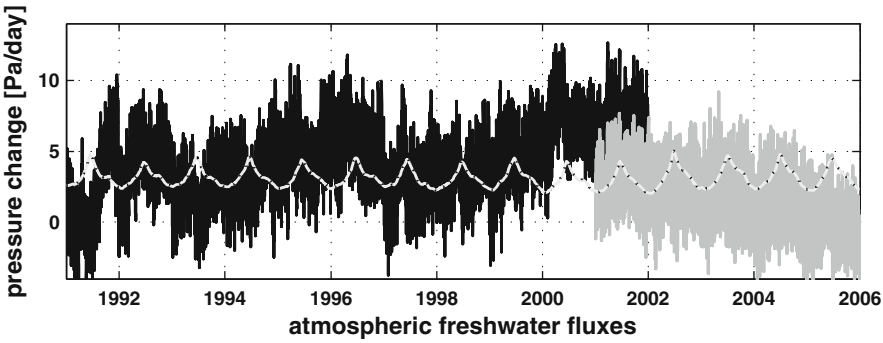

Fig. 4 Globally integrated daily freshwater fluxes into the ocean from ERA-40 reanalysis data (*solid black*), operational ECMWF data (*solid grey*), as well as from the continental hydrosphere as simulated by HDM, each expressed in globally homogeneous changes of ocean bottom pressure

integrations of precipitation and evaporation indicate a mass gain of the global oceans from the atmosphere. However, due to continuous improvements of the representation of the hydrological cycle in the operational ECMWF model, this bias has been significantly reduced during the last years, and is expected to become even smaller in the near future.

Due to that bias, total ocean masses would raise steadily, if atmospheric freshwater fluxes are uncorrected accounted for. At first order, an apparent trend of total ocean mass change is reduced from the data independently for both ERA-40 and the operational ECMWF data. However, due to the aforementioned changes in the model configurations and satellite data availability, a multi-year trend removal generates strong interannual variations of the total ocean mass from atmospheric freshwater fluxes alone (Fig. 5), which is physically unreasonable due to the restricted capacities of water vapor storage in the atmosphere. Therefore, a linear trend of changes in total ocean mass due to atmospheric freshwater fluxes has

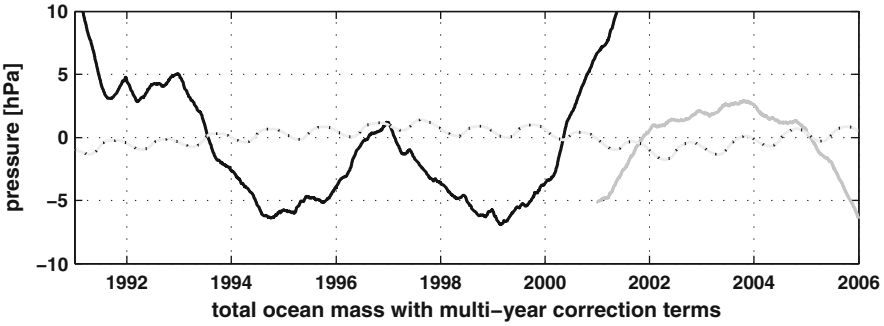

Fig. 5 Changes of total ocean mass due to atmospheric freshwater fluxes from ERA-40 reanalysis data (*solid black*), operational ECMWF data (*solid grey*), as well as due to continental runoff as simulated with HDM (*dotted*)

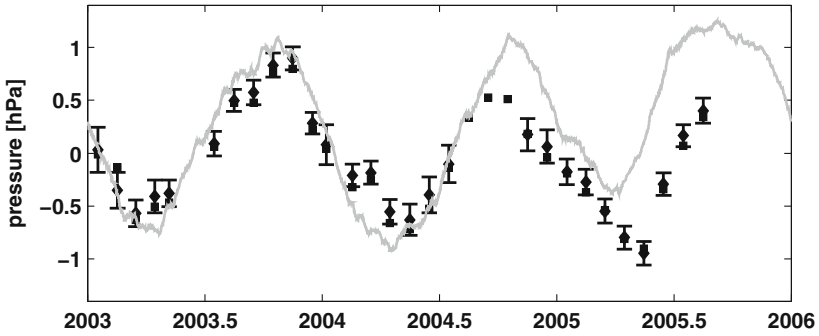

Fig. 6 GRACE based total ocean mass anomalies expressed in homogeneous changes of ocean bottom pressure from CSR release 01 fields (*black diamonds* with error bars), from CSR release 01 constrained fields (*black squares*), and ocean mass anomalies as simulated with OMCT caused by yearly de-trended freshwater fluxes due to precipitation, evaporation and run-off (*grey line*)

been reduced for every single year, reducing all interannual variability but retaining the seasonal variations only (Fig. 6). For consistency, similar trends have been removed from the hydrological data, although these data are much less subject to such dubious interannual changes.

Simulated ocean mass variations from yearly de-trended atmospheric and continental freshwater fluxes are contrasted to corresponding GRACE estimates of total ocean mass anomalies according to Chambers et al. (2004) as provided by J. Wahr (2006, personal communication; Fig. 6). In general, the seasonal variations of total ocean mass are reproduced reasonably, the results are frequently close to the uncertainties of GRACE derived values. This is especially encouraging, since cryospheric mass fluxes were not considered in the model simulations and ECMWF derived freshwater fluxes exhibit several problems as indicated above. Improvements in assimilating rain and clouds within the ECMWF model (Andersson et al., 2005) as

well as the use of more sophisticated models of continental hydrology and the incorporation of cryospheric mass fluxes might lead to even better agreement between GRACE observations and numerical models, hopefully allowing for the analysis of interannual variations as well.

However, for operational purposes the application of a yearly de-trending is not applicable. Experimental attempts to predict correction terms for an approximate de-trending of the freshwater fluxes have not been successful. They are leading to arbitrary long-term trends or variations in the total ocean mass, which might cause spurious effects in the GRACE gravity field time-series if contained in the AOD products. For operational purposes, it has been therefore agreed to consider the dynamic effects of atmospheric freshwater fluxes, to disregard the continental ones, and to artificially correct freshwater induced total ocean mass variations in OMCT by adding or removing a globally homogeneous layer of mass at each time-step of the simulation. Variations in total ocean mass are therefore not reduced during the de-aliasing process of GRACE and are consequently contained in the monthly mean gravity fields.

6 Conclusions

Various simulations have been performed with the numerical Ocean Model for Circulation and Tides (OMCT) in order to identify an optimal model configuration for de-aliasing non-tidal ocean mass anomalies within the GRACE processing. Short-term ECMWF forecasts have been considered as alternative atmospheric forcing fields, since they provide increased temporal resolution of up to 3 h and accumulated wind stress information compared to the typically used 6-hourly analysis fields. However, sensitivity experiments indicate that forecast errors well outweigh the benefits of the accumulated wind stresses, so that ECMWF forecasts are no longer considered for GRACE de-aliasing purposes. Atmospheric and continental freshwater fluxes have been found to have only minor impacts on ocean mass anomalies. While atmospheric freshwater fluxes vary on shorter time-scales and are therefore considered in the operational ocean simulations for GRACE processing, continental discharges change primarily on seasonal time-scales, which allows them to be safely neglected for GRACE purposes. Finally, the treatment of variations of the total ocean mass within the OMCT simulations has been discussed. Although reasonable variations are obtained from OMCT simulations by yearly de-trending of the freshwater fluxes, this concept cannot be applied in an operational setting. For the operational GRACE simulation, the total ocean mass is therefore artificially held constant at each time-step. However, since the total ocean mass varies globally homogeneous and on seasonal time-scales only, its variations do not cause aliasing effects and can be therefore directly obtained from the GRACE monthly mean solutions.

Acknowledgments We thank Deutscher Wetterdienst, Offenbach, Germany, and European Centre for Medium-Range Weather Forecasts, Reading, U.K., for providing data from ECMWF's

operational forecast model. This work was supported by the German Ministry of Education and Research (BMBF) and the Deutsche Forschungsgemeinschaft within the GEOTECHNOLOGIEN research program under grant 03F0423D.

References

Andersson E, Bauer P, Beljaars A, Chevallier F, Holm E, Janiskova M, Kallberg P, Kelly G, Lopez P, McNally A, et al. (2005) Assimilation and modelling of the atmospheric hydrological cycle in the ECMWF forecasting system. Bull. Am. Meteorol. Soc. 86(3), 387–401.

Bretagnon P, Francou G (1988) Planetary theories in rectangular and spherical variables: VSOP87 solutions. Astron. Astrophys. 202, 309–315.

Chambers DP, Wahr J, Nerem RS (2004) Preliminary observations of global ocean mass variations with GRACE. Geophys. Res. Lett. 31, L13310.

Conkright ME, Locarnini RA, Garcia HE, O'Brien TD, Boyer TP, Stephens C, Antonov JI (2002) World Ocean Atlas 2001: Objective Analysis, Data Statistics, and Figures, National Oceanographic Data Center, Silver Spring, MD, 17 pp.

Dobslaw H (2007) Modellierung der allgemeinen ozeanischen Dynamik zur Korrektur und Interpretation von Satellitendaten. Scientific Technical Report 07/10, GeoForschungsZentrum, Potsdam, Germany, 113 pp.

Dobslaw H, Thomas M (2005) Atmospheric induced oceanic tides from ECMWF forecasts. Geophys. Res. Lett. 32, L10615.

Dobslaw H, Thomas M (2007a) Impact of river run-off on global ocean mass redistribution. Geophys. J. Int. 168(2), 527–532.

Dobslaw H, Thomas M (2007b) Periodic and transient short-term mass variations in numerical simulations of atmosphere-ocean dynamics. Geotechnol. Sci. Rep. 11, 122–126.

Drijfhout S, Heinze C, Latif M, Maier-Reimer E (1996) Mean circulation and internal variability in an ocean primitive equation model. J. Phys. Oceanogr. 26, 559–580.

Flechtner F (2007) AOD Product Description Document. GRACE 327-750, rev. 3.1, GeoForschungsZentrum, Potsdam, Germany, 43 pp.

Greatbatch RJ (1994) A note on the representation of steric sea level in models that conserve volume rather than mass. J. Geophys. Res. 99(C6), 12767–12771.

Gross RS, Fukumori I, Menemenlis D (2003) Atmospheric and oceanic excitation of the Earth's wobbles during 1980–2000. J. Geophys. Res. 108(B8), 2370.

Hagemann S, Dümenil L, (1998) A parametrization of the lateral water flow for the global scale. Clim. Dyn. 14, 17–31.

Hagemann S, Arpe K, Bengtsson L (2005) Validation of the Hydrological Cycle of ERA-40. ERA-40 Project Report Series, 24, 42 S, European Centre for Medium-Range Weather Forecasts, Reading, UK.

Hellerman S, Rosenstein M (1983) Normal monthly wind stress over the world ocean with error estimates. J. Phys. Oceanogr. 13, 1093–1104.

Hibler III WD (1979) A dynamic thermodynamic sea ice model. J. Phys. Oceanogr. 9, 815–846.

Klinker E, Rabier F, Kelly G, Mahfouf J-F (2000) The ECMWF operational implementation of four dimensional variational assimilation, Part III: Experimental results and diagnostics with operational configuration. Q. J. R. Meteorol. Soc. 126, 1191–1215.

Latif M, et al. (2003) Reconstructing, monitoring and predicting decadal scale changes in the north Atlantic thermohaline circulation with sea surface temperature. J. Clim. 17, 1605–1613.

Levitus S (1982) Climatological Atlas of the World Ocean. NOAA Professional Paper 13, U.S. Department of Commerce, 173 pp.

Meeus J (1991) Astronomical Algorithms, Willmann-Bell Inc., Richmond, VA, 460 pp.

Persson A (2003) User Guide to ECMWF Forecast Products, 123 S, European Centre for Medium-Range Weather Forecasts, Reading, UK.

Ponte RM, Stammer D (2000) Global and regional axial ocean angular momentum signals and length-of-day variations (1985–1996). J. Geophys. Res. 105, 17161–17171.

Thomas M (2002) Ozeanisch induzierte Erdrotationsschwankungen – Ergebnisse eines Simultanmodells für Zirkulation und ephemeridische Gezeiten im Weltozean, Dissertation, Institut für Meereskunde, Universität Hamburg, Hamburg, 128 pp.

Thomas M, Sündermann J, Maier-Reimer E (2001) Consideration of ocean tides in an OGCM and impacts on subseasonal to decadal polar motion excitation. Geophys. Res. Lett. 28(12), 2457–2460.

Thomas M, Dobslaw H (2010) Representation of ocean tide dynamics in a global baroclinic ocean model based on analytical luni-solar ephemerides. Geophys. Res. Lett. (submitted).

Wahr J, Molenaar M, Bryan F (1998) Time variability of the Earth's gravity field: Hydrological and oceanic effects and their possible detection using GRACE. J. Geophys. Res. 103, 30205–30229.

Walter C (2007) Simulationen hydrologischer Massenvariationen und deren Einfluss auf die Erdrotation. Dissertation, Institut für Planetare Geodäsie, Technische Universität Dresden, 196 pp.

Wolff JO, Maier-Reimer E, Legutke S (1997) The Hamburg Ocean Primitive Equation Model HOPE. Technical Report 13, Deutsches Klimarechenzentrum, Hamburg, 103 pp.

Wünsch J, Thomas M, Gruber T (2001) Simulation of oceanic bottom pressure for gravity space missions. Geophys. J. Int. 147, 428–434.

Improved Non-tidal Atmospheric and Oceanic De-aliasing for GRACE and SLR Satellites

Frank Flechtner, Maik Thomas, and Henryk Dobslaw

1 Introduction

The initial force field considered during Precise satellite Orbit Determination (POD) of CHAMP and GRACE includes – besides Earth and third bodies gravity effects or non-gravitational forces observed by on-board accelerometers – temporal gravity variations due to solid Earth, atmosphere and ocean tides by the use of appropriate tidal models (Reigber et al., 2005). Modern missions such as CHAMP, GRACE and GOCE which derive the Earth's static and time-variable gravity field with unprecedented accuracy with monthly or even sub-monthly resolution are sensitive to short-term (weekly or shorter) non-tidal mass variations due to mass transports and mass redistribution phenomena in the atmosphere, the oceans and the continental water storage. The correction of these high-frequency impacts, which can reach up to 2 mm in terms of geoid height at wavelengths of 500 km according to analysis of GRACE real data or simulations performed by Thompson et al. (2004), by appropriate models, is commonly called "de-aliasing" in the GRACE community.

Precise global hydrological models with high spatial and temporal resolution are not yet available and are therefore not taken into account during gravity field determination. Non-tidal high-frequency atmospheric and oceanic mass variation models, however, are routinely generated at GFZ Potsdam as so-called GRACE Atmosphere and Ocean De-aliasing Level-1B (AOD1B) products to be added to the background static gravity model during GRACE monthly gravity field determination. Consequently, the outputs of the GRACE mission are spherical harmonic coefficients that signify the sum of all unmodelled mass redistribution in the system Earth during given months. Neglecting small scale or small amplitude effects such as post glacial rebound or ocean mass variability the prime result are therefore monthly maps of global continental water mass redistribution (e.g., Schmidt et al., 2006).

F. Flechtner (✉)
Helmholtz Centre Potsdam, GFZ German Research Centre for Geosciences,
Department 1: Geodesy and Remote Sensing, Telegrafenberg, 14473 Potsdam, Germany
e-mail: frank.flechtner@gfz-potsdam.de

F. Flechtner et al. (eds.), *System Earth via Geodetic-Geophysical Space Techniques*,
Advanced Technologies in Earth Sciences, DOI 10.1007/978-3-642-10228-8_11,

Additionally, GRACE data have also been studied to analyse various geophysical phenomena, such as mass balance of ice sheets in Antarctica and Greenland, the corresponding contribution to sea level change, ocean mass variability and redistribution, ocean tides, sterical effects when combined with satellite altimetry, post glacial rebound in Canada and Fennoscandia, vertical crustal displacements when combined with GPS, or relativistic effects such as dragging of inertial frames.

The GRACE AOD1B products are 6-hourly series of spherical harmonic coefficients up to degree and order 100 which are routinely provided to the GRACE Science Data System and the user community with only a few days time delay. These products reflect spatiotemporal mass variations in atmosphere and oceans deduced from operational atmospheric weather data and corresponding ocean dynamics simulated as response to wind stresses, atmospheric pressure as well as heat and freshwater fluxes provided by an ocean model (Flechtner et al., 2006). Due to its huge vertical extension, atmospheric mass anomalies cannot be taken into account by means of a thin layer approximation via surface pressure (SP) data, but have to be deduced from a vertical integration (VI) over pressure levels. This so-called 3D problem has been studied by various authors (e.g., Boy and Chao, 2005 or Velicogna et al., 2001) and can result in weighted root mean square (wRMS) geoid height errors of some tens of a millimeter. The variability is derived by subtraction of a long-term mean of vertical integrated atmospheric mass distributions and a corresponding mean of ocean bottom pressure as simulated with an ocean general circulation model.

For AOD1B RL00 (release 0) and RL01 the barotropic ocean model PPHA (developed by Pacanowski, Ponte, Hirose and Ali; Hirose et al., 2001) based on a 2001 mean field was used. As summarized in Flechtner et al. (2006), this model has deficiencies which influence the quality of the GRACE gravity field solutions: Due to the exclusion of the Arctic Ocean a pure inverse barometric response of the sea surface has to be applied north of 65° latitude; PPHA has less variance in ocean bottom pressure than other comparable models and shows reduced level of energy compared to in-situ ocean bottom pressure data (Kanzow et al., 2005). Dedicated gravity field modeling tests based on PPHA, the barotropic MOG2D (Carrère and Lyard, 2003) and the baroclinic OMCT (Ocean Model for Circulation and Tides Thomas et al., 2001) models gave the conclusion that PPHA should be substituted by MOG2D or OMCT for GRACE data reprocessing. Therefore the production of RL01 has been stopped on June 30, 2007 and since RL03 OMCT is used for operational AOD1B model generation (RL02 was an intermediate test series which was only made available for some dedicated months).

The latest AOD1B product version RL04 (Flechtner, 2007) is, as all other previous releases, still based on 6-hourly meteorological analysis fields of the Integrated Forecast System of the European Centre for Medium-Range Weather Forecasts (ECMWF) and output from OMCT forced by these analyses. The mean field was extended to the period 2001+2002.

In the following chapters the basic improvements of OMCT RL04 version and the implications from an enhanced temporal resolution of 3 h for the AOD1B model and related gravity field models are described. Finally, the AOD1B model

has been reprocessed back to 1976 for a consistent processing of and combination with Satellite Laser Ranging data.

2 OMCT Configuration for AOD1B RL04

Ocean mass anomalies for AOD1B product release 04 are obtained from the Ocean Model for Circulation and Tides (OMCT; Thomas, 2002). OMCT has been previously used to investigate the impact of ocean circulation and tides on the Earth's rotation and the gravity field (Thomas et al., 2001; Wünsch et al., 2001; Dobslaw and Thomas, 2005). Further information about the model physics can be obtained from chapter "Numerical Simulations of Short-Term Non-tidal Ocean Mass Anomalies" by Dobslaw and Thomas (this issue) or Flechtner (2007).

For the RL04 simulations, the bathymetry of the model based on the ETOPO5 topography (NOAA, 1988) has been augmented by water depth estimates below Antarctic ice-shelves obtained from Padman et al. (2002). The total ocean mass is held constant at each time-step by adding a globally homogeneous layer of mass (Greatbatch, 1994), correcting for artificial mass changes due to the model formulation as well as for changes in the total ocean mass due to time-varying freshwater fluxes.

RL04 ocean mass anomalies have been simulated by starting from a quasi steady state circulation obtained from an initial model spun up for 265 years using climatological wind stresses (Hellerman and Rosenstein, 1983) and mean sea surface temperatures and salinities according to Levitus (1982). Subsequently, OMCT has been forced by 6-hourly wind stresses, atmospheric surface pressure, 2m-temperatures and freshwater fluxes due to precipitation and evaporation obtained from the ERA-40 reanalysis project of the European Centre for Medium-Range Weather Forecasts (ECMWF) covering 1958 until 2000. From January 2001 onwards, forcing fields are taken from ECMWF's operational analyses, allowing to simulate the general ocean circulation with OMCT nearly in real-time. Ocean mass anomalies as well as additional data-sets including sea surface height anomalies have been stored every 6 h concurrent with the application of new atmospheric forcing fields.

Since GRACE typically provides monthly mean gravity fields, ocean mass variations on time-scales shorter than 30 days have to be corrected for during the de-aliasing process. In turn, variability on longer time-scales is expected to be observable by means of monthly mean gravity fields. Variability of simulated ocean mass anomalies has been therefore separated into monthly mean and sub-monthly contributions (Fig. 1) by basically applying a 30 days low pass filter (see Dobslaw and Thomas, 2007a). Mass anomalies potentially observable by GRACE reach 6 hPa in various parts of the Southern Ocean as well as in the Northern Pacific. Distinct signals with smaller spatial extent are additionally found in various shallow seas, like the Bering Strait and around the Indonesian Archipelago. Sub-monthly variability reaching up to 10 hPa is significantly stronger in most parts of the global

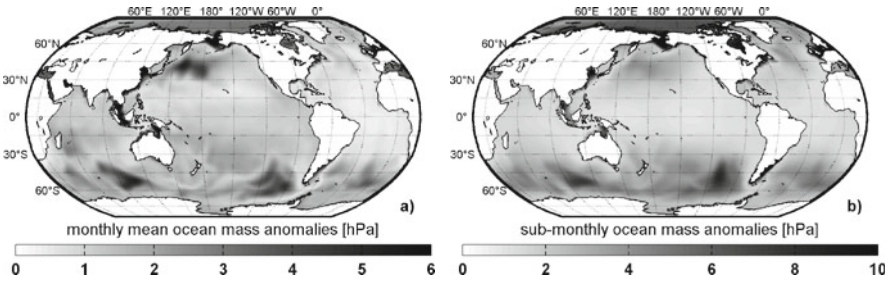

Fig. 1 Monthly mean (**a**) and sub-monthly (**b**) ocean mass variability as simulated with OMCT for AOD product release 04

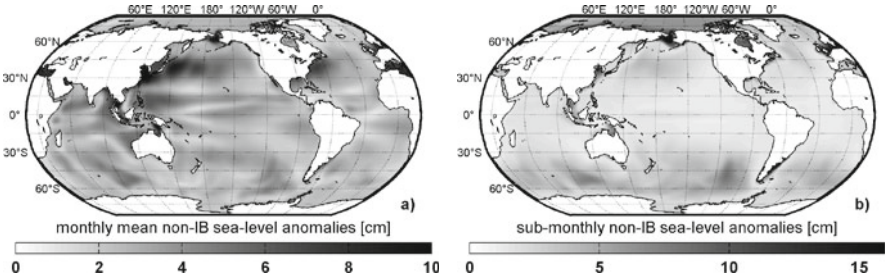

Fig. 2 Monthly mean (**a**) and sub-monthly (**b**) sea-level anomalies as simulated with OMCT that have been corrected for static effects of atmospheric loading by means of the inverse barometric assumption

ocean, underlining once more the necessity of de-aliasing the short-term non-tidal ocean mass anomalies from the GRACE observations.

Besides ocean mass anomalies, OMCT additionally provides three-dimensional fields of ocean dynamics that can be used to consistently combine GRACE observations with other geodetic observations. Since sea-level variability is routinely observed by satellite altimetry, sea-surface height estimates from OMCT (Fig. 2) can be used to decompose the various contributors to sea-level changes (see e.g. Dobslaw, 2007). The model is also able to provide insight into the physical processes generating certain signals in sea-level or ocean mass variability, allowing to relate observations to geophysical aspects of the ongoing global changes on our planet.

For operational purposes of generating the AOD product, OMCT is run daily with about 4 days delay mainly due to the availability restrictions of the ECMWF analysis fields. Ocean mass anomalies, sea surface elevations, and other relevant quantities are routinely visualised on a newly designed web site at http://www.gfz-potsdam.de (follow Home > Structure > Departments > Department 1 > Earth System Modelling > Services > Operational OMCT) and presented by means of flash animations for the past 14 days. After the performance of additional manual quality controls, the OMCT data are currently released fortnightly for the AOD product generation.

3 Increase of the Temporal Resolution of AOD1B

As stated above, the GRACE RL04 AOD1B dealiasing product is based on 6-hourly ECMWF Integrated Forecast System meteorological data and output from the baroclinic ocean model OMCT. Within GFZ's Precise Orbit Determination for GRACE, which is usually performed with 5 s integration step size, the 6-hourly AOD1B products are treated as follows: First, the atmospheric tide, which is included in the ECMWF pressure data and thus in the atmospheric part of the AOD1B, is removed from the spherical harmonic AOD1B coefficients using the model of Biancale and Bode (2006) to avoid double-bookkeeping with the atmospheric tide correction which is also based on the Biancale and Bode model and applied every integration step size during POD. Secondly, these 6-hourly "atmospheric-tide free" AOD1B spherical harmonics are then linearly interpolated to the 5 s integration time steps to be used in POD as disturbing force besides other sources such as static gravity field, atmospheric tides, Earth and ocean tides or accelerometer measured non-gravitational forces.

The OMCT component of the AOD1B product has been generated with a 6-hourly surface pressure forcing where the S2-tide (the dominant component of the atmospheric tides) has been reduced using a strategy suggested by Ponte and Ray (2002). This avoids double-bookkeeping with the atmospheric part of the ocean tide model S2 constituent during POD.

An interesting question is, if there could be any benefit if the AOD1B 6-hourly temporal resolution could be further increased. Besides operational 6-hourly analysis data used to generate the AOD1B products, ECMWF also provides daily updated 10-days forecast data. Here, the first 3 days have a 3-hourly resolution; the rest is provided on a 6-hourly time scale. Generally, the differences between the two data sets at 6-hourly (0, 6, 12 and 18 h) time steps are very small, i.e., generally less than 0.2 mm in terms of geoid heights. However, the differences at intermediate time steps (3, 9, 15 and 21 h) based on linear interpolation and direct observation show a typical S2 tide signal with an amplitude of about 1.5 mm in terms of geoid heights which cannot be tracked by the 6-hourly sampling of the analysis data. But, as stated above, this signal is corrected for during POD using the atmospheric tide model of Biancale and Bode (2006).

Nevertheless, any real 3-hourly data might contain advantages with respect to a pure model correction. Therefore, alternative 3-hourly RL04 AOD1B products for August 2003 and February 2004 have been calculated which are based on atmospheric forecast data and corresponding ocean simulations. In the next step, precise orbits and gravity fields were derived where the processing strategy and standards only differ in the applied de-aliasing product, i.e., standard 6-hourly or alternative 3-hourly temporal resolution.

Accelerations caused by the different AOD1B products are generally below $2 \cdot 10^{-9}$ m/s^2 and the resulting orbit differences are below 1 mm in all three directions. Consequently, no difference can be seen neither in the resulting K-band and GPS observation residuals nor in the resulting GRACE geoids or in the corresponding comparisons with external gravity functionals (e.g. NIMA gravity anomalies

Table 1 GPS phase, GPS code and K-band range-rate residuals for August 1, 2003 using different combinations of AOD1B products and atmospheric tide corrections

	GPS phase (cm)	GPS code (cm)	K-band range-rate (μm/s)
6-hourly with S2 correction	37.890	0.703	0.255
6-hourly without S2 correction	37.991	0.701	0.253
3-hourly with S2 correction	37.798	0.714	0.255
3-hourly without S2 correction	37.798	0.711	0.255

or CLS01-ECCO derived oceanic geoid). Results do generally not significantly change, even when no atmospheric tide model is applied to compensate the interpolation error. Exemplarily, Table 1 shows the GPS phase, GPS code and K-band range-rate residuals for August 1, 2003 for all 4 combinations (6-hourly/3-hourly time resolution and with/without S2 atmospheric tide correction).

This rather unexpected result is confirmed by a simulation study (see Meyer et al., 2009). Figure 3 shows the GRACE baseline accuracy as simulated before launch (Kim, 2000) and the present GRACE error level introduced to the simulations, which is about a factor of 15 higher. Between these two curves the error when neglecting the S2 atmospheric tide is shown. Regardless of the accelerometer and

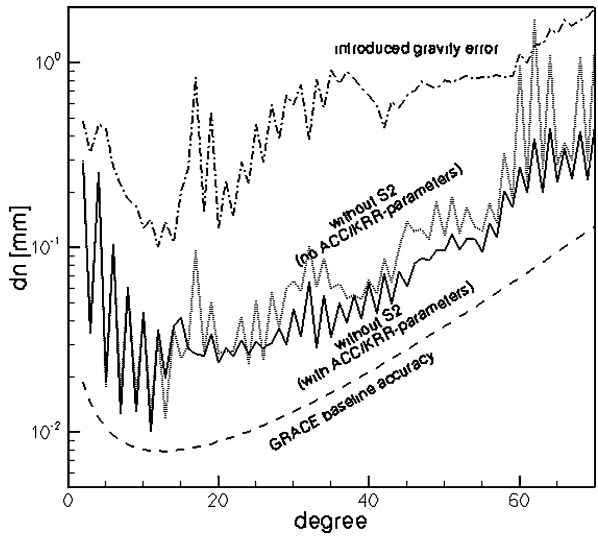

Fig. 3 Simulation study result showing the current GRACE error level, the pre-launch GRACE baseline accuracy and the error when neglecting an atmospheric S2 tide correction, both with and without adjustment of accelerometer (ACC) and K-band range-rate (KRR) parameters (in [mm] geoid height)

K-band parameters being adjusted (as done in the regular GRACE processing) or not, both results are well below the current GRACE error level.

To combine the advantages of both analyses and forecasts and thus, to reveal the impact of 3-hourly atmospheric forcing fields on short-term transient atmosphere-ocean variability, 3-hourly resolved atmospheric forecasts were adjusted to 6-hourly analyses according to Dobslaw and Thomas (2005). The semidiurnal pressure tide S2 is well resolved in 3-hourly sampled data only, which otherwise aliases into a standing wave when data with 6-hourly spacing are used. However, it turned out that the enhanced temporal resolution provides only limited additional information of up to about 1 hPa in mid-latitude regions of the atmosphere and approximately 1.5 cm sea level variability in selected coastal areas (Dobslaw and Thomas, 2007b), which is beyond the present accuracy threshold of GRACE.

To conclude, a higher temporal resolution of the AOD1B product is not necessary, because the applied atmospheric tide model (Biancale and Bode, 2006), based on 6-hourly and 3-hourly ECMWF surface pressure data, already corrects the S2-tide signal in the interpolated 6-hourly AOD1B products sufficiently. Additionally, if no other improvements towards the GRACE baseline will be implemented, GRACE is presently not able to detect the small signal caused by atmospheric tides.

4 AOD1B RL04 Time Series for Consistent SLR Data Processing

So far, AOD1B RL04 products have been generated for CHAMP and GRACE processing for the period January 2001 until present. Figure 4 shows gravity variations in terms of geoid heights as deduced from 6-hourly ECMWF vertical integrated pressure data, 6-hourly ocean bottom pressure fields as simulated with OMCT, monthly continental water height changes resulting from the Water Gap Hydrological Model (WGHM, Döll et al., 2003), and the sensitivity of LAGEOS, CHAMP, GRACE and GOCE to these signals. While GOCE is primarily sensitive to atmospheric mass variations up to approximately degree 15, CHAMP and even more GRACE results are highly influenced by all three kinds of signals. Obviously, there is a clear indication that for the very first degrees also LAGEOS is sensitive to atmospheric and, to a lesser extent, to oceanic mass variations. In contrast to GRACE, a correlation with hydrological mass variations is not obvious. However, it can be concluded that for a consistent comparison of low degree coefficients the AOD1B model has to be accounted for during LAGEOS processing as well.

A consistent prolongation back to 1976, when LAGEOS-1 was launched, cannot be performed directly due to a change of atmospheric data within the period covered by LAGEOS data; consequently, the necessary OMCT model output is based on two principally different atmospheric forcing models, too. While until 2001 atmospheric forcing fields provided by ECMWF's reanalysis project ERA-40

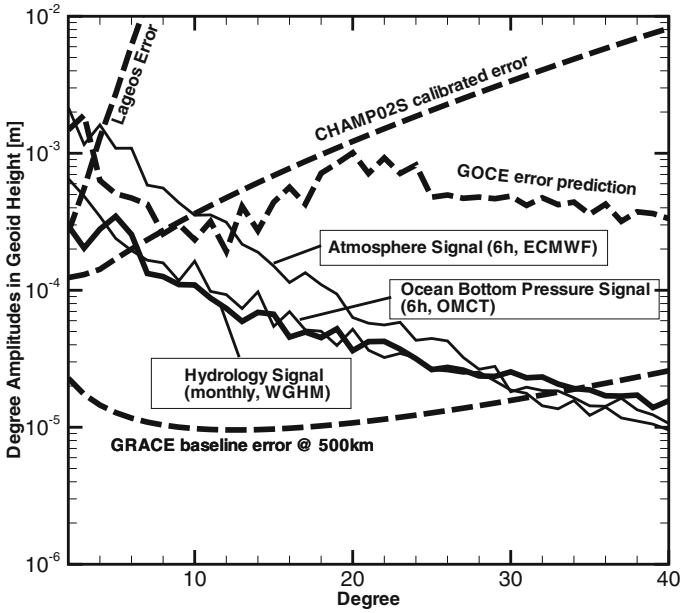

Fig. 4 Gravity variations in terms of geoid height estimated from ECMWF 6-hourly vertical integrated pressure, 6-hourly OMCT ocean bottom pressure and monthly WGHM continental water height changes (*solid lines*) and the sensitivity of LAGEOS, CHAMP, GRACE and GOCE to this signals (*long dashed lines*)

were applied, oceanic mass variations for recent years since 2001 were simulated with ECMWF's operational analysis data. This change in forcing was done because of the superiority of ERA-40 compared to operational analysis data at least up to 1999 (Uppala et al., 1999), the increase of the 4D-Var operational analysis assimilation window from 6 to 12 h on September 12, 2000, and the increase of the spatial resolution of the operational analysis data from T320 (corresponding to 0.56°) to T520 (0.35°) on November 21, 2000.

Therefore, to generate consistent atmospheric and oceanic non-tidal mass anomalies for processing of LAGEOS data, two sensitivity tests have been performed with two additional AOD1B test series for 2004. Firstly, the vertical structure of the atmospheric masses has been neglected by global substitution of the vertical integration (VI) by surface pressure (SP) data. Secondly, ocean bottom pressure variations over the oceans have been set to zero what corresponds to the simplified assumption that the sea surface reacts exactly like an inverse barometer (IB) and density variations within the local water column are negligible. According to the resulting C_{20} variations, the difference between VI and SP is insignificant for the processing of LAGEOS data, while the omission of oceanic mass variations results again in seasonal signals similar to the values obtained without AOD1B, but here with slightly smaller amplitude (see Flechtner et al., 2008). Thus, for LAGEOS data analysis back to 1976 an AOD1B product based on OMCT mass anomalies and atmospheric

surface pressure has been processed and made available to the user community in the GFZ Integrated System and Data Center (ISDC).

Exemplarily for the period 1993–2006, various experiments have been performed in order to reveal the impact of the application of AOD1B within LAGEOS data processing. This includes the change in correlation of the annual and semi-annual signals as well as the effect on LAGEOS orbits and SLR residuals. The major findings are that the

- unresolved bias between LAGEOS and GRACE has not been changed significantly when applying the AOD1B model and remains in the order of $2 \cdot 10^{-10}$.
- influence of AOD1B on the LAGEOS SLR (and K-band for GRACE) residuals and orbital fits can be neglected.
- correlation between the "standard" LAGEOS C20 time series processed without applying an AOD1B model and the primarily hydrological or atmospheric annual signals of WGHM, AOD1B and GRACE is very high (0.74–0.95).
- short-term non-tidal atmosphere/ocean corrected LAGEOS solution is not only sensitive to primarily annual hydrological mass variations, but also to semi-annual additional seasonal signals of unknown nature (Fig. 5) which also reduces the overall correlation with the above time series by 30–50%.

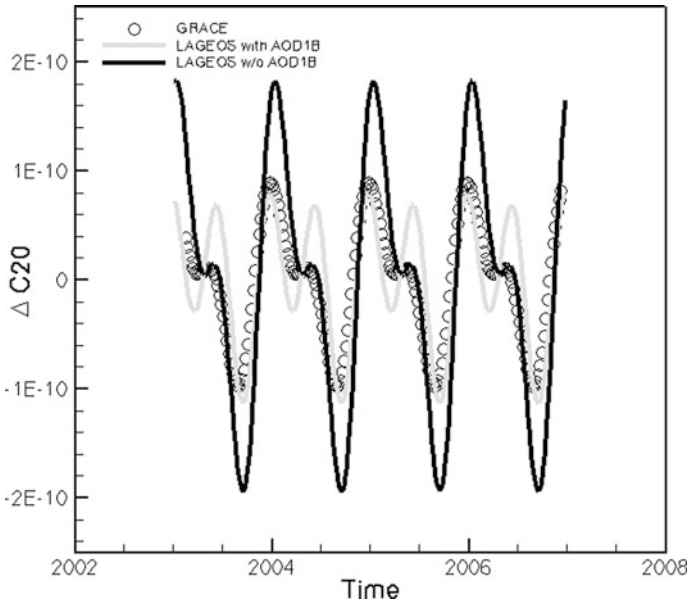

Fig. 5 Annual plus semi-annual C_{20} variations for the period 2003 till 2006 derived from weekly LAGEOS data analysis without (*black*) and with applying AOD1B (*grey*) time series and from GRACE (*dots*). For better representation the high-frequency LAGEOS and GRACE signals are not shown

The last finding is in opposite to what one would expect, i.e. a better agreement between GRACE and LAGEOS if common standards are applied, and has to be analyzed in more detail in the future. Additionally, it should be investigated in the near future if the AOD1B model needs to be applied for processing of other geodetic satellites such as AJISAI, STARLETTE and others. For further details please refer to Flechtner et al. (2008).

5 Conclusions

GFZ Potsdam routinely generates non-tidal high-frequency atmospheric and oceanic mass variation models (AOD1B) for GRACE data processing. These models are based on 6-hourly meteorological analysis fields of the Integrated Forecast System of the European Centre for Medium-Range Weather Forecasts (ECMWF) and output from an ocean general circulation model. For AOD1B release 0 (RL00) and 1 (RL01) the barotropic ocean model PPHA was used. As this model has shown several deficiencies the latest versions of AOD1B are based on the baroclinic Ocean Model for Circulation and Tides (OMCT). The OMCT output for near real time AOD1B RL04 generation is based on a bathymetry augmented by water depth estimates below the Antarctic ice-shelves and a total ocean mass which is held constant at each time-step by means of adding a globally homogeneous layer of mass, correcting for artificial mass changes due to the model formulation as well as for changes in the total ocean mass due to the time-varying freshwater fluxes.

As the temporal resolution of AOD1B products is 6 h and therefore S2 air tide signals are not accounted for properly, some experiments have been made to investigate the influence of 3-hourly meteorological forcing on the resulting GRACE orbits and gravity fields. It turned out that the atmospheric tide model used to correct for interpolation errors is accurate enough and even the error caused by a complete neglect of atmospheric tides is below the current GRACE error level.

Finally, the AOD1B RL04 model has been reprocessed back to 1976 based on ERA40 re-analysis data, a simplified surface pressure assumption and corresponding OMCT output to be used for a consistent processing of Satellite Laser Ranging data and a subsequent combination with GRACE data. First results of LAGEOS derived C20 values with those from GRACE show higher correlations for the annual amplitudes but also semi-annual signals of unknown nature.

Acknowledgments This is publication no. GEOTECH-1268 of the programme GEOTECHNOLOGIEN of BMBF and DFG, grant 03F0423. We thank ECMWF for provision of meteorological data necessary to generate AOD1B time series.

Notes

- The operational AOD1B RL04 products based an ECMWF analysis data for the period 2001 until present and the AOD1B RL04 products before 2001 based on ERA40 data are available at the Information System and Data Center (ISDC) at GFZ Potsdam (http://isdc.gfz-potsdam/grace).

- Details on the operational RL04 products as well as on the precursor releases can be found in the AOD1B Product Description Document for Product Releases 01 to 04 (Rev. 3.1, April 13, 2007) which can be downloaded at ISDC.
- A quality monitoring page for the period 2001 until present is available at http://www-app2.gfz-potsdam.de/pb1/op/grace/results.

References

Biancale R, Bode A (2006) Mean annual and seasonal atmospheric tide models based on 3-hourly and 6-hourly ECMWF surface pressure data. Scientific Technical Report STR06/01, Deutsches GeoForschungsZentrum, Potsdam, Germany.

Boy JP, Chao BF (2005) Precise evaluation of atmospheric loading effects on Earth's time-variable gravity field. J. Geophys. Res. 110(B), doi: 10.1029/2002JB002333.

Carrère L, Lyard F (2003) Modeling the barotropic response of the global ocean to atmospheric wind and pressure forcing comparisons with observations. Geophys. Res. Lett. 30(6), 1275, doi: 10.1029/2002GL016473.

Dobslaw H (2007) Modellierung der allgemeinen ozeanischen Dynamik zur Korrektur und Interpretation von Satellitendaten. Scientific Technical Report 07/10, Deutsches GeoForschungsZentrum, Potsdam, Germany, 113 pp.

Dobslaw H, Thomas M (2005) Atmospheric induced oceanic tides from ECMWF forecasts. Geophys. Res. Lett. 32, L10615.

Dobslaw H, Thomas M (2007a) Impact of river run-off on global ocean mass redistribution. Geophys. J. Int. 168(2), 527–532.

Dobslaw H, Thomas M (2007b) Periodic and transient short-term mass variations in numerical simulations of atmosphere-ocean dynamics. Geotechnol. Sci. Rep. 11, 122–126.

Döll P, Kaspar F, Lehner B (2003) A global hydrological model for deriving water availability indicators: Model tuning and validation. J. Hydrol. 270, 105–134.

Flechtner F, Schmidt R, Meyer U (2006) De-aliasing of short-term atmospheric and oceanic mass variations for GRACE. In: Flury J, Rummel R, Reigber C, Rothacher M, Boedecker G, Schreiber U (eds.), Observation of the Earth System from Space, ISBN 3-540-29520-8, Springer, Berlin, pp. 83–97.

Flechtner F (2007) AOD1B Product Description Document. GRACE 327-750, rev. 3.1, Deutsches GeoForschungsZentrum, Potsdam, Germany, 43 pp.

Flechtner F, Thomas M, König R (2008) A long-term model for non-tidal atmospheric and oceanic mass redistributions and its implications on LAGEOS-derived solutions of Earth's oblateness. Scientific Technical Report 08/12, Deutsches GeoForschungsZentrum, Potsdam, Germany, 24 pp.

Greatbatch RJ (1994) A note on the representation of steric sea level in models that conserve volume rather than mass. J. Geophys. Res. 99(C6), 12767–12771.

Hellerman S, Rosenstein M (1983) Normal monthly wind stress over the world ocean with error estimates. J. Phys. Oceanogr. 13, 1093–1104.

Hirose N, Fukomori I, Zlotnicki V, Ponte R (2001) High-frequency barotropic response to atmospheric disturbances: Sensitivity to forcing, topography, and friction. J. Geophys. Res. 1006, 30987.

Kanzow T, Flechtner F, Chave A, Schmidt R, Schwintzer P, Send U (2005) Seasonal variation of ocean bottom pressure derived from Gravity Recovery and Climate Experiment (GRACE): Local validation and global patterns. J. Geophys. Res. (Oceans) 110(C9), 9001, doi: 10.1029/2004JC002772.

Kim J (2000) Simulation Study of a Low-Low Satellite-to-Satellite Tracking Mission. Technical Report, University of Texas at Austin, TX.

Levitus S (1982) Climatological Atlas of the World Ocean. NOAA Professional Paper 13, US Department of Commerce, 173 pp.

Meyer U, Frommknecht B, Flechtner F (2009) Global gravity fields from simulated Level-1 GRACE data. In: Flechtner F, Gruber T, Güntner A, Mandea M, Rothacher M, Schöne T, Wickert J (eds.), Satellite Geodesy and Earth System Science, Springer-Verlag, Berlin, Heidelberg.

NOAA (1988) Data Announcement 88-MGG-02, Digital Relief of the Surface of the Earth, NOAA, National Geophysical Data Center, Boulder, CO.

Padman L, Fricker H A, Coleman R, Howard S, Erofeeva S (2002) A new tidal model for the Antarctic ice shelves and seas. Ann. Glaciol. 34, 247–254.

Ponte R, Ray R (2002) Atmospheric pressure corrections in geodesy and oceanography: A strategy for handling air tides. Geophys. Res. Lett. 29, 6.

Reigber C, Schmidt R, Flechtner F, König R, Meyer U, Neumayer KH, Schwintzer P, Zhu SY (2005) An Earth gravity field model complete to degree and order 150 from GRACE: EIGEN-GRACE02S. J. Geodyn. 39, 1–10.

Schmidt R, Schwintzer P, Flechtner F, Reigber C, Güntner A, Döll P, Ramillien G, Cazenave A, Petrovic S, Jochmann H, Wünsch J (2006) GRACE observations of changes in continental water storage. Global Planet. Change 50, 112–126.

Thomas M (2002) Ozeanisch induzierte Erdrotationsschwankungen – Ergebnisse eines Simultanmodells für Zirkulation und ephemeridische Gezeiten im Weltozean, Dissertation, Institut für Meereskunde, Universität Hamburg, Hamburg, 128 pp.

Thomas M, Sündermann J, Maier-Reimer E (2001) Consideration of ocean tides in an OGCM and impacts on subseasonal to decadal polar motion excitation. Geophys. Res. Lett. 28(12), 2457–2460.

Thompson PF, Bettadpur SV, Tapley BD (2004) Impact of short period, non-tidal, temporal mass variability on GRACE gravity estimates. Geophys. Res. Lett. 31, doi: 10.1029/2003GL019285.

Uppala S, Gibson JK, Fiorino M, Hernandez A, Kallberg P, Li X, Onogi K, Saarinen S (1999) ECMWF's second generation reanalysis – ERA-40. Proceedings of the Second International Conference on Reanalyses, Wokefield Park, Mortimer, Reading, UK, 23–28 August 1999.

Velicogna I, Wahr J, Van den Dool H (2001) Can surface pressure be used to remove atmospheric contributions from GRACE data with sufficient accuracy to recover hydrological signals? J. Geophys. Res. 106, 16415–16434, doi: 10.1029/2001JB000228.

Wünsch J, Thomas M, Gruber T (2001) Simulation of oceanic bottom pressure for gravity space missions. Geophys. J. Int. 147, 428–434.

Global Gravity Fields from Simulated Level-1 GRACE Data

Ulrich Meyer, Björn Frommknecht, and Frank Flechtner

1 Introduction

At the time of writing, the twin Gravity Recovery and Climate Experiment (GRACE, Tapley et al., 2004) satellites are in orbit for nearly 7 years. They deliver gravity data of unprecedented quality, but the baseline accuracy that was computed in a pre-launch simulation study (Kim, 2000) has not yet been reached by a factor of 7.5 (static field) and 15 (time variable field), respectively (Flechtner et al., 2009). The reasons are manifold and a complex simulation study is necessary to identify the error sources and to reach conclusions for an optimized processing strategy.

In a first step of our simulation study noise free observations are simulated by the Earth Parameter and Orbit System – Orbit Computation (EPOS-OC) software, the same software that is used at the German Research Centre for Geosciences (GFZ) for the routine processing of GRACE data. In a closed-loop simulation the gravity field is reconstructed from these observations for a prove of concept. In a second step empirical parameters that are designed to absorb systematic effects in the noise of the accelerometers, the inter-satellite K-Band link, and the receiver clocks onboard the GRACE satellites are introduced, and their correlations with the coefficients of the gravity field are studied. Further on, different errors in the background models (e.g. ocean and atmosphere tides and de-aliasing of short time non-tidal mass variations (AOD1B product, Flechtner et al., 2006)) are introduced to quantify their influence on the gravity field recovery. Additionally, the orbit sampling and omission errors are studied. Finally, colored observation noise from the end-to-end mission simulator (Frommknecht, 2007) at the Technical University of Munich (TUM) is added to the simulated observations. For the accelerometers, the star sensors and the K-Band link this noise resembles the instrument characterizations given in Thomas (1999). For GPS observations only white noise is added. The influence of the noise on the gravity field recovery is quantified and the effectiveness

U. Meyer (✉)
Helmholtz-Zentrum Potsdam, Deutsches GeoForschungsZentrum (GFZ),
D-82234 Weßling, Germany; Astronomical Institute, University of Bern, 3012 Bern, Switzerland,
e-mail: ulrich.meyer@aiub.unibe.ch

F. Flechtner et al. (eds.), *System Earth via Geodetic-Geophysical Space Techniques*,
Advanced Technologies in Earth Sciences, DOI 10.1007/978-3-642-10228-8_12,

of the instrument parameters is shown. The experiments with erroneous background models are repeated under the presence of observation noise.

2 Simulation of Observations

Starting from orbital elements of the two GRACE satellites on 01/08/2003, 00:00:00 UTC, monthly arcs were numerically integrated for both satellites. Since the gravity recovery is based on daily arcs, 31 daily orbital elements were extracted from the monthly arcs and the orbit integration was repeated for each day. In this way discontinuities at the arc boundaries are minimized (simple cutting of the monthly arcs into 31 daily pieces led to inconsistencies in the gravity recovery step due to necessary interpolation of Earth rotation parameters at the arc boundaries).

For the orbit integration all forces acting on the satellites have to be modeled. The biggest non-gravitational force is the atmospheric drag that was computed by the DTM94 atmosphere model (Berger et al., 1998) and a surface model of the GRACE satellites. It is completed by solar pressure and Earth albedo (Knocke et al., 1988). To model the static Earth gravity field, EIGEN-CG03C (Förste et al., 2005) was introduced up to degree and order 70. The lunar gravity field (Ferrari and Bills, 1977) was taken up to degree 4, whereas the Sun and the planets (Mercury, Venus, Mars, Jupiter and Saturn) were considered as point masses. The ocean tides were computed from FES2004 (Lyard et al., 2006) and the atmospheric tides according to Bode and Biancale (2006). Short-term mass variations of the atmosphere and oceans were interpolated from 6-hourly ECMWF meteorological data (Flechtner, 2007) and the Ocean Model for Circulation and Tides (OMCT, Thomas et al., 2001). With these background models the simulation follows the standards of the routine release 04 processing of GRACE data at GFZ (Flechtner et al., 2009) except that the measured accelerations are, of course, replaced by the surface forces.

Simulated K-Band SST range and range-rate observations were computed every 5 s from the orbital arcs of GRACE-A and -B taking into account the displacement of the K-Band antennas from the centers of mass of the satellites. The roll, pitch and yaw attitude angles were assumed to be zero. To simulate GPS observations, the SP3 orbits of the GPS satellites during August 2003 were taken from the routine GRACE processing. As long as no noise is introduced, code and phase observations do not differ and represent the distances between the GPS satellites and the corresponding GRACE satellites. Neither ambiguities nor cycle slips were introduced.

To test the simulation mode and the numerical stability of EPOS-OC, the simulated K-Band and GPS observations were reentered into EPOS-OC and the program was then used in the parameter estimation mode. Here, all background models and force models were kept unchanged. The resulting RMS of the GPS residuals between observed (simulated) and computed (during parameter estimation) observations is at the level of 0.022 μm (identical for code and phase observations). The

RMS of the K-Band range residuals drops from 0.012 μm at the beginning of august to 0.010 μm at the end of the month. Since the range observations are computed from absolute satellite positions (about 7,000 km from the origin of the geocentric coordinate system), the size of the apparent trend in the K-Band residuals is below the machine accuracy for double precision variables (15 significant digits). From this and from the near-zero residuals we conclude that the simulation mode of EPOS-OC is in accordance with the parameter estimation mode and the simulated observations can be trusted.

3 Estimation of Arc Specific Parameters and Gravity Field Coefficients

In the next step a slightly modified clone of GGM02C (Tapley et al., 2005) was introduced as a priori gravity field (C_{20}, C_{21}, S_{21} and the drift rates of low degree harmonics were set equal to EIGEN-CG03C to avoid differential once-per-rev accelerations). In a first parameter estimation run the initial elements of the satellite arcs were adjusted. In a second run partial derivatives for gravity field coefficients up to degree and order 70 were set up together with the partials for the initial orbital conditions and assembled in daily normal equations. The initial conditions were reduced from the normal equations (implicitly solved) and the daily normal equations were accumulated to monthly ones. Finally, corrections to the coefficients of the a priori gravity field were estimated from a full month of simulated observations by a least squares process. Details on the processing of GRACE data at GFZ can be found e.g. in Schmidt (2007).

The resulting gravity field was then compared to the "true" gravity field EIGEN-CG03C. In Fig. 1a the corresponding degree variances of the differences as well as the baseline accuracy and the remaining errors after adjustment of the gravity field coefficients are shown. These errors are due to the non-linearity of the problem and numerical noise. If GPS and K-Band range-rate observations are used in the adjustment process, the remaining errors are two orders of magnitude below the baseline accuracy. Even if only GPS observations are used, the solution fulfills the requirements up to degree 60. As soon as K-Band range observations are introduced, the accuracy drops. This points at a problem in the processing of the range observations, which has to be further investigated. A possible reason could be the limited accuracy of the numerical integration process at the sub-micrometer level.

In all figures showing difference degree variances between the "true" gravity field and adjusted gravity field coefficients, three lines are repeated for better orientation: the solution from noise free GPS and K-Band range observations as the best possible case, the baseline accuracy as our goal, and the difference between the a priori and the "true" gravity field as upper bound for the errors. Consequently, three kinds of results may be achieved with each individual experiment: As long as the effect of an experiment on the solved gravity field coefficients stays below the baseline accuracy, it is not really significant. If the errors rise above the differences introduced in the a priori field, the assumptions of the experiment were too pessimistic, since

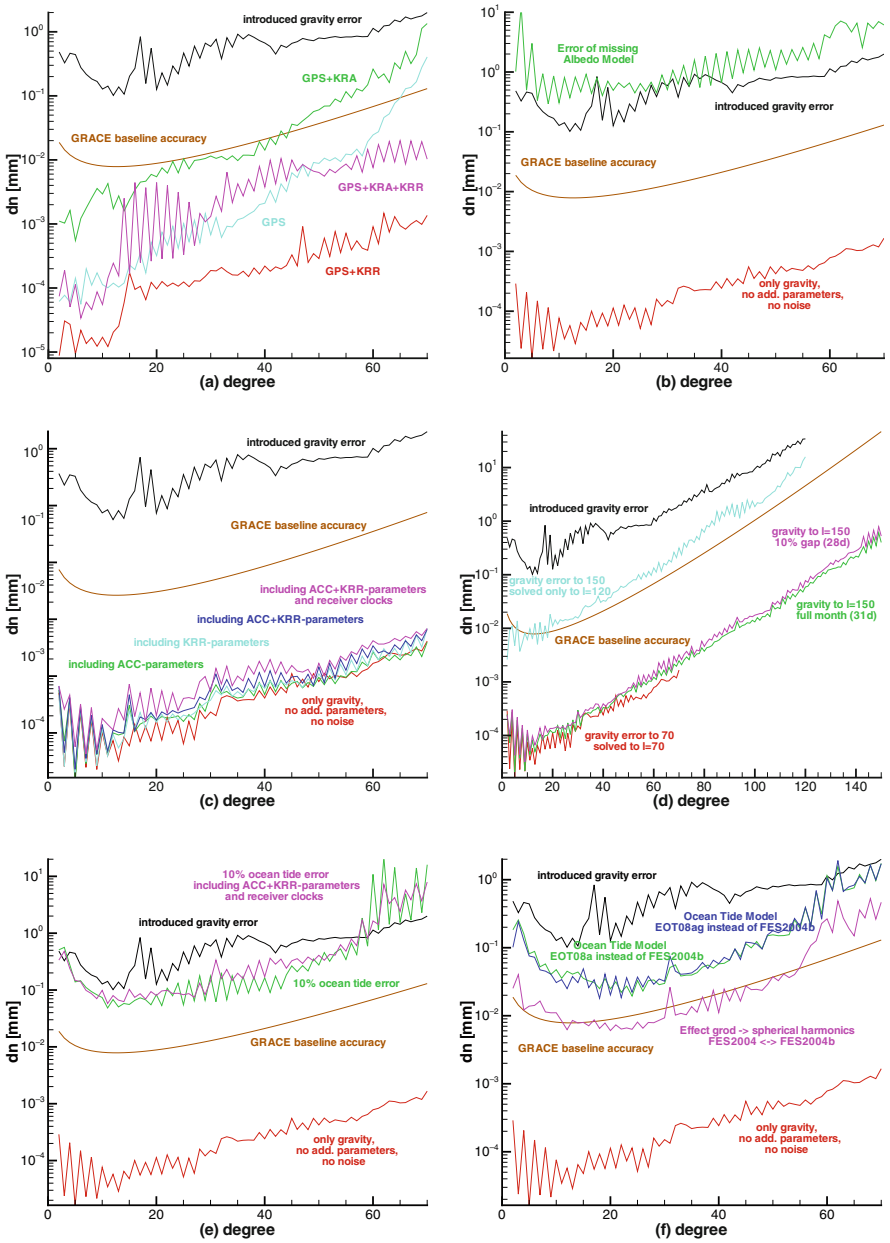

Fig. 1 (**a**) Shows the difference degree variances between a priori and adjusted gravity fields from GPS only, GPS and K-Band range (KRA), GPS and range-rate (KRR) as well as GPS, KRA and KRR together. (**b**) Shows the effect of the albedo model on the gravity field recovery. (**c**) Shows the correlation of different instrument parameters with the gravity field coefficients. (**d**) Expands the results from Fig. 1a to degree 150 and shows the effects of a data gap and omission error. (**e**) Shows the effect of a 10% ocean tide model error. (**f**) Shows the effect of two recent ocean tide models on the gravity field solution

no improvements in the coefficients could be achieved. If the remaining differences after the gravity field adjustment stay between the baseline accuracy and the errors introduced by the a priori field, the error sources studied in the experiment do play a role in the real data processing and significantly add to the error budget of the estimated gravity fields.

To assess the influence of the surface forces on the satellite trajectories, and especially the effect of errors in these models on the estimation of gravity field coefficients, the albedo model was set to zero in a next parameter estimation run. The effect on the adjusted gravity field coefficients is dramatic. As shown in Fig. 1b, the estimated parameters do not longer converge to the correct values. The differences between adjusted and "true" gravity field model grow bigger than the differences between the a priori and the "true" model. This emphasizes the necessity of either good non-gravitational models, sufficient empirical accelerations to compensate model deficiencies, or the direct measurement of the surface forces by onboard accelerometers as in case of GRACE. No further experiments with direct solar pressure or atmospheric drag were made, since the size of these surface forces is even bigger than that of albedo.

In order to simulate the direct measurement of the surface forces by the onboard accelerometers, the modeled forces were added up and stored as GRACE Level-1B ACC1B observation data files. In a similar way, the simulated K-Band observations were written to KBR1B files, and the attitude angles were transformed into quaternions and stored as SCA1B files. The change to GRACE Level-1B format includes a transformation between inertial coordinates and satellite system coordinates. Moreover, some digits are lost due to the formatted output of the EPOS-OC files. To check this effect, the parameter estimation run with GGM02C as a priori field was repeated, this time based on the simulated Level-1B observation files instead of force models. The result of the gravity field recovery using GPS and K-Band range-rate data is also shown in Fig. 1b. It does not differ significantly from the results shown in Fig. 1a. The oscillations between even and odd low degree coefficients are a phenomenon often observed in simulation studies in the absence of observation noise and are commonly attributed to the influence of the polar gap of the satellite orbits (GRACE has an inclination of 89.5°). As a result of the tests carried out so far, we conclude that the EPOS-OC software is able to simulate observations and to estimate gravity field coefficients with sufficient accuracy both for this study and for the routine processing of GRACE data.

4 Estimation of Instrument Parameters

In the routine processing of real GRACE data some empirical parameters, referred to as instrument parameters, are introduced to account for systematic effects like drifts or periodic errors in the observation noise. In this section their correlation with gravity field coefficients is described. The instrument parameters include scale factors for the along-track accelerations (FAT) and accelerometer biases in along-track (P1T), cross-track (P1N), and radial (P1R) direction that are estimated at the

beginning and the end of each daily arc. The K-Band instrument parameters include biases in range (P0) and range-rate (P1) as well as a rate-drift (P2) that are estimated once-per-rev (every 90 min). Additionally, sine and cosine parameters (S0 and C0) according to the revolution period of the satellites are estimated every 180 min, whereas corrections to the GPS receiver clocks are estimated every 30 s. In the routine processing also GPS ambiguities are estimated, but they are omitted at this point of the simulation study.

Four different parameter estimation runs were made. The first run comprised initial conditions, accelerometer instrument parameters, and gravity field coefficients. In a second experiment the accelerometer parameters were replaced by the K-Band instrument parameters. The third test included accelerometer parameters and K-Band parameters in combination. Finally, the estimation of the receiver clocks was added. In all of these runs our modified version of GGM02C was taken as a priori gravity field model and GPS and K-Band range-rate observations were used for the recovery (therefore no P0 parameters could be estimated). Figure 1c shows the degree variances of the remaining differences between the adjusted a priori and the "true" gravity field. None of the instrument parameters led to a significant degradation of the results. Therefore, we conclude that the correlations between the instrument parameters and the gravity field coefficients can be neglected.

The instrument parameters are treated like the initial conditions, i.e. they are estimated a first time during the orbit adjustment process and a second time together with the gravity field coefficients (since they are arc specific parameters, they are solved implicitly for each day prior to the accumulation of the normal equations to reduce the number of parameters in the monthly normal equation). It shall not be concealed that they reduce the size of the observation residuals after the orbit adjustment runs significantly, so they do influence the satellite orbits and absorb some gravity signal. But it seems that this signal is correctly assigned back to the gravity field coefficients as soon as they are estimated together with the instrument parameters. It is also worth mentioning that the P2 parameters are strongly correlated with the accelerometer parameters as shown in Table 1. This is in agreement

Table 1 Instrument parameters estimated during the four test runs. Since neither scales nor biases were introduced into the simulated observations, the scales are estimated close to one and the biases close to zero. Note the change in P2 as soon as ACC-parameters are estimated

	ACC-parameters	KBR-parameters	ACC+KBR	ACC+KRR+Clocks
P1R	$-5.35e^{-09}$		$-5.36e^{-09}$	$-8.93e^{-09}$
P1T	$-6.54e^{-11}$		$-6.50e^{-11}$	$-6.41e^{-11}$
P1N	$-1.83e^{-10}$		$-1.83e^{-10}$	$-2.19e^{-10}$
FAT	0.99960		0.99960	0.99960
P1		$-9.17e^{-09}$	$-10.16e^{-09}$	$-10.08e^{-09}$
P2		$-11.78e^{-13}$	$0.87e^{-13}$	$-0.40e^{-13}$
C0		$-1.89e^{-05}$	$-1.43e^{-05}$	$-0.98e^{-05}$
S0		$-4.21e^{-05}$	$-1.28e^{-05}$	$-1.57e^{-05}$

with the observation that a dense parameterization of the K-Band instrument can be replaced by a dense parameterization of the accelerometers (and vice versa).

5 Orbit Geometry and Omission Error

So far, the resolution of the gravity field has been limited to degree and order 70 for all experiments to reduce the computation time. To ensure that the results can be extrapolated to higher degrees, one example with a gravity field of higher resolution was investigated. Therefore, observations were simulated using EIGEN-CG03C up to degree and order 150 (corresponding to the maximum degree solved for in GRACE long-term static gravity fields at GFZ). As a priori model GGM02C was introduced to the same maximum degree of 150. The results of the adjustment of the gravity field coefficients from GPS and K-Band range-rate are shown in Fig. 1d. In principle, they can be linearly extrapolated from the corresponding experiment with a maximum degree of 70. Only a slight degradation in all degrees is visible, although this degradation is negligible even if a data gap of 3 days is introduced (matching the situation in some of the real GRACE monthly solutions). Apparently, the orbit geometry and data sampling is not a problem (as long as periods of repeat orbits are avoided; Klokočník et al., 2008).

Different results are obtained if observations were simulated with a high degree "true" field, but recovered to a lower degree of 120 only (with GGM02C to degree and order 120 as a priori field). The so-called omission error surpasses the baseline accuracy for almost all degrees. In reality the true gravity field is not limited, but the instrument noise limits the sensitivity of the observations. Anyway, one has to be careful to exploit the full sensitivity of the observables (see also Gunter et al., 2006). All following experiments were again limited to degree and order 70.

6 Effect of Errors in the Background Models

Another error source are the background models. While some of the perturbations like the gravitational accelerations by the Sun and the planets are either very small or can be modeled with sufficient accuracy, other effects like the short-term mass variations in the atmosphere and the corresponding response of the oceans are very difficult to model, or are critical due to their sheer size (like the mass variations due to ocean tides). For example, a Fourier analysis of a time series of 4 years of weekly gravity field solutions up to degree and order ten revealed strong signals not only at yearly and half-yearly frequency (as expected due to seasonal hydrological mass variations not modeled so far), but also at 4- and 2-weekly frequencies (Fig. 2). This is a strong indicator that the tidal signal could not be completely removed by the background models.

To assess the effect of errors in the background models on the gravity field recovery, the model of interest may be altered during the parameter estimation run by an amount that represents the expected error of the model. If the size of the model error

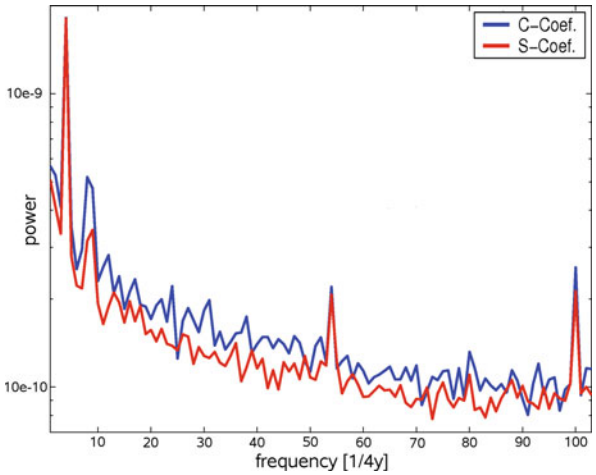

Fig. 2 Mean Fourier coefficients of time series of weekly gravity field coefficients up to degree 10. The length of the time series is $T = 4$ years. Peaks at $4/T$ and $8/T$ represent seasonal signal (water cycle), peaks around $54/T$ (˜monthly) and $100/T$ (˜twice per month) might be of tidal origin

is not known, at least the complete effect of the model on the gravity field recovery can be assessed by complete omission of the model. Both kinds of experiments are shown in this section. Additionally, the ability of the instrument parameters to absorb some of the model errors is studied.

As already pointed out, the ocean tide model is a probable error source. Since the size of the error is not well known, the amplitudes of all tides were randomly altered by up to 10%, and the manipulated model was reintroduced into the parameter estimation run. The result, shown in Fig. 1e, is well above the baseline accuracy. The estimation of instrument parameters does not change the results significantly.

The alteration of the long wavelength part of the ocean tide model by up to 10% may be too pessimistic and the experiment was therefore repeated with two recently generated ocean tide models instead of the manipulated FES2004 model. In EOT08a (Savcenko and Bosch, 2008) altimetry data was used to mainly enhance the coastal regions. In EOT08ag (T. Mayer-Gürr, private communication) specific ocean tides were additionally estimated from GRACE data. Both models are based on FES2004, so the differences represent rather optimistic error estimates. Both models were given on grids and first had to be expanded into spherical harmonics, which is not a trivial task. Therefore, to check the algorithm, also a gridded version of FES2004 was transformed into spherical harmonics and called FES2004b.

The effects of all three models on gravity field recovery are shown in Fig. 1f. While the expansion of the grids into spherical harmonics yields errors at the level of the baseline accuracy, the effect of EOT08a and EOT08ag is somewhat smaller than the effect of our arbitrarily altered FES2004, but still is significant. The real effect probably lies somewhere in-between of these two extremes and therefore very likely accounts for part of the degradation from baseline accuracy experienced in the

processing of real GRACE data. Note that these experiments are not suited to draw any conclusions about the quality of the different ocean tide models.

The atmospheric tides were much discussed in the past years. They may be modeled, but they are also visible in the observed surface pressure that is used to compute the atmosphere and ocean de-aliasing products (AOD1B) and in the response of the oceans to the surface pressure of the atmosphere. To avoid double bookkeeping, they are reduced from the ocean model forcing meteorological data and from the AOD1B product before modeled in EPOS-OC during orbit integration. Even complete omission of the biggest component, the S2 tide, leads to smaller degradations in the gravity field than the error found in the ocean tide model in the previous experiments (Fig. 3a). Consequently, atmospheric tides surely do not play a major role in the error budget of GRACE.

The error of the de-aliasing product (AOD1B) itself is difficult to access. Complete omission leads to an error even bigger than the one found for the ocean tides (Fig. 3b). This shows that the AOD1B product plays a vital role in the estimation of the monthly GRACE gravity fields. Further investigations to derive realistic error estimates for the AOD1B products would be very helpful. This is a task investigated in the German Special Priority Program "mass transports and mass distribution in the system Earth (Ilk et al., 2005)" project IDEAL-GRACE (Improved De-aliasing for GRACE).

7 Colored Observation Noise

To get closer to reality, colored noise which was created within the GEOTECHNOLOGIEN project "Improved Level-1 products and their validation by ocean bottom pressure" following the definitions given by Thomas (1999), i.e. $1e^{-20}(1+0.005/f)$ m^2s^4/Hz for the two sensitive axes of the accelerometer and $1e^{-18}(1+0.01/f)$ m^2s^4/Hz for the less sensitive axis (cross-track) is added to the simulated observations in the next step. The K-Band noise is composed of the system noise $1e^{-12}(2\pi f)^2 m^2s^4$/Hz and the oscillator noise $(2\pi f)^2(1-e^{-0.002\pi f})^2(4e^{-15} + 3e^{-11}/f^2 + 2e^{-12}/f^3 + 3e^{-15}/f^4) m^2s^4$/Hz. The system noise dominates the high frequencies, whereas the oscillator noise dominates the low frequencies. The star camera noise is $1e^{-8}$ rad/Hz on all three axes. For the GPS observations white noise was produced by EPOS-OC and directly added during the simulation run. It amounts to 35 cm for code and 0.85 cm for phase observations (these values correspond to the RMS of GPS residuals found by processing of real GRACE data).

While one type of simulated observations was replaced by noisy observations in a parameter estimation run, the other observations were kept free of noise. In this way the influence of each type of noise on the gravity field was determined separately. Only GPS and K-Band noise had to be introduced together in the same parameter estimation run. Otherwise the gravity field would have been determined completely from the noise free observation type. Therefore, the relative weighting of GPS and K-Band observations plays an important role. Each experiment was first performed with standard weights (2 m for GPS code, 2 cm for GPS phase and 1 μm/s for

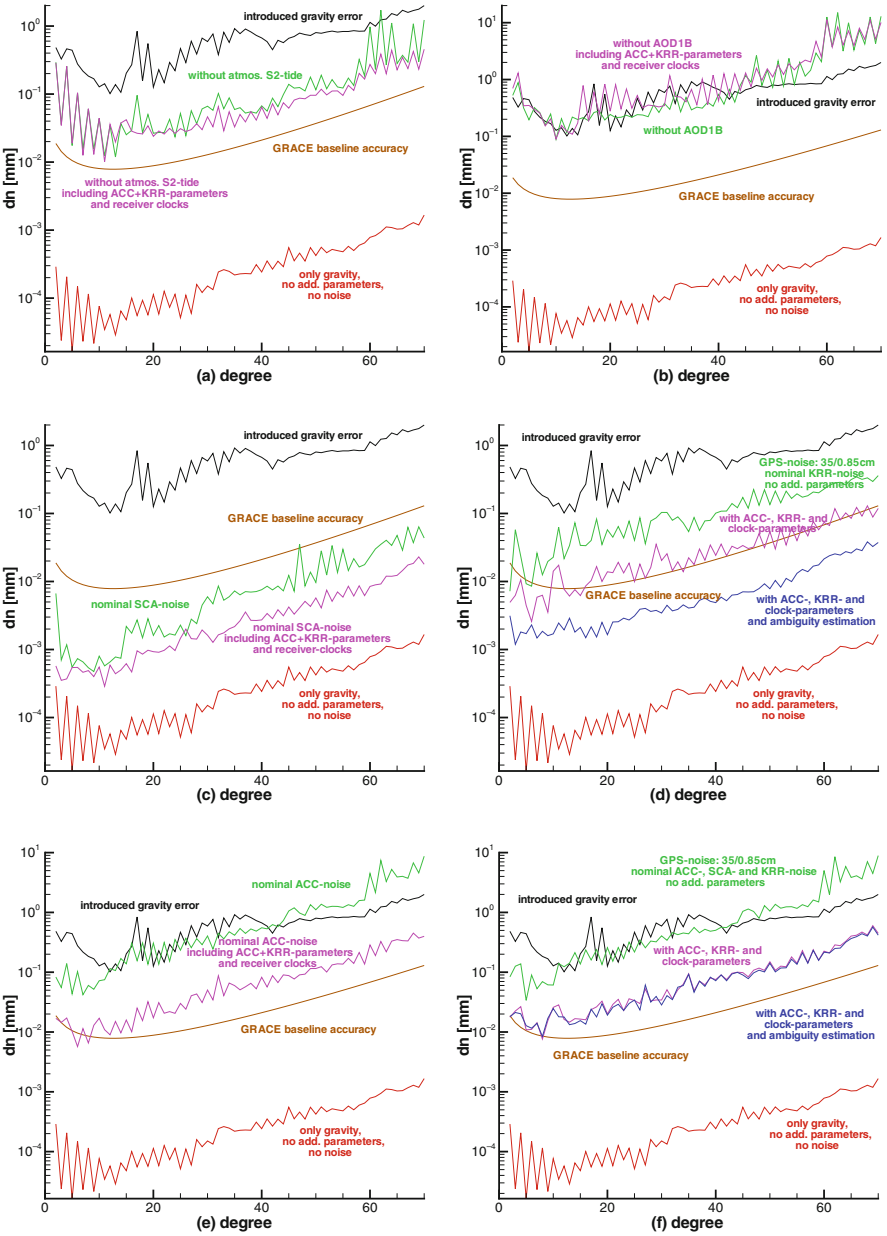

Fig. 3 (**a**) Shows the effect of the atmospheric S2 tide on gravity field recovery. (**b**) Shows the effect of the atmosphere and ocean de-aliasing (AOD1B). (**c**) Shows the effect of star camera noise, with and without estimation of instrument parameters. (**d**) Shows the combined effect of K-Band and white GPS noise, for a first time also GPS ambiguities are estimated. (**e**) Shows the effect of accelerometer noise. (**f**) Shows the combined effect of accelerometer, star camera, K-Band and GPS noise. The accelerometer noise dominates the results, while the estimation of GPS ambiguities does not show significant improvements

K-Band range-rate). After orbit adjustment the weights were adjusted to represent the size of the RMS of the residuals and the orbit adjustment was repeated until convergence. Generally, the weights converged quickly to their final values.

The results of these experiments are shown in Fig. 3c (star camera noise), 3d (GPS and K-Band noise), and 3e (accelerometer noise), respectively. Each experiment was performed twice, once without and once with estimation of instrument parameters. It turned out that the instrument parameters start to play a vital role, since they absorb the systematic effects in the observation noise to a large extent and to the benefit of the gravity field coefficients. The star camera noise itself does not play an important role, its impact on the gravity field stays well below the baseline accuracy. Systematic effects of the misalignment of the star cameras on the accelerometer observations were already accounted for in the accelerometer noise. GPS and K-Band noise lead to a significant degradation of the gravity field, but their effect drops to baseline level when instrument parameters are introduced. As soon as ambiguities are estimated, the noise drops to insignificance (note that the white noise on GPS might be too optimistic).

The results are completely different for the accelerometer noise. Without instrument parameters no improvement of the gravity field coefficients can be achieved. And even in the presence of instrument parameters the degradation of the gravity field stays above the baseline accuracy. In combination with star camera, K-Band and GPS noise the accelerometer noise clearly dominates the results (Fig. 3f). Even the iteration of the solution after introduction of the adjusted gravity field as new a priori field does not help (Fig. 4a). It can be stated that the baseline accuracy cannot be reached with the actual instrument parameterization and processing strategy of GFZ, and that the accelerometer noise is definitely one of the reasons.

Some of the experiments with erroneous background models were repeated in the presence of observation noise. To separate the effect of the erroneous model from the effect of the observation noise, always two solutions were calculated: one with a correct background model and one with an erroneous model. In Fig. 4b the differences between the two corresponding solutions in the case of missing atmospheric S2 tide, a 10% error in the ocean tide model, or a completely missing de-aliasing product are shown. It turns out that the size of the effects is slightly smaller than predicted by the experiments with noise-free observations. This phenomenon is most probably linked to the non-linearity of the gravity field estimation process and has been observed in other simulation studies as well. However, these results do not change the conclusions drawn in the former chapters.

8 Variation of the Arc Length and the Number of Instrument Parameters

An important error source that was identified above is the accelerometer noise. This noise enters directly into the satellite orbits since no corrections are estimated for the observed accelerations and only a few instrument parameters are adjusted to account for unknown biases and scales. To investigate this effect, two experiments

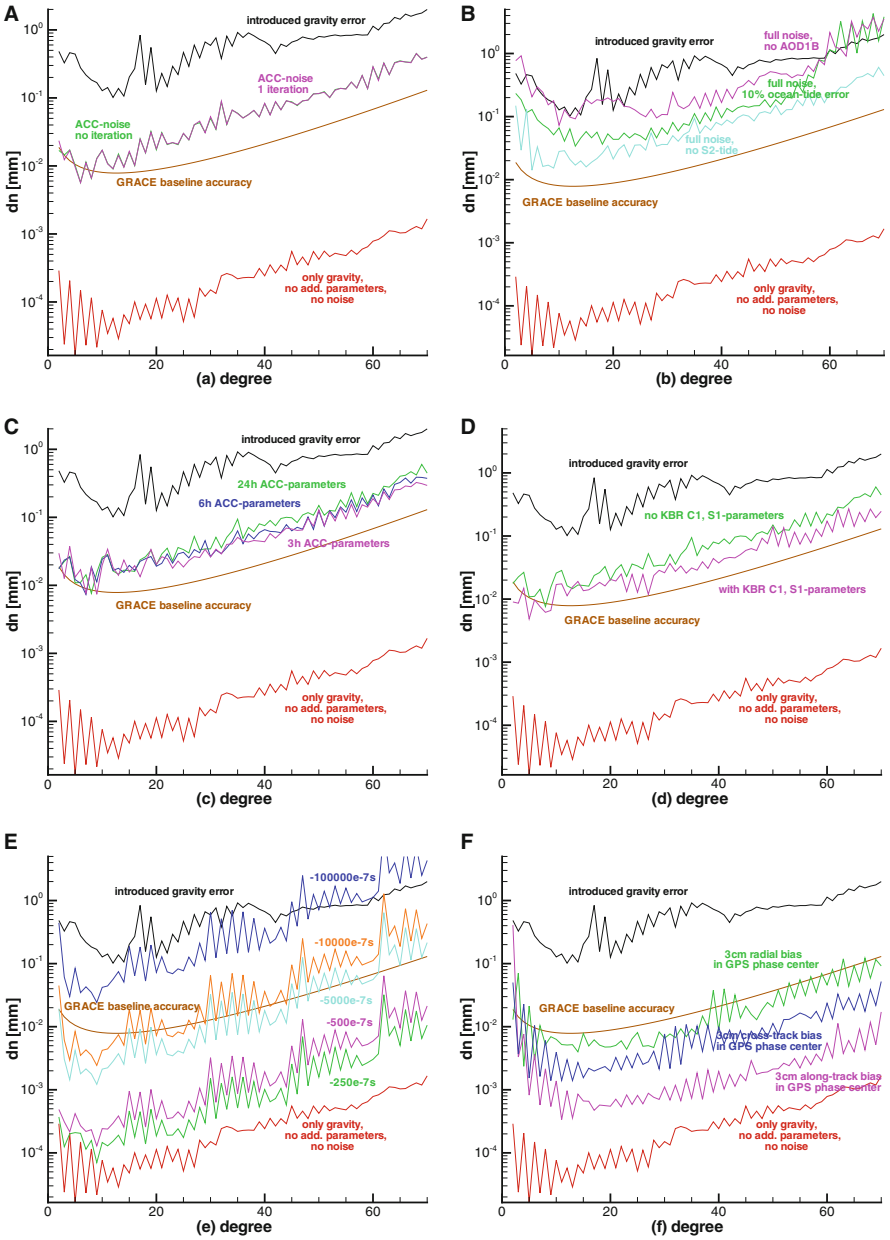

Fig. 4 (**a**) Shows the effect of iteration of the adjustment of the gravity field, no improvement is visible. (**b**) Repeats some model errors (compare Figs. 1e, 3a and 3b), this time in the presence of observation noise. (**c**) Shows the effects of the introduction of more accelerometer parameters (only valid in the simulation case). (**d**) Shows the effect of additional K-Band parameters (only valid in the simulation case). (**e**) Shows the effect of different K-Band time tag biases on the gravity field estimation. (**f**) Shows the effect of biases in the phase centre of the GPS receiver antenna on one of the GRACE satellites. Mainly the even low degree coefficients are affected

were performed. In the first experiment the number of scale factors is increased to 4 or even 8 per day. A slight improvement was achieved (Fig. 4c), but this result could not be verified with real data. More promising results with real data were achieved, by a shortening of the arc length from 24 to 6 h, which implicitly leads to more instrument parameters, since scale factors are estimated at the beginning and at the end of each arc. A significant improvement is visible when the resulting gravity fields are compared with altimetry data and terrestrial gravity anomalies (not shown here).

Kim (2000) suggests periodic range-rate parameters (C1 and S1) to be estimated every 90 min that were tested in a second experiment. Figure 4d shows the positive effect of these parameters on the gravity field estimation. But again, the results could not be verified with real data. It seems that the solution is over-parameterized. It is not clear, why the simulation study does not produce valid results in this case. No further experiments concerning the instrument parameterization were made so far.

9 Special Experiments Concerning the C_{20} Coefficient

All gravity field solutions from real GRACE data including the K-Band observations show a constant bias in the C_{20} coefficient. The size of this bias relative to solutions from the Laser Geodynamic Satellites (LAGEOS) is approximately $2e^{-10}$. If only GPS observations are taken for the gravity field adjustment, this bias vanishes. It is therefore assumed that the reason for the bias is related to the K-Band observations. These may be wrong in relation to GPS either in time or in position. To check the influence of errors in the time tagging of the K-Band observations, different biases were added to the time stamps. The effect on the gravity field is shown in Fig. 4e. Not only C_{20} is affected, but the whole spectrum of coefficients is shifted. To change C_{20} by $2e^{-10}$, an unrealistic large time-bias would be needed. Therefore, the time tags do not seem to be responsible for the C_{20} bias.

Another explanation could be that the K-Band observations are referred to the wrong positions relative to the GPS observations. The absolute distance between the K-Band antennas is not known due to a phase ambiguity of the measurements. It is estimated from the GPS-positions of the satellites. Therefore, it does not help to move the K-Band antennas relative to the centre of mass of the satellites. This change in position would be absorbed by the estimation of a different range-bias. On the other hand the position of the GPS-antennas relative to the centre of mass of the satellites may be changed by introduction of receiver antenna phase centre biases. In this way the whole satellites including their centers of mass and K-Band antennas are shifted. Since the K-Band observations characterize the relative movement of the satellites, represented by their centers of mass, this change also influences the range-rate observations and cannot be absorbed by a range bias.

This is confirmed by experiments. Figure 4f shows the results of the gravity field adjustment when the phase centre of the GPS antenna is moved by 3 cm in along-track, cross-track, or radial direction. In the case of a shift in along-track, only the

coefficients of degree 2 are affected significantly. It turns out that a GPS antenna phase centre bias of 5 cm on each of the two satellites is sufficient to scale C_{20} to the value of the LAGEOS solutions, while the effect on all other coefficients stays below baseline accuracy. We conclude that an along-track bias of 10 cm (which may be arbitrarily split for the two satellites) in the phase centre of the GPS antennas may be responsible for the observed bias in C_{20}.

10 Summary and Conclusions

With GFZ's EPOS-OC software package it is possible to simulate non-gravitational accelerations, K-Band range and range-rate, and GPS code as well as phase observations for the two GRACE satellites. It is not yet possible to simulate star camera observations that differ from the nominal orientation of the satellites. From 1 month of simulated noise-free K-Band range-rate observations it is possible to derive gravity field coefficients up to degree and order 150 with an accuracy approximately two orders of magnitude better than the pre-launch simulated GRACE baseline. The use of K-Band range observations leads to problems yet unsolved.

To absorb systematic effects on the gravity field coefficients caused by realistic colored noise that was added to the simulated observations, various instrument parameters are introduced. When gravity fields are estimated from these noisy observations, it turns out that the effect of accelerometer noise is above the baseline accuracy. It does not help to introduce more instrument parameters, but a shortening of the arcs gives promising results. Further investigations are needed to optimally adjust the instrument parameterization on shortened arcs.

Among the background models the ocean tides play an important role. Experiments with recent models showed that the probable errors in these models lead to a degradation of the gravity field coefficients that is significantly above the baseline accuracy. Further research on ocean tide models and probably also on estimating selected ocean tide constituents from GRACE observations is needed. The atmosphere and ocean de-aliasing also plays an important role. It would be very helpful to derive error measures for the AOD1B product. The atmospheric tides on the other hand are of lesser importance due to their smaller size and reliable models.

Special attention was paid to the C_{20}-coefficient of the gravity field that is biased in all GRACE solutions that include K-Band observations relative to SLR-based solutions. It is suggested that this bias is due to an along-track error in the phase centers of the GPS receiver antennas onboard the GRACE satellites. The gravity field coefficients are not sensitive to the along-track component of the GPS observations. Thus, this error does not show up in pure GPS solutions of the gravity field, but it leads to a scaling of C_{20} as soon as K-Band range-rate observations referring to a wrong position of the centers of mass of the satellites are used.

While improvements in the ocean tide models are not easy to achieve and remain a goal for further research, short arcs with adjusted instrument parameterization and

along-track biases in the GPS receiver antennas may be implemented in the routine processing of GRACE data and hopefully lead to improvements in the gravity field solutions in the near future.

Acknowledgment This is publication no. GEOTECH-1269 of the GEOTECHNOLOGIEN programme of BMBF, grant 03F0423A.

References

Berger C, Biancale R, Ill M, Barlier F (1998) Improvement of the empirical thermospheric model DTM: DTM-94- comparative review on various temporal variations and prospects in space geodesy applications. J. Geod. 72, 161–178.

Bode A, Biancale R (2006) Mean annual and seasonal atmospheric tide models based on 3-hourly and 6-hourly ECMWF surface pressure data. Scientific Technical Report STR06/01, GeoForschungsZentrum Potsdam, Potsdam.

Ferrari J, Bills BG (1977) A harmonic analysis of lunar topography. Icarus 31(2), 244–259.

Flechtner F (2007) AOD1B Product description document for product releases 01 to 04, GRACE Project Document, JPL 327–750, rev. 3.1, JPL Pasadena, Ca.

Flechtner F, Schmidt R, Meyer U (2006) De-aliasing of short-term atmospheric and oceanic mass variations for GRACE. In: Flury J, Rummel R, Reigber C, Rothacher M, Boedecker G, Schreiber U (eds.), Observation of the Earth System from Space, Springer-Verlag, Berlin, Heidelberg.

Flechtner F, Dahle CH, Neumayer KH, König R, Förste CH (2009) The release 04 CHAMP and GRACE EIGEN gravity field models. In: Flechtner F, Gruber T, Güntner A, Mandea M, Rothacher M, Schöne T, Wickert J (eds.), Satellite Geodesy and Earth System Science, Springer-Verlag, Berlin, Heidelberg.

Förste C, Flechtner F, Schmidt R, Meyer U, Stubenvoll R, Barthelmes F, König R, Neumayer KH, Rothacher M, Reigber Ch, et al. (2005) A New High Resolution Global Gravity Field Model Derived from Combination of GRACE and CHAMP Mission and Altimetry/Gravimetry Surface Gravity Data. http://www-app2.gfz-potsdam.de/pb1/op/grace/results

Frommknecht B (2007) Integrated Sensor Analysis of the GRACE Mission. Institute for Astronomical and Physical Geodesy, Technical University Munich, Germany.

Gunter B, Ries J, Bettadpur S, Tapley B (2006) A simulation study of the errors of omission and commission for GRACE RL01 gravity fields. J. Geod. 80, 341–351.

Ilk KH, Flury J, Rummel R, Schwintzer P, Bosch W, Haas C, Schröter J, Stammer D, Zahel W, Miller H, et al. (2005) Mass Transport and Mass Distribution in the Earth System – Contribution of the New Generation of Satellite Gravity and Altimetry Missions to Geosciences, 2nd ed., Proposal for a German Priority Research Program, GOCE Project Office Germany, Technical University Munich, GeoForschungsZentrum Potsdam.

Kim J (2000) Simulation Study of a Low-Low Satellite-to-Satellite Tracking Mission. University of Texas at Austin, Austin, TX.

Klokčoník J, Wagner CA, Kostelecký J, Bezdek A, Novák P, McAdoo D (2008) Variations in the accuracy of gravity recovery due to ground track variability: GRACE, CHAMP, and GOCE. J. Geod., doi: 10.1007/s00190-008-0222-0.

Knocke PC, Ries JC, Tapley BD (1988) Earth radiation pressure effects on satellites. AIAA-88-4992-CP. In: Proc. of the AIAA/AAS Astrodynamics Conference (1988), pp. 577–586.

Lyard F, Lefevre F, Letellier T, Francis O (2006) Modelling the global ocean tides: Modern insights from FES2004. Ocean Dyn. 56, 394–415.

Savcenko R, Bosch W (2008) EOT08a – Empirical Ocean Tide Model from Multi-Mission Satellite Altimetry. Deutsches Geodätisches Forschungsinstitut, München.

Schmidt R (2007) Zur Bestimmung des cm-Geoids und dessen zeitlicher Variationen mit GRACE. GeoForschungsZentrum Potsdam, Potsdam

Tapley B, Bettadpur S, Watkins M, Reigber C (2004) The gravity recovery and climate experiment: Mission overview and early results. Geophys. Res. Lett. 31, L09607.

Tapley B, Ries J, Bettadpur S, Chambers D, Cheng M, Condi F, Gunter B, Kang Z, Nagel P, Pastor R, et al. (2005) GGM02 – An improved earth gravity field model from GRACE. J. Geod. 79, 467–478.

Thomas J (1999) An Analysis of the Gravity Field Estimation Based on Dual-1-Way Intersatellite Biased Ranging. Jet Propulsion Laboratory, Pasadena, CA.

Thomas M, Sündermann J, Maier-Reimer E (2001) Consideration of ocean tides in an OGCM and impacts on subseasonal to decadal polar motion excitation. Geophys. Res. Lett. 12, 2457.

ITG-GRACE: Global Static and Temporal Gravity Field Models from GRACE Data

Torsten Mayer-Gürr, Annette Eicker, Enrico Kurtenbach, and Karl-Heinz Ilk

1 Introduction

As a result of the dedicated space-borne gravity field mission GRACE (Gravity Recovery and Climate Experiment – Tapley et al., 2004), a breakthrough in terms of accuracy and resolution of the gravity field determination has been achieved. The innovative character of this mission is due to the highly precise line-of-sight range and range-rate K-band measurements between the twin satellites. In addition, the surface forces acting on the satellites are measured by a 3D accelerometer and can be removed properly during the recovery procedure. As a result of this mission, various global gravity field models, satellite-only and combined ones, have been derived, such as the recent combined models EGM2008 (Pavlis et al., 2008) or EIGEN-5C (Förste et al., 2008) and the satellite-only models EIGEN-5S (Förste et al., 2008) or GGM03 S (Tapley et al., 2007). The classical approach of satellite geodesy in gravity field recovery consists basically in deriving the spherical harmonic coefficients representing the gravitational potential from an analysis of accumulated orbit perturbations of the satellites. Here, it is an indispensable requirement to analyze medium or long satellite arcs covering at least 1 day or more in order to cover the characteristic periodic and secular disturbances caused by the small corrections to the approximate force function. It has been demonstrated that this requirement is not necessary anymore for the new generation of dedicated gravity satellites. These new satellite missions can be characterized by a modeling concept which acts more in-situ than by analyzing accumulated orbit perturbations (Ilk et al., 2006). Results can be achieved with these new in-situ techniques which are able to compete with the results of the classical analysis procedures (e.g., Mayer-Gürr et al., 2007). In Sect. 2 of this article the computation procedure for processing the observations of the GRACE mission is sketched. In Sect. 3 the recent solution ITG-Grace03s is presented, providing a static and a time variable part and covariance information. Section 4 concludes this article with a summary.

T. Mayer-Gürr (✉)
Institute of Geodesy and Geoinformation, University of Bonn, 53115 Bonn, Germany
e-mail: mayer-guerr@geod.uni-bonn.de

F. Flechtner et al. (eds.), *System Earth via Geodetic-Geophysical Space Techniques*, Advanced Technologies in Earth Sciences, DOI 10.1007/978-3-642-10228-8_13,

2 Physical Model

The principal characteristic of the method presented here is the use of short arcs of the satellite's orbit in order to avoid the accumulation of modeling errors and a rigorous consideration of correlations between the range observations in the subsequent adjustment procedure.

2.1 Model Setup

The mathematical-physical model for a single satellite is based on the formulation of Newton's equation of motion,

$$\ddot{\mathbf{r}}(t) = \mathbf{f}(t,r,\dot{r}), \tag{1}$$

as a boundary value problem,

$$\mathbf{r}(\tau) = (1-\tau)\mathbf{r}_A + \tau\ \mathbf{r}_B - T^2 \int_0^1 K(\tau,\tau')\mathbf{f}(\tau')d\tau', \tag{2}$$

with the integral kernel,

$$K(\tau,\tau') = \begin{cases} \tau'(1-\tau) & \text{for } \tau' \le \tau \\ \tau(1-\tau') & \text{for } \tau' > \tau, \end{cases} \tag{3}$$

the normalized time variable,

$$\tau = \frac{t - t_A}{T} \quad \text{with} \quad T = t_B - t_A, \tag{4}$$

and the unknown boundary positions $\mathbf{r}_A$ at t_A and $\mathbf{r}_B$ at t_B. Equation (2) represents an observation equation for the positions determined by onboard GPS (Mayer-Gürr et al., 2005). The mathematical model for range observations can be derived by projecting the relative vector to the line-of-sight connection,

$$\rho = \mathbf{e}_{12}(\tau) \cdot (\mathbf{r}_2(\tau) - \mathbf{r}_1(\tau)) \,. \tag{5}$$

Analog formulae can be derived for range-rates and range accelerations, but for the determination of ITG-Grace03 s only ranges have been used. The quantity $\mathbf{e}_{12}(\tau)$ is the unit vector of the line-of-sight direction of the two GRACE satellites with the positions $\mathbf{r}_1(\tau)$ and $\mathbf{r}_2(\tau)$. This vector is known within a few milliarcseconds, assuming that the satellite positions are measured with an accuracy of a few cm and taking into account the distance of approximately 200 km between the two satellites. However, this accuracy is not adequate compared to the high accuracy of the range measurements in the size of some μm. Therefore, a model refinement is necessary which improves implicitly also the relative orbit. Details are not shown because

of space, refer to Mayer-Gürr (2006). Further details to the physical model of the gravity field recovery technique based on GRACE low-low SST data can also be found in Mayer-Gürr et al. (2006).

The functional model in Eq. (5) describes the dependency of the range observables on the satellite positions which again depend on the force function **f**. This force function contains among others the unknown gravity field which can be represented by the unknown gravity field parameters **x** as described below. This is a non-linear relation which has to be linearized,

$$\rho = \rho_0 + \left.\frac{\partial \rho}{\partial \mathbf{x}}\right|_{x_0} \cdot (\mathbf{x} - \mathbf{x}_0) + \cdots \tag{6}$$

where

$$\frac{\partial \rho}{\partial \mathbf{x}} = \frac{\partial \rho}{\partial \mathbf{r}} \frac{\partial \mathbf{r}}{\partial \mathbf{f}} \frac{\partial \mathbf{f}}{\partial \mathbf{x}}. \tag{7}$$

The first term at the right hand side can be derived from Eq. (5), the second term from Eq. (2), and the third term contains the gravity field representation as will be described in Sect. 2.3. If all linearized observation equations are collected for one short arc then we get the following matrix equation

$$\mathbf{l} = \mathbf{A}\mathbf{x} + \mathbf{e}. \tag{8}$$

with the range observations **l**, the unknown parameters **x** and the error vector **e**. The design matrix **A** is composed of the partial differentials as shown in Eq. (7).

The arc-related parameters, such as boundary positions, are eliminated before the arcs are merged to the complete system in order to reduce the dimension of the adjustment problem. Every short arc builds a (reduced) partial system of observation equations. Separate variance factors for each arc have been determined to combine the design matrices and to consider the variable precision. These variance factors are computed by means of a variance component estimation procedure described in Koch and Kusche (2001). The details of the iterative combination scheme combined with the variance component estimation are described in Mayer-Gürr (2006).

2.2 Stochastic Model

The reduced ranges between the twin satellites are strongly correlated. Therefore, an appropriate selected stochastic model has to be introduced for each short arc by a variance-covariance matrix,

$$\mathbf{C}(\mathbf{l}) = \sigma^2 \mathbf{P}^{-1}. \tag{9}$$

The consideration of this variance-covariance matrix acts as a decorrelation of the observations and the decorrelated adjusted residuals should show white noise. The derivation of a realistic variance-covariance matrix is very important: in case

of a correct decorrelation one can claim that the solution is optimal in the statistical sense, and it is not necessary to introduce calibration parameters for the K-band measurements. The formal errors of the adjustment results should not require any calibration. The variance-covariance matrix is composed of two parts: the first part describes the noise of the K-band measurements, $\sigma_p^2\mathbf{F}\ \mathbf{C}(\mathbf{p})\mathbf{F}^T$, and the second one the noise of the accelerometer measurements, $\sigma_a^2\mathbf{B}\ \mathbf{C}(\mathbf{a})\mathbf{B}^T$. The matrix $\mathbf{F}$ describes the filtering of the phase observations and $\mathbf{B}$ a corresponding integration and filtering matrix for the accelerometer measurements (cf. Mayer-Gürr, 2006; Thomas, 1999; Wu et al., 2004).

The variance covariance matrix results in,

$$\mathbf{C}(\mathbf{l}) = \sigma_p^2\mathbf{F}\ \mathbf{C}(\mathbf{p})\mathbf{F}^T + \sigma_a^2\mathbf{B}\ \mathbf{C}(\mathbf{a})\mathbf{B}^T. \tag{10}$$

2.3 Representation of the Gravity Field

2.3.1 Static Gravity Field Representation

The gravitational potential $V(\lambda,\vartheta,r)$ of the static gravity field model is represented by a spherical harmonic expansion,

$$V(\lambda,\vartheta,r) = \frac{GM}{R}\sum_{n=0}^{N}\left(\frac{R}{r}\right)^{n+1}\sum_{m=-n}^{n} c_{nm}Y_{nm}(\lambda,\vartheta), \tag{11}$$

with the unkown potential coefficients c_{nm}. In case of a regional recovery the potential can be modeled by parameters of space localizing basis functions as well as shown, e.g., in Eicker (2008), Mayer-Gürr et al. (2006), and Schmidt et al. (2007).

2.3.2 Representation of the Time Variable Gravity Field

In the time domain the gravity field variations can be modeled as linear combination of time dependent basis functions $\phi_i(t)$ according to

$$V(\lambda,\vartheta,r,t) = \sum_i V_i(\lambda,\vartheta,r)\phi_i(t), \tag{12}$$

where $V(\lambda,\vartheta,r)$ are the unknown, position-depending coefficients of the basis functions in the time domain. The position-dependency can be expressed by a series of spherical harmonics according to Eq. (11) or alternatively by an expansion in terms of space-localizing basis functions. The solutions provided by the official GRACE Science Data System (Center of Space Research, Texas and Deutsches GeoForschungsZentrum, Potsdam) generally model the time variabilitiy as series of monthly mean fields. Expressed in terms of Eq. (12), this results in temporal basis functions according to

$$\phi_i(t) = \begin{cases} 1 & \text{if} \quad t_i \le t < t_{i+1} \\ 0 & \text{otherwise.} \end{cases} \tag{13}$$

Here t_i denotes the beginning of the respective month i. This way, each month is processed independently of the other months. It is well known that those GRACE solutions are disturbed by high frequency temporal gravity field variations (aliasing problem). Several groups try to overcome this problem by increasing the sampling of the mean solutions (e.g. 10-days or weekly means). The drawback of this approach is the fact that the increased temporal resolution involves a loss in spatial resolution and accuracy. One alternative approach is the smooth representation of the temporal variations by continuous base functions such as splines. As the gravity field itself changes smoothly in time as well, this choice appears to be appropriate. In case of ITG-Grace03s, the temporal variations are parameterized by quadratic splines, resulting in the following basis functions:

$$\phi_i(t) = \begin{cases} \frac{1}{2}\tau_{i-1}^2 & \text{if } t_{i-1} \le t < t_i \\ -\tau_i^2 + \tau_i + \frac{1}{2} & \text{if } t_i \le t < t_{i+1} \\ \frac{1}{2}\tau_{i+1}^2 + \tau_{i+1} + \frac{1}{2} & \text{if } t_{i+1} \le t < t_{i+2} \\ 0 & \text{otherwise,} \end{cases} \tag{14}$$

with the normalized time τ_i for each interval,

$$\tau_i = \frac{t - t_i}{t_{i+1} - t_i}. \tag{15}$$

These quadratic splines are illustrated in Fig. 1.

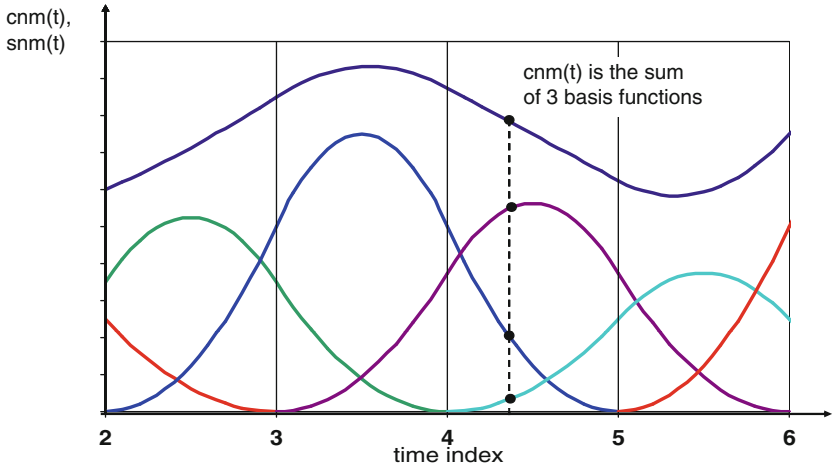

Fig. 1 Schematic illustration of quadratic splines as continuous temporal basis functions

3 Gravity Field Solution ITG-Grace03s

The gravity field model ITG-Grace03s consists of three parts: the static high resolution model up to a spherical harmonic degree of 180, the temporal variations up to degree 40 and the full variance-covariance matrix for the static solution. All three parts are publically available and can be accessed via the website http://www.geod.uni-bonn.de/itg-grace03.html

3.1 Data Set and Estimated Parameters

For the determination of the static and time variable gravity field model ITG-Grace03 K-band range measurements of the GRACE twin satellite mission have been used for the period September 2002 until April 2007 covering approximately 4.5 years. The approximately 29 million ranges are corrected for the tides caused by Sun, the Moon and the planets. The ephemerides are taken from the JPL405 data set (Standish, 1998). Effects originating from the deformation of the Earth caused by these tides are modeled according to the IERS 2003 conventions (McCarthy and Petit, 2004). Ocean tides are computed using the FES2004 model (Le Provost, 2001). Effects of high frequency non-tidal atmosphere and ocean mass redistributions are removed prior to the processing by the GFZ AOD RL04 de-aliasing products (Flechtner, 2005). Only the K-band range measurements have been used as observations, the Level 1B GRACE orbits have only served as approximation values for the linearized observation equations. As already mentioned the data have been split into short arcs of approximately 30 min arc length, taking data gap into account. In addition to the gravity field parameters (see below) a K-band range bias and an accelerometer bias in three dimensions have been estimated for each arc as well.

3.2 Temporal Variations

One of the main objectives of the GRACE mission is the determination of the Earth's time variable gravity field in order to deliver an important contribution to our knowledge of many phenomena in the dynamic system Earth. Within the frame of ITG-Grace03s, temporal variations have been calculated covering the complete time span from September 2002 until April 2007. As parameterization in the time domain the quadratic splines described in Sect. 2.3.2 have been applied with a nodal point distance of half a month. In the spatial domain the temporal variations are modeled by a spherical harmonic expansion of degree $n = 2...40$. In the estimation process the variations are filtered by applying a Kaula type regularization matrix for each set of spherical harmonic coefficients. For each regularization matrix an individual weight is determined by the variance component estimation method. One example for the application of these results shall be demonstrated by analyzing the hydrological cycle in the Amazon basin. Figure 2 shows the estimated mass variations expressed in terms of equivalent water heights. The results from gravity field solutions provided by the official Science Data System have been plotted as well. To be comparable to the regularized ITG-solution, they have been restricted to degree

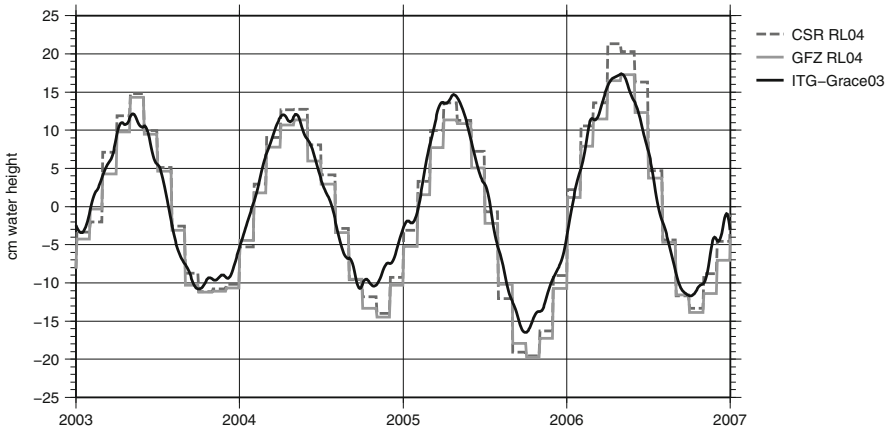

Fig. 2 Temporal mass variations in the Amazon basin expressed in terms of equivalent water heights

$n = 40$ and filtered using a Gauss filter with 500 km radius. The smooth approximation of the ITG-Grace solution due to the use of continuous temporal basis functions becomes apparent.

3.3 Static Solution

The signal of the static part of the gravity field is order of magnitudes larger than the temporal variations and can therefore be determined with much higher spatial resolution from GRACE data. Figure 3 illustrates the static part of ITG-Grace03s in terms of gravity anomalies up to degree $n = 150$; the solution has even been calculated up to degree $n = 180$ resulting in 32,757 unknown gravity field parameters. The temporal variations estimated before, as described in Sect. 3.2, were used to reduce the observations. This led to a damping of the typical error stripe pattern usually present in the GRACE solutions.

The static part of ITG-Grace03s has been selected as basic pure satellite based gravity field model for the new international accepted high resolution gravity field model EGM2008 (Pavlis et al., 2008).

3.4 Covariance-Matrix

For the static part of ITG-Grace03s a full variance-covariance matrix is provided which has a size of about 8 GB. The full matrix is required to obtain correct accuracies and correlations of derived quantities. As an example, Fig. 4 shows the standard deviations of geoid heights calculated by variance propagation from this variance-covariance matrix. In Fig. 5 correlations are displayed of one point ($\lambda = \varphi = 0$) and its neighboring points. The correlation pattern is apparently non-isotropic and reflects the error stripes well-known for GRACE.

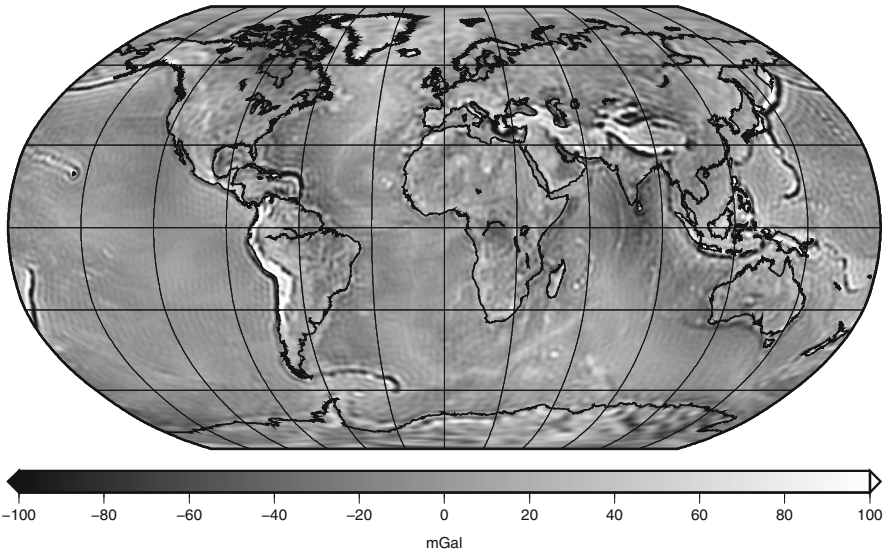

Fig. 3 Gravity anomalies of the static part of ITG-Grace03s up to degree 150

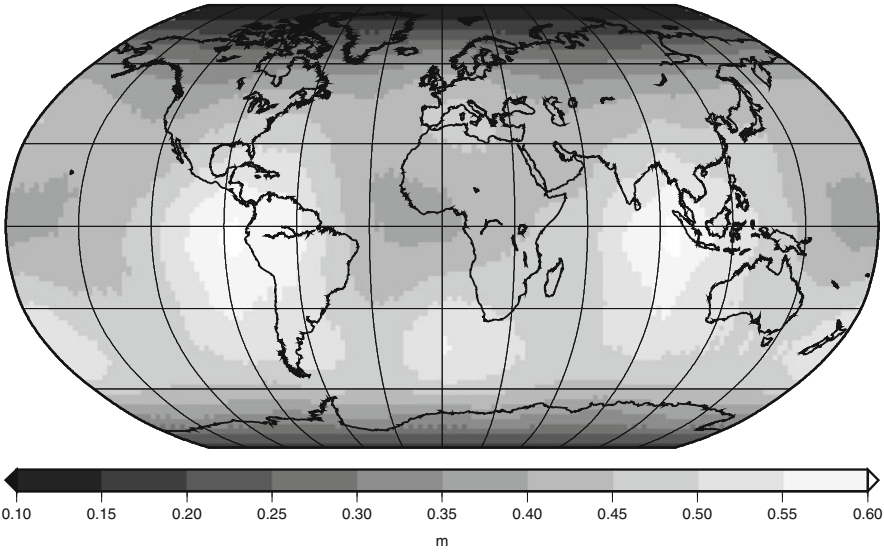

Fig. 4 Standard deviations of geoid heights calculated by variance propagation from full variance-covariance matrix of ITG-Grace03s

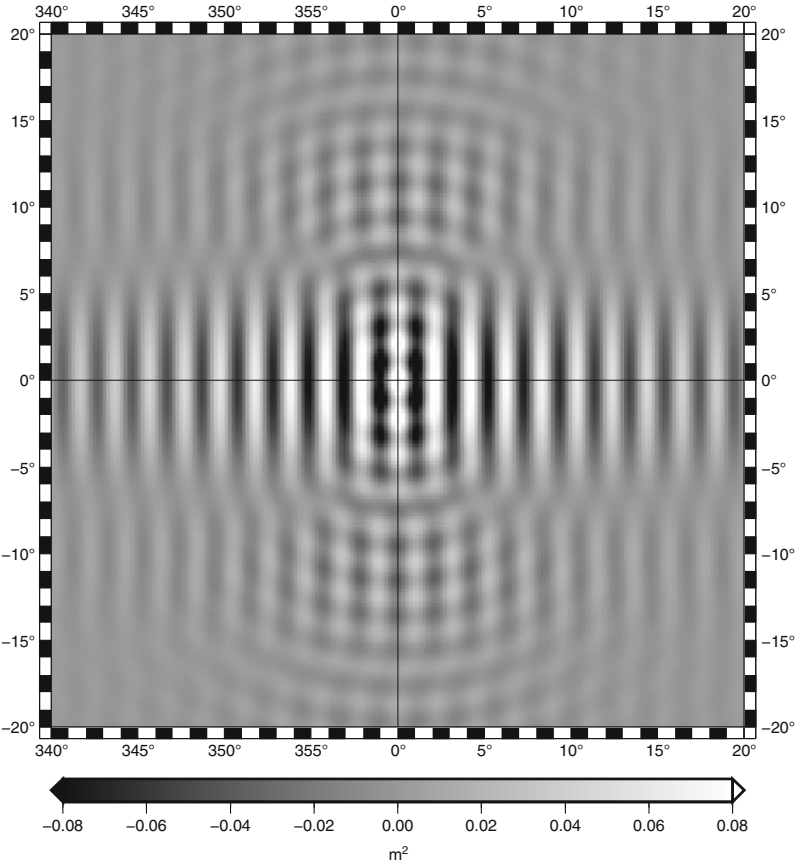

Fig. 5 Covariances in terms of geoid heights between one point ($\lambda = \varphi = 0$) and neighboring points

4 Conclusions

In this article the gravity field model ITG-Grace03s with its three parts, static high resolution model, temporal variations and the full variance-covariance matrix for the static solution has been presented. The temporal gravity field variations are parameterized by continuous basis functions in the time domain. ITG-Grace03s has been calculated using the unitized Gravity Recovery Object-Oriented Programming System (GROOPS) developed at the University of Bonn. It is tailored to the in-situ observables of the new generation of gravity satellite missions, and thus many modules of GROOPS will also be used for processing GOCE data.

Acknowledgments The support by BMBF (Bundesministerium fuer Bildung und Forschung) and DFG (Deutsche Forschungsgemeinschaft) within the frame of the Geotechnologien-Programm is gratefully acknowledged.

References

Eicker A (2008) Gravity Field Refinement by Radial Basis Functions from In-Situ Satellite Data. Dissertation University of Bonn, Schriftenreihe Institut für Geodäsie und Geoinformation, Bonn.

Flechtner F (2005) AOD1B Product Description Document. Technical Report GRACE 327-750, Jet Propulsion Labratory. http://podaac.jpl.nasa.gov/grace/documentation.html

Förste C, Flechtner F, Schmidt R, Stubenvoll R, Rothacher M, Kusche J, Neumayer K-H, Biancale R, Lemoine J-M, Barthelmes F, et al. (2008) EIGEN-GL05C – A new global combined high-resolution GRACE-based gravity field model of the GFZ-GRGS cooperation. General Assembly European Geosciences Union (Vienna, Austria). Geophys. Res. Abstr. 10, Abstract No. EGU2008-A-06944.

Ilk KH, Löcher A, Mayer-Gürr T (2006) Do we need new gravity field recovery techniques for the new gravity field satellites? Proceedings of the VI Hotine –Marussi Symposium of Theoretical and Computational Geodesy: Challenge and Role of Modern Geodesy, May 29–June 2, 2006, Wuhan, China.

Koch KR, Kusche J (2001) Regularization of geopotential determination from satellite data by variance components. J. Geod. 76(5), 259–268.

Le Provost C (2001) Ocean tides. In: Fu LL, Cazenave A (eds.), Satellite Altimetry and Earth Sciences, Springer, Berlin, pp. 267–303.

Mayer-Gürr T, Ilk KH, Eicker A, Feuchtinger M (2005) ITG-CHAMP01: A CHAMP gravity field model from short kinematical arcs of a one-year observation period. J. Geod. 78, 462–480.

Mayer-Gürr T (2006) Gravitationsfeldbestimmung aus der Analyse kurzer Bahnbögen am Beispiel der Satellitenmissionen CHAMP und GRACE. Dissertation at the Institute of Theoretical Geodesy, University Bonn, URL: http://hss.ulb.uni-bonn.de/diss_online/landw_fak/2006/mayerguerr_torsten

Mayer-Gürr T, Eicker A, Ilk KH (2006) Gravity field recovery from GRACE-SST data of short arcs. In: Flury J, et al. (eds.), Observation of the Earth System from Space, Springer, Berlin, pp. 131–148.

Mayer-Gürr T, Eicker A, Ilk KH (2007) ITG-Grace02s: A GRACE gravity field derived from short arcs of the satellites orbit. Proceedings of the 1st International Symposium of the International Gravity Field Service "Gravity Field of the Earth", Istanbul, pp. 193–198.

McCarthy DD, Petit G (eds.) (2004) IERS Conventions 2003. Number 32 in IERS Technical Notes. Verlag des Bundesamts fuer Kartographie und Geodäsie, Frankfurt am Main.

Pavlis NK, Holmes SA, Kenyon SC, Factor JK (2008) An earth gravitational model to degree 2160: EGM2008. Presented at the 2008 General Assembly of the European Geosciences Union, Vienna, Austria, April 13–18, 2008.

Schmidt M, Fengler M, Mayer-Gürr T, Eicker A, Kusche J, Sanchez L, Han SC (2007) Regional gravity modeling in terms of spherical base functions. J. Geod. 81(1), 17–38.

Standish EM (1998) JPL Planetary and Lunar Ephemerides DE405/LE405, Jet Propulsion Laboratory, Pasadena.

Tapley BD, Bettadpur S, Watkins M, Reigber Ch (2004) The gravity recovery and climate experiment: Mission overview and early results. Geophys. Res. Lett. 31, L09607, doi: 10.1029/2004GL019920.

Tapley B, Ries J, Bettadpur S, Chambers D, Cheng M, Condi F, Poole S (2007) The GGM03 mean earth gravity model from GRACE. Eos Trans. AGU 88(52), Fall Meet. Suppl., Abstract G42A-03, 2007.

Thomas JB (1999) An Analysis of Gravity-Field Estimation Based on Intersatellite Dual-1-Way Biased Ranging. Number 98-15 in JPL Publication, Jet Propulsion Laboratory, Pasadena, CA.

Wu SC, Kruizinga G, Bertiger W (2004) Algorithm Theoretical Basis Documents for GRACE Level-1B Data Processing V1.1. Technical Report GRACE 327-741, Jet Propulsion Laboratory, Pasadena, CA.

Validation of GRACE Gravity Fields by In-Situ Data of Ocean Bottom Pressure

Andreas Macrander, Carmen Böning, Olaf Boebel, and Jens Schröter

1 Introduction

The GRACE (Gravity Recovery and Climate Experiment) satellite mission observes the gravity field of the Earth with unprecedented accuracy. Its potential to measure the temporal variability of the geoid due to mass redistribution on Earth's surface has opened the possibility to study mass trends of continental ice sheets and in the lithosphere, or the hydrologic cycle in monsoon regions.

Over the oceans, variability of the gravity field primarily represents oceanic and atmospheric mass redistribution. This corresponds to changes in ocean bottom pressure (OBP), which is an integral measure of the oceanic (and atmospheric) mass above any given location at the sea floor, explained by the hydrostatic equation:

$$p(-H) = g \int_{-H}^{0} \rho(z) dz$$

with pressure p at depth $-H$, acceleration of gravity g and density ρ as a function of depth z. For oceanographers, OBP is a relevant quantity to assess sea level and ocean currents. While satellite altimetry observes the actual sea level, the combination of altimetry and gravimetry allows to distinguish between thermal expansion (steric effect) and mass increase (which is captured by GRACE, and OBP). Further, temporal changes of the horizontal OBP gradient dp/dx correspond to abyssal geostrophic current velocity anomalies (chapter "On the Representation of Transport Variability of the Antarctic Circumpolar Current in GRACE Gravity Solutions and Numerical Ocean Model Simulations" by Böning et al., 2010). Hence, GRACE may provide a world-wide monitoring of changes of ocean circulation, at least on scales larger than ≈500 km and longer than months.

However, monthly mass variability over the oceans is much smaller than over the continents, where GRACE observes up to 15 cm of water column equivalent

A. Macrander (✉)
Alfred Wegener Institute for Polar and Marine Research, D-27570 Bremerhaven, Germany
e-mail: Andreas.Macrander@awi.de

F. Flechtner et al. (eds.), *System Earth via Geodetic-Geophysical Space Techniques*, Advanced Technologies in Earth Sciences, DOI 10.1007/978-3-642-10228-8_14,

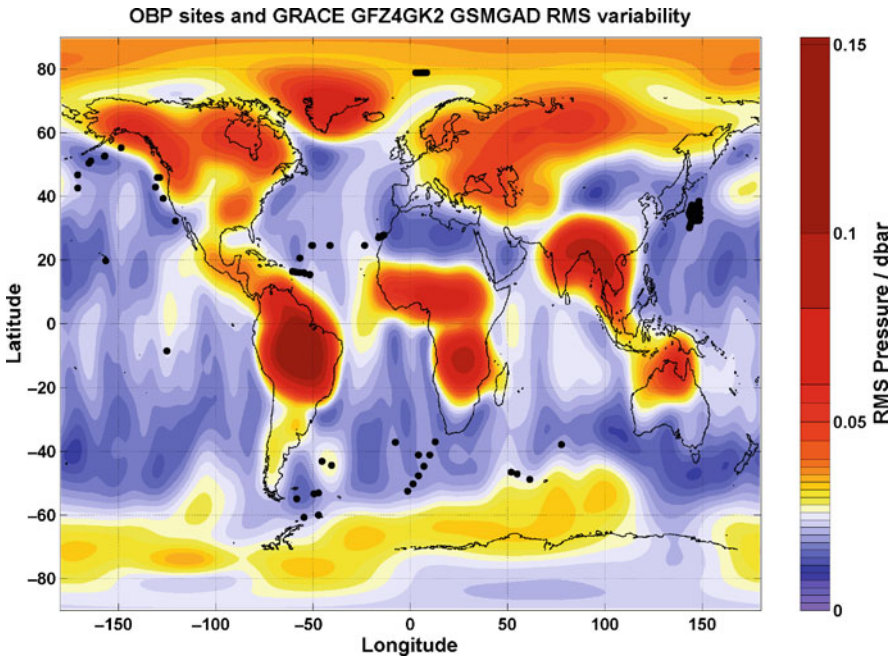

Fig. 1 RMS standard deviation of the monthly GFZ Release 04 GSM+GAD product. Note the high values over the continents, and in the Arctic and Southern Ocean. *Small black dots* mark positions of in-situ OBP observations used in this study

RMS variability in some monsoon regions. Typical monthly oceanic RMS variability ranges from about 1 cm in many tropical regions to 5 cm in the Arctic and Southern Oceans (Fig. 1). These comparatively small changes are close to the accuracy limit of the GRACE solutions. Further, large short-term variability, particularly tides reaching amplitudes of about 1 m in the open ocean, makes de-aliasing essential for realistic estimates of the monthly geoid, which is calculated from hundreds of satellite orbits. Meyer et al. (2007) showed, that even small modelling errors in ocean tide prediction significantly degrade the accuracy of the GRACE solutions.

Hence, a validation with in-situ OBP measurements is critical to assure that GRACE realistically captures oceanic mass redistribution. The main challenges in comparing satellite and in-situ OBP result from the differences in spatial and temporal scales: Due to the orbit height of the satellites, GRACE data represent spatial averages over several hundreds of kilometres. In contrast, in-situ time series depict OBP at a single point – which is not necessarily representative for the surrounding hundreds of kilometres. Particularly, close to oceanic fronts (like the Polar Front in the Southern Ocean) and in regions with highly localised variability (like close to some coastlines or western boundary currents) GRACE may show spatially smoothed variability not representative for local in-situ observations. Temporal short-term variability can be fully captured by in-situ instruments, thus the calculation of monthly means matching the time axis of GRACE data is not critical. If

the same tide model is used as for GRACE data, errors from longer periodic tides should disappear. Nevertheless, the smaller sampling rate of the GRACE satellites (i.e. the less frequent overflights of a given region, compared to sampling rates of 15 s to 30 min for moored in-situ instruments) is the reason why de-aliasing of tidal and non-tidal short-term variability is critical to obtain realistic monthly gravity field solutions. Any discrepancies between GRACE and in-situ data can hence result from (a) differences in captured spatial scales, (b) errors in the numerical de-aliasing models used for the GRACE solutions, and (c) actual measurement errors in either in-situ pressure sensors or the GRACE satellites data.

During the last years, a number of studies compared GRACE and in-situ OBP time series provided by pressure sensors deployed on the sea floor at selected positions. These showed good agreement in some (Rietbroek et al., 2006; Morison et al., 2007; Park et al., 2008), but not all cases (Kanzow et al., 2005). Here, a global comparison at one hundred locations in all oceans is presented, which may allow first conclusions on the overall skill of GRACE to observe ocean mass variability. Significant differences between different GRACE solutions and different regions are discussed.

2 Data

2.1 In-Situ Ocean Bottom Pressure

OBP is measured in-situ by instruments deployed at the sea floor for time periods of up to several years. Typically, the resonance frequency of a piezo crystal which is deformed by the ambient pressure is measured and converted into pressure data. The widely used pressure sensors from Paroscientific, for example, achieve a resolution of 0.001 dbar (University of Rhode Island, 2006). (1 dbar $= 10^4$ Pa, equivalent to ≈ 1 m of water column). Thus, short-term pressure anomalies corresponding to a change of 1 mm in sea surface height are detectable. A significant issue is, however, the long-term stability of these pressure sensors. A sensor drift of 0.1 dbar, and in some cases up to 1 dbar, occurs in many deployments, and needs to be corrected to allow a proper comparison with GRACE, which will be explained below.

For this study, all available in-situ OBP time series were collected from cooperating institutes and fed into an OBP database at AWI. At present (February 2009), the database comprises 168 data sets from 152 deployments at about 100 different locations, covering the mission period of GRACE from 2002 to present. The length of most time series is between 1 and 2 years; in total, about 200 years of OBP observations are available. Table 1 gives an overview of the data; the positions are shown in Fig. 2 in the following section.

Most deployment sites primarily serve oceanographic purposes, e.g. observation of meridional overturning circulation (MOVE, RAPID), monitoring of ocean current variability (e.g. in Drake Passage or the Kuroshio extension) and inter-basin fluxes (e.g. Fram Strait), or detection of tsunami waves (DART). In a few projects, a 2-dimensional layout of the mooring sites was specifically chosen to aid

Table 1 Data inventory of the in-situ OBP database at AWI. The site number and time span refers to the data presently available in the database; in some cases, more recent data are not yet publicly available and will be included later. An "x" in the timespan marks ongoing projects where further data is expected in the future. References are either project websites or relevant publications

Project	Area, number of deployment sites, duration	Institution, contact person; reference
GRACE/AWI	ACC, 2D-array, 9 sites, 2002–2008 + x	AWI, Olaf Boebel
DAMOCLES	Fram Strait, 79°N, 6 sites, 2003–2008 + x	AWI, Agnieszka Beszczynska-Möller
KESS	Kuroshio Extension, 2D-array, 46 sites, 2004–2006	URI, Randy Watts; Park et al. (2008); http://uskess.org/
"Kerguelen"	Southern Ocean near Kerguelen, 2 sites, 2002–2004	CNES, Pascal LeGrand; Rietbroek et al. (2006)
MOVE	Atlantic at 16°N, 2D-array, 6 sites, 2002–2008 + x	IFM-GEOMAR, Johannes Karstensen; SIO, Uwe Send; Kanzow et al. (2005)
DART	Pacific tsunami early warning system, 15 sites, 2002–2005 + x	NOAA, Christian Meinig; http://www.ndbc.noaa.gov/
POL/ACCLAIM	Drake Passage and ACC, 10 sites, 2002–2005	POL, Chris Hughes; http://www.pol.ac.uk/psmsl/programmes/acclaim.info.html
RAPID	Atlantic at 24–27°N, 10 sites, 2004–2005 + x	NOC, Stuart Cunningham, Robin McCandliss; http://www.noc.soton.ac.uk/rapid/rapid.php

the comparison with GRACE, since a 2-D array captures large-scale coherent OBP variability (which is observed by GRACE) better than single points or lines of moorings. Namely the MOVE, KESS and AWI/ACC arrays represent this dedicated 2-D pattern.

So far, the database is used in this project for GRACE/in-situ OBP validation, as well as for validation of ocean tide and ocean circulation models (see next chapter in this volume). For the future, public access to the database is planned.

An essential issue before using the in-situ for an automatic correlation analysis with all GRACE products is a homogenization of the many different data formats, and quality control to eliminate measurement errors. Following, all steps that were performed before the GRACE validation are explained:

(1) *Data format:* The OBP time series from different institutes come in all kinds of formats. The data were converted to a uniform format allowing an automatic data processing of all deployments.
(2) *Quality control*: Outliers and other obvious errors like zero values from the surface at begin and end of a deployment, were removed. The most critical issue, however, is the sensor drift introduced above (Fig. 2). Typically, the drift is largest during the first weeks and months of a deployment, and reduces to a slower drift during later part of a time series. The nonlinear trend prohibits a

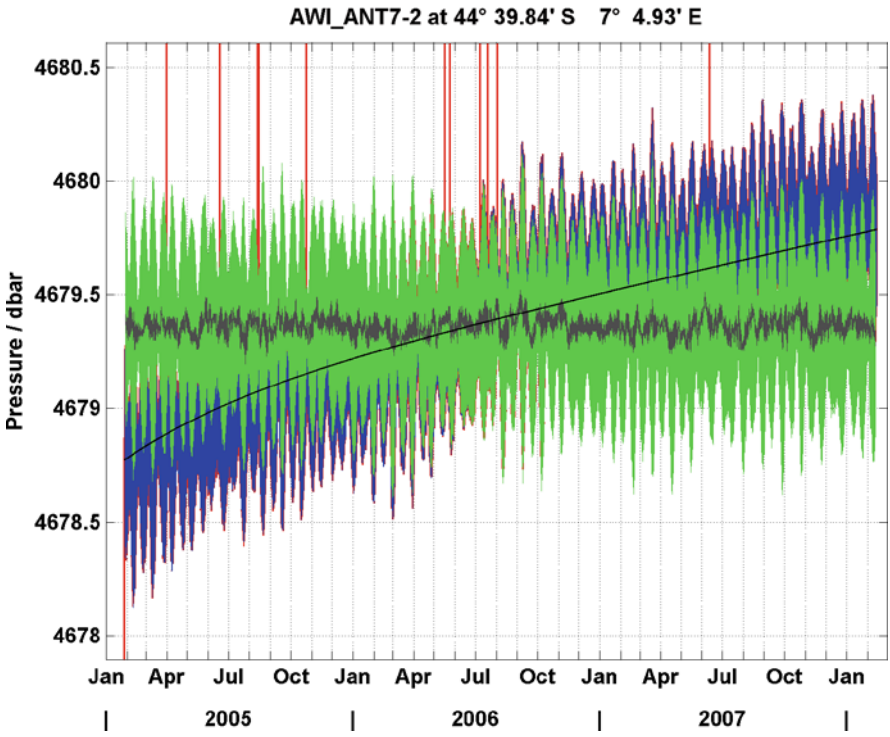

Fig. 2 Example of in-situ ocean bottom pressure, here at location ANT7 in the AWI-operated ACC array at 45°S 7°E. *Black* shows uncorrected raw data, with single outliers. A drift of 1 dbar over the period of 3 years is visible. The *black line* depicts the empirical fit function and *light grey* the resulting de-drifted time series. *Dark grey* marks the de-drifted and de-tided time series used to calculate monthly averages for GRACE validation

linear interpolation between pre- and post-deployment calibrations (if these are available at all). Therefore, sensor drift was eliminated by an exponential-linear fit function empirically determined with a least squares fit (e.g. Kanzow et al., 2006; Park et al., 2008), after the time series were first de-tided evaluating the FES2004 tide model (Lyard et al., 2006) at the deployment location. Finally the tides were re-added to retain the originally observed short term tidal variability. The de-tiding, however, avoids the possibility that the fit function itself is influenced by tides. A downside of the drift correction is, that information of longperiodic pressure signals and trends is lost. Hence in most cases no conclusions about interannual oceanic variability or deformation of the ocean floor related to e.g. Glacial Isostatic Adjustment can be obtained from in-situ OBP observations, since normally the sensor drift is much larger (0.1–1.0 dbar/year).

Small gaps in the time series (shorter than the periods of the semidiurnal tides) and other short-term errors were interpolated. Longer gaps often imply that the remaining time series are effectively separated, since “jumps” in the pressure values can be related to either sensor drift in the meantime, or real,

e.g. seasonal variability, or both. Time series too short to calculate several consecutive monthly means are hence not compared with GRACE, since the correlations become insignificant with only 2 or 3 data points.

(3) *Final time series:* For a comparison with GRACE, the FES2004 tides are subtracted from the de-drifted in-situ time series. From this data set, monthly averages are calculated over the same time periods as in the GRACE data set. Tides need to be removed since GRACE represents monthly averages of a de-tided ocean (see next subsection). Instead of an empirical tidal fit (which could easily be calculated from any in-situ data), the FES2004 model was used here, since FES2004 is also used for de-tiding in GRACE data processing (chapter "The Release 04 CHAMP and GRACE EIGEN Gravity Field Models" by Flechtner et al., 2010a). Any errors in the tide model would influence GRACE, but not the in-situ data if these were de-tided with a "perfect" empirical fit. Nevertheless, tides may still have different effects on in-situ and GRACE data: Due to the frequent sampling of in-situ instruments, short period tides are perfectly averaged in monthly means, only long-periodic tides (fortnightly and longer) may cause aliasing if not properly modelled by FES2004. In contrast, the short period tides play a major role for GRACE, which has a lower sampling rate (see below).

2.2 GRACE

The GRACE gravity field solutions analysed here are provided by the SDS data centres CSR, GFZ and JPL as well as ITG and GRGS as monthly (or shorter) temporal averages. The science data system (SDS) "standard" products consist of a monthly geoid GSM, and the monthly averages of the non-tidal de-aliasing models GAx. For ocean bottom pressure, GAC, and – in newer releases – the special OBP-optimized GAD product which mostly eliminates land signals is recommended (Flechtner, 2007). Ocean tides, that produce large, but regular short-term OBP fluctuations and hence orbit disturbances, are de-aliased by the FES2004 tide model (chapter "The Release 04 CHAMP and GRACE EIGEN Gravity Field Models" by Flechtner et al., 2010a). Thus, the full solution for bottom pressure in a tide-free ocean is given by

$$\mathbf{OBP} = \mathbf{GSM} + \mathbf{GAC/D}$$

The GAC/D values represent monthly averages of the OBP variability predicted by the non-tidal de-aliasing OMCT model (Dobslaw and Thomas, 2010; chapter "Improved Non-tidal Atmospheric and Oceanic De-aliasing for GRACE and SLR Satellites" by Flechtner et al., 2010b). The residual de-tided variability measured by the satellites which is not explained by the FES2004 and OMCT models constitutes the GSM field.

Both the GSM+GAx and the GSM or GAx fields alone, respectively, were compared with in-situ OBP to evaluate the skill of GRACE to capture oceanic mass

redistribution realistically. This allows also to assess whether good (or poor) agreement between in-situ and GRACE measurements at a specific location is a result of good (or poor) de-aliasing models, or the actual satellite observations given by the sum of GSM and GAx fields. The comparison of earlier and more recent releases allows to quantify advances made due to improved data processing and de-aliasing model. Further, in months with poor GRACE data coverage, both constrained and unconstrained solutions are analysed.

Additionally to the CSR, GFZ and JPL fields, GRACE solutions from ITG and GRGS were analysed. The ITG fields represent a different computational approach with gravity fields calculated from short arc intervals instead of modelling the satellite orbit over longer timespans. Further, the ITG Spline solution describes the temporal variability using smooth quadratic spline functions instead of monthly means (Mayer-Gürr et al., 2006). Here, however, monthly averages of the spline functions are taken, reducing the effects of potential errors from short term tide-de-aliasing in both GRACE and in-situ data. The GRGS fields, finally, are provided in 10-day intervals, using overlapping weighted 30-day means (Lemoine et al., 2007). The higher temporal resolution allows to capture shorter-term OBP variability, although the reduced number of satellite orbits may potentially increase the noise level, and tide de-aliasing becomes more critical.

For a complete overview, all GRACE products used in this study are listed in Table 2.

Table 2 GRACE products included in this study. In all cases, all available combinations, i.e. GSM only, GAC/D only, GSM+GAC and GSM+GAD were evaluated. For references, see text

Data centre	Releases	Products	Remarks
CSR	01, 02, 04	GSM, GAC, GAD (Rel. 04 only)	Monthly means
GFZ	03, 04	GSM, GAC, GAD (Rel. 04 only)	Monthly means
JPL	02, 04, 04.1	GSM, GAC, GAD (Rel. 04.1 only)	Monthly means
GRGS	2006, 2007		10-day timeaxis
ITG	02, 03	GSM, GAC, GAD (Rel. 03 only)	Monthly means, rel. 03 based on quadratic splines

For a uniform representation, all GRACE fields were expanded from degree and order 2 to 50 (ITG: 2–40). A 750 km Gauss filter was applied to mostly eliminate meridional striping and other unrealistic artifacts. This spatial filter scale represents a reasonable compromise between high resolution and noise-reduction, and is comparable with filter scales used in other studies comparing GRACE and in-situ OBP (Kanzow et al., 2005; Rietbroek et al., 2006).

A full analysis that would include the effects of different degree and order expansions, Gauss filter radii and advanced non-isotropic (Swenson and Wahr, 2006) and pattern filters (Böning et al., 2008), is planned for the near future (Böning and Macrander, in preparation). That study will also include fine step temporal evolution of the ITG Spline solutions, Mascon solutions provided by JPL which represent a completely different approach, modelling discrete mass concentrations on Earth's

surface, and the recent weekly fields provided by GFZ (chapter "The Release 04 CHAMP and GRACE EIGEN Gravity Field Models" by Flechtner et al., 2010a), which may better capture short-term variability.

3 Methods

The skill of GRACE to realistically capture OBP variability was assessed with a correlation analysis. The de-tided in-situ OBP time series were time-averaged corresponding to the considered GRACE product, and correlated with GRACE. For averaged estimates over several in-situ sites, correlations were weighted with time series length, since longer time series attain higher significance levels of correlations while correlations calculated from short time series spanning a few months only are hardly meaningful. Additionally to the correlations, the amplitude of variability was compared, since particularly in regions with a significant seasonal cycle, correlations can be high, even though GRACE may greatly overestimate the actual variability.

4 Results

A first view on the comparison of in-situ OBP with GRACE reveals moderate to good correlations at many, but not all locations of the OBP database. Figure 3 shows the results for the recent GFZ release 04 GSM+GAD solution. Particularly in the tropical Atlantic, coastal northern Pacific and in Drake Passage, some sites with weak or negative correlations are found, whereas in higher latitudes correlations are normally higher than 0.5, reaching values of up to 0.9.

Following, the different regions will be considered in more detail, including both correlation and amplitudes of variability for different GRACE solutions. Characteristic features will be shown in selected time series which are typical for each region, before an integrated comparison of all sites with all GRACE solutions is discussed.

(1) *Southern Ocean*: The Antarctic Circumpolar Current (ACC) is the largest current of the oceans, carrying about 130 Sv (1 Sv $= 10^6$ m^3/s) around the Antarctic Continent (Orsi et al., 1995; Swart et al., 2008). Its strong barotropic component, and coherent OBP variability observed along the Antarctic coast (Hughes et al., 2003; chapter "On the Representation of Transport Variability of the Antarctic Circumpolar Current in GRACE Gravity Solutions and Numerical Ocean Model Simulations" by Böning et al., 2010) imply a high signal amplitude to be detected by GRACE. In fact, GRACE GFZ release 04 GSM+GAD and other GRACE solutions display increased oceanic RMS variability in the Southern Ocean, reaching 0.05 dbar (corresponding to 5 cm of sea level change) on monthly timescales (Fig. 1), which is comparable with in-situ observations.

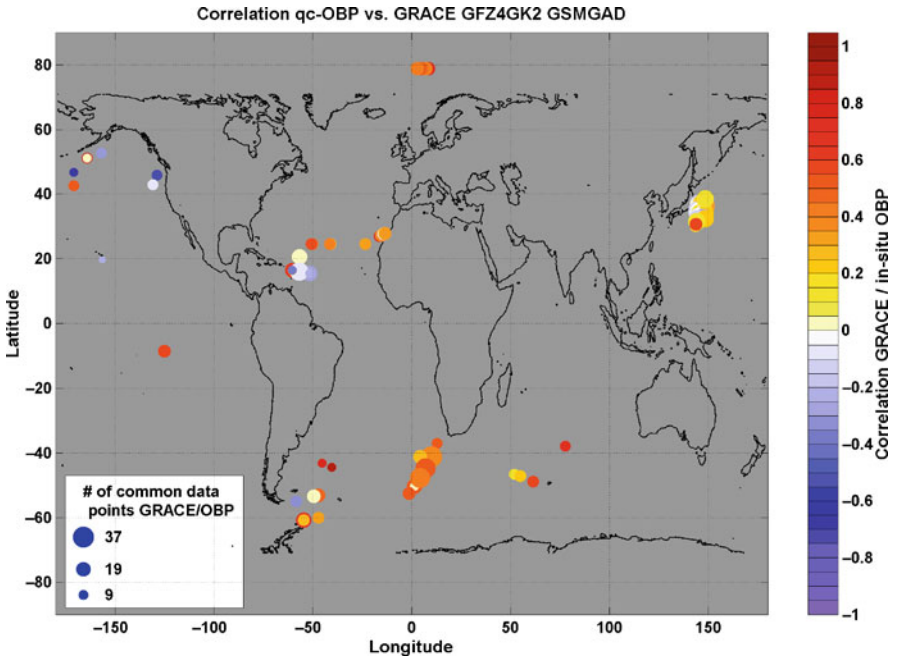

Fig. 3 Correlation of in-situ OBP with GRACE GFZ Release 04 GSM+GAD; constrained GRACE solutions were used for months with incomplete GRACE raw data. Colour of *dots* depicts correlation level, the dotsize corresponds with the length of the time series in months. Correlations with in-situ time series shorter than 5 months are not shown

Since 2002, up to 9 pressure sensors were deployed by AWI in the Atlantic sector of the Southern Ocean in a 2-dimensional pattern to detect large scale coherent OBP variability which was also found in the numerical FESOM ocean model (chapter "On the Representation of Transport Variability of the Antarctic Circumpolar Current in GRACE Gravity Solutions and Numerical Ocean Model Simulations" by Böning et al., 2010). The region is also far away from continents, where leakage effects from the hydrological cycle might degrade the GRACE solutions.

Indeed, both phase and amplitude of GRACE agree comparatively well with the in-situ time series (Fig. 4a shows an example from site ANT7). Further, some advances are evident for the recent GFZ release 04 (GSM+GAD; correlation coefficient $r = 0.56$) vs. release 03 (GSM+GAC; $r = 0.50$). The GAD de-aliasing model alone, however, shows much smaller variability than actually observed both by GRACE and the in-situ instrument and a lower correlation ($r = 0.31$).

Comparing the correlations of all GRACE products with all ACC array moorings (Fig. 4b), CSR performs slightly better than GFZ solutions. While for the GFZ products, the weighted average correlations changed

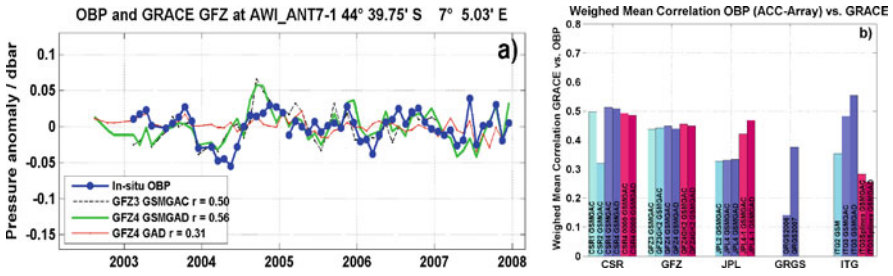

Fig. 4 (**a**) In-situ OBP time series at site ANT7 (45°S 7°E) in the ACC array (*blue*), and different GRACE GFZ products (*dashed black*: release 03 GSM+GAC; *green*: release 04 GSM+GAD; *red*: GAD only). Correlation coefficients are 0.50, 0.56 and 0.31, respectively. (**b**) Averaged correlations for all ACC array moorings, grouped according to GRACE products. From *left* to *right*: CSR: releases 01, 02 GSM+GAC (*light blue*); release 04 GSM+GAC, GSM+GAD (*blue*); release 04 with constrained solutions GSM+GAC, GSM+GAD (*magenta*). Similarly, the second group depicts GFZ rel. 03 and 03 constrained (*light blue*), 04 GSM+GAC, GSM+GAD (*blue*), 04 constrained GSM+GAC and GSM+GAD (*magenta*). Third group JPL rel. 02 (*light blue*), 04 (*blue*), 04.1 (*magenta*). Fourth group: GRGS (2006, 2007). Last group ITG rel. 02 (*blue*), 03 (monthly means) GSM+GAC, GSM+GAD (*magenta*)

little from release 03 to 04 (the improvements here are mainly due to reduction of noise amplitude; not shown), the JPL solutions improved significantly from releases 02 and 04 to 04.1. Recent GRGS and especially the monthly averages of the ITG release 03 spline solutions perform quite well in this region. At some individual sites – depending on their position relative to oceanic fronts which separate different regions of coherent OBP variability – correlations reach 0.7 for 750 km Gaussian filter. Advanced filtering techniques like the ocean-model derived pattern filter achieve even better correlations (Böning et al., 2008). The generally good agreement of GRACE and in-situ OBP time series of the ACC array is corroborated by a study of Rietbroek et al. (2006) in the Kerguelen region, which showed high correlations, here for the 10-day GRGS solutions.

(2) *Fram Strait*: Located between Greenland and Svalbard, Fram Strait represents the deepest connection between the Atlantic Ocean and the Arctic Mediterranean. GRACE observes strong OBP variability (O(0.05 dbar)) in the Arctic (Fig. 1). At 79°N, several pressure sensors are operated since 2003 to monitor the exchange of water masses between both basins. From all regions analysed in this study, Fram Strait exhibits by far the best agreement between in-situ OBP and GRACE.

During 4 years of mooring deployments at the F8 site, GRACE GSM+GAC/D closely follows the observed in-situ OBP (Fig. 5a). In this example, the average correlation is 0.73 (GFZ release 03), but over individual deployments in the entire Fram Strait array, correlations better than 0.9 are reached regularly.

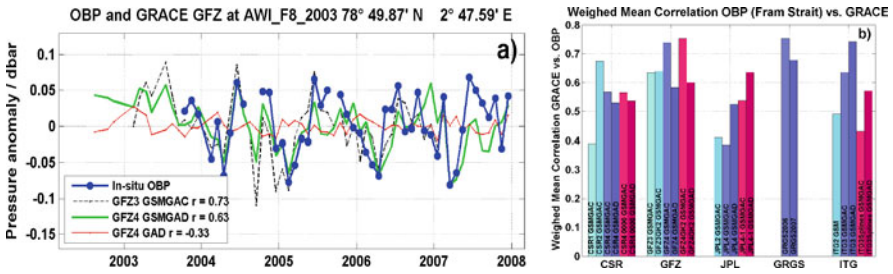

Fig. 5 (**a**) In-situ OBP time series at site F8 (79°N 3°E) in Fram Strait (*blue*), and different GRACE GFZ products (*dashed black*: release 03 GSM+GAC; *green*: release 04 GSM+GAD; *red*: GAD only). Correlation coefficients are 0.73, 0.63 and –0.33, respectively. (**b**) Averaged correlations for all Fram Strait moorings. For explanation, see legend of Fig. 4b

The figure shows also, that the GAC/D de-aliasing models alone do not capture the observed variability – hence, the actual satellite measurements are necessary, and not just good models.

The high correlation is found for all GRACE solutions (Fig. 5b), with the best results obtained by the GFZ RL04 GSM+GAC, GRGS and ITG RL03 GSM+GAD solutions. As in the Southern Ocean, the JPL solutions exhibit the largest improvements from early to recent releases. Interestingly, the GSM+GAC fields of GFZ (but not CSR and JPL) are slightly better than the OBP-optimized GSM+GAD solutions – obviously GAD does not always improve the results. Nevertheless, GRACE shows almost perfect skill to observe oceanic mass variability in Fram Strait; this agrees also with central Arctic Ocean OBP studied by Morison et al. (2007).

(3) *Subtropical north Atlantic*: As part of the MOVE and RAPID projects, several of OBP sensors are deployed at 16°N and 26°N to monitor the Atlantic meridional overturning circulation. The MOVE array was extended to a 2-dimensional layout to capture coherent OBP variability, which is observed by GRACE. Kanzow et al. (2005) showed that GRACE greatly overestimated the annual cycle of OBP. These findings are still true: Despite unrealistic annual cycles were significantly reduced in some recent GRACE releases (e.g. from GFZ, less so in e.g. JPL), the correlations of GRACE with in-situ OBP are still small (Fig. 6). In some cases, the GAC/D de-aliasing models alone perform even better than the full GSM+GAC/D solutions. Apparently, the small signal amplitude (O(0.01 dbar)) and the wider spacing of satellite groundtracks in low latitudes make realistic observations of oceanic mass variability with GRACE more challenging. A particular artifact of many GRACE solutions (especially CSR, JPL, ITG) is a northward extension of the hydrologic signal from South America. Its annual cycle is evident in e.g. the JPL solutions shown in Fig. 6b.

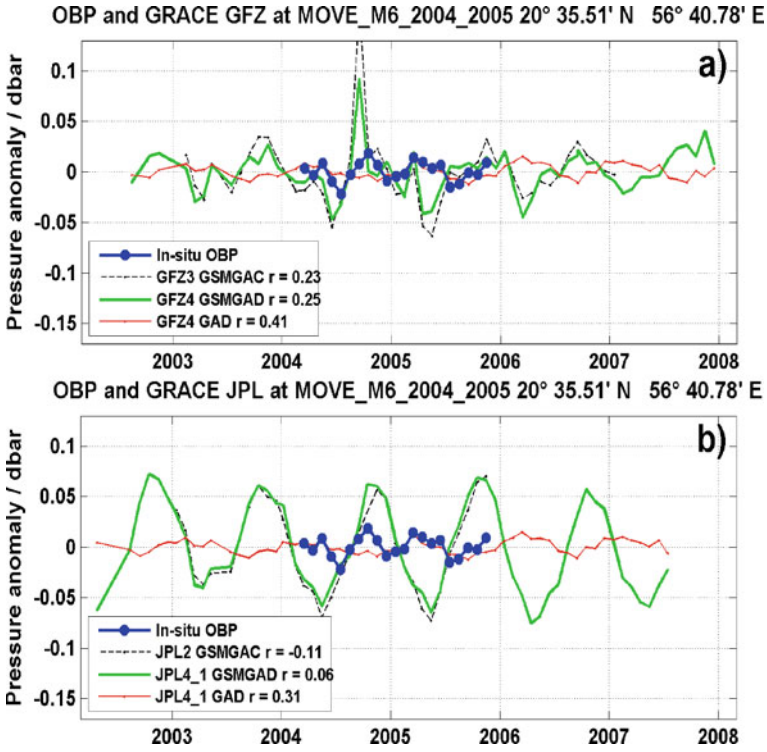

Fig. 6 (**a**) In-situ OBP time series at site M6 (near 21°N 57°W) of the MOVE array (*blue*), and different GRACE GFZ products (*dashed black*: release 03 GSM+GAC; *green*: release 04 GSM+GAD; *red*: GAD only). Correlation coefficients are 0.23, 0.25 and 0.41, respectively. (**b**) As above, but for JPL releases 02 and 04.1. Correlations are –0.11, 0.06 and 0.31, respectively. Note the large annual cycle in the JPL GSM+GAx solutions, which is likely affected from South America hydrology

At 26°N (RAPID array), correlations appear to be somewhat better (not shown, but c.f. Fig. 7 later), but here, only 1-year long time series were investigated in this study, with some higher correlations resulting from annual cycles of both in-situ and satellite data in phase, even though amplitude and short-term variability are still quite different.

(4 and 5) *Coastal north east Pacific; Drake Passage*: In these regions covered by the DART tsunami early warning system, and oceanographic moorings collected in the POL database, respectively, GRACE/in-situ OBP correlations differ from one station to the next. Some time series are in excellent agreement, suggesting, that GRACE generally captures OBP variability also in these regions quite well. Nevertheless, these regions require further investigations since at some positions GRACE data might be influenced by leakage of continental signals, and some positions in areas with highly localized variability may be not well sampled with the 750 km

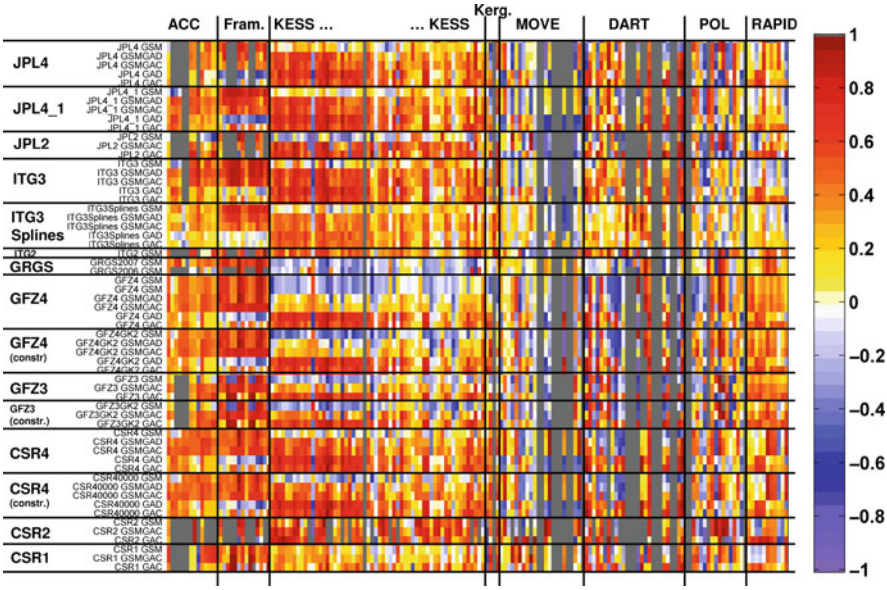

Fig. 7 Checkerboard plot showing correlation of in-situ OBP (x axis) with all different GRACE products (y axis). OBP sites are grouped according to Table 1. Only time series with more than 5 common data points with at least one GRACE solution are plotted. For clarity the 155 individual site names of these time series are not shown here. GRACE products are grouped into data centre/release. In each group, GSM-only constitutes the *top row*, followed by GSM+GAC (and GSM+GAD in recent releases) as "official" OBP products. The *bottom rows* of each group are the GAC (and GAD) de-aliasing models alone. Colour denotes correlation from +1 (*dark red*) to –1 (*blue*). *Grey* fields mark where GRACE and in-situ time series have not enough overlap (less than 5 common data points). This is the case where early GRACE releases are discontinued before the start of certain OBP time series, or in case of some short-term deployments or data gaps due to instrument problems

Gaussian filter used in this study. Böning et al. (2008) showed significant improvements using an ocean-model derived pattern filter technique to select the region for which each in-situ instrument is representative. Finally, all in-situ time series need to be cross-checked again to ensure that all measurement errors are corrected as good as possible.

(6) *Kuroshio extension*: In this highly energetic western boundary current, an extensive array of pressure sensors was deployed in the framework of the KESS experiment. Park et al. (2008) found good agreement between in-situ and GRACE data (GFZ, and especially CSR, JPL), particularly in the northern and western part of the array. This underlines that a point measurement (in-situ) may or may not be representative for a larger region sampled by the spatially averaging GRACE data.

Overview: Space does not allow here to discuss each of the 168 in-situ time series and the 53 GRACE products and combinations in detail. After the introduction of six characteristic regions sampled by in-situ instruments, an overview of

the comparison of all in-situ data with all GRACE data is given below. At first glance, the full picture showing all correlations (Fig. 7) is somewhat confusing, but it shall be attempted to indentify the key features: In the high-latitude ACC and Fram Strait arrays, all GRACE releases agree well with the in-situ observations. Generally, the best correlations are achieved by the GSM only, or the GSM+GAC/D fields, suggesting that the monthly oceanic variability is mostly captured by the satellites, but not the de-aliasing models. This is particularly the case in the 79°N Fram Strait array. In contrast, the de-aliasing models are clearly necessary in the Kuroshio extension, where almost all GRACE GSM+GAC/D solutions perform well, but not the GSM-only fields. The GFZ solutions are the only ones in the Kuroshio extension that show considerably lower correlations – whereas in the subtropical Atlantic at 26°N (RAPID) GFZ provides the comparatively best solutions. North east Pacific (DART) and Drake Passage (POL) reveal mixed results as discussed above. Nevertheless, JPL and ITG appear to be slightly better in the north east Pacific, while GFZ better captures Drake Passage.

5 Summary and Conclusions

Summarizing the results of the comparison of all different GRACE products with all OBP time series, some characteristic features can be found, whose background (e.g. de-aliasing, spatial scales of OBP variability) require further investigations. The key findings are:

(1) Recent vs. early GRACE product releases: Generally, more recent GRACE releases appear to be better than early ones. This is mostly evident in the reduction of unrealistically large annual OBP cycles and leakage effects of continental variability into the oceans. Nevertheless, the increase in actual correlation between in-situ time series and GRACE is often small. Further, the OBP-tailored GAD product does not always improve the correlations when compared with GAC.
(2) "Good regions": In some regions, particularly in the Southern Ocean (ACC array, Kerguelen) and the Arctic Ocean (Fram Strait), all GRACE solutions agree well with in-situ observations both in amplitude and phase. Further, the high correlation levels of GSM+GAx vs. in-situ OBP are mainly achieved by the GSM contribution, and not by the GAx de-aliasing models alone. This implies, that the actual satellite observations are necessary to determine the real oceanic variability. Generally, GRACE appears to realistically capture OBP variability in higher latitudes.
(3) "Partially good regions": In other parts of the oceans, correlations in-situ OBP vs. GRACE disagree among different GRACE products. For example, in the subtropical Atlantic at 26°N (RAPID array), GRACE solutions from GFZ generally reach the best correlations. The same holds for several GAC/D de-aliasing models, but *not* for the GSM geoids. Obviously, the numerical models capture

at least some of the OBP variability in low-latitude regions (e.g. the annual cycle), but the actual satellite observations degrade the final solution. This is in marked contrast to the high-latitude regions mentioned above. Another example is the Kuroshio extension in the Pacific Ocean – here, JPL and CSR perform quite well, but not GFZ (Park et al., 2008). Further, the GRGS solutions, which show excellent skill in the ACC array, Kerguelen region (Rietbroek et al., 2006) and Fram Strait, attain only weak or even negative correlations in the Kuroshio extension.

(4) "Problematic regions": All GRACE solutions exhibit low correlations with in-situ OBP in the tropical Atlantic at 16°N (MOVE, Kanzow et al., 2005) where signal amplitudes are very small, and leakage from South America hydrology is found in many GRACE solutions. Also in areas with strong small-scale variability like in parts of the Drake Passage or different sites close to coastlines in the Pacific (DART), correlations are either weak, or completely different from one site to the next.

The good skill of GRACE in high latitudes conforms with the denser sampling pattern due to the polar satellite orbits, and the generally higher signal amplitudes in polar oceans, which are mostly barotropic, in contrast to lower latitudes, where OBP variability is smaller, with warm surface and abyssal layers mostly decoupled. The poor skill in some areas with localized variability and coastal regions can be attributed to the small spatial scales which are not captured by GRACE. More challenging, however, are the remaining, "partially good" regions: Obviously, data processing and de-aliasing models play a major role in defining the skill of GRACE to realistically observe OBP variability. But, the "best" solution or model does not exist so far – products that perform well in one region, are poor in another part of the ocean, where a different GRACE product is better. The irregular distribution of "good" and "poor" regions makes it also impossible to guess how realistic a particular GRACE solution is elsewhere in the ocean, where no in-situ ground truth observations exist.

A continued global validation of GRACE offers the perspective to further improve GRACE data processing, and, in particular, tidal and non-tidal de-aliasing. Therefore, the AWI OBP database is continuously extended as more recent observations become available. Automatic validation tools are under development to allow a rapid assessment of improvements or degradations achieved by new GRACE products. A full analysis of GRACE/in-situ OBP correlation will include the effects of different degree/order expansions, recognition of characteristic geographic or temporal patterns in the correlations, and their dependence on tidal de-aliasing and filtering mechanisms such as Gaussian, anisotropic and ocean-circulation model aided pattern filter (Böning et al., 2008). Also, a validation of the temporal evolution of spline solutions, "Mascon" solutions of GRACE, which are based on a completely different approach to gravity field variations, and weekly GRACE solutions, which capture more short-term variability while reducing spatial resolution, will provide interesting results.

Until a GRACE solution is found which shows good skill at all ground-truth sites OBP remains a challenge for GRACE, and hence the validation of GRACE with in-situ observations is essential for realistic estimates of oceanic mass redistribution.

Acknowledgments This is publication no. GEOTECH-1271 of the GEOTECHNOLOGIEN programme of BMBF, grant 03F0436A.

We are grateful to all those who kindly provided in-situ OBP time series, namely Agnieszka Beszczynska-Möller (AWI, DAMOCLES), Chris Hughes (POL, ACCLAIM), Johannes Karstensen (IFM-GEOMAR) and Uwe Send (SIO, MOVE), Christian Meinig (NOAA, DART), Pascal LeGrand (CNES) and Roelof Rietbroek (GFZ) and Bert Wouters (TU Delft, Kerguelen), Randy Watts (URI, KESS), Stuart Cunningham (NOC) and Torsten Kanzow (NOC) and Robin McCandliss (NOC) for RAPID. This study uses data from the Rapid Climate Change programme, provided by the British Oceanographic Data Centre and supported by the Natural Environment Research Council.

We thank M. Thomas for the helpful comments which significantly improved the manuscript.

References

Böning C, Timmermann R, Macrander A, Schröter J (2008) A pattern-filtering method for the determination of ocean bottom pressure anomalies from GRACE solutions. Geophys. Res. Lett. 35, L18611, doi: 10.1029/2008GL034974.

Böning C, Timmermann R, Danilov S, Schröter J (2010) On the representation of transport variability of the Antarctic Circumpolar Current in GRACE gravity solutions and numerical ocean model simulations. In: Flechtner F, Gruber T, Güntner A, Mandea M, Rothacher M, Schöne T, Wickert J (eds.), Satellite Geodesy and Earth System Science, Springer-Verlag, Berlin, Heidelberg.

Dobslaw H, Thomas M (2010) Numerical simulations of short-term ocean mass anomalies. In: Flechtner F, Gruber T, Güntner A, Mandea M, Rothacher M, Schöne T, Wickert J (eds.), Satellite Geodesy and Earth System Science, Springer-Verlag, Berlin, Heidelberg.

Flechtner F (2007) AOD1B Product Description Document for Product Releases 01 to 04. Rev. 3.0, GRACE project documentation 327–750.

Flechtner F, Dahle Ch, Neumayer KH, König R, Förste Ch (2010a) The Release 04 CHAMP and GRACE EIGEN gravity field models. In: Flechtner F, Gruber T, Güntner A, Mandea M, Rothacher M, Schöne T, Wickert J (eds.), Satellite Geodesy and Earth System Science, Springer-Verlag, Berlin, Heidelberg.

Flechtner F, Thomas M, Dobslaw H (2010b) Improved non-tidal atmospheric and oceanic dealiasing for GRACE and SLR satellites. In: Flechtner F, Gruber T, Güntner A, Mandea M, Rothacher M, Schöne T, Wickert J (eds.), Satellite Geodesy and Earth System Science, Springer-Verlag, Berlin, Heidelberg.

Hughes CW, Woodworth PL, Meredith MP, Stepanov V, Whitworth T, Pyne AR (2003) Coherence of Antarctic sea levels, Southern Hemisphere Annular Mode, and flow through Drake Passage. Geophys. Res. Lett. 30(9), 1464, doi: 10.1029/2003GL017240.

Kanzow T, Flechtner F, Chave A, Schmidt R, Schwintzer P, Send U (2005) Seasonal variation of ocean bottom pressure derived from Gravity Recovery and Climate Experiment (GRACE): Local validation and global patterns. J. Geophys. Res. 110, C09001, doi: 10.1029/2004JC002772.

Kanzow T, Send U, Zenk W, Chave A, Rhein M (2006) Monitoring the integrated deep meridional flow in the tropical North Atlantic: Long-term performance of a geostrophic array. Deep Sea Res. I 53(3), 528–546, doi: 10.1016/j.dsr.2005.12.007.

Lemoine, J-M, Bruinsma S, Loyer S, Biancale R, Marty J-C, Perosanz F, Balmino G (2007) Temporal gravity field models inferred from GRACE data. Adv. Space Res. 39, 1620–1629, doi: 10.1016/j.asr.2007.03.062.

Lyard F, Lefevre F, Letellier T, Francis O (2006) Modelling the global ocean tides: Modern insights from FES2004. J. Ocean Dyn., doi: 10.1007/s10236-006-0086-x.

Mayer-Gürr T, Eicker A, Ilk KH (2006) Gravity field recovery from GRACE-SST data of short arcs. In: Flury J, Rummel R, Reigber C, Rothacher M, Boedecker G, Schreiber U (eds.), Observation of the Earth System from Space, ISBN 3-540-29520-8, Springer, Berlin, pp. 131–148.

Meyer U, Frommknecht B, Schmidt R, Flechtner F (2007) Global gravity fields from simulated L1 products. In: Observation of the System Earth form Space: Status Seminar, Geotechnologien Science Report No. 11, Bavarian Academy of Sciences and Humanities, Munich, November 22–23, 2007.

Morison J, Wahr J, Kwok R, Peralta-Ferriz C (2007) Recent trends in Arctic Ocean mass distribution revealed by GRACE. Geophys. Res. Lett. 34, L07602, doi: 10.1029/2006GL029016.

Orsi AH, Whitworth T, Nowlin WD (1995) On the meridional extent and fronts of the Antarctic Circumpolar Current. Deep Sea Res. Part I 42, 641–673.

Park JH, Watts DR, Donohue KA, Jayne SR (2008) A comparison of in situ bottom pressure array measurements with GRACE estimates in the Kuroshio extension. Geophys. Res. Lett. 35, L17601, doi: 10.1029/2008GL034778.

Rietbroek R, LeGrand P, Wouters B, Lemoine J-M, Ramillien G, Hughes CW (2006) Comparison of in situ bottom pressure data with GRACE gravimetry in the Crozet-Kerguelen region. Geophys. Res. Lett. 33, L21601, doi: 10.1029/2006GL027452.

Swart S, Speich S, Ansorge IJ, Goni GJ, Gladyshev S, Lutjeharms JRE (2008) Transport and variability of the Antarctic Circumpolar Current south of Africa. J. Geophys. Res. 113, C09014, doi: 10.1029/2007JC004223.

Swenson S, Wahr J (2006) Post-processing removal of correlated errors in GRACE data. Geophys. Res. Lett. 33, L08402, doi: 10.1029/2005GL025285.

University of Rhode Island (2006) Inverted Echo Sounder User's Manual, revised report, University of Rhode Island, Narragansett.

Antarctic Circumpolar Current Transport Variability in GRACE Gravity Solutions and Numerical Ocean Model Simulations

Carmen Böning, Ralph Timmermann, Sergey Danilov, and Jens Schröter

1 Introduction

The ACC attracts attention of oceanographers due to its unique role in the world ocean. It circles the globe providing connections between major ocean basins and has thus important implications for climate variability. Understanding the driving forces of the ACC variability presents a challenging task for both theoretical and observation based investigations. The theoretical principles underlying the ACC dynamics have been discussed in many papers (see Olbers et al., 2004 for a recent study on the dynamical balance, transport and circulation).

The zonal geostrophic transport is connected to a meridional pressure gradient. The latter is a consequence of the westerlies over the Southern Ocean which produces a northward Ekman transport leading to slope in the sea surface and, on larger time scale, affecting the oceanic density distribution. Altogether this induces the meridional pressure gradient and hence an eastward geostrophic flow.

Changes in the atmospheric pressure gradient between the low pressure system over Antarctica and the high pressure system at mid-latitudes are modulating the strength of westerlies. Due to this relation atmospheric fluctuations are connected to the transport in the ACC.

Variability of atmospheric patterns over the Southern Hemisphere is dominated by the Antarctic Oscillation (AAO) or Southern Annular Mode (SAM). This mode explains 20–30% of the total variance in the wind fields (Thompson and Marshall, 2002). Since short-term transport fluctuations in the ACC are found to be mainly barotropic, the relationship between oceanic transport variability and the SAM is of special interest for understanding the ACC.

Meredith et al. (2004) found a connection between the SAM index and volume transport derived from model simulations on an annual time scale. A correlation of about 0.68 significant at a 99% level of the SAM index to sea surface pressure measurements south of Drake Passage could be observed. Interannual month-by-month

C. Böning (✉)
Alfred Wegener Institute for Polar and Marine Research, D-27570 Bremerhaven, Germany
e-mail: carmen.boening@jpl.nasa.gov

F. Flechtner et al. (eds.), *System Earth via Geodetic-Geophysical Space Techniques*, Advanced Technologies in Earth Sciences, DOI 10.1007/978-3-642-10228-8_15,

trends from 1990 to 1999 in the SAM agree well with observations of ocean bottom pressure south of Drake Passage. They concluded that the transport variability is therefore related to the SAM.

These findings contradict recent investigations of ACC transport variability (Cunningham and Pavic, 2007) based on observations of surface geostrophic currents through a section across Drake Passage. SAM was found to be only weakly correlated to the transport variability observed in Drake Passage. A positive trend detected in the SAM (Thompson and Solomon, 2002) that is related to strengthening of the westerly winds and thus expected to influence the ACC transport has not been found in the measurements. This controversy invites new studies based on both observations and numerics to clarify the connections behind the ACC transport variability. This study contributes in this direction by combining the GRACE data with analysis of output of a primitive-equation general circulation model driven with realistic forcing.

The GRACE mission provides monthly solutions of the Earth's gravity field over the ocean, from which anomalies of ocean bottom pressure can be derived. Ocean bottom pressure fluctuations are a proxy for oceanic mass redistribution and yield a relation to the transport variations via the momentum equations. The region of the Southern Ocean is a good candidate for the validation of GRACE data with respect to their ability to capture transport variability. Barotropic variations in the ACC induced by the SAM can be expected to imprint a signature in the GRACE ocean bottom pressure data. Quantification of transport variability as seen in GRACE can then improve our understanding of the mass variability in the Southern Ocean and the ACC in particular.

First encouraging results regarding the issue of observing ACC transport variability with GRACE have been obtained by Zlotnicki et al. (2006). They compared GRACE-derived (JPL RL02) ocean bottom pressure along 40°S and 65°S and the difference between them for each basin with results obtained from the ocean models ECCO and ROMS. Furthermore, they used QuikSCAT wind observations to underline the relation between wind fluctuations and changes in zonally (along the southern boundary of the ACC) averaged bottom pressure. A high agreement in phase was found for each basin between the models and GRACE-derived differences as the amplitude was generally overestimated by GRACE filtered with a 500 km Gaussian filter. A 3-year decreasing trend has been detected in all three data sets in the average along the southern ACC boundary which was related to weakening of winds.

Due to aliasing artefacts in the GRACE solutions errors in the amplitudes of OBP anomalies continue to introduce uncertainties into the determination of the range of variability. However, these errors are apparently reduced in the new GRACE releases as well as by new filtering mechanisms.

Since 2006 new releases of GRACE data with reduced errors have been produced by the different processing centres. The time series are now spanning the period 2003–2008. Corrections for geocenter motion and post-glacial rebound (PGR) are included in the post-processed fields based on Chambers (2006).

We investigated the representation of the ACC in the currently available GRACE solutions. For this purpose transport variability derived from GRACE OBP anomalies has been compared to results obtained by Zlotnicki et al. (2006) as well as to variations derived from simulated OBP anomalies and Drake Passage volume transport. We utilized the Finite Element Sea Ice – Ocean Model (FESOM) described in detail by Timmermann et al. (2009) which provides ocean bottom pressure anomalies as well as the total transports.

In addition to the estimation of transport variability we analyzed the representation of SAM in the GRACE-derived OBP. We determined the connection between the atmospheric variability (as represented by SAM) and transport variability that can be derived from GRACE retrievals and model simulations. This analysis gives an insight into how the atmospheric variability influences the mass distribution measured by GRACE.

2 Data

We investigate the representation of ACC and SAM variability in GRACE using the so-called de-striped solutions based on Chambers (2006). The de-striping algorithm is based on the method developed by Swenson and Wahr (2006). They found the errors, which manifest themselves as north-south stripes of opposite signs and dominate spherical harmonic solutions, to be correlated – which allows for a systematic correction of the data. However, they noted that due to their empirical method signals can be attenuated. Chambers (2006) optimized this algorithm for the purpose of oceanic investigations with GRACE. The data (RL04) are provided by the three JPL, CSR, and GFZ as monthly means of GRACE-derived ocean bottom pressure for the period from January 2003 to April 2008. The de-striped data are available on a $1^\circ \times 1^\circ$ regular grid additionally smoothed with a 300, 500 or 750 km Gauss filter (http://grace.jpl.nasa.gov/data/mass/). A time average over the complete data set has been removed from the data. Since GRACE is not able to observe spherical harmonics of degree and order 1 which are related to the geocenter motion, those values have been derived from an estimation of geocenter motion. A PGR model was used to correct the data for the effect of post-glacial rebound (see Chambers, 2006).

We found that applying information about the oceanic circulation derived from our ocean model FESOM for the filtering of GRACE solutions helps to obtain a higher agreement of GRACE and in-situ data (Böning et al., 2008). As an update of our work we used our algorithm of including properties of ocean bottom pressure into the de-striped solutions of release 04. The 300 km Gauss filtered solutions were first interpolated to our model domain. Instead of larger scale Gaussian filtering we applied spatially varying patterns of coherent ocean bottom pressure anomalies. Typical length scales for these patterns are 1,000 km in the Southern Ocean (Böning et al., 2008). The results are time series that are more likely to represent fluctuations in OBP than when applying an isotropic Gaussian filter. Our 300 km de-striped

pattern filtered solutions are found to have an equivalent level of variability as the 500 km de-striped only solutions.

The ocean model is the Finite Element Sea Ice – Ocean Model (FESOM) based on Timmermann et al. (2009). In order to represent oceanic mass redistribution properly in this Boussinesq model, contributions to the surface elevation from net precipitation, surface runoff and sea ice were added and a correction for steric effects has been applied (Greatbatch, 1994; see also Böning et al., 2008).

Simulations cover the period from 1958 to 2007 and are forced with data provided by the NCEP-NCAR daily re-analysis, except for runoff which was derived from the Hydrological Discharge Model (HDM; Walter, 2007). Data are provided as monthly means which suits the GRACE solution. For the matter of flux consistency, runoff from the ECMWF-forced HDM is assumed to be balanced by the net precipitation on time scales of approximately 5 years. Based on this assumption a correction of the runoff has been applied.

The SAM index used in this study is a station-based index constructed from measurements of air pressure at 12 stations located at 40°S and 65°S. The data is provided on a monthly basis for the period from 1957 to 2008 (Marshall, 2003). Another SAM index derived from the NCEP-NCAR reanalysis (Hughes et al., 2003) is available. Meredith et al. (2004) who constructed a SAM index based on the measurements in the same way as in Marshall (2003) found a correlation to annual means of this other index of about 0.86 for the period from 1981 to 2000. This indicates a good agreement between the two indices, but also points to some independence of the two data sets. In the following we base the comparison of our model output not on the analysis of the NCEP-NCAR forcing fields but on the original station data.

3 Transport Variability and Ocean Bottom Pressure

According to Hughes et al. (1999) we can expect a relation between the barotropic transport and ocean bottom pressure. His formula describing total transport between two stations a and b reads:

$$T = \int_a^b \int_{-H}^0 u \, ds \, dz,$$

where H is the total depth from the ocean bottom to sea surface, and u is a component of velocity normal to the path connecting a and b. The transport splits into a geostrophic part and the part stemming from the Ekman transport and other ageostrophic contributions. Assuming a flow with geostrophic velocities u_g independent of depth, we can write:

$$T = \int_a^b H u_g \, ds + T_{Ek},$$

where T_{Ek} is the Ekman part of the transport (plus any ageostrophic contribution). Geostrophy gives a relation between the depth-independent geostrophic velocity u_g and pressure p:

$$f u_g \rho_0 = \frac{\partial p}{\partial s}$$

which leads to a geostrophic transport through a/b:

$$T_g = \int_a^b \frac{H}{f\rho_0} \frac{\partial p}{\partial s}\, ds$$

If a and b lie on the same contour of H/f the integration can follow this path and H/f can be taken as constant. In this case we arrive at a geostrophic transport

$$T_g = \frac{H}{f\rho_0}(p_b - p_a) \tag{1}$$

If a and b are not on the same contour of H/f the path of integration is dependent on the path of the flow and the correlation between the depth-independent transport and difference of ocean bottom pressure between a and b weakens.

In order to derive ACC transport variability estimates from GRACE OBP, Zlotnicki et al. (2006) averaged OBP anomalies along the northern- and southernmost fronts of the ACC (i.e. the Subtropical Front and the southern boundary of the ACC; Orsi et al., 1995). Transport variations are estimated through the differences between the northern and southern averaged OBP anomalies. However, as the paths of integration across the ACC do not follow H/f contours the derived estimate is an approximation of the total transport variability. Using formula (1) a rough conversion factor between bottom pressure and transport variations can be determined.

The average depths of the paths along the fronts are estimated to lie between 4,000 and 4,700 m. Taking a nominal latitude of 60°S, one arrives at a conversion factor of 3.1 Sv (cm H_2O)$^{-1}$ which leads with an average density of 1,027 kg/m^3 and a gravitational acceleration of 9.806 m/s^2 to a conversion factor between OBP anomalies and transport variations of 307 Sv (dbar)$^{-1}$.

Comparing the averaged OBP anomalies along the fronts for each ocean basin, Zlotnicki et al. (2006) found that GRACE-derived OBP anomalies in the south as well as north-south differences are in better agreement with results of ECCO and ROMS models than anomalies in the north. They attributed these differences to the correlated errors in the GRACE solutions which are more pronounced in the mid and low latitudes. As fluctuations in the north were found to be small, transport variations are associated with the average of OBP anomalies over the southern front with insignificant contribution of the northern fluctuations.

In order to compare the current GRACE products to their findings, we integrated the de-striped, pattern filtered GRACE solutions along the southern ACC boundary.

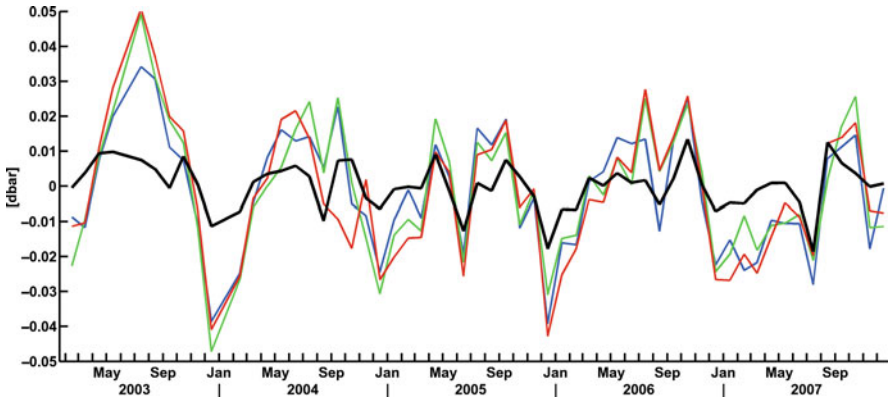

Fig. 1 OBP averaged over the southern ACC boundary from FESOM (*black*) and GRACE retrievals (*cyan*: JPL, *red*: GFZ, *green*: CSR)

We found peak-to-peak variations, i.e. maximum and minimum of the annual cycle, of OBP of about 0.02–0.04 dbar (Fig. 1). With the estimated scaling factor of 307 Sv $(\text{dbar})^{-1}$, we arrive at a transport variability at annual and semiannual periods of approximately 6–9 Sv in the GRACE solutions. This compares well with the value found for the JPL RL02 which was estimated to be 9 Sv with an estimated error of about ± 5.9 Sv for the southern path average.

The annual cycle which was a dominant feature in the JPL RL02 solutions used for the study by Zlotnicki et al. (2006) is less pronounced in the RL04 de-striped products from all three processing centers (JPL, GFZ, CSR). The differences between the JPL RL02 and the RL04 results are most likely indicative of the recent development of the GRACE solutions. Improvements of background models for example helped to overcome issues like tidal aliasing to a substantial extent. However, the de-striping is a potential source for attenuation of signals which may also induce the observed reduction of the amplitudes of derived OBP variations.

FESOM OBP anomalies are by a factor of 3 smaller than the variations measured by GRACE. However, the phase of both, GRACE and FESOM, are highly correlated. FESOM OBP anomalies have a correlation of 0.77 to the JPL, 0.7 to the CSR, and 0.71 to the GFZ solution at a 99% significance level (Fig. 2).

Volume transport through Drake Passage derived from model simulations yields the same range of variability as the quasi-zonally averaged OBP anomalies. On annual and semiannual periods variations of about 2–3 Sv are calculated. The phase of volume transport variations agrees with the phase of gradients of OBP anomalies. We obtain a correlation of 0.76 at a significance level of 99% which indicates that variations in volume transport through Drake Passage in our model simulations are to a large extent explainable by variations in OBP (in the south or north-south gradients). The explained variance by the averaged OBP is approximately 57% of the simulated total transport variations.

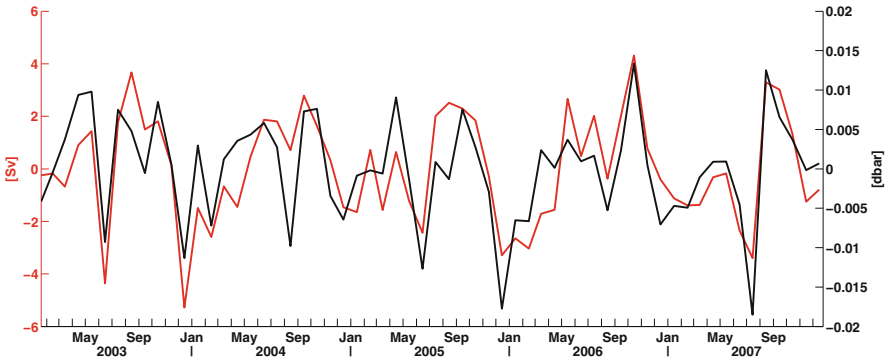

Fig. 2 Volume transport (*grey*) through Drake Passage and OBP anomalies (*black*) derived from FESOM simulations

4 SAM in GRACE Ocean Bottom Pressure

The Southern Annular Mode (SAM) can be defined as the leading principal component of the 850-hPa geopotential height anomaly south of 20°S (or of the sea level pressure; the corresponding time series displaying a correlation of 0.99; Lefebvre et al., 2004). A positive (negative) SAM is associated with lower (higher) than normal sea level pressure at high latitudes and higher (lower) than normal sea level pressures at low latitudes. As a consequence, during years with a positive SAM index, the westerlies are intensified in the region of the ACC.

Various studies (e.g. Meredith et al., 2004) found transport of the ACC through Drake Passage related to SAM and indicate a possible use of SAM index as a proxy for ACC transport variability. A connection between fluctuations in the Southern Ocean wind field and transport variations was established on scales of 10–220 days (Hughes et al., 1999). On longer time scales the growing influence baroclinicity weakens the relation between atmospheric and oceanic variability. SAM as a measure for atmospheric variations can be expected to be related to transport on similar time scales.

Recent comparisons of the SAM-related fluctuations and fluctuations derived from in-situ measurements of Drake Passage transport indicate only a weak relation between SAM index and transport fluctuations. In a comprehensive study by Cunningham and Pavic (2006) who used current meter as well as satellite and hydrographic measurements to determine transport variability over the period 1992–2004 only a weak correlation of transport variations and SAM was observed. They concluded that SAM is not likely to yield a good proxy for ACC transport variability.

Being aware of these contradicting results, we revisit the relation of SAM to the variability of mass redistribution derived from GRACE gravity solutions. We also compare SAM to transport and OBP anomalies derived from the model to get additional support to the existence of correlation.

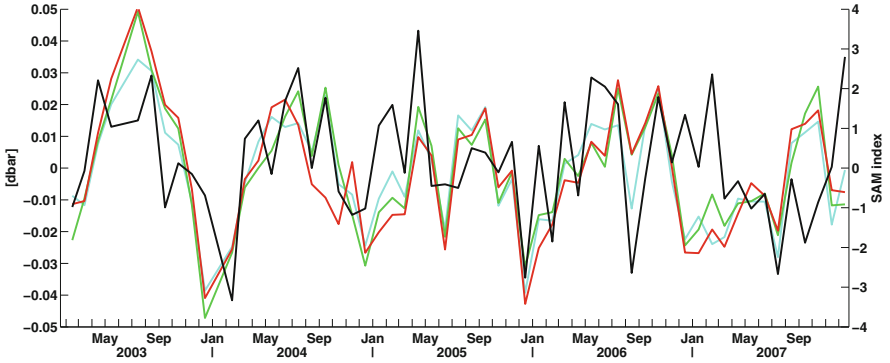

Fig. 3 *Black line* indicates SAM index, *colored lines* GRACE OBP anomalies averaged along the southern ACC boundary (JPL: *blue*, GFZ: *red*, CSR: *green*)

Findings of Zlotnicki et al. (2006) have already indicated a relation between GRACE-derived OBP anomalies averaged along the southern ACC boundary and the atmospheric variability as seen in the QuikSCAT wind stress measurements. Our study here is complementary to this earlier study by using newly available GRACE solutions and simulations performed with FESOM.

Changes in large scale atmospheric variability are represented by the SAM index. Those variations are found to be related to the GRACE-derived OBP anomalies. Extremes on a seasonal or even shorter time scale in SAM are captured by GRACE. As OBP is connected to transport, this relation supports the assumption of a connection between SAM and transport variability. However, on longer (larger than annual) time scales a weakening of this relation is expected and is confirmed by the GRACE solutions (Fig. 3).

By comparing SAM index and FESOM Drake Passage volume transport variations, we found a correlation of only 0.4 between both but at a high significance level of 99%. As can be seen in Fig. 4, showing the temporal derivatives as monthly

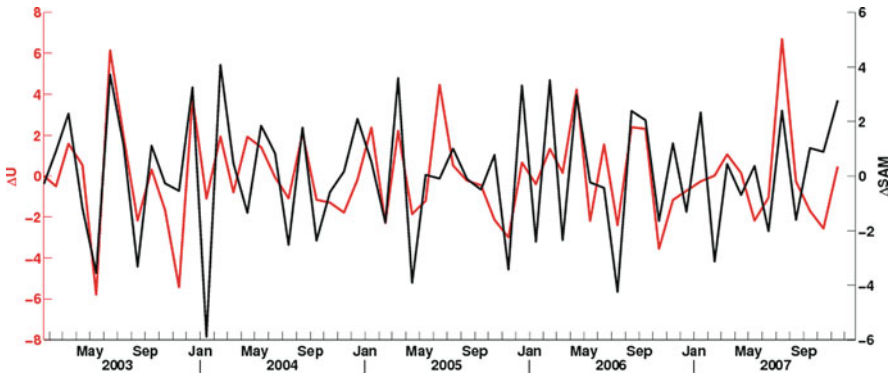

Fig. 4 Monthly changes of SAM index (*black*) and FESOM volume transport anomalies through Drake Passage (*grey*)

changes in SAM and FESOM volume transport anomalies, a change in SAM from high to low, or vice versa, indicates a similar change in the transport. This indicates a connection between both quantities on a monthly time scale. However, on inter-annual time scales this relation apparently weakens.

Studies by Lettmann and Olbers (2005) show that Drake Passage transport variations are related to OBP in the Southern Ocean with correlation patterns connected to *f/H* contours. Variations in transport are connected to OBP anomalies around Antarctica over a highly (negative) correlation. Measurements of OBP support the model results. OBP in the south of Drake Passage were found to be negatively correlated to the ACC transport derived from an ocean model (Hughes et al., 2003).

FESOM simulations yield similar results. We obtained spatial patterns of coherence between OBP and Drake Passage transport. As SAM is connected to the volume transport in Drake Passage in FESOM simulations, we find the same patterns when correlating SAM and OBP (Fig. 5). The patterns follow *f/H* contours and show high negative correlation around Antarctica.

These findings are not confined to model simulations only. The connection between SAM and OBP can also be detected in GRACE solutions (Fig. 6). Plotting

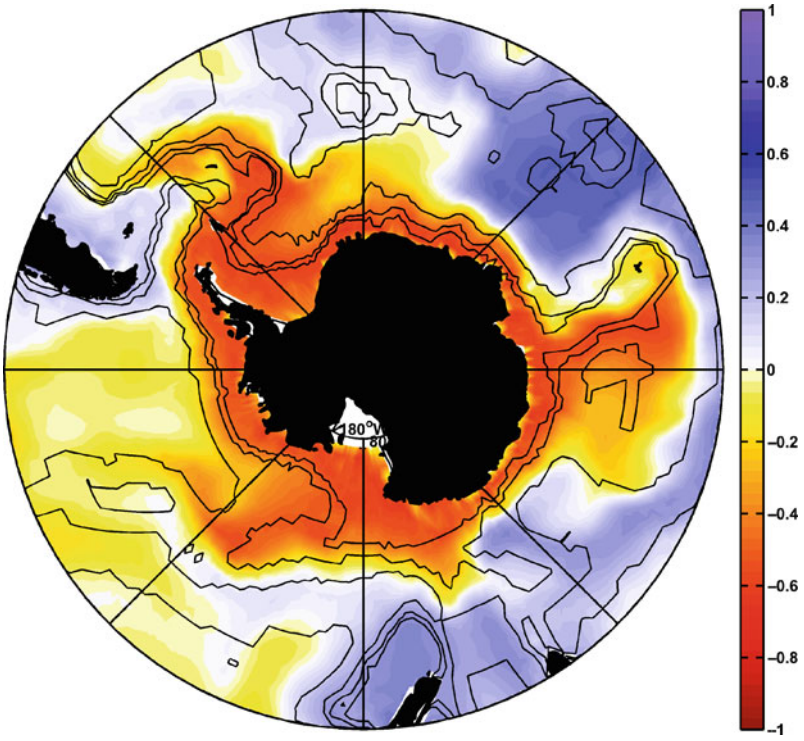

Fig. 5 *Color* indicates correlation between the SAM index and FESOM OBP. Isolines denote *f/H* contours

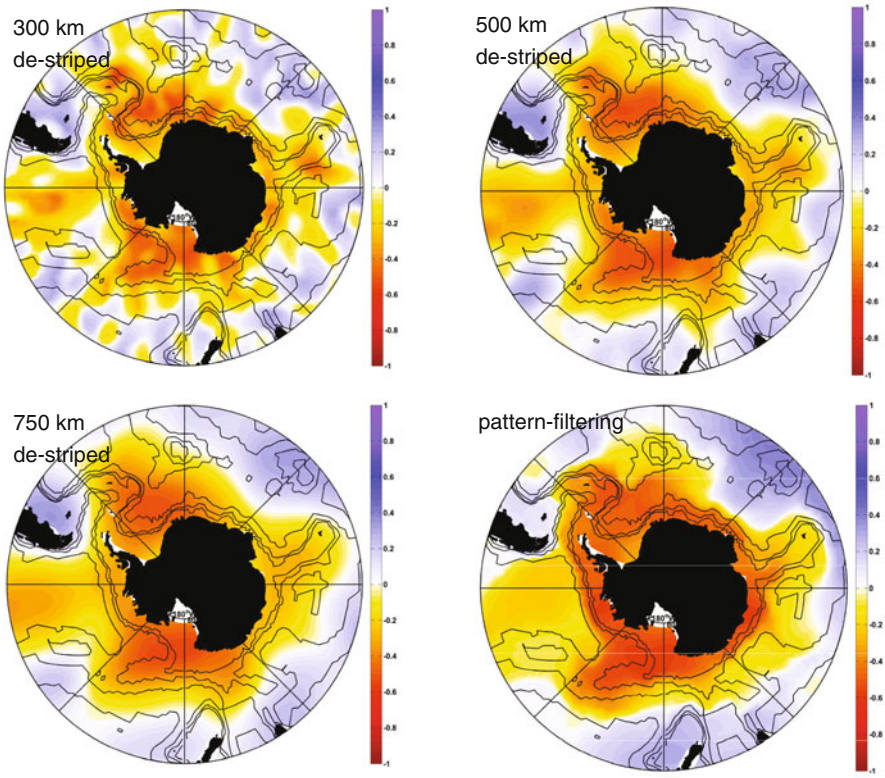

Fig. 6 Correlation between the SAM index and GRACE-derived OBP in *color*. Isolines denote *f*/*H* contours

f/*H* contours on the patterns of correlation between SAM and OBP derived from the three de-striped and the pattern-filtered solutions shows that we can find the same *f*/*H*-related patterns in GRACE retrievals as well.

Apparently, the 300 km de-striped solution is still influenced by the aliasing effects in the GRACE data. The correlation between the 300 km solution and SAM (Fig. 6, top left panel) shows circle-like small-scale patterns of switching high and low correlation. However, the mode of variability following the *f*/*H* contours as seen in FESOM can be clearly identified.

In the 500 km de-striped solution (Fig. 6, top right panel) the noise is highly reduced and the spatial shape of the correlation with SAM is more pronounced. A higher smoothing radius as seen in the 750 km de-striped solution (Fig. 6, bottom left panel) causes a weakening in the relationship between the SAM/GRACE-OBP correlation and the *f*/*H* contours.

Using information on the circulation by applying the pattern filter to the 300 km de-striped GRACE solution (Fig. 6, bottom right panel) reduces striping artefacts and additionally induces a more spatially refined SAM/GRACE-relation.

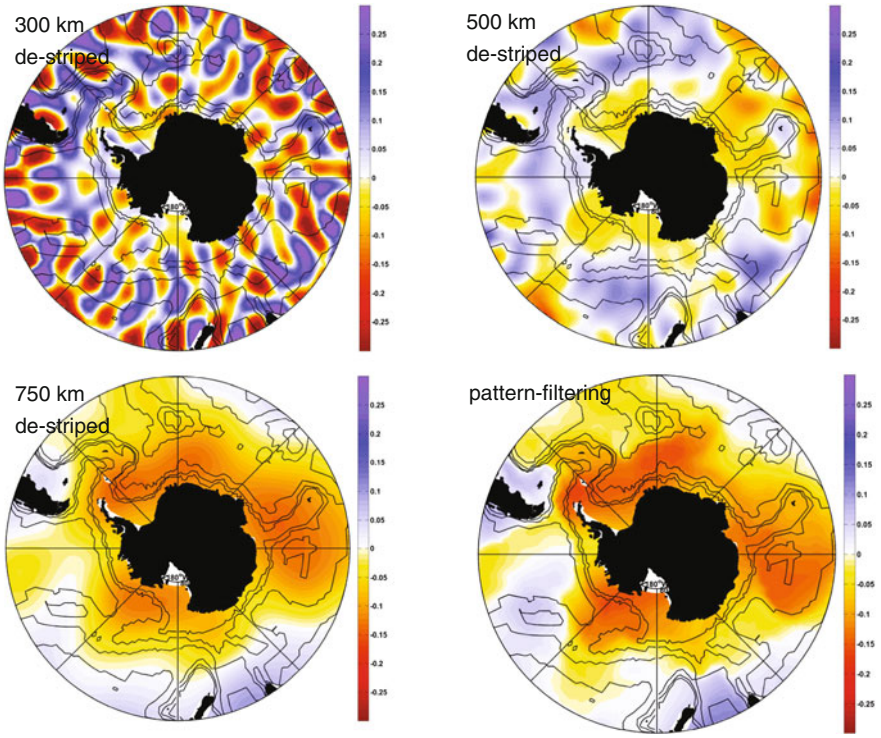

Fig. 7 First EOF of GRACE-derived OBP anomalies. Isolines denote *f*/*H* contours

An EOF analysis indicates that GRACE OBP anomalies from the 300 and 500 km de-striped solutions are dominated by striping artefacts (Fig. 7). The first EOF of the 300 km de-striped solution, showing small circle-like spatial patterns, explains 62% of the variance. In the 500 km de-striped solution those patterns can still be identified to be dominant, but the explained variance is reduced to 23%. The 750 km de-striped and the pattern-filtered solution show a mode that encircles Antarctica and can be related to *f*/*H* contours. The explained variance is 22% in case of the 750 km and 25% for the pattern-filtered solution. Comparing this mode to the correlation found with SAM (Fig. 6) which features similar spatial patterns indicates that a considerable part of the GRACE-OBP signals are connected to the atmospheric variability described by SAM.

5 Discussion

Simulations with FESOM indicate that a part of the ACC transport variability is connected to OBP variability averaged along the southern ACC boundary. A high correlation of 0.76 was found i.e. approximately 57% of the variance are explained by the averaged OBP anomalies.

Estimates of transport variability derived from GRACE OBP show higher amplitudes but similar phase compared to model results. The current de-striped pattern filtered solutions show a variations on semi-annual and annual scales of 6–9 Sv whereas the model indicates fluctuations of about 2–3 Sv.

We found a relation between the OBP variability measured by GRACE and the SAM index. Their coherence pattern reflects a southern mode of variability around the Antarctic continent and follows *f*/*H* contours. Model simulations with FESOM indicate a similar spatial distribution of coherence. These findings agree with studies by Hughes et al. (1999), who found the wind-related fluctuations of the flow following *f*/*H* contours encircling Antarctica.

This connection can be detected in all de-striped and in the pattern-filtered GRACE solutions. It is thus not created by the pattern-filtering procedure, which obviously introduces information on *f*/*H* contours by considering simulated ocean circulation, but also appears in completely independent datasets. Signals related to SAM are found to be highest in the 300 km filtered solution. However, aliasing artefacts dominate the spatial distribution and weaken the relation of the patterns to *f*/*H* contours. In the 750 km filtered solution, striping is no longer visible, but the connection of the SAM/GRACE-OBP relation to the geostrophic contours weakens due to the larger smoothing radius. The 500 km de-striped and the pattern-filtered solution show the clearest signal of the southern mode of oceanic variability related to atmospheric fluctuations. Recent studies mainly based on model simulations draw the conclusion that the variability as seen in SAM explains a large part of the volume transport through Drake Passage. Existing observation-based studies cannot confirm a strong correlation between this large-scale atmospheric and the oceanic variability. A reason behind this might be that in-situ measurements are highly influenced by local effects. Small scale features in the wind field most likely affect the circulation locally. Therefore, model simulations forced by a coarse resolution wind field might indicate a stronger response of the transport to the variability seen in SAM.

A relation between SAM and GRACE OBP along the southern boundary of the ACC was found. This indicates a connection between the transport variability which can be explained by OBP and the variability captured by SAM. However, the correlation weakens on longer time scales due to higher influence of baroclinicity on those low frequencies.

In general, we found that GRACE-derived ACC transport fluctuations agree with the simulated transport showing correlations around 0.7. Although the atmospheric variability as induced by SAM is related to simulated and GRACE-derived fluctuations, only weak correlation was found. Thus, most likely SAM cannot be used as a proxy for the ACC transport variability. However, the high correlation between model transport and GRACE-derived OBP indicates that GRACE is able to reproduce a large part of the ACC variability.

Acknowledgments For the filtering (de-striping) of the three GRACE RL04 products the data were processed by D. P. Chambers, supported by the NASA Earth Science REASoN GRACE Project, and are available at http://grace.jpl.nasa.gov

References

Böning C, Timmermann R, Macrander A, Schröter J (2008) A pattern-filtering method for the determination of ocean bottom pressure anomalies from GRACE solutions. Geophys. Res. Lett. 35, L18611, doi: 10.1029/2008GL034974.

Chambers DP (2006) Evaluation of new GRACE time-variable gravity data over the ocean. Geophys. Res. Lett. 33(17), LI7603.

Cunningham SA, Alderson SG, King BA, Brandon MA (2003) Transport and variability of the Antarctic Circumpolar Current in Drake Passage. J. Geophys. Res. 108(C5), 8084, doi: 10.1029/2001JC001147.

Cunningham S, Pavic M (2007) Surface geostrophic currents across the Antarctic Circumpolar Current in Drake Passage from 1992 to 2004. Prog. Oceanogr. 73, 296–310, doi: 10.1016/j.pocean.2006.07.010.

Greatbatch R (1994) A note on the representation of steric sea level in models that conserve volume rather than mass. J. Geophys. Res. 99, 767–771.

Hughes C, Meredith MP, Heywood K (1999) Wind-driven transport fluctuations through Drake Passage: A Southern Mode. J. Phys. Oceanogr. 29, 1971–1992.

Hughes CW, Woodworth PL, Meredith MP, Stepanov V, Whitworth T, Pyne AR (2003) Coherence of Antarctic sea levels, Southern Hemisphere Annular Mode, and flow through Drake Passage. Geophys. Res. Lett. 30(9), 1464, doi: 10.1029/2003GL017240.

Lefebvre W, Goosse H, Timmermann R, Fichefet T (2004) Influence of the Southern Annular Mode on the sea ice – Ocean system. J. Geophys. Res. 109, C09005.

Lettmann K, Olbers D (2005) Investigation of ACC transport and variability through Drake Passage using the simple ocean model BARBI. CLIVAR Exch. 10(4), 30–32.

Marshall GJ (2003) Trends in the Southern Annular Mode from observations and reanalyses. J. Clim. 16, 4134–4143.

Meredith MP, Woodworth PL, Hughes CW, Stepanov V (2004) Changes in the ocean transport through Drake Passage during the 1980s and 1990s, forced by changes in the Southern Annular Mode. Geophys. Res. Lett. 31(21), L21305, doi: 10.1029/2004GL021169.

Olbers D, Borowski D, Völker C, Wolff J-O (2004) The dynamical balance, transport and circulation of the Antarctic Circumpolar Current. Antarct. Sci. 16(4), 439–470, doi: 10.1017/S0954102004002251.

Orsi AH, Withworth T, Nowlin WD (1995) On the meridional extent and fronts of the Antarctic Circumpolar Current. Deep Sea Res. I 42(5), 641–673.

Swenson S, Wahr J (2006) Post-processing removal of correlated errors in GRACE data. Geophys. Res. Lett. 33, L08402, doi: 10.1029/2005GL025285.

Thompson DWJ, Solomon S (2002) Interpretation of recent Southern Hemisphere climate change. Science 296, 895–899.

Timmermann R, Danilov S, Schröter J, Böning C, Sidorenko D, Rollenhagen K (2009) Ocean circulation and sea ice distribution in a finite element global sea ice-ocean model. Ocean Modelling 27(3–4), 114–129, ISSN 1463-5003, doi: 10.1016/j.ocemod.2008.10.009.

Walter C (2007) Simulations of hydrological mass variations and their influence on the Earth's rotation, http://nbn-resolving.de/urn:nbn:de:bsz:14-ds-1205946097808-36130

Zlotnicki V, Wahr J, Fukumori I, Song YT (2006) Antarctic Circumpolar Current transport variability during 2003–05 from GRACE. J. Phys. Oceanogr. 37, 230–244, doi: 10.1175/JPO3009.1.

Part III
GOCE

Gravity and Steady-State Ocean Circulation Explorer GOCE

Reiner Rummel and Thomas Gruber

1 Introduction

"The intergovernmental Panel on Climate Change (IPCC) was established to provide the decision-makers and others interested in climate change with an objective source of information about climate change" (first sentence of "IPCC mandate", http://www.ipcc.ch/about/index.htm). Its first report was published in 1990. The fourth assessment report published in 2007, points out a rather rapid climate change. It also claims that to a large extent this change may be anthropogenic. During its preparation it has been debated in several publications that the key to more certainty in our understanding of the complexity of the Earth as a system is more and better data (Hogan, 2005 and the references therein). For sure, satellite data are playing a prominent role in removing this data deficiency. They are global, repetitive and uniform, near-simultaneous and near-real-time. In the mid-nineties the importance of a consistent observing and modelling strategy of the Earth as a system has been formulated by the European Space Agency (ESA). The Agency's "Living Planet" Programme for Earth Observation (ESA, 1999a) is aiming at an improved understanding of the various components of the Earth System as well as their interactions. The programme has been revisited and new challenges been formulated in 2006, resulting in the new document "The Changing Earth" (ESA, 2006).

The Gravity and steady-state Ocean Circulation Explorer (GOCE) is the first core mission of this ESA programme. It has been selected in 1999 (ESA, 1999b) and developed since then. Its launch has been delayed several times, it took finally place on March 17, 2009. In the near future also two other missions of the "Living Planet" programme will go into orbit: the ice altimetry satellite mission CryoSat-2 and the soil-moisture and ocean salinity mission SMOS. The mission objective of GOCE is the determination of the Earth's gravity field and geoid with high accuracy and maximum spatial resolution. More specifically geoid heights will be determined

R. Rummel (✉)
Institute of Astronomical and Physical Geodesy, Technische Universiät München, Munich, Germany
e-mail: rummel@bv.tum.de

F. Flechtner et al. (eds.), *System Earth via Geodetic-Geophysical Space Techniques*, Advanced Technologies in Earth Sciences, DOI 10.1007/978-3-642-10228-8_16,

with cm-accuracy and gravity variations with 1 part-per-million of "g", in both cases with a spatial resolution of about 100 km on the Earth's surface. It should be noted that these mission objectives are complementary to those of the GRACE mission. The primary goal of GRACE is the measurement of the temporal variations of the Earth's gravity field, caused by the transport of masses and their redistribution in the Earth system. While the goal of GOCE is maximum spatial resolution, the GRACE mission aims at maximum precision at some expense in terms of highest spatial resolution. Both types of gravity field information are complementary and important for Earth system science. The GRACE time series shows the path and size of mass movements, related to processes such as melting ice shields, the global seasonal water cycle, sea level variations, post glacial mass re-adjustments and others. For the first time it is now possible to quantify – so-to-say to weigh – global mass re-distribution. GOCE, on the other hand, will give one global and detailed map of spatial gravity and geoid variations. The geoid can be viewed as one global, Earth encompassing level. It corresponds to the world oceans at complete rest, their surface purely determined by gravity, without any exterior forces from winds, pressure variations or tides. The geoid serves as reference for studies of dynamic ocean topography (DOT). DOT is the small deviation of the global mean ocean surface from the geoid. It is derived from comparing the geoid with the mean ocean surface as measured by radar ocean altimetry. Altimetric observations of the ocean surface are available since more than twenty years and will continue in the future. Assuming geostrophic balance, DOT can be translated into global ocean surface circulation. The effect of climate change on ocean circulation patterns and on mass and heat transport will show up as changes in ocean circulation. The temporal gravity changes as measured by GRACE relate to variations of ocean bottom pressure and add therefore information about ocean circulation at depth. Again one can see the complementarity of the two missions. The geoid as derived from GOCE will also serve as a uniform global height reference, not only for DOT estimation but as well for sea level research and civil engineering. Tide gauges will become referenced to one level surface and their sea level records will become comparable on a global scale. Gravity anomalies, the second of GOCE's mission objectives, provide a look into the Earth's interior, albeit not a unique one. One is faced with an inverse problem. Gravity anomalies represent a detailed picture of the total of the gravitational attraction of all masses. It is difficult to distinguish individual effects. Nevertheless gravity anomalies contain a wealth of information about the composition of the Earth's interior and its dynamics. Gravity anomalies are a measure of mass imbalance; they represent therefore a "frozen" picture of the geodynamics of the past hundred millions of years, in particular of the continental and ocean lithosphere and the Earth's upper mantle. There is no direct way to look into the interior. Inversion requires joint modelling based on all available information such as seismic tomographic data, magnetic data, topographic and crustal models, plate tectonic models and laboratory results about structure and composition.

Another more practical GOCE application will be the ability to convert any GPS (ellipsoidal) height into a height above sea level. All national mapping agencies will take advantage of this possibility and many secondary benefits will result from it.

GOCE will also contribute to a better reconstruction of ocean bathymetry, in ocean areas where no direct soundings are available.

GOCE is a cornerstone of the Global Geodetic Observing System (GGOS), a flagship project of the International Association of Geodesy (IAG) – compare also this volume. A central objective of GGOS is to provide "metric" to Earth system measurements. This requires the unification of all geodetic space techniques in one Earth-fixed coordinate system with a precision of one-part-per-billion (1 ppb). While techniques such as geodetic VLBI, satellite laser ranging and GPS will help to tie the Earth's geometric shape, as well as all changes of shape, to this coordinate frame, GOCE will help to establish a corresponding height reference. These are heights above sea level, or more accurately, above the geoid, i.e. physical heights as determined by the geometry of the Earth's gravity field. Since Earth processes in the atmosphere, hydrosphere and cryosphere take place under the action of gravity, geoid and plumb lines are the natural geometric reference for monitoring these processes.

2 The GOCE Mission

The GOCE satellite mission is unique in several ways. In the following we will summarize its main characteristics. The mission consists of two complementary gravity sensing systems. The large scale spatial variations of the Earth's gravitational field will be derived from its orbit, while the short scales are measured by a so-called gravitational gradiometer. Even though satellite gravitational gradiometry has been proposed already in the late fifties (Carroll and Savet, 1959), the GOCE gradiometer will be the first instrument of its kind to be put into orbit. The principles of satellite gradiometry are described in Rummel (1986), compare also Colombo (1989) and Rummel (1997). The purpose of gravitational gradiometry is the measurement of the second derivatives of the gravitational potential. In total one could measure nine second-derivatives in the orthogonal coordinate system of the instrument. Due to symmetry only six of them are independent; because of LAPLACE condition holding for the diagonal terms, only five components remain independent. The GOCE gradiometer is a three axis instrument and its measurements are based on the principle of differential accelerometry. It consists of three pairs of orthogonally mounted 3-axis accelerometers (see Fig. 1). The gradiometer baseline of each axis is 50 cm. The precision of each accelerometer is 10^{-12} m/s^2/$\sqrt{\text{Hz}}$ along two axes, the third axis has much lesser sensitivity because of required pre-calibration on ground. From the measured gravitational acceleration differences the three main diagonal terms and one off-diagonal term of the gravitational tensor can be determined with high precision. These are the three diagonal components {xx}, {yy}, {zz} as well as the off-diagonal component {xz}, while the components {xy} and {yz} are less accurate. Thereby the coordinate directions of the instrument are in flight direction (x), cross direction (y) and in radial direction (z). The extremely high gradiometric performance of the instrument is confined to the so-called measurement bandwidth (MBW).

Fig. 1 GOCE gravitational gradiometer

The gradiometric principle based on differential accelerometry does only hold if all six accelerometers (three pairs) are perfect twins and if all accelerometer test masses are perfectly aligned. In real world small deviations from such an idealisation are unavoidable. Thus, calibration of the gradiometer is of utmost importance. Calibration is essentially the process of determination of the differential parameters of an affine transformation between an ideal and the actual set of accelerometer measurements. The unknown calibration parameters are therefore differential scale factors, rotations and mis-alignments. They are derived in orbit by randomly shaking the satellite by means of a set of cold gas thrusters and comparing the actual output with the theoretically correct one. Before calibration the non-linearities of each accelerometer are removed electronically, i.e. the capacitive electronic feedback system of proof mass and electrodes is brought into its linear range.

The gradiometric signal is superimposed by the effects of angular velocity and angular acceleration of the satellite in space. Knowledge of the latter is required for angular control and for the removal of the angular effects from the gradiometer data. The separation of angular acceleration from the gradiometric signal is possible from a specific combination of the measured nine acceleration differences. The angular rates (in the MBW) from the gradiometric data in combination with the angular rates as derived from the star sensor readings are used for attitude control of the spacecraft. The satellite has to be guided well controlled and smoothly around the Earth. While being Earth pointing, it performs one full rotation per orbit revolution. Angular control is attained via magnetic torquers, i.e. using the Earth's magnetic field lines as orientation. This approach leaves, however, uncontrolled one directional degree of freedom at any moment. In order to prevent non-gravitational forces, in particular atmospheric drag, that act on the spacecraft to "sneak" into the measured differential accelerations as secondary effect, the satellite is kept "drag-free" in along-track direction by means of a pair of ion thrusters. The necessary control signal is derived from the available "common-mode" accelerations (sum instead of differences of the measured accelerations) along the three orthogonal axes of the accelerometer pairs of the gradiometer. Some residual gradiometric and angular contribution will also add to the common mode acceleration. This is a result of the imperfect symmetry of the gradiometer relative to the spacecraft centre of mass and has to be modelled.

The second gravity sensor device is a newly developed European GPS receiver. From its measurements the orbit trajectory is computed to within a few centimetres, either purely geometrically, a so-called kinematic orbit, or by the method of reduced dynamic orbit determination. As the spacecraft is kept in an almost drag-free mode (at least in along-track direction) the orbit motion can be regarded as purely gravitational. It complements the gradiometric gravity field determination by covering the long wavelength part of the gravitational signal.

The orbit altitude is extremely low, only about 255 km. This is essential for a high gravitational sensitivity. No scientific satellite has been flown at such low altitude so far. Its altitude is maintained through the drag-free control and additional orbit manoeuvres, which are carried out at regular intervals. Again, this very low altitude results in high demands on drag-free and attitude control. Finally, any time varying gravity signal of the spacecraft itself must be excluded. This results in extreme tight requirements on metrical stiffness and thermal control.

In summary, GOCE is a technologically very complex and innovative mission. The gravitational field sensor system consists of a gravitational gradiometer and GPS receiver as core instruments. Orientation in inertial space is derived from star sensors. Common mode and differential mode accelerations from the gradiometer and orbit positions from GPS are used together with ion thrusters for drag-free control and together with magneto-torquers for angular control. The satellite and its instruments are shown in Fig. 2. The system elements are summarized in Table 1.

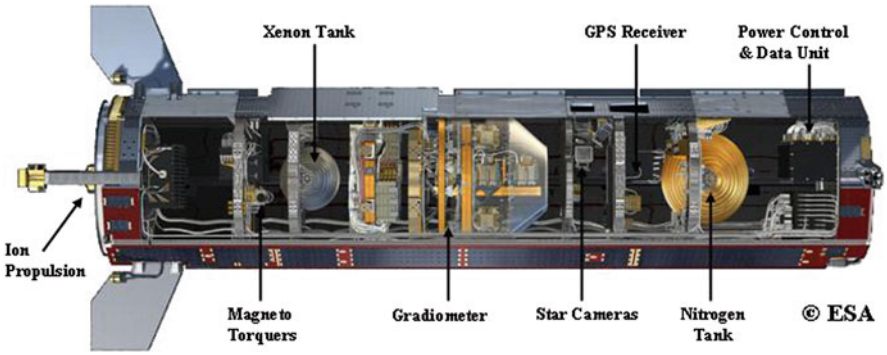

Fig. 2 GOCE satellite and instruments

Table 1 Sensor elements and type of measurement delivered by them (approximate orientation of the instrument triad: x = along track, y = out-of-orbit-plane, z = radial)

Sensor	Measurements
3-axis gravity gradiometer	Gravity gradients Γ_{xx}, Γ_{yy}, Γ_{zz}, Γ_{xz} in instrument system and in MBW (measurement bandwidth) Angular accelerations (highly accurate around y-axis, less accurate around x, z axes) Common mode accelerations
Star sensors	High rate and high precision inertial orientation
GPS receiver	Orbit trajectory with cm-precision
Drag control with 2 ion thrusters	Based on common mode accelerations from gradiometer and GPS orbit
Angular control with magnetic torquers	Based on angular rates from star sensors and gradiometer
Orbit altitude maintenance	Based on GPS orbit
Internal calibration (and quadratic factors removal) of gradiometer	Calibration signal from random shaking by cold gas thrusters (and electronic proof mass shaking)

3 GOCE in the Context of the Geotechnology-Programme

GOCE is the first mission of its kind. As already described above it consists of two gravitational sensing systems. The first one is the orbit itself. It is derived from inter-satellite tracking to the satellites of the Global Positioning System (GPS), the second one is the gravitational gradiometer. From the orbit the long wavelength part of the gravitational field will be recovered, from the gradiometer measurements its short spatial scales. The German science community has been and is heavily involved in the preparation of this mission. The GOCE-GRAND project helped to strengthen this involvement and to make optimal scientific use of the mission. The first phase of the project (2002–2004) was dedicated to the development of a gravity analysis system for GOCE data. It included kinematic orbit computation,

the determination of the long wavelength gravity field from these orbits and from common mode accelerometry based on the so-called energy conservation method, several gradiometric gravity analysis methods and development of algorithms for data reduction (temporal effects) and for external calibration and internal validation. The results are published in Flury et al. (2006). GOCE-GRAND II, which will be summarized here, focuses on refinement and extension of the developed algorithms with the objective to adapt these algorithms to the final characteristics of the sensor system as it has now been brought into orbit. This implies that all design changes are taken into account, realistic stochastic models are developed for all sensor components and the analysis algorithms are capable to cope with a large number of measurements and unknown parameters. In addition GOCE-GRAND II addresses questions concerning the combined GRACE/GOCE data analysis and validation of the GOCE results by means of methods such as GPS-levelling, astronomical levelling and ocean dynamic topography.

More specifically GOCE GRAND-II aims at the accurate high resolution gravity modelling from a combined analysis of gravitational gradiometry measurements and high-low GOCE to GPS tracking taking into account the actual GOCE sensor configuration, orbit characteristics and mission profile. It also contains the combination of GOCE, CHAMP and GRACE data as well as regional terrestrial data. The objective is to attain best possible global and regionally refined gravity and geoid products. Finally, it includes analyses of concepts of a comprehensive external calibration, quality assessment and validation based on independent data. This is to be achieved before the background of the novelty of the sensor system and spacecraft characteristics as well as the expected high quality of the GOCE gravity and geoid products. The project leads to fully operational processing modules that will be applied to actual GOCE mission data. GOCE GRAND II relies thereby on the algorithms and findings of GOCE GRAND I.

The sections are divided into three blocks, optimal gravity field modelling from GOCE sensor data, combination of GOCE gravity with complementary data sets and satellite gravity missions, and calibration and validation of the gravity models using independent data sets.

There are several factors that contribute to an optimal gravity field modelling based on GOCE:

Adequate exploitation of the high resolution gravity sensor system requires a very large and complex system of equations to be solved; this will be discussed by Brockmann et al. (2009, chapter “GOCE Data Analysis: From Calibrated Measurements to the Global Earth Gravity Field”, this book).

The gravity gradiometer on-board of GOCE has a limited measurement bandwidth. Thus, at long wavelengths the gravity gradiometer data has to be complemented by high-low GPS to GOCE tracking. This, in turn requires very precise orbit determination, high quality gravity reconstruction from these orbits and an optimal mechanism of data combination of satellite-to-satellite tracking with gradiometry taking into account the characteristic stochastic models of the sensors; a possible strategy is discussed in Brockmann et al. (2009, chapter “GOCE Data Analysis: From Calibrated Measurements to the Global Earth Gravity Field”, this book).

The GOCE sensor system had to be modified. The originally planned field emission electric propulsion system had to be replaced by angular control by magneto-torquing. This change has severe implications on the measurement model, on the gravity field recovery procedure and on the stochastic model of the gradiometer components. The results of these modifications are also discussed by Brockmann et al. (2009, chapter "GOCE Data Analysis: From Calibrated Measurements to the Global Earth Gravity Field", this book), too.

It is expected that global gravity representation e.g. in terms of a spherical harmonic series does not fully exploit the information content in certain regions with high gravity variations. As shown by Eicker et al. (2009, chapter "Regionally Refined Gravity Field Models from In-Situ Satellite Data", this book), regional adaptive methods will lead to local focussing in these areas.

GOCE will have a sun-synchronous orbit. As a result the polar caps with an opening circle of 6.5° will not be covered with data. Adequate analysis strategies and complementary polar gravity data are needed to cope with this problem. The current state-of-the-art of this is treated by Baur et al. (2009, chapter "Spectral Approaches to Solving the Polar Gap Problem", this book).

The GOCE and GRACE global gravity field models and terrestrial data sets complement each other in various ways. GOCE models will contribute to the highly accurate medium and short wavelength gravity field components up to degree and order 200 and higher in terms of spherical harmonics, while GRACE is able to provide the long wavelength part and the temporal variations of Earth's gravity potential. Global and regional terrestrial data sets add shorter wavelength field structures (above degree and order 200). Hence, global and local combination solutions of GOCE, GRACE and terrestrial data have the potential to provide the complete geoid spectrum covering all wavelengths from very long to very short with an accuracy of about 1–3 cm.

For global solutions, several terrestrial and altimetric data sets are collected and unified in one homogenous data base. These data will be combined on the basis of rigorous normal equations, with all available GOCE and GRACE data, in particular GOCE satellite gravity gradiometer data, using the classical direct combination method, and block diagonal techniques only for the short wavelength part. The resulting high resolution gravity field model, complete up to degree and order 360, will serve as basis for local refinements. Strategies for global combination solutions are shown by Stubenvoll et al. (2009, chapter "GOCE and Its Use for a High-Resolution Global Gravity Combination Model", this book).

Within a regional validation and combination experiment in Germany, terrestrial gravity and terrain data, GPS/levelling data and deflections of the vertical are employed. Before combination, the terrestrial gravity data are validated by spot-checks with absolute gravity data at selected points. In addition, a transportable zenith camera is used for the observation of deflections of the vertical along two profiles in Germany, one North-South and one East-West with a length of several hundred kilometres each. This allows a cross validation of GPS/levelling and astronomical levelling results. The validated terrestrial data sets can then be combined with GOCE geopotential models using various modelling techniques. Regional combinations applying such data are discussed by Ihde et al. (2009,

chapter "Validation of Satellite Gravity Field Models by Regional Terrestrial Data Sets", this book).

A first quality assessment of GOCE gradiometer measurements can be performed at satellite level by comparing the observed gravity gradients with reference gradients. These reference values are computed from existing geopotential models and from terrestrial gravity data by upward continuation. A near real-time validation by cross-over (XO) analysis is investigated and planned to be applied operationally. In addition, regional gravity data are upward continued to gradients at GOCE altitude, serving as reference gradients for the calibration and validation of the GOCE data. In this context, also the functional model for the external calibration is investigated, and appropriate statistical quality parameters are defined to assess the calibration results. This part is described in Müller et al. (2009, chapter "Quality Evaluation of GOCE Gradients", this book).

The gravity models are validated by means of independent gravity field information, i.e. information not already included in the GOCE gravity field determination. Thus, validation means independent assessment or control of GOCE gravity field models with data and in regions where they can be regarded as superior to GOCE gradiometry. Such independent information is:

- terrestrial point or mean gravity anomalies (based on gravity measurements and levelling),
- ocean point, profile or mean gravity anomalies (based on ship gravimetry or satellite altimetry),
- geoid height differences (derived from GPS and levelling),
- dynamic ocean topography (from ocean modelling or ocean levelling),
- assimilation of GOCE fields in ocean circulation models for estimation of ocean circulation and transports,
- satellite orbits,
- gravity models (from previous missions such as GRACE, CHAMP and others).

A fundamental difficulty of any validation experiment is that GOCE is expected to provide the best possible gravity field model ever. In other words, the GOCE gravity field model is expected to be the best global gravity information in the spectral band up to its maximum degree and order. At most, the independent validation data sets can be expected to be of comparable (or better) quality regionally and/or in certain spectral windows. Employing for validation regional data sets with point or mean values leads to the problem of how to compare their signal content and quality with that of a set of spherical harmonics, representing global but band limited information. In Ihde et al. (2009, chapter "Validation of Satellite Gravity Field Models by Regional Terrestrial Data Sets", this book) a technique is described, which uses wavelets for filtering.

A quite different approach of validation is the analysis of oceanographic information, such as dynamic ocean topography. This idea is elaborated in more detail in Stammer et al. (2009, chapter "Comparison of GRACE and Modelbased Estimates of Bottom Pressure Variations Against Global Bottom Pressure Measurements", this book).

4 Conclusions

After mission completion, GOCE will provide the global geoid with an accuracy of a few cm and gravitational accelerations on the level of 1 part-per-million of "g". This is reached by a space gravitational gradiometer instrument together with a novel GPS receiver, a very low orbit and a drag-free system compensating non-gravitational forces. The determination of the GOCE gravity field model from the instrument-satellite system requires a dedicated processing approach. Within the "Geotechnology" Programme several universities and research institutions in Germany prepared a complete analysis chain from the instrument calibration, via analysis of the gradiometer and supporting data to global gravity field solutions from GOCE and complementary sources, as well as their external validation. The involved groups are well prepared and will apply the developed algorithms and techniques to the real mission data as soon as they will be released.

References

Carroll JJ, Savet PH (1959) Gravity difference detection. Aerosp. Eng. 18, 44–47.

Colombo O (1989) Advanced techniques for high-resolution mapping of the gravitational field. In: Sansò F, Rummel R (eds.), Theory of Satellite Geodesy and Gravity Field Determination, Lecture Notes in Earth Sciences, Vol. 25, Springer, Heidelberg, 335–369.

ESA (1999a) Introducing the "Living Planet" Programme – The ESA Strategy for Earth Observation; ESA SP-1234, ESA Publication Division.

ESA (1999b) Reports for Mission Selection "The Four Candidate Earth Explorer Core Missions" – Gravity Field and Steady-State Ocean Circulation Mission; ESA-SP12333(1), ESA Publication Division.

ESA (2006) The Changing Earth – New Scientific Challenges for ESA's Living Planet Programme; ESA SP-1304, ESA Publication Division.

Flury J, Rummel R, Reigber Ch, Rothacher M, Boedecker G, Schreiber U (eds.) (2006) Observation of the System Earth from Space, Springer-Verlag, New York, ISBN 10: 3-540-29520-9, ISBN 13: 978-3-540-29520-4.

Hogan J (2005) Warming debate highlights poor data. Nature 436, 896, 18 August 2005.

Rummel R (1986) Satellite gradiometry. In: Sünkel H (eds.), Mathematical and Numerical Techniques in Physical Geodesy, Lecture Notes in Earth Sciences, Vol. 7, Springer, Berlin, pp. 317–363, ISBN (Print) 978-3-540-16809-6, doi: 10.1007/BFb0010135.

Rummel R (1997) Spherical spectral properties of the Earth's gravitational potential and its first and second derivatives. In: Sansò F, Rummel R (eds.), Geodetic Boundary Value Problems in View of the One Centimeter Geoid, Lecture Notes in Earth Sciences, Vol. 65, Springer, Berlin, pp. 359–404, ISBN: 3-540-62636-0.

GOCE Data Analysis: From Calibrated Measurements to the Global Earth Gravity Field

Jan Martin Brockmann, Boris Kargoll, Ina Krasbutter, Wolf-Dieter Schuh, and Martin Wermuth

1 Introduction

The goal of the GOCE satellite mission is the modeling of the time-invariant component of the Earth's gravity field to the accuracy of at least 1 mGal for gravity anomalies and 1 cm for the geoid at a spatial resolution of at least 100 km (cf. Drinkwater et al., 2007; ESA, 1999). This model consists of a finite series of globally defined spherical harmonics (cf. ESA, 2006).

From a mathematical viewpoint, the least-squares estimation of the more than 70,000 coefficients of these basis functions from more than one hundred million GPS satellite-to-satellite tracking (SST) and satellite gravity gradiometry (SGG) observations constitutes an extremely high-dimensional, inverse, and ill-conditioned data-fitting problem in terms of a linear Gauss-Markov model. The numerical solution of the combined normal equations resulting from this problem is further complicated by the strong data correlations as well as by the different weighting of the three data types. The rigorous solution of such a large least-squares problem puts strong requirements on computer resources and can at present only be solved by computer clusters (cf. Plank, 2004). Therefore several alternatives have been developed. One alternative is the so-called space-wise approach, which is based on a transformation of the data onto a regular spatial grid leading to a block-diagonal system of normal equations (cf. Miggliacchio et al., 2007). Another alternative is the so-called semi-analytic approach, which uses the assumption of a circular Hill-orbit (see also Sneeuw, 2000). This results in a simplified and very efficient solution, but at the cost of accuracy (errors are about twice as large as for a rigorous solution).

Another alternative, which provides an efficient solution with high accuracy has been implemented at the Department of Theoretical Geodesy at the Institute of Geodesy and Geoinformation (IGG-TG) of the University of Bonn into the operational GOCE data processing software PCGMA, and will be explained in more detail in the following. The key feature of PCGMA (Preconditioned Conjugate

W.-D. Schuh (✉)
Institute of Geodesy and Geoinformation, University of Bonn, Bonn, Germany
e-mail: schuh@uni-bonn.de

F. Flechtner et al. (eds.), *System Earth via Geodetic-Geophysical Space Techniques*, Advanced Technologies in Earth Sciences, DOI 10.1007/978-3-642-10228-8_17,

Gradient Multiple Adjustment) consists in the iterative solution of the normal equations via the preconditioned conjugate gradient method and the in-situ processing of the observation equations (Schuh, 1996). These topics will be explained in more detail in Sect. 2. The advantages that result from this combination are twofold: firstly, the in-situ analysis allows for a direct access to and modelling of the correlations present in the SGG data; secondly, the iterative procedure allows for the quick computation of a reasonably accurate approximative solution, which requires only a few iteration steps, but also for a nearly exact solution with a sufficient number of iteration steps.

As stated earlier, two types of complications in GOCE data analysis result from the fact that both the colored measurement noise of the GOCE gradiometer and the distinct weighting of the different groups of GOCE data (SGG, SST, and regularizing prior information) must be accurately estimated and taken into account if the stochastic model is to be consistent. The iterative parameter estimation of spherical harmonic coefficients using CG must therefore comprise additional steps for adapting the variance component and the SGG noise model. To handle the huge amount of data, this procedure must be implemented on a massive parallel computer cluster. This approach will be explained in Sect. 3.

2 Processing Strategy for the Different Data Types

The concept of the GOCE mission is based upon the fusion of different sensors. For the global gravity field determination especially the instruments observing functionals of the gravity field are important. Firstly, the lower frequency terms can be determined accurately from the GPS observations, tracking the satellite in a precise way via SST in high-low mode. On the other hand, the gradiometer observations (SGG) are sensitive to the higher frequencies. The third observation group (REG) consists of regularizing prior information according to the degree variances of state-of-the-art gravity field models or Kaula's rule of thumb, leading to a (weak) smoothness condition regarding the parameters. The sensitivity of these observation groups is shown in Fig. 1 in terms of degree variances for a model in a closed loop simulation. The purpose of the following subsections is to demonstrate how these three data types are preprocessed in the light of a subsequent joint least-squares adjustment in terms of a linear Gauss-Markov model.

2.1 Processing of the SST Data

The main observable of hl-SST (high-low satellite-to-satellite tracking) is the GPS tracking of the low orbiting GOCE satellite, which is used to determine the satellite orbit. As there is no linear relation of the orbit to the spherical harmonic gravity field coefficients the observation equations must be linearized. Several approaches for this linearization have been developed. The one discussed here – the so-called Energy-Balance approach (cf. Reigber, 1969) – has been developed almost 40 years

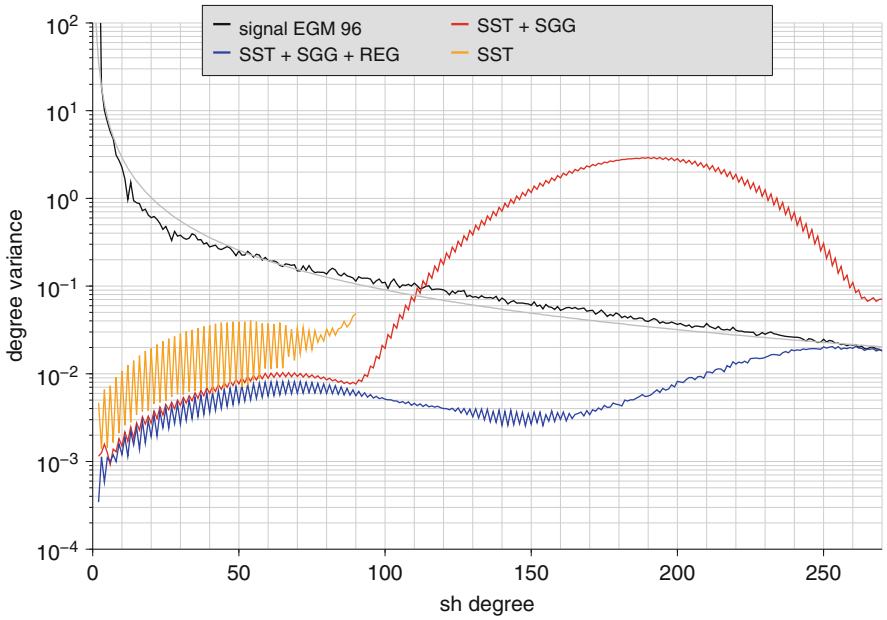

Fig. 1 Degree variances for different models, SST only model, SST combined with SGG, and regularized solution, i.e. SST and SGG combined with REG group

ago, but became only feasible with the continuous tracking of an on-board GPS receiver on the CHAMP satellite (Gerlach et al., 2003).

The approach is based on the law of energy conservation, which states that in a conservative force field, the sum of potential and kinetic energy is constant. Written for unit mass (and using the geodetic sign convention for potential) it reads:

$$C = \frac{1}{2}\dot{\mathbf{r}}^2 - V\,, \tag{1}$$

where C is an unknown constant with the physical unit of a potential. This equation relates the gravitational potential V to the satellite orbit or the velocity $\dot{\mathbf{r}}$, respectively. The determination of the satellite orbit positions from GPS observations and the derivation of velocities is an import part of this approach and will be discussed in Sect. 2.1.1. The satellite is subject to non-conservative forces like air-drag, solar radiation pressure or forces from its own propulsion system. These forces are measured by the common mode of the gradiometer and have to be corrected for. This is explained in Sect. 2.1.2.

2.1.1 Kinematic Orbit and Velocity Determination

The state-of-the-art orbit determination method is reduced-dynamic POD (precise orbit determination) (cf. Yunck et al., 1990). It is based on the integration of

accelerations (or more precisely specific forces acting on the satellite) which are computed from physical models (e.g. gravity model, atmospheric drag model, solar radiation pressure model etc.). Various parameters like the initial coefficients or corrections to the employed physical models are estimated in a least-squares adjustment using the GPS-tracking as observations in order to fit the integrated orbit to the observations. In addition the deterministic models are extended by statistical parameters to allow for a better fit. The orbit velocities are a by-product of the orbit integration. The resulting orbits have a high accuracy, are very smooth and are barely affected by short data gaps, as the orbit integration smoothes measurement noise and bridges data gaps. However, the velocities are strongly correlated with the employed models (especially the a priori gravity model), as they are basically obtained by the integration of accelerations determined by these models. It has been shown by Gerlach et al. (2003) that no significant improvement of the a priori gravity model can be achieved by the Energy Balance Approach using reduced dynamic orbits.

In contrast to the model-based methods kinematic POD was developed (Svehla and Rothacher, 2002). It is a geometric technique which is purely based on observations (mainly GPS) and uses no a priori models to describe the motion of the satellite. Thus the orbits are better suited to be used with the Energy Balance Approach. Nevertheless they have some disadvantages: they contain more high frequency errors and more data-gaps than reduced dynamic orbits. As each point is computed independently using only the observations of the given epoch, kinematic POD can not provide velocities. Thus velocities have to be derived by numerical differentiation. Numerical differentiation has the disadvantage that high-frequency measurement errors are amplified. Hence it is important to choose a differentiation method which smoothes high-frequency noise, but preserves as much of the gravity signal as possible (cf. Wermuth, 2008). A common method for numerical differentiation is to use interpolating polynomials and differentiate them analytically. A polynomial of nth degree passes n+1 sample points exactly and uniquely. If the n+1 sample points are chosen symmetrically around the point for which the velocity should be derived, the whole orbit can be differentiated in a moving window process, where the sample point window is shifted over the time series. In this case a polynomial of degree $n = 7$ has been used for numerical differentiation.

2.1.2 Energy Integral

As mentioned above, the law of energy conservation is only valid for conservative force fields in closed mechanical systems. All accelerations, which originate from non-conservative forces, have to be integrated along the satellite orbit and corrected for. One can distinguish the principal sources of non-conservative forces, which have to be treated differently:

1. *Surface forces*: The satellite is subject to external forces like air-drag or solar radiation pressure and internal forces from the satellite's propulsion system. All these forces act on the satellite's surface and are non-conservative, which

means that they either extract energy from the system by friction or add energy by thrust. In order to maintain the energy balance, the accelerations caused by surface forces $\mathbf{a}_s$, which are measured by the onboard accelerometer have to be integrated along the orbit and the resulting quantity has to be used for correction.

2. *Temporal variations and tides*: All mass transports in the Earth system (including oceans and atmosphere) cause temporal variations in the Earth's gravity field. Also the direct attraction from other celestial bodies such as the moon, the sun and other planets is time variable due to the motion of the bodies w.r.t. the Earth. In addition they cause indirect tidal effects due to the deformation of the Earth. These gravitational effects cannot be considered conservative as the integral along the orbit depends on the integration path due to the movement of the gravitating masses and have to be treated as non-conservative surface forces. The accelerations due to temporal variations and tides $\mathbf{a}_t$ can be computed from models and have to be integrated along the orbit as well.
3. *Fictitious forces*: If the computation is done in the Earth-fixed frame, fictitious forces which occur only in the rotating frame have to be considered. The fictitious forces are Coriolis force, Euler force and centrifugal force. As the Coriolis force is perpendicular to the satellite's velocity vector, the integral over the orbit becomes zero. The Euler forces, which originate from the change of the Earth rotation can be neglected as the change of the Earth's rotation can be considered very small within the considered time span. Only the centrifugal accelerations have to be integrated along the orbit. This can be done analytically and leads to the centrifugal potential:

$$V_{\text{cent}} = \frac{1}{2}\left(\boldsymbol{\omega} \times \mathbf{r}\right)^2 \tag{2}$$

If all these forces are considered, Eq. (1) is extended by three terms which account for non-conservative forces:

$$C = \frac{1}{2}\dot{\mathbf{r}}^2 - V - \frac{1}{2}\left(\boldsymbol{\omega} \times \mathbf{r}\right)^2 - \int \mathbf{a}_s \mathrm{d}\mathbf{r} - \int \mathbf{a}_t \mathrm{d}\mathbf{r}. \tag{3}$$

The integration constant C_{cent} from Eq. (3) has been included in the global unknown constant C. The potential V can be split up in the normal potential U, which is the potential of a level ellipsoid (often denoted as Somigliana-Pizzetti field) and the disturbing potential T, which represents the deviations from the reference field. It is numerically more stable to use the disturbing potential T for the gravity field determination instead of the full potential V as the values are several orders of magnitude smaller, therefore (3) is rewritten as:

$$T = \frac{1}{2}\dot{\mathbf{r}}^2 - U - \frac{1}{2}\left(\boldsymbol{\omega} \times \mathbf{r}\right)^2 - \int \mathbf{a}_s \mathrm{d}\mathbf{r} - \int \mathbf{a}_t \mathrm{d}\mathbf{r} - C. \tag{4}$$

It should be noted that all quantities are given in the Earth-fixed frame. The time series of disturbing potential values T then enters the least-squares estimation

of potential coefficients as pseudo-observable, resulting in the normal equations $\mathbf{N}_{SST}\mathbf{x}=\mathbf{n}_{SST}$. The unknown potential constant C can be estimated together with the potential coefficients or can be determined before the adjustment using a priori gravity field information and be reduced from the data. Experience from the CHAMP mission (cf. Wermuth, 2008) shows that after data gaps longer than several minutes the coherence of the disturbing potential time series is lost, and a separate potential constant C has to be estimated for each separate data arc. The size of the various quantities of Eq. (4) is listed in Table 1. If the signals are compared to the residuals after adjustment, one can see that starting from a potential signal of $2.9{\cdot}10^7 \mathrm{m}^2/\mathrm{s}^2$ the gravity signal can be extracted with an accuracy of $\delta \approx 1\ \mathrm{m}^2/\mathrm{s}^2$.

Table 1 Magnitudes of the effects modeled in Eq. (4)

Effect		Signal
Kinetic energy	$1/2\dot{\mathbf{r}}^2$	$2.9{\cdot}10^7 \pm 3{\cdot}10^5\ \mathrm{m}^2/\mathrm{s}^2$
Normal potential	U	$5.8{\cdot}10^7 \pm 3{\cdot}10^5\ \mathrm{m}^2/\mathrm{s}^2$
Unknown constant	C	$2.9{\cdot}10^7\ \mathrm{m}^2/\mathrm{s}^2$
Centrifugal potential	$-1/2(\boldsymbol{\omega}\times\mathbf{r})^2$	$\pm 5{\cdot}10^4\ \mathrm{m}^2/\mathrm{s}^2$
Surface forces	$\int \mathbf{a}_s d\mathbf{r}$	$\pm 1{\cdot}10^5\ \mathrm{m}^2/\mathrm{s}^2$
Temporal variations	$\int \mathbf{a}_t d\mathbf{r}$	$400\ \mathrm{m}^2/\mathrm{s}^2$
Systematic instrument errors	–	$8{,}000\ \mathrm{m}^2/\mathrm{s}^2$
Disturbing potential	T	$1{,}000\ \mathrm{m}^2/\mathrm{s}^2$
Residuals	σ_0	$1.1\ \mathrm{m}^2/\mathrm{s}^2$

2.2 Processing of the SGG Data

The SGG data set consists of the gravity gradients in the six directional components V_{xx}, V_{yy}, V_{zz}, V_{xy}, V_{xz} and V_{yz} describing the whole gravity tensor $\mathbf{T}$ in the gradiometer reference frame (GRF), defined by the mass-center of the six accelerometer test masses, observed throughout time t. Each tensor $\mathbf{T}(\mathbf{r}(t))$ has a designated position $\mathbf{r}(t)$ in the Earth-fixed reference frame (EFRF).

In the framework of the High-level Processing Facility (HPF), which is responsible for the official computation of ESA's GOCE gravity field products, these observed gradients are calibrated (see e.g. Bouman et al., 2008; Visser, 2008) and corrected for physical disturbing effects like ocean tides or temporal gravity signals (see e.g. Bouman et al., 2008; ESA, 2006). After this preprocessing, the observations are assumed to contain only the static part of the gravity field signal and colored measurement noise.

As a consequence of the accelerometer design, the components V_{xy} and V_{yz} are determined with relatively low accuracies and are therefore not used in our approach to SGG data processing. Furthermore, the third off-diagonal component neglected for computational reasons (our simulations have shown that the resulting loss of accuracy is insignificant).

2.2.1 Functional Model for In-Situ SGG Data Processing

As mentioned earlier, the in-situ approach to SGG data processing avoids transformations of the data. Instead, to obtain the observation equations, the functional model has to be expressed in the GRF. To begin with, the equation describing the gravitational potential of the Earth at a position with spherical coordinates (r, ϑ, λ) in the EFRF, in terms of a spherical harmonic series up to d/o $l_{\max}$, reads

$$V(r,\vartheta,\lambda) = \frac{GM}{a}\sum_{l=0}^{l_{\max}}\left(\frac{a}{r}\right)^{l+1}\sum_{m=0}^{l}\left(c_{lm}\cos m\lambda + s_{lm}\sin m\lambda\right)P_l^m(\cos\vartheta), \qquad (5)$$

where l and m denote the spherical harmonic degree and order, c_{lm} and s_{lm} the unknown coefficients of spherical harmonic expansion, a the equatorial radius of the Earth reference ellipsoid, $P_l{}^m(\cos\vartheta)$ the fully normalized associated Legendre functions, and GM the geocentric gravitational constant.

The first and second derivatives of Eq. (5) with respect to r, ϑ, λ in the EFRF can be found e.g. in Hausleitner (1995). These derivatives are transformed into a local north-oriented frame (LNOF), that is, an $\hat{x},\hat{y},\hat{z}$ frame, where $\hat{x}$ is pointing positive to the north, $\hat{y}$ positive east and $\hat{z}$ positive along the radius; the resulting second derivatives $V_{\hat{x}\hat{x}}, V_{\hat{y}\hat{y}}, V_{\hat{z}\hat{z}}, V_{\hat{x}\hat{y}}, V_{\hat{x}\hat{z}}$ and $V_{\hat{y}\hat{z}}$ are found to be certain combinations of the first and second-order derivatives in the EFRF (Hausleitner, 1995), and are thus also linear functions of the spherical harmonic coefficients. The corresponding design matrix $\mathbf{A}_{\text{LNOF},i}$ is composed of 6 rows (one for each of the non-redundant tensor components) and m columns (one for each spherical harmonic coefficient) for each position $\mathbf{r}_i := \mathbf{r}(t_i)$ (with $i \in \{1,\ldots,n\}$).

Finally, the transformation of the design matrix $\mathbf{A}_{\text{LNOF},i}$ into the GRF has to be found. For this purpose, we use the rotation between the LNOF and the GRF via the inertial reference system (IRF) by means of the rotation matrices $\mathbf{R}_{\text{LNOF-GRF}}$ and $\mathbf{R}_{\text{IRF-GRF}}$. The former is derived from GPS tracks and Earth rotation models, the latter from star tracker data (reflecting the orientation of the satellite in space), and can be combined to $\mathbf{R}_{\text{LNOF-GRF}} = \mathbf{R}_{\text{IRF-GRF}}\,\mathbf{R}_{\text{LNOF-IRF}}$. This combined rotation is applied to the tensor $\mathbf{T}_{\text{LNOF},i}$ by pre- and post-multiplication with $\mathbf{R}_{\text{LNOF-GRF}}$, that is, $\mathbf{T}_{\text{GRF},i} = \mathbf{R}_{\text{LNOF-GRF}}\mathbf{T}_{\text{LNOF},i}\mathbf{R}^{T}_{\text{LNOF-GRF}}$. This yields six equations in the non-redundant elements of $\mathbf{T}_{\text{GRF},i}$, each of which is a linear function of the elements of $\mathbf{T}_{\text{LNOF},i}$. These can therefore be written as $\mathbf{t}_{\text{GRF},i} = \mathbf{M}_{\text{LNOF-GRF}}\,\mathbf{t}_{\text{LNOF},i}$ (where $\mathbf{M}_{\text{LNOF-GRF}}$ is a 6×6 matrix, and $\mathbf{t}_{\text{GRF},i}$, $\mathbf{t}_{\text{LNOF},i}$ denote the vectorized six non-redundant tensor elements of $\mathbf{T}_{\text{GRF},i}$ and $\mathbf{T}_{\text{LNOF,i}}$, respectively). Substituting the parametric model for the tensor components $\mathbf{t}_{\text{LNOF},i}$ it is seen that the design matrix in the GRF results from $\mathbf{A}_{\text{LNOF},i}$ by premultiplication of $\mathbf{M}_{\text{LNOF-GRF}}$, that is, $\mathbf{A}_{\text{GRF},i} = \mathbf{M}_{\text{LNOF-GRF}}\,\mathbf{A}_{\text{LNOF},i}$.

As we do not use the mixed tensor components V_{xy}, V_{xz}, V_{yz}, the dimension of $\mathbf{A}_{\text{GRF},i}$ is reduced to $3\times m$ per position by deleting the rows of the unused tensor components. Then we can write the in-situ observation equations with respect to the given data $\mathbf{l}_i$ (the observed gravity gradients V_{xx}, V_{yy}, V_{zz}), unknown residuals $\mathbf{v}_i$ and

point-wise given design matrix $\mathbf{A}_{GRF,i}$ (with $i \in \{1,\ldots,n\}$), as

$$\begin{bmatrix} \mathbf{l}_1 \\ \vdots \\ \mathbf{l}_n \end{bmatrix} + \begin{bmatrix} \mathbf{v}_1 \\ \vdots \\ \mathbf{v}_n \end{bmatrix} = \begin{bmatrix} \mathbf{A}_{GRF,1} \\ \vdots \\ \mathbf{A}_{GRF,n} \end{bmatrix} \mathbf{x},$$

or in short $\mathbf{l}_{SGG} + \mathbf{v}_{SGG} = \mathbf{A}_{SGG}\mathbf{x}$ to express the fact that Eq. (6) represents the full SGG observation equation system.

Since the measurement frequency of GOCE is 1 Hz throughout the two measurement phases, each of which is of approximately 6 months duration, the number of positions is then $n > 30{,}000{,}000$. With three processed tensor components per position and the number of parameters m given by $m = (l_{max}+1)^2 - 4$ (as the coefficients with respect to degrees zero and one are not estimable) the resulting design matrix $\mathbf{A}_{SGG}$ will have approximately 100,000,000 rows and 73,437 columns (assuming a resolution of $l_{max} = 270$), requiring more than 50,000 GB of memory. Thus it becomes evident that a numerically highly efficient adjustment algorithm must be applied which is capable of processing such a huge amount of data.

2.2.2 Stochastic Model of SGG Data

GOCE SGG data are auto-correlated in their three components V_{xx}, V_{yy} and V_{zz} because the gradiometer produces a flat error spectrum only within a certain measurement bandwidth in which the gradiometer measures most accurately (ESA, 1999). The three components are assumed to have negligible cross-correlations in these simulations, which must still be validated for the real data. From simulations we know the typical features and the approximate shape of the normalized spectral density function (i.e. the Fourier transform of the autocorrelation function) of the SGG data (see Fig. 2). Besides its aforementioned flat behaviour within the measurement bandwidth between 0.005 and 0.1 Hz, the error spectrum is mainly characterized by an inverse proportional dependence (approx. f^{-2}) and a large number of sharp peaks on frequencies ranging from 0 to 0.005 Hz.

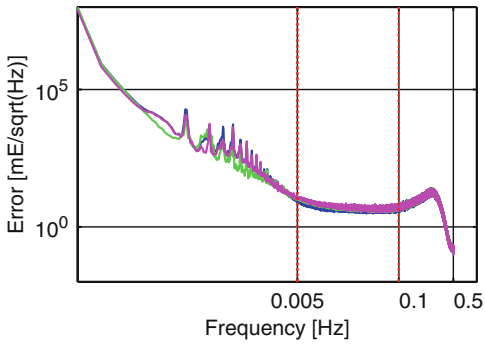

Fig. 2 Simulated error spectra of the three main diagonal tensor components

When estimating the gravity field parameters via a rigorous least-squares adjustment, this correlation pattern would normally have to be taken into account by including the known data covariance matrix into the normal equations. However, due to the huge number of SGG data, this covariance matrix cannot be stored considering a memory requirement of more than 20 PetaByte. An effective solution to this problem consists in a full decorrelation of the SGG data before the evaluation of the normal equations. Such a decorrelation can be performed effectively through an application of digital filters to the SGG observation equations. To achieve a full decorrelation, the autocorrelation pattern must be completely reversed in the frequency domain. For this purpose, we used a sequential cascade of high-pass filters (levelling the strongly correlated and inaccurate low-frequency part of the error spectrum; see Schuh, 2002), notch filters (eliminating the narrow peaks; see e.g. Siemes, 2008; Schuh, 2003), and ARMA filters (flattening the entire residual spectrum; see Schuh, 1996 and e.g. Klees et al., 2003). Although these three filter steps are recursive by design, the combined filter operation acting on the SGG observation equations can be expressed via the linear transformation relations $\mathbf{F}(\mathbf{l}_{SGG} + \mathbf{v}_{SGG}) = \mathbf{F}\mathbf{A}_{SGG}\mathbf{x}$ (cf. Siemes, 2008) resulting in the decorrelated observation equations

$$\bar{\mathbf{l}}_{SGG} + \bar{\mathbf{v}}_{SGG} = \bar{\mathbf{A}}_{SGG}\mathbf{x} \text{ with } \Sigma\left\{\bar{\mathbf{l}}_{SGG}\right\} = \mathbf{I}. \tag{7}$$

In principle, the true autocorrelations are unknown as ground simulations cannot replace GOCE in its operational mode in space. The above mentioned spectral density function is therefore considered as an approximate model to be adapted to the real data in the course of the overall GOCE real data analysis (see Sect. 3).

2.3 Introduction of Regularizing Prior Information

Due to power supply requirements, the GOCE satellite has to take a sun synchronous orbit, with an orbit of an inclination of about 96.5°. This results in data gaps, because the satellite will never cross the polar regions (cf. Fig. 3).

Fig. 3 GOCE orbit on the earth surface after 1 day, 1 week and 1 month mission duration

The combined normal equation system, resulting from Sects. 2.1 to 2.2 with respect to the SST and SGG data (see also Sect. 2.4) is ill-conditioned as a consequence of both the absence of measurements above the polar regions (see Sneeuw and van Gelderen, 1997; Kusche and Ilk, 2000, for this so-called polar gap problem) and the attenuation of the gravity field signal at the satellite's altitude. To stabilize the gravity field solution, some kind of regularization is necessary, usually by adding a third group of normal equations to the SGG and SST normal equations (see e.g. Ditmar et al., 2003; Metzler and Pail, 2005).

The information contained in this additional group can be interpreted as pseudo-observations (i.e. stochastic prior information in a Bayesian sense)

$$c_{lm} = s_{lm} = 0, \qquad \text{for } l \in \{l_{\min} \dots l_{\max}\}, m \in \{0 \dots l\}, \tag{8}$$

reflecting the fact that the coefficients tend to zero with higher degrees (accounted for by smoothness conditions in Hilbert space). The assumed standard deviations

$$\sigma_{c_{lm}} = \sigma_{s_{lm}} = 10^{-5} \frac{1}{l^2}, \qquad \text{for } l \in \{l_{\min} \dots l_{\max}\}, m \in \{0 \dots l\} \tag{9}$$

of the coefficients (8) are specified according to Kaula's rule of thumb (cf. Kaula, 1966) and realistically rescaled by variance component estimation (cf. Sect. 3.2).

In summary, this group of (pseudo-)observation equations serves the purpose of smoothing the parameter estimates and regularizing the effect of the polar gap and the downward continuation; they take the form

$$\mathbf{l}_{\mathrm{REG}} + \mathbf{v}_{\mathrm{REG}} = \mathbf{A}_{\mathrm{REG}}\mathbf{x}, \qquad \Sigma_{\mathbf{REG}} = \mathrm{diag}\left(\sigma^2_{c_{lm}}\right) \tag{10}$$

which results in the normal equations

$$\mathbf{A}^T_{\mathrm{REG}}\Sigma^{-1}_{\mathrm{REG}}\mathbf{A}_{\mathrm{REG}}\mathbf{x} = \mathbf{A}^T_{\mathrm{REG}}\Sigma^{-1}_{\mathrm{REG}}\mathbf{l}_{\mathrm{REG}} \quad \Leftrightarrow \quad \Sigma^{-1}_{\mathrm{REG}}\mathbf{x} = \mathbf{0} \tag{11}$$

due to the fact that, firstly, the design matrix $\mathbf{A}_{\mathrm{REG}}$ is the identity-matrix and secondly, the pseudo-observations are zero. Coefficients for which the pseudo-observations are not introduced (i.e. which are not regularized) are omitted by setting the corresponding weights in $\sum^{-1}_{\mathrm{REG}}$ equal to zero.

2.4 Combination of All Observation Groups

Assuming the three observation types SST, SGG and REG to be uncorrelated, the joint normal equation system is found by adding up the normal equations of each observation group,

$$\left(\omega_{\mathrm{SST}}\mathbf{N}_{\mathrm{SST}} + \omega_{\mathrm{SGG}}\bar{\mathbf{A}}^T_{\mathrm{SGG}}\bar{\mathbf{A}}_{\mathrm{SGG}} + \omega_{\mathrm{REG}}\Sigma^{-1}_{\mathrm{REG}}\right)\mathbf{x} = \omega_{\mathrm{SST}}\mathbf{n}_{\mathrm{SST}} + \omega_{\mathrm{SGG}}\bar{\mathbf{A}}^T_{\mathrm{SGG}}\bar{\mathbf{l}}_{\mathrm{SGG}}, \tag{12}$$

where ω_k, $k \in \{\text{SST,SGG,REG}\}$ denote factors by which the individual normal equations are weighted optimally. Besides the solution of this combined normal equation system for the unknown parameters $\mathbf{x}$, also the unknown weight factors ω_k must be estimated. From a numerical point of view, it is recognized from the normal equation matrices in Eq. (12) that the memory requirements are to a great extent due to the SGG group, whereas they are negligible for the preprocessed SST data (which cover only a small subset of the parameter space and is zero outside) and the (diagonally structured) regularizing prior information (see Table 2).

Table 2 Matrix sizes of the data types for different resolutions (with 1 year of GOCE data)

d/o	m	$\mathbf{N}_{\text{SST}}$ [MB]	Σ_{REG} [MB]	$\mathbf{A}_{\text{SGG}}$ [TB]	Σ_{SGG} [PB]	Remark
90	8,277	523.19	0.06	5.62	20.62	Specified Resolution GOCE (SST only)
180	32,757		0.25	22.24		Resolution of current GRACE models
200	40,397		0.31	27.43		Specified resolution of GOCE (SST+SGG)
270	73,437		0.56	49.86		Expected maximum resolution of GOCE

Thus the computation of the normal equation matrix $\mathbf{N}_{\text{SGG}} = \bar{\mathbf{A}}_{\text{SGG}}^T \bar{\mathbf{A}}_{\text{SGG}}$ is seen to be particularly expensive and is therefore avoided in our algorithm. Consequently, this consideration applies also to the joint normal equation matrix $\mathbf{N} = \omega_{\text{SST}}\mathbf{N}_{\text{SST}} + \omega_{\text{SGG}}\bar{\mathbf{A}}_{\text{SGG}}^T\bar{\mathbf{A}}_{\text{SGG}} + \omega_{\text{REG}}\Sigma_{\text{REG}}^{-1}$. Instead, Eq. (12) is solved by applying a tailored algorithm based on the method of conjugate gradients, which allows data combination based upon both normal and observation equations as described in the following Sect. 3.

3 Solving the Combined Normal Equation System

We will now give an outline of the iterative PCGMA algorithm (see Fig. 4), which avoids the solution of the joint normal equation system in Eq. (12) via computation of the combined normal equation matrix $\mathbf{N}$. The core of PCGMA (Schuh, 1995, 1996) is an advanced version of the conjugate gradient (CG) method (Hestenes and Stiefel, 1952; Schwarz, 1970), which allows for the combination of both normal equations (in our case given by the SST group) and additional observation equations (such as given by the SGG and REG groups). PCGMA has been extended recently by features such as data-adaptive preconditioning (Boxhammer and Schuh, 2006), efficient decorrelation filters (cf. Sect. 2.2.2 and Siemes, 2008), Monte-Carlo-based variance/covariance estimation (Alkhatib and Schuh, 2007; Alkhatib, 2007), and implementation on a massive parallel computer cluster based on a client/master concept (Boxhammer, 2006).

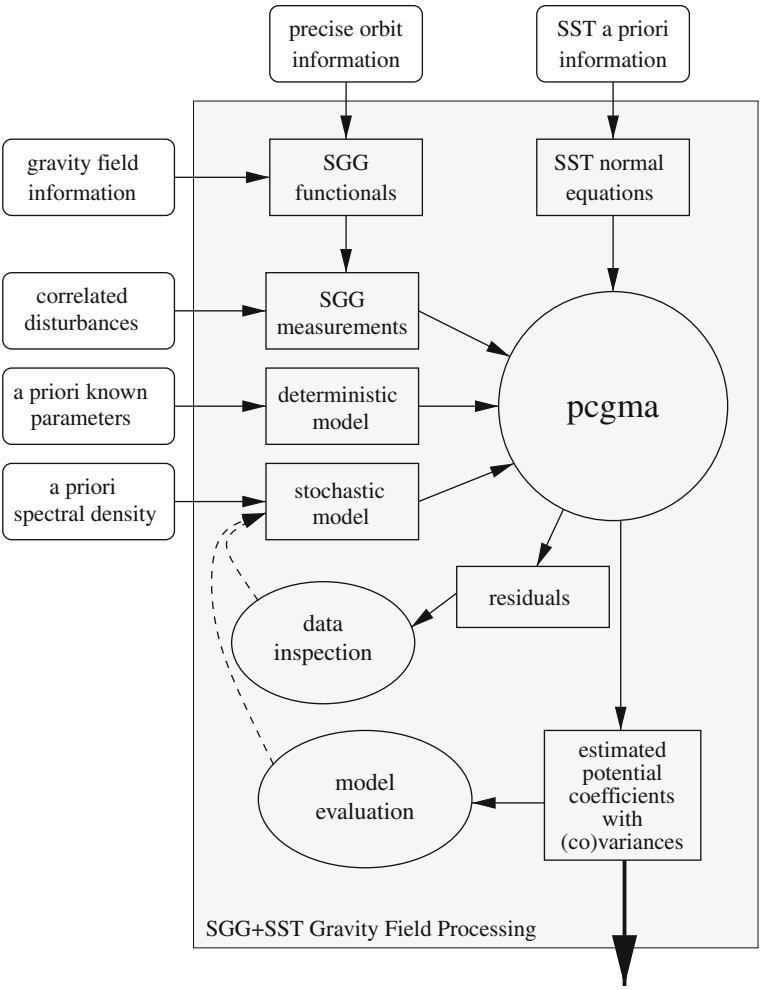

Fig. 4 Processing chain for the in-situ adjustment of GOCE data

3.1 Preconditioned Conjugate Gradients Multiple Adjustment

The basic idea of PCGMA is to combine the CG method based on normal equations (Hestenes and Stiefel, 1952) with the CG method based on observation equations (Schwarz, 1970). Thus, any number of uncorrelated heterogeneous data types can be adjusted jointly. If we tentatively assume that the weight factors ω_k, an initial solution $\mathbf{x}^{(0)}$ and the fully decorrelated SGG observation equations are known, then Eq. (12) can be solved directly by PCGMA. Within each iteration step, the standard CG algorithm for normal equations requires knowledge of the residual-dependent search direction and step length (resulting in a parameter update $\mathbf{\Delta x}$). The residuals

$\mathbf{r} = \mathbf{N}\mathbf{x}$–$\mathbf{n}$ of the combined normal equation system is found after rearranging terms in Eq. (12)

$$\begin{aligned}\mathbf{r} &= \left(\omega_{\mathrm{SST}}\mathbf{N}_{\mathrm{SST}} + \omega_{\mathrm{SGG}}\bar{\mathbf{A}}_{\mathrm{SGG}}^{T}\bar{\mathbf{A}}_{\mathrm{SGG}} + \omega_{\mathrm{REG}}\Sigma_{\mathrm{REG}}^{-1}\right) \\ &\quad \mathbf{x} - \left(\omega_{\mathrm{SST}}\mathbf{n}_{\mathrm{SST}} + \omega_{\mathrm{SGG}}\bar{\mathbf{A}}_{\mathrm{SGG}}^{T}\bar{\mathbf{l}}_{\mathrm{SGG}}\right) \\ &= \left(\omega_{\mathrm{SST}}\mathbf{N}_{\mathrm{SST}}\mathbf{x} - \omega_{\mathrm{SST}}\mathbf{n}_{\mathrm{SST}}\right) + \left(\omega_{\mathrm{SGG}}\bar{\mathbf{A}}_{\mathrm{SGG}}^{T}\bar{\mathbf{A}}_{\mathrm{SGG}}\mathbf{x} - \omega_{\mathrm{SGG}}\bar{\mathbf{A}}_{\mathrm{SGG}}^{T}\bar{\mathbf{l}}_{\mathrm{SGG}}\right) \\ &\quad + \left(\omega_{\mathrm{REG}}\Sigma_{\mathrm{REG}}^{-1}\mathbf{x}\right) \\ &= \left(\omega_{\mathrm{SST}}\mathbf{r}_{\mathrm{SST}}\right) + \left(\omega_{\mathrm{SGG}}\bar{\mathbf{A}}_{\mathrm{SGG}}^{T}\left(\bar{\mathbf{A}}_{\mathrm{SGG}}\mathbf{x} - \bar{\mathbf{l}}_{\mathrm{SGG}}\right)\right) + \left(\omega_{\mathrm{REG}}\Sigma_{\mathrm{REG}}^{-1}\mathbf{x}\right)\end{aligned}$$

Introducing the observation residuals $\bar{\mathbf{v}}_{\mathrm{SGG}} = \bar{\mathbf{A}}_{\mathrm{SGG}}\mathbf{x} - \bar{\mathbf{l}}_{\mathrm{SGG}}$, we obtain

$$\mathbf{r} = \left(\omega_{\mathrm{SST}}\mathbf{r}_{\mathrm{SST}}\right) + \left(\omega_{\mathrm{SGG}}\bar{\mathbf{A}}_{\mathrm{SGG}}^{T}\bar{\mathbf{v}}_{\mathrm{SGG}}\right) + \left(\omega_{\mathrm{REG}}\Sigma_{\mathrm{REG}}^{-1}\mathbf{x}\right). \tag{13}$$

Note that the residuals $\mathbf{r}$ can be computed very efficiently since the expensive computation of $\bar{\mathbf{A}}_{\mathrm{SGG}}^{T}\bar{\mathbf{A}}_{\mathrm{SGG}}$ is thereby reduced to two matrix-vector products $\bar{\mathbf{A}}_{\mathrm{SGG}}\mathbf{x}$ and $\bar{\mathbf{A}}_{\mathrm{SGG}}^{T}\bar{\mathbf{v}}_{\mathrm{SGG}}$. In the following iteration steps both types of residuals ($\mathbf{r}$ and $\mathbf{v}$) can be updated by recursion formulas (see e.g. Schuh, 1996).

The convergence and stability of the CG algorithm just described can be accelerated considerably by preconditioning the combined normal equation system, i.e. by premultiplying Eq. (12)

$$\mathbf{N}_{\oplus}^{-1}\mathbf{N}\mathbf{x} = \mathbf{N}_{\oplus}^{-1}\mathbf{n}, \tag{14}$$

where $\mathbf{N}_{\oplus}$ is chosen to be a sparse preconditioning matrix, approximating the dominant structure of $\mathbf{N}$. It constitutes the weighted sum of the non-zero entries of $\mathbf{N}_{\mathrm{SST}}$, the diagonal matrix $\sum_{\mathrm{REG}}^{-1}$, and a subset of $\bar{\mathbf{A}}_{\mathrm{SGG}}^{T}\bar{\mathbf{A}}_{\mathrm{SGG}}$. The latter is computed within the so-called Kite structure (Boxhammer, 2006; Boxhammer and Schuh, 2006), i.e. only the block-diagonal correlations and the near-zonal correlations are modeled. To achieve a most simple sparse structure within $\mathbf{N}_{\oplus}$ it is useful to rearrange the elements of the parameter vector $\mathbf{x}$ according to the Free Kite Numbering (FKN) scheme (Boxhammer, 2006), which allows one in particular (i) to keep the SST parameters within a single coherent block, (ii) to maintain the block-diagonal structure, and (iii) to model additional zonal correlations.

The residuals $\boldsymbol{\rho}$ of the preconditioned problem Eq. (14) are given by

$$\boldsymbol{\rho} = \mathbf{N}_{\oplus}^{-1}\mathbf{N}\mathbf{x} - \mathbf{N}_{\oplus}^{-1}\mathbf{n} = \mathbf{N}_{\oplus}^{-1}\left(\mathbf{N}\mathbf{x} - \mathbf{n}\right) = \mathbf{N}_{\oplus}^{-1}\mathbf{r} \tag{15}$$

i.e. the new residuals $\boldsymbol{\rho}$ result from preconditioning the original residuals $\mathbf{r}$ which are computed in an efficient way by Cholesky reduction of the sparse preconditioner. With these tools at hand the standard CG algorithm can be applied (see e.g. Schuh, 1996). This procedure is easily modified to enable the solution of Eq. (12) for multiple right-hand sides, which allows for efficiently estimating the unknown weight

factors or the variance/covariance matrix of the spherical harmonic coefficients by Monte-Carlo methods (Alkhatib, 2007).

3.2 Integration of VCE into PCGMA

In Sect. 3.1 the optimal weights of the observation groups $k \in \{\text{SST,SGG,REG}\}$ in the combination were treated as known quantities, which is however not a realistic assumption. Interpreting these weights as variance factors $\omega_k = 1/\sigma_{0k}^2$, they can be estimated via variance component estimation (VCE). These variance components may be determined for uncorrelated groups by (see e.g. Koch and Kusche, 2002)

$$\sigma_{0k}^2 = \frac{1}{\omega_k} = \frac{\mathbf{v}_k^T \mathbf{P}_k \mathbf{v}_k}{n_k - m_k} = \frac{\Omega_k}{n_k - m_k} \tag{16}$$

where n_k denotes the (known) number of observations within observation group k. The unknown weighted squared sum of residuals Ω_k as well as the number of parameters m_k, determined by the corresponding observation group k, can be computed from the normal equations as well as directly from the observation equations by evaluating the trace of $\mathbf{N}_k\mathbf{N}^{-1}$ or $\mathbf{A}_k{}^T\mathbf{A}_k\mathbf{N}^{-1}$ using a stochastic trace estimator (see e.g. Alkhatib, 2007; Brockmann and Schuh, 2008 for the convergence behavior). As the residuals on the one hand change within each CG step but also depend on the weights used for parameter estimation, the two iterative methods CG and VCE are nested loops. Starting with initial guesses $\omega_k^{(0)}$, the CG steps are repeated until convergence. The residuals of the final CG step $\nu_{\max}$ are used to compute updated weight factors, which in turn are used to solve Eq. (12) again for new parameter estimates:

```
for τ = 1...τ_max //VCE − iterations
    for ν = 1...ν_max //CG − iterations
        Δx^(ν) = estimateParameterUpdate(ω_k^(τ));
        x^(ν+1) = x^(ν) + Δx^(ν);
    end
    ω_k^(τ+1) = estimateWeights();
end
```

3.3 Integration of the Decorrelation Filters into PCGMA

Variance component estimation as described in the previous section requires that the SGG observation equations have been decorrelated according to Eq. (7). As we do not know the true PSD of the SGG data, but only an approximation thereof

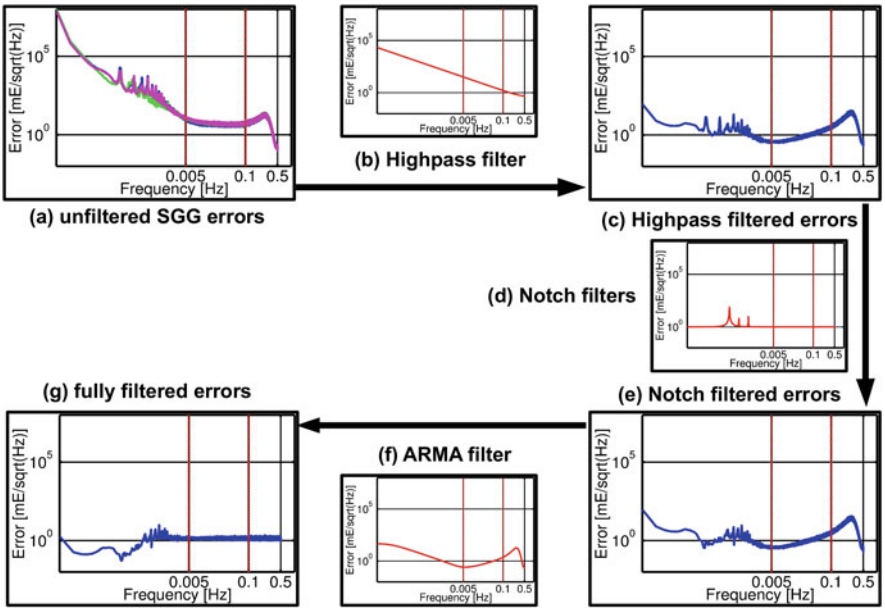

Fig. 5 Visualization of the power spectral densities (PSD) of the decorrelation process

from ground simulations, the PSD is estimated from the real data itself. As the presence of the spherical harmonic trend function distorts the PSD estimate, it must be first eliminated from the data. Evidently, the trend at this stage is still unknown so that some start values for the spherical harmonic coefficients (or for the PSD) may be used instead; eliminating the trend thus approximately results in start residuals, whose PSD takes a form such as in Fig. 5a.

The goal is to filter the residuals (and thus the given observation equations) such that their initial PSD (a) is transformed into a flat spectrum, reflecting uncorrelatedness of the observations (g). This is achieved by applying three consecutive filter steps: Firstly, a high-pass filter in the form of a difference or Butterworth filter (b) is used to reduce the amplitudes below the measurement bandwidth (<0.005 Hz). The thus filtered residuals then still exhibit multiple sharp peaks below the measurement bandwidth (c). These can, secondly, be reduced by using notch filters, wherein each of these corresponds to one peak (d). The resulting filtered residuals with PSD as in (e) is in turn, thirdly, filtered by means of an ARMA filter (f) which is specifically designed to flatten primarily the spectrum within the high-priority measurement bandwidth. The final PSD (g) of the filtered residuals should be practically flat, which is statistically verified via white-noise tests (cf. Schuh and Kargoll, 2004). Once these filters have been adjusted to the start residuals, they may be applied to the given SGG observation equations via linear transformations. After a subsequent CG step (including VCE), improved trend coefficients and residuals will be available, which in turn enable a more realistic adjustment of the decorrelation filter components along the same steps as just explained (Fig. 5).

4 Conclusion and Outlook

The presented methods were applied to closed-loop simulations using synthetic GOCE observations based on the EGM96 (Lemoine et al., 1998), and the latest error models. Details of the simulation results concerning the modeling and processing of SST data, implementation and convergence behaviour of PCGMA, variance component estimation and filter design can be found in Wermuth (2008), Boxhammer (2006), Alkhatib (2007), Brockmann and Schuh (2008), and Siemes (2008), respectively. With these developments PCGMA is ready for the processing of the real data, expected as of mid-2009.

Acknowledgments Parts of this work were financially supported by the BMBF Geotechnologien program GOCE-GRAND II and the ESA contract No. 18308/04/NL/MM. The computations were performed on the JUMP supercomputer in Jülich. The computing time was granted by the John von Neumann Computing Institute (project 1827).

References

Alkhatib H (2007) On Monte Carlo methods with applications to the current satellite gravity missions. Schriftenreihe des Instituts für Geodäsie und Geoinformation der Universität Bonn No. 7. PhD thesis. http://hss.ulb.uni-bonn.de/diss_online/landw_fak/2007/alkhatib_hamza/

Alkhatib H, Schuh WD (2007) Integration of the Monte Carlo covariance estimation strategy into tailored solution procedures for large-scaled least squares problems. J. Geod. 70, 53–66.

Boxhammer C (2006) Effiziente numerische Verfahren zur sphärischen harmonischen Analyse von Satellitendaten. Mitteilungen aus den Geodätischen Instituten der Rheinischen Friedrich-Wilhelms-Universität Bonn, No. 94. PhD thesis. http://hss.ulb.uni-bonn.de/diss_online/landw_fak/2006/boxhammer_christian/

Boxhammer C, Schuh WD (2006) GOCE gravity field modeling: Computational aspects – Free kite numbering scheme. In: Rummel R, Reigber C, Rothacher M, Boedecker G, Schreiber U, Flury J (eds.), Observation of the Earth System from Space, Springer, Berlin/Heidelberg.

Bouman J, Rispens S, Gruber T, Koop R, Schrama E, Visser P, Tscherning CC, Veicherts M (2008) Preprocessing of gravity gradients at the GOCE high-level processing facility. J. Geod., doi: 10.1007/s00190-008-0279-9.

Brockmann JM, Schuh WD (2008) Fast variance component estimation in GOCE data processing. In: Mertikas S (ed.), Gravity, Geoid and Earth Observation, IAG Symposia 135, Springer, Berlin.

Ditmar P, Kusche J, Klees R (2003) Computation of spherical harmonic coefficients from gravity gradiometry data to be acquired by the GOCE satellite: regularization issues. J. Geod. 77, 465–477.

Drinkwater MR, Haagmans R, Muzi D, Popescu A, Floberghagen R, Kern M, Fehringer M (2007) The GOCE gravity mission: ESA's first core Earth explorer. Proceedings of the 3rd International GOCE User Workshop in Frascati, Italy.

ESA (1999) Gravity field and steady-state ocean circulation mission. Report for Mission Selection of the Four Candidate Earth Explorer Missions. ESA-Document SP-1233(1).

ESA (2006) GOCE Level 2 Product Data Handbook. ESA-Document GO-TN-HPF-GS-0111.

Gerlach C, Földváry L, Svehla D, Gruber T, Wermuth M, Sneeuw N, Frommknecht B, Oberndorfer H, Peters T, Rothacher M, et al. (2003) A CHAMP-only gravity field model from kinematic orbits using the energy integral. Geophys. Res. Lett. 30(20), 2037.

Hausleitner W (1995) Orbit and SGG Data Simulations. CIGAR III/Phase 2, Final Report, Part 1.

Hestenes M, Stiefel E (1952) Methods of conjugate gradients for solving linear systems. J. Res. Natl. Bur. Stand. 49(6), 2379.

Kaula W (1966) Theory of Satellite Geodesy, Blaisdell, Waltham, MA.
Klees R, Ditmar P, Broersen P (2003) How to handle colored noise in large least-squares problems. J. Geod. 76, 629–640.
Koch KR, Kusche J (2002) Regularization of the geopotential determination from satellite data by variance components. J. Geod. 76, 259–268.
Kusche J, Ilk KH (2000) The polar gap problem. In: Sünkel H (ed.), From Eötvös to Milligal, Final Report. ESA/ESTEC Contract No. 13392/98/NL/GD.
Lemoine FG, Kenyon SC, Factor JK, Trimmer RG, Pavlis NK, Chinn DS, Cox CM, Klosko SM, Luthcke SB, Torrence MH, et al. (1998) The Development of the Joint NASA GSFC and the National Imagery and Mapping Agency (NIMA) Geopotential Model EGM96. NASA/TP-1998-206861, Greenbelt.
Metzler B, Pail R (2005) GOCE data processing: The spherical cap regularization approach. Stud. Geophys. Geod. 49, 441–462.
Migliacchio F, Reguzzoni M, Sansó F, Tscherning CC, Veicherts M (2007) The latest tests of the space-wise approach for GOCE data analysis. Proceedings of the 3rd International GOCE User Workshop in Frascati, Italy.
Plank G (2004) Numerical solution strategies for the GOCE mission by using cluster technologies. PhD thesis. Institut für Navigation und Satellitengeodäsie, TU Graz.
Reigber C (1969) Zur Bestimmung des Gravitationsfeldes der Erde aus Satellitenbeobachtungen. Deutsche Geodätische Kommission, Reihe C, No. 137, Munich.
Schuh WD (1995) SST/SGG tailored numerical solution strategies. CIGAR III/Phase 2, Final Report, Part 2.
Schuh WD (1996) Tailored numerical solution strategies for the global determination of the earth's gravity field. Mitteilungen der Geodätischen Institute der TU Graz, No. 81, Graz.
Schuh WD (2002) Improved modeling of sgg-data sets by advanced filter strategies. In: Sünkel H (ed.), From Eötvös to mGal+, Final Report. ESA/ESTEC Contract No. 14287/00/NL/DC.
Schuh WD (2003) The processing of band-limited measurements – Filtering techniques in the least squares context and in the presence of data gaps. Space Sci. Rev. 108(1–2), 67–78.
Schuh WD, Kargoll B (2004) The numerical treatment of the downward continuation problem for the gravity potential. In: Sansó F (ed.), V Hotine-Marussi Symposium on Mathematical Geodesy, IAG Symposia 127, Springer, Berlin, pp. 22–31.
Schwarz HR (1970) Die Methode der konjugierten Gradienten in der Ausgleichsrechnung. ZfV 95, 130–140.
Siemes C (2008) Digital filtering algorithms for decorrelation within large least squares problems. PhD thesis. http://hss.ulb.uni-bonn.de/diss_online/landw_fak/2008/siemes_christian/
Sneeuw N, van Gelderen M (1997) The polar gap. In: Sansó F, Rummel R (eds.), Geodetic Boundary Value Problems in View of the One Centimeter Geoid, Lecture Notes in Earth Sciences, Vol. 65, Springer, Berlin, pp. 559–568.
Sneeuw N (2000) A semi-analytical approach to gravity field analysis from satellite observations. Deutsche Geodätische Kommission, Reihe C, No. 527, Munich.
Svehla D, Rothacher M (2002) Kinematic orbit determination of LEOs based on zero or double difference algorithms using simulated and real SST GPS data. In: Adam J, Schwarz KP (eds.), Vistas for Geodesy in the New Millennium, IAG Symposia 125, Springer, Heidelberg, pp. 322–328.
Visser P (2008) GOCE gradiometer: Estimation of biases and scale factors of all six individual accelerometers by precise orbit determination. J. Geod. 83, 69–85.
Wermuth M (2008) Gravity field analysis from the satellite missions CHAMP and GOCE. PhD thesis. TU Munich.
Yunck TP, Wu SC, Wu JT, Thornton CL (1990) Precise tracking of remote sensing satellites with the global positioning system. IEEE Trans. Geosci. Remote Sens. 28(1), 108–116.

GOCE and Its Use for a High-Resolution Global Gravity Combination Model

Richard Shako, Christoph Förste, Oleg Abrikosov, and Jürgen Kusche

1 Pre-GOCE Satellite-only Models

The determination of the global Earth gravity field is one of the major tasks of geodesy. Until the end of the last century, a satisfactory solution for the Earth gravity field could only be obtained by combining data from a large number of satellites at different altitudes and inclinations. The processing of these different data resulted in the so-called "satellite-only" normal equation matrix (for instance cf. Biancale et al., 2000).

Important milestones on the way to a more precise, satellite-based global Earth gravity model were then set with the CHAMP and especially the GRACE missions. By using data of these satellites alone, the Earth gravity field could be resolved with an accuracy of 1 cm for half-wavelengths down to approximately 270 km (e.g. EIGEN-GRACE02S; Reigber et al., 2005 or GGM02S; Tapley et al., 2005). Furthermore, solutions had been derived which made use of combined CHAMP/GRACE-data or combined GRACE/LAGEOS-data (e.g. EIGEN-GL04S1; Förste et al., 2008b) which resulted in an even more accurate Earth gravity model. Compared to the past, where a conglomerate of satellites contributed to the solution, it is of great advantage that the long to medium wavelength features of the Earth gravity field are now homogeneously derived from only few satellites' data. This is one part of the milestone. The other part is the improved accuracy of the GRACE-models of more than two orders of magnitude compared to the latest pre-CHAMP satellite-only model GRIM5-S1 (Biancale et al., 2000).

Figure 1 illustrates the progress by means of some GFZ and GFZ/GRGS derived satellite-only models plotted in their internal unregularized versions. In this figure, the degree amplitudes between degrees 90 and 160 are displayed together with the combination solution EIGEN-5C (Förste et al., 2008a), serving as a reference for a realistic spectral behaviour of the satellite-only solutions. The degree variances of

R. Shako (✉)
Helmholtz Centre Potsdam, GFZ German Research Centre for Geosciences,
Department 1: Geodesy and Remote Sensing, Telegrafenberg, 14473 Potsdam, Germany
e-mail: rst@gfz-potsdam.de

F. Flechtner et al. (eds.), *System Earth via Geodetic-Geophysical Space Techniques*,
Advanced Technologies in Earth Sciences, DOI 10.1007/978-3-642-10228-8_18,

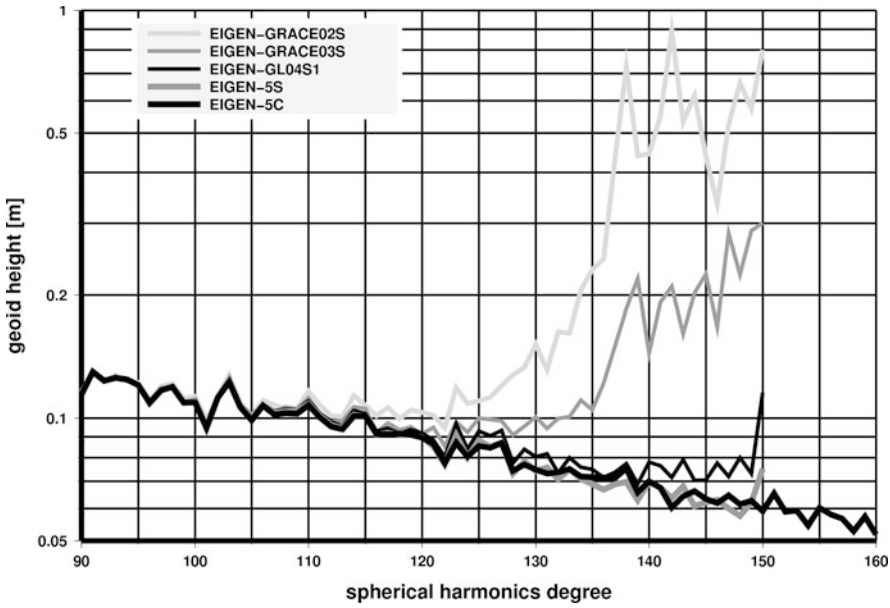

Fig. 1 Signal amplitudes per degree in terms of geoid heights for various satellite-only gravity field models derived at GFZ and GFZ/GRGS with the combination model EIGEN-5C as reference

the satellite-only models show a run-off at higher degrees. This run-off and its unrealistic increase in power is an indication for the limited sensitivity of the satellite data, and therefore a measure for the stability at higher degrees of a satellite-only model. For the earliest version, EIGEN-GRACE02S, the run-off starts at about 125, while for EIGEN-GL04S1 it starts at about 140. The version EIGEN-5S does not show a run-off at all, but only a spike at the end of the spectrum, probably a truncation error effect. The fact that from version to version the run-off is gradually suppressed can be simply explained by the amount of included GRACE data, which increased over the course of the time as well. The latest version, EIGEN-5S, is the best and most accurate performing model, since its degree variances are most close to the combination solution. While for EIGEN-GL04S1 the sensitivity limit is around degree/order (d/o) 140, Fig. 1 gives no information about the sensitivity limit of EIGEN-5S. It can be concluded that GRACE-based satellite-only gravity models are stable beyond degree 150, if enough observations are accumulated.

2 GOCE and Satellite-only Models

The recently launched GOCE-mission with its gradiometry observations is to be expected the next milestone in geopotential modeling.

For geosciences, the satellite-gravity-gradiometry (SGG) measurements are a very new type of observations. Already in early studies (for instance CIGAR IV,

1996, or Abrikosov et al., 2004) it was shown that the gravity gradients observed by GOCE will allow for the determination of the geopotential with a resolution of 80–100 km half-wavelength (corresponding to about d/o 200–250 in terms of spherical harmonics). Thus GOCE is expected to increase the quality of Earth gravity field models significantly in the short and medium wavelength ranges. Unfortunately this is not true for the long wavelengths due to the characteristic gradiometer bandwidth and the specific GOCE orbit configuration. This problem, however, can be simply tackled by combining GOCE with GRACE data (which are much better for the long wavelengths).

Another issue is caused by the GOCE mission profile. Since GOCE will have two separate observation periods of only six months each, its data are not perfect for the determination of a static gravity field. Indeed, the data will be contaminated by seasonal and high-frequency signals caused by mass variations of the oceans, in the atmosphere and by hydrological effects. Neglecting these seasonal and high-frequency effects will result in fundamental systematic distortions. Therefore, data corrections by de-aliasing and reduction techniques are necessary to use the GOCE-SGG data at their best (Stubenvoll, 2006). During the last years, GFZ worked intensely on the development of software and strategies in order to de-alias and reduce these annual and high-frequency signals in the GOCE-SGG data. It has turned out that, again, GRACE will be of big benefit: by using GRACE time-variable models for the reduction of seasonal hydrology mass variations and by using proper models for the high-frequency signals in the ocean and the atmosphere, the GOCE-data can be cleaned in a pre-processing step such that they contain only information of the static gravity field. The GRACE-models seem to be more reliable than, for instance, hydrology derived models (Petrovic et al., 2004; Schmidt et al., 2008). Note that the use of GRACE models is possible, because the two missions overlap in time.

In order to predict the quality of a future GOCE gravity model and to develop software and processing strategies, a simulation study has been performed on behalf of ESA by the GOCE High Performance Facility HPF (Rummel et al., 2004). Within the GOCE-HPF processing system three different strategies for GOCE gravity field determination have been adapted, these are the timewise approach (Pail et al., 2005), the spacewise approach (Migliaccio et al., 2004), and the direct approach (Abrikosov and Schwintzer, 2004). In the following the focus is set on the direct approach which is used at GFZ. The simulated GOCE observations used for the study were the E2E data as provided by ESA within the GOCE-HPF community (Catastini et al., 2007). They had been processed by the HPF teams in the context of the Acceptance Review 3 (AR3) in the framework of the HPF-development, and cover 58 days, representative for a nominal mission scenario. The satellite-to-satellite-tracking (SST) and SGG data were generated with the EGM96 model to d/o 200 and 360, respectively. In fact, the GOCE SST normal equations (up to d/o 150) and the SGG normal equations (up to d/o 200) both computed for AR3 were used in this study. In order to close the polar gaps, these data were combined with simulated surface gravity anomalies (using EGM96 (Lemoine et al., 1998) gravity model at $30' \times 30'$ grid covering polar areas bounded by latitudes $\pm 80.25°$). Random

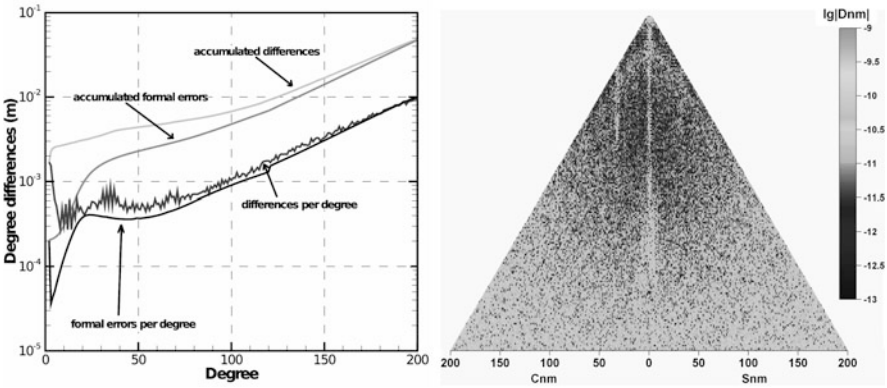

Fig. 2 Results of a study using simulated GOCE observations: (**a**) Spectrum of geoid-errors in mm w.r.t. EGM96 (*left*); (**b**) Errors of harmonic coefficients w.r.t. EGM96 (*right*)

noise with an rms of 2.5 mGal was added to these simulated values. Then gravity anomalies computed from EGM96 coefficients up to d/o 45 were subtracted from these data, and normal equations for harmonics up to d/o 200 have been computed using the latitude-dependent weighting and standard deviation of 2 mGal.

In this study, the GOCE mission objectives (1–2 cm accumulated geoid error at degree 200) cannot be attained, because only two months of simulated data were available. Figure 2a, b show the study results in the spectral domain. The spectrum of the resulting geoid-errors (Fig. 2a) demonstrates that the individual errors coincide almost perfectly with the formal errors. The mentioned problems at low degrees (up to d/o 15) are visible (due to the fact that the study did not use any GRACE data). The typical run-off (as known from Fig. 1) does not show up, which emphasizes that GOCE will be able to give accurate information for wavelengths beyond d/o 200. The accumulated error passes the 2 cm threshold at about d/o 150. Figure 2b shows the errors of the individual harmonic coefficients. The low order coefficients have about the same error as the high order ones. Also, the zonal coefficients are less accurate. Figure 2b backs up the conclusion that GOCE will give accurate information for wavelengths beyond d/o 200.

Figure 3 shows the results in the spatial domain. The polar regions exhibit much higher errors. The global rms is 5 cm, while the rms of the non-polar regions is 4 cm. This is a very good result, because only 58 days of data had been used. It can be estimated that – once the complete period of GOCE observations is available – the mission goal is reachable. Finally, it can be concluded that by proper treatment of the GOCE-SGG data and by optimal combination with GRACE-SST and GOCE-SST observations, GOCE will increase the resolution and quality of satellite-only Earth gravity models significantly. While the current pre-GOCE models have an accuracy of about 4 cm at 200 km half-wavelength, the expected GOCE accuracy is about 1–2 cm at 100 km half-wavelength. Thus, GOCE will open the door to a new age of geopotential modeling.

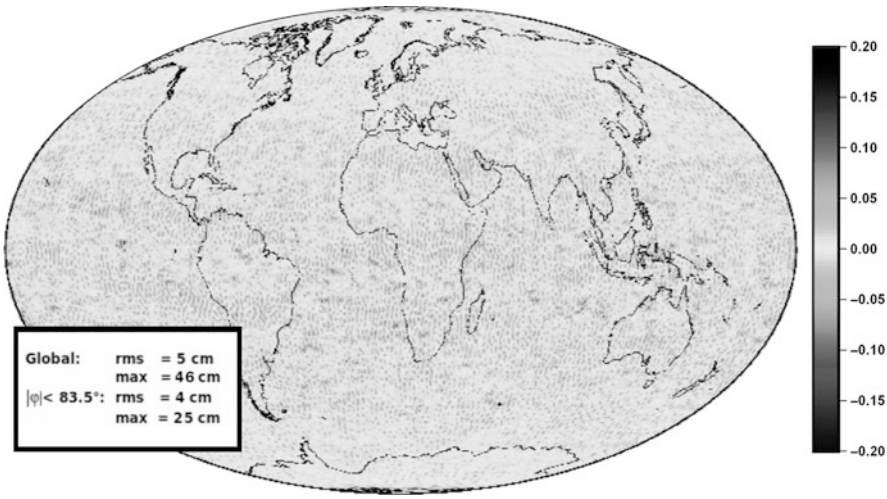

Fig. 3 Results of a study with simulated GOCE observations: geoid-errors w.r.t. EGM96 in cm

3 GOCE and Global Gravity Field Combination Models

3.1 Surface Data

The focus of the preceding section was set on satellite-only models. In order to enhance the resolution of the gravity model to degree and order 360 (and higher) the shortest wavelengths must be determined from surface gravity data. In the following, the GFZ strategy for the combination of GOCE with surface data is discussed.

The currently existing surface data sets (compiled from satellite altimetry, ship and airborne gravimetry over the oceans, and airborne and terrestrial gravimetry over land) provide – except for Antarctica – an almost complete global coverage. Due to inconsistencies between the various data sets and regionally varying accuracies, the surface data do not contain precise long to medium wavelengths gravity information. However, if properly preprocessed and thoroughly combined with satellite-only normal equations, the resolution of the global model can be extended down to at least 55 km half-wavelength.

For preprocessing the surface data, it is of great importance to: (a) unify the different data sets in order to eliminate errors in the geodetic datum; (b) apply the necessary correction terms (for instance free air correction, linear and quadratic terms of the normal gravity field gradient, ellipsoidal correction terms, atmospheric correction); (c) choose a high quality sea surface topography model, if sea surface heights derived from satellite altimetry are used.

After these steps the different surface data sets are condensed to regular gridded block mean values ($30' \times 30'$ grids). Then, these gridded data can be used for the combination with satellite-only normal equations. Basically two approaches exist:

1. Combine the satellite data with full normal equations of the surface data up to a certain d/o of spherical harmonics; for the higher degrees the surface data contribute in form of block-diagonal normal equations to the solution.
2. Combine the satellite-data with full normal equations of the surface data only.

The reason for following two different approaches is the amount of computer memory (RAM and hard disk) needed for a full normal equation up to a certain degree. For instance, one full normal equation up to d/o 180 (32,761 unknowns) has the size of 4.3 GB (if stored as triangle matrix), while one full normal equation up to d/o 360 (130,321 unknowns) has the size of 67.9 GB. The computation time for setting up these normal equations behaves similarly exponential. Due to the fact that each surface data set is handled as an individual normal equation system, the necessary computer memory is 10–20 times larger (depending on the number of different data sets). This is quite enormous for high d/o-solutions. Until the recent past there was just no other way than to use block-diagonal techniques for these solutions, since hard disk memory and RAM was too limited. With the use of block-diagonal techniques, the size of the normal equation is reduced drastically, that is to 0.008 GB (for d/o 180) and 0.063 GB (for d/o 360), so that the higher d/o could be easily calculated.

However, in order to make use of block-diagonal techniques, the used surface data set must fulfill some requirements (Gruber, 2000):

- They must be complete and of the same data type.
- They must be gridded regularly and in equatorial symmetry.
- The weighting of the data must be constant for a certain latitude.
- The weighting of the data must be equator-symmetric.

If all these conditions are fulfilled, the resulting normal equations fall apart into blocks due to the orthogonality of trigonometric functions. In particular, all correlations are zero for (Gruber, 2000):

- all C- and S-coefficients (e.g., $C_{21}S_{21}$, $C_{21}S_{40}$).
- all coefficients of different order (e.g., $C_{21}C_{20}$, $S_{21}S_{53}$).
- all coefficients of the same order if one coefficient is of even degree while the other is of uneven degree (e.g., $C_{20}C_{30}$, $S_{43}S_{33}$).

3.2 Combination Models Derived from Full and Block-Diagonal Normal Equations

The block-diagonal techniques offer the opportunity to calculate a high-resolution model, whereby correlations between coefficients are not neglected (thus it is outperforming the numerical integration approach). On the downside there are the mentioned requirements for the input data, which for instance do not allow merging

gravity anomalies with geoid undulation as input data. Also, an individual weighting is not possible. Therefore it must be the goal to use full normal equation for as high degrees as computer resources allow.

Until the GFZ/GRGS-model EIGEN-5C (complete up to d/o order 360) block-diagonal techniques had been used. In the following the strategy for a block-diagonal combination is explained, using EIGEN-5C (Förste et al., 2008a) as pars pro toto. Of course, the presented strategy is optimized for the used GRACE data. Its basic principle, however, can be adapted to GOCE very simple.

First, the satellite-only normal equation system (consisting of LAGEOS (complete to d/o 30) and GRACE (complete to d/o 150)) was added to the full surface data normal equation system (complete to d/o 280) in such a way that the surface- and satellite-based coefficients up to degree 70 were kept separate (see Fig. 4). That means the surface data did not contribute to the solution for $n, m = 1 \ldots 70$; therefore the mentioned surface data problems in the long wavelengths (low degrees) are avoided. The relative weights for the individual surface data normal equations were chosen in accordance with the standard deviations of their underlying terrestrial data. Furthermore, the surface data used for the complete normal equations had been filtered for frequencies higher than d/o 260 in order to avoid truncation errors, which means that they do not contribute to the solution for $n, m = 261 \ldots 280$.

In the overlapping spectral band, where both satellite and surface data are contributing to the solution, there is a degree range where the information of both data types is completely used (from $n, m = 70 \ldots 90$), followed by a degree range where the satellite data are kept separate but bound together with the surface data by introducing degree-dependent weighted pseudo-observations

$$C/S_{nm\_\mathrm{Surf.}} - C/S_{nm\_\mathrm{Sat.}} = 0 \quad \text{with weight } p = 1/(0.8696 \cdot 10^{-10} \cdot \mathrm{e}^{(n-90)/24.6})^2$$

so that a smooth transition in the degree amplitude spectrum within the overlapping part of the surface and satellite normal equations is assured, while the information

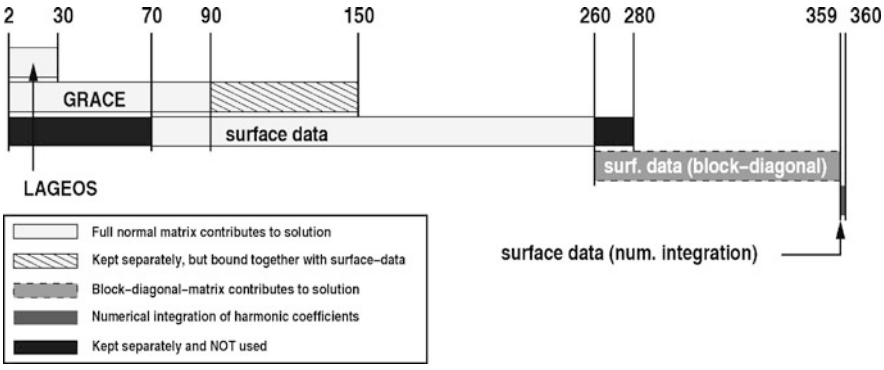

Fig. 4 Details of the EIGEN-5C combination

of the satellite-only gravity field model is kept up to its maximum d/o 150. The optimum degree dependence of the weights in the above formula was found empirically by testing a dedicated range of the therein given numbers after evaluating the formal errors of the spherical harmonics of previous satellite-only models. The finally resulting combined normal equation system was solved by Cholesky decomposition.

Last, the block diagonal system was solved separately and the resulting solution was used to extend the spherical harmonic coefficients from degree 261 to degree 359, and the degree 360 coefficients (obtained through numerical integration) were added for completeness.

3.3 The GOCE-Model: Combination with Full Normal Equations Only

As mentioned in the previous subsection, the use of block-diagonal techniques is less preferable than the use of full normal equations. Due to the enormous development in computer technology, which led to the availability of huge *and* affordable hard disk and RAM memory, the handling of a dozen of 70 GB sized normal equations is not a too big problem anymore. The problem of the long processing time has vanished due to the much higher speed of computer processors. Furthermore, the use of clusters offer an alternative for massive parallel processing.

Furthermore, the software existing at GFZ has been optimized significantly. Table 1 demonstrates the huge speed-up. While the old software version, which used internal compiler parallelization, was not able (due to technical reasons caused by the code) to set up normal equations up to d/o 250, the new mpi-parallelized software can in a reasonable time frame. When using 15 processors on a SUN V890 workstation, the computation of a complete global set of normal equation up to d/o 359 takes about 2 days.

In the following, the up-to-date strategy for the combination of GOCE-SGG observations with GRACE, LAGEOS, and surface data sets is discussed. This strategy is targeting at a geopotential model complete up to d/o 360.

Table 1 Computation times for setting up one normal equation for 3,800 observations on a SUN V890 workstation using 6 processors

Maximum degree	Normal equation size (GB as triangle matrix)	Old software version (s)	New version (s)	Increase of speed (new/old)
100	0.4	2,036	91	2,237%
200	6.5	34,950	1,287	2,716%
250	15.8	Technically impossible	3,248	∞
300	32.8	Technically impossible	6,348	∞
359	67.9	Technically impossible	9,862	∞

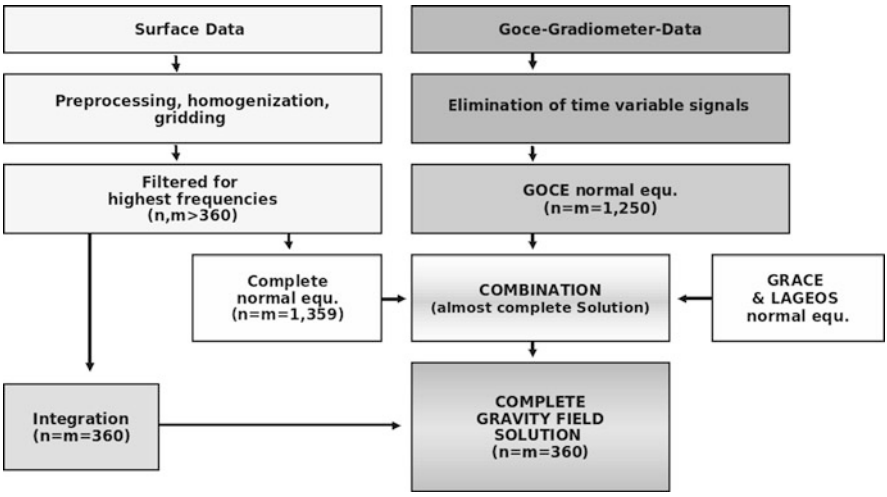

Fig. 5 Combination scheme for GOCE-SGG data with GRACE, LAGEOS, and surface data

Figure 5 shows the planned combination scheme. On the left hand side the processing of surface data is displayed. As discussed in Sect. 3.1, the surface data are preprocessed, homogenized and gridded in $30' \times 30'$-resolution. Following this, they will be filtered for degrees higher than the resolution of the targeted geopotential model (d/o 360). This is necessary for avoiding truncation errors and aliasing effects of higher frequencies. Then, complete normal equations are computed up to d/o 359 (one normal equation for each individual surface data set). Since a $30' \times 30'$-grid cannot provide an invertible normal equation for the coefficients of degree 360, these coefficients are calculated by numerical integration.

On the right hand side of Fig. 5 the processing of GOCE-SGG observations is displayed. After the preprocessing and the elimination of time variable signals, the GOCE normal equations are obtained (complete up to d/o 250), which are then combined with both the surface normal equations and the GRACE/LAGEOS normal equations (see below for further details). An almost complete gravity field model up to d/o 359 will result. The final step is to extend this model with the results of the numerical integration in order to make it complete up to d/o 360.

Figure 6 shows the details of the combination step in the current stage of planning. First of all, it does not seem necessary to include CHAMP- and GOCE-SST data. Internal studies have shown that their contribution to the quality of the solution does not justify their use. LAGEOS data, however, are very advantageous for the accurate estimation of the C_{20}-coefficient. In analogy to the combination of the EIGEN-5C model, LAGEOS will contribute to the solution from d/o 2 up to d/o 30 with complete normal equations, and GRACE will contribute with complete normal equations up to d/o 150. The information of GOCE and surface data is eliminated up to d/o 30 and d/o 120, respectively. This is done by keeping their low degree

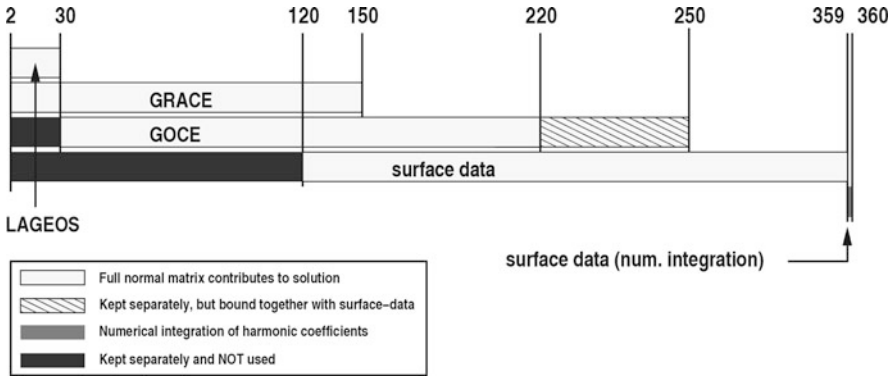

Fig. 6 Details of the planned GOCE-combination-model

coefficients separately during the solution of the normal equation system. In the transition zone from d/o 220 up to d/o 250, the coefficients solved by GOCE are bound to together with the surface data coefficients by introducing degree-weighted pseudo-observations as discussed in Sect. 3.2. After finding the optimum weighting for the surface normal equations, the resulting combined normal equation system is solved by Cholesky decomposition. For the optimum weighting a variance component estimation will be established. Finally, the degree 360 coefficients (obtained through numerical integration) are added for completeness.

Once the first real GOCE observations are available, it may be necessary to adapt the strategy to the real characteristics of GOCE gradiometry measurements. For instance, the reality may show that introducing a transition zone for the highest GRACE degrees is necessary, or that the transition zone for GOCE should start earlier or later, or that the contribution of the surface data should not begin at 120, but at 90. Once the real GOCE observations are accessible, the details will be fixed both by thoroughly computation and validation of the results.

When surface data of global coverage with higher resolution than $30' \times 30'$ become publicly available (for instance the $5' \times 5'$ data-set used for the NGA EGM2008 model; Pavlis et al., 2008), the goal will be to solve for a higher resolution model as well; for instance, a $15' \times 15'$ global surface data set would allow for a model up to d/o 720. The strategy will be then a composition of the two previously discussed approaches. For degrees higher than d/o 360, the surface data will contribute to the solution as block-diagonals.

4 Conclusions

With the GOCE gradiometry measurements, the door to a new age in geopotential modelling will be opened, not only for satellite-only models, but for combination solutions as well. GFZ is waiting for the first GOCE observations with an improved strategy, based on longterm experiences in gravity field determination. A gravity

field model, complete up to at least 360 (in terms of spherical harmonics) with an improved accuracy and quality will result. Surface data will contribute to d/o 359 as complete normal equations. The use of block-diagonal-techniques is planned if future surface data sets allow for a higher resolution.

References

Abrikosov O, Jarecki F, Müller J, Petrovic S, Schwintzer P (2004) GOCE-GRAND: Gradiometer data reduction, combination and processing. GEOTECHNOLOGIEN Statusseminar, GFZ Potsdam, 5 July 2004 (Poster).

Abrikosov O, Schwintzer P (2004) Recovery of the Earth's gravity field from GOCE satellite gravity gradiometry: A case study. Proceedings of the Second International GOCE User Workshop "GOCE, the Geoid and Oceanography", 8–10 March 2004, ESA-ESRIN, Frascati, Italy, ESA SP-569.

Catastini G, Cesare S, de Sanctis S, Dumontel M, Parisch M, Sechi G (2007) Predictions of the GOCE in-flight performances with the end-to-end system simulator. Proceedings of the 3rd International GOCE User Workshop, 6–8 November 2006, Frascati, Italy, ESA SP-627, pp. 9–16.

CIGAR IV (1996) Study of Advanced Reduction Methods for Spaceborne Gravimetry Data, and of Data Combination with Geophysical Parameters, Final Report. ESA contract No. 152163 – ASA study ESTEC/JP/95-4-137/MS/nr.

Biancale R, Balmino G, Lemoine J-M, Marty J-C, Moynot B, Barlier F, Exertier P, Laurain O, Gegout P, Schwintzer P, et al. (2000) A new global Earth's gravity field model from satellite orbit perturbations: GRIM5-S1. Geophys. Res. Lett. 27, 3611–3614.

Förste C, Flechtner F, Schmid R, Stubenvoll R, Rothacher M, Kusche J, Neumayer H, Biancale R, Lemoine J-M, Barthelmes F, et al. (2008a) EIGEN-GL05C – A new global combined high-resolution GRACE-based gravity field model of the GFZ-GRGS cooperation, General Assembly European Geosciences Union (Vienna, Austria, 2008), Geophysical Research Abstracts, Vol. 10, Abstract No. EGU2008-A-06944/2008.

Förste C, Schmidt R, Stubenvoll R, Flechtner F, Meyer U, König R, Neumayer H, Biancale R, Lemoine JM, Bruinsma S, et al. (2008b) The GeoForschungsZentrum Potsdam/Groupe de Recherche de Gèodésie: Spatiale satellite-only and combined gravity field models: EIGEN-GL04S1 and EIGEN-GL04C. J. Geod. 82, 331–346, doi: 10.1007/s00190-007-0183-8.

Gruber T (2000) Hochauflösende Schwerefeldbestimmung aus Kombination von terrestrischen Messungen und Satellitendaten über Kugelfunktionen. Scientific Technical Report STR00/16, GeoForschungsZentrum, Potsdam.

Lemoine FG, Kenyon SC, Factor JK, Trimmer RG, Pavlis NK, Chinn DS, Cox CM, Klosko SM, Luthcke SB, Torrence MH, et al. (1998) The Development of the Joint NASA GFSC and NIMA Geopotential Model EGM96. NASA/TP-1998-206861, Goddard Space Flight Center, Greenbelt, MD.

Migliaccio F, Reguzzoni M, Sanso F (2004) Space-wise approach to satellite gravity field determination in the presence of coloured noise. J. Geod. 78, 304–313, doi: 10.1007/s00190-004-0396-z.

Pail R. Schuh W-D, Wermuth M (2005) GOCE gravity field processing. In: Jekeli C, Bastos L, Fernandez J (eds.), Gravity, Geoid and Space Missions, Springer, Berlin, ISDN 978-3-540-26930-4, pp. 36–41.

Pavlis NK, Holmes SA, Kenyon SC, Factor JK (2008) An Earth Gravitational Model to Degree 2160: EGM2008. EGU General Assembly 2008. Vienna, Austria, 2008. Geophysical Research Abstracts, Vol. 10, Abstract No. EGU2008-A-01891/2008.

Petrovic S, Reigber C, Schmidt R, Flechtner F, Wünsch J, Güntner A (2004) Comparing temporal gravity variations derived from GRACE satellite observations and existing physical models. Geophysical Research Abstracts, Vol. 6, EGU04-A-06903.

Reigber C, Schmidt R, Flechtner F, König R, Meyer U, Neumayer K-H, Schwintzer P, Zhu SY (2005) An Earth gravity field model complete to degree and order 150 from GRACE: EIGEN-GRACE02S. J. Geodyn. 39, 1–10, doi: 10.1016/j.jog.2004.07.001.

Rummel R, Gruber T, Koop R (2004) High level processing facility for GOCE: Products and processing strategy. Proceedings of the 2nd International GOCE User Workshop, 8–10 March 2004, Frascati, Rome, Italy, ES SP-569.

Schmidt R, Petrovic S, Güntner A, Barthelmes F, Wünsch J, Kusche J (2008) Periodic components of water storage changes from GRACE and global hydrological models. J. Geophys. Res. 113, B08419.

Stubenvoll R (2006) GOCE and Terrestrial Data: A High Resolution Earth Gravity Combination Model, GEOTECHNOLOGIEN Statusseminar "Beobachtung des Systems Erde aus dem Weltraum", Bonn, 18.-19.09.2006 (Poster).

Tapley B, Ries J, Bettadpur S, Chambers D, Cheng M, Condi F, Gunter B, Kang Z, Nagel P, Pastor R, et al. (2005) GGM02: An improved Earth gravity field model from GRACE. J. Geod. 79, 467–478, doi: 10.1007/s00190-005-0480-z.

Spectral Approaches to Solving the Polar Gap Problem

Oliver Baur, Jianqing Cai, and Nico Sneeuw

1 Introduction

Launched on March 17, 2009, the GOCE (Gravity field recovery and steady-state Ocean Circulation Explorer) satellite mission will upgrade our present knowledge about the Earth's gravitational structure considerably. The mission's major concern is recovering the short-scale features of the terrestrial gravity field, the gravitational potential or geopotential respectively, with an anticipated geoid accuracy of about 2 cm, and a spatial resolution around 100 km (ESA, 1999).

In order to continuously supply the spacecraft with energy, the surface of the satellite is equipped with solar panels, hence has to be oriented towards the sun during the whole mission lifetime as good as possible. Due to the low satellite altitude of around 250 km, the sun-synchronous orbit constraint causes the orbit inclination to be around $I \approx 96.6°$. Consequently, in terms of data coverage, the satellite ground track leaves out two circular-shaped polar areas completely. The lack of observations in these regions is referred to as the polar gap problem (PGP). In case of GOCE, the polar caps enclose 0.66% of the total Earth surface, adversely affecting gravity field determination from the satellite's observations.

Conventionally, the geopotential is parameterized in spherical harmonics. This representation can be interpreted as a two-dimensional Fourier expansion on the sphere. Two base function indices characterize the individual spectral constituents, referred to as degree l and order m. Based on spherical harmonics, the GOCE observation equations assembly is straightforward (e.g., Rummel et al., 1993; Ditmar et al., 2003; Baur et al., 2008). Inversion, e.g. by means of least-squares (LS) adjustment, of the resulting normal equations system yields the unknown series coefficients.

As a matter of fact, the lack of observations in the polar caps leads to a reduced numerical stability of the normal equations, i.e., the system becomes ill-posed (Metzler and Pail, 2005). Consequently, spatial data gaps map into non-resolvable

O. Baur (✉)
Institute of Geodesy, University of Stuttgart, 70174 Stuttgart, Germany
e-mail: oliver.baur@gis.uni-stuttgart.de

F. Flechtner et al. (eds.), *System Earth via Geodetic-Geophysical Space Techniques*, Advanced Technologies in Earth Sciences, DOI 10.1007/978-3-642-10228-8_19,

spectral constituents. Particularly the low-order constituents can not be recovered at all. In turn, reduced spectral domain resolvability for low orders implicates poor spatial results in the polar caps. Moreover, the limited observation geometry distorts gravity field modelling in regions nearby the polar areas as well, although there is high data coverage (Sneeuw and van Gelderen, 1997; Metzler and Pail, 2005). According to van Gelderen and Koop (1997) the maximum non-resolvable order $m_{\max}$ depends on both the orbital inclination I and the spectral degree l subject to the rule of thumb $m_{\max} \approx \mid 0.5\pi - I \mid l$, with I in radian. Hence, the number of non-resolvable spherical harmonic coefficients per degree increases with increasing spectral resolution.

Solving the PGP means minimizing its impact on data analysis. In order to determine the terrestrial gravity field as good as possible, various methods have been proposed for and applied to the GOCE observation geometry. From the data point of view they can be separated in approaches either using GOCE observations only, or considering additional external data such as provided by space-borne gravimetry. Alternatively, one can distinguish spectral and spatial domain approaches. As we point out later, from the computational point of view, spectral domain approaches are more convenient to overcome the PGP in the context of GOCE.

In this contribution we investigate two approaches to solving the PGP. Both strategies are spectral domain methods. The first one incorporates external data in terms of spectral a priori information. The combination of both the GOCE data and the additional spectral information is performed by tailored regularization. The second approach belongs to the class of GOCE-only solutions. It is based on the parameterization of the geopotential in band-limited base functions that are optimally concentrated on the area of GOCE data coverage.

The next section gives a brief, referenced overview on selected strategies to solve the PGP. In Sects. 3 and 4 we address the two spectral domain approaches mentioned before in more detail. Finally, Sect. 5 summarizes the major conclusions of this contribution.

2 Selected Strategies – A Review

2.1 Stabilization with External Data

As outlined in Fig. 1, stabilization approaches including external data combine GOCE observations with measurements provided by terrestrial, airborne or space-borne gravimetry. GRACE (Gravity Recovery And Climate Experiment) observations, for example, have global coverage, as the GRACE spacecraft orbit the Earth on an almost polar orbit (Tapley et al., 2004). Incorporating GRACE data in terms of a combined analysis results in an additional (linear) model between observed gravity field functionals on the one hand and the unknown parameters of the geopotential on the other hand. Opposed to the combination on the observation level, the GRACE gravity field information may be introduced by means of simulated GOCE measurements. The method would require the conversion of GRACE spherical harmonic

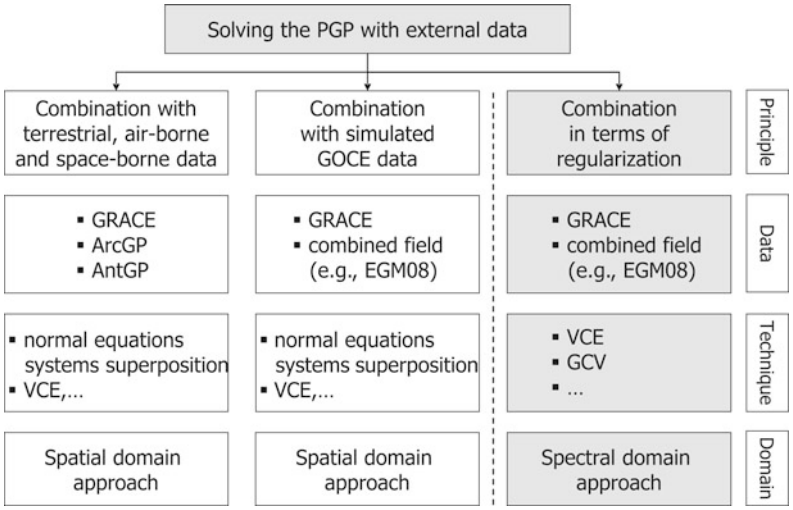

Fig. 1 Selected strategies to solving the polar gap problem with external data

coefficients to simulated gravitational gradients in the spatial domain. The performance of this combination approach depends on a variety of yet unsolved issues such as the preferable spatial density of the simulated gradients and their weigthing against the GOCE observations.

As a matter of fact, GRACE only resolves long- and medium-scale gravity field features. Terrestrial gravity observations such as provided by the Arctic gravity project (ArcGP) and the Antarctic geoid project (AntGP) essentially augment the satellite data (Forsberg and Kenyon, 2004; Scheinert, 2005). The individual observation models, normal equations systems respectively, are superposed in terms of a joint LS adjustment procedure. Variance component estimation (VCE) may be applied for the proper weighting of each kind of observation (e.g., Kusche, 2003).

Alternatively to the combination approach in the spatial domain, external gravity field information can also be introduced in the spectral domain. In this case, the combination is performed in terms of regularization. The consideration of additional spatial data exclusively in the polar areas has its spectral analogue in the regularization of non-resolvable orders only. The regularization of the whole spectrum, on the other hand, corresponds to globally available external data. In the framework of spectral domain stabilization techniques, we prefer the adoption of a combined terrestrial gravity field model, such as EGM08, as it contains terrestrial, airborne as well as spaceborne measurements. Combined models are best fitting the presently available data sets.

The selected strategies in Fig. 1 outline a broad variety to solve the PGP with external data. Within GOCE-GRAND II we focused on combination in terms of regularization. We prefer spectral over spatial domain approaches for practical reasons. Spectral approaches entail lower computational costs opposed to their spatial counterparts. Predominantly the assembly of various additional normal equations

systems is a challenging task. Incorporating external (spectral) information in "post-processing" avoids any superposition effort. The GOCE normal equations system is simply extended by some additional terms. From the computational point of view, this extension is largely independent of the spectral a priori information used. Consequently, the impact of different a priori information can be evaluated without significant additional implementation effort. In Sect. 3, we address the combination in terms of regularization in more detail.

2.2 Stabilization without External Data

As a matter of fact, gravity field solutions solely based on GOCE data do not constitute the best state-of-the-art global description of the terrestrial gravitational features as they do not include all presently available gravity field information. However, GOCE-only solutions are characterized by the outstanding property to be internally consistent, hence not prone to systematic errors of additional data sets. This is the reason for the ESA (European Space Agency) requirement for the determination of the Earth's gravity field from GOCE data only (ESA, 1999).

Without introducing any additional external data, a solution of the PGP leads to the minimization of numerical instabilities and distortions within the data analysis process, i.e., avoiding the normal equations to be ill-conditioned. Making no claim to be complete, Fig. 2 gives an overview on possible strategies.

Most stabilization methods applied in practice are related to tailored regularization. Tikhonov-Phillips regularization (Phillips, 1962; Tikhonov, 1963), in particular, is a commonly applied tool in satellite geodesy to treat ill-posed problems. The method stabilizes spectral constituents subject to a so-called penalty term, which is added to the LS optimization functional. Its impact on the normal equations matrix depends on the choice of the regularization matrix and the regularization parameter. To fix both, numerous proposals exist in literature (e.g., Kusche

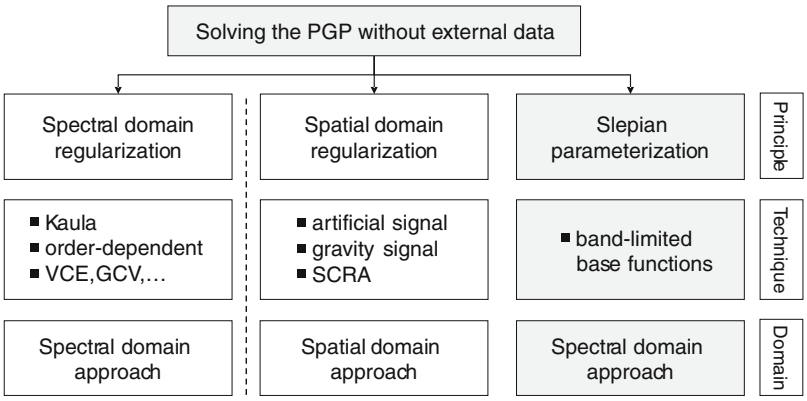

Fig. 2 Selected strategies to solving the polar gap problem without external data

and Klees, 2002). With regard to the PGP, the regularization of low orders only may be the appropriate approach.

Alternatively, spatial domain regularization techniques force the geopotential towards a pre-defined artificial or gravity signal at discrete locations. The spherical cap regularization approach (SCRA), for example, implies a continuous function, which is exclusively defined in the polar regions (Metzler and Pail, 2005).

Both the combination principles in Sect. 2.1 and the regularization approaches mentioned before try to adapt the GOCE measurements to the gravity field model parameterized in spherical harmonics. A completely different approach starts from the other point of view, i.e., not to adapt the observation geometry to the modeling but instead, to adapt the parameterization of the geopotential to GOCE observations. This results in band-limited base functions, also called Slepian functions that are optimally concentrated on the spherical belt of GOCE data coverage. The Slepian parameterization of the geopotential will be discussed in Sect. 4.

3 Regularization and Combination

In order to solve the PGP by spectral domain stabilization, we use a priori information in terms of spherical harmonic coefficients. Augmenting the minimization of squared residuals $\mathbf{r} = \mathbf{A}\mathbf{x} - \mathbf{y}$ by a parameter component $\mathbf{x} - \mathbf{x}_0$

$$\min_{\mathbf{x}}\{||\mathbf{A}\mathbf{x} - \mathbf{y}||^2_{\Sigma_\mathbf{y}^{-1}} + \alpha||\mathbf{x} - \mathbf{x}_0||^2_{\mathbf{R}}\} \tag{1}$$

yields the normal equations system

$$\hat{\mathbf{x}} = (\mathbf{A}^\mathrm{T}\Sigma_\mathbf{y}^{-1}\mathbf{A} + \alpha\,\mathbf{R})^{-1}(\mathbf{A}^\mathrm{T}\Sigma_\mathbf{y}^{-1}\mathbf{y} + \alpha\,\mathbf{R}\mathbf{x}_0)\ . \tag{2}$$

In Eqs. (1) and (2), $\Sigma_\mathbf{y}$ is the variance-covariance matrix of the observations $\mathbf{y}$, and $\mathbf{R}$ indicates the regularization matrix, which is typically symmetric and positive definite. The parameter α denotes the (a priori unknown) regularization parameter. It balances the residual norm $||\mathbf{A}\mathbf{x} - \mathbf{y}||$ against the (reduced) parameter norm $||\mathbf{x} - \mathbf{x}_0||$. Amongst alternative (predominantly heuristic) approaches, Cai (2004) developed a method to compute the optimal regularization parameter analytically.

Equation (2) accounts for both regularization and combination. When $\mathbf{x}_0 = \mathbf{0}$, i.e. the a priori information consisting of null pseudo-observables, the penalty term in Eq. (1) only impacts the normal equations matrix. This is the case of regularization. In its simplest form, the regularization matrix may be set to identity, $\mathbf{R} = \mathbf{I}$, often referred to as ordinary ridge regression. Commonly, however, the Kaula matrix is used for regularization (Reigber, 1989). Its entries follow a simple power law, approximating the signal content per spherical harmonic degree.

Data combination in the spectral domain is achieved by incorporating non-trivial a priori information $\mathbf{x}_0 \neq \mathbf{0}$, yielding the mixed estimator with additional information as stochastic linear restrictions (Rao and Toutenburg, 1999). The regularization

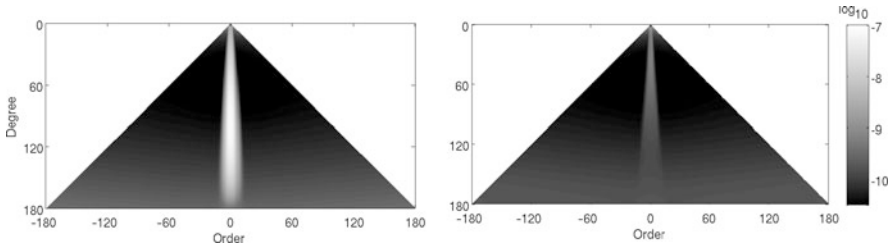

Fig. 3 Formal errors of GOCE spherical harmonic coefficients (negative orders indicate sine, positive orders cosine coefficients). *Left panel*: non-stabilized solution; *right panel*: Kaula-regularized solution

matrix becomes the inverse error variance-covariance matrix of the parameter vector $\mathbf{x}_0$. Both $\mathbf{x}_0$ and its error variance-covariance information are derived by the analysis of observations either collected in the polar areas or over the whole globe. Here we incorporate the gravity field model EGM08 as spectral a priori information, as it includes a multitude of currently available data sets. In order to deal with a diagonal structure of the regularization matrix, we restrict ourselves on the error variances.

The left panel in Fig. 3 presents the a posteriori error standard deviations of GOCE spherical harmonic coefficients if neither regularization nor combination is performed, i.e. $\mathbf{R} = \mathbf{0}$ and $\mathbf{x}_0 = \mathbf{0}$ holds true. The PGP causes a wedge-shaped band around the zonal coefficients to be poorly resolved. Kaula regularization, cf. the right panel in Fig. 3, improves the overall quality of the parameter estimate. The formal errors of the zonal and near-zonal coefficients decrease by roughly two orders of magnitude. However, the estimator turns out to be not complete due to the non-proper introduction of a priori information in terms of zero observations.

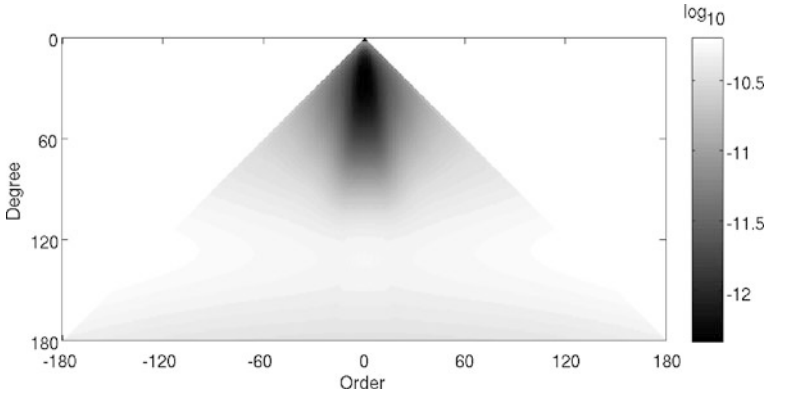

Fig. 4 Formal errors of spherical harmonic coefficients for the mixed estimator solution, incorporating EGM08 spherical harmonic coefficients and their variances as a priori information (negative orders indicate sine, positive orders cosine coefficients); different scale opposed to Fig. 3 applied

Figure 4 displays the formal errors of spherical harmonic coefficients incorporating the mixed estimator with a priori parameters $\mathbf{x}_0 \neq \mathbf{0}$ and appropriate variance information. For the combined solution, the quality of the parameter estimate improves considerably. The different options for stabilization in the spectral domain, cf. Eq. (2) and Figs. 3 and 4, outline the range of the regularization and combination performance. The more accurate the a priori information the better the accuracy of the coefficient estimate.

4 Slepian Parameterization

Any strategy to solving the PGP using spherical harmonics faces the problem that globally defined base functions are forced to model spatially limited signals. The orthogonality of Legendre functions, though, does not hold within a spatially limited area. The misfit causes the normal equations to be ill-conditioned, and hence the need to overcome the resulting numerical instabilities, cf. Sect. 3. With regard to GOCE data analysis, opposed to Legendre functions, band-limited base functions that are optimally concentrated on the spherical belt of data coverage are much more convenient to ensure the consistency between the observations and the gravity field modelling.

The methodology of deriving band-limited base functions traces back to Slepian (1978). Originally developed in communication theory to optimally transmit band-limited signals in limited time he referred them to as prolate spheroidal wave functions. Later, the simple term "Slepian functions" became more popular. Slepian himself solved the concentration problem on the line only. However, the approach can be easily transferred to the sphere as shown in Albertella et al. (1999), Pail et al. (2001) and Simons et al. (2006). Concerning GOCE, the basic idea of the Slepian parameterization approach is to find a set of base functions that are optimally concentrated within the data-covered spherical belt $B = \{0 \leq \lambda < 2\pi;\ \theta_0 \leq \theta \leq \pi - \theta_0\}$, with θ_0 denoting the co-latitude of the (double) spherical data gap. Back in 1999, Albertella et al. (1999) investigated the method for space geodetic applications. But they only succeeded in the calculation of non-structured band-limited functions, leading to unsatisfactory results. Based on recent developments (e.g., Miranian, 2004; Simons et al., 2006) we make use of an analytical expression for the unique transformation to the Slepian base, definitively solving the concentration problem on the sphere. Simons et al. (2006), in particular, address special focus on the axisymmetric double polar cap configuration, hence the GOCE observation geometry.

Slepian functions are derived by means of a maximum concentration problem, or its equivalent algebraic eigenvalue problem (EVP):

$$\Lambda = \frac{\mathbf{g}^{\mathrm{T}}\mathbf{D}\mathbf{g}}{\mathbf{g}^{\mathrm{T}}\mathbf{g}} \stackrel{!}{=} \max \quad \Leftrightarrow \quad \mathbf{D}\mathbf{g} = \Lambda\mathbf{g}\,. \tag{4}$$

The eigenvalues Λ ($0 \leq \Lambda \leq 1$), denoted as concentration factors, are a measure for the spectral concentration of the eigenvectors $\mathbf{g}$ in B. They are dependent on the kernel $\mathbf{D}$, representing the area of base function concentration. In the special case of an axisymmetric double polar cap its elements become

$$D_{lml'} = \frac{1}{2} \int_{\theta_0}^{\pi-\theta_0} \bar{P}_{lm} \bar{P}_{l'm} \sin\theta \, d\theta \quad \Leftrightarrow \quad \mathbf{D}_m \mathbf{g}_m = \Lambda_m \mathbf{g}_m. \tag{5}$$

Due to its block-diagonal structure, the eigenvalue problem in Eq. (5) can be solved for each order m separately. The eigenvectors related to large concentration factors, i.e., $\Lambda \approx 1$, allow to set up a system of (normalized) band-limited base functions $\bar{S}_{jm}(\cos\theta)$. They result from the product between the eigenvectors $\mathbf{g}_m$ and the (normalized) associated Legendre functions $\bar{P}_{lm}(\cos\theta)$ subject to

$$\bar{S}_{jm}(\cos\theta) = \sum_{l=m}^{L} g_{lm} \bar{P}_{lm}(\cos\theta) \,, \quad m \leq j \leq L \,. \tag{6}$$

The Slepian functions are orthogonal within the spherical belt B, orthonormal on the sphere respectively. For constant order m they are constructed by a linear combination of Legendre functions of the same order. The order m is identical for both Legendre and Slepian functions. This does not hold for the first index. In the following we refer j to as the Slepian index to distinguish from the degree l.

4.1 Solving the Eigenvalue Problem

The problem Albertella et al. (1999) were faced with is that the EVP according to Eq. (5) can not be solved uniquely. The parity of most of the concentration factors, cf. the left panel in Fig. 6, only allows the non-structured computation of the eigenvectors, hence Slepian functions. Grünbaum et al. (1982) gave the key impulse to overcome this computational problem. For the axisymmetric double polar cap configuration they found a commuting EVP to the original one. As outlined in Fig. 5, the commuting matrices $\mathbf{D}_m$ and $\mathbf{T}_m$, subject to $\mathbf{D}_m\mathbf{T}_m = \mathbf{T}_m\mathbf{D}_m$, generate the same

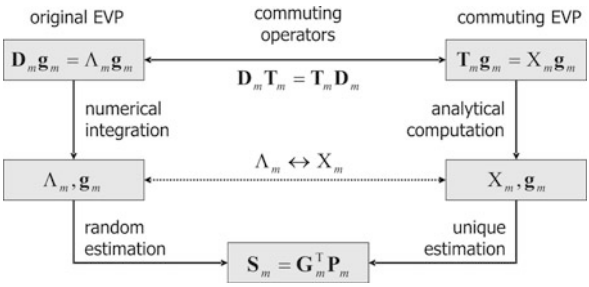

Fig. 5 Slepian functions computation via commuting operators

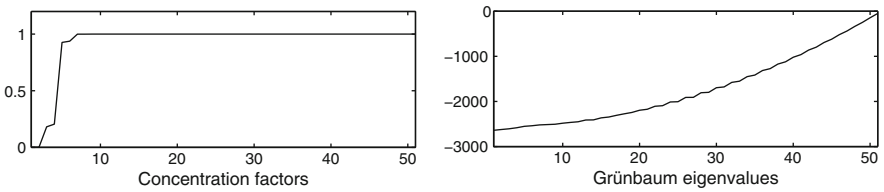

Fig. 6 Spectrum of concentration factors (*left panel*) and Grünbaum eigenvalues (*right panel*); exemplary for order $m = 0$ and spectral resolution $L = 50$

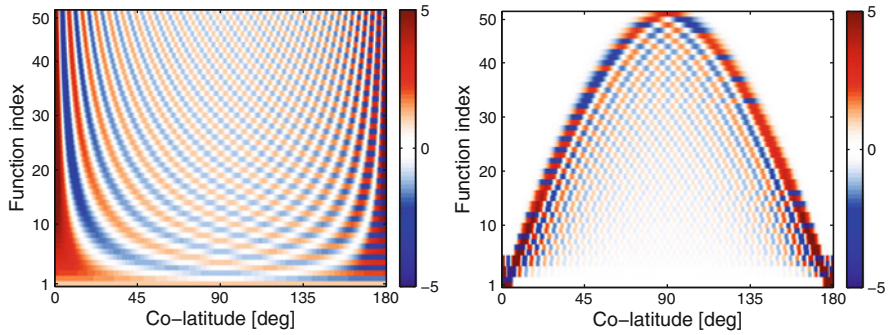

Fig. 7 Spatial oscillation of Legendre functions (*left panel*) and Slepian functions (*right panel*); exemplary for order $m = 0$ and spectral resolution $L = 50$

eigenvectors but different eigenvalues. Hence, in terms of Slepian functions computation both the original and the commuting EVP are equivalent: $\mathbf{D}_m\mathbf{g}_m = \Lambda_m\mathbf{g}_m \leftrightarrow \mathbf{T}_m\mathbf{g}_m = \mathbf{X}_m\mathbf{g}_m$.

The spectrum of the so-called Grünbaum eigenvalues $\mathbf{X}_m$, cf. the right panel in Fig. 6, allows the unique estimation of the eigenvectors and hence Slepian functions. Moreover, as $\mathbf{T}_m$ turns out to be tridiagonal with its elements following simple analytical expressions, the computation of the eigenvectors is highly efficient.

Figure 7 displays Slepian functions opposed to Legendre functions, exemplary for the order $m = 0$ and a spectral resolution of $L = 50$. As already mentioned before, Legendre functions exhibit no spatial concentration. Independent of the function index l, they oscillate over the whole sphere. Slepian functions, on the other hand, clearly demonstrate their band-limited nature. Low function indices j represent base functions that are exclusively concentrated in the polar caps, followed by a small transmission zone, with signal content in both the polar caps and the spherical belt. From the seventh base function on there is negligible signal in the polar caps. Hence (for $m = 0$ and $L = 50$), these Slepian functions constitute a system of orthogonal band-limited base functions that are optimally concentrated on the spherical belt of GOCE data coverage.

The Slepian parameterization definitively solves the PGP in the "Slepian world". In this context, it may be interpreted as a method for regional gravity field determination, as the polar caps are totally ignored within the analysis process. We have to

point out that the Slepian approach has no benefit compared to the Legendre parameterization of the geopotential for GOCE data analysis on a global scale (Baur and Sneeuw, 2007).

5 Conclusions

The GOCE satellite's ground tracks leave out a double polar cap with a radius of more than six degrees. As a consequence, GOCE data analysis based on spherical harmonics is confronted with numerical instabilities, as the spatial data gaps map into non-resolvable low-order constituents. Spectral approaches are efficient and powerful to solve the PGP. We stabilize the normal equations system by tailored regularization. In terms of a combination approach, we incorporate EGM08 to provide a global GOCE-based gravity field model. In this context we recommend the mixed estimator with additional information as stochastic linear restrictions.

Besides stabilization with external a priori information, the parameterization of the Earth gravity field by means of band-limited base functions, or Slepian functions, ultimately solves to PGP. The transformation of base functions is done by solving an algebraic eigenvalue problem. Commuting matrices allow the unique estimation of the new base. The philosophy of the Slepian approach is not to adapt the observation scenario to the modeling but instead, to adapt the parameterization of the geopotential to GOCE observations. Hence it can be interpreted as method for regional gravity field determination, meeting the ESA requirement for the recovery of the Earth's gravity field from GOCE data only.

Acknowledgments This is publication no. GEOTECH-1243 of the programme GEOTECHNOLOGIEN, Grant 03F0421C. We gratefully acknowledge the support of the BMBF (Bundesministerium für Bildung und Forschung) and the DFG (Deutsche ForschungsGemeinschaft). Furthermore, we kindly acknowledge helpful comments by W.-D. Schuh and an anonymous reviewer of the manuscript.

References

Albertella A, Sansò F, Sneeuw N (1999) Band-limited functions on a bounded spherical domain: The Slepian problem on the sphere. J. Geod. 73, 436–447.

Baur O, Sneeuw N (2007) Slepian approach revisited: New studies to overcome the polar gap. Proceedings of GOCE User Workshop, ESA SP-627.

Baur O, Sneeuw N, Grafarend EW (2008) Methodology and use of tensor invariants for satellite gravity gradiometry. J. Geod., doi: 10.1007/s00190-007-0178-5.

Cai J (2004) Statistical inference of the eigenspace components of a symmetric random deformation tensor. DGK Series C 577, Munich.

Ditmar P, Klees R, Kostenko F (2003) Fast and accurate computation of spherical harmonic coefficients from satellite gravity gradiometry data. J. Geod., doi: 10.1007/s00190-002-0298-x.

ESA (1999) The four candidate Earth explorer core missions – gravity field and steady-state ocean circulation mission. ESA Report SP-1233(1), Granada.

Forsberg R, Kenyon S (2004) Gravity and geoid in the arctic region – The Northern polar gap now filled. Proceedings of GOCE User Workshop, ESA-ESRIN.

van Gelderen M, Koop R (1997) The use of degree variances in satellite gradiometry. J. Geod. 71, 337–343.
Grünbaum FA, Longhi L, Perlstadt M (1982) Differential operators commuting with finite convolution integral operators: some non-abelian examples. SIAM J. Appl. Math. 42, 941–955.
Kusche J (2003) A Monte-Carlo technique for weight estimation in satellite geodesy. J. Geod., doi: 10.1007/s00190-002-0302-5.
Kusche J, Klees R (2002) Regularization of gravity field estimation from satellite gravity gradients. J. Geod. 76, 359–368.
Metzler B, Pail R (2005) GOCE data processing: The spherical cap regularization approach. Stud. Geophys. Geod. 49, 441–462.
Miranian L (2004) Slepian functions on the sphere, generalized Gaussian quadrature rule. Inv. Prob. 20, 877–892.
Pail R, Plank G, Schuh W-D (2001) Spatially restricted data distributions on the sphere: The method of orthonormalized functions and applications. J. Geod. 75, 44–56.
Phillips DL (1962) A technique for the numerical solution of certain integral equations of the first kind. J. ACM 9, 54–97.
Rao CR, Toutenburg H (1999) Linear Models, Springer, Berlin, Heidelberg.
Reigber C (1989) Gravity field recovery from satellite tracking data, theory of satellite geodesy and gravity field determination. In: Sansò F, Rummel R (eds.), Lecture Notes in Earth Science, Vol. 25, Springer, Berlin, Heidelberg, pp. 197–234.
Rummel R, Sansò F, van Gelderen M, Brovelli M, Koop R, Miggliaccio F, Schrama E, Scerdote F (1993) Spherical harmonic analysis of satellite gradiometry. Netherlands Geodetic Commission, New Series 39.
Scheinert M (2005) The Antarctic geoid project: Status report and next activities. In: Jekeli C, Bastos L, Fernandes J (eds.), Gravity, Geoid and Space Missions, Vol. 129, Springer, Berlin, Heidelberg, pp. 137–142.
Simons FJ, Dahlen FA, Wieczorek MA (2006) Spatiospectral localization on a sphere. SIAM Rev. 48, 504–536.
Slepian D (1978) Prolate spheroidal wave functions, Fourier analysis and uncertainty. V. The discrete case. Bell. Syst. Tech. J. 57, 1371–1430.
Sneeuw N, van Gelderen M (1997) The polar gap. In: Sansò F, Rummel R (eds.), Geodetic Boundary Value Problems in View of the One Centimeter Geoid. Lecture Notes in Earth Science, Vol. 65, Springer, Berlin, pp. 559–568.
Tapley BD, Bettadpur S, Watkins M, Reigber C (2004) The gravity recovery and climate experiment: Mission overview and early results. Geophys. Res. Lett., doi: 10.1029/2004GL019920.
Tikhonov AN (1963) Regularization of incorrectly posed problems. Sov. Mat. Dokl. 4, 1035–1038.

Regionally Refined Gravity Field Models from In-Situ Satellite Data

Annette Eicker, Torsten Mayer-Gürr, Karl-Heinz Ilk, and Enrico Kurtenbach

1 Introduction

The third satellite in the sequence of dedicated gravity satellite missions after CHAMP (CHAllenging Minisatellite Payload – Reigber et al. 1999) and GRACE (Gravity Recovery and Climate Experiment – Tapley et al., 2004) will be GOCE (Gravity field and steady-state Ocean Circulation Explorer – ESA, 1999). The gravity field will thereby be measured with unprecedented accuracy by a gravity gradiometer consisting of six three-axes accelerometers which determine in-orbit gravity gradients in three spatial directions.

In the past decades several gravity field analysis techniques tailored to this new kind of observables have been proposed and tested based on various realistic simulation scenarios. One problem is the processing of the extremely large amount of observations and in solving the huge unstable adjustment problem. Another problem seems to be related to the representation of the gravity field by an appropriate set of basis functions and the associated gravity field parameters. The usual way is to model the gravity field by spherical harmonics up to a certain degree. This degree is limited by the significance of the gravity field signal in the observations and its ratio to the observation noise. Because of the inhomogeneous gravity field of the Earth the signal content varies in the space domain. The gravity field in regions with rough gravity field features should be recovered up to a higher degree than within regions with smooth gravity field features. This means that the degree of instability of the gravity field recovery process, which increases with increasing high frequencies in the gravity field signal, varies with the specific gravity field characteristics in different regions. A gravity field representation with basis functions of global support must be regularized globally. However, a global regularization causes an overall filtering of the observations leading to a mean dampening of the global gravity field features. As a consequence, the high frequent gravity field signal in the observations is lost again in some geographical regions.

A. Eicker (✉)
Institute of Geodesy and Geoinformation, University of Bonn, 53115 Bonn, Germany
e-mail: annette@geod.uni-bonn.de

F. Flechtner et al. (eds.), *System Earth via Geodetic-Geophysical Space Techniques*, Advanced Technologies in Earth Sciences, DOI 10.1007/978-3-642-10228-8_20,

An alternative approach, presented here, is to determine a global gravity field solution with high long and medium wavelength accuracy and improve this global solution in regions with characteristic gravity field features by an adapted regional recovery procedure. The global solution is parameterized by spherical harmonic coefficients up to a moderate degree and the regional solutions are represented by space localizing basis functions, e.g., by spherical splines. This procedure provides several advantages. The regional approach allows the exploitation of the individual signal content in the observations and a tailored regularization for regions with different gravity field characteristics. The advantage compared to a uniform global regularization is that the regularization factor is selected for each region individually. By an individually adapted regularization it is possible to extract more information out of the given data than with a global gravity field determination process. Regions with a smooth gravity field signal, for example, can be regularized stronger without dampening the signal. In addition, the resolution of the gravity field determination can be chosen for each region individually according to the spectral behavior of the signal in the specific region. Furthermore, the regional approach has the advantage of dealing with regions with different data coverages more easily. If no data at all is available (e.g. the polar gap) the regional refinement can be skipped. For regions with sparse data coverage a coarser parameterization can be selected. Another aspect, especially relevant for the GOCE mission with its potential to recover the high resolution gravity field, is the fact that regional solutions contain less unknown parameters and therefore the computation procedure is simplified. This enables a significant reduction of computation costs.

If desired, several regional solutions with global coverage can be merged by means of quadrature methods to obtain a global solution, in principle, up to an arbitrary degree. Simulation results are presented to demonstrate this approach. Due to the regionally adapted strategy this method provides better results than calculating a spherical harmonic solution by recovering the potential coefficients directly (see also Eicker et al., 2004 and Eicker, 2008).

2 Mathematical Model

The gradiometer as primary observation device in case of the GOCE mission for the determination of the high frequency part of the gravity field, measures the gravity gradient consisting of the second derivatives of the gravitational potential. To use these measurements in the gravity field determination process, a mathematical model has to be established that links the particular observations to the gravity field parameters. The unknown gravity field parameters are then determined by a least-squares adjustment procedure. Therefore, the gravity field has to be parameterized in terms of basis functions. In the approach presented here, a global reference solution, parameterized by spherical harmonics is refined by regional solutions modeled by spherical splines as space localizing basis functions. The design of these basis functions will be described in Sect. 2.1. When solving the system of normal equations, special emphasis is put on the ill-posedness of the downward continuation process

that is inevitable when dealing with satellite data and aiming at the determination of the gravity field on the Earth's surface. The use of space localizing basis functions offers the opportunity to regionally adapt the necessary regularization process as will be explained in Sect. 2.2.

The observations are given in the reference frame of the gradiometer (GRF), oriented along the three axes of the gradiometer instrument with origin in the nominal intersection of the three one-axis gradiometers. In contrast to that, the gravity field representation is formulated in an Earth-fixed reference frame (ITRF) with its origin located in the geocenter, z-axis directed to the pole, x-axis fixed in the equatorial plane in the direction of the Greenwich meridian, and y-axis as completion to a right-handed system. Therefore, the observation equation has to be transformed from the ITRF into the GRF.

In a real data analysis, the influence of non-gravitational forces have to be corrected for. These disturbing forces, such as tides (direct tidal forces of sun and moon, ocean tides, Earth tides polar tides) and short periodic variations of atmospheric masses and the reaction of the ocean to theses masses, can be approximated by appropriate models. In anticipation of being able to process real GOCE observations in the near future, these background models have been implemented in the software and have been used for real-data GRACE analysis as well. In the simulation scenario described in Chap. 3 they have not been considered for simplification.

2.1 Basis Functions

As mentioned above, the parameterization of the gravitational potential is performed in terms of spherical harmonics for the global solution, in case of a regional gravity field recovery the potential has to be parameterized by space localizing basis functions. The gravitational potential $V(\mathbf{r})$ at a given field point $\mathbf{r}$ can be modeled as a sum of basis functions as follows,

$$V(\mathbf{r}) = \sum_{i=1}^{I} a_i \Phi_i(\mathbf{r},\mathbf{r}_i), \tag{1}$$

with the field parameters a_i arranged in a column matrix and the basis functions located at the nodal point $\mathbf{r}_i$ being denoted by $\Phi_i(\mathbf{r},\mathbf{r}_i)$. These are chosen as isotropic and homogeneous harmonic spline functions (Freeden et al., 1998) and can therefore be expanded into a series of Legendre polynomials,

$$\Phi(\mathbf{r},\mathbf{r}_i) = \frac{GM}{R} \sum_{n=2}^{N} k_n \left(\frac{R}{r}\right)^{n+1} P_n(\mathbf{r},\mathbf{r}_i). \tag{2}$$

R is the mean equator radius of the Earth, r the distance of a field point from the geo-centre, and $P_n(\mathbf{r},\mathbf{r}_i)$ are the normalized Legendre polynomials of degree n. The coefficients k_n define the shape of the basis functions. In our approach these shape coefficients are chosen to ensure that the basis functions become decorrelated

with respect to the inner product in a reproducing kernel Hilbert space defined by the smoothness characteristics of the gravity field as reproducing kernel, for more details see Eicker (2008). This leads to the following choice for the coefficients k_n with σ_n^2 describing the degree variances of the gravity field spectrum,

$$k_n = \frac{\sigma_n}{\sqrt{2n+1}} \qquad \text{with} \qquad \sigma_n^2 = \sum_{m=-n}^{n} c_{nm}^2. \tag{3}$$

The nodal points as locations for the basis functions are generated on a grid by a uniform subdivision of an icosahedron of 20 equal-area spherical triangles. In this way the global pattern of spline nodal points $\mathbf{r}_i$ shows approximately uniform nodal point distribution as illustrated in Eicker (2008). For an overview of regional gravity field parameterizations used in satellite geodesy see for example Schmidt et al. (2007).

The observation equation for gradiometer measurements is obtained by differentiating the potential twice. It reads in case of a regional gravity field refinement,

$$\nabla\nabla V(\mathbf{r}) = \sum_{i=1}^{I} a_i \nabla\nabla \Phi_i(\mathbf{r},\mathbf{r}_i). \tag{4}$$

2.2 Regionally Adapted Regularization

Due to the ill-posedness of the downward continuation process the solution has to be regularized. Here the Tikhonov regularization has been applied and the regularization parameter has been determined by means of variance component estimation as proposed by Koch and Kusche (2001).

The process of variance component estimation yields the optimal regularization parameter under consideration of the given signal-to-noise ratio. In case of a regional gravity field determination, this results in one regularization parameter tailored optimally to the respective recovery region. This is an improvement in comparison to a global gravity field parameterization which allows only one regularization factor for the complete Earth, resulting in an overall mean damping of the gravity field features. But even within smaller geographical areas, the gravity field features may vary significantly. Therefore, it seems reasonable to further adapt the regularization procedure. The proposed approach does not take into account only one regularization matrix with one associated regularization parameter per region, but allows several matrices with respective parameters $\frac{1}{\sigma_i^2}$,

$$\mathbf{N} = \frac{1}{\sigma_\varepsilon^2}\mathbf{A^T P A} + \frac{1}{\sigma_1^2}\mathbf{R_1} + \cdots + \frac{1}{\sigma_n^2}\mathbf{R_n}. \tag{5}$$

Here, $\mathbf{N}$ denotes the combined normal equation matrix. The first term on the right hand side contains the accumulated observation equations with the corresponding

variance factor σ_ε^2. For each regional regularization group i, the regularization matrix $\mathbf{R}_i$ is a diagonal matrix featuring a "one" for each regional spline parameter located inside the corresponding region and a "zero" for parameters belonging to basis functions outside the regularization group,

$$R_i(j,j) = \begin{cases} 1 & \text{for} \quad j \text{ inside } i \\ 0 & \text{for} \quad j \text{ outside } i, \end{cases} \tag{6}$$

$$\mathbf{R}_1 + \cdots + \mathbf{R}_K = \mathbf{I}. \tag{7}$$

The possibility of adapting the regularization procedure in this particular way is a unique feature of a field parameterization by space localizing basis functions, as each unknown parameter is related to a particular geographical location. This is an inevitable premise when the elements of the regularization matrix are supposed to be assigned to a certain region. The approach assumes that the original regularization matrix used for a global calculation can be approximated by the unit matrix. This is achieved by the specific choice of the space localizing basis functions as described in Sect. 2.1 and the orthogonality relations emerging from it, as explained in Eicker (2008). The separation of a geographical region into different regularization areas is exemplarily illustrated in Fig. 1. Here the two regularization areas are the continental and the oceanic regions. The separation into land and ocean areas can propose a reasonable choice in certain regions, where the gravity field information over the oceans is significantly less rough compared to the continental areas. In the presence

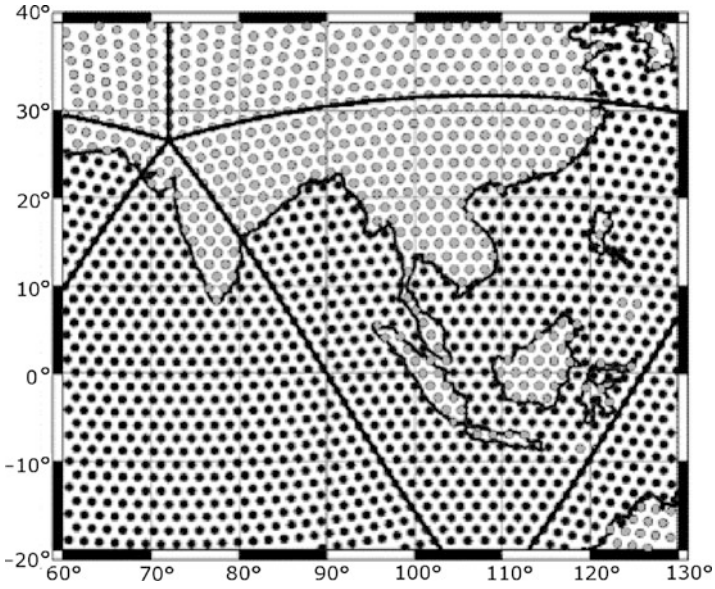

Fig. 1 Two different regularization areas and the location of the unknown parameters belonging to each area

of deep sea trenches or rough ocean bottom topography, however, this might not always be a valid assumption. In this case, different choices for the regularization areas are inevitable.

3 Simulation Scenario

Due to the lack of real GOCE observations, the following calculations were performed in the frame of a simulation scenario. The simulation example is supposed to demonstrate that a regional refinement strategy cannot only be applied to refine global solutions, but it can be utilized to combine different data sets as well. In the scenario at hand, GRACE-observations supposed to be combined with those of GOCE. The GRACE solution serves as the global reference field, as GRACE provides excellent results especially in the long and medium wavelength part of the gravity field spectrum. The regional refinements of this solution are then calculated on the basis of GOCE-like observations, as they cover the short periodic part of the gravity field spectrum with superior accuracy. As additional reference field for the higher frequencies, the OSU91 (Rapp et al., 1991) was introduced from degree $n = 150$ to $n = 300$. An extension of this combination approach is suitable to include terrestrial or airborne gravity data as well.

In order to achieve a consistent data set, both the GRACE and the GOCE solution were calculated from simulated observations on the basis of the EGM96 (Lemoine et al., 1998) up to degree $n = 300$. The observations for GRACE as well as for GOCE were simulated for a period of 30 days with a sampling rate of 5 s. In case of the GRACE satellites, the simulated orbit positions were corrupted by a white noise with a standard deviation of 3 cm and the intersatellite ranges between the GRACE twin satellites with a white noise of 10 μm. Regarding the GOCE satellite, the gradiometer observations were corrupted by a colored noise model with a standard deviation of 1.2 mE. In this model, the power spectrum is assumed as constant in the measurement band of the gradiometer and features increasing energy in the long wavelength part of the spectrum, as the gradiometer is not able to recover these low frequencies. For the satellite positions again an accuracy of 3 cm was assumed. From this simulated data set, first the GRACE solution up to a harmonic degree of $n = 150$ was derived. The analysis of the GRACE data was conducted using the integral equation approach as described in Mayer-Gürr (2006). The regional refinements from GOCE observations were then calculated as residual fields to this global solution. Using a parameterization by splines as space localizing basis functions, the spline kernels are to represent the gravity field features to be determined. Therefore, up to degree $n = 150$, the error degree variances of the (simulated) GRACE solution were applied in Eq. (3) as coefficients in the series expansion of the spline kernel. These error degree variances represent the signal which is still in the data in addition to the GRACE solution. Above degree $n = 150$, the degree variances were approximated by Kaula's rule of thumb. The resulting basis function is displayed in Fig. 2.

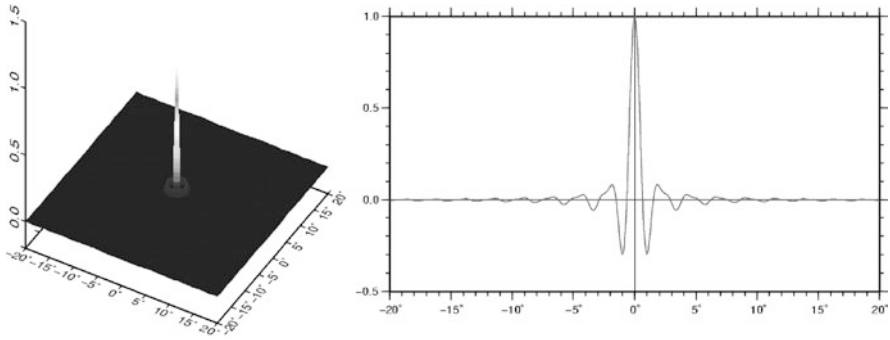

Fig. 2 Spline kernel used in the combined GRACE-GOCE simulation scenario: developed until degree $n = 300$, formal errors of simulated spline solution up to degree $n = 150$, above $n = 150$ Kaula's rule

The basis functions were located at the nodes of a triangular grid with an average nodal point distance of about 74 km. This results in a resolution slightly higher than a spherical harmonic degree of $n = 300$. From the setting described above regional solutions were calculated. The results for an individual regional refinement are displayed in Fig. 3 for the area of the Andes. The figure shows the differences to the pseudo-real field EGM96 in terms of geoid heights.

The comparison was only performed up to degree $n = 240$, because the higher degrees are too strongly corrupted by noise. The left part of the figure shows the result with one uniform regularization parameter determined for the region, the

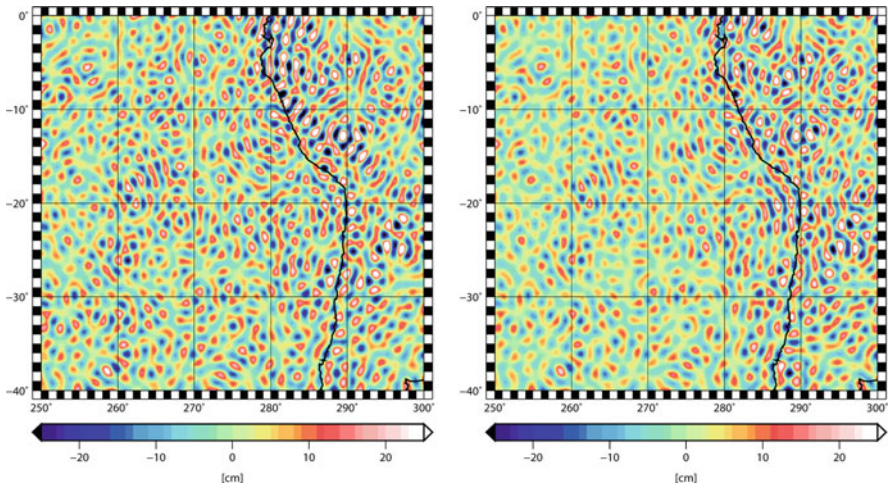

Fig. 3 Differences between spline solution from combined GRACE/GOCE analysis (simulation study) and the pseudo-real field EGM96: one uniform regularization parameter (*left*, RMS: 9.24 cm), two adapted regularization parameters for land and ocean (*right*, RMS: 8.08 cm)

right part demonstrates the improvement that was achieved using the regionally refined regularization procedure described in Sect. 2.2 with adapted regularization for ocean and continental area. The RMS value is reduced from 9.24 to 8.08 cm. This corresponds to an improvement of 12.5%.

Subsequently, regional refinements were calculated covering the complete surface of the Earth, with an overlapping border of 10° having been taken into account at the boundaries to avoid truncation effects. The individual patches have a size of $\Delta\lambda = 40° \times \Delta\varphi = 50°$, complemented by two spherical caps with an aperture angle of 30° covering the poles. The pattern of the refinement regions is illustrated in Fig. 4. It leads to a number of about 5,000–9,000 spline parameters to be determined for each region, the size of the patches being limited by storage restrictions.

From the individual spline solutions the gravity field functionals were predicted to the nodes of a Gaussian grid with a spacing of $\Delta\lambda = 0.5°$. From the global field, a spherical harmonics expansion was calculated using the Gauss-Legendre quadrature, for the specific grid and the respective quadrature method see, for example, Stroud and Secrest (1966) or Sneeuw (1994). For the global solution, again compared up to degree $n = 240$, the global RMS amounts to 6.51 cm, including the poles. Only the solution with the adapted land/ocean regularization is presented in Fig. 4, as on a global scale the differences between the use of one or two regularization parameters are not easily detectable. The problem arises that for many of the patches the choice of continental and oceanic regions does not pose an ideal option. Here a more tailored adjustment of the regularization areas would be advisable.

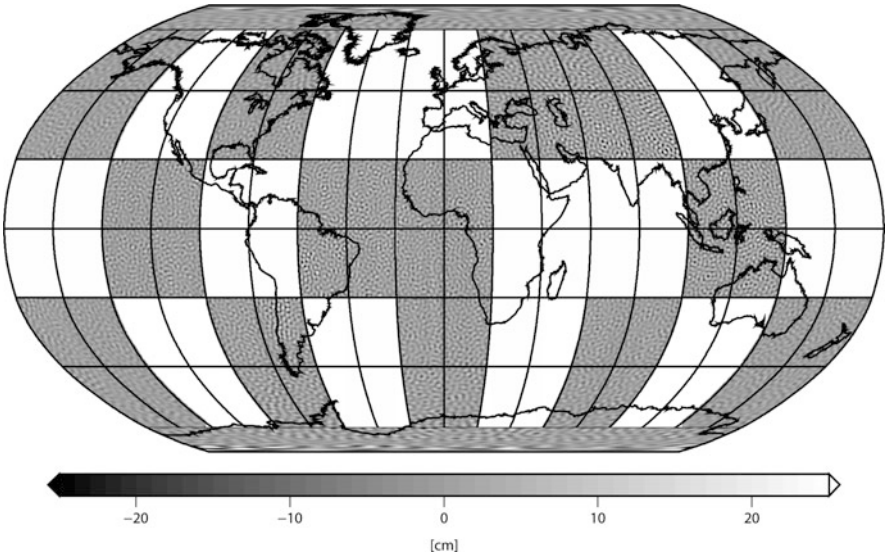

Fig. 4 Individual refinement patches, differences in geoid heights between combined GRACE/GOCE solution and EGM96, RMS for global coverage: 6.51 cm

4 Conclusions

The concept of taking a global solution and calculating regional refinements to the global solution presents an elegant method of combining different data sets. The lower resolution data set can serve as global reference, and observations with assumed higher resolution can be exploited for the regional refinements. The regularization parameters are determined individually for different geographical areas by variance component estimation. With this procedure the regularization parameter is optimally chosen according to the given signal-to-noise ratio in the respective regularization area. In this way the dampening can be adjusted in accordance with the residual signal content (i.e. the information additional to the global reference solution).

It shall be pointed out that the direct computation of the spherical harmonic coefficients by solving the improperly posed downward continuation cannot provide a stable solution up to an (arbitrarily) high degree as it can be achieved by means of the quadrature method. Finally, the regional recovery procedure offers a chance to deal with the polar gap problem in a tailored way, as in regions without any data the regional refinement can either be skipped or the regularization parameter can be adjusted accordingly.

Acknowledgements The support by BMBF (Bundesministerium fuer Bildung und Forschung) and DFG (Deutsche Forschungsgemeinschaft) within the frame of the Geotechnologien-Programm is gratefully acknowledged.

References

Eicker A, Mayer-Gürr T, Ilk KH (2004) Global gravity field solutions based on a simulation scenario of GRACE SST data and regional refinements by GOCE SGG observations. Proceedings of the International Conference Gravity, Geoid and Space Missions – GGSM2004, 2004 August 30–September 3, Porto, Portugal.

Eicker A (2008) Gravity field refinement by radial basis functions from in-situ satellite data. Dissertation University of Bonn. URN: urn:nbn:de:hbz:5N–13754, URL: http://hss.ulb.uni-bonn.de/diss_online/landw_fak/2008/eicker_annette.

ESA (1999) Gravity field and steady-state ocean circulation mission. Reports for Mission Selection, ESA, SP-1233(1). European Space Agency Publications Division, Nordwijk.

Freeden W, Gervens T, Schreiner M (1998) Constructive Approximation on the Sphere. Oxford University Press, Oxford.

Koch KR, Kusche J (2001) Regularization of geopotential determination from satellite data by variance components. J. Geod. 76(5), 259–268.

Lemoine FG, Kenyon SC, Factor JK, Trimmer RG, Pavlis DS, Chinn NK, Cox CM, Klosko SM, Luthcke SB, Torrence MH, Wang YM, Williamson RG, Pavlis EC, Rapp RH, Olson TR (1998) The Development of the Joint NASA GSFC and NIMA Geopotential Model EGM96. NASA Goddard Space Flight Cent., Greenbelt, MD.

Mayer-Gürr T (2006) Gravitationsfeldbestimmung aus der Analyse kurzer Bahnbögen am Beispiel der Satellitenmissionen CHAMP und GRACE. Dissertation at the University of Bonn. URN: urn:nbn:de:hbz:5N–09047, URL: http://hss.ulb.uni-bonn.de/diss_online/landw_fak/2006/mayerguerr_torsten

Rapp RH, Wang YM, Pavlis NK (1991) The Ohio State 1991 geopotential and sea surface topography harmonic coefficient models. Number 410 in Reports of the Department of Geodetic Science. Ohio State University (OSU), Columbus, OH.

Reigber C, Schwintzer P, Lühr H (1999) The CHAMP geopotential mission. Boll. Geof. Teor. Appl. 40, 285–289.

Schmidt M, Fengler M, Mayer-Gürr T, Eicker A, Kusche J, Sanchez L, Han SC (2007) Regional gravity modeling in terms of spherical base functions. J. Geod. 81(1), 17–38.

Sneeuw N (1994) Global spherical harmonic analysis by least squares and numerical quadrature methods in historical perspective. Geophys. J. Int. 118, 707–716.

Stroud AH, Secrest D (1966) Gaussian Quadrature Formulas. Prentice Hall, Englewood Cliffs, NJ.

Tapley BD, Bettadpur S, Watkins M, Reigber CH (2004) The gravity recovery and climate experiment: mission overview and early results. Geophys. Res. Lett. 31, L09607, doi: 10.1029/2004GL019920.

Quality Evaluation of GOCE Gradients

Jürgen Müller, Focke Jarecki, Insa Wolf, and Phillip Brieden

1 Cross-Over Analysis

The first ESA Earth Explorer Core Mission GOCE (Gravity Field and Steady-State Ocean Circulation Explorer) entered the operational measurement phase in September 2009. Before gravity field processing, the quality of the GOCE gradients has to be assessed. Here, two procedures have been developed in Hanover, the mutual comparison and analysis of observed gradients in satellite track cross-overs and the application of terrestrial gravity data which are upward continued and transformed into reference gradients for the GOCE observations. As shown in Jarecki et al. (2006), comparison of the gravity tensor elements in satellite ground track cross-overs ("XO analysis") offers a good opportunity to validate the gradients measured by a satellite gravity gradiometer. There, closed loop results are presented, with accuracies fitting well into the margins of the overall GOCE gradiometer performance. The radial tensor component can be reproduced with an accuracy of better than 3 mE, just using the un-filtered measurements in corresponding track parts and a recent high-resolution geopotential model like the combined GRACE/terrestrial model (e.g. EIGEN-GL04C, Förste et al., 2006). The XOs are identified by a measurement oriented search algorithm (independent of the predicted orbit characteristics) resulting in the actual position of the ground track crossing. Gradiometer measurements and auxiliary data are interpolated into the position of the XO along each of the crossing orbit tracks. Gradient differences from differing orbit altitudes and orientations of the measurement reference frame are reduced by applying the geopotential model (and auxiliary data). These closed loop tests show, that residual gradient differences in the XO can be assigned to measurement errors, as they should vanish in the absence of noise and systematic errors. Such noise and systematic errors have been modelled for the integrated gradiometer (single components of the system, like specific accelerometers, are not treated separately)

J. Müller (✉)
Institut für Erdmessung, Leibniz Universität Hannover, 30167 Hannover, Germany
e-mail: mueller@ife.uni-hannover.de

F. Flechtner et al. (eds.), *System Earth via Geodetic-Geophysical Space Techniques*, Advanced Technologies in Earth Sciences, DOI 10.1007/978-3-642-10228-8_21,

by Koop et al. (2002), with model refinements by Denker et al. (2003), as

$$V_{ij}^{\text{meas}}(t) = V_{ij}^{\text{real}}(t) + V_{ij}^{*} + o(t)\, V_{ij}^{*} + V_{ij}{}'t + \sum_{k=1}^{n} a_k \cos(k\omega t) + b_k \sin(k\omega t) + \varepsilon(t). \quad (1)$$

In the XOs, differences of the measured gradients are further investigated. But not all modelled systematic errors project into those XO differences according to Eq. (2). Temporally constant or, due to the relation to a discrete point on the earth sphere, locally constant features $V_{ij}{}^{*}$ vanish. The first vanishes because of the relative nature of this internal validation approach, the latter could also be characterised as some kind of geographical signal (and therefore not as measurement error). Constant biases $V_{ij}{}^{*}$, which are not present in the whole time series investigated $o(t) \neq \text{const}$, can project into the XO differences. A linear trend $V_{ij}{}'$ projects linearly (with the measurement time difference $\Delta t_{\text{XO}} = t_2 - t_1$ in the XO) into the investigated value $\Delta V_{ij}{}^{\text{meas}}$. Fourier harmonics $a_k \cos(k\omega t) + b_k \sin(k\omega t)$ sum up to combined terms and are still present in the gradient differences. Contrary to the trend (and polynomial parameters of higher degree) where only time differences Δt_{XO} show up, they carry absolute time information into the differences, modelled as t_1 and t_2. The noise parameter $\epsilon(t)$ represents the stochastic noise. Thus, the following systematic parts of the gradients' differences remain in the XOs:

$$\begin{aligned} \Delta V_{ij}^{\text{meas}} = {} & \big(o(t_2) - o(t_1)\big)\, V_{ij}^{*} + V_{ij}{}'\, \Delta t_{XO} \\ & + \sum_{k=1}^{n} a_k \big(\cos(k\omega t_1) - \cos(k\omega t_2)\big) + b_k \big(\sin(k\omega t_1) - \sin(k\omega t_2)\big). \end{aligned} \quad (2)$$

Consequently, the XO approach is (only) capable to detect three kinds of systematic errors, namely linear trends (and polynomial drifts), Fourier-type periodic disturbing effects and biases which are only present in short parts of the data (called Short Term Biases). The latter may reach from single outliers (affecting just one special measurement) to larger portions of the data set under investigation.

In the following sections, it will be discussed if and under which conditions those systematic errors can be detected, and which approaches might be used to get robust, accurate and reliable results. The studies are shown for the tensor component V_{zz}, for the ease of formulation and readability, but similar results are achieved for the other diagonal and off-diagonal tensor components.

1.1 Short Term Biases

Biases which are not present in the whole data set (called sequential outliers) project into XO gradient differences in contrast to biases affecting the whole data set. In the first case there is some data left which can be considered as "reference data". The amount and the coverage (and, of course, the quality) of reference data is the main criterion to decide, whether the detection of outliers and short term biases works: On the one hand, there has to be enough reference data to intersect with the erroneous part of the track at all. On the other hand, shorter erroneous parts of the track (leaving more correct reference data) might be hidden between the single XOs, especially

Table 1 Single and sequential outliers as detected with the XO method when a threshold is applied to the XO differences of the tensor component V_{zz}. The 30 d 1 Hz input data have been superposed by 4,400 single outliers of 10 mE affecting 1,633 XOs and by three series of sequential outliers (10 and 15 mE) affecting 6,045 XOs. Type 1 error indicates the rate of theoretically detectable outliers not detected, while type 2 error means false alarms

	No. of alarms		Error (%)	
Threshold	Total	Correct	Type 1	*Type*2
Single outliers				
1.5 mE	1,773	1,399	14.3	22.9
2 mE	1,508	1,152	29.5	21.8
Sequ. outliers				
1.5 mE	6,018	6,001	0.72	0.28
2 mE	6,007	6,001	0.72	0.09

in the mid latitudes where the XO coverage is sparse. The latter problem becomes especially clear, when dealing with single outliers. Those single erroneous gradients cannot be detected by the XO method, if they appear in parts of the track, where no crossing arc is present. Moreover, even if they affect an XO, it cannot be determined which of the four (in case of linear interpolation) measurements contributing to the XO is the erroneous one.

The capability of the XO approach can simply be tested by applying a threshold to gradient differences, where artificial outliers in single values of V_{zz} are added or V_{zz} is disturbed constantly during single revolutions of the satellite track. In a test case (see Table 1) roughly 4,400 single outliers were artificially introduced in a simulated 30 d 1 Hz V_{zz} GOCE test data set. Of the 1,633 affected XOs, nearly 30% remained undiscovered or led to false alarms. While the errors of type 1, undiscovered outliers, can be reduced by carefully choosing the threshold (and most likely by using a more sophisticated test method), the type 2 errors, or false alarms, seem to remain in the same range when changing the threshold. This is due to the threshold being chosen close to the accuracy of the measurements themselves. The detection of sequential outliers works much more effectively and is not as sensitive to the choice of the threshold. This is mainly due to the structure of the outliers, which affect all the measurements used in the XO interpolation and therefore severely project into the XO difference.

For single outlier detection, the detection mode should be more sophisticated to significantly identify most outliers. Another important improvement would be the identification of a single erroneous measurement rather than a suspicious XO, e.g., by changing the interpolation algorithm systematically. Those refinements were not planned for the present study, as other methods, like along-track interpolation (see Bouman and Koop, 2003) show complementary behaviour and are recommended (and adopted in the official GOCE processing) for use in outlier detection.

1.2 Trend

According to Eq. (2) a linear trend projects linearly into the XO gradient differences with respect to the measurement time differences and independently of the

Table 2 Statistics of estimated trend factors for all 475 ascending arcs from least-squares and from robust estimation on the basis of XO differences from different time spans

XOs with tracks from		Mean trend (mE/d)	Abs. error (mE)	Std (mE/d)	Min trend (mE/d)	Max trend (mE/d)
30 days	Least squares	6.7979	0.0005	0.0014	6.7033	6.9407
	Robust	6.7974	0.0000	0.0001	6.7967	6.7980
10 days	Least squares	6.7994	0.0020	0.0330	6.6339	7.1368
	Robust	6.7974	0.0000	0.0001	6.7971	6.7978
1 day	Least squares	6.7992	0.0018	0.0168	6.7742	6.9150
	Robust	6.7975	0.0001	0.0001	6.7972	6.7977

actual measurement epochs. Therefore, all XOs contribute to the determination of a single (constant) trend factor. Consequently, its determination is possible with high accuracy and reliability, when large data sets are used. Dealing with shorter data sets, single outliers might severely affect the standard least-squares estimation of a trend parameter. This is a typical example for the application of robust estimation methods (Huber, 1981). The formal application of the Huber approach for trend estimation from XO differences has been described in Jarecki and Müller (2009). There, a robust estimator is successfully applied to estimate (artificial) trend factors for single and half revolution GOCE data sets. Table 2 summarises the benefits of robust trend estimation with respect to short reference data sets. Least-squares estimation gives reasonable (mean) results and a good standard deviation for the trend factor (introduced as 6.7974 mE/d) when using all 30 d of test data. Taking just the XOs from the surrounding day(s) produces larger deviations and absolute estimation errors. However, trend factors from robust estimation fit very well and deviate less. In Fig. 1, the estimated trend factors for each of the 475 ascending arcs of a 30 d test data set is shown, as estimated with the least-squares and robust

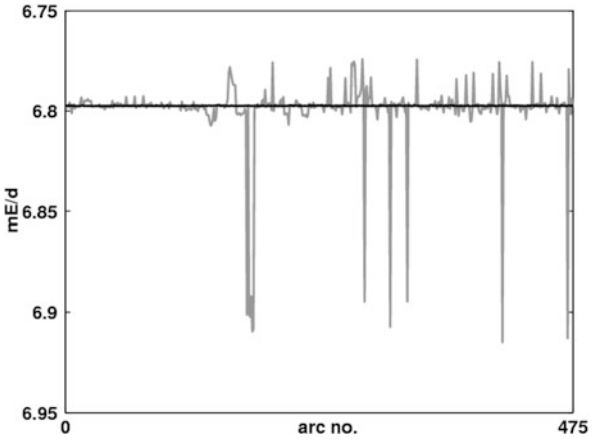

Fig. 1 Estimated trend factor for each of the 475 ascending arcs of a 30 d test data set with an artificial trend of 6.7974 mE/d superposed. The estimates are based on XO differences from 1 day of surrounding data. Robust results are shown in *black*, least-squares results in *grey*

approach, using 16 XOs. While several least-squares estimates obviously suffer from outliers in the reference data, the robust estimates look smooth and correct. A change in trend factors would easily be observable in the timeline of arc-wise estimates.

The long-term trend estimation assesses the overall coherence of the data set, but neglects time-variable physical effects on the measurements. Repeated determination of trend factors for short parts of the data and their comparison is a fast and easy method to monitor the behaviour of the measurement system. Robust trend estimation provides those features and will be applied in the GOCE project as part of the validation activities of the CalVal-Team (ESA, 2006).

1.3 Fourier Coefficients

Periodic systematic errors do not project directly into the gradient differences, i.e. their effect is not independent from the measurement epoch and therefore they give a different feature in XO gradient differences. Nevertheless, they can be represented in a linear model (assuming fixed frequencies) and estimated as well by standard least-squares or with robust methods. Thus, the results from the trend part regarding overall data quality assessment and instrument monitoring also hold for low-degree Fourier coefficients, e.g., up to degree four (Bouman et al., 2004). Medium and high degree coefficients on the other hand, which would be valuable to gain information about the gradiometer's performance in its highly accurate measurement bandwidth MBW (5–100 mHz), are not accessible via this way. As all coefficients up to the desired degree (100 mHz means approx. $n = 500$ based on complete cycles) have to be estimated in the complete Fourier decomposition, large numbers of XO differences had to enter the computation. Short data sets as adopted for the revolution-wise trend monitoring do not deliver such a big amount of data. Consequently, a repeated estimation of Fourier coefficients in the MBW is not possible. But in principle, global assessment of the gradiometer performance in the MBW is possible from rather long data sets. This is illustrated in Fig. 2, where the amplitudes for the (revolution based) Fourier frequencies 1–110 cpr are plotted, as estimated from 500 or 20,000 XO differences, respectively. In a pre-processing step, both, the simulated measurements of V_{zz}, which have been superposed by a perturbation of 100 cpr which is in the MBW, and the applied reductions have been filtered with a bandpass butterworth filter to cut out the signal content in the MBW. To filter the time-independent reductions, they have been computed from differences of another time series of simulated V_{zz}. This is a straightforward method to deal with the problem of filtering the reductions. Figure 2 shows the disturbing signal clearly and significantly detected even with less "reference data". But to rely on the absolute amplitude estimated and to suppress wrongly estimated signals in the longer wavelengths, much more data is needed. Finally, even the amplitude calculated from 20,000 XO differences is off by about 10% but at least the (non-existing) signals in the other frequencies vanish.

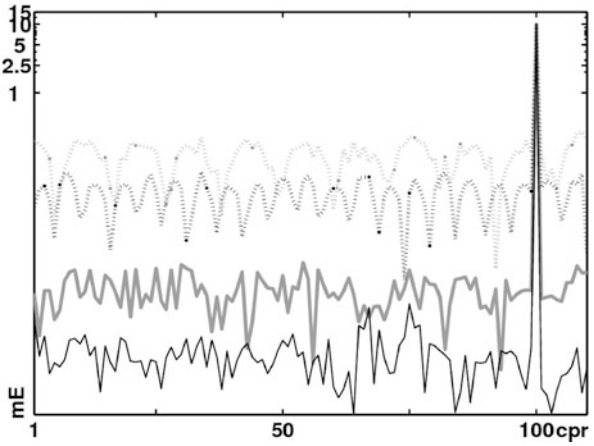

Fig. 2 Fourier amplitudes (1–110 cpr) estimated from 500 (*grey*) and 20,000 (*black*) V_{zz} XO differences with standard least squares (*dotted*) and robust methods (*solid lines*). Measurement and reduction data have been filtered to cover the MBW. A superposed disturbing signal of 100 cpr is detected significantly, even in case of sparse XO data while the lower frequencies are misfits (note the logarithmic scale)

2 Accuracy Analysis of External Reference Gradients in the Frequency Domain

To prove the planned accuracy level, the gradiometer measurements will be calibrated and validated internally and externally. Internal calibration will be performed by industry and ESA. External evaluation is done by comparing measured gradients with reference data, where we worked in the frequency domain, as it easily allows a comparison with the given baseline accuracy. Here, the highest accuracy level of the gradiometer within the MBW is 11 mE/$\sqrt{\text{Hz}}$, valid for the sum of the main diagonal components of the gravitational tensor (1 mE $= 10^{-12}$ 1/s^2). We took this value as worst case assumption for single tensor components, too.

One strategy of an external evaluation includes the use of gravity data on ground upward continued to satellite altitude (e.g., Bouman et al., 2004; Denker, 2003; Pail, 2003; Wolf, 2007). The evaluation can only be applied regionally, because sufficiently accurate ground data are only available for selected areas. Therefore, a global potential model, representing the long wavelength part, is introduced in a remove-restore procedure. The error estimation for the external reference data is carried out empirically in a synthetic environment permitting closed-loop validation in all points.

2.1 Spectral Combination Method

In the present study, the radial tensor component V_{zz} is computed using integral formulas, see Wolf (2007) for the other five components. In the following the

tensor component V_{zz} is considered with respect to the disturbing potential T as T_{zz}. Applying the remove-restore technique residual gravity anomalies $\Delta g^{\mathrm{R}} = \Delta g^{\mathrm{T}} - \Delta g^{\mathrm{M}}$ as differences between the terrestrial gravity anomalies Δg^{T} and those from a geopotential model Δg^{M} are used in the computations. The resulting residual tensor component $\hat{T}^{R}_{zz}$ has to be restored using again the GPM ($\hat{T}^{M}_{zz}$): $\hat{T}_{zz} = \hat{T}^{M}_{zz} + \hat{T}^{R}_{zz}$.

Integral formulas with spectral weighting are applied to combine regional terrestrial gravity data with a geopotential model for the computation of the tensor component based on the remove-restore procedure. For more theoretical details see Wolf (2007). The spectral weights are based on the error degree variance information of the GPM and of the terrestrial gravity data.

2.2 Synthetic Data

The input data (Δg^{T}, Δg^{M}) and the output data ($T_{[ij]}$) are based on a synthetic Earth model composed of a Digital Topography Model (DTM) and a GPM. Simulated noise is added to the input data. The ground-truth GPM (SYNGPM1300S) consists of the EIGEN-GRACE02S ($n = 2\ldots104$, Reigber et al., 2005), the EGM96 ($n = 105\ldots360$, Lemoine et al., 1998) and the GPM ($n = 361\ldots1{,}300$, Wenzel, 1999). The characteristics of the synthetic scenarios are chosen based on a statistical accuracy estimation using least-squares estimation (Wolf, 2007). From the SYNGPM1300S, the test data sets are derived. The gravity anomalies Δg^{M} are based on the SYNGPM1300S up to a spherical harmonic degree $n_{\max} = 360$, the appropriate noise is generated according to the coefficients' standard deviations of the SYNGPM1300S. For the terrestrial data Δg^{T}, the complete synthetic model is used and different noise scenarios are investigated: 1 mGal uncorrelated (1UC), 1 mGal correlated (1C) and 5 mGal correlated (5C).

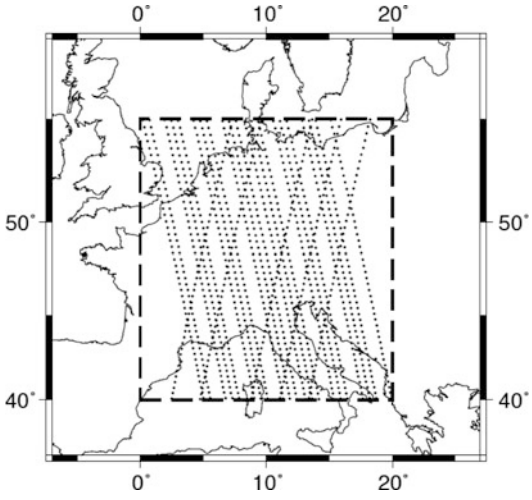

Fig. 3 A number of 26 tracks from a 29-days global data set cover the test area

The test area is located in Central Europe (Fig. 3), the data sets are computed in a 0.1° geographical grid. The spectral signal content of the synthetic data is limited to a resolution of about 8′ ($n_{\max} = 1{,}300$). The synthetic gravity data represent gravity anomalies reduced from the gravitational effect of a residual terrain model (RTM reduction). The gravity anomalies Δg^{T} have a mean signal content of 10.07 $\pm$ 33.36 mGal, the tensor values 2,747.107 $\pm$ 0.187 E.

2.3 Closed-Loop Differences in the Frequency Domain

The differences between the tensor component values directly computed from the SYNGPM1300S and the values derived from the noisy synthetic gravity anomalies (Δg^{M}, Δg^{T}) are analysed in an inner area (marked in Fig. 3) to avoid edge effects. For the frequency domain analysis, the following steps are performed:

(a) computation of all tensor components in points of a three dimensional grid (spherical surfaces with a 6′ data grid; 5 km height difference between each interpolation level),
(b) interpolation into points of a simulated GOCE orbit (SCVII, 2000) using a cubic spline approach,
(c) rotation of the tensor into the gradiometer reference frame (according to ESA, 2006),
(d) derivation of closed-loop differences with error-free tensor values (directly computed from SYNGPM1300S),
(e) computation of the spectral densities from the times series based on the closed-loop differences.

Due to the limited regional data area, only parts of the GOCE tracks can be evaluated. Within the test area, a number of 26 tracks from a global 29-days time series cover each at least a time span of 225 s (Fig. 3).

In Fig. 4 the spectral density (for V_{zz}) of the simulated noise of the synthetic GPM based on the global time series (grey) is compared with the spectral density computed as mean curve from the 26 tracks (black). Within the MBW (dark grey box) the track-wise computed spectral density can be used as approximation of the global one. The solid lines in white mark the accuracy level of 7 and 11 mE/$\sqrt{\mathrm{Hz}}$, respectively. The white dashed lines mark the interesting frequency band for GOCE. The line at 0.019 Hz corresponds to a spherical harmonic degree 105. The peak formed by the spectral density based on the global times series is caused by the much higher noise of the SYNGPM1300S in this frequency band resulting from the EGM96. A similar peak can also be found in the spectral density curve when the noise simulation is based on the accuracy of the EIGEN-GL04C, the current combination model from GRACE, altimetry, terrestrial and other data (Förste et al., 2006). The line at 0.036 Hz corresponds to a spherical harmonic degree of 200. Here, the signal of the tensor components approaches zero at GOCE altitude and the noise decreases, too.

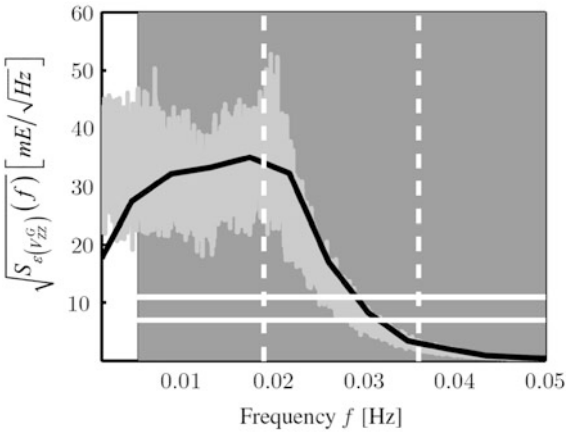

Fig. 4 Spectral densities of simulated noise in V_{zz} of the synthetic GPM based on the global time series (*light grey*) and based on the 26 tracks (*black*)

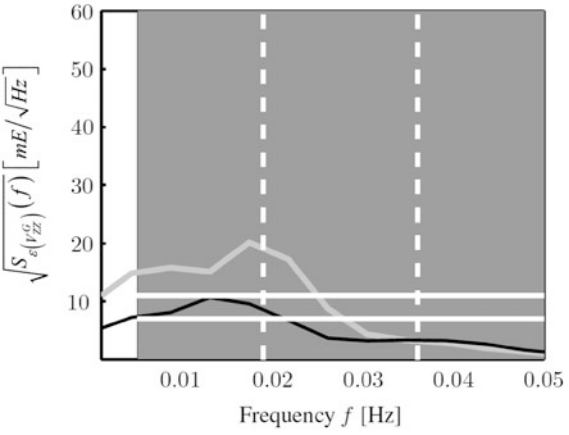

Fig. 5 Spectral densities of the remaining noise in V_{zz} from the combined solution adding terrestrial data to the GPM information. Scenario 1C in *black*, scenario 5C in *light grey*

In Fig. 5 the spectral density of the remaining noise in V_{zz} based on the combined solution using the GPM and terrestrial data with a noise level of 5 mGal (5C, light grey) and with a noise level of 1 mGal (1C, black) are shown. The curves are clearly closer to zero than the spectral density based on the pure GPM solution. In scenario 1C the required accuracy (the Laplace threshold of 11 mE/$\sqrt{}$Hz is indicated as upper white solid line) can be reached. This holds for the other tensor components as well, for detailed figures see Wolf (2007).

3 Generation of Quality Reports

To document the quality of the investigated GOCE gradients' measurements, the results of both analysis procedures discussed above are represented in dedicated quality reports. Those reports are implemented according to the ESA (2006) and shall be included in the frame of the CMF activities as auxiliary validation tool.

The performance of the input data (tensor elements, position, velocity, time and orientation information) is monitored by calculating and representing XO differences, parameters of the error model according to Sect. 1 and some statistical measures. The double-computation of XOs that have already been computed in the past is avoided by strict distinction of "new data" and "reference data". Within the "new data" XOs have to be searched in crossings of new ascending and descending arcs. In addition, XOs also result from the combination of "new arcs" and already validated "reference arcs". While the first group assesses the internal quality of the newly obtained data, the second group validates all data on a long-term basis. Thus, potential "wrong measurements" can be identified. The quality report is divided into four parts:

(a) All essential data files in the computation flow, the used reduction model (see Jarecki et al., 2006) as well as applied thresholds are represented.
(b) The operational procedures in the calculation (e.g., selected models, algorithms, codes) are documented.
(c) The most important part of the report comprises the results for the XO differences of the six components of V_{ij}. To trace their quality behaviour, general statistics of all XOs is illustrated. The differences of the gravity gradients at each XO are also reported with respect to the contributing orbit.
(d) In addition, the fourth part summarizes statistics, where XO differences that belong to a certain portion of the orbit (like each single arc) are analyzed. Here, ascending and descending arcs as well as XOs from "new data" and "reference data" are distinguished. Also a trend and several Fourier coefficients (e.g., up to degree four) are estimated. Moreover, a plot of each data set under evaluation and its XOs is generated, see Fig. 6.

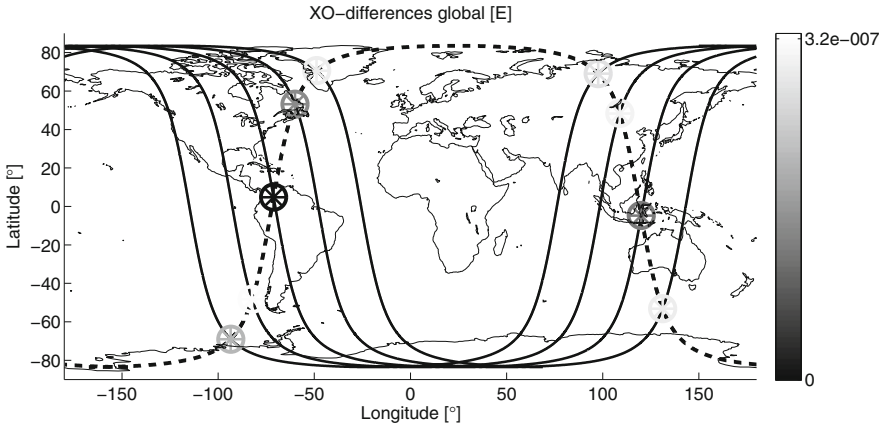

Fig. 6 Ground tracks of nine arcs of "reference data" (*solid line*) and two arcs of "new data" (*dashed line*). The cross-overs (XOs) are indicated with *asterisk-in-circle* symbols that are *gray-coded* with respect to the XO difference in V_{zz}

Similar reports are generated for the differences of observed GOCE gradients and reference gradients based on upward-continued terrestrial gravity data as described in Sect. 2. There, (a) and (b) correspond to the XO case, (c) represents the quality of the upward-continued terrestrial data, and (d) provides the relevant information for the gradients' differences.

4 Conclusions

Cross-over analysis is a helpful tool for monitoring the quality of the GOCE gradients at the required accuracy level during data acquisition. In addition, a selection of so-called calibration parameters can be determined, where, however, the investigated data span and the kind of the parameter (bias, trend, periodic term) plays a significant role.

From upward (and transformed) terrestrial gravity data, highly accurate reference gradients in GOCE altitude can be obtained. Our study shows that the remaining noise of the computed reference values of the tensor component V_{zz} is well below the required accuracy level of 11 mE/$\sqrt{\text{Hz}}$ for the Laplace condition when combining recent global potential models with RTM reduced terrestrial gravity data having a noise level of better than 1 mGal.

The performance of the GOCE gradients as obtained by applying the two discussed procedures is monitored in special quality reports. There, the latter method delivers information about the overall spectral quality of the gradients, whereas the first method indicates an anomalous behaviour of the gradiometer.

References

Bouman J, Koop R (2003) Error assessment of GOCE SGG data using along track interpolation. Adv. Geosci. 1, 27–32.

Bouman J, Koop R, Tscherning CC, Visser P (2004) Calibration of GOCE SGG data using high–low SST, terrestrial gravity data and global gravity field models. J. Geod. 78(1–2), 124–137.

Denker H (2003) Computation of gravity gradients over Europe for calibration/validation of GOCE data. In: Tziavos IN (ed.), Proceedings of IAG International Symposium "Gravity and Geoid", Thessaloniki, Greece, Aug 26–30, 2002, pp. 287–292.

Denker H, Jarecki F, Müller J, Wolf J (2003) Calibration and validation strategies for the gravity field mission GOCE. Status Seminar "Observation of the System Earth from Space", Geotechnologien Science Report, No. 3, Potsdam, pp. 32–35.

ESA (2006) GOCE Calibration & Validation Plan for L1b Data Products. EOP-SM/1363/MD-md, ESTEC, Nordwijk.

Förste C, Flechtner F, Schmidt R, König R, Meyer U, Stubenvoll R, Rothacher M, Barthelmes F, Neumayer KH, Biancale R, Bruinsma S, Lemoine J-M (2006) A mean global gravity field model from the combination of satellite mission and altimetry/gravimetry surface gravity data. Geophy. Res. Abstr. 8, 03462.

Huber PJ (1981) Robust Statistics, John Wiley, New York.

Jarecki F, Wolf KI, Denker H, Müller J (2006) Quality assessment of GOCE gradients. In: Flury J et al. (eds.), Observation of the Earth System from Space, Springer, New York, pp. 271–285.

Jarecki F, Müller J (2009) Robust trend estimates from GOCE SGG satellite track cross-over differences. In: Sideris M (ed.), Observing Our Changing Earth. IAG Symposia 133, Springer, New York, pp. 363–370.

Koop R, Bouman J, Schrama EJO, Visser P (2002) Calibration and error assessment of GOCE data. In: Adam J et al. (eds.), Vistas for Geodesy in the New Millenium. IAG Symposia 125, Springer, New York, pp. 167–174.

Lemoine FG, Kenyon SC, Factor JK, Trimmer RG, Pavlis NK, Chinn DS, Cox CM, Klosko SM, Luthcke SB, Torrence MH, Wang YM, Williamson RG, Pavlis EC, Rapp RH, Olson TR (1998) The Development of the Joint NASA GSFC and NIMA Geopotential Model EGM96, NASA/TP-1998-206861. Technical Report, NASA, Greenbelt, MD.

Pail R (2003) Local gravity field continuation for the purpose of in-orbit calibration of GOCE SGG observations. Adv. Geosci. 1, 11–18.

Reigber C, Schmidt R, Flechtner F, König R, Meyer U, Neumayer K-H, Schwintzer P, Zhu SY (2005) An earth gravity field model complete to degree and order 150 from GRACE: EIGEN-GRACE02S. J. Geodynamics 39(1), 1–10.

SCVII (2000) Simulation Scenarios for Current Satellite Missions. IAG Special Commission VII, http://www.geod.uni-bonn.de/apmg/lehrstuhl/simulationsszenarien/sc7/satellitenmissionen.php (July 13, 2006).

Wenzel H-G (1999) Schwerefeldmodellierung durch ultra-hochauflösende Kugelfunktionsmodelle. ZFV 124(5), 144–154.

Wolf KI (2007) Kombination globaler Potentialmodelle mit terrestrischen Schweredaten für die Berechnung der zweiten Ableitungen des Gravitationspotentials in Satellitenbahnhöhe. Deutsche Geodätische Kommission, Reihe C, Nr. 603.

Validation of Satellite Gravity Field Models by Regional Terrestrial Data Sets

Johannes Ihde, Herbert Wilmes, Jan Müller, Heiner Denker, Christian Voigt, and Michael Hosse

1 Introduction

The gravity field mission GOCE aims at providing the global geoid and gravity anomalies with accuracies of about 1–2 cm and 1 mGal (1 mGal = 10^{-5} m/s^2), respectively, both at a spatial resolution of 100 km (ESA, 1999). For this purpose, a three-axis gravity gradiometer and high-low satellite-to-satellite-tracking from GPS satellites are combined to derive the gravity field information. In this respect, many error sources affect the final GOCE products, and thus the calibration (procedure to achieve "correct" observations) and validation (procedure to assess the quality of end products) are essential tools for reaching the mission goals (Bouman and Koop, 2003). Calibration and validation (cal/val) includes on-ground and in-orbit techniques with internal and external (independent) data.

Within the GOCE-GRAND II project, internal and external cal/val procedures were investigated. Internal cal/val studies included the use of cross-over differences for accuracy and integrity monitoring (chapter "Quality Evaluation of GOCE Gradients" by Müller et al., 2009, this book; Jarecki and Müller, 2007) as well as the utilization of the integrals of motion (Löcher and Ilk, 2007). External cal/val procedures were developed using terrestrial gravity field data and ocean data (chapter "Comparison of GRACE and Model-Based Estimates of Bottom Pressure Variations Against In Situ Global Bottom Pressure Measurements" by Stammer et al., 2009, this book). Further investigations involved upward continued regional gravity field data for the external calibration and validation of the GOCE gravity gradient observations (chapter "Quality Evaluation of GOCE Gradients" by Müller et al., 2009, this book; Wolf, 2007).

In this contribution, the emphasis is put on the development of highly accurate terrestrial data sets for the external validation of the GOCE products. This was also one of the main issues of the regional validation and combination experiment carried out in Germany within the framework of the GOCE-GRAND II project. In this

J. Ihde (✉)
Bundesamt für Kartographie und Geodäsie (BKG), D-60598 Frankfurt am Main, Germany
e-mail: johannes.ihde@bkg.bund.de

F. Flechtner et al. (eds.), *System Earth via Geodetic-Geophysical Space Techniques*, Advanced Technologies in Earth Sciences, DOI 10.1007/978-3-642-10228-8_22,

subproject, two extensive measurement campaigns were performed in order to internally validate the terrestrial data sets and to provide ground truth data for the GOCE mission results.

The Earth's gravity field can be completely described by the gravity vector $\boldsymbol{g}$ and the (scalar) gravity potential W, which after linearization leads to the disturbing potential T and the gravity anomaly and gravity disturbance vectors $\Delta\boldsymbol{g}$ and $\delta\boldsymbol{g}$, respectively. The disturbing potential T can be derived from the solution of the geodetic boundary value problem or from GNSS/levelling in discrete points. In this context, the spectral sensitivity, the data spacing and coverage as well as the noise characteristics of different gravity field parameters are important.

Mostly terrestrial gravity observations and terrain data are available with highest resolution. In Germany, more than 260,000 gravity values exist in data bases. The area coverage varies between one point per 1 km^2 to one point per 25 km^2. The random error is in general smaller than 0.1 mGal and reaches values up to 0.01 mGal for 1st order stations. The existing gravity data bases include measurements from different epochs and instruments and also the data processing was not done in a homogeneous way. Hence, the real accuracy, especially at long wavelengths, is largely unknown. This was also the main reason for absolute gravity control observations at about 100 points over the territory of Germany with an absolute gravity meter A-10. In Sect. 2, the new absolute gravity observations are analyzed and the differences to the existing gravity values from the national data base are reported.

Section 3 describes the GPS/levelling control points available for Germany. The data set includes about 900 GPS/levelling stations, which are more or less homogeneously distributed with spacing of 20–30 km. The GPS/levelling control points are employed for the evaluation of gravimetric geoid computations as well as in combination solutions. An evaluation of different global geopotential models by the national GPS/levelling data set is given at the end of Sect. 3.

Section 4 deals with the development of gravimetric quasigeoid models for Germany with a resolution of about 2 km and the cross-validation with the national GPS/levelling data.

Section 5 includes the results of the second extensive measurement campaign, consisting of about 300 astrogeodetic vertical deflections observed with the zenith camera system TZK2-D. The astrogeodetic results are cross-validated with GPS/levelling data and gravimetric quasigeoid models and the differences between low-pass filtered astrogeodetic vertical deflections and various global geopotential models are presented. As the astrogeodetic vertical deflections are completely independent of all other gravity field data sets, they are quite valuable for manifold validation purposes.

A general problem of the comparisons between point observations and global geopotential models is the different spectral and spatial resolution and sensitivity. In Sect. 6, a validation procedure is proposed for the comparison of point observations with global gravity field models, employing a filter technique based on wavelets.

2 Gravity Data

High quality and high resolution regional gravity data sets are important independent data sources for the validation of the GOCE products. Furthermore, the combination of the terrestrial data with the GOCE global gravity field models will allow to determine the complete gravity field spectrum (all wavelengths) with high accuracy (about 0.01 m for geoid and 1 mGal for gravity). In this connection, a thorough check of the existing gravity data sources with respect to systematic errors (e.g., errors due to the used gravity reference stations, network structure or gravimeter calibrations) and random errors is mandatory (Denker et al., 2007).

Within the project GOCE-GRAND II, Germany is used as a test area for validation and combination experiments. About 260,000 terrestrial gravity observations with a spacing of 2–5 km are available for the territory of Germany at the Bundesamt für Kartographie und Geodäsie (BKG), Frankfurt am Main, and the Institut für Erdmessung (IfE), Leibniz Universität Hannover (see Fig. 1, left). In Germany, a gravity base network (DSGN94) exists, which includes 30 station groups observed with FG-5 absolute gravity meters in 1994/1995 (Torge et al., 1999). This network was densified in the Eastern German states with relative gravimeters by the state survey agencies, yielding the first order network DHSN96 with stations about 30 km apart. In the Western German states older and already existing relative gravity measurements of the DHSN were transformed to the level of the DSGN94 and both are forming the DHSN96.

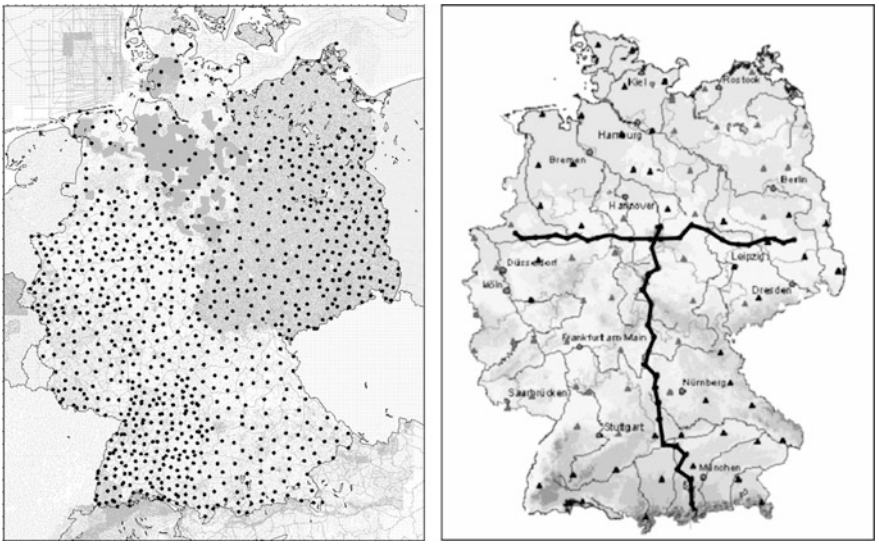

Fig. 1 *Left*: Terrestrial gravity data (*thin dots*) and GPS and levelling control points (*thick dots*) for Germany; *Right*: Gravity control points in Germany observed with absolute gravity meter A-10 (*triangles*) and astrogeodetic profiles (*thick lines*)

Then the 2nd and 3rd order relative networks of the German federal states were mounted to the DHSN96 network. Unfortunately, many of the other available terrestrial gravity data suffers from clear information about the gravity and position reference systems.

In order to check the quality of the terrestrial gravity data base for Germany, spot-checks at 100 evenly distributed stations (see Fig. 1, right) were performed by BKG with two A-10 absolute gravity meters. Purposes of these measurements were detection of systematic errors and level differences within the existing terrestrial gravity data (mainly within 1st order gravity network), because all further measurements are dependent on this hierarchy.

The selected stations are spaced about 60–80 km and cover the entire territory of Germany. Stations are mostly part of the DHSN96 1st order gravity network and all of them are field stations. Hence, an absolute gravity meter of type A-10 had to be employed, as it is the only instrument which can work under field conditions (the more accurate FG-5 instruments works only under laboratory conditions).

The A-10 accuracy was specified by the manufacturer as 10 μGal (1 μGal = 10^{-8} ms^{-2}) for an observation time of about one hour, but it was found that it can be increased by the following special measurement procedure and certain accuracy criteria: On each site, two instrument set-ups in opposite directions (North and South) were used to check for gross errors. The differences between both set-ups should not exceed a value of 8 μGal. Furthermore, the entire observation procedure was examined and optimized with respect to the number of measured drops and sets as well as a proper instrument setup, wind shielding and power supply.

The frequencies of the HeNe-laser of the A-10 gravimeter were checked on a regular basis at BKG using an iodine stabilized HeNe-laser and the Rubidium frequencies were compared with the Cs-frequency standard at BKG to monitor long-term stability of instrumental standards.

In order to check the accuracy of the A-10 instruments over the total project time span, comparisons were done at three stations of the German GREF network, that were measured with FG-5 periodically and, more importantly, with FG-5 results at the reference station in Bad Homburg before and after each particular field campaign. The gravity station Bad Homburg serves as a reference station with a highly precise absolute gravity value due to periodic FG-5 observations with different instruments and availability of long-term time series from two superconducting gravity meters.

The synopsis of all above described approaches and more than 25 existing comparisons at the reference station Bad Homburg confirm the accuracy specification of the manufacturer and, moreover, prove the accuracy increase to better than 10 μGal for most of the occupied field stations.

Between July 2006 and September 2008 a total of 13 field campaigns were carried out. Supplementary to the A-10 observations, the vertical gravity gradients were measured using a Scintrex CG-5 relative gravity meter and a tripod with special design. The gradient measurements became necessary in order to transfer the observed absolute gravity values (sensor height about 0.7 m) to the corresponding bench marks without loss of accuracy. On some locations the absolute gravity meter

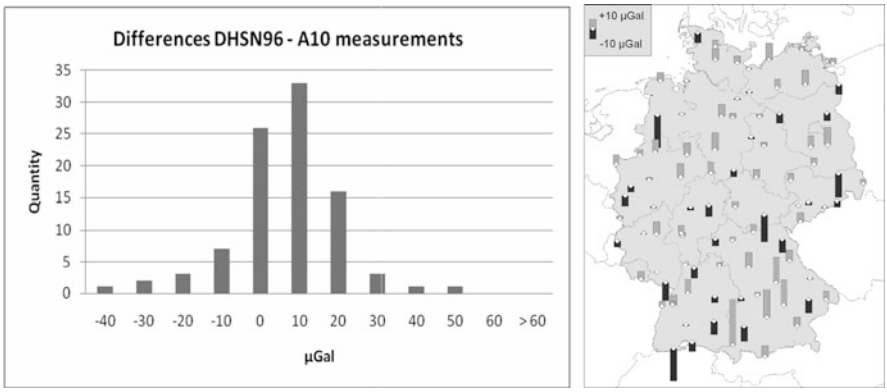

Fig. 2 *Left*: Histogram of differences between A-10 observations and DHSN96 1st order network gravity values; *Right*: Spatial distribution of differences between A-10 absolute gravity observations and corresponding values from DHSN96 1st order network in Germany

could not be placed directly above the intended measurement point. In these cases eccentric observations were connected to the corresponding bench marks using relative measurements as well. The necessary height transfer from the absolute sites to the DHSN96 bench marks was done by spirit levelling.

In order to evaluate the accuracy of the DHSN96 1st order gravity network, the gravity values were compared with the observed A-10 absolute gravity values at 93 field stations, measured during the GOCE-GRAND II project (7 points were left out due to instrumental problems or environmental issues). The differences between the A-10 and DHSN96 gravity values (which are influenced by observation errors of the A-10 absolute and CG-5 relative gravimeter as well as by the errors of the DHSN96 values themselves) show a mean of ± 0.2 µGal and a standard deviation of ± 18.7 µGal (see Fig. 2). About 90% of the measured points differ by not more than 20 µGal from the DHSN96 values. With the results presented above, the accuracy estimates for the DHSN96 network were confirmed, and thus no systematic impacts on geoid modelling have to be worried about. The quality of subordinate networks or independent data sets is still questionable and requires further investigations. Regarding the source, measurement method, accuracy and homogeneity, the existing data base includes a variety of different data sets. A proper weighting strategy of these different data sets in the course of the quasigeoid modelling should be derived from this evaluation in the future.

Furthermore, the existing gravity data base, e.g., used for the computation of the national quasigeoid model GCG05 (German Combined QuasiGeoid 2005; Liebsch et al., 2006), was validated by the new A-10 absolute gravity observations. For this purpose, Bouguer anomalies were predicted from the GCG05 data base, which were then compared with corresponding values for the A-10 stations. However, since the accuracy of the predicted values is two orders of magnitude worse than the accuracy of the absolute measurements, meaningful conclusion appear to be impossible.

3 GPS and Levelling Data

GPS and levelling data are essential in two respects. First, they are important for the direct validation of global gravity field models including the ones from the GOCE mission, and secondly they can be used for cross-validating astrogeodetic and gravimetric geoid and quasigeoid models. Moreover, the GPS and levelling data can be combined with the aforementioned data sets. In this context, the fitting of gravimetric geoid and quasigeoid models to GPS and levelling control points has become a standard procedure for GPS height determination with a targeted accuracy of about 1 cm.

In Germany, a national GPS and levelling data was collected by BKG, consisting of 907 stations with a spacing of 25–30 km. The GPS coordinates are based on the re-adjusted SAPOS reference station coordinates, which were introduced at the beginning of 2004 (Beckers et al., 2005). However, the Federal States of Germany used individual procedures to implement the new SAPOS reference frame, ranging from re-observation and re-adjustment to different transformation procedures, which may have introduced some inhomogeneities in the GPS coordinates. The gravity field related heights are normal heights referring to the official DHHN92 system (AdV, 1995). For further details cf. Liebsch et al. (2006). In this context, future improvements will result from the renewal of the German 1st order levelling network until 2011 in connection with a parallel GNSS observation campaign in 2008.

The German GPS/levelling data set was compared with the global geopotential models EGM1996 (Lemoine et al., 1998), EGM2008 (Pavlis et al., 2008) and several models developed at the Helmholtz Centre Potsdam, GFZ German Research Centre for Geosciences (ICGEM, 2009). All geopotential models include terrestrial gravity and satellite altimeter data in combination with satellite observations. Apart from EGM1996, all other models are based on data from the GRACE mission. Table 1 provides the statistics of the differences between the German GPS/levelling data set and the above mentioned geopotential models. In all cases, a constant bias was subtracted from the differences in order to account for different zero levels and very long wavelength errors in all data sets involved (GPS, levelling, quasigeoid).

Table 1 Comparison of 907 GPS and levelling stations in Germany with different global geopotential models. A constant bias is subtracted. Units are m

Geopotential model	Maximum degree used	RMS	Min	Max
EGM1996	360	0.251	–0.588	+1.187
EGM2008	360	0.135	–0.552	+0.663
EGM2008	2,190	0.030	–0.107	+0.144
EIGEN-CG01C	360	0.211	–0.734	+0.693
EIGEN-CG03C	360	0.189	–0.723	+0.704
EIGEN-GL04C	360	0.180	–0.736	+0.724
EIGEN-5C	360	0.153	–0.541	+0.756

From the models to spherical harmonic degree 360, EGM2008 performs best with a RMS difference of 0.135 m, while the latest EIGEN-5C models yields a RMS difference of 0.153 m, compared to 0.251 m for EGM1996. This shows the significant improvements due to the inclusion of the GRACE data but also due to the improved terrestrial data sets. Regarding the EIGEN models from GFZ, it can be observed that the results improve with time and the inclusion of GRACE data over a longer time period. Finally, with the EGM2008 model to degree 2,190, a RMS difference of only 0.030 m is obtained, which is close to the best regional quasigeoid models.

4 Gravimetric Quasigeoid Models

The computation of regional high-resolution geoid and quasigeoid models is commonly based on the remove-restore technique, combining terrestrial gravity data (with a spacing of a few km), a detailed digital terrain model (with a grid size down to 30 m) and a global geopotential model. In this context, the global geopotential model and the regional data sets complement each other in a favorable manner, i.e., the global model provides the long wavelength gravity field structures with high accuracy, while the regional data sets contribute the medium and short wavelength gravity field components, which are not included in the global model. Up-to-date global geopotential models are based on the GRACE satellite mission (e.g., EGM2008; Pavlis et al., 2008) and provide the global geoid with an unprecedented accuracy of about 1 mm to spherical harmonic degree 40 and 1 cm to degree 80. On the other hand, high quality regional terrestrial gravity field data sets exist in several parts of the world and can be combined with a global model. In the combination approach, e.g., least-squares collocation or spectral combination techniques, the signal and error characteristics of all involved data sets have to be taken into account. As a result, the long wavelength components of the regional geoid and quasigeoid models and of the global geopotential model match to a great extent. Therefore, comparisons of regional geoid and quasigeoid models with GPS/levelling data can be regarded also as a validation tool for the underlying global geopotential models.

In the following, the high resolution European quasigeoid models derived within the framework of the European Gravity and Geoid Project (EGGP) are considered as representative examples (cf. Denker et al., 2009). The latest model EGG2008 was computed on the basis of the 2008 European gravity and terrain data sets and the EGM2008 global model, utilizing the spectral combination approach. In order to show the improvement with time, the 2008 terrestrial data was also combined with other recently published global models as well as the EGM1996 model (Lemoine et al., 1998). In addition, the previous European quasigeoid model EGG1997 is considered as a reference. All results were evaluated by comparisons with the German GPS/levelling data set. Table 2 shows the statistics of differences between the GPS/levelling data and different European quasigeoid models. A constant bias was subtracted from the differences. First, the results based on

Table 2 Comparison of 907 GPS and levelling stations in Germany with different quasigeoid models. A constant bias is subtracted. Units are m

Terrestrial data	Underlying geopotential model	RMS	Min	Max
1997 (EGG1997)	EGM1996	0.094	–0.185	+0.327
2008	EGM1996	0.072	–0.132	+0.296
2008	EIGEN-CHAMP03S	0.049	–0.118	+0.258
2008	EIGEN-GRACE01S	0.038	–0.113	+0.148
2008	EIGEN-GRACE02S	0.037	–0.081	+0.119
2008	EIGEN-GL04S1	0.028	–0.096	+0.082
2008	EIGEN-5S	0.027	–0.097	+0.070
2008	EIGEN-5C	0.027	–0.098	+0.073
2008 (EGG2008)	EGM2008	0.026	–0.090	+0.074

EGM1996 show that the updated terrestrial data sets improve the results; the RMS difference reduces from 0.094 m for the 1997 terrestrial data to 0.072 m for the 2008 data. Then further significant improvements can be found when using a CHAMP based model (EIGEN-CHAMP03S, 0.049 m RMS) and the GRACE based EIGEN and EGM2008 models. It can be observed that the GRACE based models improve with time with the recent EIGEN-5C/S and EGM2008 models resulting in a RMS difference of 2.7 and 2.6 cm, respectively. In total, this is a very significant improvement of more than 70%, as compared to the previously published EGG1997 quasigeoid model. Hence, the new satellite mission data have a significant impact on

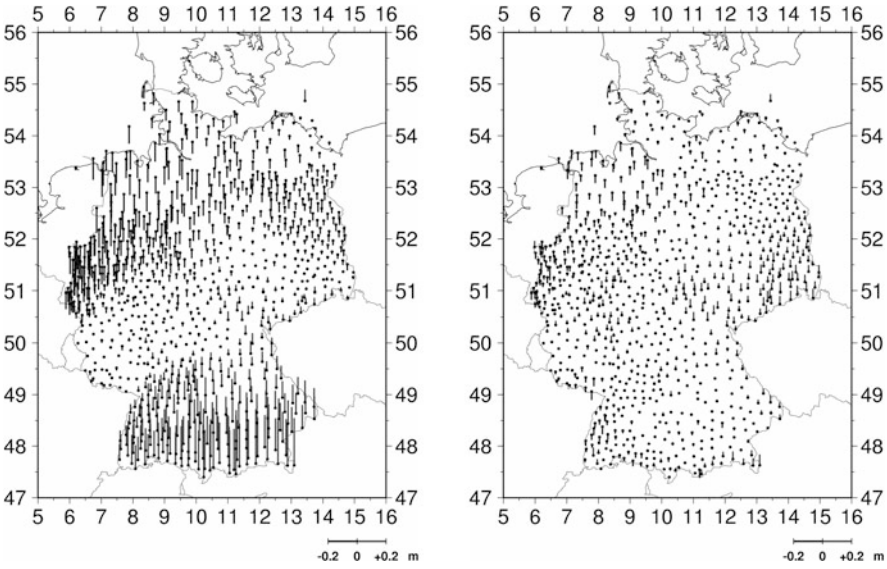

Fig. 3 Comparison of 907 GPS and levelling stations in Germany with the quasigeoid solutions EGG1997 (*left part*) and EGG2008 (*right part*). A constant bias is subtracted. Stations (*dots*) and differences (positive: *up*; negative: *down*) are depicted

the performance of the regional quasigeoid models and further improvements down to the level of about 1 cm can be expected from the GOCE mission. However, on the other hand, also the quality of the terrestrial data sets is of vital importance. In the end, Fig. 3 depicts the differences between the German GPS/levelling data set and the EGG1997 and EGG2008 gravimetric quasigeoid models.

Furthermore, the GPS/levelling data can be included as input data in the quasigeoid modelling. This was done in Germany and lead to the combined GCG2005 quasigeoid model (Liebsch et al., 2006). This model was developed as a joint effort of BKG and IfE and serves as a standard in Germany for the conversion between GPS ellipsoidal heights and normal heights. The evaluation of the model with independent GPS and levelling points suggested an accuracy of about 1–2 cm (Liebsch et al., 2006).

5 Astrogeodetic Vertical Deflections

In recent years, a new generation of zenith camera systems has become available for the determination of astrogeodetic vertical deflections. The increased accuracy of $0.1''$ or better (Hirt, 2004) and the automation of the vertical deflection processing are the main improvements. Two very similar zenith camera systems exist in Europe, namely the TZK2-D at IfE (Hirt, 2004) and DIADEM at ETH Zurich (Bürki et al., 2004). After an extensive test phase, both systems were applied in high-resolution gravity field modelling investigations. The TZK2-D was employed extensively in the local validation of gravimetric geoid models along profiles in the German Alps (Hirt and Flury, 2007) and in the Harz Mountains (Hirt et al., 2008). The results showed the great accuracy potential of the astrogeodetic vertical deflections within local test areas.

Within the framework of the GOCE-GRAND II project, the IfE zenith camera system TZK2-D was employed in extensive campaigns to collect vertical deflections on longer profiles of several hundred kilometres length (regional scales), aiming at an independent regional validation of other gravity field data sets such as GPS/levelling data, regional quasigeoid models or global geopotential models. Between 2006 and 2008, astrogeodetic vertical deflections were determined on 148 stations along a North-South profile and on 134 stations along an East-West profile. The observations were collected during 54 nights in total.

Both profiles have a spacing of about 2.5–5 km between adjacent stations, resulting in a total length of 540 km (North–South) and 533 km (East–West), respectively. In addition, astrogeodetic vertical deflections observed within previous projects (Hirt and Flury, 2007; Hirt et al., 2008) were embedded in the North-South profile, resulting in a unique data set of in total 498 highly accurate astrogeodetic vertical deflections (see Fig. 1, right). Due to the high degree of automation of the TZK2-D system, up to 12 vertical deflection stations could be observed in a single night, but it should also be pointed out that unfavourable nightly weather conditions may significantly limit the efficiency of the astronomical observation technique.

In order to assess the quality of the astrogeodetic vertical deflections, repeated observations were carried out at 48 identical stations in different nights. The standard deviation of the differences was found to be 0.16″ for both ξ and η. However, these values were affected by observations with a reduced accuracy due to worse weather conditions, e.g. fog; after excluding corresponding observations from the analysis, the repeatability agrees well with the stated accuracy of 0.1″ for the TZK-2D system (Hirt, 2004). Furthermore, vertical deflection determinations and calibrations were carried out regularly at the IfE astronomic reference station in Hannover (Hirt and Seeber, 2007) in order to verify the instrumental stability.

5.1 Astrogeodetic Validation of GPS/Levelling Data and Gravimetric Quasigeoid Models

In order to allow a cross-validation with the national GPS/levelling data set, the astrogeodetic profiles traverse through 46 nearby GPS/levelling control points in total (see Fig. 1). The method of astronomic levelling was used to compute quasigeoid height differences (Torge, 2001). In this context, a digital terrain model with a grid size of 1″ × 1″ was utilized in order to smooth the observed vertical deflection data (Voigt and Denker, 2007). The accuracy estimate for the quasigeoid height difference over an entire profile length of more than 500 km is 2.2 cm, implying random noise with a magnitude of 0.1″ for the vertical deflection data and neglecting omission errors. The results of the comparisons between the astrogeodetic quasigeoid profiles and the GPS/levelling data as well as the gravimetric quasigeoid models German Combined QuasiGeoid 2005 (GCG05; Liebsch et al., 2006) and the European Gravimetric Quasigeoid 2008 (EGG2008; Denker et al., 2009) are shown in Table 3 and Fig. 4. Since the astrogeodetic method only provides differences of height anomalies, the absolute level is taken from the GCG05 model at the first station.

The cross-validation of the astrogeodetic results, based on the method of astronomic levelling, with GPS/levelling and gravimetric quasigeoid data revealed partly systematic differences in the order of a few cm over some 100 km length (Voigt et al., 2009), which could not be fully explained so far, although repeat and densification observations were carried out with the TZK2-D instrument. Possible reasons for the discrepancies in the cross-validation may be inhomogeneities in the GPS

Table 3 Statistics (cm) of the differences Δζ between the astrogeodetic quasigeoid heights and GPS/levelling as well as gravimetric models along the North–South and the East–West profile

	North–South profile				East–West profile			
Data set	No	Std	Min	Max	No	Std	Min	Max
GPS/lev	23	3.5	−1.3	10.7	23	2.7	–6.8	2.1
GCG05	364	3.4	−1.1	9.9	134	2.6	–6.3	2.0
EGG08	364	4.3	0.0	12.3	134	1.4	–0.6	4.0

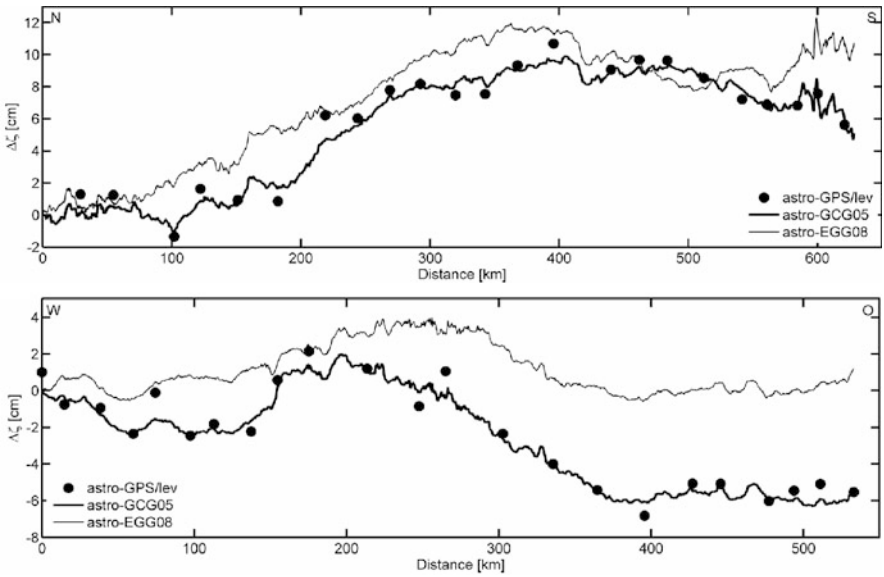

Fig. 4 Comparison of the astrogeodetic quasigeoid solution with GPS/levelling and quasigeoid models GCG05 and EGG2008 along the North–South profile (*top*) and the East–West profile (*bottom*)

results due to different processing strategies used in the individual Federal States of Germany (ranging from re-observation and re-adjustment to different transformation procedures), systematic effects or insufficient spacing of the vertical deflection observations, and to some extent also large-scale levelling errors. It is mandatory to further study and enlighten the reasons for the discrepancies by additional observations, data re-processing and development of realistic error models.

5.2 Astrogeodetic Validation of Global Geopotential Models

The main difference between the astrogeodetic vertical deflections and corresponding values derived from a global geopotential model (GGM) is the different spectral content. Whereas the GGM deflections have only a limited spectral content due to the limited degree of the spherical harmonic series, the astrogeodetic deflection data contain the complete spectrum (all frequencies).

In order to filter out all high-frequency signals from the terrestrial data, which are not included in the GGM (i.e. outside the measurement bandwidth with regard to GOCE), the Gaussian filter technique was applied with a radius of 50 km. Due to the delay of the GOCE mission, the analyses were carried out using the currently available models EGM96 (Lemoine et al., 1998), EIGEN-GL04C (Förste et al., 2008a) and the ultra-high degree model EGM2008 (Pavlis et al., 2008). Figure 5 shows the unfiltered and Gaussian filtered differences of the vertical deflection components ξ

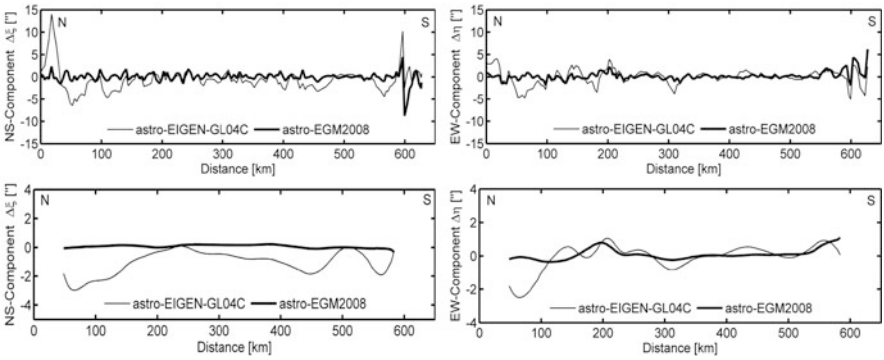

Fig. 5 Comparison between the unfiltered (*top*) and Gaussian filtered (*bottom*) astrogeodetic and GGM vertical deflection components ξ and η along the North–South profile

and η along the North–South profile. The comparisons with the models EGM96 and EIGEN-GL04C show RMS values from 1.7″ to 2.8″ for the unfiltered differences and 0.8″–2.1″ for the Gaussian filtered values, with mean values of 1.0″ or below. The validation of the ultra-high degree model EGM2008 shows RMS values from 0.6″ to 1.2″ for the unfiltered differences – slightly better than the RMS differences of 1.1″ to 1.3″ in CONUS (Contiguous United States) and Australia (Pavlis et al., 2008) – and 0.1″ to 0.3″ for the Gaussian filtered values, with mean differences of 0.2″ or below. These results confirm the high accuracy level of the EGM2008 model and show that the astrogeodetic vertical deflections are suitable for an external and completely independent validation of the GGM data.

6 Global Model Validation by Wavelet Techniques

In general there are two kinds of gravity field validation. The first one is a global approach: the gravity field covering the whole Earth is compared to another global gravity field. Both fields are spectrally band limited. There are some well-known techniques to filter and to estimate the errors introduced by the chosen filter.

The second approach is to compare a global gravity field with regional point observations, covering only a small part of the Earth. These two data sets are not compatible. The global gravity field is spectrally band limited, while the local observations are not. Thus, validation has to be performed on the observation points and it has to be band-limited by low pass filtering the terrestrial validation data set. Apart from the filtering, additional uncertainties in such a validation process might result from the data combination technique and regularization method applied in the global (GOCE) gravity field analysis and from possible datum off-sets, biases and trends in the terrestrial validation data sets. Because available data sets cover only a small part of the Earth, validation results might not be representative for the globe and long wavelengths of the global model might not be well represented in the test data sets.

Table 4 Available GPS/levelling data sets

Country/continent	Number of points	References
Australia	197	Johnston and Manning (2003, personal communication)
Canada	430	Verroneau (2007, personal communication)
Europe	1,233	Kenyeres et al. (2006)
Germany	675	Ihde and Sacher (2002)
Japan	837	Nakagawa (2003, personal communication)
USA	5,167	NGS (1999)

For all approaches it is necessary to use data sets of sufficient consistency and precision for the global model validation. Astrogeodetic vertical deflections (see Sect. 5) and GPS/levelling observations (see Sect. 3) are natural candidates for this. In the following study, GPS/levelling heights in different areas of the world are applied for validating global models. In particular it is referred to the German GPS/levelling observations described in Sect. 3. As already pointed out, it is expected that GOCE gravity field models will have a precision of a few centimeters in geoid height with a resolution of 100 km or better. Hence, the regional data must have the same or even better precision. As a further requirement for a satisfactory validation there should exist different data sets evenly spread over the whole Earth. Table 4 specifies the GPS/levelling geoid height data sets applied for GOCE gravity field validation. As one can see in Table 4, only very few data sets are available for validation. Especially there are no test data in South America, Africa and most parts of Asia.

The input data and the results of this work will be stored in a newly designed validation database. This database is able to store all validation data as well as the GOCE gravity field results. It is hosted on a server at IAPG. A second server is used as a web interface to the database. With the web interface one can access all data in the validation database. The interface assists the user by showing only those data sets that match the selections already made. As a last step, the data can be downloaded in various graphical and textual formats.

6.1 Filtering Terrestrial Data by Second Generation Wavelets

The calculation of global gravity fields is commonly done with spherical harmonics. They have a lot of well-known advantages for computing global fields, but for locally bounded problems this globality is a disadvantage, because spherical harmonics cannot be restricted in frequency and space simultaneously without loss of accuracy. As mentioned before, in order to make both data sets compatible, it is necessary to filter regional data with respect to the frequency content, because the global field is band limited in the frequency domain. There are several filter techniques to achieve this: Least-Square-Collocation (LSC), Spherical-harmonic synthesis (SHS) with ultra-high degree spherical harmonic models and second generation wavelets (SGW). The latter approach is described in the following paragraphs.

Wavelets can filter a data set in the frequency and space domains simultaneously. This makes wavelets suitable for filtering regional data in order to compare them with global models. Usually wavelets rely on regularly spaced data because of an underlying Fourier transform, requiring a regular grid of data. To apply a wavelet transform to GPS/levelling data, the data would have to be interpolated to this regular grid. However, interpolating data can add aliasing to data and removes (mainly high-frequency) information (Soltanpour et al., 2006). To avoid this interpolation, Sweldens (1998) developed wavelets usable for irregular spaced data, the so called second generation wavelets (SGW). Besides the ability to work on irregular data, there are some other differences to "normal" wavelets: First generation wavelet functions are dyadic translations and dilations of one mother wavelet

$$\psi_{j,m}(x) = \psi(2^j x - m).$$

So each wavelet $\psi_{j,m}$ at a level j and location m can be retrieved from the mother wavelet ψ. This is not possible with second generation wavelets. In terms of signal processing this means that the new wavelets have different filter characteristics for each level depending on the underlying data.

In a first step, the wavelet coefficients have to be determined. In general one needs to know the neighbours of each calculation point. With one-dimensional calculation, only the direct neighbours have to be taken into account. With two dimensional data, the determination of the neighbourhood of each vertex is not a trivial task anymore. In this work, the Delaunay triangulation (Fig. 6 left) is used for this purpose as proposed by Delouille et al. (2006).

To determine the area of support of the scaling functions, the Voronoi polygons (Fig. 6 right) have to be built for each vertex. At the finest level, the integral of the scaling functions is initialized with the area of the Voronoi polygon around the vertex it was calculated for, i.e. v_0. After that, the vertex with the smallest area is removed, the surrounding vertices are updated to keep the support constant, and the triangulation has to be partly rebuilt. On each level, only one new wavelet coefficient is calculated for a vertex. These steps are repeated until only boundary vertices remain. Figure 7 shows the calculated coefficients. In this case, the first

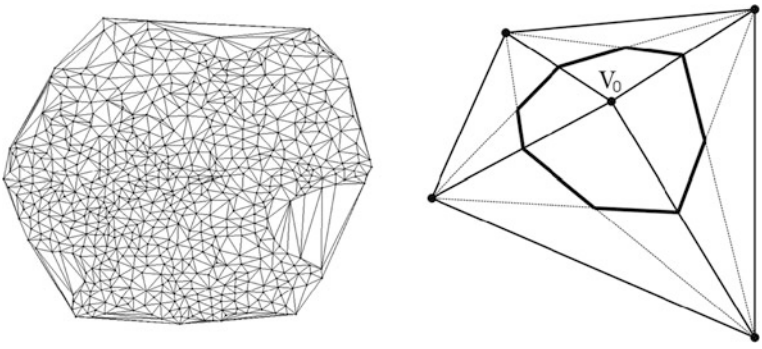

Fig. 6 Delaunay triangulation

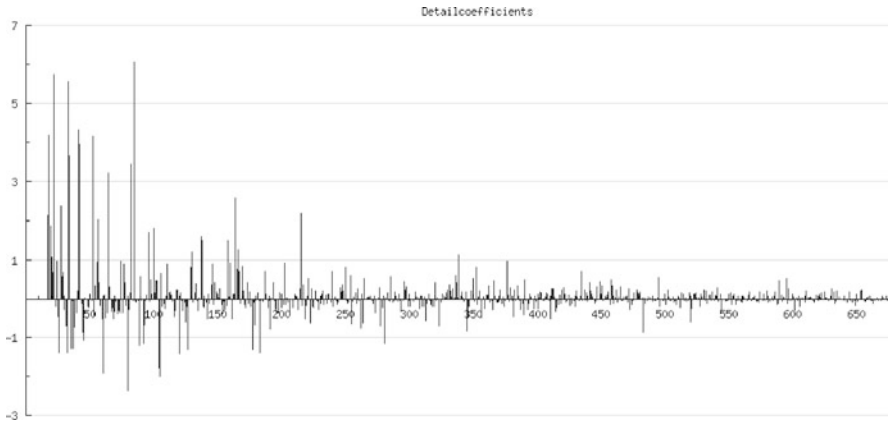

Fig. 7 Wavelet detail coefficients. x-axis shows the level of wavelet coefficient, y-axis shows the difference in height between vertex and the plane through the surrounding vertices

16 coefficients are not shown because they are located on the border and so it was not possible to determine surrounding vertices.

The coefficients are sorted by level. The coefficients of the finest level (i.e. the observations) with the smallest area support are shown on the right, those of the coarsest level on the left. The smaller these coefficients are, the smoother is the underlying data. The coefficients are the differences of the observations to a least squares plane through the surrounding vertices. This step is called prediction. There are several ways to determine this plane. In this work, a least-squares prediction of order one is used, as proposed in Jansen et al. (2001). Delouille et al. (2003, 2006) describe several other prediction operators. Besides the wavelet coefficients, the prediction provides a weight matrix. The weight matrix shows the relationship between the predicted vertex and its surrounding vertices. It is possible to display this matrix in a banded structure. For that purpose the vertices have to be sorted by their coordinates. This depicts the localizing effect of this wavelet transformation as only correlated vertices have values not equal to zero.

For de-noising the data (i.e. low pass filtering in terms of wavelets), the smallest coefficients are replaced by zeros. Therefore, the reconstructed signal will only consist of the remaining coefficients. This step is called thresholding. It is very important to find an optimal threshold value. A small threshold value will leave noise in the data, while a large value could remove parts of the signal. To find the optimal threshold value, Jansen et al. (1997) proposed the generalized cross-validation (GCV) function:

$$GCV(\lambda) = \left[\frac{1}{N}\,\|\tilde{\omega} - \tilde{\omega}_\lambda\|_2\right]\left[\frac{N_0}{N}\right]^{-2}$$

In this equation $\tilde{\omega}$ is the vector of normalized coefficients, $\tilde{\omega}_\lambda$ is the vector of thresholded normalized coefficients and N_0/N is the fraction of coefficients

replaced by zero for a particular threshold value λ. In most cases, this function has a minimum. This minimum is the optimal threshold value. It also minimizes the mean square error of the result as compared to the noise free coefficients.

To use this function, the wavelet coefficients have to be normalized as the noise standard deviation is different for each coefficient, as shown in Jansen et al. (1997). This is done by using the correlation matrix of the input. In case of GPS/leveling data, this matrix is often not known but can be approximated by their covariance function. This might fail if the GCV function does not have a minimum. In this case one must choose another appropriate threshold value. All coefficients with a value below the minimum of the GCV will be set to zero. In a last step, the vertices will be reproduced.

6.2 First Results with Second Generation Wavelets

While LSC and SHS use a fixed order for filtering, with SGW the optimal filter limit only depends on the data. In case of SGW, there are two possible ways to validate: Filtering before or after building differences. In the first case, both data sets must be filtered on their own. Each data set will have its own coefficients and threshold value. In the second case, there will be only one set of coefficients and one threshold value.

While filtering after building differences has the advantage of a faster calculation, filtering before building differences has some advantages that make it preferable. In case of filtering after building differences some signal might be filtered out which is relevant for the validation.

Coefficient comparison can give a first overview about the quality of the data. Both sets of coefficients must have a high correlation. Different threshold values will give a hint about the signal-to-noise ratio of both data sets. Especially with the already band limited global data, a threshold value indicates a high noise level for that type of data.

The following results are calculated with the German GPS/levelling data set (Ihde and Sacher 2002) and three different geopotential models. For each model, geoid heights of each point were calculated. These heights were filtered and compared point-wise to the filtered measured geoid heights.

Figure 8 shows the distribution of differences between original and filtered data for different geoid models. Depending on the maximum degree of the model, the maximum differences vary between ± 0.20 and ± 0.07 m. On the one hand, this shows the different quality of the input data. On the other hand, it demonstrates the low-pass filtering by the wavelet filter. The less the maximum degree, the less points were changed by the filter. With this in mind it should be possible to determine the inherent maximum degree of a data set that depends on the geographical distribution of the points.

Table 5 shows the resulting RMS, comparing the measured geoid heights (GPS/levelling) to the three calculated geoid height data sets (geopotential models).

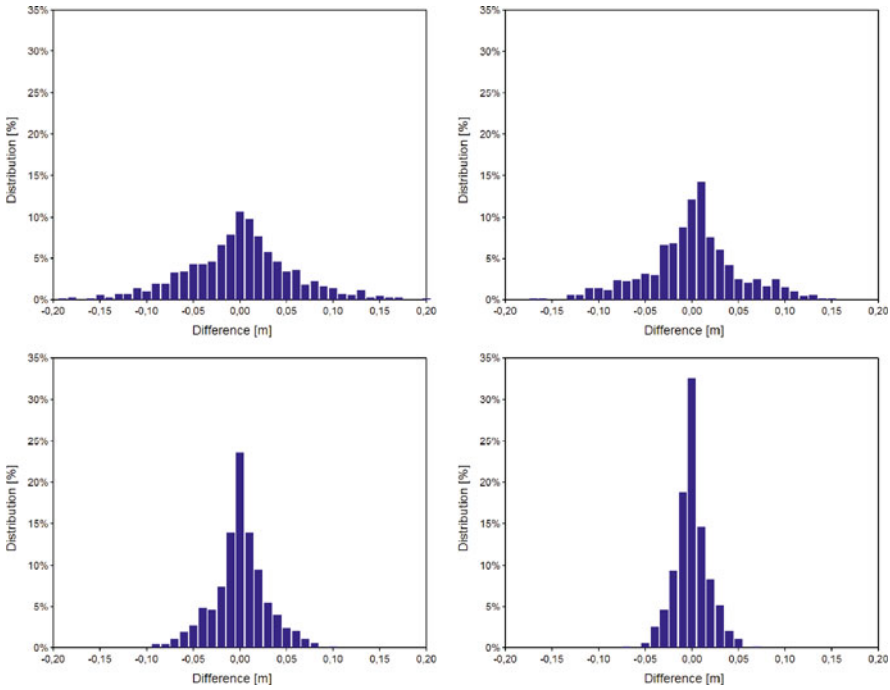

Fig. 8 Differences geoid heights original vs. filtered. Measured geoid heights (*left top*), EGM 2008 to degree 2,160 (*right top*), EIGEN 5C to degree 360 (*left bottom*) and EIGEN 5C to degree 200 (*right bottom*)

Table 5 RMS of centered differences

Model	Max. degree	RMS (m)
EGM 2008 (Pavlis et al., 2008)	2,160	0.039
EIGEN 5C (Förste et al., 2008b)	360	0.154
EIGEN 5C (Förste et al., 2008b)	200	0.295

Obviously these results are only a first attempt. Because the wavelet filter depends on the data, some tuning will be necessary when validating real GOCE data. There are also still several topics for further investigations: It should be possible to determine the degree and order of the filtered data by means of spherical harmonics, and also the quality of the validation has to be investigated. For this purpose it must be analyzed which errors can be detected and how they will show up.

7 Conclusions

A regional validation and combination experiment was carried out within the framework of the GOCE GRAND II project and lead to valuable regional terrestrial gravity field data sets, including gravity data, GPS and levelling control points,

astrogeodetic vertical deflections and gravimetric quasigeoid models. Spot-checks with the A-10 absolute gravimeter have proved the high quality of the existing terrestrial gravity data base for Germany. The detected gravity differences are insignificant with regard to geoid and quasigeoid computations with an envisaged accuracy level of about 1 cm. The astrogeodetic observations and GPS/levelling data are completely independent of all other gravity field data sets. Therefore they are very valuable for manifold validation purposes.

The existing GPS/levelling quasigeoid heights are not yet at the 1 cm accuracy level. Reasons for this are the inhomogeneities of the three-dimensional coordinates, especially the ellipsoidal heights, resulting from different measurement epochs and processing schemes within the Federal States of Germany, but also the levelling may contribute to this. With regard to the renewal of the German 1st order levelling network until 2011 and the parallel GNSS campaign 2008, considerable improvements are expected.

Approximately 300 astrogeodetic vertical deflections with an accuracy of about $0.1''$ were collected. This data set is independent of the other terrestrial data sets and can be considered as unique worldwide. However, the cross-validation with GPS and levelling data and gravimetric quasigeoid models revealed partly systematic differences in the order of several cm over a few 100 km length, which could not be fully explained within this project. The validation of GGM vertical deflections, however, showed the high accuracy potential of the astrogeodetic data. Hence, they can be used as another independent external validation tool for GOCE data, taking into account a reasonable low-pass filtering of the surface data.

With regard to the gravimetric quasigeoid models, the new satellite mission data have a significant impact on the performance. Further improvements down to the level of about 1 cm can be expected from the GOCE mission.

References

AdV (1995) Deutsches Haupthöhennetz 1992 (DHHN 92). Arbeitsgemeinschaft der Vermessungsverwaltungen der Länder der Bundesrepublik Deutschland (AdV). Bayerisches Landesvermessungsamt München.

Beckers H, Behnke K, Derenbach H, Faulhaber U, Ihde J, Irsen W, Lotze J, Strerath M (2005) Diagnoseausgleichung SAPOS – Homogenisierung des Raumbezugs im System ETRS89 in Deutschland. ZFV 130(4), 203–208.

Bouman J, Koop R (2003) Geodetic methods for calibration of GRACE and GOCE. Space Sci. Rev. 108, 293–303.

Bürki B, Müller A, Kahle H-G (2004) DIADEM: the new digital astronomical deflection measuring system for high-precision measurements of deflections of the vertical at ETH Zurich. IAG GGSM 2004, Porto, Portugal, CD-ROM Proceedings.

Delouille V, Jansen M, von Sachs R (2003) Second Generation Wavelet Methods for Denoising of Irregularly Spaced Data in Two Dimensions, Institut de Statistique, Université Catholique de Louvain, Belgium.

Delouille V, Jansen M, von Sachs R (2006) Second generation wavelet methods for denoising of irregularly spaced data in two dimensions. Signal Process. 86, 1435–1450.

Denker H, Voigt C, Müller J, Ihde J, Lux N, Wilmes H (2007) Terrestrial data sets for the validation of GOCE products. In: Observation of the System Earth from Space. Geotechnologien Science Report No. 11, pp. 85–92.

Denker H, Barriot J-P, Barzaghi R, Fairhead D, Forsberg R, Ihde J, Kenyeres A, Marti U, Sarrailh M, Tziavos IN (2009) The development of the European gravimetric Geoid Model EGG07. In: Sideris M (ed.), Observing Our Changing Earth, Proceedings of the IAG General Assembly, Perugia, July 2–13, 2007. IAG Symposia Series No. 133, Springer, New York, pp. 177–186.

ESA (1999) Gravity field and steady-state ocean circulation mission. Reports for Mission Selection, The Four Candidate Earth Explorer Core Missions, ESA SP-1233(1).

Förste C, Schmidt R, Stubenvoll R, Flechtner F, Meyer U, König R, Neumayer H, Biancale R, Lemoine J-M, Bruinsma S, Loyer S, Barthelmes F, Esselborn S (2008a) The GeoForschungsZentrum Potsdam/Groupe de Rechereche de Gèodésie Spatiale satellite-only and combined gravity field models: EIGEN-GL04S1 and EIGEN-GL04C. J. Geod. 82(6), 331–346.

Förste C, Flechtner F, Schmidt R, Stubenvoll R, Rothacher M, Kusche J, Neumayer K-H, Biancale R, Lemoine J-M, Barthelmes F, Bruinsma J, König R, Meyer U (2008b), EIGEN-GL05C – A new global combined high-resolution GRACE-based gravity field model of the GFZ-GRGS cooperation, General Assembly European Geosciences Union (Vienna, Austria 2008), Geophysical Research Abstracts, Vol. 10, Abstract No. EGU2008-A-06944, 2008.

Hirt C (2004) Entwicklung und Erprobung eines digitalen Zenitkamerasystems für die hochpräzise Lotabweichungsbestimmung. Wissenschaftliche Arbeiten der Fachrichtung Vermessungswesen der Universität Hannover Nr. 253.

Hirt C, Flury J (2007) Astronomical-topographic levelling using high-precision astrogeodetic vertical deflections and digital terrain model data. J. Geod. 82(4–5), 231–248.

Hirt C, Seeber G (2007) Accuracy analysis of vertical deflection data observed with the Hannover Digital Zenith Camera System TZK2-D. J. Geod. 82(6), 347–356.

Hirt C, Feldmann-Westendorff U, Denker H, Flury J, Jahn C-H, Lindau A, Seeber G, Voigt C (2008) Hochpräzise Bestimmung eines astrogeodätischen Quasigeoidprofils im Harz für die Validierung des Quasigeoidmodells GCG05. ZFV 133, 108–119.

Ihde J, Sacher M (2002), EUREF Publication 11/I, Mittelungen des Bundesamtes für Kartographie und Geodäsie, Band 25, Frankfurt/Main, ISBN 3-89888-869-X.

International Centre for Global Earth Models, URL: http://icgem.gfz-potsdam.de/ICGEM/ICGEM.html, 2009

Jansen M, Malfait M, Bultheel A (1997) Generalized cross validation for wavelet thresholding. Signal Process. 56, 33–44.

Jansen M, Nason G, Silverman B (2001) Scattered data smoothing by empirical Bayesian shrinkage of second generation wavelet coefficients. In: Wavelet Applications of Signal and Image Processing IX, Proceedings of SPIE (4478), pp. 87–97.

Jarecki F, Müller J (2007) GOCE gradiometer validation in satellite track cross-overs. Proceedings of the 1st International Symposium of the International Gravity Field Service, "Gravity Field of the Earth", Harita Dergisi, Special Issue 18, Ankara, Turkey, pp. 223–228.

Kenyeres A, Sacher M, Ihde J, Denker H, Marti U (2006) EUVN_DA: Establishment of a European continental GPS/levelling network. Presentation, 1st International Symposium of the International Gravity Field Service (IGFS), "Gravity Field of the Earth", Istanbul, Turkey, August 28–September 1, 2006.

Lemoine FG, Kenyon SC, Factor JK, Trimmer RG, Pavlis NK, Chinn DS, Cox CM, Klosko SM, Luthcke SB, Torrence MH, Wang YM, Williamson RG, Pavlis EC, Rapp RH, Olson TR (1998) The Development of the Joint NASA GSFC and NIMA Geopotential Model EGM96. NASA/TP-1998-206861, Technical Report, NASA, Greenbelt, MD.

Liebsch G, Schirmer U, Ihde J, Denker H, Müller J (2006) Quasigeoidbestimmung für Deutschland. DVW-Schriftenreihe 49, 127–146.

Löcher A, Ilk K-H (2007) A validation procedure for satellite orbits and force function models based on a new balance equation approach. International Association of Geodesy Symposium, Vol. 130, Springer Verlag, New York, pp. 280–287.

NGS (1999) See http://www.ngs.noaa.gov/GEOID/GPSonBM99/gpsbm99.html

Pavlis NK, Holmes SA, Kenyon SC, Factor JK (2008) An Earth Gravitational Model to Degree 2160: EGM2008. EGU General Assembly, Vienna, Austria, April 13–18.

Soltanpour A, Nahavandchi H, Featherstone WE (2006) The use of second-generation wavelets to combine a gravimetric quasigeoid model with GPS-levelling data. J. Geod. 80(2), 82–93.

Sweldens W (1998) The lifting scheme: a construction of second generation wavelets. SIAM J. Math. Anal. 29(2), 511–546.

Torge W (2001) Geodesy, 3rd ed., W. de Gruyter, New York.

Torge W, Falk R, Franke A, Reinhart E, Richter B, Sommer M, Wilmes H (1999) Das Deutsche Schweregrundnetz 1994 – Band 1 – DGK B309, München.

Voigt C, Denker H (2007) A Study of High Frequency Terrain Effects in Gravity Field Modelling. Proceedings of the 1st International Symposium of the International Gravity Field Service, "Gravity Field of the Earth", Harita Dergisi, Special Issue 18, Ankara, Turkey, pp. 342–347.

Voigt C, Denker H, Hirt C (2009) Regional astrogeodetic validation of GPS and levelling data and quasigeoid models. In: Sideris M (ed.), Observing Our Changing Earth, Proceedings of the IAG General Assembly, Perugia, July 2–13, 2007. IAG Symposia Series No. 133, Springer, New York, pp. 413–420.

Wolf KI (2007) Kombination globaler Potentialmodelle mit terrestrischen Schweredaten für die Berechnung der zweiten Ableitungen des Gravitationspotentials in Satellitenbahnhöhe (Diss.). Wiss. Arb. Fachr. Geodäsie u. Geoinformatik der Leibniz Universität Hannover, ISSN 0174-1454, Nr. 264.

Comparison of GRACE and Model-Based Estimates of Bottom Pressure Variations Against In Situ Bottom Pressure Measurements

Detlef Stammer, Armin Köhl, Vanya Romanova, and Frank Siegismund

1 Introduction

Regional changes of the ocean to a large extent are caused by changes of the barotropic circulation, i.e., the vertically averaged circulation. This component of the general circulation is primarily controlled by the wind forcing at the surface, but also by the interaction with the bottom topography. Uncertainties in our knowledge of the wind stress or insufficient representation of topographic effects in circulation models do lead to uncertainties in our knowledge of the barotropic flow field. However, a detailed knowledge of the ocean's barotropic circulation is required to discriminate between mass-induced and sterically driven changes in sea level, to better understand the uptake and transport of heat in the ocean, and to describe the ocean's response to mass loss of polar ice caps. Understanding variations in ocean bottom pressure will also be of fundamental importance, e.g., for obtaining new insight into the Earth's angular momentum changes and the torques imposed on the solid Earth by the ocean.

Associated with the changes in the barotropic ocean circulation are changes in the local bottom pressure p_b which can be measured by bottom pressure gauges located at the sea floor. However, we know from the current generation of ocean models and ongoing comparisons of model simulations with time series of ocean p_b gauges, that pressure fluctuations on the sea floor are broadband, i.e., they occur over a broad range of temporal and spatial scales. Observing p_b fields globally to improve our understanding of the barotropic circulation therefore does pose a serious observational challenge that requires measurements from space.

Changes in mass are associated with changes in gravity which in principle can be observed by satellites. The U.S.-German joint gravity mission GRACE is designed to measure time-varying gravity fields on spatial scales of more than 1,000 km and temporal scales of a month and longer. Through these novel measurements, the mission in principle is able to provide unprecedented information about the

D. Stammer (✉)
Institut für Meereskunde, KlimaCampus, Universität Hamburg, Hamburg, Germany
e-mail: detlef.stammer@zmaw.de

F. Flechtner et al. (eds.), *System Earth via Geodetic-Geophysical Space Techniques*, Advanced Technologies in Earth Sciences, DOI 10.1007/978-3-642-10228-8_23,

changing barotropic circulation and associated bottom pressure fields of the ocean. The Nyquist frequency of these data is 1/2 cycle/month (2-months period), with shorter periods being aliased. For studies of the ocean using GRACE data, we are primarily concerned with the analysis of p_b variability from GRACE data at annual and shorter periods, including all resolvable signals at periods >2 months. On the other hand, the shorter periods of p_b variability are very energetic (about 50% of the energy resides on periods shorter than 10 days) and will be strongly aliased by the GRACE sampling. The processing of GRACE data depends on the assumption that ocean models are skillful in predicting mass variations on short-time scale, but do have deficits on scales longer than the GRACE Nyquist frequency of about 2 months. This is an assumption that needs to be tested against bottom pressure data.

The extent to which the GRACE mission provides new information about the barotropic circulation to a large degree depends (1) on our ability to discriminate in the GRACE signal between terrestrial groundwater signal and ocean mass signal, close to continental boundaries and over the open ocean, (2) on the extent to which models actually deviate from observed changes in mass at high and low frequencies (relative to the mission's Nyquist frequency) and (3) on the degree to which we can use GRACE time-varying gravity fields jointly with altimetric observations and data from the ARGO array to constrain ocean models. Each of the above steps, directly or indirectly, depends on our ability to test the results of circulation models against observations of bottom pressure gauges and thereby to test the skill of model predictions of p_b variations as a function of time scale. At the same time, existing GRACE retrievals also have to be tested against model simulations as well as bottom pressure data to document the degree of difference between models and GRACE but also to obtain an estimate of uncertainties present in the GRACE data and compare it with the formal uncertainty provided by the project in form of an error covariance.

Another way to test the accuracy of time-varying geoid field estimates (time mean as well as its variability) is the procedure of ocean state estimation. This procedure is associated with the combination of gravity data in form of geoid fields (time mean and variability) with all available information about the changing ocean circulation and with the dynamics embedded in numerical ocean circulation models. This step is very much akin to assimilation in numerical weather predictions and allows us to compare prior and posterior estimates of the ocean circulation with prior statistics, e.g., provided about the accuracy of the time-varying geoid fields. Any inconsistency of the model's dynamics with those observations would result in residual model-data misfits that have to be tested against prior assumptions of errors. Examples of the use of ocean state estimation for detecting geoid uncertainties are provided by Stammer et al. (2007).

As a prerequisite to the assimilation of GRACE data into ocean models, our focus here is on the ocean's bottom pressure (pb) signals, their representation in ocean models (i.e., how variations in bottom pressure are being simulated by ocean models as function of space and time scales), and their relation to gravity changes as observed by GRACE.

2 Methodology

Our approach is to use several data sets available to investigate the variability of p_b, to infer its space and time scale, and to investigate to what extent respective information agrees or differs in the available data sets. In detail the analysis involves:

(1) A comparison of results available from various models with simultaneous measurements of ocean bottom pressure to understand the dependence of model results on the model resolution and numerical details.
(2) A comparison of bottom pressure time series with GRACE data.
(3) A statistical analysis of GRACE and model results in terms of slow (annual and longer) variations in bottom pressure and the respective spatial structure.

Data sets analyzed in this study include (a) time series of bottom pressure observations, (b) results from various models, specified below, (c) GRACE monthly products available from 2003 through 2007. Bottom pressure time series, available to us from various locations of the world ocean, are summarized in Fig. 1. Data used in our analysis were obtained from the Proudman Oceanographic Laboratory, the IFM-GEOMAR (MOVE – Meridional Overturning Variability Experiment) and the Oregon State University. As can be seen from the figure, most of those time series reside in the Southern Ocean or the Indian Ocean; only a few bottom pressure data are available in the Pacific, and in the North Atlantic the only time series available are located at about 15°N in the western subtropical gyre.

For our analysis we use GRACE monthly solution from GeoForschungsZentrum (GFZ), Potsdam and Center for Space Research (CSR), University of Texas. In

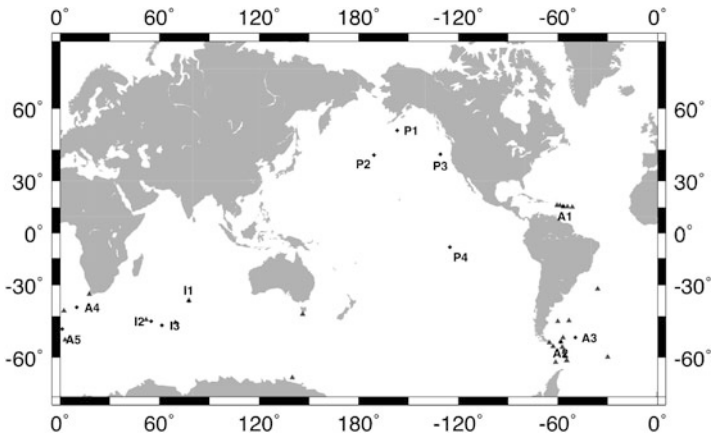

Fig. 1 Positions where bottom pressure measurements exist. Positions of bottom pressure recorders, used for comparison with GRACE and GECCO monthly bottom pressure variability, are marked by labels

general terms, GRACE measures the time-varying gravity field of the Earth once per month (although higher temporal resolution seems possible). When using GRACE level-2 data for investigations on ocean mass variability, two specific aspects have to be considered, which are described in more detail by Siegismund et al. (2010). First, ocean and atmospheric variability that was subtracted before processing level-2 data to prevent aliasing into monthly variability, has to be restored. Second, the maps have to be smoothed in a way that leakage of strong land signals is prevented as much as possible. Restoring of variability is done using the GAD product that is provided together with the other GRACE products from the GRACE processing centers. GAD contains non-tidal ocean and atmosphere variability as provided by the ocean model OMCT and the ECMWF analysis fields, respectively. Smoothing of the data is done using a sequence of filters. As first step we use the Swenson and Wahr (2006) de-correlation filter. Still in spectral domain a 200 km Gaussian filter is applied. After transformation to physical space, signals over land and over a 500 km wide stripe of ocean following the coastline, is masked out. Finally a 600 km spatial Gaussian filter is applied. With this approach we reduce land to ocean leakage substantially since smoothing on large spatial scales is done on the physical maps rather than in the spectral domain.

To test the consistency of model simulations with bottom pressure observations, we use the output from different models and syntheses. They differ in the period they simulate, in details of the numerics, but also in horizontal resolution. We used four models here during the intercomparison:

(1) 1^{o} GECCO first guess and synthesis (1952–2001, Köhl and Stammer, 2008a, b)
(2) 1^{o} ECCO-GODAE synthesis (1992–2004, Wunsch and Heimbach, 2006)
(3) 1^{o} GECCO-2 first guess and synthesis (2002–2007, Köhl et al., 2009)
(4) 2^{o} OMCT (2001–2008, Thomas, 2002).

The ECCO-GODAE and GECCO synthesis products are nearly identical in their methodology, numerical model, and the assimilated data, but cover different periods. In particular, GECCO does not overlap with GRACE. In contrast, GECCO-2 features a truly global extent, higher horizontal and vertical resolution, an ice model and the inclusion of the Arctic Ocean. In all cases, the assimilation method builds on the adjoint method, which was first implemented with the ECCO/MITgcm by Stammer et al. (2002, 2003). The subsequent products were built on this ECCO modeling and assimilation framework but assimilated additional data. The standard types of data now include hydrographic data from TOGA/TAO, XBT/MBT, CTD, and Argo profiles, satellite altimeter, and SST data. The assimilation procedure estimates surface boundary conditions for heat, freshwater and momentum. The prior for this forcing that was also used in first guess is based on the NCEP reanalysis. OMCT (Ocean Model for Circulation and Tides) is the model being used during the GRACE data processing and forced with ECMWF analysis data. This particular version does not include lunisolar tidal dynamics but additional to the other products atmospheric pressure forcing.

3 Comparison of Results with Bottom Pressure Sensors

To evaluate model simulations of bottom pressure, we compare time series of bottom pressure available from several model runs against bottom pressure measurements at all those positions shown as black marks in Fig. 1. Such a comparison is a first step to test the quality of model results in various frequency bands, notably the frequencies above and below the GRACE Nyquist frequency of about 1/(2 months). We show in Fig. 2 time series from three selected positions located in the Atlantic and Indian

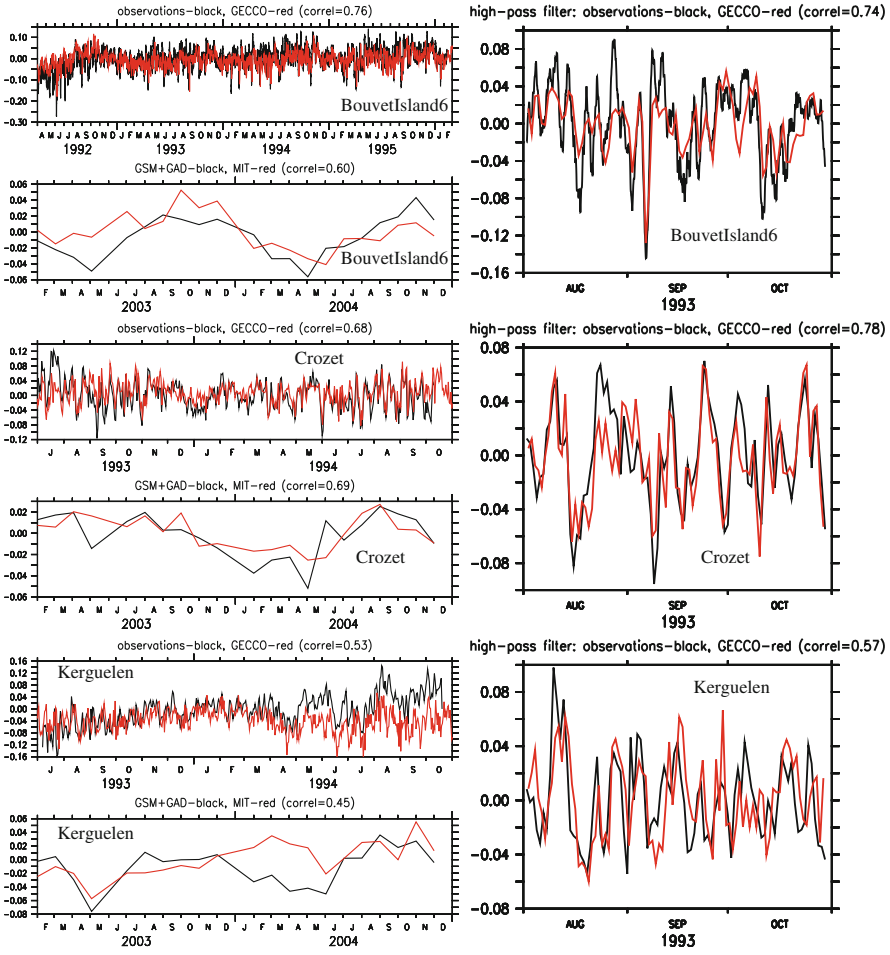

Fig. 2 (*Left column*, 1st, 3rd, 5th panels, from top to bottom): Time series of bottom pressure (*black*) and the GECCO synthesis (*red*) at Bouvet Island 6 (Southern Ocean, 3.0E, 54.3S); Crozet Island (Indian Ocean, 51.9E, 46.4S); Kerguelen (Indian Ocean, 52.3E, 46S); in every second panel we show a comparison of the ECCO-GODAE synthesis and monthly GRACE results. Units are in m equivalent water height. (*Right column*): High-pass filtered time series of bottom pressure (*red*) and the GECCO synthesis at the same geographic locations, but shown as blow-up for only 3 months during 2003

Ocean sector of the Southern Ocean: positions near the Kerguelen Islands, near CK2 in the Indian Ocean and near the Bouvet Islands. The figure illustrates the high degree of skill of the models on high frequencies leading to a correlation up to 0.72 at Kerguelen Islands.

The correlation coefficients between model simulations and all bottom pressure measurements available to us are provided in Table 1. We note that the GECCO synthesis does show about a 10% increase in correlation after assimilating all available ocean data. This suggests that a best possible input data set for the GRACE processing is the model that is being constrained by data. The GECCO model shows skill in simulating the high frequency variability in the p_b fields. At some locations correlation coefficients are around 0.8 and demonstrate a good agreement with the data but low correlations of around 0.4 are found at other locations. The discrepancies between the model and the measured data at these latter positions may be due to the unresolved mesoscale activity of the model or coarse topography resolution.

4 Comparison of GRACE Results with Model Simulations and Bottom Pressure Sensors

During the GRACE period, the few bottom pressure data available do not suffice for a quantitative comparison with GRACE results. Nevertheless, we can compare GRACE and model results. We show in Fig. 2 a comparison of the ECCO-GODAE synthesis and GRACE monthly fields, again at the same geographical positions used before in the comparison with in situ bottom pressure fields. The comparison is shown here first for the years 2003 and 2004 at the same geographic position for which a comparison of GECCO-bottom pressure data was shown before for earlier years. We note a clear agreement between GRACE and ECCO-GODAE time series in terms of amplitude and general temporal structure. In some cases even short-period variations agree, while during other periods some differences can be noted. It will be our task in the future to find out which of those time series do represent more the ocean and how we can use both to obtain an improved estimate of the barotropic ocean circulation.

A longer comparison of GRACE results and model simulations is provided in Fig. 3, showing time series of two GRACE retrievals at several geographic positions shown by black labels in Fig. 1, and time series of the GECCO-2 run, before and after assimilating all ocean data. Also shown are the few bottom pressure time series available during short periods at those locations. As before, the signal strength of the GRACE solutions is comparable to the bottom pressure sensor data. In contrast, mass variations from both GECCO-2 runs are smaller than observed, except for the Pacific sites, where all the bottom pressure time series exhibit comparable variability. We also note that the GECCO-2 assimilation correlates substantially better with the sensor data than the unconstrained reference run (Fig. 4), while the underestimation of the signal strength still remains. This suggests that the assimilation of GRACE fields should have a significant impact on the estimate of the strength of the seasonal changes in the barotropic circulation.

Table 1 Correlation coefficients between daily bottom pressure time series and (a) the GECCO simulation (iter0), (b) the GECCO synthesis (iter11), (c) the OMCT model (OMCT)

Mooring name	Position	Depth (m)	Time period	OMCT	GECCO Ref.	GECCO	High pass	Low pass
NORTH13	44.12S, 146.22E	1,025	2.1.1994–6.1.1996	X	0.31	0.24	0.33	0.10
SOUTH14	65.56S, 139.85E	1,010	16.1.1994–15.3.1996	X	0.46	0.55	0.47	0.75
CAPETWN1	34.60S, 17.80E	985	27.3.1992–10.11.1993	X	0.43	0.42	0.40	0.55
CAPETWN2	34.59S, 17.80E	991	27.3.1992–5.2.1996	X	0.17	0.25	0.30	0.17
CAPETWN15	34.59S,17.81E	990	10.11.1993–3.8.1997	X	0.20	0.24	0.18	0.37
SHANNONT3	42.59S, 2.34E	745	1.6.1992–10.3.1994	X	0.51	0.52	0.65	0.40
SHANNONT4	42.99S, 2.34E	809	1.6.1992–10.2.1996	X	0.24	0.27	0.60	−0.12
BOUVET5	54.34S, 3.02E	972	2.4.1992–20.3.1994	X	0.74	0.77	0.75	0.86
BOUVET6	54.34S, 3.02E	964	2.4.1992–13.2.1996	X	0.75	0.76	0.75	0.80
SANAE7	70.14S, 2.64 W	979	13.3.1992–26.12.1993	X	0.32	0.33	0.17	0.65
SANAE18	70.13S, 2.62 W	889	26.12.1993–21.1.1997	X	0.42	0.42	0.27	0.63
CAPEHRN95	55.17S, 65.21 W	1,028	29.10.1995–25.12.1998	0.38	0.20	0.18	0.08	0.37
Fram F2	78.83 N, 8.33E	793	2.9.2004–16.8.2005	0.54	X	X		
Fram F6	78.83 N, 5.01E	2,712	2.9.2004–17.8.2005	0.58	X	X		
Fram F8	78.84 N, 2.80E	2,496	2.9.2004–5.8.2005	0.51	X	X		
P127 (M1)	15.3 N, 51.3 W	4,965	29.1.2000–2.1. 2001	0.04	0.24	0.24	0.38	−0.09
	15.3 N, 51.3 W	4,965	10.1.2001–26.1.2002	–0.03	0.29	0.35	0.46	0.01
P165 (M2)	15.6 N, 56.7 W	4,978	02.2.2000–01.1.2001	0.01	0.26	0.39	0.41	0.18
	15.6 N, 56.7 W	4,978	12.1.2001–25.1.2002	–0.15	0.13	0.20	0.43	−0.11
P005 (M2.5)	16.16 N, 58.71 W	5,688	07.7.2004–24.4.2006	0.24	X	X		
P012 (M1.5)	15.7 N, 54.2 W	5,450	07.7.2004–24.4.2006	0.23	X	X		
P123 (M3)	16.35 N, 60.48 W	4,960	05.7.2004–18.2.2006	0.37	X	X		
dpnns956_i4d	56.83S, 57.50 W	2,096	27.11.1995–16.11.1996	X	0.02	0.0	0.12	−0.10
dpn9496a_a4d	58.38, 54.94S	1,052	17.11.1994–13.11.1996	X	0.14	0.14	0.20	0.11
nd1_9192_a	56.49S, 62.98 W	3,925	23.12.1991–05.11.1992	X	0.17	–0.13	0.10	−0.21
nd2_9293_a	54.94S, 58.39 W	1,010	16.11.1992–20.11.1993	X	0.13	0.15	0.26	−0.06
nd2_9394_a	54.94S, 58.39 W	1,007	23.11.1993–14.11.1994	X	0.04	0.04	0.21	−0.11
nd2_9496	54.94S, 58.38 W	1,050	17.11.1994–13.11.1996	X	0.03	0.04	0.12	−0.07

Table 1 (continued)

Mooring name	Position	Depth (m)	Time period	OMCT	GECCO Ref.	GECCO	High pass	Low pass
nd2_96_97	54.94S, 58.38 W	1,050	04.12.1996–19.12.1997	0.51	–0.06	–0.04	0.08	−0.19
dps9496_i4d	60.85S, 54.71 W	1,040	22.11.1994–19.11.1996	X	0.51	0.58	0.64	0.48
dps9697_i4d	60.84S, 54.72 W	1,170	21.11.1996–29.12.1997		0.53	0.56	0.71	0.43
ck2_9394.c	46.87S, 53.47 W	3,600	10.3.1993–02.3.1994	X	0.65	0.66	0.72	0.45
fs1_9292_acc	53.52S, 57.03 W	2,800	13.1.1992–19.7.1992	X	0.48	0.44	0.33	0.62
fs3_9292_acc	47.16 W,60.05S	2,267	08.1.1992–19.11.1992	X	0.51	0.56	0.55	0.61
sd1_9192_a	61.47S, 61.29 W	3,946	24.12.1991–06.11.1992	–	0.37	0.56	0.60	0.50
sd2_9293_a	54.71 W, 60.85S	1,020	14.11.1992–25.11.1993	–	0.18	0.33	0.60	−0.03
sd2_9394_a	54.71 W, 60.85S	1,020	28.11.1993–20.11.1994	–	0.52	0.54	0.72	−0.21
sd2_94_96	54.72 W, 60.85S	1,040	22.11.1994–19.11.1996	–	0.41	0.52	0.53	0.49
sd2_96_97	54.72 W, 60.85S	1,107	20.11.1996–30.12.1997	0.38	0.41	0.45	0.59	0.27
NNS	57.50 W, 56.84S	2,096	26.11.1995–17.11.1996	–	0.16	0.14	0.16	0.16
CD	56.35 W, 58.36S	3,776	19.11.1994–18.11.1996	–	0.13	0.11	0.25	−0.29
crozet_9394	51.94E, 46.40S	160	02.7.1993–09.10.1994	–	0.65	0.69	0.78	0.42
dpc9496a_i4d	56.35 W, 58.36S	3,776	20.11.1994–17.11.1996	–	0.16	0.13	0.29	−0.11
dpc9496a_i4d	56.35 W, 58.36S	3,776	20.11.1994–14.7.1996	X	0.17	0.25	0.27	0.10
Kerguelen	69.36E, 47.66S	185	07.7.1993–20.10.1994	–	0.36	0.53	0.57	0.51
marfrio_4p_a	36.01 W, 31.99S	2,604	02.5.1995–04.5.1996	–	0.41	0.46	0.52	0.04
myr9296_a1d	55.49 W, 59.72S	3,690	14.11.1992–07.8.1996	–	0.13	0.11	0.15	0.08
Amsterdam	37.88S, 77.58E	350	02.5.1992–10.7.1993	–	0.58	0.58	0.60	0.58
Amsterdam	37.88S, 77.58E	350	12.7.1993–23.10.1994	–	0.58	0.59	0.40	0.75
Weddell CH1	30.1 W, 59.867S	2,823	18.1.1998–08.4.1999	0.32	0.65	0.69	0.79	0.35
Weddell CH2	34.62 W, 73.69S	2,826	21.1.1998–17.2.1999	0.54	0.54	0.57	0.70	0.36
Weddell MS2	32.01 W, 76.58S	389	10.2.1998–21.2.1999	0.52	0.50	0.51	0.52	0.35

Grey fields indicate maximum correlations.

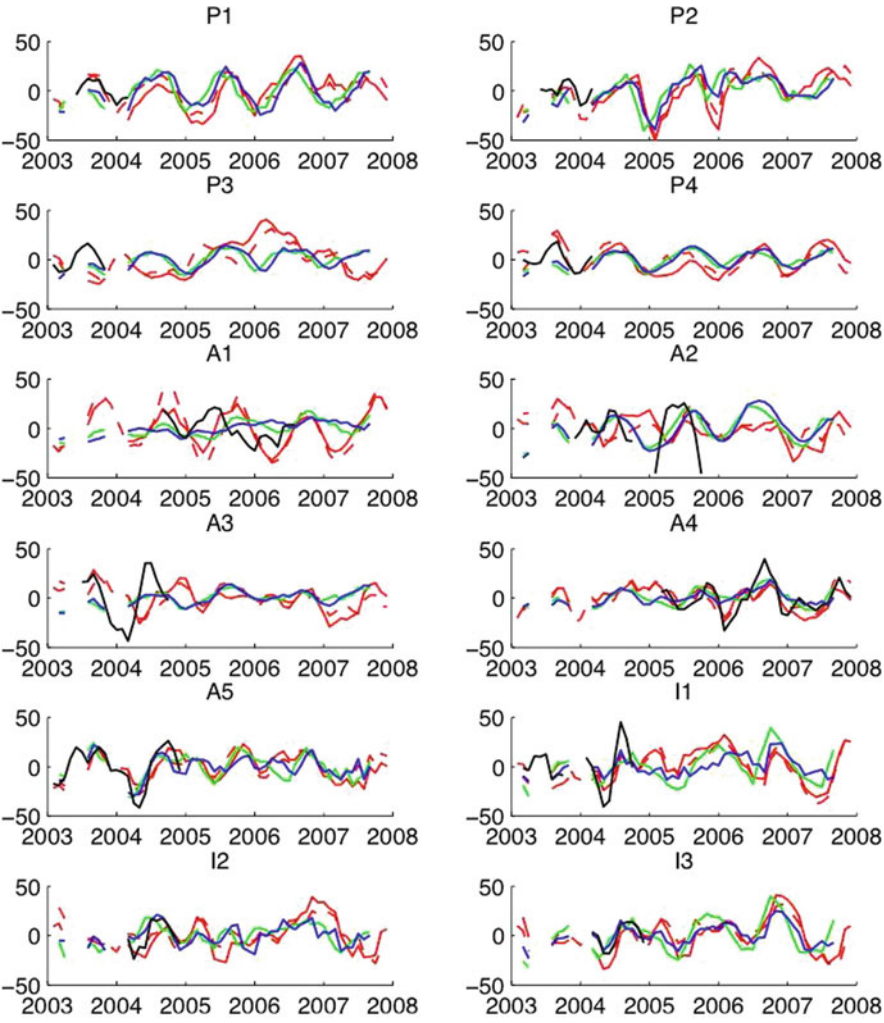

Fig. 3 Three-months running mean bottom pressure (mm equivalent water height) for various locations as calculated from bottom pressure sensors (*black*), GECCO (*green*: reference run, *blue*: assimilation run) and GRACE Level-2 (*red*; solid: GFZ, *dashed*: CSR) solutions. For positions see Fig. 1

In the Pacific, GRACE bottom pressure variations compare well with the GECCO-2 synthesis, which is substantially higher correlated with the few available bottom sensor data than the reference run (Fig. 4). An exception can be found at site P3; here the bad performance of GRACE data might be due to artificial leakage of landmass signals from the nearby U.S. mainland (Munekane, 2007, site 46405 therein). In the North Atlantic (A1) GRACE variability is slightly stronger than observed by the ocean bottom pressure recorder (compare Kanzow et al., 2005).

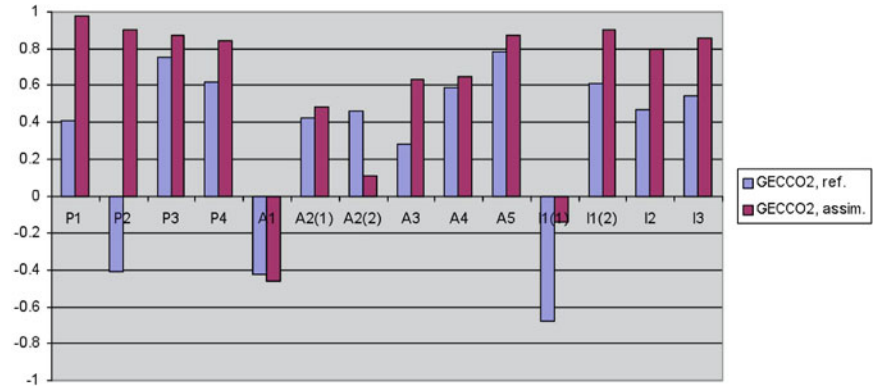

Fig. 4 Correlation of GECCO ocean bottom pressure with observations from sensors. For positions see Fig. 1

In contrast, GECCO-2 strongly under-estimates the observed OBP variations. In the Drake Passage (A2), no strong correlation between GRACE, GECCO-2 and sensor data is found; however, downstream of Drake Passage (A3), the GECCO synthesis strongly correlates with the in situ observation, albeit the variability is strongly underestimated. For the two sites near and north of Bouvet Island (southwest of Capetown, A4 and A5) GRACE compares fairly well with the in situ data and also the GECCO-2 estimates correlate but under-estimate the signal strength. In the Indian Ocean, finally, I1 is the only site where sensor data exhibit much stronger variability than the GRACE models. The correlation between in situ sensor measurements and GRACE is low for the first period in 2003, but high for the second measurement period in 2004. The same holds for GECCO. In the Crozet-Kerguelen region signal strength is comparable to sensor data for both GRACE and GECCO OBP, with high correlation of the GECCO assimilation with in situ data.

5 Global EOF Fields of GRACE and Model p_b Variations

EOFs are a valuable tool for describing and comparing the large-scale variability present in GRACE retrievals and model simulations of p_b. We show in Fig. 5 the first EOF from GRACE monthly p_b fields and the associated GECCO-2 monthly bottom pressure anomalies, both evaluated over the identical period 2003 through 2007. As can be seen from the respective loading time series (Fig. 5c) the first mode EOF essentially represents the seasonal variability in bottom pressure associated with a redistribution of mass which explains close to 25% of the total variance, i.e., it represents a significant fraction of the total variance present in the monthly p_b fields. We note from the figure that the phases of the seasonal cycle match very well between the GRACE retrievals and the model simulations although there are small month-to-month discrepancies. Likewise, spatial patterns of the EOFs are in clear agreement

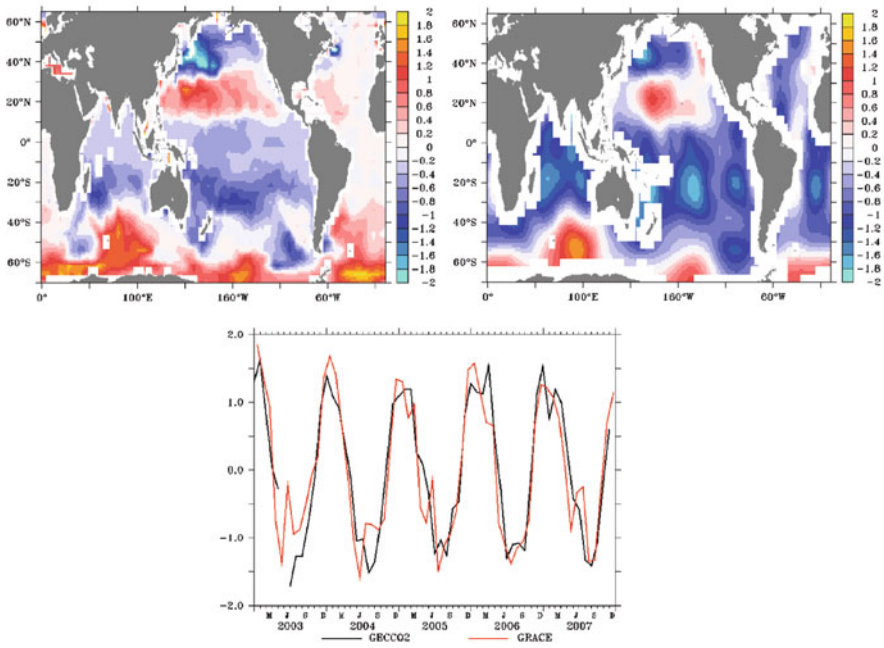

Fig. 5 First EOF of (**a**) GECCO2 (*top left*, 25%) and (**b**) GRACE (*top right*, 24%) bottom pressure anomalies. The *color bar* is in cm and percentages indicate the percent variance explained (*bottom*). Loading time series of EOF for GECCO2 and the CSR GRACE product (normalized, dimensionless)

indicating the great progress that was made in processing the GRACE gravity fields, but also in simulating the bottom pressure variations. The associated redistribution is mainly characterized by a transport of mass from the polar/subpolar regions towards the subtropical gyres in response to a seasonally changing barotropic circulation. The two fields differ mostly in the Atlantic, showing a smaller signal for GECCO-2 and no transport of mass in the northern hemisphere for GRACE. Otherwise even regional highs, such as those observed along the ACC do agree well in amplitude and spatial structures.

We conclude from this comparison, that the model simulations and GRACE retrievals of seasonal bottom pressure variations appear consistent with each other on the seasonal time scale and that it is timely to try to investigate the value of GRACE data for improving the barotropic variations through incorporating them into the model through data assimilation.

6 Concluding Remarks

The goal of this work was to test the skill of ocean models in simulating observed bottom pressure changes as function of time scale and to quantify the differences between existing ocean syntheses (i.e., models that were constrained by ocean

data) and monthly GRACE retrievals of bottom pressure variations. The comparison between model simulations and bottom pressure data does reveal a substantial agreement between models and pressure measurements on high frequencies, but also some clear differences on longer time scales (> 1 year) that need to be corrected in order to improve estimates of the barotropic circulation. Equally important, we find a good agreement between monthly GRACE solutions and ECCO/GECCO syntheses that encourage us now to use the GRACE fields as constraints in ocean synthesis efforts. Differences of the order of a few centimeters appear consistent with previously estimated uncertainties provided by Quinn and Ponte (2008), see also Ponte et al. (2007), Bingham and Hughes (2006), Park et al. (2008) and Rietbroek et al. (2006). Differences can partly be rationalized as land effects leaking out over the ocean and thereby corrupting the GRACE solutions. Other differences still have to be interpreted in terms of uncertainties in the model and data.

A valuable tool to decipher uncertainties in gravity fields is the approach of data assimilation, i.e., the combination of gravity fields with ocean circulation models and other ocean data. Uncertainties in the gravity data are expected to stand out as residuals (e.g., Stammer et al., 2007), which subsequently can be used to improve the gravity models. But there appears also the possibility that GRACE data might correct the small seasonal variations in bottom pressure in the model, especially over the Atlantic, as well as other model deficiency. Respective work is underway and we are thereby at the verge of finally improving the time-varying ocean circulation estimates through the use of time-variable gravity models on top of what we learn from ocean data alone.

Acknowledgment Helpful comments from R. Ponte are gratefully acknowledged. Thanks also go to the ECCO-GODAE and OMCT groups for providing their model results and to the data centers providing bottom pressure data. Funded, in part, through the DFG Projects STA410/9-1 and STA410/14-1, the DFG SFB 512, TP E1. as well as the BMBF GEOTECHNOLOGIEN project GOCE-GRAND-II (03F0421E). Contribution to the GECCO effort at the KlimaCampus of the University of Hamburg.

References

Bingham RJ, Hughes CW (2006) Observing seasonal bottom pressure variability in the North Pacific with GRACE. Geophys. Res. Lett. 33, L08607, doi: 10.1029/2005GL025489.

Kanzow T, Flechtner F, Chave A, Schmidt R, Schwintzer P, Send U (2005) Seasonal variation of ocean bottom pressure derived from gravity recovery and climate experiment (GRACE): Local validation and global patterns. J. Geophys. Res. (Oceans) 110, C09001 doi: 10.1029/2004JC002772.

Köhl A, Stammer D (2008a) Decadal sea level changes in the 50-year GECCO ocean synthesis. J. Clim. 21, 1876–1890.

Köhl A, Stammer D (2008b) Variability of the meridional overturning in the North Atlantic from the 50-year GECCO state estimation. J. Phys. Oceanogr. in press.

Köhl A, Stammer D, Cornuelle B (2007) Interannual to decadal changes in the ECCO global synthesis. J. Phys. Oceanogr. 37(2), 313–337.

Munekane H (2007) Ocean mass variations from GRACE and tsunami gauges. J. Geophys. Res. (Solid Earth) 112(B11), 7403?+, doi: 10.1029/2006JB004618.

Park J-H, Watts DR, Donohue KA, Jayne SR (2008) A comparison of in situ bottom pressure array measurements with GRACE estimates in the Kuroshio Extension. Geophys. Res. Lett. 35, L17601, doi: 10.1029/ 2008GL034778.

Ponte RM, Quinn KJ, Wunsch C, Heimbach P (2007) A comparison of model and GRACE estimates of the large-scale seasonal cycle in ocean bottom pressure. Geophys. Res. Lett. 34, L09603, doi: 10.1029/2007GL029599.

Quinn KJ, Ponte RM (2008) Estimating weights for the use of time-dependent gravity recovery and climate experiment data in constraining ocean models. J. Geophys. Res. (Oceans) 113(C12), 12013?+, doi: 10.1029/2008JC004903.

Rietbroek R, LeGrand P, Wouters B, Lemoine J-M, Ramillien G, Hughes CW (2006) Comparison of in situ bottom pressure data with GRACE gravimetry in the Crozet-Kerguelen region. Geophys. Res. Lett. 33, L21601, doi: 10.1029/2006GL027452.

Swenson S, Wahr J (2006) Post-processing removal of correlated errors in GRACE data. Geophys. Res. Lett. 33, L08402.

Siegismund F, Romanova V, Köhl A, Stammer D (2010) Bottom Pressure and Circulation Changes Estimated from GRACE and Ocean Synthesis. Manuscript in preparation.

Stammer D, Wunsch C, Giering R, Eckert C, Heimbach P, Marotzke J, Adcroft A, Hill CN, Marshall J (2002) The global ocean circulation during 1992–1997, estimated from ocean observations and a general circulation model. J. Geophys. Res. 107(C9), 3118, doi: 10.1029/2001JC000888.

Stammer D, Wunsch C, Giering R, Eckert C, Heimbach P, Marotzke J, Adcroft A, Hill CN, Marshall J (2003) Volume, heat and freshwater transports of the global ocean circulation 1993–2000, estimated from a general circulation model constrained by World Ocean Circulation Experiment (WOCE) data. J. Geophys. Res. 108(C1), 3007, doi: 10.1029/2001JC001115.

Stammer D, Wunsch C, Giering R, Zhang Q, Marotzke J, Marshall J, Hill CN (1997) The global ocean circulation estimated from TOPEX/POSEIDON altimetry and the MIT general circulation model. MIT Center for Global Change Science, Report 49.

Stammer D, Ueyoshi K, Köhl A, Large WB, Josey S, Wunsch C (2004) Estimating air-sea flux estimates through global ocean data assimilation. J. Geophys. Res. 109, C05023, doi: 10.1029/2003JC002082.

Stammer D, Köhl A, Wunsch C (2007) Impact of accurate geoid fields on estimates of the ocean circulation. J. A. O. Tech. 24, 1464–1478.

Thomas M (2002) Ocean induced variations of Earth's rotation – Results from a simultaneous model of global circulation and tides. PhD dissertation, University of Hamburg, Germany.

Wunsch C, Heimbach P (2006) Estimated decadal changes in the north Atlantic meridional overturning circulation and heat flux 1993–2004. J. Phys. Oceanogr. 36, 2012–2024.

Part IV
SEAVAR

Sea Level Variations – Prospects from the Past to the Present (SEAVAR)

Tilo Schöne and Jens Schröter

Climate change and climatic fluctuations are a natural phenomenon and have occurred over different temporal scales during the Earth's history. In addition to this natural variability, the question of human-induced changes of climate has gained increasing public awareness. This interest is caused by indications of recent global warming, which has been related to increasing portions of anthropogenic greenhouse gases in the atmosphere. The importance of sea level when studying climate change is, that it responds as a highly sensitive indicator of climate change, the main causal connections being the mass exchange between land ice and ocean water and the thermal expansion of the ocean water.

Besides this monitoring function of climate change, sea level itself is of public concern. This is a consequence of the fact that a large portion of the human population lives close to the coast and, therefore, would be directly affected by a sea level rise as expected for global warming. Thus, irrespective of whether the current changes are governed by natural or by anthropogenic processes, it is of prime interest to determine sea level and sea level changes with high accuracy, to study the likely sources and to predict future sea level changes.

Measuring sea level variations with tide gauges and radar altimetry and modeling the associated effects by general ocean circulation models is the primary means to derive consistent statements about regional and global sea level change patterns. Moreover, in combination with the new series of gravity field models derived from CHAMP and GRACE, steps are made towards the separation of mass and density changes for parts of the world ocean.

For the last two decades altimetry has played an important role in detecting sea level change on a global scale. A strong regional variability even for decadal periods has been measured from satellites. A main pitfall of altimetry is that no single mission covers the whole time span with sufficient accuracy. The series of radar altimetry satellites started in 1985 with the launch of GEOSAT but was discontinued in 1989 till 1992. Since than a series of high quality satellite missions have been

T. Schöne (✉)
Helmholtz Centre Potsdam, GFZ German Research Centre for Geosciences,
Department 1: Geodesy and Remote Sensing, Telegrafenberg, 14473 Potsdam, Germany
e-mail: t.schoene@gfz-potsdam.de

F. Flechtner et al. (eds.), *System Earth via Geodetic-Geophysical Space Techniques*,
Advanced Technologies in Earth Sciences, DOI 10.1007/978-3-642-10228-8_24,

followed or paralleled each other. However, the analysis of the results of all missions does not lead to unique sea level estimates. Depending on the choice of corrections algorithms distinctly different trends are found. With the consistent reprocessing of satellite orbits (chapter "Radar Altimetry Derived Sea Level Anomalies – The Benefit of New Orbits and Harmonization" by Schöne et al., this issue) for the first time comparable accuracies for sea level anomalies and mean sea level was achievable.

The derivation of long-term trends is complicated by the fact, that climate-induced decadal and secular sea level changes can be concealed by seasonal, annual and interannual variations, which may act as noise masking long-term trends. Long-term time series of sea level measurements are available only from tide gauges (TGs), which are also sensitive to vertical land movements and are, thus, records of relative rather than absolute sea level. Another difficulty comes from the inhomogeneous distribution of TGs over the globe. An optimal analysis of TG records requires assimilating the data into a global ocean model with the goal of extrapolating these data over the entire domain in a dynamically consistent way. However, most of global ocean circulation models are not capable of resolving the ocean coastline in a sufficiently accurate way which is also necessary to fully exploit the fine resolution of the Gravity Field and Steady-State Ocean Circulation (GOCE) Mission.

The accurate determination of sea level, the prediction of its future changes and its use as an indicator of climate change is linked to our understanding of the governing processes in the strongly interactive dynamic system Earth. This confronts scientists with the following tasks:

- Accurate determination of absolute sea level using multi-mission satellite altimetry supported by space and surface techniques from GEOSAT till today (chapter "Radar Altimetry Derived Sea Level Anomalies – The Benefit of New Orbits and Harmonization" by Schöne et al., this issue).
- Estimation of vertical rates of GPS benchmarks at TGs and combination with TG measurements to derive absolute sea level change records with high resolution and long history (chapter "Reanalysis of GPS Data at Tide Gauges and the Combination for the IGS TIGA Pilot Project" by Rudenko et al., this issue).
- Improved estimates of historical global sea level variability by combining TG measurements and radar altimetry (RA) through empirical orthogonal functions (EOF) (chapter "A 15-Year Reconstruction of Sea Level Anomalies Using Radar Altimetry and GPS-Corrected Tide Gauge Data" by Schön et al., this issue).
- Estimation of regional and global sea level change for 20 years and more to fill the gap between the GEOSAT and TOPEX/Poseidon altimeter missions by ocean modeling and assimilation (chapter "Sea Level Rise in North Atlantic Derived from Gap Filled Tide Gauge Stations of the PSMSL Data Set" by Reinhardt et al., this issue).
- Refinement of ocean model resolution for better description of boundary currents, assimilation of absolute dynamic topography in conjunction with hydrographic measurements from autonomous profiling floats and preparation of the use of

a fine resolution geoid (chapter "Using ARGO, GRACE and Altimetry Data to Assess the Quasi Stationary North Atlantic Circulation" by Richter et al., this issue).
- Consistent assimilation of altimetry derived sea level anomalies from GEOSAT to TOPEX/Poseidon into an ocean circulation model (chapter "Combining GEOSAT and TOPEX/Poseidon Data by Means of Data Assimilation" by Wenzel and Schröter, this issue).

A major step forward made in SEAVAR is the consistent reprocessing of satellite orbits (chapter "Radar Altimetry Derived Sea Level Anomalies – The Benefit of New Orbits and Harmonization" by Schöne et al., this issue) starting from GEOSAT (1985–1989), ERS-1 (1992–1996), ERS-2 (since 1995) to TOPEX/Poseidon (1992–2005). Small inconsistencies still exist since the older satellites had different satellite tracking technologies. Nevertheless, the main improvement came from the consistent use of up-to-date gravity field models and improved tracking station coordinates. The new orbits for the first time allowed estimating high quality sea level anomalies for the period covering 1985 till now. This improvement had allowed to (i) assimilating a long time series into the general ocean circulation model and (ii) to estimate sea level variability over the past 15 years using a combination of radar altimetry and tide gauges.

To construct long time series of sea level anomalies for e.g., the past 50 years, tide gauges can be used as a proxy. PSMSL (UK) provides revised tide gauge time series for a global set of gauges; however, the time series are affected by local vertical land movement. In 2001 the Tide Gauge Benchmark Monitoring Pilot Project (TIGA) was initiated by the International GNSS Service and GLOSS to process and provide estimates of vertical land movement. GFZ is contributing from the beginning, providing consistent time series of vertical motion at tide gauges. Within SEAVAR a new attempt has been made to reprocess a much larger data set of GPS data at tide gauges (chapter "Reanalysis of GPS Data at Tide Gauges and the Combination for the IGS TIGA Pilot Project" by Rudenko et al., this issue). Now, vertical estimates for more than 280 sites are available. In combination with solutions of other contributors, a global and unified GPS solution is now available.

Both the GPS corrected time series and the newly derived sea level anomalies have been used to construct sea level anomalies (chapter "A 15-Year Reconstruction of Sea Level Anomalies Using Radar Altimetry and GPS-Corrected Tide Gauge Data" by Schön et al., this issue). A major contribution is the study of the sensitivity of the reconstruction to the geographical distribution of the tide gauges, which is of importance for reconstructions of sea level anomalies over longer periods back in time.

Combining the altimetry data and tide gauge data with ocean circulation models opens further perspectives in assessing sea level rise over time spanning GEOSAT and TOPEX/Poseidon missions. Data assimilation studies carried out at AWI (chapter "Combining GEOSAT and TOPEX/Poseidon Data by Means of Data Assimilation" by Wenzel and Schröter, this issue) rely on tide gauge data to bridge

the gap between the missions and find that ocean warming accounts for one third of the global sea level rise and concludes that the inflow of fresh water adds another 2 mm/year.

A reconstruction of the sea level rise for the North Atlantic relying on tide gauge data for 1950–2006 and the Inverse Finite Element Ocean Model (IFEOM) show 1.18 mm/year sea level rise for this period (chapter "Sea Level Rise in North Atlantic Derived from Gap Filled Tide Gauge Stations of the PSMSL Data Set" by Reinhardt et al., this issue). About 27% are explained by steric expansion of the ocean while the remaining 73% are due to inflow of water from land or surrounding oceans.

SEAVAR successfully demonstrated the advantage of a consistent and combined approach in using radar altimetry, tide gauges, GPS and ocean circulation models.

Radar Altimetry Derived Sea Level Anomalies – The Benefit of New Orbits and Harmonization

Tilo Schöne, Saskia Esselborn, Sergei Rudenko, and Jean-Claude Raimondo

1 Introduction

Satellite radar altimetry (RA) has proven to be a reliable and efficient method to monitor the global sea level and its short- and long-term changes. With currently five active RA missions (ERS-2, JASON-1, ENVISAT, GFO-1, JASON-2), the global sea level can be observed with reasonable accuracy. Exploiting the already completed missions of GEOSAT, ERS-1 and TOPEX/Poseidon sea level time series of more than two decades can be constructed. Due to the different orbital parameters, accuracy, long-term system stability and spatial coverage, all satellites, however, give slightly different results in terms of regional sea level change and sea surface variability.

In the past several attempts have been made to calibrate and long-term monitor individual as well as to cross-calibrate different RA missions. For JASON-1 and TOPEX/Poseidon this has been successfully demonstrated (e.g., Ablain et al., 2009). However, the poor orbit quality of especially GEOSAT has heavily constrained studies on decadal sea level variability. With the recently developed gravity field models EIGEN-GRACE04Sp (Foerste et al., 2008) and improvements in orbit modeling new orbits have been computed for various RA missions (GEOSAT, ERS-1, ERS-2, TOPEX/Poseidon). For GEOSAT the improvement is most clearly visible, reducing the RMS of single crossover differences from 15 to 9 cm which is almost the level of ERS-2.

2 The Altimeter Database and Processing System (ADS)

For accurate analyses of local and global sea level it is vital to use consistently processed data from active and completed altimeter missions incorporating state of the art correction models. In order to integrate, process, update, and harmonize

T. Schöne (✉)
Helmholtz Centre Potsdam, GFZ German Research Centre for Geosciences,
Department 1: Geodesy and Remote Sensing, Telegrafenberg, 14473 Potsdam, Germany
e-mail: t.schoene@gfz-potsdam.de

F. Flechtner et al. (eds.), *System Earth via Geodetic-Geophysical Space Techniques*,
Advanced Technologies in Earth Sciences, DOI 10.1007/978-3-642-10228-8_25,

data from different radar altimeter missions the Altimeter Database and Processing System (ADS) has been developed since several years at GFZ. Using the ADS system it is possible to correct the data for various instrumental and environmental effects as well as to merge different correction models optimized for the desired application.

The ADS consists on the one hand of a database holding data from most completed and recent RA missions (GEOSAT, ERS-1, ERS-2, TOPEX, GFO-1, Jason-1) as well as state of the art instrumental, orbital, and environmental correction models. This structure allows for integrating upcoming data corrections and new correction models in a timely manner. The parallel storage of different correction models for the same effects allows for testing their influence on derived quantities, such as mean sea levels and crossover statistics.

In addition ADS provides tools to extract and process data – starting from the extraction of uncorrected data or correction models at given coordinates and times up to the derivation of statistical quantities like crossover point statistics, collinear analysis, and the derivation of mean sea surface height and sea level anomaly models. The data is provided along-track as well as interpolated onto regular geographical grids. A web interface (http://adsc.gfz-potsdam.de) allows external users to retrieve and process data and to derive many statistical quantities.

3 Harmonization of Different Altimetric Missions

Almost all past and recent RA missions are using different processing standards and different environmental correction models. As long as single mission studies are performed, these differences can be neglected. However, when comparing or combining different RA data, a harmonization is necessary.

Some environmental effects can be corrected using the same correction models, e.g. tidal effects or the reaction on atmospheric pressure changes. For those effects, state of the art correction models are provided consistently for all missions available at the ADS. Other correction models, like the ionospheric or wet tropospheric correction, rely on the satellite hardware. Harmonization is done by using the most accurate corrections available for the individual missions. For the selection of correction models studies have been performed to identify systematic differences between the different models. Other correction models including e.g. sea state bias and orbits it is possible to re-calculate them at least in a similar manner. In this paper, however, we will concentrate on the consistent recomputation of satellite orbits and their effects on sea level anomalies derived from GEOSAT data.

For the calculation of mean sea level and sea level anomaly maps discussed here the best-available correction models, orbits, and data upgrades (e.g., Rudenko and Schöne, 2007; Rudenko et al., 2006; Scharroo et al., 2000; Scharroo et al., 2004; AVISO, 2008) have been used. In case several state of the art models were available the “best model” was selected by minimization of single- and inter-mission crossover differences (Figs. 1 and 2). It can also be seen that the sea level trends

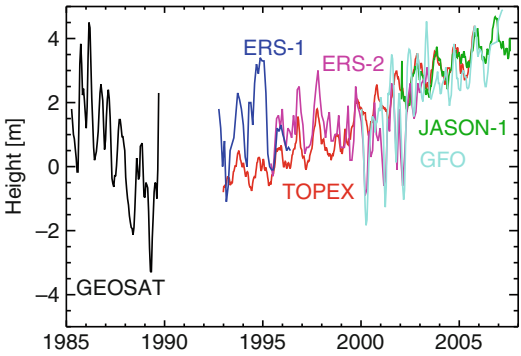

Fig. 1 Sea level time series derived using the selection of best-performing correction models and reprocessed orbits

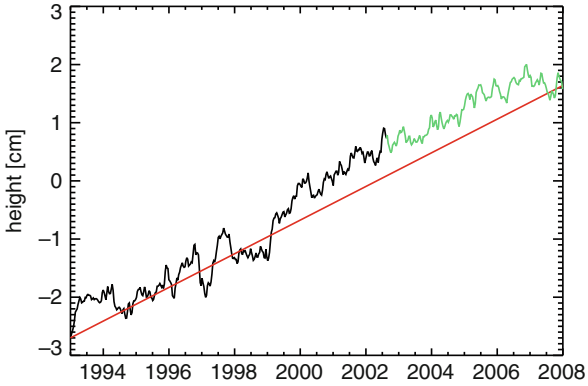

Fig. 2 Sea level time series derived from the combination of TOPEX and JASON-1 altimetry

still differ between the missions. These are artifacts originating from orbit insufficiencies, problems in the external calibration, as well as from some of the correction models.

4 The Effects of New Orbits

Precise orbits of RA satellites GEOSAT (March 1985–December 1989), ERS-1 (August 1991–June 1996), TOPEX/Poseidon (September 1992–October 2005) and ERS-2 (May 1995–February 2006) were derived using GFZ's EPOS-OC software in the same ITRF2000 reference frame (Boucher et al., 2004) for all satellites using common models (Table 1) for the time periods given above. The orbits were computed using the following types of observations: GEOSAT orbit was calculated using Doppler and single RA crossover (SXO) data, ERS-1 and ERS-2 orbits using satellite laser ranging (SLR) and SXO data and TOPEX/Poseidon orbit using SLR and Doppler Orbitography Integrated by satellite (DORIS) observations.

Table 1 The main models, input data and corrections used for the RA satellite orbit determination

Forces, input data, corrections	Model used
Geopotential	EIGEN-GRACE04Sp up to $n = m = 80$ (70 for TOPEX/Poseidon) (Foerste et al., 2008)
Third body gravitational attraction	Sun, Moon, Mercury, Venus, Mars, Jupiter, Saturn (DE405, LE405) (Standish, 1998)
Atmosphere density	MSIS-86 (Hedin, 1987), CLS F10.7 cm solar flux and Ap coefficients
Solar radiation pressure	Umbra, penumbra modeled
Albedo and infrared radiation of the Earth	Knocke and Ries (1987)
Solid Earth tides	IERS Conventions 2003 (McCarthy and Petit, 2003)
Ocean tides	FES2004, up to $n = m = 50$ (Letellier, 2004)
Atmospheric tides	Biancale and Bode (2006)
Earth rotation parameters	IERS EOP 05 C04 series with IERS2003 daily and sub-daily corrections (http://www.iers.org/MainDisp.csl?pid=36-9)
Nutation model	Wahr model with VLBI corrections (McCarthy and Petit, 2003)
Initial station coordinates	ITRF2000, if available, or estimated
Station velocities	ITRF2000, if available, or NNR-NUVEL1A model
Troposphere correction	Marrini-Murray (1973) with Herring correction for SLR data, Hopfield (1969) model for Doppler and DORIS data
Ocean loading effect on stations	GFZ, based on FES2004 ocean tide model
Atmospheric loading effect on stations	GFZ, based on ECMWF atmosphere data
Relativistic corrections	Post-Newtonian correction, relativistic corrections for SLR measurements (McCarthy and Petit, 2003)

The 7-day orbital arcs with 2-day overlaps were used for GEOSAT, ERS-1 and ERS-2 and 12-day arcs for TOPEX/Poseidon. Shorter arcs were used in case of orbit maneuvers. The orbit quality was evaluated using root mean square (RMS) fits of measurements, orbital arc overlaps, RMS and mean crossover differences. The use of the new models, in particular the EIGEN-GRACE geopotential models (Flechtner et al., 2006) and an optimal parameterization for each satellite (Rudenko and Schöne, 2007) allowed improving the satellite orbits significantly (Rudenko et al., 2006, 2007), as compared to the orbits derived in the standard distribution of altimetry data. As a result, e.g., the mean value of RMS crossover differences reduces from 11.7 cm for ERS-2 orbit derived using PGM055 geopotential and other rather old models (Massmann et al., 1997) to 7.1 cm for the new orbit. Improved parameterization and new models also significantly enhance the GEOSAT orbit, especially for the period of high solar activity (MJD 47,400–47,900) (Fig. 3). The mean value of RMS crossover differences is 15.4 cm for NASA JGM-3 orbit (GEOSAT Handbook, 1997) and 9.0 cm for GFZ EIGEN-GRACE04S orbit of GEOSAT.

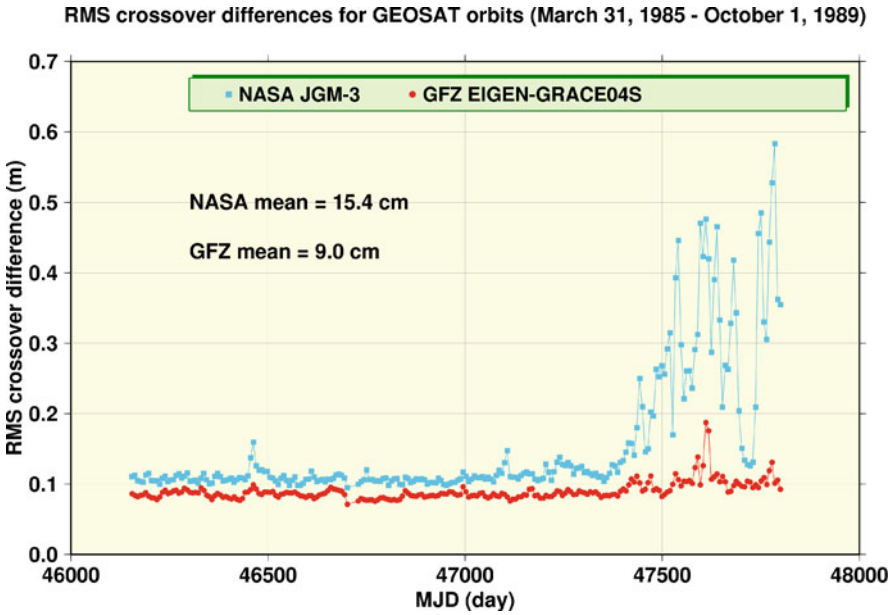

Fig. 3 RMS crossover differences for GEOSAT orbits computed at NASA (GEOSAT Handbook, 1997) and GFZ; x-axis in Modified Julian Days (March 1985–December 1989)

Since the GEOSAT original orbit was based on the JGM-3 gravity field model (GEOSAT Handbook, 1997), the progress in orbit modeling, in particular, use of a new gravity field model and improved parameterization significantly enhances the derived sea level quantities especially for the final phase (Figs. 4 and 5). Although

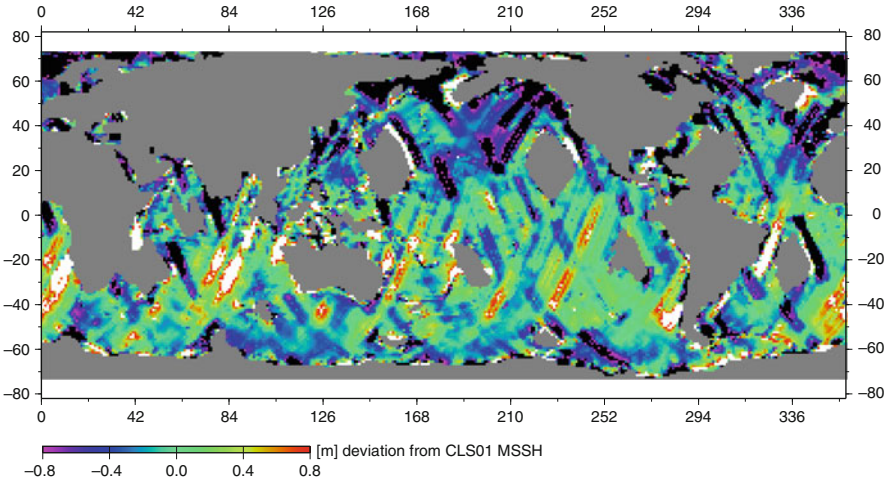

Fig. 4 Sea level anomalies of GEOSAT (May 1988) derived using the original JGM-3 based orbits

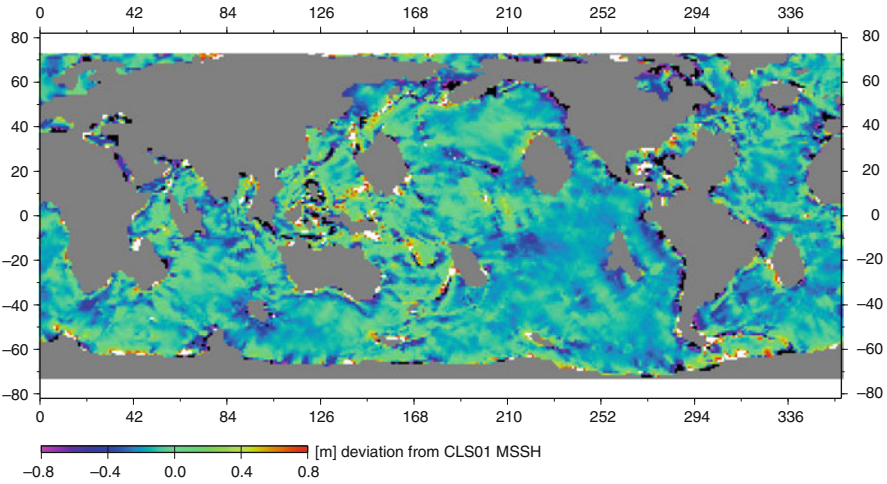

Fig. 5 Sea level anomalies of GEOSAT (May 1988) derived using the GFZ reprocessed EIGEN-GRACE04Sp orbits

the global weighted sea level change value remains almost identical, regional differences can be observed. Notable differences occur especially in the Northern Pacific and Northern Atlantic. In addition the half-monthly sea level anomalies (SLA) are less noisy and, thus more suitable, for assimilation into ocean circulation models.

5 Summary and Outlook

As a result of the reprocessing and harmonization of GEOSAT and other RA mission data, a radar altimetry data set is now available for studies of decadal sea level variability. Using improved or new models and modeling approaches for instrumental and environmental corrections has further improved the consistency of derived sea level anomalies. Especially the orbit recomputation for different RA missions allows studies in a consistent reference frame for the first time.

The GEOSAT mission still suffers from a negative trend in sea level. Already a few attempts have been made to calibrate this mission using tide gauge data but leaking for the correct geo-referencing of the tide gauges. Having now a reprocessed orbit, GPS correction for tide gauges, and upgraded altimetry data will allow for calibrating GEOSAT RA data.

So far, there is still a biannual fluctuation visible in the GEOSAT derived SLA values. Most likely data from one ore more individual tracking stations are causing this effect, although no single station was identified so far.

Acknowledgments ILRS (Pearlman et al., 2002) and IDS (Tavernier et al., 2006) data were used. GEOSAT Doppler data were provided by C.K. Shum (Ohio). RA data are provided by ESA

for ERS-1 and ERS-2, by NASA/CNES for TOPEX/Poseidon and JASON-1, and by NOAA for GEOSAT. This is publication no. GEOTECH-1252 of the GEOTECHNOLOGIEN programme of BMBF, grant 03F0434A. Altimetry and orbit data is available through the ADS system at GFZ http://adsc.gfz-potsdam.de/ads.

References

Ablain M, Cazenave A, Valladeau G, Guinehut S (2009) A new assessment of global mean sea level from altimeters highlights a reduction of global trend from 2005 to 2008. Ocean Sci. Discuss. 6, 31–56.

AVISO (2008) SMM-MU-M5-OP-13184-CN, Edition 4.1, October 2008, http://www.aviso.oceanobs.com/fileadmin/documents/data/tools/hdbk_j1_gdr.pdf

Biancale R, Bode A (2006) Mean annual and seasonal atmospheric tide models based on 3-hourly and 6-hourly ECMWF surface pressure data. GFZ Scientific Technical Report 06/01, doi: 10.2312/GFZ.b103-06011.

Boucher C, Altamimi Z, Sillard P, Feissel-Vernier M (2004) The ITRF2000. IERS Technical Note, No. 31.

Flechtner F, Schmidt R, Meyer U, Schöne T, Esselborn S, Förste C, Stubenvoll R, Rudenko S, Neumayer KH, Rothacher M, König R (2006) The benefit of EIGEN gravity field models for altimetry and vice versa. In: International Symposium on "15 Years of Progress in Radar Altimetry" Symposium (Venice 2006).

Foerste C, Schmidt R, Stubenvoll R, Flechtner F, Meyer U, König R, Neumayer H, Biancale R, Lemoine JM, Bruinsma S, Loyer S, Barthelmes F, Esselborn S (2008) The GeoForschungsZentrum Potsdam/Groupe de Recherche de Geodesie Spatiale satellite-only and combined gravity field models: EIGEN-GL04S1 and EIGEN-GL04C. J. Geod. 82(6), 331–346, doi: 10.1007/s00190-007-0183-8.

GEOSAT Handbook (1997) http://ibis.grdl.noaa.gov/SAT/gdrs/geosat_handbook

Hedin AE (1987) MSIS-86 thermospheric model. JGR 92, 4649–4662.

Hopfield HS (1969) Two-quadratic tropospheric refractivity profile for correction satellite data. JGR 74(18), 4487–4499.

Knocke P, Ries J (1987) Earth radiation pressure effects on satellites. Technical Memorandum CSR-TM-87–01. Center for Space Research, The University of Texas at Austin, USA.

Letellier T (2004) Etude des ondes de marée sur les plateux continentaux. Thèse doctorale, Université de Toulouse III, Ecole Doctorale des Sciences de l'Univers, de l'Environnement et de l'Espace, 237 pp.

Marini JW, Murray CW (1973) Correction of laser range tracking data for atmospheric refraction at elevations above 10 degrees. NASA GSFC X-591-73-351.

Massmann FH, Neumayer KH, Raimondo JC, Enninghost K, Li H (1997) Quality of the D-PAF ERS orbits before and after inclusion of PRARE data. Proceedings of the 3rd ERS Symposium on Space at the service of our Environment, Florence, Italy, 17–21 March 1997, ESA SP-414, 3 Vols.

McCarthy DD, Petit G (eds.) (2003) IERS Conventions. IERS Technical Note 32.

Pearlman MR, Degnan JJ, Bosworth JM (2002) The international laser ranging service. Adv. Space Res. 30(2), 135–143, doi: 10.1016/S0273-1177(02)00277-6.

Rudenko S, Schöne T (2007) Influence of parameterization on the accuracy of altimetry satellite orbits. Geophy. Res. Abstr. 9, 07492.

Rudenko S, Schöne T, Gendt G, Zhang F, Thaller D (2007) Precise orbits of altimetry satellites and analysis of GPS data at tide gauges for sea level research. In: Observations of the System Earth from Space: status seminar, 22–23 November 2007, Bavarian Academy of Sciences and Humanities, Munich; Programme & Abstracts, Koordinierungsbüro GEOTECHNOLOGIEN, 41–46.

Rudenko S, Schöne T, Raimondo JC (2006) Precise orbits of altimetry satellites ERS-1, ERS-2 and TOPEX/Poseidon. In: International Symposium on “15 Years of Progress in Radar Altimetry” (Venice 2006).

Scharroo R, Schrama EJO, Naeije M, Benveniste J (2000) A recipe for upgrading ERS altimeter data. Proceedings of ERS-ENVISAT Symposium, Gothenburg, 2000.

Scharroo R, Lillibridge JL, Smith WHF, Schrama EJO (2004) Cross-calibration and long-term monitoring of the microwave radiometers of ERS, TOPEX, GFO, Jason, and Envisat. Mar. Geod. 27, 279–308.

Standish EM (1998) JPL Planetary and Lunar Ephemerides, DE405/LE405, JPL IOM 312. F-98-048.

Tavernier G, Fagard H, Feissel-Vernier M, Le Bail K, Lemoine F, Noll C, Noomen R, Ries JC, Soudarin L, Valette JJ, Willis P (2006) The international DORIS service: genesis and early achievements. In: DORIS Special Issue, P. Willis (ed.), J. Geod. 80(8–11), 403–417, doi: 10.1007/s00190-006-0082-4.

Combining GEOSAT and TOPEX/Poseidon Data by Means of Data Assimilation

Manfred Wenzel and Jens Schröter

1 Introduction

The global sea level is exceedingly reacting on variations of the climate. A warming of the world ocean or the melting of large continental ice sheets for example would lead to a sea level rise that would affect directly a large part of mankind. These effects are reasonable well studied on the global scale but they are still uncertain on regional or even local scale. For the period of the TOPEX/Poseidon altimetric measurements Wenzel and Schröter (2006, 2007) showed that the sea level trends vary substantially in space and time and that they are closely associated with heat and salt anomalies in the ocean. By assimilating the TOPEX/Poseidon measurements into a global ocean circulation model they were able to separate the individual parts contributing to the sea level change (steric effects, oceanic fresh water budget). But longer time-series of the global distribution of sea level variability are needed to confirm these results because the climate-induced decadal and secular sea level changes may be concealed by seasonal, annual and interannual variations, which may act as noise masking long-term trends. One step in this direction is to utilize sea surface height (SSH) data from the GEOSAT altimetric mission (1987–1989) in combination with the TOPEX/Poseidon data (1993–2000). Both datasets will be assimilated into a global ocean circulation model. By doing this the data gap between GEOSAT and TOPEX/Poseidon can be filled in a dynamically consistent manner. We will then be in a position to separate sea level rise due to inflow of continental waters from warming of the ocean for a much longer time period and reduce estimation error.

2 Model and Data

For our purpose we use the Hamburg Large Scale Geostrophic model (LSG, Maier-Reimer and Mikolajewicz, 1991; Maier-Reimer et al., 1993). In conjunction with its adjoint this model has been used successfully for ocean state estimation (e.g. Wenzel

M. Wenzel (✉)
Alfred Wegener Institute for Polar and Marine Research, 27570 Bremerhaven, Germany
e-mail: manfred.wenzel@awi.de

F. Flechtner et al. (eds.), *System Earth via Geodetic-Geophysical Space Techniques*, Advanced Technologies in Earth Sciences, DOI 10.1007/978-3-642-10228-8_26,

and Schröter, 2006, 2007). It has 2 × 2 degree horizontal resolution, 23 vertical layers (varying from 20 m thickness for the top layer to 750 m for the deepest ones) and the implicit formulation in time allows for a time step of 10 days. The utilized global OGCM has a free surface. Mass conservation is achieved by taking into account the volume and mass of the surface freshwater flux as well as by including the steric effects of thermal expansion and haline contraction. This offers the possibility to combine altimetric measurements with hydrographic data in a dynamically consistent manner. Details about the assimilation procedure can be found e.g. in Hellmer et al. (2005).

Here we perform two assimilation experiments. First we make use of all available data from altimetry of both satellite missions called GEOSAT-TOPEX/Poseidon (GETO). It is mostly a substantial extension of the previous work reported in Hellmer et al. (2005) and Wenzel and Schröter (2007). The relative reference between the satellite altimeters is uncertain, as there was no period of overlap. We accept this fact by referencing GEOSAT to its own temporal mean. The gap to TOPEX/Poseidon is filled by the ocean model. As it turned out the results for this gap were not satisfactorily and a second assimilation experiment was performed using additional data.

The only continuous dataset for sea level for the whole assimilation period is land based and consists of tide gauge records. In a preliminary study it was found that the direct use of sea level time series at tide gauge stations has only little influence on the general model behaviour. There are simply too many reasonable dynamically consistent solutions for a local sea level that are the effect of regional changes in wind forcing or local density variations in the ocean which are inside the observed variability We therefore produced a global dataset for sea surface height which is reconstructed from tide gauges and observed variability patterns as measured by TOPEX/Poseidon in analogy to the study by Church and White (2006). The second experiment is then denoted GEOSAT-TOPEX/Poseidon-Reconstructed (GETORC).

Let us next describe the datasets used in the experiment GETO in detail:

- Monthly sea surface temperatures (SST) for the period 1987–2000 (Reynolds et al., 2002).
- Gridded fields of 10 day averages of sea surface height anomalies (SSHA) as measured by the TOPEX/Poseidon altimetric mission for the period 1993–2000, provided by GeoForschungsZentrum Potsdam (GFZ; S. Esselborn, pers. communication). These anomalies are combined with the SHOM98.2 mean sea surface height (MSSH; available online at the time of writing at: http://www.cls.fr/html/oceano/projets/mss/cls_shom_en.html) referenced to the EIGEN-GRACE01S geoid (available online at the time of writing at: http://www.gfz-potsdam.de/grace/results/grav/g001_eigen-grace01s.html) to give absolute dynamic height values.
- Preliminary re-processed gridded fields of 10 day averages of sea surface height anomalies (SSHA) as measured by the GEOSAT altimetric mission for the period 1987–1989, provided by GeoForschungsZentrum Potsdam (chapter "Radar Altimetry Derived Sea Level Anomalies – The Benefit of New Orbits

and Harmonization" by Schöne et al., 2009, this issue). These anomalies are referenced to their own temporal mean.
- Temporal mean transports of mass, freshwater and heat as obtained by different authors and as they are summarized e.g. by Bryden and Imawaki (2001) and by Wijffels (2001). Transport constraints are not applied for the Antarctic Circumpolar Current (ACC).
- The climatological mean temperatures and salinities from the WOCE Global Hydrographic Climatology (WGHC; Gouretski and Koltermann, 2004) in combination with the mean annual cycle from the World Ocean Atlas (WOA01; Conkright et al., 2002). These data are supplied to the assimilation procedure with small weights thus serving only as background information.
- The mean annual cycle of temperatures, salinities and horizontal velocities on two sections in the Weddell Sea area and on four sections in the Ross Sea. These data are taken from high resolution model experiments of the Weddell Sea (Schodlok et al., 2002) and the Ross Sea (Assmann and Timmermann, 2005) whose water mass characteristics and circulation are in good agreement with local observations.

In the second experiment GETORC, we additionally use SSHA fields that are reconstructed from tide gauges and an EOF basis deduced from the TOPEX/Poseidon data, in analogy to Church and White (2006). These data will be applied for the whole period 1987–2000.

3 Results

The data assimilation produces minor changes in atmospheric forcing which is in agreement with observed atmospheric variability. Further, the initial temperature and salinity fields of the ocean can be adjusted. Both changes result in a temporal evolution of the modelled ocean which is as close to the observations in space and time as possible and follows the exact model equations. All ocean fields are in dynamic equilibrium and data counterparts can be modelled in satisfactory agreement with the observed values. It is found that the initial state has only little influence on the evolution. The most important changes are in the wind and thermal forcing. Freshwater fluxes have small local effects, however their global integral directly influences the global sea level variation.

Figure 1 shows the modelled global mean sea level anomaly (GMSLA) after assimilation for the experiment GETO in comparison to the above mentioned satellite measurements. While the model reproduces the GMSLA derived from TOPEX/Poseidon quite well this is not the case for GEOSAT. Even the trend during the period 1987–1989 is not reproduced. The model prefers a positive trend while the data show a negative one. Anyhow, the modelled positive trend seems to be more realistic to some extent as one can conclude from the GMSLA reconstructed by Church and White (2006) from tide gauge records that shows a positive trend throughout the period 1986–2000. Furthermore, Fig. 1 shows that from hydrographical data alone the assimilation has no reason to produce a sea

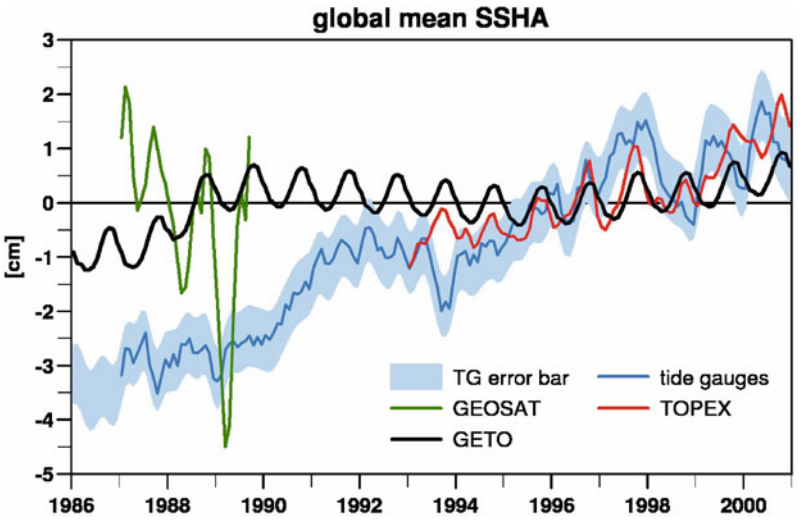

Fig. 1 Temporal evolution of the global mean of the sea level anomaly from assimilation experiment GETO compared to the satellite data used. Because the GEOSAT data are anomalies only with no own reference, they are adjusted to have the same temporal mean as the model solution. For comparison the SSHA data reconstructed from tide gauges (*blue curve*) are included together with the error bars (*blue shading*) taken from Church and White (2006)

level rise as strong as given by Church and White (2006), although its steric part during this period appears to be reasonable. To demonstrate the latter Fig. 2 shows the evolution of the oceans heat content from experiment GETO. Its trend fits well to the results of Levitus et al. (2005). Therefore, the missing part must contribute to the oceanic fresh water budget (eustatic sea level change) that remains unrestricted during most of the assimilation period as long as the models SSHA is constrained by data only for disconnected sub-periods that do not have a common reference, i.e. as for TOPEX/Poseidon an absolute reference is needed for the GEOSAT data before reliable statements are possible for the past 20 years. Another possibility to improve the situation would be to link the different SSHA datasets by additional information about the evolution of the sea level during the whole assimilation period.

Consequently we produced the second experiment GETORC. The SSHA data reconstructed from tide gauges are utilized as additional information during the whole assimilation period. Also for GETORC the negative trend from the GEOSAT data during 1987–1989 is not reproduced (Fig. 3). Nevertheless, now the temporal evolution of the GMSLA fits well to the one given by Church and White (2006) for the whole period 1987–2000. Beside this, during the time with the TOPEX/Poseidon SSHA employed (1993–2000) it is even further improved. This improvement is not only confined to the GMSLA. It also applies to the spatial structure of the sea level. The root mean square (RMS) value for the difference between the modelled SSH and the data is only slightly smaller for GETORC than for GETO during the GEOSAT period (1987–1989), but it is significantly reduced

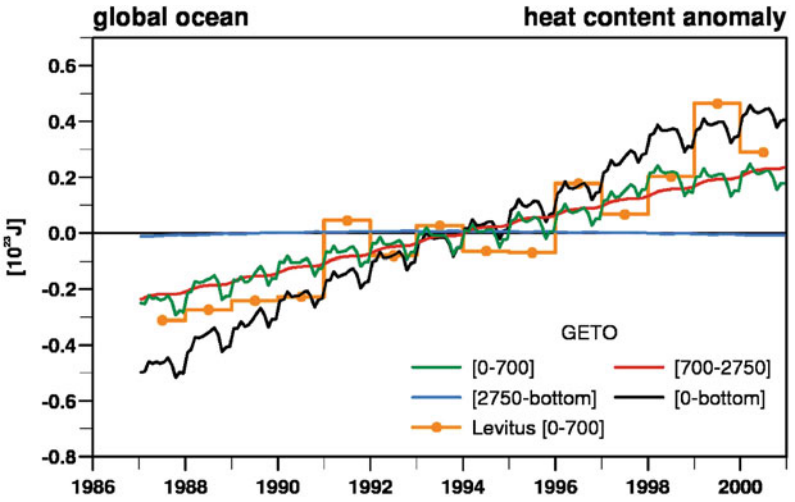

Fig. 2 Temporal evolution of the global oceans heat content anomaly for the depth ranges [0–700 m], [700–2,750 m] and [2,750 m-bottom]. For the upper 700 m the corresponding annual mean values derived from Levitus et al. (2005) are included

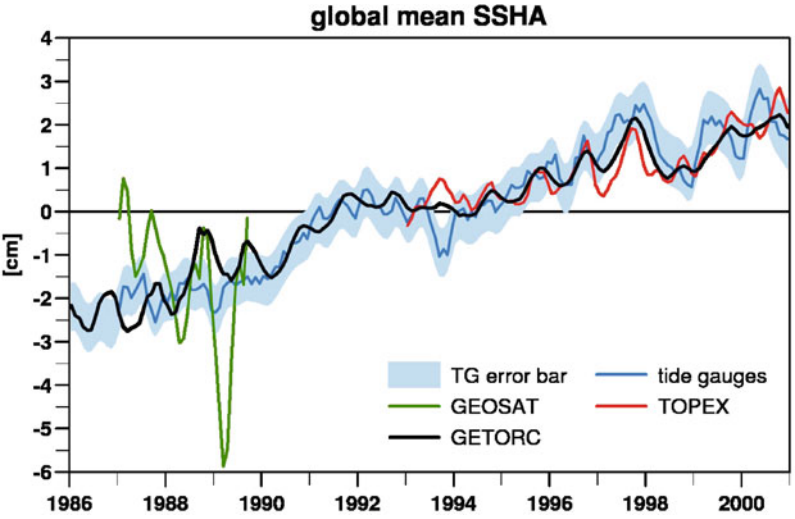

Fig. 3 Temporal evolution of the global mean of the sea level anomaly from assimilation experiment GETORC compared to the satellite data used. Note that in this experiment the SSHA data reconstructed from the tide gauges are assimilated!

for the TOPEX/Poseidon period (Fig. 4a, b). In general the RMS differences now coincide approximately with the values that result from the differences between the SSHA data derived from altimeter and the ones reconstructed from tide gauges. Accordingly the spatial correlations between model and data have increased for

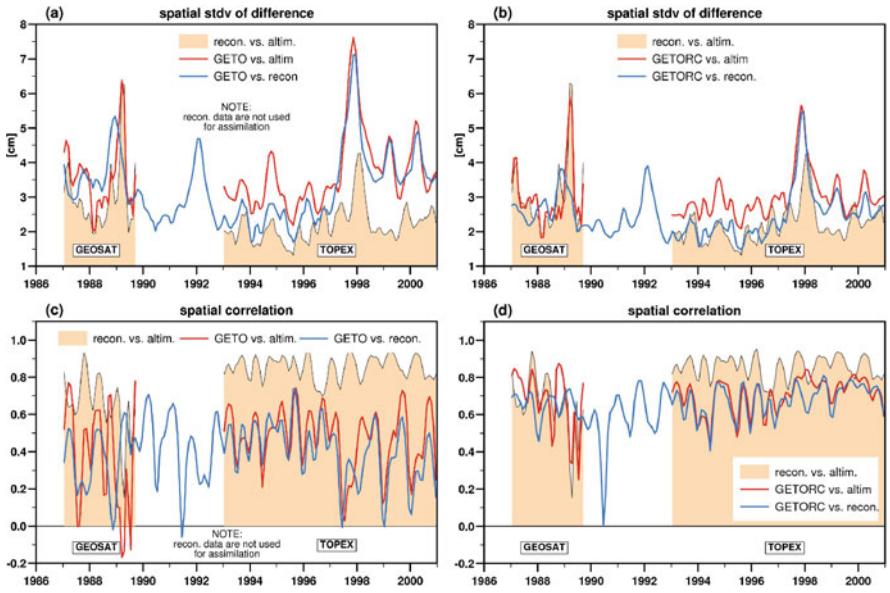

Fig. 4 *Upper row*: temporal evolution of the spatial RSM of the difference between the model SSHA and the data. *Lower row*: the corresponding correlations for the two experiments GETO (*left*: **a**, **c**) and GETORC (*right*: **b**, **d**). For comparison the *light grey* shading gives the corresponding values for the difference between the tide gauge reconstruction and the satellite data

both periods (Fig. 4c, d). Both facts strongly indicate that the model solution profits from assimilating this additional dataset that bridges the gap between GEOSAT and TOPEX/Poseidon.

To analyse the regional distribution of the modelled sea level trend (Fig. 5) in more detail it is dissected into the parts that stem from the eustatic contribution, i.e. the ocean fresh water budget, and from the steric effects, i.e. thermal expansion and haline contraction. On global average the eustatic part (Fig. 5b) contributes about two thirds (1.98 mm/year) to the total sea level rise (2.95 mm/year, Fig. 5a) although on regional to local scale it is less important than the thermosteric (Fig. 5c) and the halosteric part (Fig. 5d). Both, the thermosteric and the halosteric changes, are of the same order of magnitude locally and they nearly compensate in large parts of the world ocean, as has been demonstrated already by Wenzel and Schröter (2006, 2007), whereas on global average the halosteric trend is negligible (0.05 mm/year) compared to the thermosteric (0.92 mm/year).

A further inspection of the results on a global scale shows, that about half of the thermosteric sea level rise stems from an upper ocean warming (0–700 m). The development of the heat content of this layer (Fig. 6a) is mainly constrained via the sea surface temperature and by the climatological hydrographic annual cycle and it fits well to the estimates of Levitus et al. (2005), even better than for experiment GETO (Fig. 2). In the lower depth ranges (700–2,750 m and 2,750 m-bottom) we find ocean warming, an increasing heat content too. Both layers add about one quarter to the total heat surplus each, i.e. together as much as the upper 700 m. Thus, the

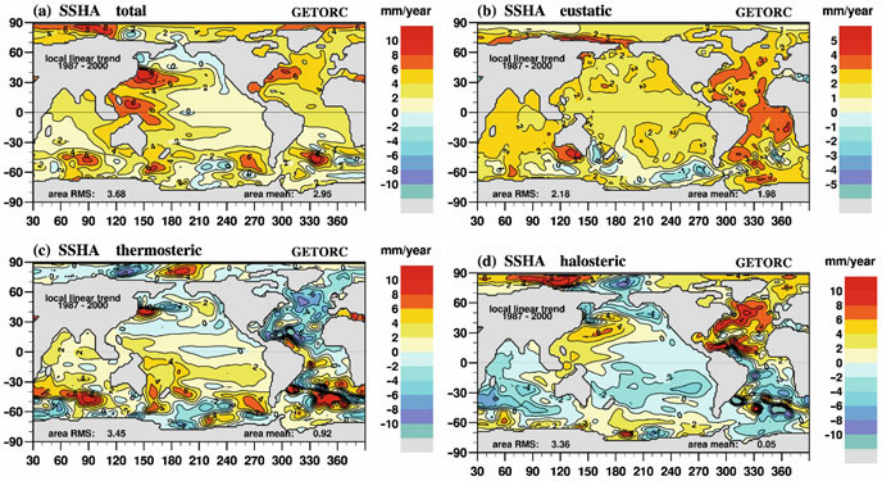

Fig. 5 (**a**) Local sea level trend dissected into its (**b**) eustatic, (**c**) thermosteric and (**d**) halosteric contribution. Note the enlarged colour scale for the eustatic part!

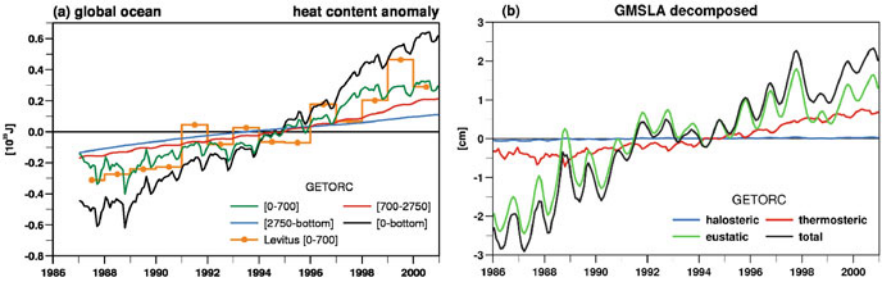

Fig. 6 (**a**) Temporal evolution of the global oceans heat content anomaly for the experiment GETORC as in Fig. 2, (**b**) the resulting global mean sea level anomaly dissected into its thermosteric, halosteric and eustatic contribution

deep ocean adds an essential contribution to the total (thermo)steric sea level rise. In any case, the global steric sea level variations give only about one third of the total trend. The subordinate importance of the steric trend compared to the eustatic during this period has already been stressed by Jevrejeva et al. (2008). Furthermore, in comparison with the eustatic variations, the steric show a much weaker annual cycle that is out of phase (Fig. 6b), a well known result from hydrology.

4 Summary and Conclusions

In order to assess the sea level rise for periods longer than the continuous observations by TOPEX/Poseidon we performed two assimilation experiments. Both use the GEOSAT mission data additionally and bridge the gap between these observations

in a dynamically consistent manner in accordance with standard ocean observations. It is found that the global fresh water fluxes of the ocean remain uncertain to such an extent that the evolution of the sea level cannot be concluded from measurements of fluxes or estimates of land ice melting. Without continuous records of the sea level no reliable estimates can be made, as has been demonstrated in the experiment GETO.

We therefore used additional observations provided by time series of sea level at tide gauges. From these data global maps of sea level anomalies were constructed using the EOF technique applied in Church and White (2006). These maps are subsequently assimilated in addition to the sea surface height anomalies from altimetry. Experiment GETORC then provides the answer to the total sea level rise and to its temporally and spatially varying contributions. Ocean warming accounts for one third of global sea level rise by steric expansion. Half of it is confined to the upper 700 m of the ocean, in good agreements with the independent analysis of Levitus et al. (2005). The other half of oceanic thermosteric expansion is found in equal parts above and below the depth of 2,750 m. That is we diagnose very strong warming of the deep ocean which cannot be deducted from the very sparse in situ observations alone. In addition to warming of the ocean we find an inflow of fresh water with amplitude close to 2 mm/year. This value is also on the high side but it is supported by the analysis of Jevrejeva et al. (2008). Wrapping up we can conclude that a relative reference has been found between the satellite missions GEOSAT and TOPEX/Poseidon which is physically reasonable and in accordance with oceanic observations, in particular tide gauge records.

Acknowledgement This is publication no. GEOTECH-1253 of the GEOTECHNOLOGIEN programme of BMBF, grant 03F0434B. We are grateful to the anonymous reviewer for helpful comments and suggestions.

References

Assmann KM, Timmermann R (2005) Variability of dense water formation in the Ross Sea. Ocean Dyn. 55(2), 68–87, doi: 10.1007/s10236-004-0106-7.

Bryden HL, Imawaki S (2001) Ocean heat transport. In: Siedler G, Church J, Gould J (ed.), Ocean Circulation and Climate, Academic Press, New York, International Geophysics Series Vol. 77, pp. 455–474.

Church JA, White NJ (2006) A 20th century acceleration in global sea-level rise. Geophys. Res. Lett. 33, L01602, doi: 10.1029/2005GL024826.

Conkright ME et al. (2002) World Ocean Atlas 2001: objective analysis, data statistics and figures, CD-ROM Documentation, National Oceanographic Data Center, Silver Springs, MD, 17 pp.

Gouretski VV, Koltermann KP (2004) WOCE Global Hydrographic Climatology, A Technical Report, Berichte des Bundesamtes für Seeschifffahrt und Hydrographie, No. 35, 50 pp + 2 CD-ROM

Hellmer HH, Schodlok MP, Wenzel M, Schröter J (2005) On the influence of adequate Weddell Sea characteristics in a large-scale global ocean circulation model. Ocean Dyn. 55, 88–99.

Jevrejeva S, Moore JC, Grinstead A (2008) Relative importance of mass and volume changes to global sea level rise. J. Geophys. Res. 113, D08105, doi: 10.1029/2007JD009208.

Maier-Reimer E, Mikolajewicz U (1991) The Hamburg large scale geostrophic ocean general circulation model (Cycle 1), Technical Report, 2, Deutsches Klimarechenzentrum, Hamburg

Maier-Reimer E, Mikolajewicz U, Hasselmann K (1993) Mean circulation of the Hamburg LSG OGCM and its sensitivity to the thermohaline surface forcing. J. Phy. Oceanogr. 23, 731–757.

Levitus S, Antonov J, Boyer T (2005) Warming of the world ocean, 1955–2003. Geophys. Res. Lett. 32, L02604, doi: 10.1029/2004GL021592.

Reynolds RW et al. (2002) An improved in situ and satellite SST analysis for climate. J. Clim. 15, 1609–1625.

Schodlok MP et al. (2002) On the transport, variability, and origin of dense water masses crossing the South Scotia Ridge. Deep Sea Res. II 49, 4807–4825.

Wenzel M, Schröter J (2006) Understanding measured sea level rise by data assimilation. In: "Proceedings of the Symposium on 15 Year of Progress in Radar Altimetry", SP-614, ESA Publication Division, Noordwijk, The Netherlands, ISBN 92-9092-925-1, ISSN 1609-042X, CD-ROM.

Wenzel M, Schröter J (2007) The global ocean mass budget in 1993–2003 estimated from sea level change. J. Phy. Oceanogr. 37(2), 203–213, doi: 10.1175/JPO3007.1.

Wijffels SE (2001) Ocean transport of fresh water. In: Siedler G, Church J, Gould J (eds.), Ocean Circulation and Climate, Academic Press, New York, International Geophysics Series Vol. 77, pp. 475–488.

Reanalysis of GPS Data at Tide Gauges and the Combination for the IGS TIGA Pilot Project

Sergei Rudenko, Daniela Thaller, Gerd Gendt, Michael Dähnn, and Tilo Schöne

1 Introduction

Analysis of tide gauge measurements for sea level change research requires a well defined reference frame. Such reference frame can be realized through precise positions of GPS stations located at or near tide gauge benchmarks. Establishment, maintenance and expansion of the network of GPS stations at tide gauges and establishment of such a reference frame are the primary purposes of the IGS GPS Tide Gauge Benchmark Monitoring Pilot Project (TIGA) (Schöne et al., 2009). Presently, six TIGA analysis centres (TAC) contribute to the project, namely, Geoscience Australia (AUT), a consortium of University of Canberra, University of Tasmania and Australian National University (CTA), German Geodetic Research Institute (DGF), EUREF (ETG) through Federal Agency for Cartography and Geodesy (Germany), German Research Centre for Geosciences (GFT) and University La Rochelle (ULR). Three TAC (CTA, GFT and ULR) contribute with global station network solutions, whereas AUT, DGF and ETG provide regional station network solutions for the regions Pacific/Australia/Antarctica, Atlantic and Europe, respectively. Different TAC provided their solutions in 2002–2006. However, with the switch within the IGS from using a relative model for antenna phase centre variations (PCV) to an absolute PCV model primarily affecting the station height a reprocessing became necessary within the TIGA project.

2 Reprocessing of GPS Data at Tide Gauge Benchmarks at GFT

GPS data of the global network of 403 GPS stations (Fig. 1) at the time interval from March 1998 till December 2007 were processed using EPOS-PV2 software (Gendt et al., 1994) improved in the recent years. The main improvements

S. Rudenko (✉)
Helmholtz Centre Potsdam, GFZ German Research Centre for Geosciences,
Department 1: Geodesy and Remote Sensing, Telegrafenberg, 14473 Potsdam, Germany
e-mail: sergei.rudenko@gfz-potsdam.de

F. Flechtner et al. (eds.), *System Earth via Geodetic-Geophysical Space Techniques*,
Advanced Technologies in Earth Sciences, DOI 10.1007/978-3-642-10228-8_27,

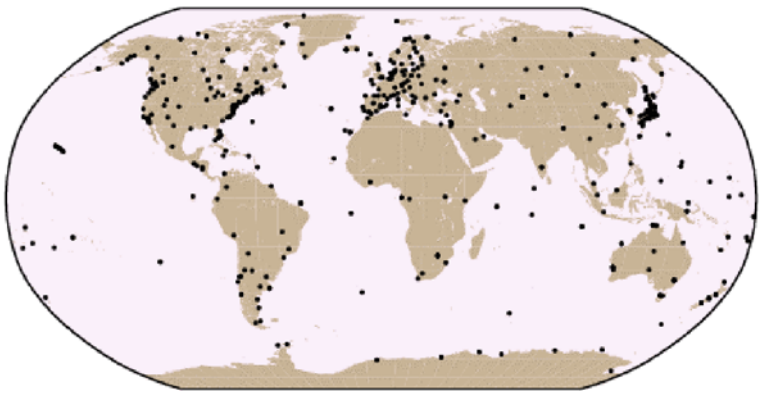

Fig. 1 Global station distribution of the GFT solution

include use of the absolute PCV model, implementation of IERS Conventions 2003 (McCarthy and Petit, 2004), development of a new ambiguity fixing scheme allowing to fix 95 vs. 80% of ambiguities (Ge et al., 2005), implementation of a new data processing strategy for huge GNSS networks (Ge et al., 2006) allowing to process GPS data from a few hundred stations in one network solution and other improvements.

The GPS analysis follows the scheme described in Zhang et al. (2007) with the following modifications. The absolute PCV model is used instead of relative one. The total number of stations in the GFT solution increased from 372 (Zhang et al., 2008) to 403 by adding 31 new TIGA stations located in Europe, Asia, Africa, Australia, Pacific, North and South America. The global network of GPS stations includes 216 IGS stations and 187 GPS TIGA stations. ITRF2005 (Altamimi et al., 2007) is used as a priori reference frame. Initial coordinates of 197 stations not present in the ITRF2005 are estimated ones and their velocities are computed using NNR-NUVEL1A model (McCarthy and Petit, 2004). A procedure based on the GFZ rapid product generation was created to compute satellite clocks using the global network of up to 98 IGS stations. The derived satellite clocks and orbits are used for data cleaning within precise point positioning (PPP), namely, for detecting cycle slips, outliers and bad observation periods. The EIGEN-GL04S1 Earth gravity model with the time variations of C20, C30 and C40 is used instead of JGM2. The Earth gravity model truncation level increased from 8 to 12.

The final results are given in the SINEX format and include weekly sets of GPS station coordinates, daily values of Earth rotation parameters and their rates, as well as satellite antenna offsets. The mean value of RMS fits of L3 ionosphere-free linear combination of phase observables is 6.9 mm.

Weekly station coordinates of the GFT solution were compared with those of the solutions of two TACs, namely, CTA and ULR, and with the solutions of three IGS Analysis Centres (AC), namely, GFZ (GF1), Massachusetts Institute of Technology, USA (MI1) and National Geodetic Survey, NOAA, USA (NG1) ACs (Fig. 2). The

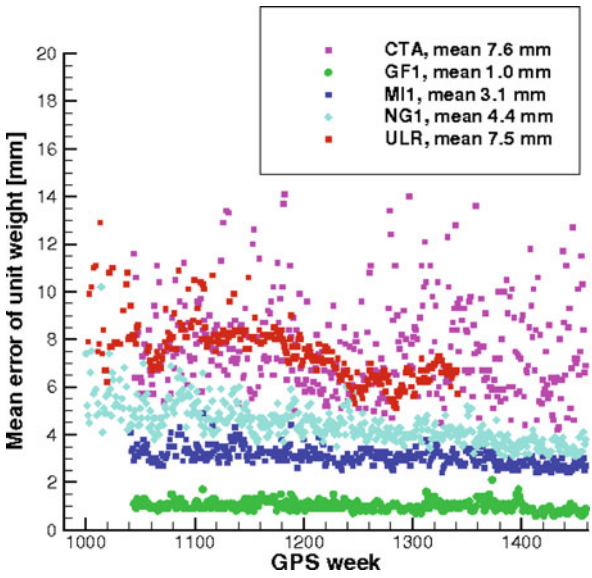

Fig. 2 Comparison of weekly station coordinates of the GFT solution and the solutions of other TIGA and IGS analysis centres

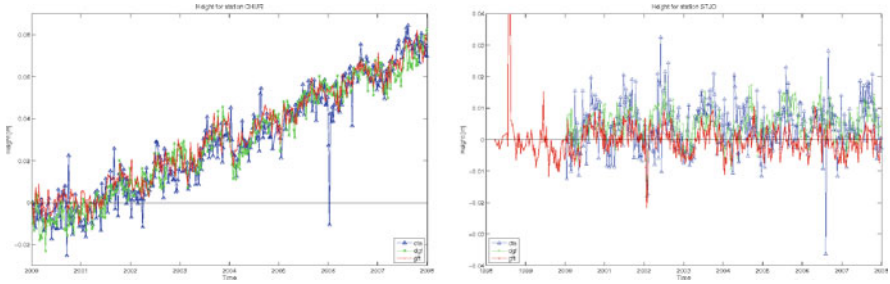

Fig. 3 Time series of station heights derived from the individual TAC solutions for two TIGA sites

mean RMS difference of station coordinates of GFT and GF1 solutions is 1.0 mm, and of GFT and four other IGS and TIGA AC solutions is 3–8 mm. The differences can be caused by using different models, software packages, data processing strategies, etc.

Figure 3 shows the time series of station height derived from the GFT solution in the comparison with two other TIGA analysis center solutions, namely, CTA and DGF. The temporal behavior agrees quite well. After removing the linear trend (10.2 mm/year for the GFT solution) from the time series of station CHUR (Churchill, Canada), the weighted RMS values of the residuals are 8.1, 6.0 and 5.5 mm for the CTA, DGF and GFT solution, respectively. In the case of STJO (St. John's, Canada), the vertical trend is much smaller (–0.2 mm/year for the GFT solution). The weighted RMS values are 7.3, 4.1 and 6.4 mm for the three series.

3 Combination of Weekly TIGA Solutions

As the TACs perform the processing on a best-effort basis, not all could manage it to fully reprocess all data. Table 1 summarizes the actual status of the reprocessed solutions (20/10/2009).

In order to minimize the so-called analysis noise and to provide station coordinates for all TIGA observing stations (TOS) in one common reference frame, a combination of the individual contributions is indispensable. Hence, a similar procedure that is already applied for the official weekly IGS product (see Ferland et al., 2005) is done for the TIGA project as well. The individual contributions are provided as weekly solutions using the SINEX format, so that the full variance-covariance matrix and the information on a priori constraints are provided in addition to the solution itself. Therefore, it is possible to fully remove the constraints applied to the individual contributions, i.e. mainly datum definition, and, thus, to derive datum-free normal equation systems (NEQs). The availability of datum-free NEQs is the precondition for a rigorous combination of all TAC contributions. The combination is done using the Bernese GPS Software version 5.0 (Dach et al., 2007) with further modifications implemented at GFZ in order to be able to handle all contributions as best as possible. The weekly combined solutions are aligned to the IGS realization of the ITRF2005 (Altamimi et al., 2007) using no-net-rotation and no-net-translation conditions for the set of reference frame stations used within the IGS.

Figure 4 shows the time series of station heights derived from the weekly combined solutions exemplarily for two TOS. Metsahovi (METS, Fig. 4a) is one of the stations with a clearly pronounced annual signal, e.g. coming from atmospheric or hydrological loading. Contrary, the station Townsville (TOW2; Fig. 4b) has even almost no annual signal; however, a comparably large linear trend is visible.

The time-series of combined coordinates of the TOS were used to reconstruct sea level anomalies and it turned out that the time series perform very well for such applications (see Schöne et al., 2009).

Table 1 Status of reprocessed TAC contributions that were computed using the new IGS standards

TAC	First week	Last week	No. of weeks available	No. of weeks missing	No. of stations
AUT	0887	1,512	626	0	∼80
CTA	1,043	1,474	432	0	∼130
DGF	1,043	1,511	469	0	∼60
ETG	1,400	1,548	149	0	∼40
GFT	939	1,459	515	6	∼400
ULR	834	1,511	678	0	∼300

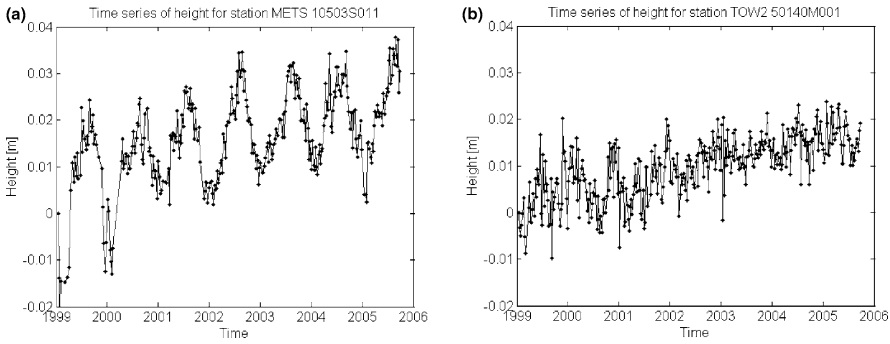

Fig. 4 Time series of weekly combined station heights for Metsahovi (METS) and Townsville (TOW2)

4 Summary and Conclusions

Reanalysis of GPS data at tide gauges allows establishing a reference frame to be used to correct tide gauge measurements and tie them to the ITRF. GPS data of stations located at or near tide gauge benchmarks (TIGA stations) have been reprocessed at six TIGA analysis centres. The improvements and results of reprocessing of GPS data from the global network of 403 stations at the time span from March 1998 till December 2007 at GFT TAC are described. The mean RMS difference of weekly station coordinates of GFT and GFZ IGS AC solutions is 1.0 mm, and of GFT solution and the solutions of four other IGS and TIGA ACs is 3–8 mm. The procedure and some results of the combination of the solutions of six TACs are given.

Acknowledgments Use of GPS data from IGS (Dow et al., 2005) and TIGA stations is acknowledged. We are grateful to F. Zhang, M. Ge, Th. Nischan and A. Brandt for useful discussions and some help and to the anonymous reviewer for the comments improved the paper. This publication no. GEOTECH-1250 of the programme GEOTECHNOLOGIEN of the German Ministry of Education and Research (BMBF), grant 03F0434A.

TAC solutions are available at TIGA web page http://adsc.gfz-potsdam.de/tiga/index_TIGA.html.

References

Altamimi Z, Collilieux X, Legrand J, Garayt B, Boucher C (2007) ITRF2005: A new release of the International Terrestrial Reference Frame based on time series of station positions and Earth Orientation Parameters. J. Geophys. Res. 112, B09401, doi: 10.1029/2007JB004949.

Dach R, Hugentobler U, Fridez P, Meindl M (2007) Bernese GPS Software 5.0, Astronomical Institute University of Bern, Bern, Switzerland.

Dow J, Neilan R, Gendt G (2005) The International GPS Service: Celebrating the 10th anniversary and looking to the next decade. Adv. Space Res. 36(3), 320–326, doi: 10.1016/j.asr.2005.05.125.

Ferland R, Gendt G, Schöne T (2005) IGS reference frame maintenance. In: Meindl M (ed.), Celebrating a Decade of the International GPS Service, Workshop and Symposium 2004, Proceedings. Astronomical Institute University of Bern, Switzerland.

Ge M, Gendt G, Dick G, Zhang FP (2005) Improving carrier-phase ambiguity resolution in global GPS network solutions. J. Geod. 79, 103–110, doi: 20.2007/s00290-005-0447-0.

Ge M, Gendt G, Dick G, Zhang FP, Rothacher M (2006) A new data processing strategy for huge GNSS networks. J. Geod. 80, 199–203, doi: 10.1007/s00190-006-0044-x.

Gendt G, Dick G, Mai W, Nischan T, Sommerfeld W (1994) Nutzerhandbuch zum Programmsystem EPOS.P.V2 (Earth Parameters and Orbit determination System) für die Analyse von GPS-daten. GeoForschungsZentrum Potsdam, Bereich "Rezente Kinematik und Dynamik der Erde", February 18, 1994.

McCarthy D, Petit G (2004) IERS Conventions (2003). IERS Technical Note 32.

Schöne T, Schön N, Thaller D (2009) IGS tide gauge benchmark monitoring pilot project (TIGA): Scientific benefits. J. Geod. 83, 249–261, doi: 10.1007/s00190-008-0269-y.

Zhang F, Gendt G, Ge M (2007) GPS data processing at GFZ for monitoring the vertical motion of global tide gauge benchmarks: Technical report for projects TIGA and SEAL. GeoForschungsZentrum Potsdam Scientific Technical Report STR07/02, 28p.

Zhang F, Wünsch J, van Dam T, Gendt G, Ge M, Schöne T (2008) Vertical crustal motion at tide gauges derived by analyzing GPS time series. GeoForschungsZentrum Potsdam Scientific Technical Report STR08/03, 106p.

Sea Level Rise in North Atlantic Derived from Gap Filled Tide Gauge Stations of the PSMSL Data Set

Heiko Reinhardt, Dimitry Sidorenko, Manfred Wenzel, and Jens Schröter

1 Introduction

Sea level in the second half of the last century has been observed at a large number of tide gauges. The major difficulty in deriving a consistent analysis of sea level rise is caused by temporal data gaps and vertical shifts in tide gauge positions. Additionally vertical land motion has to be separated from sea level change.

In the past years the tide gauge stations data have been efficiently used for many coastal and global ocean applications as well as for validation of ocean models. Thus Jevrejeva et al. (2006) used the global set of gauges to compute the sea level rise variability for the time period spanned by Permanent Service for Mean Sea Level (PSMSL, web page http://www.pol.ac.uk/psmsl) data set. They follow two approaches, one using simple mean of all active gauge stations and the other using averaging of the next-neighbouring-stations. The resulting global averaged trend is 1.8 mm/year for the time period 1900–2000. Church et al. (2004) used PSMSL data set together with TOPEX/POSEIDON satellite mission to estimate the spatio-temporal pattern for the world ocean leading to an averaged linear trend of 1.8±0.3 mm/year for the last 50 years. Other works concentrate on regional applications as exemplified by Zervas (2001) and Holgate and Woodworth (2004).

Most of these studies however neglect the temporal data gaps or just omit such series from the analysis. Our concern is therefore to reconstruct the missing data. Including reconstructed series into analysis would serve for the improvement of the regional distribution of the gauge data. Following we describe the dataset and present the methods for closing the gaps. The validation of these methods is demonstrated. The reconstructed data is further used together with IFEOM model to obtain the spatial trend and variability patterns in the North Atlantic for the period from 1950 to 1994.

H. Reinhardt (✉)
Stiftung Alfred Wegener Institut für Polar und Meeresforschung,
27570 Bremerhaven, Germany
e-mail: heiko.reinhardt@awi.de

F. Flechtner et al. (eds.), *System Earth via Geodetic-Geophysical Space Techniques*,
Advanced Technologies in Earth Sciences, DOI 10.1007/978-3-642-10228-8_28,

2 The PSMSL Gauge Data Set

Proudman Oceanographic Institute UK maintains the Permanent Service for Mean Sea Level (PSMSL), and provides us with the revised local referenced data set (RLR), consisting of time series of mean monthly sea level at gauge stations in a common time reference frame.

Gauge stations are mainly confined to the coasts of the continents, mostly Europe and North America and a few stations on islands in the open ocean. Few stations show data before 1900. This number increases in decades afterwards. A sufficient number of active stations can be seen after 1950. We consider the gauge stations in the region of IFEOM model (the North Atlantic) and the time-span from January 1950 to December 2006. Only the gauges providing time series for longer than 5 years were used.

Each gauge station rests on the ground below it, using it as its local reference frame. To compare data from different tide gauges, shifts in the reference frame must be corrected for each tide gauge. Land movements are mostly due to glacial isostatic adjustment (GIA), where the land still moves since the last glacial maximum 10,000 years ago. Oil or groundwater drilling or constructions near the gauge stations complicate the situation.

A way to reduce the time series from land movement would be with the help of GPS signals which can give a very precise value at sensor locations. GPS data however was not used in this study due to its limited availability at gauge stations and other drawbacks (see Snay et al., 2007). Results including GPS corrections are subject of a separate study.

Here, we use a correction for GIA by Peltier, which can be accessed via PSMSL (see Peltier, 1998). These values are based on theoretical assumptions and neglect some local effects of land movement.

We group the gauge stations of the North Atlantic into 10 regions as shown in Fig. 1. Typically tide gauges in the same region show similar behaviour expressed by their covariance structure. This is used in our gap-filling method.

Area Name	Ratio Gap/Data	# gauges
North UK	0.47	14
South UK	0.60	16
France	0.55	11
Iberia	0.60	16
Africa	0.69	13
Caribbean	0.56	13
Texas	0.40	12
Florida	0.51	13
Central USA	0.54	5
North-East America	0.51	16

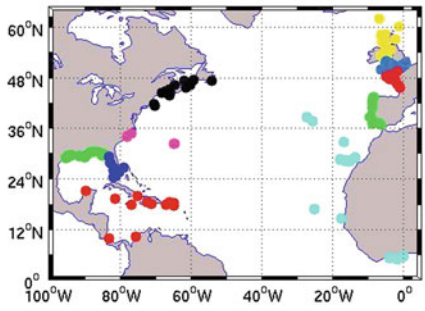

Fig. 1 Regional distribution of the gauge stations in North Atlantic used for gap filling (*right*) and details of each region

Our grouping of gauges takes into account gauge stations that are lying close together at the same continental coast line. Exceptions are the regions Caribbean and Africa. The stations in the Caribbean and on the coast of Central America were taken into one group due to large data gaps at the end of few time series in these regions. The stations on the Canaries, Azores islands and African coast were taken in one group because there are a few stations in that region.

The table within Fig. 1 (left part) summarizes the regions as well as the percentage of missing values in the data. The total number of missing values in one region should not exceed 60% of the total number of data values in that region.

3 Theoretical Background and Used Method

Multi-Channel-Singular-Signal-Analysis (MSSA): The MSSA method is mostly used for noise reduction, but can be also used for filling of data gaps. This work strongly relies on Ghil et al. (2002) where a detailed description of MSSA can be found. MSSA is based on a time lagged grand covariance matrix C, where the covariance of N time series (channels) each with a lag of M time steps to the other is calculated according to:

$$(C_{l,l'})_{j,j'} = \frac{1}{\tilde{N}} \sum_{\max(1,1+j-j')}^{\min(N,N+j-j')} x_l(t) x_{l'}(t+j-j')$$

$\check{N}$ is a normalising factor. l and l' denote the respective time series, j and j' are the indices of the entries of sub-block matrices. The grand covariance matrix is made up of N^2 sub matrices each containing a lagged covariance matrix of time series l and l'.

From Matrix C $N{*}M$ eigenvectors (M for each time signal) and $N{*}M$ eigenvalues can be calculated. By projecting each time series to the according eigenvector one gets $M{*}N$ principal components (PCs) showing the temporal behaviour. By projecting the PCs on the according time series one obtains $N{*}M$ reconstructed components (RCs).

Summing over all the according RCs fully reconstructs each time series. Every RC explains a certain percentage of variance of the time series, given by the normalised eigenvalues. So with the first few RCs the dominant behaviour of the signal can be explained, while higher RCs can be neglected as noise. This is important for our gap-filling method, since we try to reconstruct only information for long term variations in the data gaps and filter the time series after reconstruction.

Method for gap-filling: For gap-filling we considered the years from 1950 to 2006. Our aim was to get consistent time-series for all gauges for this period. The time series of the gauges are used as channels in MSSA in each region. While a few gauge stations have data for almost the entire time span, most gauge stations show large data gaps. There are several possibilities to treat with gaps in time series, the simplest being linear interpolation thereby neglecting variabilities in the time signal. Other methods as e.g. EOFs only consider covariances in space, e.g. transform

information from neighbouring gauge stations into data gaps. Our method of preference is based on Multi-Channel-Singular-Signal-Analysis (MSSA) as explained in detail in Kondrashov and Ghil (2006). Here the inserted information in the data gaps comes from the spatio-temporal covariance structure of the other gauges in the same region.

The procedure begins with inserting zeros instead of the data gaps (though one gets the same results when inserting random numbers or linear trends). We use a two-fold iteration. The inner iteration uses the following steps:

1. Calculate the leading RC of the new time-series (with inserted zeros) using MSSA.
2. At the position of the data gap insert the values of the RC.
3. Recalculate the leading RC again and insert these (new) values at the data-gaps.
4. Carry out these operations until convergence of the new (inserted) values is reached.
5. Perform the same with the next RC by starting with the resulting reconstructed time-series of the previous RC.

When a sufficient number of RCs is calculated, we get a first gap-filled signal. This result is then again inserted in step 1. We perform this outer iteration until convergence is reached. This is done for each region of gauges separately.

Best Parameters: The dominant oscillation of the plain time series is the annual cycle. In our study we only are interested in multi-annual oscillations and the linear trend. Therefore the annual cycle is removed by subtracting the mean of all Januarys from each January and accordingly with the other months. In order to have a common frame of variance, all variances where normalized to var $= 1$.

As shown in Kondrashov and Ghil (2006) the ideal window length M depends on the type of signal to be reconstructed. Since we are interested in multi-year oscillations and trends, we choose multiples of 1 year i.e. $M = 12; 24; 36; 48$ months. A larger M would reduce the ratio of filter epoch versus total time and consequently the degrees of freedom.

We want to reconstruct only the dominant behaviour of the signal in the data gaps. It turns out that only the first two RCs need to be considered. In Fig. 2 an example is shown as a test case. Into the measurements at tide gauge Fort Myers/Florida shown in grey (right panel) a large artificial gap from 1967 to 1975 is introduced. The left panel shows time series of the RC's for this gap where our method of reconstructing sea level from surrounding station data is tested. The measurements at the artificial gap were withheld from the analysis and filled with our method depicted as black curve in Fig. 1 (left). Comparison with the original data shows good agreement. The correlation between both, original and filled gap, is 0.97. Thus the gap filling method appears to be reasonable and successful.

Signal filtering: MSSA can also be used to split the signal in trend, oscillations and high-frequent noise. In the gauge data (without annual cycle) the dominant signal is the trend. Time series analysis of the 1st RC shows that low frequencies (i.e. a linear trend) dominate the signal. In higher RCs the major frequencies are in the

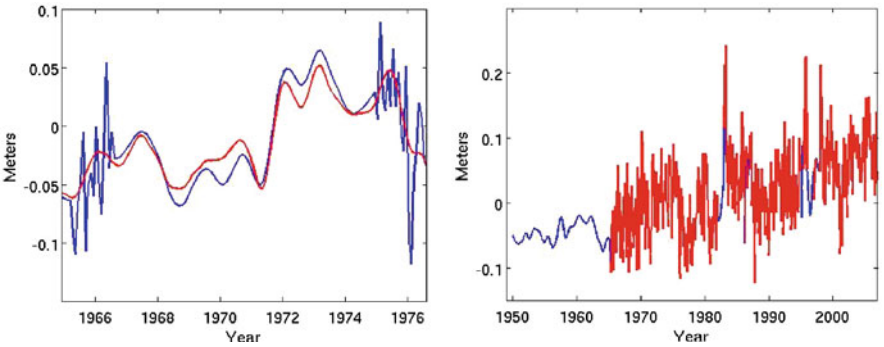

Fig. 2 The *left panel* shows in *grey* the sum of RCs 1 and 2 of the original time series of gauge Fort Myers/Florida ($M = 12$). An artificial gap for the years 1967 to 1975 was filled with our method (*black*). The correlation between both for the years 1967–1975 is 0.97. The *right panel* shows the full measured time (*grey*) and the how the original data gaps were filled (*black*)

annual to sub-annual scale. This is depicted in Fig. 3 the 1st RC (black) and 2nd RC (grey) are displayed together with their respective trends. The window length is $M = 60$.

In the following section we calibrate the sea surface height of IFEOM model with the time series of the reconstructed tide gauges. The IFEOM fields are provided as pentads (5 year means) from 1950 to 1994 which result from an analysis of historic fields of temperature and salinity (Lozier et al., 1995). Accordingly, gap-filled tide gauge time series are smoothed with MSSA using a window length $M = 60$ for the gap-filled time span of 1950–2006. We used the resulting smoothed time-series from 1950–1994 to calibrate IFEOM. In Fig. 3 the trend of the gap filled time series

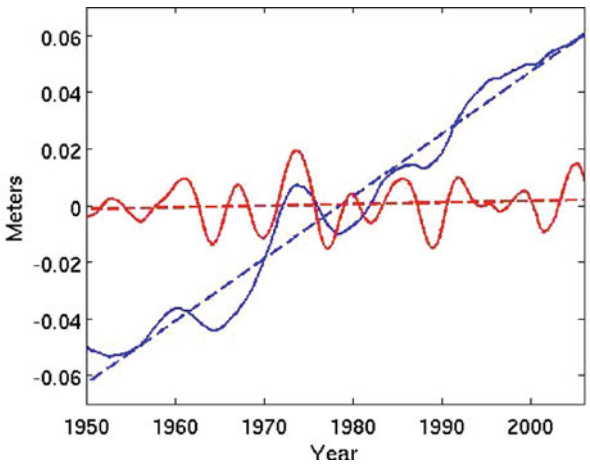

Fig. 3 The gap filled time series at gauge Fort Myers/Florida, the 1. RC (*black*) and 2. RC (*grey*) and their respective trends. The window length is $M = 60$. The trend is confined to 1. RC

is confined completely to 1st RC. Including only the 1st RC for calibration of 5-year mean values seems to be reasonable.

4 Reduced Number of Gauges and Calibration of IFEOM

Next we consider a series of results from the Inverse Finite Element Ocean Model (IFEOM) which was applied to hydrographic data to obtain a sequence of dynamic topography (Sidorenko et al., 2008). The series consists of nine realisations which are available as means for the periods from 1950–1954 to 1990–1994. The model circulation is in equilibrium with spatial gradients of dynamic topography. A bias or shift in the surface reference has no dynamic consequence and cannot be determined by the inverse model. The bias was therefore arbitrarily set to zero mean for each of the pentads. Thus an undetermined shift exists from one realisation to another. The tide gauge data were now used to determine the interpentadal shifts.

For calibration of IFEOM we want to rely on stable tide gauges only. We performed reconstructions of data gaps using different window lengths $M = 12; 24; 36; 48$ months. All gauges with correlation below 0.8 (20 gauges) and difference in regression greater 0.5 (22 gauges) for different window lengths where omitted. Six gauges of the region Texas where discarded because they possess strong positive trends, different from all other gauges. This could be explained by local land subduction due to oil exploitation, which cannot be corrected by the PGR model of Peltier. Every station containing less than 25% of data between 1950 and 1994 was omitted (26 gauges). Two remaining African stations (Santa Cruz de Tenerife and Takoradi) were excluded from calibration due to significant variance in the tide gauges resulting from unaccounted land-movements. This and the large ratio (see Fig. 1) are the reasons for gap-filling to fail here. All together 53 gauges remain for calibration from the 129 gauges originally used for gap filling (see Fig. 4).

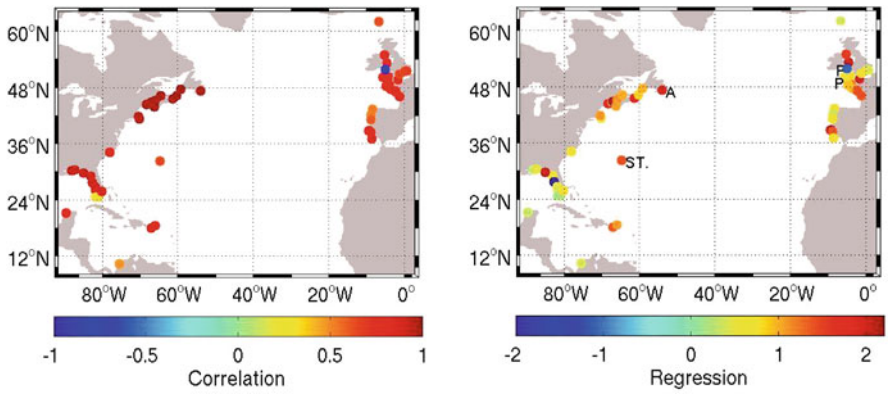

Fig. 4 Correlation and regression between 53 consistent tide gauges and calibrated IFEOM model. Good agreement is seen on the American coast, where the model input data resolution is also the best

The calibration was carried out by fitting pentadal differences of IFEOM at gauge locations to the tide gauges series in the least squares sense. The area mean reconstructions show the trend in dynamic topography of 1.18; 1.18; 1.19; 1.19 mm/year for the window lengths $M = 12; 24; 36; 48$ months, respectively.

Figure 4 shows the correlation and regression between the consistent tide gauges and the calibrated IFEOM model. Good agreement is seen along the American coast where hydrographic data used by IFEOM are dense. The gauges on the Canary Islands and the African coast differ largely, possibly as a consequence of poor data coverage in temperature and salinity fields.

A few time series of the gauges and the calibrated IFEOM Model (for the exact locations see right side of Fig. 4) are shown in Fig. 5. The signal variance is generally greater in the Western Atlantic (St. Georges and Argentia). Gauge Portsmouth is also well represented by IFEOM, whereas gauge Fishguard is anticorrelated to IFEOM. This is perhaps due to the limited capabilities of IFEOM in the Irish Sea or to undiscovered movement of the tide gauge.

The regional distribution of sea level rise calculated from calibrated IFEOM is shown in Fig. 6 (left). The resulting mean is 1.18 mm/year sea level rise (SLR) for the period of 1950–1994.

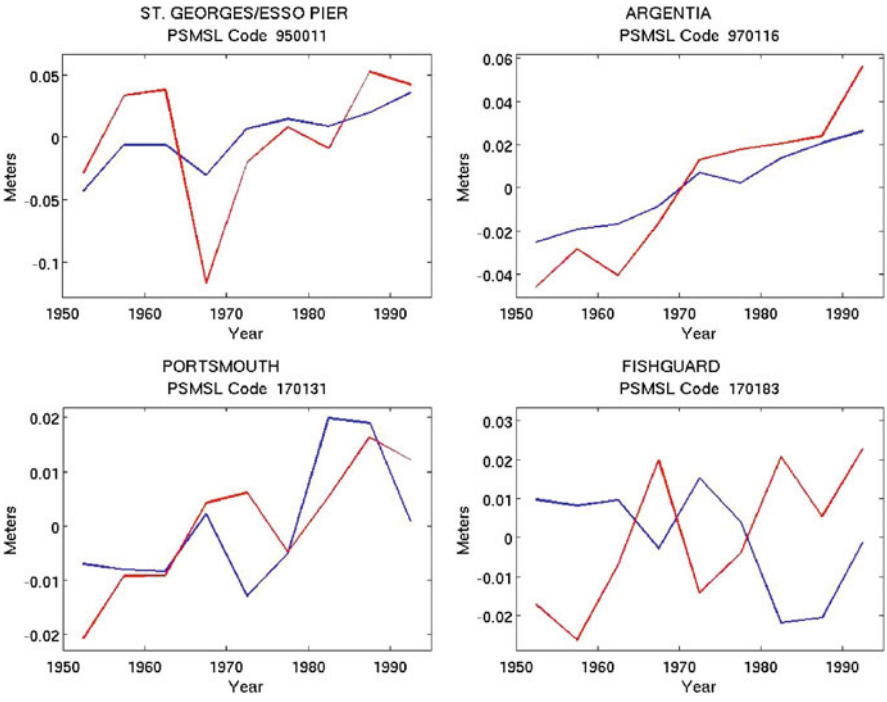

Fig. 5 Time series of tide gauges (*black*) and calibrated IFEOM Model (*grey*) at selected locations (see Fig. 4 *right*)

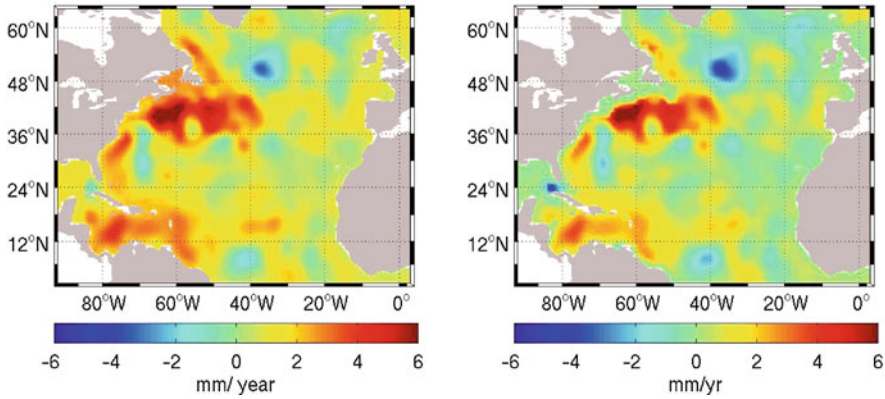

Fig. 6 The sea level rise of calibrated IFEOM for 1950–1994 (*left*). The mean sea level rise for the complete model area is 1.18 mm/year. The right figure shows the trend of steric height with a mean of 0.31 mm/year

The right panel in Fig. 6 shows the 0.31 mm/year in SLR due to steric effects. The trend in ocean bottom pressure with a mean of 0.87 mm/year is depicted in Fig. 7 (left) . It is to a large extent equally distributed over the model domain with notable exceptions near the boundaries. In the right panel of Fig. 7 the mean of the pentads for sea level, steric height and ocean bottom pressure is plotted. The fourth curve is the mean sea level calculated from all gauges directly, which leads to a trend in SLR of 1.54 mm/year. This is significantly larger than the 1.18 mm/year in SLR from the calibrated IFEOM.

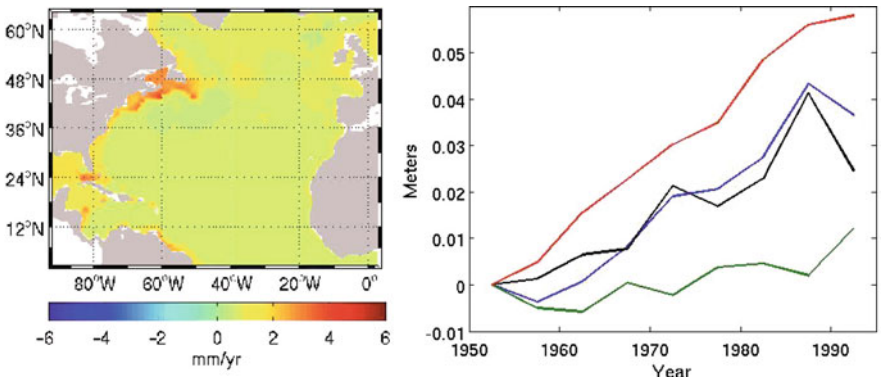

Fig. 7 The *left panel* shows the trend of bottom pressure (surface height minus steric height) with a mean of 0.87 mm/year. The *right panel* shows the mean of the pentads for the calibrated sea level of the IFEOM model (*blue*), the ocean bottom pressure (*black*), and the steric height (*green*) and for comparison the mean sea level of all gauges (*red*).

5 Conclusions

Gap filling of observed sea level data can be performed with the MSSA method and is stable with respect to different window length when long time scales are considered. MSSA can also be used for low pass filtering of the gap filled time series. Our method of calibrating the basin wide sea surface topography derived from the inverse ocean circulation model IFEOM with gauge data leads to reasonable results. The trend in SLR, calculated directly from the tide gauges used for calibration, is 1.54 mm/year. Our calibration converts this to a basin wide sea level rise of 1.18 mm/year which shows that coastal and regional sea level trends may differ substantially (see also Holgate and Woodworth, 2004). In our results 0.31 mm/year SLR are due to steric expansion while 0.87 mm/year are due to mass increase in the North Atlantic.

References

Church JA, White NJ, Coleman R, Lambeck K, Mitrovica JX (July 2004) Estimates of the regional distribution of sea level rise over the 1950–2000 period. J. Clim. 17(13), 2609\u20132625.

Ghil M, Allen MR, Dettinger MD, Ide K, Kondrashov D, Mann ME, Robertson AW, Saunders A, Tian Y, Varadi F, Yiou P (August 2002) Advanced spectral methods for climatic time series. Rev. Geophy. 40(1), 1003.

Holgate SJ, Woodworth PL (April 2004) Evidence for enhanced coastal sea level rise during the 1990s. Geophys. Res. Lett. 31(7), L07305.

Jevrejeva S, Grinsted A, Moore JC, Holgate S (September 12, 2006) Nonlinear trends and multiyear cycles in sea level records. J. Geophys. Res. Oceans 111, C9.

Kondrashov D, Ghil M (2006) Spatiotemporal filling of missing points in geophysical data sets. Nonlinear Processes Geophys. 13(2), 151\u2013159.

Lozier MS, Owens WB, Curry RG (1995) The climatology of the North Atlantic. Prog. Oceanogr. 36, 1–44.

Peltier WR (November 1998) Postglacial variations in the level of the sea: implications for climate dynamics and solid-earth geophysics. Rev. Geophys. 36(4), 603\u2013 689.

Sidorenko D, Danilov S, Schröter J (2008) Inverse solution for pentadal variability in the North Atlantic. Geophys. Res. Lett. 35, L02603.

Snay R, Cline M, Dillinger W, Foote R, Hilla S, Kass W, Ray J, Rohde J, Sella G, Soler T (April 25, 2007) Using global positioning system-derived crustal velocities to estimate rates of absolute sea level change from North American tide gauge records. J. Geophys. Res. Solid Earth 112(B4).

Zervas C (2001) Sea level variations of the United States 1854–1999, NOAA Technical Report NOS CO-OPS 036, Version July 2001.

Using ARGO, GRACE and Altimetry Data to Assess the Quasi Stationary North Atlantic Circulation

Falk Richter, Dimitry Sidorenko, Sergey Danilov, and Jens Schröter

1 Introduction

In the last years, two major observation systems have become operational. The first, satellite altimetry, maps the ocean surface quasi synoptically, and by referencing sea surface height to the GRACE geoid ocean currents are diagnosed. The second observing system is the Global Array of Profiling Floats (ARGO) adding in situ subsurface temperature and salinity data. Both types of measurements are consistent with each other to such an extent that altimetry can be used to check the quality and performance of individual temperature and salinity profiles measured by ARGO (see e.g. Ivchenko et al., 2007; Guinehut et al., 2009). It is shown that both types of measurements complement each other and a joint analysis is required in order to fully exploit the information content.

We combine the two sources of data in the context of an ocean inverse general circulation model. In this way we make use of dynamical rather than statistical correlations between the data and analyse ocean currents and transports simultaneously with the observations.

Generally, numerical ocean circulation models produce fields which differ from observations. The bias is a result of many factors, which are in both, models and measurements. On one hand models produce uncertainties due to the lack of sufficient information on the surface forcing and errors in model dynamics. On the other hand, the measurements themselves are contaminated by measurement errors and include transient effects of the ocean dynamics which are not resolved by models. Assimilating all available information into an ocean circulation model could serve the purpose of finding the compromise between model and data and obtaining improved patterns of ocean circulation. This has been successfully demonstrated in a series of works (Wenzel and Schröter, 1998; Wenzel et al., 2001; Wenzel and Schröter, 2002; Stammer et al., 2002, 2003; Losch and Schröter, 2004; Kivman et al., 2005).

F. Richter (✉)
Alfred-Wegener-Institute for Polar- and Marine Research, D-27570 Bremerhaven, Germany
e-mail: Falk.Richter@awi.de

F. Flechtner et al. (eds.), *System Earth via Geodetic-Geophysical Space Techniques*,
Advanced Technologies in Earth Sciences, DOI 10.1007/978-3-642-10228-8_29,

2 Model Setup and Data

The model used for the present study is an inverse finite-element ocean circulation model (IFEOM) which has been described in Sidorenko et al. (2005). The model solves the stationary momentum equations for velocity field and sea surface height, and treats the advective-diffusive tracer balances as soft constraints. IFEOM seeks for the temperature (T) and salinity (S) fields which give minimum to its objective function. The latter penalizes residuals in the tracer equations, deviations of model variables from data available and also the misfit between the diagnosed deep pressure gradient and the pressure gradient of a prognostic model run. The experiments reported below take into account several data sources. Gouretsky and Koltermann (2004) climatology is used in all experiments as a background for temperature and salinity.

The other dataset includes T and S profiles for the years 2005–2006 from the ARGO project, available from the official ARGO web site (www.ARGO.ucsd.edu). The ARGO data comes from a set of profiling buoys which contains seasonal and transient signals. Because of a poor spatial coverage of ARGO data on a monthly basis we restrict our results to annual model solutions. We use the annual mean of ARGO data in our experiments with the seasonal signal removed.

Altimetry data is optionally taken as gridded maps of absolute dynamic topography (MADT) provided by AVISO (Archiving, Validation and Interpretation of Satellite Oceanographic data). Absolute dynamic topography is the sum of sea level anomaly (SLA) and a mean dynamic topography (MDT). Following AVISO the Rio05 MDT is used here. The Rio05 mean dynamic topography (Rio and Hernandez, 2004 and Rio et al., 2005) is the combined product of large scale MDT, using the CLS01 mean sea surface (MSS) and the EIGEN-GRACE 03S geoid (Reigber et al., 2005), and hydrographic and Lagrangian data together with altimeter SLA over the 1993–2002 period. CLS01 shows the mean shape of the sea surface during the period covered by the altimetry data. It is corrected from seasonal variations and corresponds to the sum of geoid + mean elevation in response to ocean circulation. The annual means of MADT have been computed for the years 2005–2006.

Three experiments have been performed for each year for the period 2005–2006. First, solutions are obtained by assimilating only the ARGO data (ARGO05-ARGO06). Second, solutions that use only altimetry data (Alt05-Alt06) are found. Finally, solutions using both, ARGO and altimetry are computed (AltARGO05-AltARGO06). In the following, the adjustments produced by IFEOM in temperature and salinity fields and the resulting circulation patterns are analysed.

3 Results

The sea surface elevation corresponding to the analysis of ARGO data with the altimeter information included (AltARGO05) is presented in Fig. 1 for 2005. It exhibits all major features of the North Atlantic dynamic topography, i.e. the warm

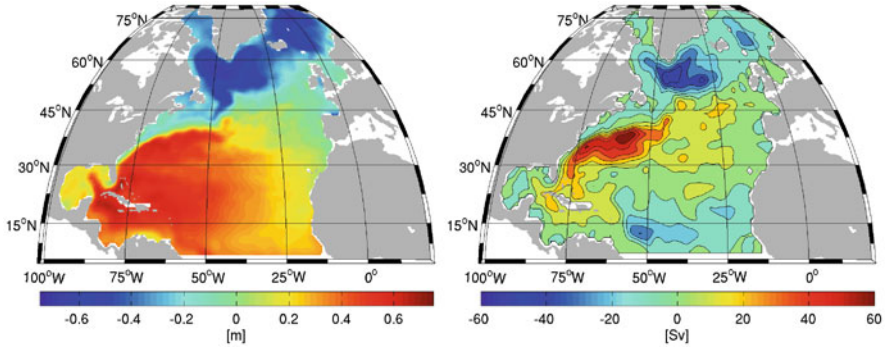

Fig. 1 *Left panel*: Modelled sea surface elevation (dynamic height) of the AltARGO05 experiment. *Right panel*: the corresponding barotropic stream function

pool with a strong gradient toward the subpolar Gyre south of Greenland, the loop current in the Caribbean basin, a strong Labrador current which continues around the Grand Banks, a northward extension of the North Atlantic Current after its separation from the American coast at Cape Hatteras, and the Azores Current. Ocean currents are in agreement with the conventional oceanic knowledge and are used for the further analysis of the North Atlantic circulation and its interannual changes.

We analyse the impact of using altimetry on the model solution. Comparing ARGO05, the experiment that excludes altimetry, with the independent altimeter sea surface (Fig. 2, left panel) we observe a large scale shift of about 80 cm, from the Caribbean Sea to the subpolar gyre which shows that the circulation derived from hydrographic data alone is far from the observed reality. Using only ocean subsurface data produces a sea surface height with large scale spatial differences to altimeter and geoid observations. Thus, the additional information on the ocean circulation is necessary, and the obvious choice is to account for altimetry data in the model. The success of this choice (AltARGO05) is demonstrated in Fig. 2,

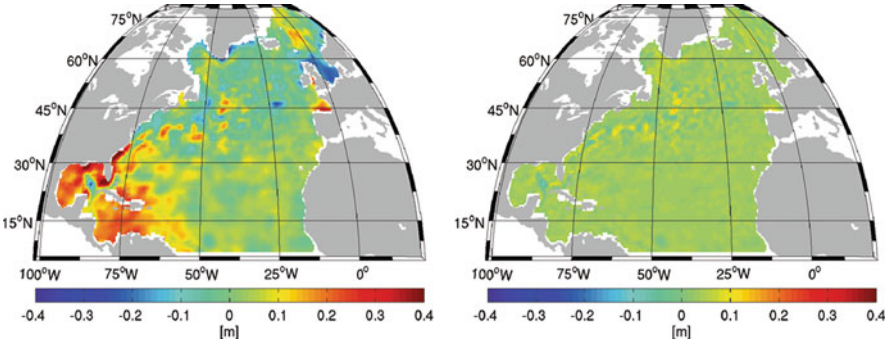

Fig. 2 Difference of modelled sea surface elevation and altimetry data in 2005. Based on ARGO only (*left panel*; ARGO05) and after including altimetry (*right panel*; AltARGO05)

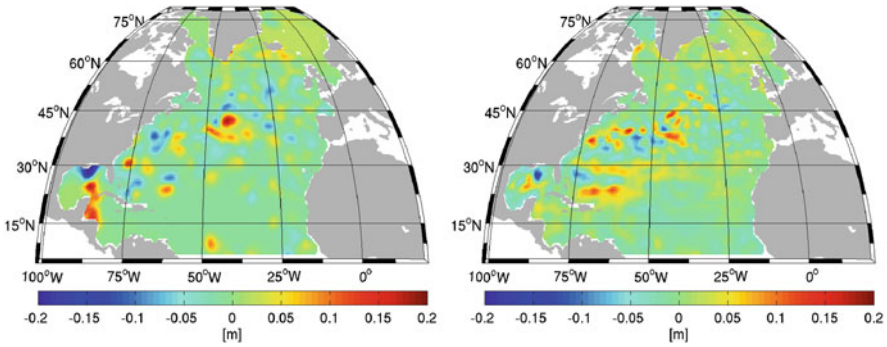

Fig. 3 Difference in modelled sea surface change based on ARGO only (*left panel*; ARGO06-ARGO05) and after including altimetry (*right panel*; AltARGO06-AltARGO05)

right panel. It shows the differences of AltARGO05 to altimetric data which are an order of magnitude smaller than those for ARGO05. Referenced altimetry and the dynamic topography of the inverse model can be matched by small adjustments in T and S to an RMS misfit of 3 cm.

One of the improvement by including altimetry is seen at an oceanographic section at 24°N. The heat transport across this line computed from AltARGO05 is 1.24 PW what compares perfectly with the values estimated by Lumpkin and Speer (2007) and Ganachaud and Wunsch (2003). Their estimates are 1.24 ± 0.25 PW and 1.27 ± 0.15 PW, respectively. ARGO05 underestimates the heat transport across 24°N providing a value of only 0.89 PW.

In order to estimate the variability contained in ARGO and altimetry data the intercomparison of temporal change in modelled topography between years 2005 and 2006 is presented in Fig. 3. The left panel shows sea surface variability based on ARGO (ARGO06-ARGO05), and the right panel displays the difference (AltARGO06-AltARGO05) when all data are used.

Both patterns suggest a sea level rise of about 5 cm in Nordic seas. The Gulf Stream region and its extension are characterized by large activity. The inter-annual differences are up to 20 cm. The differences in variability between the two plots are obviously due to the poor spatial sampling of ARGO data in comparison to altimetry. The corresponding change in the solution AltARGO06-AltARGO05 is similar to that of altimetry data (Fig. 4). It contains slightly smaller and less sharp local anomalies, but takes into account a significant part of variability contained in the data.

The model solution allows studying other characteristics of the circulation. We discuss the transport and its variability. Barotropic stream function has been determined for the inverse solution using all data (AltARGO05) and is depicted in Fig. 1 right panel. The gyre structures are well developed, the strength of the subpolar gyre is 50 Sv and is on the upper limit of most forward modelling studies (see e.g. Treguier et al., 2005). Considering the temporal changes 2006–2005 we notice differences of about 20 Sv with the maximum in Gulf Stream region seen in both ARGO and AltARGO experiments (Fig. 5, left and right panels, respectively) with

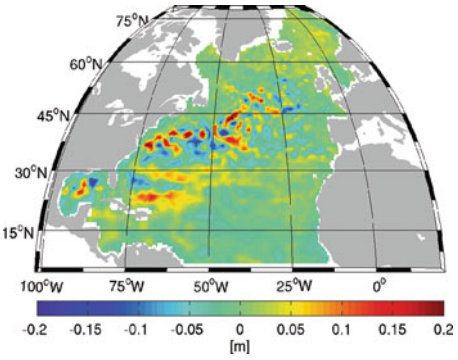

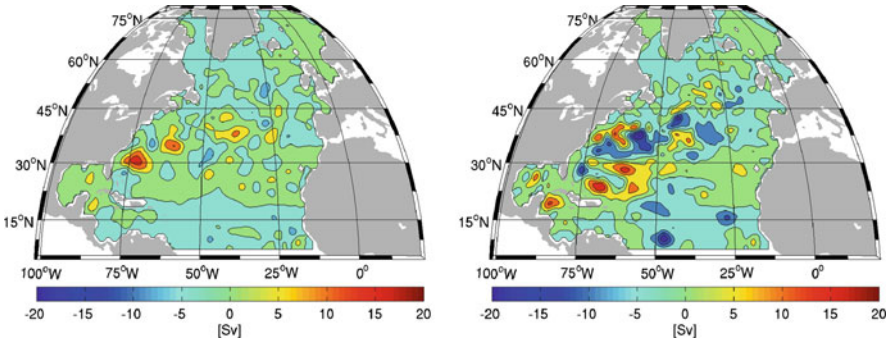

Fig. 4 Inter-annual change in altimetry data (2006–2005)

Fig. 5 Change in barotropic stream function (ARGO06-ARGO05 *left* and AltARGO06-AltARGO05 *right*). Altimetry has a stronger impact on total transports then ARGO data have

more pronounced changes in AltARGO experiments. The changes in T and S fields are distinct and quite similar between ARGO only experiments and AltARGO solutions. In accordance to these findings, only smaller modifications in T and S are needed to compensate for the misfit in surface elevation. The variability in transports can be either explained by the bottom pressure change (which is loosely constrained during the assimilation to that of a forward solution; Sidorenko et al., 2005) or the change in vertically integrated potential energy (which is the result of redistribution of T and S within the water column). Figure 6 shows the difference in vertically integrated potential energy between ARGO06-ARGO05 (left panel) and between AltARGO06-AltARGO05 (right panel).

It demonstrates that a significant part of the transport variability is due to the variability in vertically integrated potential energy. Thus, despite the fact that T and S adjustments done by IFEOM are mainly due to the ARGO anomalies, the modifications in potential energy are mainly from including altimetry. The latter in turn has a significant impact on transport variability.

Figure 7 shows the temperature change (AltARGO06-AltARGO05) across a section at 37.5°N. It is dominated by the ARGO anomalies. The changes due to the altimetry assimilation are an order of magnitude smaller and are of the same sign

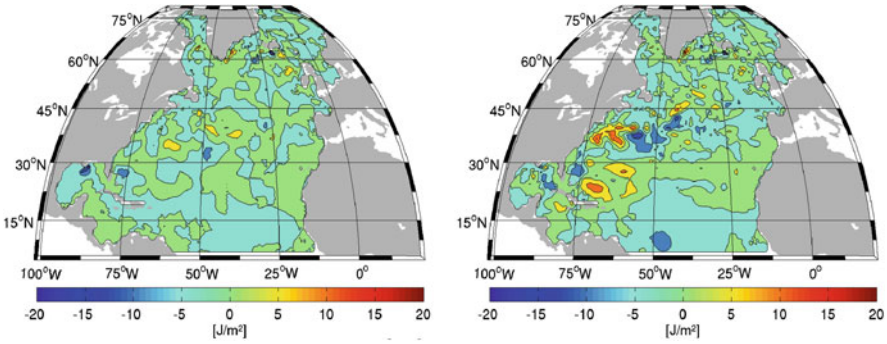

Fig. 6 Change in vertical integrated potential energy (ARGO06-ARGO05 *left* and AltARGO06-AltARGO05 *right*) scaled by 10^{-5}. The transport changes induced by using altimeter data are produced by adjusting the vertical density structure in the model

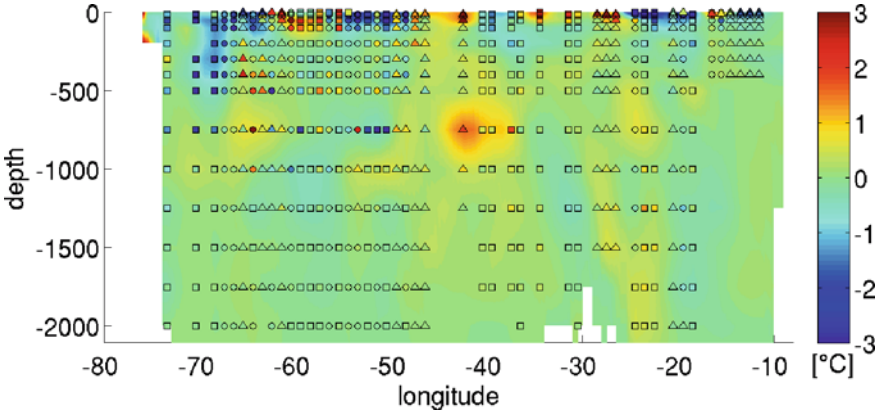

Fig. 7 Temperature change along a section through the North Atlantic at 37.5°N. Difference between solutions AltARGO06-AltARGO05 is shown in background colour. The difference in the observations (2006–2005) at ARGO positions is depicted by colour coding the following symbols: both years are present in ARGO data (*circle*), if only 1 year (2005 *square*, 2006 *triangle*) is present the difference is computed using the climatology data instead of the missing year

within the entire depth (not shown here). The plot demonstrates that the model takes into account even the transient signal which can be present in raw data. The pattern of positive anomaly at about 40°W corresponds to an unstable profile measurement (year 2005). This anomaly is partly captured by IFEOM (which accounts for the whole available information) and results in stable model solution.

4 Summary and Conclusions

The quasi-stationary circulation of the North Atlantic is estimated for the years 2005–2006 using ARGO, GRACE and altimetry data. The assimilation technique has been used to reduce the misfit between data and model by adjusting T and S

fields. It is shown that inclusion of the additional information from altimetry significantly changes the estimates of transports and variability. The sea level rise between 2005 and 2006 of about 5 cm in the Nordic seas is shown to be present in both, ARGO and altimetry data. Both datasets also reveal large variability in the Gulf Stream region and its extension which contributes to the estimated interannual differences of about 20 cm. The Gulf Stream region shows the transport variability of about 20 Sv in maximum. The changes are more pronounced for the simulations including altimetry data despite the fact that using altimetry leads to only small additional adjustments in T and S. These adjustments in turn modify the vertically integrated potential energy significantly, which explains the transport variability. Thus, the vertically integrated potential energy anomaly shows that the transport variability is dominated mainly by the altimetry information while the major changes in T and S are explained by the ARGO data.

Acknowledgment This is publication no. GEOTECH 1249 of the GEOTECHNO-LOGIEN programme of BMBF, grant 03F0434B.

References

Ganachaud A, Wunsch C (2003) Large-scale ocean heat and freshwater transports during the world ocean circulation experiment. J. Clim. 16, 696–705.

Gouretski VV, Koltermann KP (2004) WOCE Global Hydrographic Climatology. Bundesamt für Seeschifffahrt und Hydrographie, Hamburg und Rostock, Germany.

Guinehut S, Coatanoan C, Dhomps A-L, Le Traon P-Y, Larnicol G (2009) On the use of satellite altimeter data in ARGO quality control. J. Atmos. Oceanic Technol. 26, 395–402.

Ivchenko VO, Danilov SD, Sidorenko DV, Schröter J, Wenzel M, Aleynik DL (2007) Comparing the steric height in the Northern Atlantic with satellite altimetry. Ocean Sci. 3, 485–490.

Kivman G, Danilov S, Fritzsch B, Harig S, Reick C, Schröter J, Seufer V, Sidorenko D, Staneva J (2005) Improved estimates of the oceanic circulation using the CHAMP geoid. Earth Observation with CHAMP, Results from Three Years in Orbit, Springer-Verlag, Heidelberg, pp. 211–216.

Losch M, Schröter J (2004) Estimating the circulation from hydrography and satellite altimetry in the southern ocean: limitations imposed by the current geoid models. Deep-Sea Res. I 51(9), 1131–1143.

Lumpkin R, Speer K (2007) Global ocean meridional overturning. J. Phys. Oceanogr. 37, 2550–2562.

Reigber C, Schmidt R, Flechtner F, König R, Meyer U, Neumayer K-H, Schwintzer P, Yuan Zhu S (2005) An earth gravity field model complete to degree and order 150 from GRACE: EIGEN-GRACE02S. J. Geodyn. 39(1), 1–10.

Rio MH, Hernandez F (2004) A mean dynamic topography computed over the world ocean from altimetry, in situ measurements, and a geoid model. J. Geophys. Res. 109, C12032.

Rio MH, Schaeffer P, Lemoine JM, Hernandez F (2005) Estimation of the ocean Mean Dynamic Topography through the combination of altimetric data, in-situ measurements and GRACE geoid: from global to regional studies. Proceedings of the GOCINA international workshop, Luxembourg.

Sidorenko D, Danilov S, Kivman G, Schröter J (2005) On the use of a deep pressure gradient constraint for estimating the steady state ocean circulation from hydrographic data. Geophys. Res. Lett., doi: 10.1029/2005GL024716.

Stammer D, Wunsch C, Giering C, Eckart C, Heimbach P, Marotzke J, Adcroft A, Hill CN, Marshall J (2002) The global ocean circulation during 1992–1997, estimated from ocean observations and a general circulation model. J. Geophys. Res. 107(C9), 3118–3145.

Stammer D, Wunsch C, Giering C, Eckart C, Heimbach P, Marotzke J, Adcroft A, Hill CN, Marshall J (2003) Volume, heat and freshwater transports of the global ocean circulation 1993–2000, estimated from a general circulation model constrained by World Ocean Circulation Experiment (WOCE) data. J. Geophys. Res. C1, 3007.

Treguier AM, Theetten S, Chassignet EP, Penduff T, Smith R, Talley L, Beismann JO, Böning C (2005) The north Atlantic subpolar gyre in four high-resolution models. J. Phys. Oceanogr. 35, 757–774.

Wenzel M, Schröter J (1998) Combined assimilation of altimetric and hydrographic data. AVISO Newsletter 6, 122–124.

Wenzel M, Schröter J, Olbers D (2001) The global ocean circulation during 1992–1997, estimated from ocean observations and a general circulation model. Prog. Oceanogr. 48(C9), 73–119.

Wenzel M, Schröter J (2002) Assimilation of TOPEX/Poseidon data in a global ocean model: differences in 1995–1996. Phys. Chem. Earth 27, 1433–1437.

A 15-Year Reconstruction of Sea Level Anomalies Using Radar Altimetry and GPS-Corrected Tide Gauge Data

Nana Schön, Saskia Esselborn, and Tilo Schöne

1 Introduction

When estimating sea level changes over the last century, one major problem is the spatial non-uniformity. Regional estimates give a broad range of results for sea level rise. For the determination of consistent time series, satellite radar altimetry data (RA) with its short but near-global coverage must be combined with the relatively long but spatially sparse set of tide gauge time series. Church et al. (2004) developed a reconstruction scheme that takes into account the regional differences and can produce reliable estimates. In this paper, a similar reconstruction procedure is used, but improved in two aspects. First, the typical correction for land movement, commonly accomplished by employing a global isostatic adjustment (GIA) model (e.g., Davis and Mitrovica, 1996; Lambeck et al., 1998; Peltier, 2004), is replaced by applying vertical land movement trends extracted from the combined TIGA (GPS Tide Gauge Benchmark Monitoring – Pilot Project) dataset of co-located GPS stations to the tide gauge data set (Schöne et al., 2009). Second, a careful selection of the tide gauges used in the reconstruction minimizes the influence of their spatial distribution.

2 Methodology

For the reconstruction of sea level anomalies (SLA), a modified Optimal Interpolation (OI) algorithm (Kaplan et al., 1997) is applied. Fully corrected and harmonized monthly altimetric sea surface height anomaly data derived from the Altimeter Database and Processing System ADS (chapter "Radar Altimetry Derived Sea Level Anomalies – The Benefit of New Orbits and Harmonization" by Schöne et al., this issue) are gridded into $1^\circ \times 1^\circ$ maps and are used to estimate the global

N. Schön (✉)
Helmholtz Centre Potsdam, GFZ German Research Centre for Geosciences,
Department 1: Geodesy and Remote Sensing, Telegrafenberg, 14473 Potsdam, Germany
e-mail: nana.schoen@gfz-potsdam.de

F. Flechtner et al. (eds.), *System Earth via Geodetic-Geophysical Space Techniques*,
Advanced Technologies in Earth Sciences, DOI 10.1007/978-3-642-10228-8_30,

covariance structure as expressed in empirical orthogonal functions (EOFs). The amplitude of these EOFs is estimated using tide gauge records. This way, the main spatial patterns of the SLAs are extracted from the RA data, while their amplitude time series is reconstructed using the tide gauge data. For this reconstruction, the first 25 area-weighted EOFs are used, which cover over 91% of the global variability. Church et al. (2004) have argued that this number of EOFs is sufficient for an OI reconstruction.

The land movement part of the tide gauge records is GPS-corrected using vertical trends derived from the TIGA combination (chapter "Reanalysis of GPS Data at Tide Gauges and the Combination for the IGS TIGA Pilot Project" by Rudenko et al. this issue). For this study, 18 tide gauges (see Schöne et al., 2009) are selected from the global TIGA network. Tide gauge data for the period 1987–2001 are taken from the PSMSL data archive (Woodworth and Player, 2003). The selection criteria are chosen such as to comply with the recommendations of Douglas (2001) for tide gauges, as well as Blewitt and Lavallée (2002) for the GPS time series. An additional three tide gauges (La Libertad 2 (PSMSL ID 845/012), Pt. La Rue (PSMSL ID 442/007), Unalaska (PSMSL ID 820/021)) were used for the stabilization of the OI algorithm (see Schöne et al., 2009 for a detailed discussion). Only a small number of tide gauges satisfy all the necessary selection criteria. In addition to this, the influence of their geographical distribution on the reconstruction hinders a more flexible selection of tide gauges. Adaptively using all tide gauges available for a certain period of time is not recommended, since the integrity of a changing geographical distribution in time cannot be determined. Instead, a fixed configuration of tide gauges that must stay unchanged throughout the reconstruction period is chosen beforehand, which of course further diminishes the set of eligible tide gauges.

For all sea level time series only one average GPS value for the vertical velocity is applied. A comparison of the GPS land movement trends with those determined by Peltier (2004) in his VM4 GIA model (Fig. 1), shows that, especially in the Southern Hemisphere, the model trends tend to be smaller than those derived from GPS data. However, since several GPS-derived trends are extracted from very short time series only, a fully reliable comparison cannot yet be drawn.

It is assumed that the GPS vertical trends describe ongoing, long-term processes. Hence, the corrections for land movement are applied not only for the period of time over which the trend was determined, but are also projected into the past. The respective corrections are applied from the beginning of the reconstruction period

Fig. 1 (**a**) Sea level anomalies (SLA) for January 1998, TOPEX radar altimetry data. (**b**) Sea level anomalies (SLA) reconstruction for January 1998 using 18 (21) tide gauges with GPS vertical corrections. Tide gauges used in the reconstruction are depicted as *stars*. (**c**) Sea level anomalies (SLA) reconstruction for January 1998 using 18 (21) tide gauges with GIA model vertical corrections (Peltier, 2004). Tide gauges used in the reconstruction are depicted as *stars*. Three tide gauges without GPS or GIA corrections were used for stabilization of the algorithm

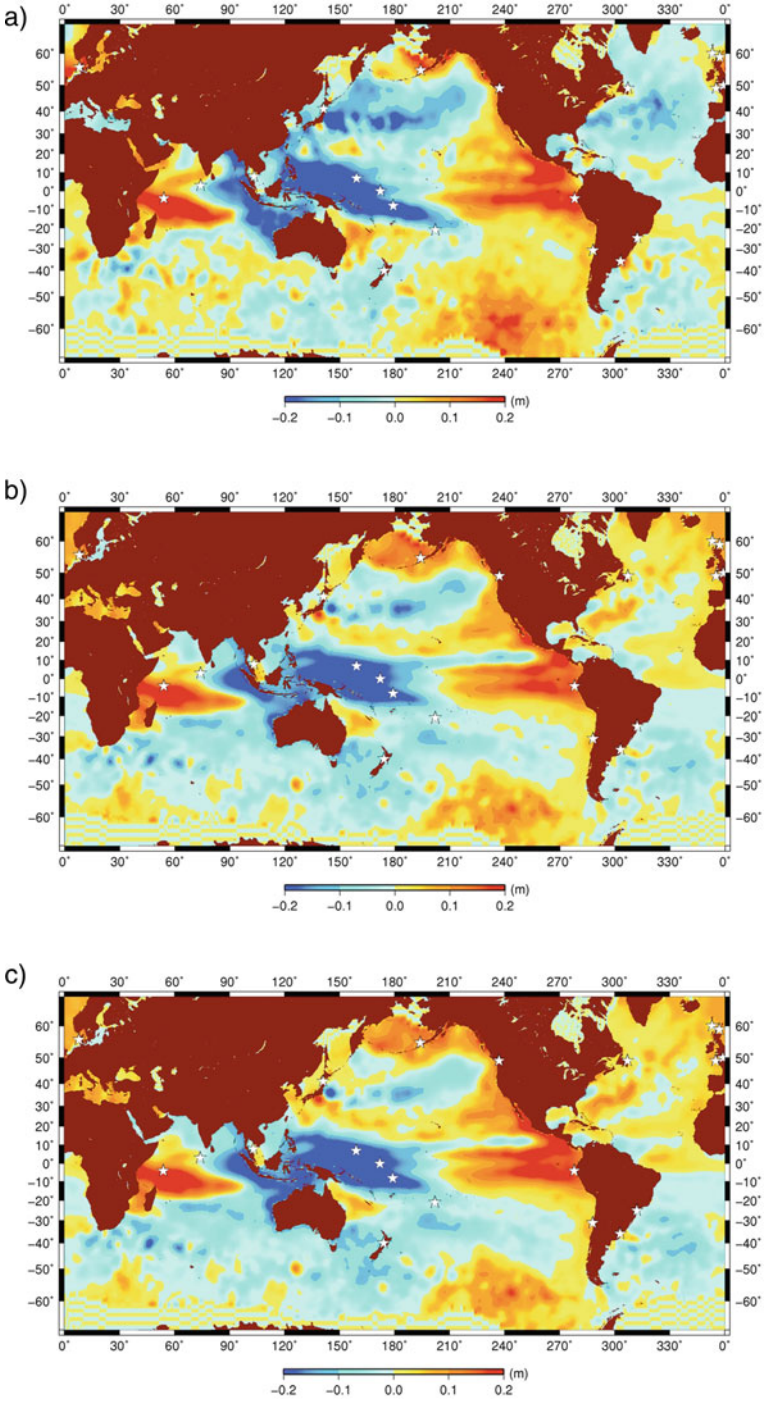
a)
b)
c)
0° 30° 60° 90° 120° 150° 180° 210° 240° 270° 300° 330° 0°
60° 50° 40° 30° 20° 10° 0° −10° −20° −30° −40° −50° −60°
−0.2 −0.1 0.0 0.1 0.2 (m)

Fig. 1 (Contd.)

(1987) to its end in 2001. An exception is Pohnpei, where a strong positive trend is derived from the GPS time series. Careful examination of the PSMSL time series suggests that the strong uplift signal is the result of a recent process and that the GPS correction should be applied only from 1999 onwards.

3 Comparison of GIA vs. GPS Corrections

The reconstruction results using GPS vertical corrections (Fig. 1b) are compared with the one using GIA model corrections (Fig. 1c) as well as the original TOPEX altimetry data (Fig. 1a) for January 1998. Here, the two dominant signals are the double tongue-shaped positive anomaly resulting from the 1997/1998 El Niño event, and the Indian Ocean Dipole event (IOD) (Feng and Meyers, 2003) with its characteristic warming (positive anomaly) in the Indian Ocean, as well as a distinct cooling (negative anomaly) in the Indonesian/Western Pacific region. Both reconstructions agree well with the original data, with RMS differences of 3.74 cm (GPS corrections) and 4.01 cm (GIA corrections), respectively.

In the comparison of the reconstructions, the advantage of the GPS-corrected reconstruction is most visible in the rendition of the negative anomaly east of Japan. Also, the intensity of the double tongue (El Niño signal) is reproduced more distinctly. In contrast, the GIA-corrected reconstruction overestimates the positive anomalies in the North Atlantic and also shows slightly more negative artifacts around New Zealand. Figure 2 shows a comparison of monthly RMS values for both reconstructions. Although, in the global scale (Fig. 2a), the RMS for the GPS corrections is slightly higher, the regional RMS comparisons for the North Atlantic (Fig. 2b) and North Pacific (Fig. 2c) show the overall improvement from the GPS correction.

In the Southern Pacific region, the GIA-corrected gives a better result. This may be due to the fact that some of the GPS trends used were derived from short time series (see Schöne et al., 2009). A recalculation has now produced significantly lower trends for the short time series (D. Thaller, personal communication May, 2009). Hence, the results for the Southern Pacific, as well as the Southern Atlantic, should be treated with care.

The effect of the GPS vs. GIA corrections on the sea level trend is depicted in Figure 3. A comparison with the trend extracted from the satellite altimetry data over the common period (1995–2001) gives a very good agreement (2.2 mm/year vs. 2.4 mm/year); with the GPS-corrected reconstruction slightly closer to the altimetry data over the whole period. The 21 uncorrected tide gauges used in the reconstruction give a considerably higher trend of 3.1 cm/year for the same period. The fact that the rendition of the seasonal cycle is not yet satisfactory is most probably due to the small number of tide gauges used. The lack of gauges causes an erroneous overestimation of anomalies, resulting in a noisy reconstruction (see also Chambers et al., 2002). The trend for the whole 15-year reconstruction period (1987–2001), is comparably low at only 0.4 mm/year for both corrections, compared to 3.6 mm/year

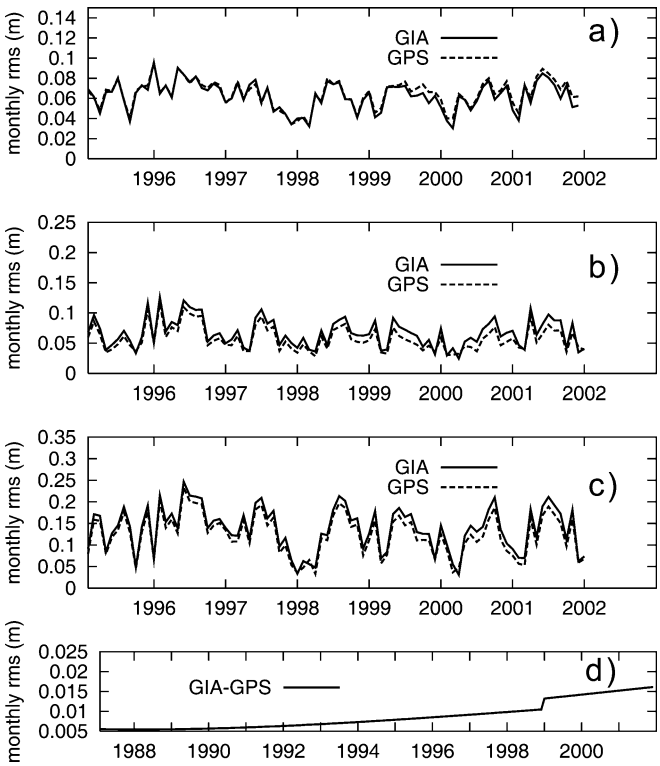

Fig. 2 Monthly RMS time series for TOPEX/Poseidon – GPS/GIA, resp. (**a**) global (**b**) North Atlantic (50°–20° Lat, 280°–360° Lon) (**c**) North Pacific (50°–30° Lat, 150°–210° Lon) (**d**) RMS difference GIA-GPS. The jump in 1999 marks the application of the Pohnpei GPS correction

from the tide gauges alone. It remains to be seen whether this low rate holds when more land movement data becomes available, or whether it is, at least in part, caused by an instability of the algorithm.

4 Conclusion

GPS corrections can markedly improve the quality of an SLA reconstruction provided that enough tide gauges are available. Especially in the North Atlantic and North Pacific, a regional improvement can be achieved (see also Snay et al., 2007). Results for the Southern Oceans must be treated with care due to the insufficient length of GPS time series in this area (see also Blewitt and Lavallée, 2002).

Acknowledgments The author would like to thank Daniela Thaller for providing the GPS data, as well as for her overall help and expertise. This is publication no. GEOTECH-1251 of the GEOTECHNOLOGIEN programme of BMBF, grant 03F0434A.

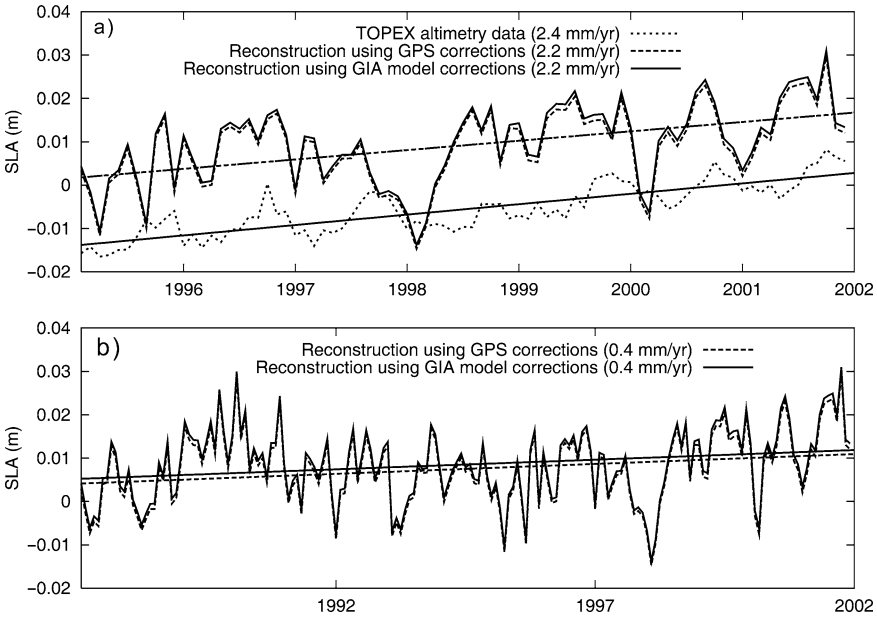

Fig. 3 (**a**) A comparison of global SLA trends for the 1995–2001 period. (**b**) Global SLA trends for the 1987–2001 period

References

Blewitt G, Lavallée D (2002) Effect of annual signals on geodetic velocity. J. Geophys. Res. 107(B7), doi: 10.1029/2001JB000570.

Chambers DP, Melhaff CA, Urban TJ, Fuji D, Nerem RS (2002) Low-frequency variations in global mean sea level: 1950–2000. J. Geophys. Res. 107(C4), 3026–3035.

Church A, White NJ, Coleman R, Lambeck K, Mitrovica JX (2004) Estimates of the regional distribution of sea level rise over the 1950–2000 period. J. Clim. 17, 2609–2625.

Davis JL, Mitrovica JX (1996) Glacial isostatic adjustment and the anomalous tide gauge record of eastern North America. Nature 379, 331–333.

Douglas BC (2001) Sea level change in the era of the recording tide gauge. In: Douglas BC, Kearney MS, Leatherman SP (eds.), Sea Level Rise – History and Consequences, Academic Press, New York, pp. 37–64.

Feng M, Meyers G (2003) Interannual variability in the tropical Indian Ocean: a two-year time-scale of Indian Ocean Dipole. Deep-Sea Res. II 50, 2263–2284.

Kaplan A, Kushnir Y, Cane MA, Blumenthal MB (1997) Reduced space optimal analysis for historical data sets: 136 years of Atlantic sea surface temperatures. J. Geophys. Res. 102, 27835–27860.

Lambeck K, Johnston P, Smither C (1998) Sea-level change, glacial rebound and mantle viscosity for northern Europe. Geophys. J. Int. 134, 102–144.

Peltier WR (2004) Global glacial isostasy and the surface of the ice-age earth: the ICE-5G (VM2) Model and GRACE, Ann. Rev. Earth Planet. Sci. 32, 111–149.

Schöne T, Schön N, Thaller D (2009) IGS tide gauge benchmark monitoring pilot project (TIGA): scientific benefits. J. Geod. 83(3–4), March 2008, doi: 10.1007/s00190-008-0269-y.

Snay R, Cline M, Dillinger W, Foote R, Hilla S, Kass W, Ray J, Rohde J, Sella G, Soler T (2007)

Using global positioning system-derived crustal velocities to estimate rates of absolute sea level change from North American tide gauge records. J. Geophys. Res. 112, B04409, doi: 10.1029/2006JB004606.

Woodworth PL, Player R (2003) The permanent service for mean sea level: an update to the 21st century. J. Coastal Res. 19, 287–295.

Part V
TIVAGAM

Continental Water Storage Variations from GRACE Time-Variable Gravity Data

Andreas Güntner

1 Surface Mass Variations from GRACE

Since 2002, the Gravity Recovery and Climate Experiment (GRACE) satellite mission monitors the Earth's gravity field. Given the unprecedented accuracy of GRACE, mass redistributions caused by geophysical and hydro-climatological processes above, at and below the Earth surface can be resolved by time-variable gravity signals of GRACE (Tapley et al., 2004). The mission sensitivity to processes in the continental water cycle (e.g. Schmidt et al., 2008a), post glacial rebound (e.g. Tamisiea et al., 2007), changes in the polar ice sheets (e.g. Velicogna and Wahr, 2006) and mass transport in the oceans (e.g. Chambers et al., 2004) has clearly been demonstrated during the last years. Also, interactions between these subsystems have been analyzed with the help of GRACE data, such as the effect of continental water storage changes on sea level rise (e.g. Chambers et al., 2007; Ramillien et al., 2008a). GRACE thus provides a unique data set to help understanding mass distributions and mass transport processes in the Earth system at continental to global scales.

The particular nature of GRACE is that the satellite gravity data integrate over all mass contributions in the Earth system. Thus, before adequate data on mass variations in a certain Earth system component are obtained, a key point is to separate the signal of interest from the other contributions included in the GRACE data. In the standard GRACE monthly gravity fields provided by the three processing centres of the GRACE mission (GFZ, CSR and JPL) (see Schmidt et al., 2008a and chapter "Improved GRACE Level-1 and Level-2 Products and Their Validation by Ocean Bottom Pressure" by Flechtner, this issue, for an overview on GRACE processing), several time-variable gravity effects such as tides of the solid Earth, oceans and the atmosphere and non-tidal mass variations due to atmospheric and oceanic dynamics are already reduced. Thus, mainly mass signals from Earth surface processes, in particular water storage changes in the continental areas including ice caps and glaciers,

A. Güntner (✉)
Helmholtz Centre Potsdam, GFZ German Research Centre for Geosciences,
Department 5: Earth Surface Processes, Telegrafenberg, 14473 Potsdam, Germany
e-mail: guentner@gfz-potsdam.de

F. Flechtner et al. (eds.), *System Earth via Geodetic-Geophysical Space Techniques*,
Advanced Technologies in Earth Sciences, DOI 10.1007/978-3-642-10228-8_31,

can be expected to be left in the time-variable gravity fields. Other mass variation components that are still contained in these reduced gravity fields are effects from post-glacial rebound and from seismic deformations of the Earth crust due to earthquakes. Any errors committed in the separation process propagate into errors of the signal of interest, such as continental water storage changes. These errors originate in particular from uncertainties in the geophysical reduction models (e.g., atmospheric and ocean circulation models) in terms of input data, model structure and parameters.

Other factors that contribute to the error budget of GRACE data on Earth surface mass variations originate from measurement errors of satellite instruments and orbit determination, and from leakage errors caused by mass signals outside the area of interest. The latter error term is again due to the integrative nature of satellite gravity data that capture all masses around the satellites, with the contribution of individual mass elements decreasing as a function of the squared distance to the satellites. Usually, gravity field models of the Earth are represented in the frequency domain by truncated global spherical harmonics series. A limitation of this type of representation is that the signal cannot be precisely located in the space domain, i.e., spatially detailed information is smeared to some extent over the whole globe.

Thus, to extract mass variations for a particular region of interest such as a river basin, either alternative GRACE processing techniques that result in regional gravity solutions (e.g., Rowlands et al., 2005) or filter functions applied to the global gravity data (e.g., Swenson and Wahr, 2002) are used. These filters have to be optimized in a way such that they minimize at the same time (1) the contamination of the river basin signal by disturbing contribution from outside the region (leakage error) and (2) GRACE measurement errors which increase markedly with the spatial detail that is to be extracted from the gravity fields. As a consequence, filters cannot follow exactly the boundary of the region of interest as this would involve unacceptably high GRACE errors, but they are gradual in space around the region and thereby incorporate some signal from the surroundings into the final basin-average estimates of water mass anomalies. A variety of filter techniques has been developed during the last years (see e.g. Kusche, 2007 for an overview). The efficiency of a particular filter type, i.e., high signal-to-noise ratio and low bias of signal amplitudes and phases, varies with the location, shape and with the signal properties in and around the region of interest. Thus, the optimum filter type to derive water storage variations for the scale of large river basins varies between the basins (Werth et al., 2009).

Near-surface mass variations on the continents are not only reflected in the Earth's gravity field as monitored by GRACE but also in solid Earth deformations. In particular, load variations such as caused by water storage changes induce an elastic deformation of the Earth surface which can be observed by geodetic GPS observations. Thus, in principle, an independent observation system exists that could be compared and combined with GRACE data to estimate large-scale continental mass variations (e.g., Davis et al., 2004; Van Dam et al., 2007).

2 Surface Mass Processes: Continental Hydrology

Continental water storage is a key component of the global hydrological cycle. By balancing precipitation, evapotranspiration and runoff, water storage has an important control over water, energy and biogeochemical fluxes and thus plays a major role in the Earth's climate system. In spite of its importance, spatial and temporal variations of continental water storage were largely unknown at regional and global scales prior to the GRACE mission because of the lack of adequate monitoring systems (Lettenmaier and Famiglietti, 2006). While disperse ground-based hydrological monitoring networks exist, point measurements of, e.g., soil water content or groundwater levels give only local estimates of water storage. It is practically impossible to upscale these observations to larger scales because of the high variability of environmental conditions, e.g., in terms of climate, geology, soils and land cover, which may cause very different water storage dynamics than what is observed at specific points. Monitoring from satellites would in principle allow for a large spatial coverage. However, remote sensing of soil water storage was limited to the surface soil layer of few centimetres in depth and to areas free of a dense vegetation cover (e.g., Wagner et al., 2003). For surface waters bodies, satellite altimetry and imaging techniques could be used to derive variations of water levels and the extent of inundated areas (e.g., Alsdorf and Lettenmaier, 2003) and water volumes by a combination of both data types (Frappart et al., 2008). A common limitation of all ground- and satellite-based observation techniques was that they only gave access to individual water storage components. *Total* continental water storage, however, is composed of storage in the form of snow, ice, soil water, groundwater and surface water in rivers, lakes, wetlands and inundation areas. The contribution of single storage components to total storage varies considerably between the Earth's climate zones (Güntner et al., 2007). Total water storage variations could not be monitored in an integrative way before GRACE.

Besides water storage, also other components of the continental water cycle are only sparsely known from observations at large spatial scales. While a global network of gauging stations for river discharge exists (Global Runoff Data Centre. Koblenz, Germany), many continental areas remain ungauged or no access to recent data is available due to the decline in station density. Measurements of evapotranspiration from the land surface are even more difficult to obtain. Thus, the description of water storage and other water balance components at continental scales primarily came from global hydrological or land-surface models prior to the GRACE mission. Theses models, however, suffer from important uncertainties in terms of climate forcing data, model structures and parameters, and the observed river discharge is usually the only observable to evaluate simulation results (e.g., Hunger and Döll, 2008). Having only this single constraint does not guarantee that the hydrological processes are correctly represented in the model and that water fluxes and storage are adequately partitioned between the different components of the water cycle. This can only be evaluated and improved by additional observation data on other hydrological state variables and fluxes.

From the absence of a global and comprehensive hydrological monitoring system and the limitations in quantifying water balance components by observations and modelling as summarized above, the extraordinary value of GRACE for the field of continental hydrology becomes apparent. GRACE is an unprecedented source of information to quantify spatio-temporal variations of the continental hydrological cycle as, for the first time ever, water storage changes for large continental areas are monitored with GRACE.

The first about 7 years of the GRACE mission have clearly demonstrated its capacity to resolve water storage variations (see Schmidt et al., 2008a and Ramillien et al., 2008a for reviews). With monthly to 10-days time-steps, maps of water storage patterns for the continental areas and time series of area-average water storage for selected regions and large river basins worldwide have been derived. The resolution and accuracy of water storage change data is in the range of 400–500 km and some ten mm water equivalent. Errors tend to increase for smaller areas and depend on various factors as explained above. GRACE water storage data were used in resolving the water balance equations for other components of the water cycle, such as evapotranspiration (e.g., Rodell et al., 2004) and river discharge (e.g., Syed et al., 2005). With the help of ancillary data, also mass variations in individual water storage compartments have been isolated from GRACE, such as snow (e.g. Frappart et al., 2006) or groundwater (e.g. Rodell et al., 2007).

The focus of many studies using GRACE data for continental hydrology was on seasonal variations of water storage as the dominant signal in the time series. In a few studies it could additionally be shown that GRACE is able to detect longer-term variations and extremes in continental water storage, for example related to large floods and droughts in Central Europe and Australia (Andersen et al., 2005; Seitz et al., 2008; Schmidt et al., 2008b). The potential of relating water storage anomalies from GRACE to large-scale inter-annual modifications of global circulation patterns such as El-Niño-Southern Oscillation (ENSO) has for the first time been shown by Morishita and Heki (2008). Ramillien et al. (2008b) analyzed trends in continental water storage and their contribution to sea level variations. Nevertheless, such analyzes of longer-term variations are still considerably limited due to the short period with available GRACE data.

Given the scarcity of other observation data at large scales, water storage variations from GRACE have a large potential to validate, calibrate and improve global hydrological and land surface models by (1) demonstrating deficiencies of the model output relative to GRACE data, (2) identifying sources of these model deficiencies in terms of model input data, model structure or model parameters, and by (3) modifying hydrological models and evaluating the modifications against GRACE observations (see Güntner, 2008 for a review). However, while qualitative comparisons of model results to GRACE data have frequently been done, only few attempts have been made so far towards a full integration of GRACE data into the modelling process. The particular nature of GRACE data requires adequate processing and modelling steps both on the hydrological and geodetic side to assure the comprehensive and consistent improvement of large-scale hydrological models. Such prerequisites include, for instance, the consistency of GRACE data and

model variables in terms of filtering, reliable error estimates, advanced methods of multi-objective model calibration or data assimilation and the full evaluation of the water balance at the river basin scale after model adjustments with GRACE (Güntner, 2008).

3 The TIVAGAM Project

Research within the project TIVAGAM (Time-Variable Gravity and Surface Mass Processes: Validation, Processing and First Application of New Satellite Gravity Data) was devoted to topics outlined above, from the adequate processing of GRACE time-variable gravity field data to their application for improved modelling and understanding of Earth surface processes, here for the example of continental hydrology. Important goals were (1) to develop strategies for signal separation from integral satellite gravity observations with emphasis on identifying typical spatio-temporal characteristics of hydrological mass signals, (2) to evaluate GRACE-based mass variations in comparison to geophysical model data and independent observations and (3) to develop methods to make use of GRACE data towards an improvement of large-scale hydrological models.

Regarding the first goal, Petrovic et al. (chapter "Surface Mass Variability from GRACE and Hydrological Models: Characteristic Periods and the Reconstruction of Significant Signals" by this issue) propose an analysis method to extract the characteristic spatio-temporal morphology of surface mass anomalies, in particular their periodic components, from time series of GRACE gravity models in the space domain. The method works as a filter to enhance the signal-to-noise ratio and was applied to reconstruct basin-average water storage signals from GRACE which were subsequently used for the calibration of a hydrological model (chapter "Calibration of a Global Hydrological Model with GRACE Data" by Werth and Güntner, this issue). With the similar aim to enhance the signal properties of GRACE data in particular for regional analyses of surface mass processes, Freeden et al. (chapter "Time-Space Multiscale Analysis and Its Application to GRACE and Hydrology Data" by this issue) introduce methods based on the theory of spherical wavelets to allow for comparing GRACE and hydrology data in a consistent way in time and space and with good localization in the space domain. The multi-resolution approach can be applied for evaluation of different hydrological data sets, i.e., towards identifying improved hydrological models.

Horwath et al. (chapter "Mass Variation Signals in GRACE Products and in Crustal Deformations from GPS: A Comparison", this issue) analyze the complementary value of GRACE gravity data and GPS surface deformation data to describe surface mass variations. They illustrate the challenges in terms of homogeneous data processing and reference systems to make the data useful for identification of errors, e.g., in hydrological or other geophysical background models to be used for GRACE processing. In addition to the atmospheric and oceanic models that are routinely applied with high temporal resolution in GRACE processing for signal separation, daily continental water storage variations are simulated with the WaterGAP

Global Hydrology Model (WGHM) by Fiedler and Döll (chapter "Monthly and Daily Variations of Continental Water Storage and Flows", this issue) and are tested for de-aliasing disturbing high frequency mass signals in the GRACE observations.

Finally, concluding the TIVAGAM research framework from GRACE satellite data to hydrological applications, Werth and Güntner (chapter "Calibration of a Global Hydrological Model with GRACE Data", this issue) propose a multi-objective calibration framework to incorporate time series of measured river discharge and GRACE water storage variations directly into the parameter tuning process of the global hydrological model WGHM. They make use of the adapted GRACE signal separation methods mentioned above and ensure consistency by applying identical processing strategies for the water storage fields of the hydrological model. Fiedler and Döll (chapter "Monthly and Daily Variations of Continental Water Storage and Flows", this issue) in a complementary study improve the process representation of water storage and transport in WGHM by adjusting flow routing and reservoir schemes in the model. In combination, both studies highlight the beneficial nature of GRACE data as a constraint for improving hydrological models and towards best estimates of continental water storage variations at large scales.

References

Alsdorf DE, Lettenmaier DP (2003) Tracking fresh water from space. Science 301, 1491–1494.

Andersen OB, Seneviratne SI, Hinderer J, Viterbo P (2005) GRACE-derived terrestrial water storage depletion associated with the 2003 European heat wave. Geophys. Res. Lett., doi: 10.1029/2005GL023574.

Chambers DP, Wahr J, Nerem RS (2004) Preliminary observations of global ocean mass variations with GRACE. Geophys. Res. Lett. 31, L13310.

Chambers D, Tamisiea ME, Nerem R, Ries J (2007) Effects of ice melting on GRACE observations of ocean mass trends. Geophys. Res. Lett. 34, L05610.

Davis JL, Elosegui P, Mitrovica JX, Tamisiea ME (2004) Climate-driven deformation of the solid Earth from GRACE and GPS. Geophys. Res. Lett., doi: 10.1029/2004GL021435.

Frappart F, Ramillien G, Biancamaria S, Mognard-Campbell N, Cazenave A (2006) Evolution of highlatitude snow mass derived from the GRACE gravimetry mission (2002–2004). Geophys. Res. Lett., doi: 10.1029/2005GL024778.

Frappart F, Papa F, Famiglietti JS, Prigent C, Rossow WB, Seyler F (2008) Interannual variations of river water storage from a multiple satellite approach: a case study for the Rio Negro River basin. J. Geophy. Res., doi: 10.1029/2007JD009438.

Güntner A, Stuck J, Werth S, Döll P, Verzano K, Merz B (2007) A global analysis of temporal and spatial variations in continental water storage. Water Resour Res. 43(5), W05416.

Güntner A (2008) Improvement of global hydrological models using GRACE data. Surv. Geophys., doi: 10.1007/s10712-008-9038-y.

Hunger M, Döll P (2008) Value of river discharge data for global-scale hydrological modeling. Hydrol. Earth Syst. Sci. 12, 841–861.

Kusche J (2007) Approximate decorrelation and non-isotropic smoothing of time-variable GRACE-type gravity field models. J. Geod. 81, 733–749.

Lettenmaier DP, Famiglietti JS (2006) Hydrology – water from on high. Nature 444(7119), 562–563.

Morishita Y, Heki K (2008) Characteristic precipitation patterns of El Niño/La Niña in time-variable gravity fields by GRACEM. Earth Plan. Sci. Lett., doi: 10.1016/j.epsl.2008.06.003.

Ramillien G, Bouhours S, Lombard A, Cazenave A, Flechtner F, Schmidt R (2008a) Land water storage contribution to sea level from GRACE geoid data over 2003–2006. Glob. Planet Change 60(3–4), 381–392.

Ramillien G, Famiglietti JS, Wahr J (2008b) Detection of continental hydrology and glaciology signals from GRACE: a review. Surv. Geophys., doi: 10.1007/s10712-008-9048–9.

Rodell M, Famiglietti JS, Chen J, Seneviratne SI, Viterbo P, Holl S, Wilson CR (2004) Basin scale estimates of evapotranspiration using GRACE and other observation. Geophys. Res. Lett., doi: 10.1029/2004GL020873.

Rodell M, Chen J, Kato H, Famiglietti J, Nigro J, Wilson C (2007) Estimating ground water storage changes in the Mississippi River basin (USA) using GRACE. Hydrogeol. J. 15, 159–166.

Rowlands DD, Luthcke SB, Klosko SM, Lemoine FG, Chinn DS, McCarthy JJ, Cox CM, Anderson OB (2005) Resolving mass flux at high spatial and temporal resolution using GRACE intersatellite measurements. Geophys. Res. Lett. 32, L04310.

Schmidt R, Flechtner F, Meyer U, Neumayer KH, Dahle C, König R, Kusche J (2008a) Hydrological signals observed by the GRACE satellite mission. Surv. Geophys., doi: 10.1007/s10712-008-9033-3.

Schmidt R, Petrovic S, Güntner A, Barthelmes F, Wünsch J (2008b) Periodic components of water storage changes from GRACE and global hydrology models. J. Geophy. Res., doi: 10.1029/2007JB005363.

Seitz F, Schmidt M, Shum CK (2008) Signals of extreme weather conditions in Central Europe in GRACE 4-D hydrological mass variations. Earth Plan. Sci. Lett. 268(1–2), 165–170.

Swenson S, Wahr J (2002) Methods for inferring regional surface-mass anomalies from Gravity Recovery and Climate Experiment (GRACE) measurements of time-variable gravity. J. Geophys. Res., doi: 10.1029/2001JB000576.

Syed T, Famiglietti J, Chen J, Rodell M, Seneviratne S, Viterbo P, Wilson C (2005) Total basin discharge for the Amazon and the Mississippi River basins from GRACE and a land-atmosphere water balance. Geophys. Res. Lett., doi: 10.1029/2005GL024851.

Tapley BD, Bettadpur S, Watkins M, Reigber C (2004) The gravity recovery and climate experiment: mission overview and early results. Geophys. Res. Lett. 31, L09607.

Tamisiea ME, Mitrovica JX, Davis JL (2007) GRACE gravity data constrain ancient ice geometries and continental dynamics over laurentia. Science 316, 881–883.

Van Dam T, Wahr J, Lavallée D (2007) A comparison of annual vertical crustal displacements from GPS and Gravity Recovery and Climate Experiment (GRACE) over Europe. J. Geophys. Res., doi: 10.1029/2006JB004335.

Velicogna I, Wahr J (2006) Acceleration of Greenland ice mass loss in Spring 2004. Nature 443, 329–331.

Wagner W, Scipal K, Pathe C, Gerten D, Lucht W, Rudolf B (2003) Evaluation of the agreement between first global remotely sensed soil moisture data with model and precipitation data. J. Geophys. Res., 108(D19), 4611, doi: 4610.1029/2003JD003663.

Werth S, Güntner A, Schmidt R, Kusche J (2009) Evaluation of GRACE filter tools from a hydrological perspective. Geophys. J. Int., doi: 10.1111/j.1365-246X.2009.04355.x.

Surface Mass Variability from GRACE and Hydrological Models: Characteristic Periods and the Reconstruction of Significant Signals

Svetozar Petrovic, Roland Braun, Franz Barthelmes, Johann Wünsch, Jürgen Kusche, and Rico Hengst

1 Introduction

Using data supplied by the Gravity Recovery and Climate Experiment (GRACE), scientists from various disciplines have for the first time been able to observe time-variable gravity signals related to mass redistributions at, on, and below the Earth's surface caused by ongoing geophysical and climatological processes. The mission's sensitivity to processes such as continental water cycle (e.g. Schmidt et al., 2006), post glacial rebound (e.g. Tamisiea et al., 2007), changes in the polar ice sheets (e.g. Velicogna and Wahr, 2006) and mass transport in the oceans (e.g. Chambers et al., 2004) has been clearly demonstrated in the recent past.

An important goal is the quantification of the mass redistribution related to the individual phenomena to improve the modelling and understanding of various geodynamic processes. A key question is the signal separation of the individual contributions contained in the integral satellite gravity observations. In order to derive the characteristic spatio-temporal morphology of the surface mass anomalies traceable in time series of GRACE gravity models we propose an analysis method to derive such features from time series of surface mass anomalies in the space domain with a focus on periodic components due to continental hydrology. The method combines a decomposition of the spatio-temporal signal using well-known Principal Components Analysis (PCA) with a specific frequency analysis method which allows for the determination of harmonic (i.e. sine and cosine) waves of arbitrary periods.

As a basic result we obtain characteristic spectra of periodic mass variations contained in the GRACE data and in independent global hydrology models. In this way it is possible to identify the hydrological components contained in the GRACE data. Based on this, we derive filtered GRACE signals reconstructed from selected components (considered significant) which can contribute to calibration of hydrological models. The proposed method is not limited to the examination of

S. Petrovic (✉)
Helmholtz Centre Potsdam, GFZ German Research Centre for Geosciences,
Department 1: Geodesy and Remote Sensing, Telegrafenberg, 14473 Potsdam, Germany
e-mail: sp@gfz-potsdam.de

F. Flechtner et al. (eds.), *System Earth via Geodetic-Geophysical Space Techniques*,
Advanced Technologies in Earth Sciences, DOI 10.1007/978-3-642-10228-8_32,

hydrological mass redistributions performed here and may therefore be valuable for further applications in other fields.

2 Input Data and Preprocessing

Our analysis is based on time series of spatial grids of surface mass anomalies from GRACE gravity fields and from water storage fields of various global hydrology models. These series are in both cases derived from time series of coefficients of spherical harmonics describing the gravity potential.

For GRACE such gravity potential coefficients are provided by the groups of the GRACE Science Data System (SDS) from the inter-satellite measurements, which are related to the gravity variations along the satellites' orbit. In the following we use our own RL04 monthly model series generated at GFZ (GFZ-RL04).

For hydrology four state-of-the-art global hydrology models are considered: the WaterGAP Global Hydrology Model (WGHM, Döll et al., 2003), the H96 model (Huang et al., 1996), the Land Dynamics (LaD) model (Milly and Shmakin, 2002), and the Global Land Data Assimilation System (GLDAS, Rodell et al., 2004). In order to be comparable with integral mass variations deduced from GRACE observations, a hydrological model should include all continental water existing in any form. This holds for no available hydrology model. Furthermore, the considered models differ with respect to several aspects of model design (Werth et al., 2009b). Nevertheless, they give a realistic representation of global hydrology. All these hydrology models are provided as total water storage variations on global grids. All the monthly maps are then expanded into sets of spherical harmonics describing the gravity potential (e.g. Wahr et al., 1998) to allow for a unified preparation of time series of grids of surface mass anomalies from GRACE and hydrological data sets.

Each monthly spherical harmonic data set is referenced to the individual long term mean to derive residual time-variable quantities. From these residual spherical harmonic coefficients time series of surface mass anomalies on $0.5° \times 0.5°$ grids are computed applying the relations given by Wahr et al. (1998). In order to suppress the correlated errors of the GRACE-based surface mass anomalies, known as striping, the following filter versions are considered:

- DDK1: decorrelation filter with parameters $a = 1 \cdot 10^{14}$, $p = 4$ (Kusche, 2007),
- DDK2: decorrelation filter with parameters $a = 1 \cdot 10^{13}$, $p = 4$ (Kusche, 2007),
- DDK3: decorrelation filter with parameters $a = 1 \cdot 10^{12}$, $p = 4$ (Kusche, 2007),
- G500: Gaussian smoothing filter with $R = 500$ km (Jekeli, 1981).

For consistent treatment, the same filter is applied both to the GRACE and the hydrological data sets. The focus in this study is on continental hydrology. Therefore, we extract from the global grids the data points located over land and data points located within 18 selected river basins worldwide. The size of the basins

ranges from $5.9 \cdot 10^6$ km^2 for the Amazon to $85 \cdot 10^3$ km^2 for the Po basin, which is at the limit of the resolution of the GRACE mission. Since the results with any of the hydrological models are in general very similar, we present mainly results of WGHM as a representative hydrological data set.

3 Methodology

The analysis consists of three main steps: (1) Principal Components Analysis (PCA), (2) search for arbitrary periods in principal components, and (3) accuracy assessment of the spectral parameters from GRACE.

Principal Components Analysis (PCA, also known as Empirical Orthogonal Functions, EOF) allows for a proper pre-processing of the data in studying the temporal characteristics of the spatial variability of surface mass anomalies from GRACE and the hydrology models. We use conventional PCA (e.g. Preisendorfer, 1988, or Wilks, 1995), where decomposition into the mode-wise pairs of eigenvectors (evs) and associated principal components (pcs) is based on the signal variance-covariance matrix of the input data. For each mode the eigenvector represents a pattern of the spatial variability. The associated principal component describes the variation of this pattern with time.

Since the input data sets are driven by climatological processes that show variability in the signal amplitude, phase and also period, both in space and time, we estimate all three quantities simultaneously. Based on the principles described in Mautz and Petrovic (2005), we estimate the amplitudes A_k, phase lags ϕ_k and frequencies ω_k of the model consisting of sinusoidal terms

$$y_k(t) = A_k \sin(\omega_k t + \phi_k) \tag{1}$$

from the principal components $y(t)$ of individual dominant modes. For discrete data this problem can be transformed into a least squares adjustment problem with the observation equations:

$$y_i = A_0 + Dt_i + \sum_{k=1}^{n} B_k \cos(\omega_k t_i) + \sum_{k=1}^{n} C_k \sin(\omega_k t_i) + \varepsilon_i\,, \quad (i = 1, \ldots, N) \tag{2}$$

where in addition to the amplitudes A_k and phase lags ϕ_k (contained in the B_k and C_k), also the unknown frequencies $\omega_k = 2\pi f_k = 2\pi/T_k$, and the trend parameter D are to be determined. The latter is estimated to avoid aliasing of secular signals into the periodic terms. The main advantage of the approach (2) is that the signal energy is mapped into few but representative frequencies, as it allows for the estimation of arbitrary periods in addition to the amplitudes and phases. This contrasts the classical Fourier analysis where the signal energy is forced into a fixed basic period and multiples of the associated basic frequency, treating only the signal amplitudes and phases as unknowns. Equation (2) represents a highly non-linear

least squares problem. In order to apply standard local optimization methods, very accurate initial values for the unknown parameters are necessary. These can only be provided by global optimization methods, which require high computational effort (e.g. Horst and Pardalos, 1995). A reasonable strategy based on a sequential algorithm is presented in Schmidt et al. (2008).

In contrast to the hydrological data sets, where only little is known about the data accuracy, it is possible to assess the accuracy of the GRACE derived amplitudes, phases and periods. This can be done based on the available GRACE gravity field model error estimates provided together with the gravity field models by the GRACE science data teams. We use a Monte Carlo method for error propagation (Gundlich et al., 2003; Kalos and Whitlock, 1988), considering the spatial correlation of the GRACE gravity field errors. Based on a scaled version of the full variance-covariance matrix of the monthly GRACE gravity model for August 2003 we create 200 spatial grids of noise in the surface mass anomalies for each of the considered river basins by a rigorous error propagation of correlated model errors by the Monte Carlo method. The noise grids are added to GRACE grids of surface mass anomalies that are constructed from the strongest periods found in the pcs of the PCA. To do this we replace the original principal components of the respective modes by the harmonic model from (2) evaluated at the epochs of the input data, and perform the inverse PCA transformation for these modes. As a result we obtain a time series of GRACE-based surface mass anomalies, containing a set of well-defined variations contaminated by authentic noise. Applying the PCA and the frequency analysis to this data we derive the standard deviations of the empirical distribution for the amplitudes, periods and phases.

4 Application to Continental Grids and River Basins

The described methodology was applied to continental grids and to 18 selected river basins. The PCA reveals that in all cases 80% and more of the total variability observed in GRACE and water storage of hydrology models is contained in the very first three to five modes (Petrovic et al., 2007; Schmidt et al., 2008). Hence, we limit the frequency analysis of the pcs and the accuracy assessment for the GRACE data to these lower modes. Some plots of the evs patterns and the associated pcs curves can be found in Petrovic et al. (2007) and Schmidt et al. (2008). Here we illustrate the results taking as example the basins of Amazon and Ganges.

Tables 1, 2, 3, and 4 summarize the periods detected in the pcs from the non-standard frequency analysis outlined in previous section. In analogy to PCA, the results are tabulated in descending order, i.e. from the strongest to the weakest periodic component. This ranking is derived based on the percentage contribution of the harmonic component to the total variability of the input grid data, i.e. from the ratio $(\mathrm{var}_{\mathrm{harm}}/\mathrm{var}_{\mathrm{total}}) \cdot 100\ [\%]$, where $\mathrm{var}_{\mathrm{total}}$ denotes the variance of the original total signal (which includes noise), and $\mathrm{var}_{\mathrm{harm}}$ is the signal variance of the spatial signal reconstructed from the harmonic components only.

Table 1 Periods, phases and amplitudes of the most dominant periodic features for Amazon deduced from GRACE time series 08/2002–09/2007. Applied decorrelation filter DDK1, amplitudes in relative units, last column displays the percentage of total signal explained

Rank	Mode	Period T (d)	Phase ϕ (d)	Amplitude A	Percentage of total
1	1	361.9 ± 0.3	114.3 ± 0.7	7.63 ± 0.06	73.9
2	2	361.5 ± 0.4	201.3 ± 0.6	3.73 ± 0.04	17.8
3	3	772.4 ± 19.5	75.1 ± 13.7	0.50 ± 0.06	1.1
4	1	459.6 ± 6.6	469.7 ± 7.9	0.90 ± 0.06	1.0

Table 2 Same as Table 1, but for the hydrology model WGHM

Rank	Mode	Period T (d)	Phase ϕ (d)	Amplitude A	Percentage of total
1	1	360.3	101.9	4.80	73.3
2	2	361.0	197.0	2.09	13.8
3	1	1,072.7	455.0	1.28	4.0
4	1	467.0	453.3	0.77	1.3

Table 3 Periods, phases and amplitudes of the most dominant periodic features for Ganges deduced from GRACE time series 08/2002–09/2007. Applied decorrelation filter DDK1, amplitudes in relative units, last column displays the percentage of total signal explained

Rank	Mode	Period T (d)	Phase ϕ (d)	Amplitude A	Percentage of total
1	1	365.2 ± 0.6	264.3 ± 1.0	2.88 ± 0.04	83.5
2	1	184.8 ± 0.7	60.2 ± 1.7	0.76 ± 0.04	5.5
3	2	358.3 ± 2.1	355.8 ± 3.8	0.47 ± 0.03	2.3

Table 4 Same as Table 3, but for the hydrology model WGHM

Rank	Mode	Period T (d)	Phase ϕ (d)	Amplitude A	Percentage of total
1	1	365.1	255.6	2.30	89.3
2	1	182.7	54.3	0.59	6.0

For the GRACE-based results the accuracy assessment according to Sect. 3 is displayed in Tables 1 and 3. For the interpretation of the errors of the amplitudes one has to note that the tabulated values have relative units, since absolute signal amplitudes are only given after the synthesis of the eigenvectors and principal components. The mean errors displayed in Tables 1 and 3 show that the four most dominant periodic variations found in Amazon and the three found in Ganges can be regarded as significant. However, the significance of the 772.4-days wave in Amazon is somewhat lower. In spite of the statistical significance of the results, it makes sense to check whether the resulting periods are independent of the filter used. Table 5 illustrates the differences in the results for three different versions of the decorrelation filter according to Kusche (2007), which represent a realistic span of smoothing. The relative differences between the periods detected based on

Table 5 Comparison of periods, phases and amplitudes estimated for data points inside the Amazon and Ganges basin from GRACE for different versions (DDK1, DDK2, DDK3) of decorrelation filter. Time span: 08/2002–09/2007

	Δ period (d)		Δ phase (d)		Amplitude ratio	
	DDK2-1	DDK3-1	DDK2-1	DDK3-1	DDK2/1	DDK3/1
Amazon	0.05	−0.02	1.03	3.04	1.09	1.12
	0.29	0.39	1.62	3.38	1.27	1.35
	–5.01	−9.70	−15.31	−5.87	1.64	2.02
	0.06	0.60	1.70	4.81	1.22	1.27
Ganges	0.06	0.04	−0.52	−3.14	1.12	1.16
	–0.14	−0.56	−2.01	−4.59	1.11	1.09
	0.46	3.56	−1.86	−1.74	1.85	2.55

the preprocessing by DDK1 and DDK2 vary between 0.01 and 0.13%, with the sole exception for the 772.4-days wave (0.69%). For the comparison of DDK1 and DDK3 these relative differences are mostly under 0.30% and reach in the worst case 1.26%. Note that the uncertainty of 0.01% corresponds to the periodic component which explains 73.9% (respectively 83.5%) of the total signal, and the uncertainty of 1.26% to the periodic term explaining only 1.1% of the total variability. In short, the determination of periods and phase lags is very stable, differences in the smoothing strength affect, as expected, primarily amplitudes, cf. Kusche et al. (2009).

Table 6 displays the results obtained for Ganges basin earlier using a simple Gaussian smoothing filter and a shorter time span (Schmidt et al., 2008). There is a very good agreement with Table 3, confirming that the detected periods are not merely an artefact of the applied filter or time interval.

The results for Amazon and Ganges presented here are representative for all investigated basins and can be summarized as follows. A major part of the total variability, usually 80% and more, is contained in a few first modes resulting from PCA. In each basin a few (2–4) significant (according to the accuracy assessment) periodic terms are detected, which explain 70–95% of the entire variability. The significance of the long-periodic terms (periods of 2 years and more) is somewhat lower due to the limited time span of the available data. Preprocessing GRACE data with different decorrelation or smoothing filters affects the determination of periods and phase lags only slightly.

Table 6 Periods, phases and amplitudes of the most dominant periodic features for Ganges deduced from GRACE time series 02/2003–12/2006. Applied Gaussian smoothing filter G500, amplitudes in relative units, last column displays the percentage of total signal explained

Rank	Mode	Period T (d)	Phase ϕ (d)	Amplitude A	Percentage of total
1	1	362.7 ± 1.0	265.1 ± 1.4	2.69 ± 0.06	79.0
2	1	183.4 ± 1.0	57.8 ± 2.3	0.71 ± 0.05	4.6
3	2	352.7 ± 5.2	358.6 ± 13.2	0.60 ± 0.06	4.6

In Tables 1, 2, 3, and 4 we see a good agreement between the periods detected from GRACE observations and from the hydrology model WGHM. The most dominant features observed are annual periodic variations (with almost identical results for the three other hydrology models considered here). They are found in all investigated basins; in most of them 70–80% of the total variability seem to be represented by annual waves. The accuracy assessment of the GRACE-based results indicates a very good resolution of the annual terms; for the Amazon and the Ganges basin the standard deviations of the derived annual periods and their phases are at the level of or even below 1 day. The detection of several annual signals in different modes, i.e. associated to different spatial patterns, is not surprising. This is caused by the spatial variability of the signal amplitudes, phases and periods inside the region of interest. For the Amazon these variations are well explicable by the distribution of the rainfall inside this basin, cf. Zeng (1999) and Güntner et al. (2007). Hence, finding several annual periods associated to different spatial patterns inside a basin is a consequence of the processes governing the mass redistributions.

Semiannual variations are found only in few investigated river basins. The contribution to the total variability is small, but can be determined significantly, as shown by standard deviations for the Ganges (Table 3). This semiannual term is found in the principal component of mode 1; hence, it has the same spatial variability pattern as the annual term. Therefore, it might be just a correction of the dominating annual term, and it is not easy to attribute the semiannual signal to some uniquely defined physical cause. However, there are several physical causes that may explain semiannual oscillations indeed, cf. Güntner et al. (2007).

The results of the frequency analysis (Tables 1 and 2) also show long-periodic variations in the range of 2 years and more. As for semiannual signals, these represent only small contributions to the total variability, too. The standard deviations for the GRACE-based estimates are much larger than for the annual and semiannual terms. This holds e.g. for the 2.1-yearly oscillation in the Amazon (Table 1), and illustrates the difficulties in clearly identifying such terms, in particular in view of the rather short period covered by GRACE so far. However, for several reasons such terms may be plausible nevertheless, cf. Schmidt et al. (2008).

5 Reconstruction of Filtered GRACE Time Series of Surface Mass Anomalies

Phase lags in Tables 1, 2, 3, and 4 show that the variations of surface mass anomalies from WGHM are ahead of the GRACE estimate for Amazon and Ganges. This holds also in general. Taking into account all investigated basins and different hydrology models, an average systematic offset of about 1 month can be detected. In order to validate and calibrate hydrology models, the GRACE time series is reconstructed taking into account only the part of the signal which can be regarded as reliably detected and representative for the hydrological variations. In order to achieve this,

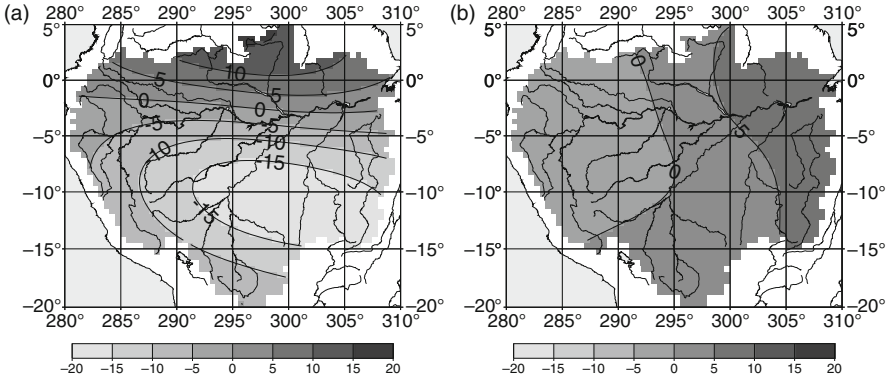

Fig. 1 (**a**) Synthesis of GRACE-based surface mass anomalies in the Amazon derived from the first four harmonic terms from Table 1 at epoch 15 August 2006. (**b**) Residual of total surface mass anomaly map minus the map shown in (**a**). Units: cm water column

we construct filtered GRACE time series of surface mass anomalies using in the PCA synthesis the harmonic components of the pcs that

- are significant according to the accuracy assessment, and
- are found also in the hydrology data.

As an example, Fig. 1(a) shows the filtered surface mass anomaly signal for the Amazon basin for the month of August 2006. This reconstruction is based on the four dominant periodic terms from Table 1. Figure 1(b) displays the residual signal obtained by subtracting the map in Fig. 1(a) from the total GRACE-based signal at that epoch. The anomalies in Fig. 1(a) represent about 94% of the total signal (Table 1), while the residual signal in Fig. 1(b) represents only about 6% of the variability. Although both maps still contain GRACE data errors, the spatial distribution of the residual signal, dominated by North-South oriented striping features well comparable to the correlated GRACE gravity model error, indicates a clear signal-noise separation obtained by the applied approach. For the Ganges, the three dominating periodic terms (Table 3) explain 91% of the total variability.

The residual signal may still contain traces of hydrological signal and cannot be interpreted as pure errors. Since the amplitude of the residual signal is relatively small (in the Amazon only 6% of the total variability, in the Ganges 9%), the potentially neglected hydrological signal should be very small, too. Conversely, the reconstructed signal from the selected harmonic terms may also contain some small portions of the error signals. However, the accuracy assessment shows that the relative contributions of errors in the derived dominating terms are much smaller than in the residual part. The percentage of the total signal explained by this reconstruction is comparably high in most of the considered basins. In this way the construction of filtered surface mass anomalies from the dominating terms is useful for the basin-specific calibration of hydrological models with respect to the dominant periodic variations of water storage, as demonstrated in Werth et al. (2009a).

6 Conclusions

We present the methodology for deriving characteristic spectra of periodic surface mass variations induced by continental hydrology observable in time series of GRACE gravity and global hydrology models. To this end we apply a combined PCA and frequency analysis method, where the latter allows for the determination of arbitrary periods from the temporal patterns of the derived PCA modes. This is an interesting alternative to conventional, Fourier-based frequency analysis of data, as it may allow for a more adequate description of time variability contained in geophysical data. For the GRACE-based spectra we perform an accuracy assessment using available GRACE error estimates and a Monte-Carlo simulation.

The characteristic features of hydrologically induced mass redistributions are dominated by annual variations which explain about 60% to more than 90% of the total data variability, and are well determined in the GRACE data. The absolute errors of the annual periods and phases are small and seem to be at the level of about $\pm$ 1 day for most of the basins. For the phases of the annual terms we observe a systematic delay between GRACE-based surface mass anomalies and the hydrology models (depending on the model and the region the phases from the hydrology models are about 1–6 weeks ahead of the GRACE estimates), which may point to systematic deficiencies in hydrological modelling. Semiannual terms do not play a significant role, at least on the global scale. For river basins only in a few regions, e.g., the Ganges, the Nile, the Congo, and the Ob, semiannual variations are traceable. Moreover long-periodic signals with periods of 2 years and more are observed. Due to the short data period covered by GRACE so far, a separability of such features may be limited.

Finally, it is possible to derive filtered GRACE surface mass anomaly data. These are reconstructed by the inverse PCA transformation where the original principal components are replaced by harmonic terms that (1) are significant according to the error estimates, and (2) are found consistently also in hydro-climatological models. Such anomaly data, revealing a distinct signal-noise separation, are of benefit for calibration and validation of hydroclimatological models. The method is not restricted to the presented study case of hydrology, and it may be of general interest for a wide set of geophysical applications in the context of an assimilation of GRACE-based surface mass data.

Acknowledgments The German Ministry of Education and Research (BMBF) supported these investigations within the geoscientific R+D programme GEOTECHNOLOGIEN "Erfassung des Systems Erde aus dem Weltraum" under grant 03F0424A. We thank P.C.D. Milly, Y. Fan and H. van den Dool, M. Rodell as well as P. Döll and J. Alcamo for providing the LaD, H96, GLDAS and WGHM model data, respectively. Thanks also go to D.W. Pierce for his Empirical Orthogonal Functions (EOF) software.

References

Chambers DP, Wahr J, Nerem RS (2004) Preliminary observations of global ocean mass variations with GRACE. Geophys. Res. Lett. 31, L13310.

Döll P, Kaspar F, Lehner B (2003) A global hydrological model for deriving water availability indicators: Model tuning and validation. J. Hydrol. 270, 105–134.
Gundlich B, Koch K-R, Kusche J (2003) Gibbs sampler for computing and propagating large covariance matrices. J. Geod. 77(9), 514–528.
Güntner A, Stuck J, Werth S et al. (2007) A global analysis of temporal and spatial variations in continental water storage. Water Resour. Res. 43, W05416.
Horst R, Pardalos PM (eds.) (1995) Handbook of Global Optimization, Nonconvex Optimization and Its Applications, Vol. 2., Kluwer Academic Publishers, Dordrecht.
Huang J, van den Dool HM, Georgakakos PK (1996) Analysis of model-calculated soil moisture over the United States (1981–1993) and applications of long-range temperature forecasts. J. Clim. 9, 1350–1362.
Jekeli C (1981) Alternative methods to smooth the Earth's gravity field. Tech Rep 327, Ohio State University.
Kalos MH, Whitlock PA (1988) Monte Carlo Methods, Wiley, New York.
Kusche J (2007) Approximate decorrelation and nonisotropic smoothing of time-variable GRACE-type gravity field models. J. Geod. 81(11), 733–749.
Kusche J, Schmidt R, Petrovic S, Rietbroek R (2009) Decorrelated GRACE time-variable gravity solutions by GFZ, and their validation using a hydrological model. J. Geod. 83(10), 903–913.
Mautz R, Petrovic S (2005) Erkennung von physikalisch vorhandenen Periodizitäten in Zeitreihen. ZFV (Zeitschrift f. Geodäsie, Geoinformation und Landmanagement) 130(3), 156–165.
Milly PCD, Shmakin AB (2002) Global modeling of land water and energy balances, Part I: The land dynamics (LaD) model. J. Hydrometeor. 3, 283–299.
Petrovic S, Schmidt R, Wünsch J et al. (2007) Towards a characterization of temporal gravity field variations in GRACE observations and global hydrology models. In: Proceedings of the 1st International Symposium of the Gravity Field Service "Gravity Field of the Earth", Istanbul, J Mapping (ISSN 1300-5790) 73, Special Issue: 18, 199–204.
Preisendorfer RW (1988) Principal Component Analysis in Meteorology and Oceanography, Elsevier Science Publishers, Amsterdam.
Rodell M, Houser PR, Jambor U et al. (2004) The global land data assimilation system. Bull. Amer. Meteorol. Soc. 85(3), 381–394.
Schmidt R, Schwintzer P, Flechtner F et al. (2006) GRACE observations of changes in continental water storage. Glob. Planet Change 50(1–2), 112–126.
Schmidt R, Petrovic S, Güntner A et al. (2008) Periodic components of water storage changes from GRACE and global hydrological models. J. Geophys. Res. 113, B08419.
Tamisiea ME, Mitrovica JX, Davis JL (2007) GRACE gravity data constrain ancient ice geometries and continental dynamics over Laurentia. Science 316(5826), 881–883.
Velicogna I, Wahr J (2006) Acceleration of Greenland ice mass loss in Spring 2004. Nature 443, 329–331.
Wahr J, Molenaar M, Bryan F (1998) Time variability of the Earth's gravity field: Hydrological and oceanic effects and their possible detection using GRACE. J. Geophys. Res. 103, 30205–30230.
Werth S, Güntner A, Petrovic S, Schmidt R (2009a) Integration of GRACE mass variations into a global hydrological model. Earth Planet Sci. Lett. 277(1–2), 166–173.
Werth S, Güntner A, Schmidt R, Kusche J (2009b) Evaluation of GRACE filter tools from a hydrological perspective. Geophys. J. Int., doi: 10.1111/j.1365-246X.2009.04355.x.
Wilks DS (1995) Statistical Methods in the Atmosphere Sciences: An Introduction, Academic Press, San Diego, CA.
Zeng N (1999) Seasonal cycle and interannual variability in the Amazon hydrologic cycle. J. Geophys. Res. 104(D8), 9097–9106.

Time-Space Multiscale Analysis and Its Application to GRACE and Hydrology Data

Willi Freeden, Helga Nutz, and Kerstin Wolf

1 Introduction

The satellite gravity mission GRACE (Gravity Recovery and Climate Experiment) (Tapley et al., 2004a, b) provides a huge amount of data which allows to quantify both temporal and spatial variations of the Earth's gravity field caused by mass transport and mass distribution (Swenson and Wahr, 2006; Swenson et al., 2003). For modelling the gravitational field of the Earth, usually, truncated Fourier series based on spherical harmonics are used where the accuracy of the approximation is given by the maximum degree. A fundamental disadvantage of this method is the localization of the spherical harmonics in the frequency domain, which leads to a smearing of the spatial detail information over the whole globe. The need of a method which allows local analysis of the gravitational potential led to the development of spherical wavelets in the Geomathematics Group of TU Kaiserslautern (Freeden, 1999; Freeden and Schneider, 1998; Freeden and Schreiner, 2009; Freeden et al., 1998). The spherical wavelets are kernel functions, which are built up using clusters of a finite number of polynomials, and, thus, guarantee a good localization in the space domain. Note that the uncertainty principle states that localization in both frequency and space domain are mutually exclusive.

Based on the theory of spherical wavelets we propose two different methods which allow a temporal and spatial wavelet analysis of monthly data sets given by the satellite mission GRACE or resulting from WGHM (WaterGAP Global Hydrology Model) (Döll et al., 2003) for a period of several years (some first results are presented in, e.g., Fengler et al., 2007). With the help of the wavelet analysis we are able to locally compare the GRACE and hydrology data in both temporal and spatial sense and, finally, to give a first idea of how to construct an improved hydrological model on the basis of a time-space multiresolution.

The layout is as follows: in Sect. 2 the combination of the spatial analysis and the temporal analysis is performed with the help of two different methods: First

W. Freeden (✉)
Geomathematics Group, Department of Mathematics, TU Kaiserslautern,
67653 Kaiserslautern, Germany
e-mail: freeden@mathematik.uni-kl.de

F. Flechtner et al. (eds.), *System Earth via Geodetic-Geophysical Space Techniques*,
Advanced Technologies in Earth Sciences, DOI 10.1007/978-3-642-10228-8_33,

we combine the classical Euclidean wavelets for the time domain with the spherical wavelets for the space domain and, second, we build up tensor product wavelets with Legendre wavelets and spherical wavelets for the time and space domain, respectively. The comparison of both wavelet methods is performed in Sect. 3, and we propose a filtering method for the extraction of an improved hydrological model in Sect. 4. In the last section some conclusions are drawn.

All computations have been performed based on 62 monthly data sets of spherical harmonic coefficients up to degree and order 70 from GRACE and WGHM for the period of August 2002 till September 2007. The data have been provided by our project partners from the German Centre for Geosciences (GFZ), Department 1: Geodesy and Remote Sensing.

2 Multiscale Analysis

This section starts with a short introduction to the theory of spherical multiresolution. For a more detailed representation see Freeden and Michel (2004), Freeden and Schneider (1998) and Freeden et al. (1998). Let $L^2(\Omega)$ be the space of all square-integrable functions on the unit sphere Ω, let $Y_{n,m}$, $n \in IN_0$, $m = 1,\ldots,2n+1$, be an $L^2(\Omega)$-orthonormal system of spherical harmonics. The idea of the spherical multiscale analysis is to choose kernel functions (so-called scaling functions) $\Phi_J(\xi,\eta) = \sum_{n=0}^{\infty} (\Phi_J)^\wedge(n) \sum_{m=1}^{2n+1} Y_{n,m}(\xi) Y_{n,m}(\eta)$ which depend on a scale $J \in IN_0$ in order to build up the scale spaces $V_J = \left\{ \Phi_J * \Phi_J * F \,\middle|\, F \in L^2(\Omega) \right\}$, where "$*$" denotes the convolution, in such a way that we get a multiresolution (i.e., a nested sequence of subspaces) of $L^2(\Omega)$: $V_0 \subset \cdots \subset V_J \subset V_{J+1} \subset \cdots \subset L^2(\Omega)$ with $L^2(\Omega) = \overline{\bigcup_{J=0}^{\infty} V_J}^{||\cdot||_{L^2(\Omega)}}$. The transmission from V_J to V_{J+1} is performed by use of the detail space $W_J = \left\{ \Psi_J * \Psi_J * F \,\middle|\, F \in L^2(\Omega) \right\}$ via $V_{J+1} = V_J + W_J$, where the wavelets are given by $\Psi_J(\xi,\eta) = \sum_{n=0}^{\infty} (\Psi_J)^\wedge(n) \sum_{m=1}^{2n+1} Y_{n,m}(\xi) Y_{n,m}(\eta)$ and the symbols of the scaling functions and the wavelets fulfill a scaling equation of the form $\left((\Psi_J)^\wedge(n)\right)^2 = \left((\Phi_{J+1})^\wedge(n)\right)^2 - \left((\Phi_J)^\wedge(n)\right)^2$. For the temporal case ($L^2([-1,1])$) we transform the spherical multiscale theory using the normalized Legendre polynomials $P_{n'}^*$, $n' \in IN_0$, instead of the spherical harmonics $Y_{n,m}$.

2.1 *Separated Wavelet Analysis with Spherical Wavelets in Space and Euclidean Wavelets in Time Domain*

The first idea we follow is to analyze the data in two steps: starting from the original data a spherical wavelet analysis is performed. The result is a time series of spherical wavelet coefficients which show more and more (spatial) details with increasing scale. In the second step we analyze this time series of spherical wavelet coefficients using Euclidean wavelets and get temporal wavelet coefficients (see Fig. 1). For the understanding of the classical Euclidean wavelet theory see, e.g., Chui (1992), Mallat and Hwang (1992) and Mallat and Zhong (1992).

In Figs. 2 and 3 the wavelet coefficients for different scales are presented. The reader should keep in mind that these coefficients represent the detail information

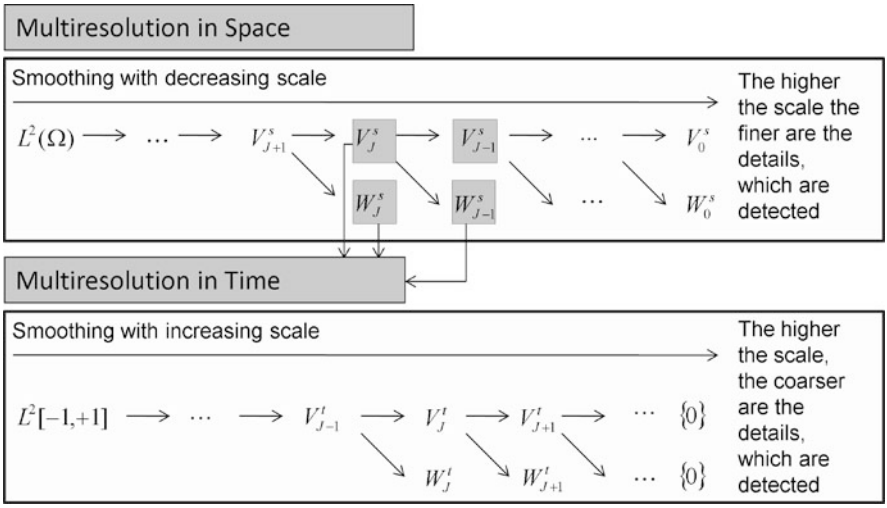

Fig. 1 Separated multiresolution in space and time using spherical and Euclidean wavelets, respectively

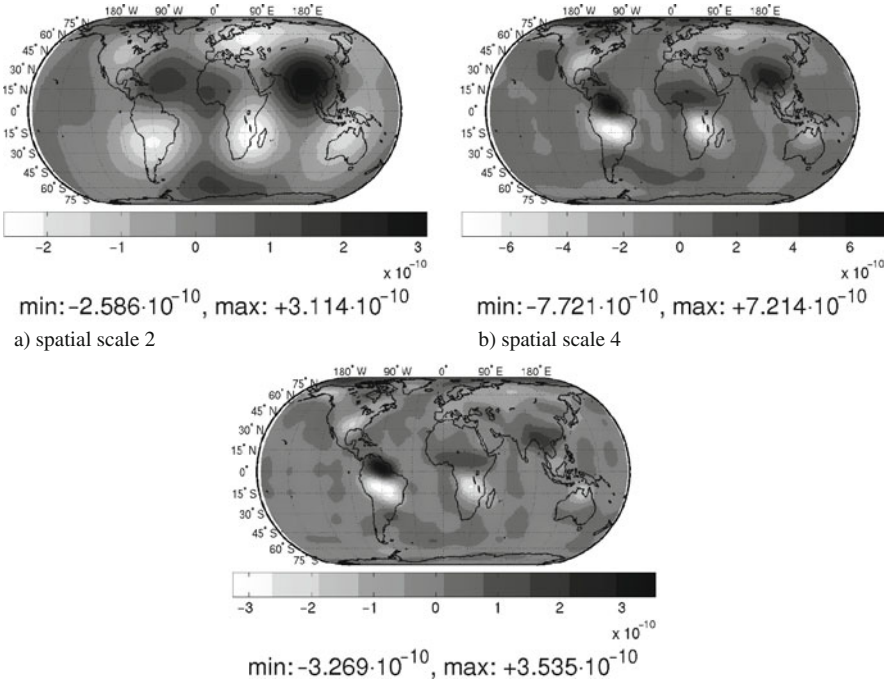

Fig. 2 Space-time wavelet coefficients of GRACE data for April 2005 computed from spherical c(ubic) p(olynomial)-wavelet coefficients with the quadratic spline wavelet at time scale 2

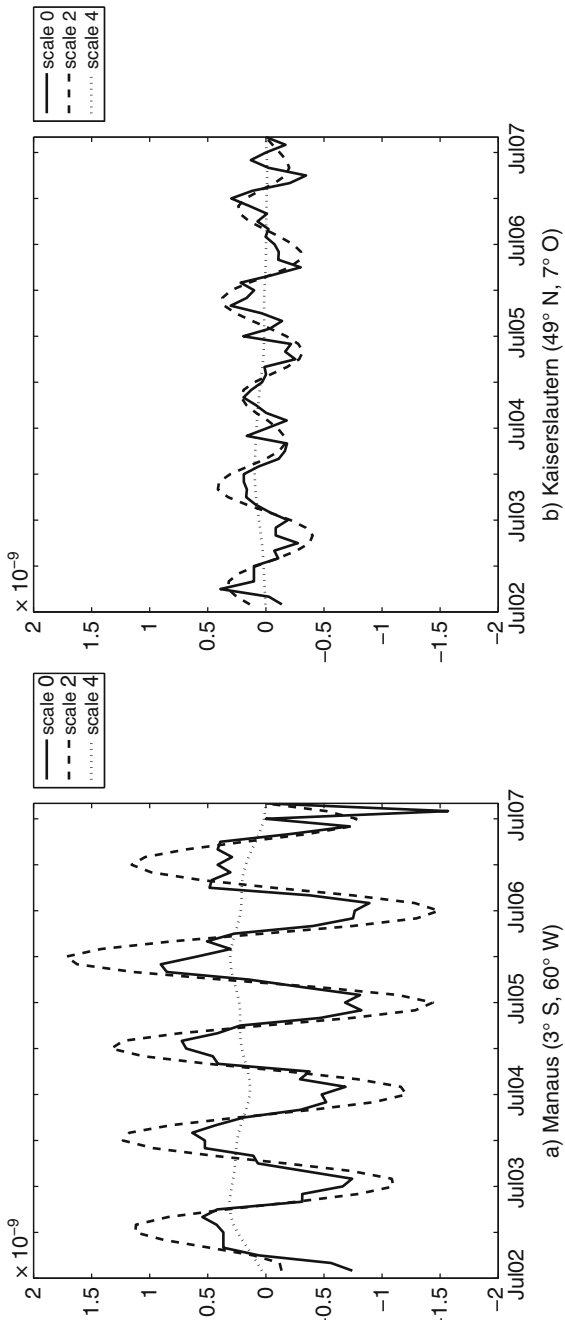

Fig. 3 Time-dependent courses of the space-time wavelet coefficients of the GRACE data in Manaus and Kaiserslautern. For the spatial analysis we used the cp-wavelet with spatial scale 3 and for the temporal analysis the quadratic spline wavelet for temporal scales 0, 2, 4

with whose help we are able to reconstruct the original signal adding detail parts (following the principle of the multiresolution shown in Fig. 1). In Fig. 2 the zooming-in effect can be seen clearly: the higher the scale the better the regions with great changes in the water balance are detected, as, e.g., in the Amazon basin, Ganges, and Mississippi. In Fig. 3 the time-dependent courses of the space-time wavelet coefficients in a selected location in the Amazon basin and the corresponding results for Kaiserslautern are shown. In both diagrams we recognize that the seasonal variations at temporal scale 2 (dimension of the details about 4 months) can be seen clearly. At time scale 4 (dimension of the details about 16 months) the course is very smooth, which indicates that it does not make sense to compute higher scales.

2.2 Tensor Product Wavelets

The principle of the tensor product wavelet analysis which is, e.g., described in Louis et al. (1998) admits the transmission of the one dimensional multiscale analysis to higher dimensions. Using the tensor product wavelet theory we are able to define the multiresolution analysis of the space $L^2([-1,1]\times\Omega)$. The theory of spherical wavelets described in Sect. 2 is transformed to the time domain using Legendre wavelets $\Psi'_J(s,t) = \sum_{n'=0}^{\infty} (\Psi'_J)^\wedge(n') P^*_{n'}(s) P^*_{n'}(t)$ and the analogously defined temporal scaling functions Φ'_J. As in the spatial case the (temporal) kernel functions Φ'_J and Ψ'_J fulfill a scaling equation. Now we are able to build the tensor product wavelets $\tilde{\Psi}^i_J$, i=1,2,3, and scaling functions $\tilde{\Phi}_J$:

$$\tilde{\Psi}^i_J(s,t;\xi,\eta) = \sum_{n'=0}^{\infty} \sum_{n=0}^{\infty} \sum_{m=1}^{2n+1} (\tilde{\Psi}^i_J)^\wedge(n';n) P^*_{n'}(s) P^*_{n'}(t) Y_{n,m}(\xi) Y_{n,m}(\eta),$$

$$\tilde{\Phi}_J(s,t;\xi,\eta) = \sum_{n'=0}^{\infty} \sum_{n=0}^{\infty} \sum_{m=1}^{2n+1} (\tilde{\Phi}_J)^\wedge(n';n) P^*_{n'}(s) P^*_{n'}(t) Y_{n,m}(\xi) Y_{n,m}(\eta),$$

with the symbols

$$(\tilde{\Psi}^1_J)^\wedge(n';n) = (\Phi'_J)^\wedge(n')(\Psi_J)^\wedge(n),\ (\tilde{\Psi}^2_J)^\wedge(n';n) = (\Psi'_J)^\wedge(n')(\Phi_J)^\wedge(n),$$

$$(\tilde{\Psi}^3_J)^\wedge(n';n) = (\Psi'_J)^\wedge(n')(\Psi_J)^\wedge(n),\ (\tilde{\Phi}_J)^\wedge(n';n) = (\Phi'_J)^\wedge(n')(\Phi_J)^\wedge(n).$$

This yields the time-space multiresolution with tensor product wavelets shown in Fig. 4.

In case of the first hybrid part we smooth in the time domain and detect details in the space domain, whereas in case of the second hybrid part it is vice versa. The pure parts in addition show details in both time and space domain. The wavelet

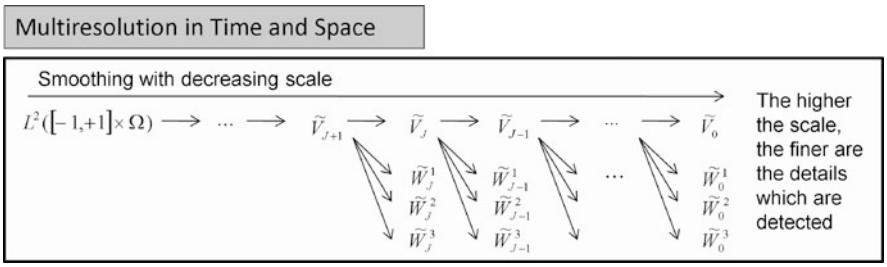

Fig. 4 Multiresolution of $L^2([-1,+1]\times\Omega)$ with tensor product wavelets

coefficients of the tensor product multiresolution demonstrate the same structures in the data sets as shown in Sect. 2.1 for the separated multiresolution using Euclidean wavelets in the time domain. With increasing scale more and more details can be recognized in both time and space. A detailed description of the tensor product wavelet theory and a sound discussion of the results can be found in Nutz and Wolf (2008).

3 Comparison of the Wavelet Methods Involving Correlation Coefficients

Considering the computing time we state that the classical Euclidean wavelet transform provides the results time-independent of the scale whereas in case of the spherical and the tensor product wavelet transform the computing time rises exponentially with increasing scale. Additionally the computing time also depends on the applied wavelets and for this reason we cannot state in general which method is faster.

As far as the interpretation of the results is concerned it does not make sense to directly compare the wavelet coefficients of both methods. This is mainly the result of the fact that the temporal and spatial details in the first method (Euclidean wavelets in the time domain) are visualized in different (spatial and temporal) scales, whereas the second method (tensor product wavelets) has one single scale for both temporal and spatial analysis which yields the necessity of three different types of details. Thus we need a tool for the evaluation of the result, and we decided to use local and global correlation coefficients. Since we average over time the methodical differences are diminished and we are able to compare, e.g., the results for the spatial scales for fixed temporal scale (Euclidean wavelets in the time domain) with the results for different scales of the pure wavelet coefficients (tensor product wavelets).

As shown in Fig. 5 we see that the results for both methods are in general quite similar, as expected, though there are regional differences which have to be interpreted in view of an improvement of existing hydrology models. Supplementary,

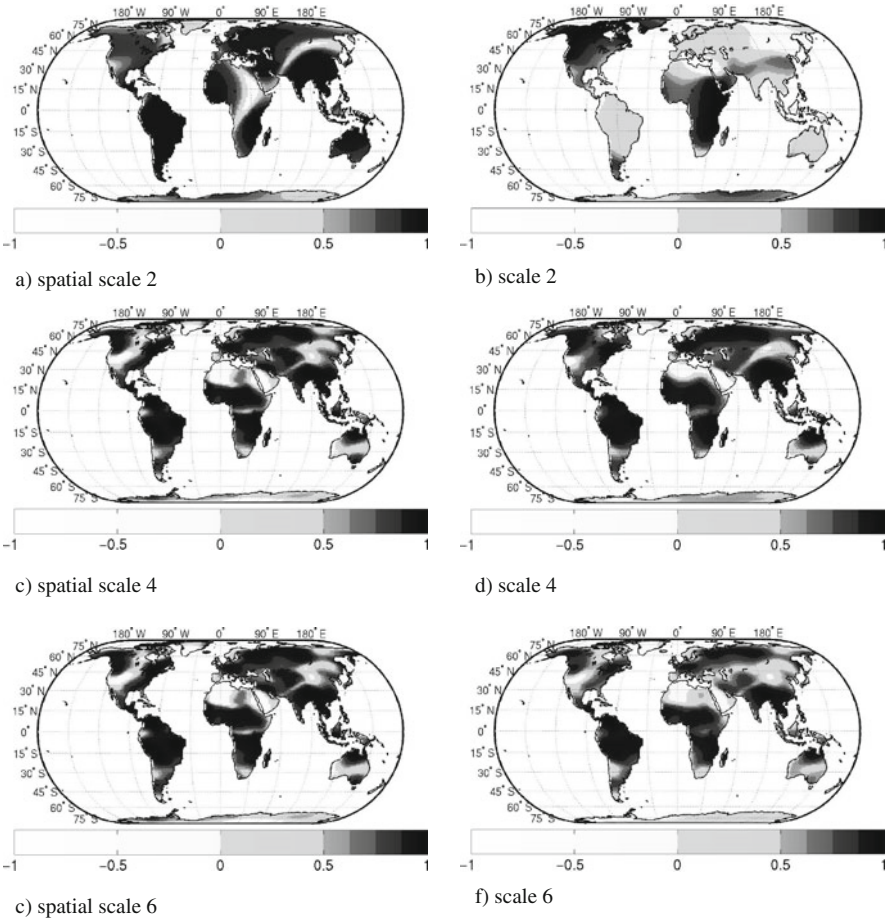

Fig. 5 Local correlation coefficients between GRACE- and WGHM-data computed from wavelet coefficients with quadratic spline wavelet of scale 2 in the time domain and cp-wavelet of different scales in the space domain (**a**, **c**, **e**) and from pure tensor product wavelet coefficients with cp-wavelet of different scales (**b**, **d**, **f**)

Table 1 (a and b) shows the global correlation coefficients for different scales. The best values are marked in light grey and dark grey.

4 Adapted Filter for the Extraction of a Hydrology Model from GRACE Data

Our aim now is to interpret the results achieved from the multiscale analysis with the aid of the correlation coefficients in view of an improvement of existing hydrology models. To this end we propose a filter based on the correlation

Table 1 Global correlation coefficients for the multiresolution (only on the continents) of GRACE and WGHM data

(a) *Separated wavelet analysis (cp-wavelet in the space domain, quadratic spline wavelet in the time domain)*

Spatial scale \ Temp. scale	0	1	2	3	4
2	0.59	0.79	0.82	0.61	0.29
3	0.68	0.84	0.86	0.66	0.52
4	0.68	0.83	0.85	0.66	0.52
5	0.65	0.82	0.84	0.64	0.49
6	0.63	0.81	0.83	0.63	0.47
7	0.62	0.80	0.83	0.63	0.47
8	0.62	0.80	0.83	0.62	0.46

(b) *Tensor product wavelet analysis with cp-wavelet in the time and space domain*

Scale	$\Phi_J * F$	$\Psi_J^1 * F$	$\Psi_J^2 * F$	$\Psi_J^3 * F$
2	0.04	0.28	0.38	0.38
3	0.33	0.49	0.58	0.72
4	0.54	0.51	0.74	0.82
5	0.66	0.62	0.74	0.82
6	0.69	0.66	0.64	0.76
7	0.68	0.67	0.53	0.66
8	0.67	0.66	0.46	0.59

coefficients and we assume that we have an improvement if the (global and local) correlation coefficients of the filtered GRACE and WGHM data are better than those of the original data. Furthermore we demand that a very large part of the original signal is reconstructed in the filtered data. Note that the improvement of the correlation coefficients and the increase of the percentage of the filtered signal from the original signal cannot be optimized simultaneously. The method is only applied for the tensor product wavelet analysis but can be transformed to the separated wavelet analysis with Euclidean wavelets in the time domain, too.

To find out an optimal filter we start with computing the local correlation coefficients $k_J^{(i)}$ on the continents for the corresponding detail parts (of the potential of GRACE and WGHM) $F * \Psi_J^{(i)} * \Psi_J^{(i)}$ and the local correlation coefficients k_J for the "reconstructions" $F * \Phi_J * \Phi_J$. In addition we compute the "global" correlation coefficients $gk_J^{(i)}$,gk_J. From the correlation coefficients we derive the weights using a weight function $w:[-1,1] \to [0,1]$ which controls the influence of the corresponding detail part on the resulting reconstructed signal:

$$F_{J_{\max}} = \left(\Phi_{J_0} * \Phi_{J_0} * F\right)(\xi) w\left(k_{J_0}(\xi)\right) + \sum_{j=J_0}^{J_{\max}-1} \sum_{i=1}^{3} \left(\Psi_j^{(i)} * \Psi_j^{(i)} * F\right)(\xi) w\left(k_j^{(i)}(\xi)\right). \tag{1}$$

The weight function is defined by

$$w(k) = \begin{cases} 0, & k \le G_1 \\ \frac{1}{G_2-G_1}k - \frac{G_1}{G_2-G_1}, & G_1 < k < G_2 \\ 1, & k \ge G_2 \end{cases}, \tag{2}$$

$k \in [-1,1]$, with the constants $G_1, G_2 \in [-1,+1]$ which help to control the region of influence: If the correlation coefficient is smaller than G_1 we do not add the corresponding part in the reconstruction formula (1), whereas in case of a correlation coefficient greater than G_2 we add the entire part. In case of a correlation coefficient $G_1 < k < G_2$ we weight the corresponding part in the reconstruction formula (1) in such a way that for higher correlation coefficients we use greater weights. In order to get the percentage of the reconstructed signal F^{rec} from the original signal F^{orig} we use the energy which is given by $||F||^2_{L^2([-1,+1]\times\Omega)} = \sum_{n'=0}^{\infty}\sum_{n=0}^{\infty}\sum_{m=1}^{\infty}\left(F^{\wedge}\left(n';n,m\right)\right)^2$ for $F \in L^2([-1,+1]\times\Omega)$, where $F^{\wedge}\left(n';n,m\right)$ are the time-space Fourier coefficients. The percentage $p(F^{\text{rec}},F^{\text{orig}})$ is then given by

$$p(F^{\text{rec}}, F^{\text{orig}}) = \frac{\|F^{\text{rec}}\|_{L^2(-1,+1]\times\Omega)}}{\|F^{\text{orig}}\|_{L^2(-1,+1]\times\Omega)}}.$$

In analogy we compute the percentage of the detail parts from the total signal.

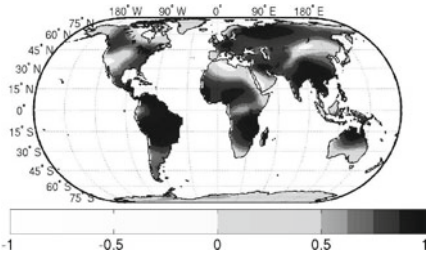

a) Original data (gk = 0.75)

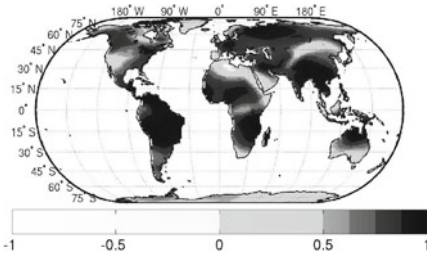

b) Reconstruction with $G_1 = -0.1$ and $G_2 = -0.09$ (90.04% gk = 0.81).

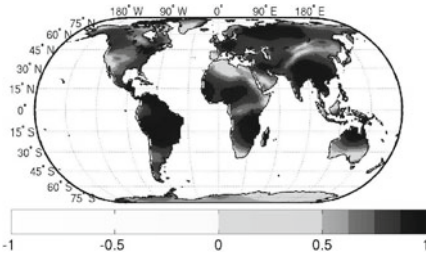

b) Reconstruction with $G_1 = 0.01$ and $G_2 = 0.53$ (80.03% gk = 0.84).

Fig. 6 Correlation coefficients between the original signals and two reconstructions with details up to scale 9 from GRACE and WGHM (gk: global correlation coefficient, G_1 and G_2 control the region of influence of the weight function cf. Eq. (2))

Table 2 Percentage of the reconstruction with details up to scale 9 from GRACE data to the original GRACE data and correlation coefficients for the corresponding reconstructions between GRACE and WGHM data for different values of G_1 and G_2

Percentage	Corr. coeff.	G_1 and G_2
Original (100)	0.75	–
95	0.77	– 0.8 and –0.68
90	0.81	– 0.1 and –0.09
85	0.83	0.1 and 0.22
80	0.84	0.1 and 0.53

In Fig. 6 the correlation coefficients between the original data (Fig. 6a) and for two reconstructions (Fig. 6b and c) are shown. In addition, Table 2 shows some more optimal results for different values G_1 and G_2.

5 Conclusions

A time-space multiscale analysis using two different methods is introduced: First a separated wavelet concept and, second, a tensor product wavelet concept is realized. Both methods turn out to be an efficient tool to extract all at once temporally and spatially local phenomena. The results of the multiresolution analysis are finally used for developing a filter that makes it possible to extract an improved hydrological model, where we have to be aware of the fact that both a complete reconstruction of the data and an improvement of the correlation coefficients are mutually exclusive.

References

1. Chui C (1992) An introduction to wavelets, Academic Press, Boston, MA.
2. Döll P, Kaspar F, Lehner B (2003) A global hydrological model for deriving water availability indicators: Model tuning and validation. J. Hydrol. 270, 105–134.
3. Fengler M, Freeden W, Kohlhaas A et al. (2007) Wavelet modelling of regional and temporal variations of the Earth's gravitational potential observed by GRACE. J. Geod. 81, 5–15.
4. Freeden W (1999) Multiscale modelling of spaceborne geodata, Teubner, Stuttgart, Leipzig.
5. Freeden W, Michel V (2004) Multiscale potential theory (with application to the geoscience), Birkhäuser, Berlin.
6. Freeden W, Schneider F (1998) An integrated wavelet concept of physical geodesy. J. Geod. 72, 259–281.
7. Freeden W, Schreiner M (2009) Spherical functions of mathematical geosciences, Springer, Heidelberg.
8. Freeden W, Gervens T, Schreiner M (1998) Constructive approximation on the sphere (with application to geomathematics), Oxford Science Publication, Clarendon.
9. Louis AK, Maaß P, Rieder A (1998) Wavelets, Teubner, Stuttgart, Leipzig.
10. Mallat S, Hwang WL (1992) Singularity detection and processing with wavelets. IEEE Trans. Inf. Theory 38(2), 617–643.

11. Mallat S, Zhong S (1992) Characterization of signals from multiscale edges. IEEE Trans. Pattern. Anal. Mach. Intell. 14(7), 710–732.
12. Nutz H, Wolf K (2008) Time-space multiscale analysis by use of tensor product wavelets and its application to hydrology and GRACE data. Stud. Geophys. Geod. 52, 321–339.
13. Swenson S, Wahr J (2006) Post-processing removal of correlated errors in GRACE data. Geophys. Res. Lett., doi: 10.1029/2004GL0119920.
14. Swenson S, Wahr J, Milly PC (2003) Estimated accuracies of regional water storage variations inferred from the gravity recovery and climate experiment (GRACE). Water Resour. Res., doi: 10.1029/2002WR001808.
15. Tapley BD, Bettadpur S, Ries JC et al. (2004a) GRACE measurements of mass variability in the earth system. Science 305, 503–505.
16. Tapley BD, Bettadpur S, Watkins MM et al. (2004b) The gravity recovery and climate experiment: Mission overview and early results. Geophys. Res. Lett., doi: 10.1029/2004GL019779.

Mass Variation Signals in GRACE Products and in Crustal Deformations from GPS: A Comparison

Martin Horwath, Axel Rülke, Mathias Fritsche, and Reinhard Dietrich

1 Introduction

Geophysical mass variations are reflected not only in variations of the gravity field which are sensed by GRACE but also in solid Earth deformations. In particular, load variations (e.g. due to the global hydrological cycle) induce an elastic deformation which can be modeled by the load Love number formalism. Such elastic deformations can be, in turn, observed by geodetic GPS observations. A cross-comparison with GRACE results and GPS results (cf. Davis et al., 2004; King et al., 2006; van Dam et al., 2007) may validate either technique and may finally contribute to the improvement of mass transport estimates. This article describes results from analyses following this strategy.

2 Crustal Deformation Time Series from GPS in a Consistent Reference Frame

With regards to GPS and other space geodetic techniques, site specific time series of residual crustal deformations are in general considered as displacements w.r.t. an a priori defined reference network geometry. Here, we make use of homogeneous results from a reprocessing of a global GPS network (Steigenberger et al., 2006) in order to realize a terrestrial reference system in a consistent way including station coordinates and velocities and low-degree spherical harmonics for surface load variations as well (Rülke et al., 2008). Given the corresponding frame, a reference network geometry can be derived for any arbitrary epoch by propagating the solved for site coordinates and velocities as well the low-degree deformation terms. Daily global GPS network solutions are then compared according to that reference on the basis of a 6-parameter similarity transformation (3 translations, 3 rotations). For each individual site, transformation residuals together with the deformation

M. Horwath (✉)
Institut für Planetare Geodäsie, Technische Universität Dresden, 01219 Dresden, Germany
e-mail: martin.horwath@legos.obs-mip.fr

F. Flechtner et al. (eds.), *System Earth via Geodetic-Geophysical Space Techniques*, Advanced Technologies in Earth Sciences, DOI 10.1007/978-3-642-10228-8_34,

time series converted from the low-degree harmonics compose the overall crustal deformation time series represented by GPS.

3 Comparison of Low-Degree Deformations from GPS and GRACE

Reprocessed GPS observations are used to directly infer spherical harmonics for surface loads (see Sect. 2). Unlike GPS, related degree-1 terms cannot be derived from GRACE only measurements as the origin of the underlying reference system coincides with the center of mass of the Earth system, i.e. CM. But higher degrees of loading are captured by both techniques. Exemplarily, Fig. 1 shows changes in C_20 obtained from the global GPS reanalysis and from GRACE (GFZ Release 04) where background fields (see Sect. 4.1) were re-added to the GRACE solution so that both the GPS and the GRACE curve show estimates of the full non-tidal variations. In this case, we find good agreement between the completely independent and complementary results.

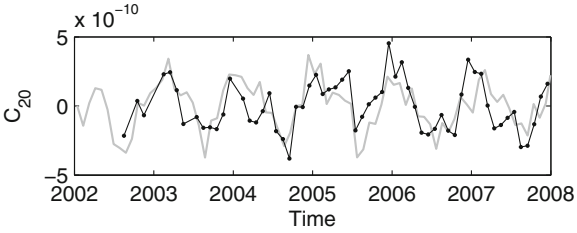

Fig. 1 Changes in C_20 obtained from the global GPS reanalysis (*gray line*) and from GRACE (GFZ Release 04, *black line*)

4 Comparison of Point-Wise Deformation Time Series

4.1 Daily GPS Versus Geophysical Models

In order to validate the GRACE background models (given in high temporal resolution), daily surface mass variations according to these models were converted to crustal load deformation time series (using the load Love number theory) and compared to daily deformation time series from GPS. The background models include the atmospheric and oceanic models routinely applied in GRACE processing and, in addition, the WGHM hydrology model (Döll et al., 2003) which was experimentally applied as a background model within the TIVAGAM project. Degree-one deformations which are present in either datasets were included using the 'Center of Figure' reference frame.

Figure 2 (left) illustrates the comparison in the vertical dimension for sample stations on all continents and on Greenland for the year 2003. Generally, the GPS time series show larger day-to-day variations. This predominantly reflects noise in

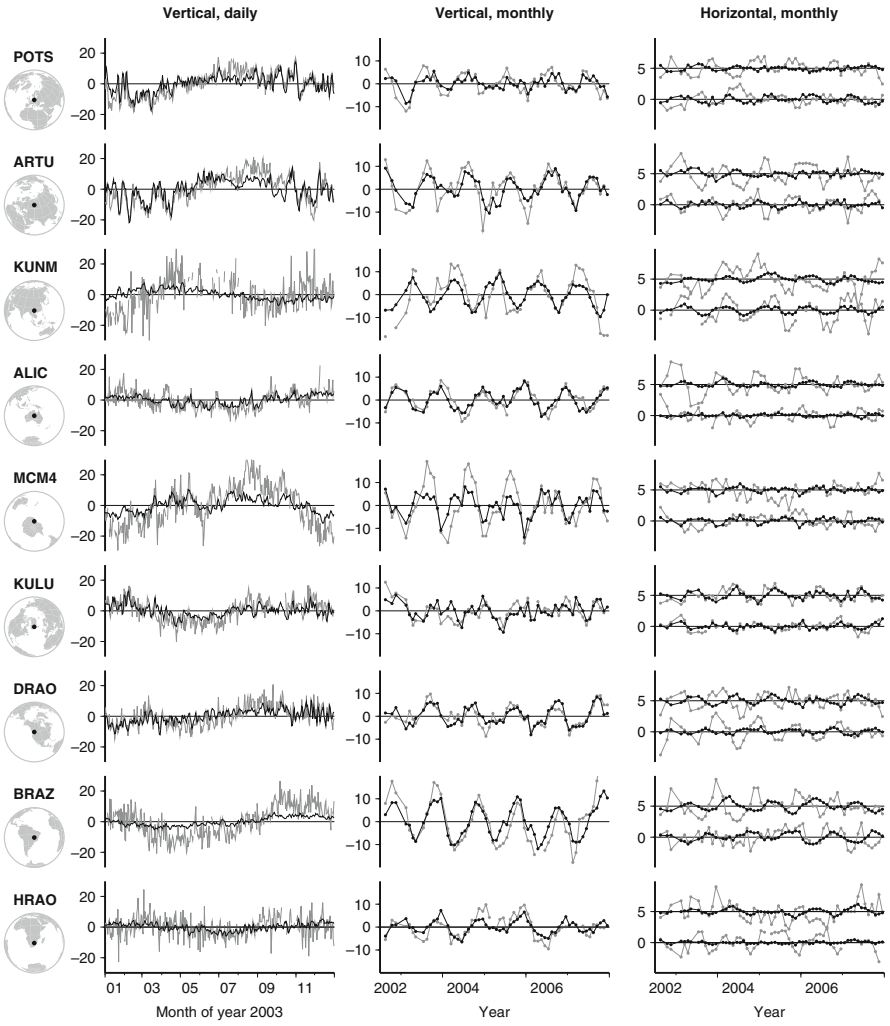

Fig. 2 Comparisons of station-wise nonlinear crustal deformations (mm) from GPS (*gray*) and from computed load deformations according to models and GRACE results (*black*). The considered GPS sites are indicated in the far left. *Left*: Daily vertical deformations in 2003. *Black curves* show GRACE background model results. *Center*: monthly vertical deformations over the GRACE period. *Black curves* show GRACE results. *Right*: Same as in the center, but for the North and East components. North components are shifted by +5 mm

the daily GPS time series. On a time scale from days to weeks where the modeled variations are dominated by atmospheric mass variations, there are remarkable agreements between both types of observations: see, e.g., the POTS and ARTU sites. This shows that the GPS vertical deformations well reflect geophysical load effects. On an annual scale, there is a clear correlation in the behavior of either time series

but the differences are also considerable, most remarkably at the BRAZ site. Errors of the hydrology model, local effects, and systematic effects in the GPS time series (see Sect. 5) are possible causes of such differences.

4.2 Monthly GPS Versus Grace

Monthly averages of GPS site displacements were compared to modeled deformations according to the GRACE monthly solutions. Here, the GRACE monthly solutions had to be filtered to dampen high-degree error effects. To avoid smoothing of hydrological signals, the WGHM hydrology model was removed before smoothing and restored afterwards. Also, the atmospheric and oceanic background models were re-added. Since degree-one components are not given by the GRACE solutions, those components were also excluded from the GPS deformations.

Figure 2 (center) illustrates the respective comparisons for the vertical component. There is a clear resemblance between GPS and GRACE at all shown sites. At the same time, significant differences remain.

For a more quantitative comparison, statistical parameters were computed: the standard deviations (STDs) of the GPS and GRACE time series as well as of their difference, σ_{GPS},σ_{GRACE} and σ_{Diff}; the correlation coefficients between GPS and GRACE; and the percentage of GPS variance explained by the GRACE time series, $(\sigma^2_{\mathrm{GPS}} - \sigma^2_{\mathrm{Diff}})/\sigma^2_{\mathrm{GPS}}$. These parameters are shown globally for every involved station in Fig. 3. The GPS variability is typically higher than the GRACE variability (Fig. 3a). This is true for almost all continental sites and is particularly pronounced for sites on small ocean islands where the geophysical signal ought to be small due to the inverse barometric compensation of atmospheric pressure variations and due to the smallness of land hydrology domains. Also, the GPS-GRACE differences are far larger than the expected error in the GRACE-derived time series (Fig. 3b).

Nonetheless, the GPS-GRACE agreement is good for most of the continental sites. There, the correlation (Fig. 3c) is typically between 50 and 80% and the percentage of explained GPS variance (Fig. 3d) is typically between 20 and 60%.

For horizontal components, examples of time series comparisons are shown in Fig. 3 (right). The GPS variability is far larger than the GRACE variability. Apart from a few exception (including KULU), there is hardly any similarity between the two kinds of time series.

5 Systematics in GPS-GRACE Discrepancies

To further illuminate the nature of the GPS-GRACE discrepancies, a principal component analysis (PCA) of these discrepancies was performed in selected regions. Here, we concentrate on the results for the analysis of the horizontal components. Figure 4 shows the PCA results for a European, an Australian and a North American sub-network. The first empirical orthogonal functions (EOFs) are almost uniform

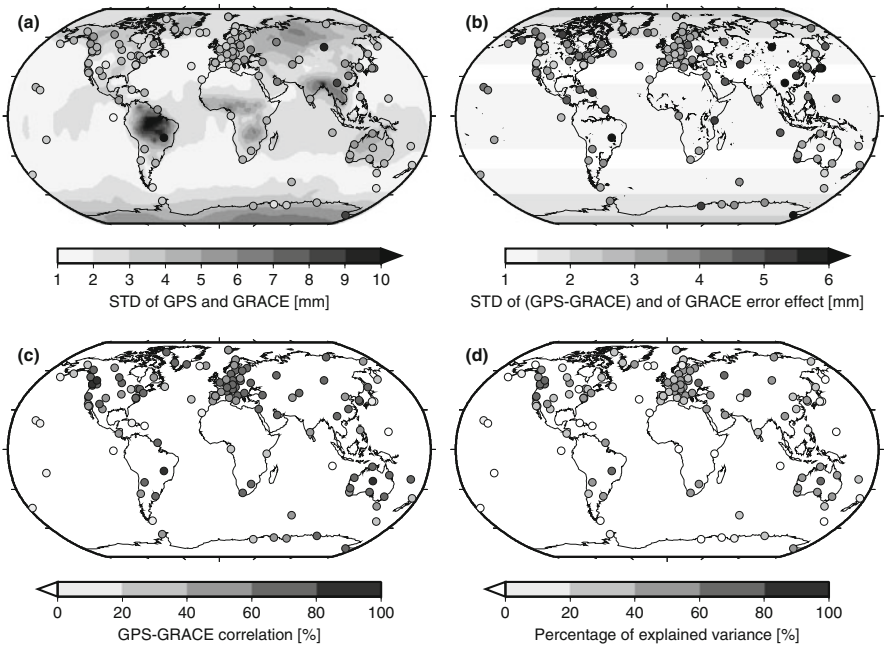

Fig. 3 Statistical parameters for the comparison of GPS and GRACE vertical deformation time series. (**a**) STDs of the GPS signal (*circles*) and the GRACE signal (background image). (**b**) STDs of the GRACE-GPS discrepancy (*circles*) and an assessment of GRACE error effects (background image) following the approach of Horwath and Dietrich (2006). (**c**) Correlation between GPS and GRACE. (**d**) Percentage of GPS signal variance explained by the GRACE signal

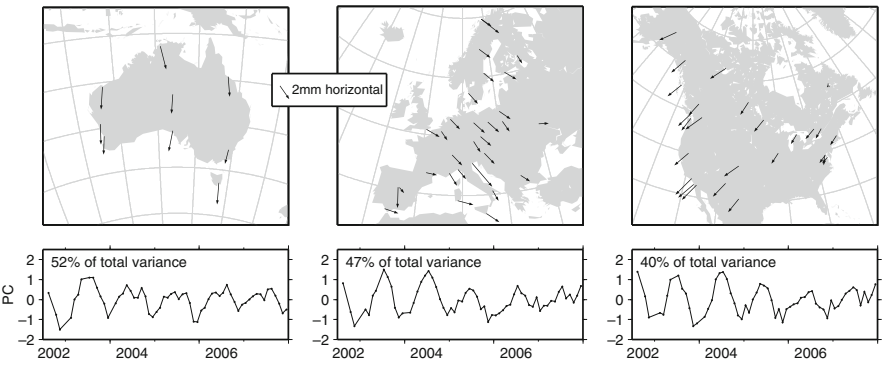

Fig. 4 Results of a principal component analysis of the horizontal GPS-GRACE discrepancies performed for regional sub-networks. The maps show the patterns of the first EOFs, the time series show the corresponding PCs. That is, multiplying the time series with the mapped patterns yields variations that make up 52, 47 and 40%, respectively, of the total variance of GPS-GRACE discrepancies

displacements of almost all involved sites. These patterns are responsible for about 50% of the variance of the GPS-GRACE discrepancies. The respective principal components (PCs) contain a large seasonal signal without being purely seasonal. The next EOFs (not shown) also contain spatially coherent patterns. In conclusion, the GPS-GRACE discrepancies are dominated by variations that are correlated over large distances.

At the moment, we address these remaining discrepancies to be caused by a remaining systematic GPS mismodeling. In fact, there are a number of possible aspects in the modeling of GPS observations such as solar radiation pressure or Earth albedo that are suitable to induce common large scale residual pattern.

6 Regionalized Comparison Studies

As a way to circumvent the systematic errors apparently present in the GPS time series we want to consider regional networks and remove their common displacements since, according to our previous analyses, we suspect systematic errors to dominate these common displacements in the GPS results. We thus aim at isolating the internal deformations of regional networks.

We choose the following realization of this general approach: For every month we perform a Helmert transformation of the monthly network geometry onto the mean network geometry. We set up four transformation parameters with respect to geocentric coordinates: three rotations and one scale parameter. By not allowing for translations, we effectively estimate independent 'shifts' in the horizontal and in the vertical directions. We then consider the residuals of the Helmert transform as the internal deformations of the regional network. We perform this procedure equally for the GPS and for the GRACE time series.

Figure 5 illustrates the procedure for the example of the Australian regional cluster. For two selected sites, the coordinate time series from the global analysis

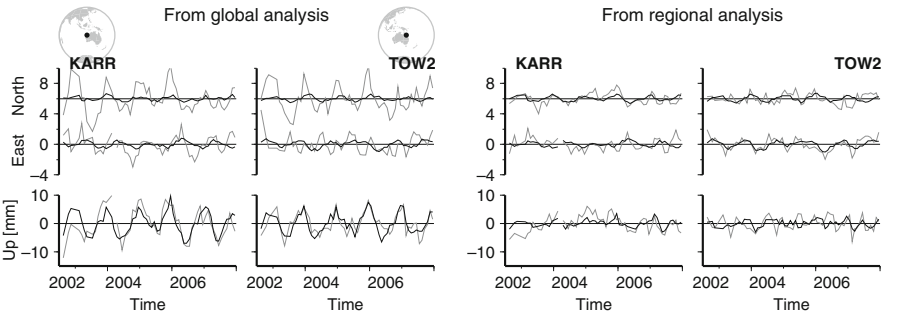

Fig. 5 Illustration of the regionalization approach outlined in Sect. 6. *Left half*: Horizontal and vertical deformation time series (mm) from GPS (*gray*) and GRACE (*black*) for two Australian sites. *Right*: The same kind of time series after regionalization

(shown in the left half of the figure) show relatively large GPS-GRACE discrepancies in the horizontal directions which are similar for both sites. The right half of the figure shows the regionalized deformation time series. For the horizontal directions, much of the presumably spurious GPS variations is reduced by the Helmert transform and the remaining variations better resemble the GRACE variations. These GRACE variations are also changed by the regionalization, but not much, because the dominant horizontal signal of the GRACE time series is a contraction and dilatation of the whole network due to continental load changes and this signal is not absorbed by the Helmert transform. For the vertical component, the regionalization reduces the (absolute) differences between the GPS and GRACE time series but it also dramatically reduces the presumable signal in both time series. This is because the dominant geophysical signal in the vertical is a unidirectional upward and downward displacement which is well absorbed by the Helmert transform.

Figure 6 shows statistical parameters of the GPS-GRACE comparison per site as in Fig. 3c and d but now for horizontal time series in six regions, converted following our regionalization approach. Table 1 shows the mean values of these parameters for each of the six regions. The GPS-GRACE resemblance after regionalization is still weak but was, nevertheless, considerably improved by the regionalization.

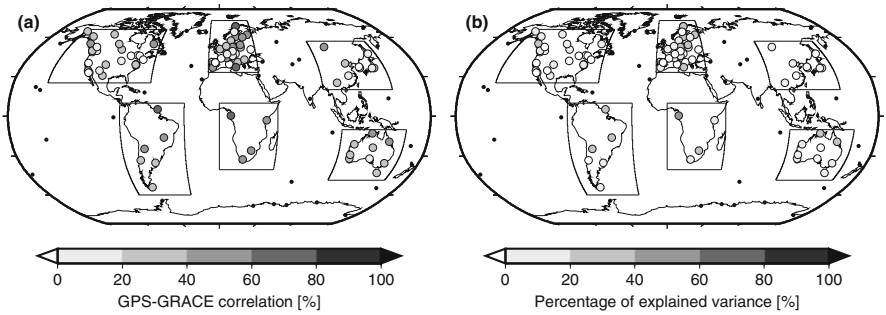

Fig. 6 Statistical parameters as in Fig. 3c, d, but now for the horizontal components after regionalization in the outlined six regional sub-networks

Table 1 Regional mean values of the statistical parameters shown in Fig. 6. In parentheses, the respective values before regionalization are shown

Region	Correlation (%)	Percentage of explained variance (%)
North America	17 (8)	0 (–4)
Europe	24 (–4)	5 (–21)
Asia	22 (15)	5 (2)
South America	46 (23)	17 (3)
Africa	51 (39)	26 (17)
Australia	38 (11)	14 (–1)

7 Conclusions

GRACE and GPS are complementary 'sensors' for surface mass variations. A comparison between both shows encouraging results. In the vertical dimension, there is typically good agreement between GPS observations and modeled deformations from GRACE-derived mass variations. This can be seen as a progress compared to previous studies using standard GPS products (e.g., van Dam et al., 2007). The remaining discrepancies, however, by far exceed expected errors in the GRACE-derived deformations. This is even more evident in the horizontal dimensions.

A likely cause of these discrepancies lies in remaining systematic errors in the GPS solution. The problem of systematic differences can be partly circumvented by analyses of internal deformations of regional subnetwork.

The work illustrates that there remain large challenges in consistently combining different space geodetic techniques into one Global Geodetic Observing System (Drewes, 2005).

References

Davis JL, Elosegui P, Mitrovica JX, Tamisiea ME (2004) Climate-driven deformation of the solid Earth from GRACE and GPS. Geophys. Res. Lett. 31, L24605, doi:10.1029/2004GL021435.

Döll P, Kaspar F, Lehner B et al. (2003) A global hydrological model for deriving water availability indicators: model tuning and validation. J. Hydrol. 270, 105–134.

Drewes H (2005) Science rationale of the global geodetic observing system (GGOS). In: Tregoning P, Rizos C (eds.), Dynamic Planet: Monitoring and Understanding a Dynamic Planet with Geodetic and Oceanographic Tools, Vol. 130 of IAG Symposia, Springer, Berlin, pp. 703–710.

Horwath M, Dietrich R (2006) Errors of regional mass variations inferred from GRACE monthly solutions. Geophys. Res. Lett. 33, L07502, doi:10.1029/2005GL025550.

King M, Moore P, Clarke P, Lavallée D (2006) Choice of optimal averaging radii for temporal GRACE gravity solutions, a comparison with GPS and satellite altimetry. Geophys. J. Int. 166(1), 1–11, doi:10.1111/j.1365-246X.2006.03017.x.

Rülke A, Dietrich R, Fritsche M, Rothacher M, Steigenberger P (2008) Realization of the Terrestrial Reference System by a reprocessed global GPS network. J. Geophys. Res. 113, B08403, doi:10.1029/2007JB005231.

Steigenberger P, Rothacher M, Dietrich R, Fritsche M, Rülke A, Vey S (2006) Reprocessing of a global GPS network. J. Geophys. Res. 111, B05402, doi:10.1029/2005JB0037472.

van Dam T, Wahr J, Lavallée D (2007) A comparison of annual vertical crustal displacements from GPS and Gravity Recovery and Climate Experiment (GRACE) over Europe. J. Geophys. Res. 112, B03404, doi:10.1029/2006JB004335.

Monthly and Daily Variations of Continental Water Storage and Flows

Kristina Fiedler and Petra Döll

1 Introduction

Continental water storage is an essential part of the global water cycle, being particularly important for the existence of many ecosystems and for the satisfaction of human demands, including water for agricultural, industrial and domestic use. Total continental water storage is the sum of water stored as snow and ice, in and on vegetation cover, in the unsaturated soil zone, in groundwater and surface waters like rivers, wetlands, lakes and reservoirs. Little is known about the spatial and temporal variability of water storage on a global scale although this information is important for understanding the global hydrological cycle. Direct estimations of storage change are often restricted to the point scale and to single components of total water storage, such as groundwater or lakes, due to the lack of an adequate monitoring network. With the GRACE satellite mission launched in 2002, estimates of the Earth's dynamic gravity field became available with unprecedented accuracy. Over land, the time variable gravity data mainly contain a hydrological signal representing continental water storage changes. In order to evaluate GRACE results, the state-of-the-art WaterGAP Global Hydrological Model (WGHM) was applied to calculate monthly continental water storage changes on a global scale during the period for which GRACE data were available. Simulated daily water storage values were intended to be used as a means to improve de-aliasing of GRACE data. To improve estimates of both water storage and river discharge, the representation of flow velocities and man-made reservoirs in WGHM was improved. Finally, a best estimate of continental water storage variations and water flows was derived.

K. Fiedler (✉)
Institute of Physical Geography, Goethe University Frankfurt am Main,
60438 Frankfurt am Main, Germany
e-mail: fiedler@em.uni-frankfurt.de

F. Flechtner et al. (eds.), *System Earth via Geodetic-Geophysical Space Techniques*,
Advanced Technologies in Earth Sciences, DOI 10.1007/978-3-642-10228-8_35,

2 Modelling of Global Continental Water Storage and Flows with WGHM

2.1 Model Overview

The WaterGAP global hydrological model (WGHM) has been developed at the Centre for Environmental Systems Research at the University of Kassel. Ongoing model development is done both in Kassel and at the University of Frankfurt. A detailed model description can be found in Döll et al. (2003). WGHM operates with an internal time step of one day and a spatial resolution of 0.5° lat/long. Calculations are based on spatially distributed physiographic characteristics and on time series of monthly climate data. A global database of lakes and wetlands is integrated to supply information on large surface water bodies. Anthropogenic water use is calculated externally: water needed for irrigation, industrial and domestic purposes is taken into account but it is assumed to be taken out of surface water bodies only. Within the model, total water storage is calculated as the sum of canopy, snow, soil and groundwater storage as well as water stored in surface water bodies (rivers, wetlands, lakes and reservoirs). A global-scale analysis of long-term average seasonal storage variations in the different compartments (for the climate normal 1961–1990) was performed by Güntner et al. (2007).

2.2 Improved Representation of Lateral Flows

In order to improve the representation of river discharge and terrestrial water storage changes in WGHM, the globally constant river flow velocity was changed to a dynamic approach and a new reservoir algorithm was introduced.

2.2.1 Variable Flow Velocity

In the standard version of WGHM, river flow velocity is set constant at 1 m/s for the whole globe. Following the work of Schulze et al. (2005), a new algorithm to calculate the flow velocity as a function of slope and discharge was applied, using the Manning-Strickler-Formula

$$v = n^{-1} \cdot R^{2/3} \cdot S^{1/3} \tag{1}$$

where v is flow velocity (m/s), n is river bed roughness (–), R is the hydraulic radius and S is river slope (m/m). The slope is derived using elevation data from the GTOPO30 global digital elevation model with a horizontal grid spacing of 30 arc seconds (approximately 1 km). The hydraulic radius is calculated based on river width (W) and depth (D). Because information on W and D is not available on a global scale, these values are estimated as a function of discharge according to Allen et al. (1994). River bed roughness is not directly measurable and varies on a very small scale. Based on data listed by Mays (1996), a global value of 0.04 is applied. Ongoing work will focus on a spatially distributed roughness value as

an input parameter depending on vegetation, land cover type, elevation, degree of industrialization etc.

2.2.2 Reservoir Algorithm

For 487 reservoirs with a total storage capacity of about 4,000 km^3, a reservoir operation algorithm was integrated into WGHM based on the approach of Hanasaki et al. (2006). Information on reservoir type (irrigation or non-irrigation), surface area and storage capacity was taken from the Global Lakes and Wetlands Database (GLWD) (Lehner and Döll, 2004). The algorithm requires the definition of a reservoir-specific operational year. The start of the operational year is defined as the first month of a release period when the mean monthly inflow into the reservoir is smaller than the mean annual inflow. Mean values for monthly and annual inflow were generated from a previous model run covering the period 1961–1990 and not taking reservoir operations into account.

At the beginning of an operational year, the *annual* total release R_y for the following year is estimated based on actual water storage and mean annual inflow:

$$R_y = \frac{S_{\text{first}}}{\alpha \cdot C} \cdot I_{\text{mean}} \tag{2}$$

where S_{first} is the storage at the beginning of the operational year, α is a constant parameter set to 0.85, C is the storage capacity and I_{mean} is the long-term average annual inflow. For large non-irrigation reservoirs, *monthly* releases are assumed to be constant during the operational year. For large irrigation reservoirs, the water demand in the downstream area (calculated as the sum of industrial, domestic, livestock and irrigation water use in a maximum distance of 5 cells downstream of the reservoir) is also taken into account. Monthly fluctuations in reservoir release occur if there is a seasonal distribution of water demand. In the case of small non-irrigation and irrigation reservoirs, monthly release is assumed to be influenced, additionally by monthly inflows, such that overflow and storage depletion are minimized. If monthly inflow exceeds storage capacity, overflow is generated.

2.3 Climate Input Data

For the period 1901–2002, WGHM is generally driven by monthly climate data from the Climate Research Unit (CRU). The CRU TS 2.1 data set provides gridded data for several climate variables like precipitation, number of rain days, temperature and cloudiness from 1901 to 2002 with a spatial resolution of 0.5° (covering the global land surface). This dataset is based on station observations and uses anomaly analysis for the spatial interpolation (Mitchell and Jones, 2005; New et al., 1999, 2000). For precipitation, another global data set was used. The Global Precipitation Climatology Centre (GPCC) provides a gridded monthly precipitation product for the global land surface which is available from 1951 to 2004 with a spatial resolution of 0.5° (Full Data Set Version 3, Rudolf and Schneider, 2005). It is based on a larger

number of station observations than the CRU data and covers the time period of the first GRACE results. For the years 2005–2007, the so-called GPCC Monitoring Product was used, which is based on a smaller number of station observations with a less intensive data processing. To run the model for the GRACE period 2002–2007, monthly temperature and cloudiness data from the ECMWF operational forecast system were used as model input. In the standard version of WGHM, monthly precipitation is distributed equally over the number of rain days within one month. For the GRACE period, daily precipitation data from ECMWF were scaled with GPCC monthly precipitation totals to create a daily precipitation dataset to be used as model input. Scaling numerical weather forecast data against observations is supposed to improve the quality of the daily data product since forecast data are highly uncertain especially with regard to precipitation intensity and peak values.

The above mentioned monthly precipitation data are not corrected for measurement errors; precipitation, in particular snow, is generally underestimated due to mainly wind induced undercatch. As this has a strong influence on simulated snow water storage, precipitation was corrected using mean monthly catch ratios from Adam and Lettenmaier (2003) and taking actual monthly temperatures into account (see Döll and Fiedler, 2008, for details).

3 Results

3.1 Impact of Dynamic Flow Velocity Algorithm on River Discharge and Storage

The flow velocity is a very sensitive parameter for the calculation of both river discharge and water storage variations. To investigate the effect of using a dynamic flow velocity approach instead of a constant global value, different model runs were carried out. Here, the Amazon basin is chosen as an example. Using a constant flow velocity of 1 m/s within the model and thus representing the standard model version, seasonal water storage variations are underestimated when compared to GRACE observations (Fig. 1). Furthermore, there is a time shift of one to two months between the modelled and observed river discharge as well as between calculated water storage change and GRACE observations. In reality, the flow regime in the Amazon basin is strongly influenced by seasonal flooding of floodplains which delays discharge peaks. However, seasonal flooding is currently only modelled in a very simple way within WGHM, and is probably underestimated. If the constant flow velocity is lowered to 0.3 m/s, the time lags of modelled river discharge and water storage change in the Amazon basin are much improved. For water storage variations, the model values are significantly increased by up to 100% and are in good correlation with GRACE amplitudes (Fig. 1).

Using the dynamic flow velocity algorithm with a roughness value of 0.04 shows very similar results to the standard model version because the applied formula leads to a comparable mean flow velocity value. However, increasing roughness to a value

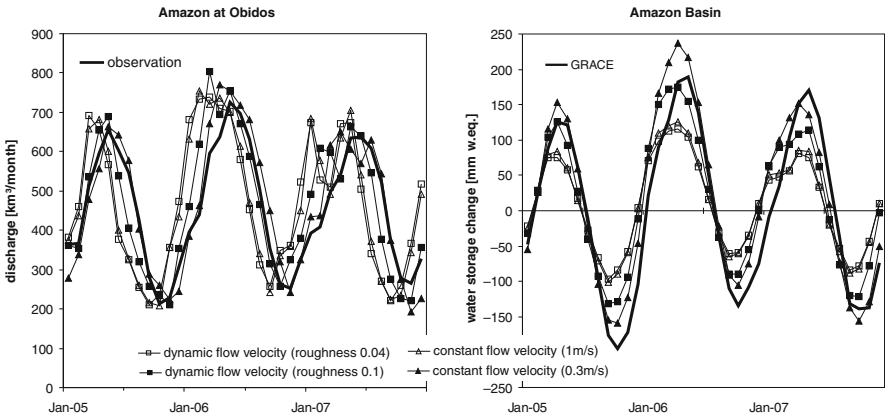

Fig. 1 River discharge and water storage change calculated with WGHM for the Amazon Basin showing the impact of different flow velocity algorithms

of 0.1 and thus decreasing the calculated flow velocity leads to a significant improvement with respect to the timing of river discharge and water storage peaks and the absolute values of water storage change for the Amazon basin. This may not be the case for other basins with a typically higher flow velocity. Since river bed roughness is a very sensitive parameter for the calculation of flow velocities, a spatially distributed value should be applied in the future.

3.2 Impact of Reservoir Algorithm on River Discharge and Storage

In order to estimate the influence of the new reservoir algorithm on modelled water storage variations and river discharge, several model runs were carried out: two *anthropogenic* model runs taking water use into account and modelling reservoirs as reservoirs (ANT) or reservoirs as lakes (ANT-LAKE), without reservoirs but still considering water use (USE) and a naturalized flow run (NAT) without reservoirs and use. For selected large river basins (like Colorado, Columbia, Volga, Ganges and Mississippi, with significant water use and/or reservoirs) both the total water storage as well as the partitioning of water storage among the different compartments (snow, soil, groundwater, surface water) differ between model runs. However, monthly variations in total water storage do not change significantly.

River discharge in the above five basins, however, is affected significantly by reservoirs and water use. The Colorado and the Columbia River are chosen here as examples: eight reservoirs in the Colorado River Basin representing a total storage capacity of 80 km^3 and 16 reservoirs in the Columbia River Basin with 73 km^3 storage volume are actually included within the reservoir algorithm.

Figure 2 showsthe results of different model runs for the long term mean period 1961–1990. Including reservoir operations strongly improves the mean monthly

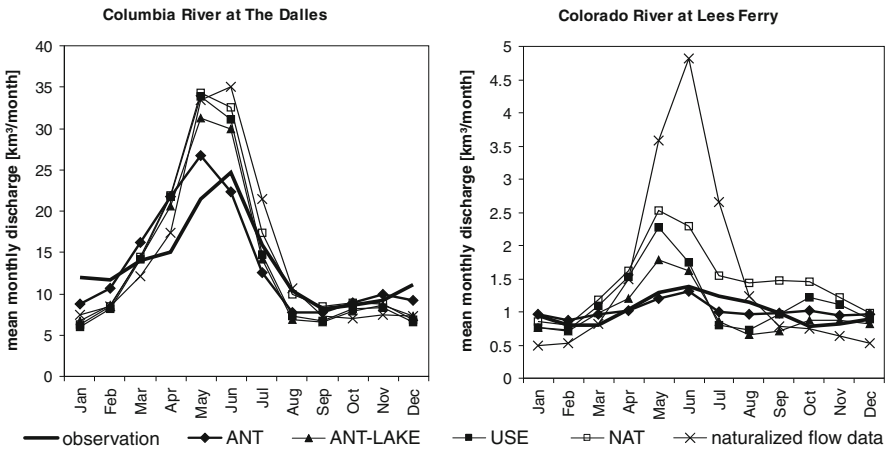

Fig. 2 Mean monthly discharge (1961–1990) for Columbia and upper Colorado River using different model versions of WaterGAP to show the impact of reservoir operation and water use (* naturalized flow data for Columbia River based on Haddeland et al., 2006, representing mean over 1980–1990)

river discharge when compared to observations. The root mean squared error (RMSE) decreased from 4.3 (ANT-LAKE) to 3.1 (ANT) for the Columbia River and from 0.27 (ANT-LAKE) to 0.13 (ANT) for the upper Colorado River. The annual peak decreased and the seasonal flow regime changed due to reservoir operations showing the typical behaviour of reservoirs used for hydropower generation with an increase of winter flows and a decrease of spring flood. Without reservoirs (USE), the seasonal flow pattern changes because discharge seasonality is not dampened by large surface water bodies, and because evaporation also decreases. The naturalized flow (NAT) shows the highest discharge volumes and seasonality as there is also no human water use in this run.

Independent estimates of naturalized flow data are available for both basins. For Columbia River at The Dalles, the agreement between modelled naturalized flow values (NAT) and independent estimates (Haddeland et al., 2006) is quite good. Naturalized flow data for Colorado River at Lees Ferry from USBR (US Department of the Interior – Bureau of Reclamation) differ significantly from the modelled naturalized flow with a peak difference of about 100%, but the model still manages to capture a large amount of the damping effects of reservoirs (and water use) on river discharge.

3.3 Daily Variations of Water Storage

Since the internal time step of WGHM is one day, global continental water storage change can also be calculated on a daily basis. It is, however, a common phenomenon that climate or weather model data like those from ECMWF underestimate

daily precipitation variability. There are too many wet days with a very low amount of precipitation, and precipitation peaks are underestimated. This is one of the reasons why simulated daily values of water storage and discharge are so unreliable that they should not be considered further for hydrological analyses at continental and global scales. However, it is meaningful to investigate which effect the computed pattern of daily storage variations has on GRACE signal processing (Han et al., 2004).

A clear aliasing effect of sub-monthly hydrological mass variations that leads to errors in the computed monthly gravity anomalies was detected. However, this effect is small compared to other effects influencing the total GRACE error like ocean tides or short term mass variations from the atmosphere and oceans. In addition, daily water storage variations may still be underestimated by WGHM due to the climate input data used. Furthermore, sub-daily variations which are larger than daily variations at least for small spatial scales are not taken into account by WGHM. Since the use of daily water storage variations for de-aliasing did not lead to a significant improvement of GRACE data processing, daily model results of water storage variations were not further investigated.

4 Best Estimate of Continental Water Storage and Flows

The standard model version of WGHM is calibrated against long-term average river discharge at 1,235 observation stations (i.e. 1,235 drainage basins) world-wide with the runoff coefficient γ as a calibration parameter. It determines how much of the effective precipitation is transformed into runoff, depending on the degree of soil water saturation. Additionally, two tuning factors are applied if γ cannot be adjusted within a predefined range (see Hunger and Döll, 2008, for details).

Another approach is the multi-objective calibration against monthly time series of river discharge *and* GRACE continental water storage for the world's 29 largest river basins. For each river basin, the most sensitive six model parameters were identified and then calibrated using a global optimization method (Werth et al., 2009).

To obtain a best global-scale estimate of continental water storages and flows, both approaches are combined. For all grid cells within the 29 largest river basins, the parameter values of the standard model version are replaced by the values determined by multi-objective calibration.

5 Conclusions

In this study, monthly and daily variations of continental water storage and river discharge were calculated with the WaterGAP global hydrological model (WGHM). Daily water storage variations were calculated to improve de-aliasing of GRACE data. However, using these data for de-aliasing did not lead to a significant improvement of GRACE data processing.

New algorithms were added to obtain improvements with respect to modelled monthly water storage and discharge values. The integration of a new reservoir operation scheme significantly improved model results. Reservoir storages and river discharge in basins with large reservoirs showed a better agreement with observations but the effect on total water storage variations was very small. With the new algorithm, WGHM can now simulate the impact of reservoirs and water use from surface water bodies on river discharge in a more realistic way.

Applying a dynamic flow velocity instead of a constant global value showed reasonable results and revealed the sensitivity of the approach to the river bed roughness parameter. It also became obvious that an improved algorithm for floodplain water storage modelling is required in some basins like the Amazon, and preferable to a mere parameter tuning (like velocity or river bed roughness). A first analysis of the results of the multi-objective calibration by Werth et al. (2009) showed that a good fit to GRACE observations and river discharge by adjusting the six most sensitive WGHM parameters is not possible in all river basins (e.g. Murray, St. Lawrence, Nelson and Niger). This indicates that structural changes of the model or improved input data and observations are necessary.

Future work will focus on investigating the reasons for discrepancies between WGHM results on the one hand and GRACE observations and observed discharge on the other hand. Next steps in model development will include the implementation of spatially distributed roughness values as input parameters for the dynamic flow velocity approach. Furthermore, the data base for reservoirs included in the reservoir operation algorithm will be regularly revised.

References

Adam JC, Lettenmaier DP (2003) Adjustment of global gridded precipitation for systematic bias. J. Geophys. Res. Atmos., doi: 10.1029/2002JD002499.

Allen PM, Arnold JG, Byars BW (1994) Downstream channel geometry for use in planning-level models. Water Resour. Bull. 30, 663–671.

Döll P, Fiedler K (2008) Global-scale modeling of groundwater recharge. Hydrol. Earth Syst. Sci. 12, 863–885.

Döll P, Kaspar F, Lehner B (2003) A global hydrological model for deriving water availability indicators: Model tuning and validation. J. Hydrol. 270(1–2), 105–134.

Güntner A, Stuck J, Werth S, Döll P, Verzano K, Merz B (2007) A global analysis of temporal and spatial variations in continental water storage. Water Resour. Res., doi: 10.1029/2006WR005247.

Haddeland I, Skaugen T, Lettenmaier DP (2006) Anthropogenic impacts on continental surface water fluxes. Geophys. Res. Lett., doi: 10.1029/2006GL026047.

Han SC, Jekeli C, Shum CK (2004) Time-variable aliasing effects of ocean tides, atmosphere, and continental water mass on monthly mean GRACE gravity field. J. Geophys. Res. Solid Earth, doi: 10.1029/2003JB002501.

Hanasaki N, Kanae S, Oki T (2006) A reservoir operation scheme for global river routing models. J. Hydrol. 327, 22–41.

Hunger M, Döll P (2008) Value of river discharge data for global-scale hydrological modeling. Hydrol. Earth Syst. Sci. 12, 841–861.

Lehner B, Döll P (2004) Development and validation of a global database of lakes, reservoirs and wetlands. J. Hydrol. 296, 1–22.

Mays LW (1996) Water Resources Handbook, McGraw-Hill, New York.
Mitchell TD, Jones PD (2005) An improved method of constructing a database of monthly climate observations and associated high-resolution grids. Int. J. Climatol. 25, 693–712.
New M, Hulme M, Jones P (1999) Representing twentieth-century space-time climate variability. Part I: Development of a 1961–90 mean monthly terrestrial climatology. J. Clim. 12, 829–856.
New M, Hulme M, Jones P (2000) Representing twentieth-century space-time climate variability. Part II: Development of 1901–96 monthly grids of terrestrial surface climate. J. Clim. 13, 2217–2238.
Rudolf B, Schneider U (2005) Calculation of gridded precipitation data for the global land-surface using in-situ gauge observations, Proceedings of the 2nd Workshop of the International Precipitation Working Group IPWG, Monterey October 2004.
Schulze K, Hunger M, Döll P (2005) Simulating river flow velocity on global scale. ADGEO 5, 133–136.
Werth S, Güntner A, Petrovic S, Schmidt R (2009) Integration of GRACE mass variations into a global hydrological model. Earth Planet Sci. Lett. 277, 166–173.

Calibration of a Global Hydrological Model with GRACE Data

Susanna Werth and Andreas Güntner

1 Introduction

Since 2002, the US-German satellite gravity mission GRACE (Gravity Recovery and Climate Experiment) monitors the Earth's gravity field and traces mass redistributions close to the Earth's surface (Reigber et al., 2005; Tapley et al., 2004). Time series of global maps of surface mass anomalies are derived from monthly GRACE gravity fields represented by coefficients of a spherical harmonic representation. Due to the global coverage and the previously unrivaled accuracy, GRACE derived mass variations give insight into processes of the Earth's subsystems. After removal of mass variations due to tides and non-tidal atmospheric and oceanic transport processes, GRACE time-variable gravity data mainly represent water mass variations on and beneath the land surface, i.e., total continental water storage change (TWSC) (see a recent overview by Schmidt et al., 2008a). Therefore, GRACE data are widely used to improve understanding and modeling of the Earth's water cycle through the observation of hydrological mass changes on the continents. For example, previous studies analyzed the contribution of TWSC to sea level variations (Ramillien et al., 2008) and the impact of climate variability or extremes on water storage (e.g. Andersen et al., 2005) or they considered components of the continental water cycle (evapotranspiration by Ramillien et al., 2006; runoff by Syed et al., 2007; groundwater in Rodell et al., 2007; snow in Frappart et al., 2006). Other studies applied TWSC data from GRACE to validate large-scale hydrological models (for a recent overview see Güntner, 2008). For example, a good general correspondence to GRACE was found for the WaterGAP Global Hydrology Model (WGHM), though seasonal TWSC signal amplitudes tend to be smaller in WGHM than in GRACE (e.g., Schmidt et al., 2006).

Beyond the mere comparison, a new challenge in hydrological modeling is model improvement by the full integration of GRACE data into the modeling process.

S. Werth (✉)
Helmholtz Centre Potsdam GFZ German Research Centre for Geosciences,
14473 Potsdam, Germany
e-mail: swerth@gfz-potsdam.de

F. Flechtner et al. (eds.), *System Earth via Geodetic-Geophysical Space Techniques*,
Advanced Technologies in Earth Sciences, DOI 10.1007/978-3-642-10228-8_36,

Güntner (2008) recently exposed some of the conditions to be met for a successful combination strategy. As first examples, Zaitchik et al. (2008) assimilated GRACE TWSC into a land surface model for the Mississippi river basin and Werth et al. (2009a use GRACE data to calibrate the global hydrological model WGHM.

In this study, we present the fundamental steps to be performed for the calibration of the global hydrological model WGHM (Sect. 2.1) using GRACE TWSC estimations and river discharge data. These steps comprise the selection of adequate calibration parameters (Sect. 2.2), the derivation of GRACE time series at the scale of river basins with an optimized error budget (Sect. 2.3) and the multi-criteria calibration approach (Sect. 2.4). Finally, results of the calibration are presented and analyzed, also with respect to identifying of possible structural model errors (Sect. 3).

2 Methods

2.1 Hydrological Model

The WaterGAP Global Hydrology Model (WGHM, Döll et al., 2003) is a conceptual global water balance model that simulates the continental water cycle with a daily time-step and a spatial resolution of 0.5°, excluding the regions of Antarctica and Greenland. Water storage compartments represented in WGHM include canopy, soil water, snow, groundwater and surface water bodies. In this study, WGHM is forced by monthly climate data such as air temperature and cloudiness of ECMWF (European Center for Medium-Range Weather Forecast) and precipitation data of GPCC (Global Precipitation Climatology Center). Disaggregation of climate data to the daily modeling time step is done within the model by simple rules. The basic model version used in this study was calibrated (i.e. tuned) by adjusting a runoff coefficient parameter against observed river discharge at 1,235 gauging stations worldwide (Hunger and Döll, 2008). A detailed analysis of spatio-temporal variations of water storage as simulated with WGHM was given by Güntner et al. (2007).

2.2 Parameter Sensitivity Analysis

The conceptual equations of WGHM comprise around 30 different parameters that belong to different hydrological storage and flow processes. In the original model version, only the runoff parameter was tuned to long-term annual averages of observed river discharge. All other parameters were fixed to physical or empirical values (Döll et al., 2003). In this calibration study, TWSC as an additional observable is used besides river discharge to constrain the simulation results and to tune additional model parameters. Especially water storage processes that are dominant in a certain river basin are to be considered and respective parameters to be calibrated. For example, snowfall is negligible in the Amazon basin whereas

surface water transport is of high importance. In order to select adequate calibration parameters, a parameter sensitivity analysis for both river discharge and TWSC was undertaken for WGHM. 2,000 parameter sets were generated with Latin-Hypercube sampling procedure and the model was run with each parameter set. By analyzing the impact of each parameter to the model output, process and parameter sensitivities were found to vary with the region. For example, parameters governing surface water transport and evapotranspiration are the most sensitive in the Amazon basin. In river basins in high latitudes, for instance, parameters driving snow accumulation and melt are among the most sensitive parameters. We also found for many areas that different parameters were the most sensitive ones for the simulation of water storage change and river discharge, respectively.

We conclude that depending on the predominant storage compartments, different parameter should be calibrated for each river basin. The six most sensitive parameters to both river discharge and TWSC were selected for the multi-objective calibration approach. For the Amazon basin, these parameters belong to surface water processes (runoff coefficient, river velocity and wetland depth), groundwater (baseflow coefficient), soil (rooting depth) and interception (maximum canopy water height) (see also Werth et al., 2009a).

2.3 GRACE Data and Filter

GRACE data are provided as monthly coefficients of a spherical harmonic representation of the gravity field. The application of filtering techniques to GRACE data is indispensable because of errors in the gravity fields in particular for signal components of higher harmonic degree, i.e., higher spatial resolution. Filtering causes a damping of the signal inside the region of interest and the leakage of signals from outside into the resulting time series for the region of interest (Swenson and Wahr, 2002). Numerous filter methods of different assumptions and design with different error characteristics are available in the literature (see examples below). A filter method that provides a reasonable balance of satellite and leakage errors in the GRACE data is desirable to obtain an optimal separation of errors from the signal. Applying a standard filter method (a Gaussian smoother of 500 km filter width), Schmidt et al. (2008b) developed a method to determine dominant signal components of the GRACE signal which were successfully applied by Werth et al. (2009a) for a calibration of WGHM. In this study, we identified and used another filter method for hydrological model calibration, considering the improvement of hydrological models and the evaluation of GRACE data as an iterative process.

To this end, we evaluated widely used filter methods and their parameter by comparing filtered data sets of GRACE and hydrological models (here WGHM). Four isotropic and anisotropic methods were analyzed: (1) a standard isotropic filter method is the widely-used Gaussian filter (GF). Designed for gravity field application by Jekeli (1981), its intensity is determined by the filter width r_g, representing the radius at which the filter weighting function declines to 50% of its maximum value. (2) A filter (OF) by Swenson and Wahr (2002) minimizes the

signal leakage from surrounding areas for a specific basin shape. The filter is of degree- and order-dependency (anisotropic) and an a-priori given maximum of the basin average satellite error Δ_{max} tunes the filter properties. The error is a-posteriori propagated from the smoothed GRACE coefficient errors. (3) Another anisotropic Swenson and Wahr (2002) technique minimizes the sum of GRACE error and signal leakage (MF). To estimate the latter, a synthesized signal of an exponential design is parameterized by the auto-correlation length G_l and standard deviation s_0 of the expected signal. Both parameters determine the MF filter design. And (4) the signal-to-noise ratio of each GRACE coefficient is optimized by the method of Seo et al. (2006). We applied the method B_4 of their study, which uses monthly GRACE coefficients as a signal estimate and calculate the filter from the variance of the monthly coefficient errors (called SF below). For regulation of the filter intensity, a dimensionless error factor f is introduced to the errors.

To ensure consistency in space for the filter evaluation, the same filtering was applied to GRACE data (GFZ, data release RL04) and simulated hydrological model results. For varying filter parameters, regionally averaged time series of TWSC for the Amazon River basin were derived from both data sets and compared by the correspondence criteria wNSC (see Werth et al., 2009b). This criterion measures the agreement of both time series in signal amplitude and phase as well as the filter induced leakage error by a comparison of filtered and unfiltered simulated

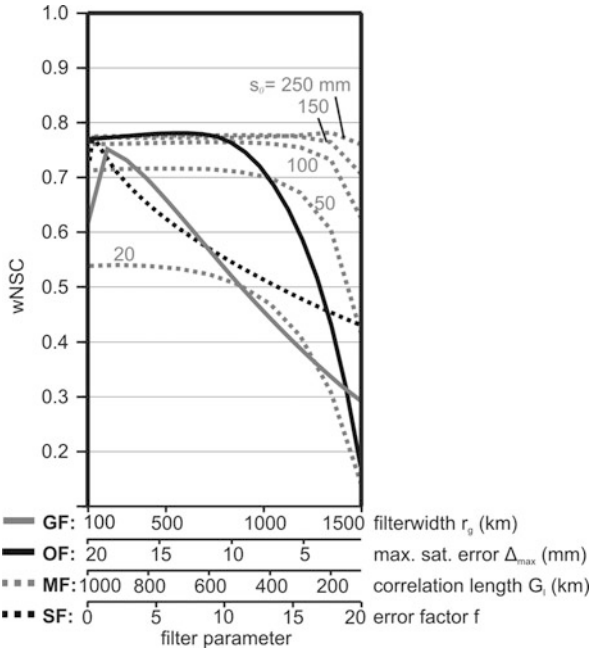

Fig. 1 Filter performance for the Amazon basin: wNSC correspondence between time series of TWSC from GRACE and WGHM for different filter types and parameter values

hydrological data. A perfect agreement corresponds to a wNSC of 1, whereas wNSC decreases for lower agreement.

For the Amazon, high filter parameter sensitivities of GF, OF, SF and for s_0 of MF were found (Fig. 1). Since the Amazon basin is located close to ocean to the east and the west (inhering different signal properties) and at the equator to the north (with shifted seasonality of water storage), basin averages for the Amazon are quite sensitive to leaking signals for high filter intensities. The second MF parameter G_l is comparatively insensitive in terms of wNSC values to correlation lengths greater than 300 km which are typical values for continental-scale water storage patterns (Güntner et al., 2007).

Among other features, basin shape and signal characteristics mostly determine which filter type is optimal for a specific basin. The results vary widely between different regions. The overall best results corresponding wNSC values for the Amazon basin are provided by the OF filter with $\Delta\max = 13$ mm and for MF with $\sigma_0 = 250$ mm and $G_l = 200$ km. For this study, we select OF filtered time series of TWSC from GRACE gravity fields for the multi-objective calibration of WGHM.

2.4 Calibration Approach

To retain the original station-based accuracy of WGHM in terms of river discharge and gain from the integrative nature of the GRACE TWSC estimations, we expect improved simulation results from a multi-objective calibration approach against several observation data. Calibration denotes an iterative method of parameter

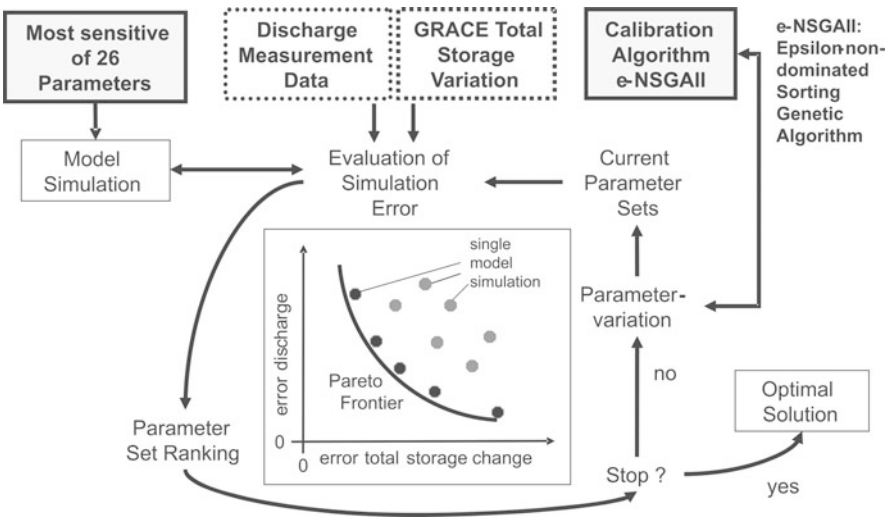

Fig. 2 Multi-objective calibration principle for the integration of GRACE data into WGHM

testing and selection based on the evaluation of simulation results against observation data (see scheme in Fig. 2). In a multi-objective calibration, parameter values are selected through the model performance against more than one objective. In this study, two observation data sets were used as evaluation objectives for the Amazon basin: (a) monthly mean river discharge from GRDC (Global Runoff Data Centre) at the most downstream gauging station in Obidos and (b) TWSC derived from optimal filtered GRACE data. For the period of 01/2003 until 12/2007, the evaluation of the calibration objectives was done by computation of the Nash-Sutcliffe-efficiency coefficient NSC (Nash and Sutcliffe, 1970) as a criterion of agreement between modeled and measured time series.

The calibration of six WGHM parameters against two objectives depicts a non-linear optimization problem. This requires a global optimization method, which searches the whole parameter space. To handle also the computational demands of WGHM we selected the efficient ϵ-Non-dominated-Sorting-Genetic-Algorithm-II (ε-NSGAII, Kollat and Reed, 2006) which solves multi-objective problems using the concept of evolutionary parameter variation (mutation, crossover and selection). Its operators were parameterized as in the original version and a population size of $N = 8$ and an ϵ-resolution of 0.05 for both objectives was used and the optimization was stopped after 2,000 iterations.

The multi-objective approach leads to a Pareto set of optimal solutions (see Fig. 2). Each Pareto optimum is an optimal solution from a multi-objective point of view in the sense that no other solution exists that provides a better simulation performance for both model output objectives. Hence, when moving from one Pareto solution to another, simulation performance increases for one objective while it decreases for the other objective. A ranking between the Pareto solutions is only possible with additional information or decision about a weighting between the objective functions.

3 Results

Calibration results of the Amazon provide an improved simulation performance for both TWSC and river discharge (Fig. 3). Improvement holds for all solutions on the Pareto frontier compared to the original model simulation. An optimal fit would give a simulation performance of 1 for each objective. A balanced improvement between both objectives is given by the metrically closest Pareto solution to an optimal fit (called the Pareto optimum in Fig. 3). The simulated TWSC time series show that the underestimated TWSC variability of the original WGHM version could be corrected in the recalibrated model (Fig. 3a). Furthermore, the phase and amplitude of the seasonal water storage regime is improved in the recalibrated model.

The better representation of TWSC simulations for the Amazon is mainly due to a lower river flow velocity in the calibrated model version (see graph B in Fig. 3) as well as a larger runoff coefficient. This causes a delay in river runoff and a longer-

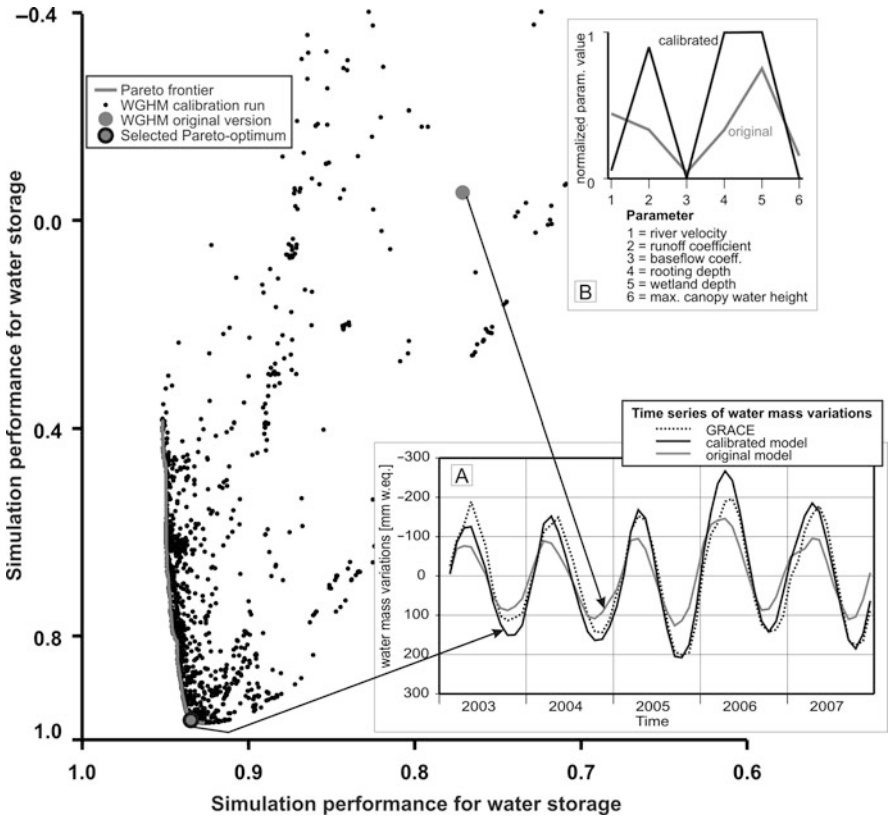

Fig. 3 Amazon calibration results in terms of simulation performance of discharge (y-axis) and total water storage (x-axis). The Pareto solution closest to the optimal fit was selected for further analyzes. Embedded graph A contains results for time series of water mass variations of GRACE, the original model and the selected Pareto optimum model. Embedded graph B compares normalized param eter values of the original model and the selected Pareto optimum model

lasting storage of more surface water in the river network of the basin. The larger river storage variability during the rainy season in the recalibrated model is also revealed by the storage time series of all individual storage compartments (Fig. 4). Furthermore , increased soil water storage is due to the larger rooting depth in the recalibrated model (see also Fig. 3b). In contrast, the larger value of the parameter wetland depth has nearly no effect on the storage variability in lakes and wetlands in spite of the large importance of wetlands and floodplains for water storage in the Amazon (e.g. Frappart et al., 2006). This may be an indication of structural model errors in representing surface water exchange processes between floodplains and the channel due to the conceptual model formulations and the cell-based simulation of surface water bodies in WGHM.

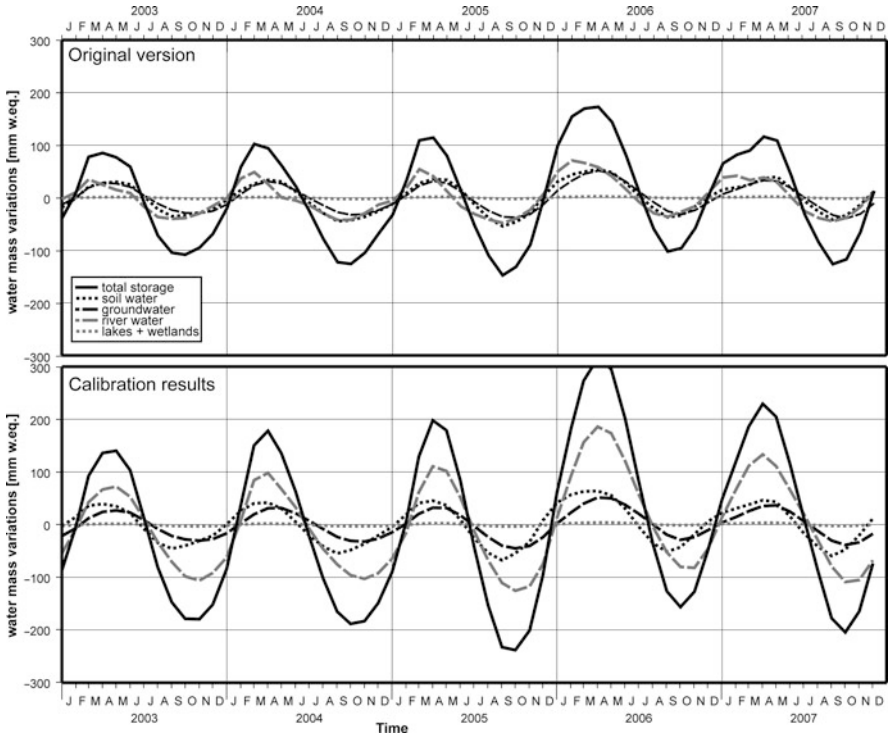

Fig. 4 Simulation of individual storage compartments of the Amazon basin by the original and the recalibrated model

4 Conclusions

The presented calibration approach for large-scale hydrological models follows three important steps: (1) selection of most sensitive and relevant process parameter of the model to be calibrated, (2) equal filtering of GRACE and hydrological data and filter optimization to achieve the best possible separation of signal and error in the GRACE data, and (3) multi-objective calibration against two observables that represent different states of the hydrological system.

This approach results in a successful calibration of WGHM with regard to both river discharge and GRACE water storage change for the Amazon basin. Furthermore, the multi-objective strategy provides comprehensible results for single storage compartments by adjusting parameter values and thus processes in a reasonable manner. Such an improved process representation is required towards more reliable simulations of the continental water cycle with regard to impacts of climate variability and water resources management. The developed approach is applicable for any large region worldwide to improve simulation performance of large-scale hydrological models. Additionally, the multi-objective nature of the calibration

technique sets a useful framework for the integration of other remote sensing data into hydrological models, such as soil moisture, surface water volumes or snow cover.

References

Andersen O, Seneviratne SI, Hinderer J, Viterbo P (2005) GRACE derived terrestrial water storage depletion associated with the 2003 European heat wave. Geophys. Res. Lett. 32, doi: 10.1029/2005GL023574.

Döll P, Kaspar F, Lehner B (2003) A global hydrologicalmodel for deriving water availability indicators: model tuning and validation. J. Hydr. 270(1–2), 105–134.

Frappart F, Ramillien G, Biancamaria S, Mognard N, Cazenave A (2006) Evolution of high-latitude snow mass derived from the GRACE gravimetry mission (2002–2004). Geophys. Res. Lett. 33(2), doi: 10.1029/2005GL024778.

Frappart F, Seyler F, Martinez J-M, León JG, Cazenave A (2006) Floodplain water storage in the Negro River basin estimated from microwave remote sensing of inundation area and water levels. Rem. Sens. Environ. 99(4), 387–399.

Güntner A (2008) Improvement of global hydrological models using GRACE data Surv. Geophys., doi: 10.1007/s10712-008-9038-y.

Güntner A, Stuck J, Werth S, Döll P, Verzano K, Merz B (2007) A global analysis of temporal and spatial variations in continental water storage. Water Resour. Res. 43(5), W05416.

Hunger M, Döll P (2008) Value of river discharge data for global-scale hydrological modeling. Hydrol. Earth Syst. Sci. 12(3), 841.

Jekeli C (1981) Alternative methods to smooth the earth's gravity field. Technical Report 329, Department of Geodetic Sciences and Surveying, Ohio State University, Columbus.

Kollat J, Reed P (2006) Comparing state-of-the-art evolutionary multi objective algorithms for long-term groundwater monitoring design. Adv. Water Res. 29(6), 792–807.

Nash JE, Sutcliffe JV (1970) River flow forecasting through conceptual models. Part-1 a discussion of principles. J. Hydr. 10(3), 282–290.

Ramillien G, Bouhours S, Lombard A, Cazenave A, Flechtner F, Schmidt R (2008) Land water storage contribution to sea level from GRACE geoid data over 2003–2006. Glob. Planet Change 60(3–4), 381.

Ramillien G, Frappart F, Güntner A, Ngo-Duc T, Cazenave A, Laval K (2006) Time variations of the regional evapotranspiration rate from gravity recovery and climate experiment (GRACE) satellite gravimetry. Water Resour. Res. 42, W10403.

Reigber C, Schmidt R, Flechtner F, König R, Meyer U, Neumayer KH, Schwintzer P, Zhu SY (2005) An earth gravity field model complete to degree and order 150 from GRACE: EigenGRACE02s. J. Geodyn. 39(1), 1–10.

Rodell M, Chen J, Kato H, Famiglietti J, Nigro J, Wilson C (2007) Estimating groundwater storage changes in the Mississippi river basin (USA) using GRACE. Hydrogeol. J. 15(1), 159.

Schmidt R, Flechtner F, Meyer U, Neumayer K-H, Dahle C, König R, Kusche J (2008a) Hydrological signals observed by the GRACE satellites Surv. Geophys., doi: 10.1007/s10712-008-9033-3.

Schmidt R, Petrovic S, Güntner A, Barthelmes F, Wünsch J, Kusche J (2008b) Periodic components of water storage changes from GRACE and global hydrology models. J. Geophys. Res. 113, B08419.

Schmidt R, Schwintzer P, Flechtner F, Reigber C, Güntner A, Döll P, Ramillien G, Cazenave A, Petrovic S, Jochmann H, Wünsch J (2006) GRACE observations of changes in continental water storage. Global and Planetary Change 50, 112–126, doi: 10.1016/j.gloplacha.2004.11.018.

Seo K-W, Wilson CR, Famiglietti JS, Chen JL, Rodell M (2006) Terrestrial water mass load changes from gravity recovery and climate experiment (GRACE). Water Resour. Res. 42, W05417.

Swenson S, Wahr J (2002) Methods for inferring regional surface-mass anomalies from gravity recovery and climate experiment (GRACE) measurements of time-variable gravity. J. Geophys. Res. 107(B9), 2193.

Syed TH, Famiglietti JS, Zlotnicki V, Rodell M (2007) Contemporary estimates of pan-arctic freshwater discharge from GRACE and reanalysis. Geophys. Res. Lett. 34(19), doi: 10.1029/2007GL031254.

Tang Y, Reed P, Wagener T (2006) How effective and efficient are multi objective evolutionary algorithms at hydrologic model calibration?. Hydrol. Earth Syst. Sci. 10, 289–307.

Tapley BD, Bettadpur S, Watkins M, Reigber C (2004) The gravity recovery and climate experiment: mission overview and early results. Geophys. Res. Lett. 31, L09607.

Werth S, Güntner A, Petrovic S, Schmidt R (2009a) Integration of GRACE mass variations into a global hydrological model. Earth Planet Sci. Lett. 277(1–2), 166–173.

Werth S, Güntner A, Schmidt R, Kusche J (2009b) Evaluation of GRACE filter tools from a hydrological perspective Geophys. J. Int., doi: 10.1111/j.1365-246X.2009.04355.x.

Zaitchik BF, Rodell M, Reichle RH (2008) Assimilation of GRACE terrestrial water storage data into a Land Surface Model: Results for the Mississippi River basin. J. Hydr., 9, 535–548 doi: 10.1175/2007jhm951.1

Part VI
NRT-RO

Near-Real-Time Provision and Usage of Global Atmospheric Data from CHAMP and GRACE (NRT-RO): Motivation and Introduction

Jens Wickert

Global and precise atmospheric satellite-based measurements with high temporal and spatial resolution are especially suited to characterize global change related atmospheric variations and to improve global numerical weather forecasts. Atmospheric research cannot be imagined without satellite measurements since the sixties, when the meteorological use of satellite data started. Especially data from passive multi-spectral radiometers contributed substantially to the understanding of global atmospheric processes. But these data from, e.g., MSU (Microwave Sounding Unit) and AMSU (Advanced Microwave Sounding Unit) are influenced by instrument and orbit changes, calibration problems, instrument drifts, and insufficient vertical resolution. Because of these shortcomings, e.g., the reliability of the derived temperature data and – in particular – its trends in the troposphere is under debate (Foelsche et al., 2007; Anthes et al., 2000).

With the installation of the US-American GPS (Global Positioning System) in the nineties an innovative technique has come up to complement the measurements of the established satellite remote sensing systems with data of a new quality: GPS radio occultation (RO) measurements (see Fig. 1). Thesedata are recorded aboard Low Earth Orbiting satellites (LEOs) and have a number of favorable characteristics, as global coverage, high accuracy and vertical resolution, all-weather capability and long-term stability (Kursinski et al., 1997). Extensive validation studies with data, generated by the classical methods, as, e.g., radiosonde measurements, and several applications demonstrated the high potential of the new data for atmospheric remote sensing on a global scale (Wickert et al., 2009, 2005; Anthes et al., 2008, 2000).

The method was successfully tested within the US-American GPS/MET-experiment (1995–1997; Rocken et al., 1997) and is currently continuously applied aboard the CHAMP and GRACE (Wickert et al., 2009, 2005), COSMIC (Anthes et al., 2008) and Metop (v. Engeln et al., 2008) satellites.

The CHAMP measurements were for a long time (2001–2006) the only operationally available RO data world-wide. It was extensively used for various scientific

J. Wickert (✉)
Helmholtz Centre Potsdam, GFZ German Research Centre for Geosciences,
Department 1: Geodesy and Remote Sensing, Telegrafenberg, 14473 Potsdam, Germany
e-mail: wickert@gfz-potsdam.de

F. Flechtner et al. (eds.), *System Earth via Geodetic-Geophysical Space Techniques*,
Advanced Technologies in Earth Sciences, DOI 10.1007/978-3-642-10228-8_37,

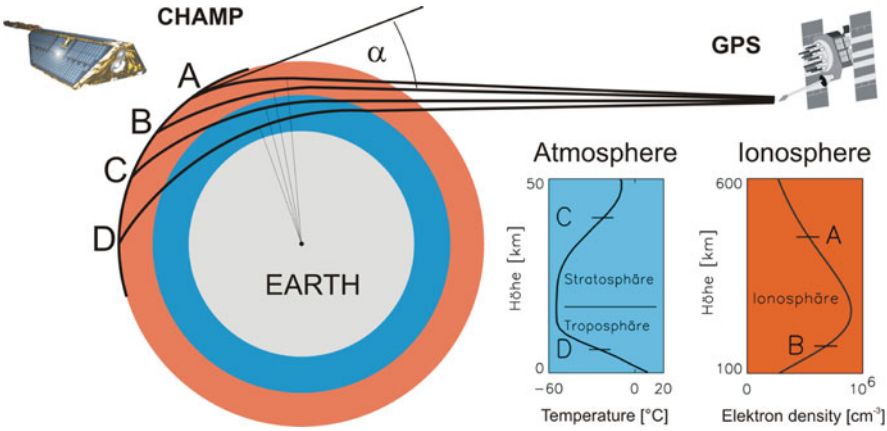

Fig. 1 Principle of GPS radio occultation measurements. A key observable is the bending angle α of the signal path between the GPS and LEO (here CHAMP) satellites. Globally distributed vertical profiles of atmospheric parameters (e.g., here temperature and electron density) can be derived from a time series (50 Hz) of bending angles, recorded during an occultation event (Figure from Wickert, 2002)

investigations (Wickert et al., 2009, 2006; Schmidt et al., 2008) including initial and very promising impact studies to improve global numeric weather forecasts at the Met Office (Buontempo et al., 2008; Healy et al., 2005) and the ECMWF (European Centre for Medium-Range Weather Forecasts; Healy, 2007; Healy et al., 2007).

A major result of these impact studies was the conclusion of the weather centers, that the GPS RO measurements would be operationally assimilated if they would be available in near-real-time. A real assimilation (based on available near-real-time data) would not only improve the forecasts, but also would reduce systematic errors in the ECMWF and Met Office model and allow for other satellite data (e.g. Atmospheric InfraRed Sounder) to be assimilated and therefore result in supplementary improvement of the global forecasts.

The promising impact study results and the above mentioned statement of the weather centers were the reasons to propose a research project, focused to provide GPS radio occultation data from CHAMP and GRACE in near-real time in 2005 (Wickert and Rothacher, 2005). It was recognized that the preconditions for an operational use of GPS RO data in numerical weather forecasts were established and is was time to push this important GPS RO application. It was the best time to take an active and leading role and to push the international activities for the operational application of the GPS RO data, based on the reliable CHAMP and GRACE measurements and before the launches of COSMIC and Metop. The proposal submission was led by GFZ, which also provided significant components of the necessary infrastructure for the planned research project (see Wickert et al., 2009; chapter "Global Atmospheric Data from CHAMP and GRACE-A: Overview and Results" by Wickert et al., this issue). The related proposal NRT-RO (Near-real-time

provision and usage of global atmospheric data from CHAMP and GRACE) was applied within the research programme GEOTECHNOLOGIEN "Observing of the System Earth from Space", funded by the German Ministry for Education and Research in 2005. The proposal application was supported by various weather prediction centers world-wide. Among them ECMWF, Met Office and DWD directly participated in the preparation of the research project.

The main objective of the proposed project was to develop, install and operate the necessary complete ground infrastructure for the operational provision of GPS RO data from CHAMP and GRACE in near-real time. These data should be operationally provided according to the timely requirements of the weather centers for the assimilation to global numerical weather forecasts. Furthermore the project partners DWD, ECMWF and the external user Met Office should assimilate the provided data to study the impact on the global forecasts. Hereby a positive impact from the occultation data was expected. A real and operational assimilation of the near-real-time RO data from CHAMP and GRACE at various weather centers should be started as highlight of the project.

According to the expectations the major success of the NRT-RO project was reached in September 2006, when the first GPS RO data ever (chapter "Global Atmospheric Data from CHAMP and GRACE-A: Overview and Results" by Wickert et al., this issue) were operationally assimilated to the global weather forecasts from Met Office. The extensive use especially of the CHAMP data for several impact studies and for operational assimilation tests since 2001 was in addition one of the major preconditions for the later begin of the operational use of COSMIC and Metop GPS RO data to improve global forecasts.

The following book chapter overviews the main results of the interdisciplinary research project NRT-RO. Wickert et al. (2009, chapter "Global Atmospheric Data from CHAMP and GRACE-A: Overview and Results", this issue) overview the project and its main results in more detail. Michalak et al. (2009, chapter "Near-Real Time Satellite Orbit Determination for GPS Radio Occultation with CHAMP and GRACE", this issue) characterize the precise orbit determination of the LEO and GPS satellites in near-real-time. Schmidt et al. (2009, chapter by "The Operational Processing System for GPS Radio Occultation Data from CHAMP and GRACE", this issue) describe the operational processing of the GPS RO data at GFZ. The use of the GPS RO data from the NRT-RO project for improving global weather forecasts is described by Pingel et al. (2009, chapter by "Assimilation of CHAMP and GRACE-A Radio Occultation Data in the GME Global Meteorological Model of the German Weather Service", this issue).

Acknowledgments We thank the CHAMP, GRACE and TerraSAR-X teams for their great work to make the GPS RO data continuously available. Our project was supported by the German Ministry for Education and Research within the GEOTECHNOLOGIEN programme (Research project NRT-RO) and also by GFZ basic funding. This project is also significantly aided by ECMWF, Met Office, Météo-France and Japan Meteorological Agency. We are very grateful for this support.

References

Anthes R, Bernhardt P, Chen Y, Cucurull L, Dymond K, Ector D, Healy S, Ho SP, Hunt D, Kuo Y-H et al. (2008) The COSMIC/FORMOSAT-3 mission: Early results. Bull. Am. Met. Soc. (March), 1–21

Anthes RA, Rocken C, Kuo Y (2000) Applications of COSMIC to meteorology and climate. Terr. Atmos. Ocean. Sci. 1(1), 115–156.

Buontempo C, Jupp A, Rennie M (2008) Operational NWP assimilation of GPS radio occultation data. Atmos. Sci. Lett. 9(3), 129–133.

v Engeln A, Andres Y, Marquardt C, Sancho F (2008) GRAS status and future European radio occultation missions, Proc. ECMWF workshop on GPS RO, 37-42, ECMWF publication, http://www.ecmwf.int/publications/library/do/references/list/11122008 .

Foelsche U, Borsche M, Steiner AK, Gobiet A, Pirscher B, Kirchengast G, Wickert J, Schmidt T (2007) Observing upper troposphere–lower stratosphere climate with radio occultation data from the CHAMP satellite. Clim. Dyn., doi: 10.1007/s00382-007-0337-7.

Healy S (Spring 2007) Operational assimilation of GPS radio occultation measurements at ECMWF. ECMWF Newslett. 111, ECMWF, 2007.

Healy SB, Wickert J, Michalak G, Schmidt T, Beyerle G (2007) Combined forecast impact of GRACE-A and CHAMP GPS radio occultation bending angle profiles. Atmos. Sci. Lett. 8(43–50), doi: 10.1002/asl.149.

Healy S, Jupp A, Marquardt C (2005) Forecast impact experiment with GPS radio occultation measurements. Geophys. Res. Lett. 32, doi: 10.1029/2004GL020806.

Kursinski ER et al. (1997) Observing Earth's atmosphere with radio occultation measurements using the Global Positioning System. J. Geophys. Res. 102, 23429–23465.

Rocken C, Anthes R, Exner M, Hunt D, Sokolovskiy S, Ware R, Gorbunov M, Schreiner W, Feng D, Herman B, Kuo YH, Zou X (1997) Analysis and validation of GPS/MET data in the neutral atmosphere. J. Geophys. Res. 102(29849–29866), doi: 10.1029/97JD02400.

Schmidt T, Wickert J, Beyerle G, Heise S (2008) Global tropopause height trends estimated from GPS radio occultation data. Geophys. Res. Lett., doi: 10.1029/2008GL034012.

Wickert J, Michalak G, Schmidt T, Beyerle G, Cheng CZ, Healy SB, Heise S, Huang CY, Jakowski N, Köhler W et al. (2009) GPS radio occultation: Results from CHAMP, GRACE and FORMOSAT-3/COS MIC. Terr. Atmos. Ocean. Sci. 20, doi: 10.3319/TAO.2007.12.26.01(F3C).

Wickert J, Schmidt T, Beyerle G, Heise S, Reigber Ch (2006) Global atmospheric sounding with GPS radio occultation aboard CHAMP. In: Flury J, Rummel R, Reigber C, Rothacher M, Boedecker G, Schreiber U (eds.), Observation of the Earth System from Space, Springer, Berlin, pp. 55–77.

Wickert J, Beyerle G, König R, Heise S, Grunwaldt L, Michalak G, Reigber Ch, Schmidt T (2005) GPS radio occultation with CHAMP and GRACE: A first look at a new and promising satellite configuration for global atmospheric sounding. Ann. Geophysicae 23, 653–658.

Wickert J, Rothacher M (2005) Near-real-time provision and usage of global atmospheric data from GRACE and CHAMP (NRT-RO), Group project proposal within the BMBF/DFG-Research program GEOTECHNOLOGIEN, GFZ.

Wickert J (2002) The GPS radio occultation experiment aboard CHAMP: Algorithms, Processing system and first results (Germ.), GFZ Scientific Technical Report STR 02/07, Potsdam.

Global Atmospheric Data from CHAMP and GRACE-A: Overview and Results

Jens Wickert, Georg Beyerle, Carsten Falck, Sean B. Healy, Stefan Heise, Wolfgang Köhler, Grzegorz Michalak, Dave Offiler, Detlef Pingel, Markus Ramatschi, Markus Rothacher, and Torsten Schmidt

1 Introduction

Recently ground and space based GPS atmospheric remote sensing techniques including the GPS Radio Occultation (GPS RO) method are more and more accepted by the meteorological community. Brief overviews on several techniques and applications are given, e.g., by Wickert and Jakowski (2007) or Wickert et al. (2007). The application of GPS RO aboard Low Earth Orbiting (LEO) satellites allows for the derivation of vertical profiles of atmospheric parameters on a global scale. Main characteristics of GPS RO measurements are: all-weather capability, calibration independence, high accuracy and high vertical resolution. A detailed introduction to GPS RO is given, e.g., by Kursinski et al. (1997). Currently GPS RO is continuously applied aboard the German CHAMP and the US/German GRACE satellites (Wickert et al., 2005, 2006, 2008, 2009a, b), the 6 satellites of the FORMOSAT-3/COSMIC mission (launched April 14, 2006; see, e.g., Anthes et al., 2008) and aboard Metop (v. Engeln et al., 2008; Launch October 18, 2006). GPS RO data are also available from the US-Argentinean satellite SAC-C (Satelite de Aplicaciones Cientificas-C). Initial GPS RO results from the German TerraSAR-X mission complete this multi-satellite RO data set.

A major application of GPS RO data is the use to improve global weather forecasts. A breakthrough for this application was reached in 2006, when operational assimilation was started by Met Office and ECMWF (e.g., Healy, 2007; Buontempo et al., 2008). In preparation of this operational phase several investigations were made at the weather centers to quantify the impact of the GPS RO data on the quality of the global forecasts. For these studies mainly data of the CHAMP mission were used (Cucurull et al., 2007; Healy and Thepaut, 2006; Healy et al., 2005, 2007). These data were operationally available already since 2003 with an average delay of about 5 h between measurement and corresponding provision of atmospheric

J. Wickert (✉)
Helmholtz Centre Potsdam, GFZ German Research Centre for Geosciences,
Department 1: Geodesy and Remote Sensing, Telegrafenberg, 14473 Potsdam, Germany
e-mail: wickert@gfz-potsdam.de

F. Flechtner et al. (eds.), *System Earth via Geodetic-Geophysical Space Techniques*,
Advanced Technologies in Earth Sciences, DOI 10.1007/978-3-642-10228-8_38,

Fig. 1 Title page of the Near-Real Time Radio Occultation (NRT-RO) research project proposal (in German). The project was performed from August 2005 until August 2008

data products (globally distributed vertical bending angle and refractivity profiles; Wickert et al., 2004).

The NRT-RO research project (see Fig. 1) was mainly initiated to reduce this delay for CHAMP and GRACE below 2 h, as required for the operational assimilation of GPS RO data to numerical weather forecasts. We briefly summarize results of this project here.

2 Status of CHAMP and GRACE Radio Occultations

CHAMP is currently expected to reach its 10th anniversary in orbit on July 15, 2010. GPS RO data are available nearly continuously from May 2001 until October 2008 (Fig. 2). The measurements from CHAMP form the first long-term RO

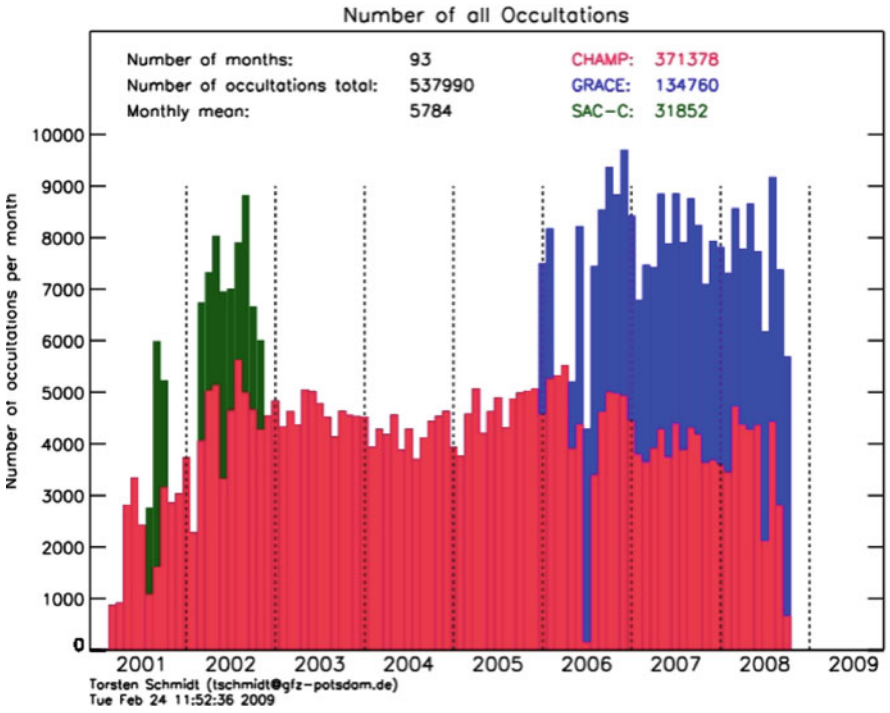

Fig. 2 Number of available monthly vertical atmospheric profiles, derived from CHAMP and GRACE-A GPS occultation measurements (GFZ processing) as of November 2008. For short periods (mid 2001 and 2002) also GFZ processing results from the US-Argentinean satellite SAC-C are available

data set, which currently also is the base for initial climatological investigations (e.g., Schmidt et al., 2008; Ho et al., 2009).

The GRACE satellites (e.g., Tapley et al., 2004) had 7th anniversary in orbit on March 17, 2009. GPS RO data from GRACE-A are continuously available since May 2006 (Fig. 2).

3 Near-Real Time Occultation Infrastructure and Data Analysis at GFZ

GFZ operates an operational infrastructure for the processing of GPS RO data (overview see Fig. 3). The GPS data (navigation and occultation) from CHAMP and GRACE are transferred to the ground via receiving antennas at Ny-Ålesund, Spitsbergen. Together with GPS data from the operational global GPS ground network (jointly operated by GFZ and JPL) these satellite observations form the main input for the automated processing systems to derive precise satellite orbit and atmospheric data (for more details, see, e.g., Wickert et al., 2009a, b and Michalak et al., 2007). For processing of the OpenLoop (Sokolovskiy, 2001) tracking data (e.g.,

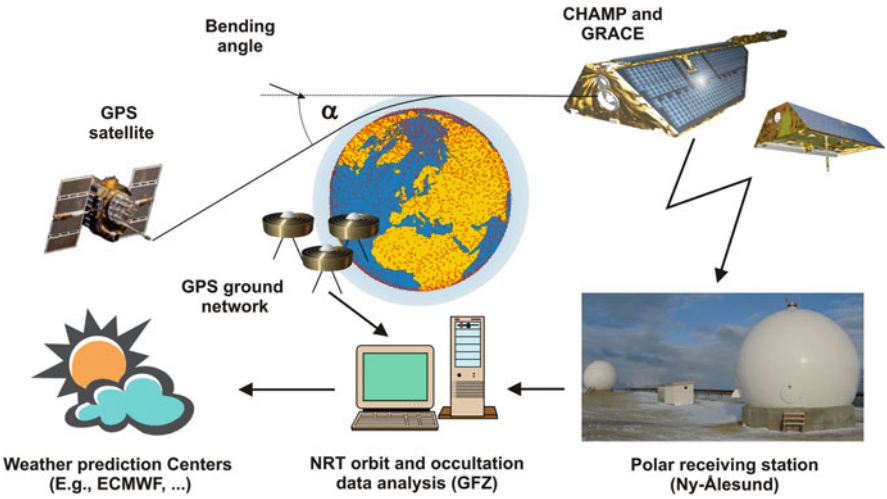

Fig. 3 GPS radio occultation infrastructure at GFZ (overview, slightly modified from Wickert et al., 2008)

TerraSAR-X), information on the navigation bit modulation of the GPS signals is required. These data is provided by selected stations of the globally distributed GFZ ground network (Beyerle et al., 2008).

The atmospheric standard data products are: atmospheric excess phases and vertical profiles of bending angles, refractivity, temperature and water vapor (Wickert et al., 2009a, b). In parallel to the standard data processing a near-real time provision of atmospheric data (excess phases and vertical profiles of bending angle, refractivity and dry temperature) was developed and demonstrated within the NRT-RO research project. The NRT data are currently provided continuously with average delay between measurement aboard the satellites and provision of corresponding analysis results at GFZ of less than 2 h (Fig. 4). Key -preconditions for this result is the successful work related to the installation of NRT-orbit and occultation processing chains, which are described in detail by Michalak et al. (2009, chapter "Near-Real Time Satellite Orbit Determination for GPS Radio Occultation with CHAMP and GRACE", this issue) and Schmidt et al. (2009, chapter "The Operational Processing System for GPS Radio Occultation Data from CHAMP and GRACE", this issue).

4 Monitoring and Assimilation of CHAMP and GRACE Data to Global Weather Models

The provision of NRT atmospheric data products from CHAMP and GRACE within the NRT-RO research project (see Fig. 4) stimulated the pioneering use of GPS-RO for numerical weather prediction, which was started during the course of the project.

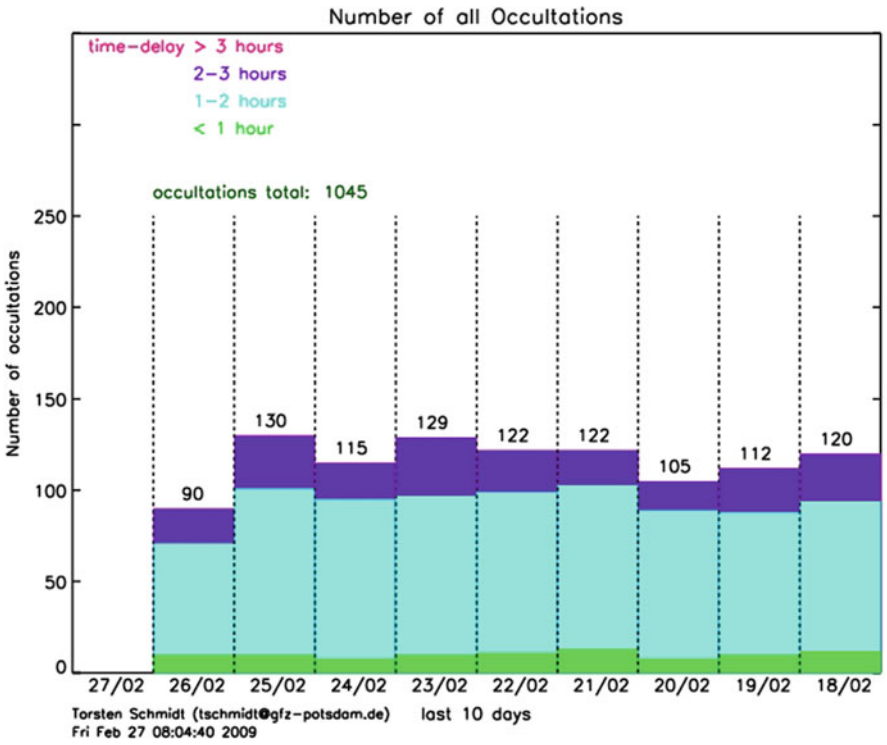

Fig. 4 GFZ provides near-real time occultation data (bending angle and refractivity profiles in BUFR) from CHAMP and GRACE-A. The figure shows a recent monitoring plot of the time delay between GRACE-A occultation measurements aboard the satellite and availability of corresponding analysis results at NRT ftp-server at GFZ. About 100% of the data is available within 3 h. Data are provided since February 2007 in BUFR format and are currently distributed also via the Global Telecommunication System (GTS)

Various weather forecast centres started the operational assimilation of GPS RO data from COSMIC, CHAMP and GRACE (beginning within September 2006). The initial operational assimilation of GPS RO data was started at Met Office with refractivity profiles from CHAMP and GRACE on September 26, 2006 (Buontempo et al., 2008), at ECMWF with RO data from CHAMP, GRACE and COSMIC on December 12, 2006 (Healy, 2007) and at NOAA with COSMIC RO data on May 1, 2007 (Cucurull, 2007). The Japanese Meteorological Agency (JMA) used CHAMP data for the first time operationally on March 22, 2007 (Shoji et al., 2008) and Météo-France started with CHAMP, GRACE and COSMIC on September 5, 2007 (Poli et al., 2008). The assimilation related activities at the Deutscher Wetterdienst (DWD) are described by Pingel et al. (2009, chapter "Assimilation of CHAMP and GRACE-A Radio Occultation Data in the GME Global Meteorological Model of the German Weather Service", this issue, 2007).

Met Office as part of the GRAS SAF (GNSS Receiver for Atmospheric Sounding Satellite Application Facility) operates an operational quality monitoring of GPS RO

data from several missions. Monitoring results are available via internet (http://garf.grassaf.org/monitoring/).

5 GPS Radio Occultation with TerraSAR-X

The German TerraSAR-X satellite was launched on June 15, 2007 with a Dnepr-1 launch vehicle from Aerodrome Baikonur (Russia). The main science instrument aboard is a new generation X-band radar (9.65 GHz) for Earth observation with up to 1–2 m resolution (spotlight mode). GFZ (together with University Texas) is operating an IGOR GPS receiver for precise orbit determination and occultation measurements.

The occultation experiment is still in the commissioning phase, but initial RO results already indicate a promising data quality. In contrast to CHAMP and GRACE, TerraSAR-X applies the OpenLoop (Sokolovskiy, 2001) signal tracking technique in the lower troposphere, which allows an improvement of the data quality compared to the Closed Loop tracking applied aboard CHAMP and GRACE-A. Figure 5 shows 2 water vapour profiles from TerraSAR-X, recorded on October 1,

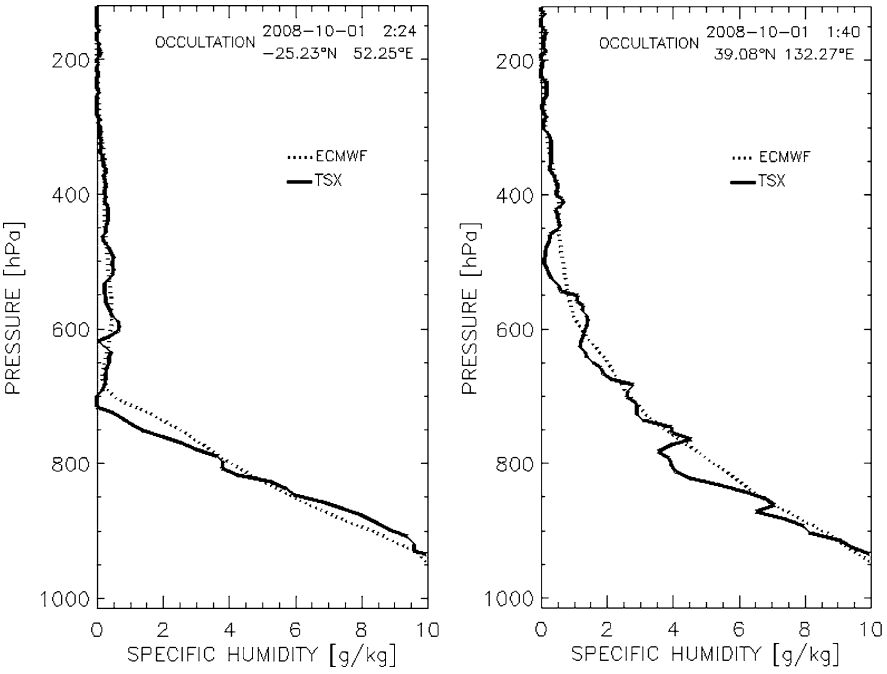

Fig. 5 Examples for initial GPS RO results from TerraSAR-X: Vertical water vapour profiles (TSX, *solid line*), compared with corresponding ECMWF analyses (*dotted line*). For details see text

2008. The OpenLoop data were analysed according to Beyerle et al. (2006) using a GFZ navigation bit data stream (Beyerle et al., 2008) and applying the Direct Water Vapor Pressure (DWVP) technique, introduced by Heise et al. (2008). Both profiles reach the last kilometre above the Earth's surface and show a good data quality, indicated by comparison with corresponding ECMWF data.

6 Summary

The joint research project of GFZ, DWD, ECMWF, and Met Office significantly contributed to the pioneering begin of the operational GPS RO data use to improve global numerical weather forecasts, which was started in 2006. Global atmospheric data from CHAMP and GRACE are provided with average latency of less than 2 h between measurements aboard the satellites and provision of corresponding analysis results at GFZ ftp-server. Usually 100% of the data is available within 3 h. The use of the operational ground infrastructure of GFZ is precondition to reach this result. Key-components are a Polar Satellite Receiving Antenna, located at Ny Ålesund (Spitsbergen), a globally distributed GPS ground network and NRT-orbit and occultation processing systems.

Several weather centres started operational assimilation of CHAMP/GRACE atmospheric data (Met Office, ECMWF, JMA, NCAR, Météo-France) during the NRT-RO project course.

Acknowledgments We thank the CHAMP, GRACE and TerraSAR-X teams for their great work to guarantee the availability of GPS occultation data. The near-real time activities at GFZ and DWD are supported by the German Ministry for Education and Research within the GEOTECHNOLOGIEN programme (Research project NRT-RO) and also by GFZ. This project is also significantly aided by ECMWF, Met Office, Météo-France and Japan Meteorological Agency. We are grateful for this support.

References

Anthes R, Bernhardt P, Chen Y, Cucurull L, Dymond K, Ector D, Healy S, Ho SP, Hunt D, Kuo Y-H et al. (2008) The COSMIC/FORMOSAT-3 mission: Early results. Bull. Am. Met. Soc. (March), 1–21.

Beyerle G, Ramatschi M, Galas R, Schmidt T, Wickert J, Rothacher M (2008) A data archive of GPS navigation messages. GPS Solut., doi: 10.1007/s10291-008-0095-y.

Beyerle G, Schmidt T, Wickert J, Heise S, Rothacher M, König-Langlo G, Lauritsen KB (2006) Observations and simulations of receiver-induced refractivity biases in GPS radio occultation. J. Geophys. Res. 111, D12101, doi: 10.1029/2005JD006673.

Beyerle G, Schmidt T, Michalak G, Heise S, Wickert J, Reigber Ch (2005) GPS radio occultation with GRACE: Atmospheric profiling utilizing the zero difference technique. Geophys. Res. Lett. 32, L13806, doi: 10.1029/2005GL023109.

Buontempo C, Jupp A, Rennie M (2008) Operational NWP assimilation of GPS radio occultation data. Atmos. Sci. Lett. 9(3), 129–133.

Cucurull L (2007) COSMIC Data to be Assimilated Operationally at NOAA, Joint Center for Satellite Data Assimilation, JCSDA Quarterly, page 1, No. 18, March.

Cucurull L, Derber JC, Treadon R, Purser RJ (2007) Assimilation of global positioning system radio occultation observations into NCEP's global data assimilation system. Mon. Wea. Rev. 135(9), 3174.

v. Engeln A, Andres Y, Marquardt C, Sancho F (2008) GRAS status and future European radio occultation missions, Proceedings of ECMWF workshop on GPS RO, 37–42, ECMWF publication, http://www.ecmwf.int/publications/library/do/references/list/11122008.

Healy S (Spring, 2007) Operational assimilation of GPS radio occultation measurements at ECMWF, ECMWF Newslett. 111, ECMWF.

Healy SB, Wickert J, Michalak G, Schmidt T, Beyerle G (2007) Combined forecast impact of GRACE-A and CHAMP GPS radio occultation bending angle profiles. Atmos. Sci. Lett. 8, 43–50, doi: 10.1002/asl.149.

Healy SB, Thepaut J-N (2006) Assimilation experiments with CHAMP GPS radio occultation measurements. Q. J. R. Meteorol. Soc. 132, 605–623, doi: 10.1256/qj.04.182.

Healy S, Jupp A, Marquardt C (2005) Forecast impact experiment with GPS radio occultation measurements. Geophys. Res. Lett. 32, doi: 10.1029/2004GL020806.

Heise S, Wickert J, Beyerle G, Schmidt T, Smit H, Cammas JP, Rothacher M (2008) Comparison of water vapor and temperature results from GPS radio occultation aboard CHAMP with MOZAIC aircraft measurements. IEEE Trans. Geosci. Remote Sens. 46(11), 3406–3411.

Ho S-P, Kirchengast G, Leroy S, Wickert J, Mannucci AJ, Steiner AK, Hunt D, Schreiner W, Sokolovskiy S, Ao CO et al. (2009) Estimating the uncertainty of using GPS radio occultation data for climate monitoring: Inter-comparison of CHAMP refractivity climate records 2002–2006 from different data centers. J. Geophys. Res., 114, D23107, doi: 10.1029/2009JD011969, in press.

Kursinski ER et al. (1997) Observing Earth's atmosphere with radio occultation measurements using the Global Positioning System. J. Geophys. Res. 102, 23429–23465.

Michalak G, Wickert J, König R, Rothacher M (2007) Near-real-time satellite orbit determination for GPS radio occultation. GEOTECHNOLOGIEN, Science Report No. 11, ISSN 1619-7399, pp. 23–25.

Poli P, Beyerle G, Schmidt T, Wickert J (2008) Assimilation of GPS radio occultation measurements at Météo-France, Proceedings of ECMWF workshop on GPS RO, 73–82, ECMWF publication, http://www.ecmwf.int/publications/library/do/references/list/11122008.

Schmidt T, Wickert J, Beyerle G, Heise S (2008) Global tropopause height trends estimated from GPS radio occultation data. Geophys. Res. Lett., doi: 10.1029/2008GL034012.

Shoji Y, Kunii M, Seko H, Ozawa E, Tsuda T (2008) Data assimilation experiments of GPS radio occultation data into numerical weather prediction models in Japan, talk at the 4th Asian Space conference, October 1–3, Taipeh, Taiwan.

Sokolovskiy SV (2001) Tracking tropospheric radio occultation signals from low Earth orbit. Radio Sci. 36(3), 483–498.

Tapley B, Bettadpur S, Watkins M, Reigber C (2004) The gravity recovery and climate experiment: Mission, overview and early results. Geophys. Res. Lett. 31, L09607, doi: 10.1029/2004GL019920.

Wickert J, Michalak G, Schmidt T, Beyerle G, Cheng CZ, Healy SB, Heise S, Huang CY, Jakowski N, Köhler W et al. (2009a) GPS radio occultation: Results from CHAMP, GRACE and FORMOSAT-3/COS MIC. Terr. Atmos. Ocean. Sci. 20, doi: 10.3319/TAO.2007.12.26.01(F3C).

Wickert J, Schmidt T, Michalak G, Heise S, Arras Ch, Beyerle G, Falck C, König R, Pingel D, Rothacher M (2009b) GPS radio occultation with CHAMP, GRACE, SAC-C, TerraSAR-X and COSMIC: Brief review of results from GFZ. Steiner, Pirscher, Foelsche, Kirchengast (eds.), New Horizons in Occultation Research: Studies in Atmosphere and Climate, Springer, Berlin Heidelberg, ISBN 978-3-642-00320-2, pp. 3–16.

Wickert J et al. (2008) CHAMP, GRACE, SAC-C, TerraSAR-X/TanDEM-X: Science results, status and future prospects, Proceedings of ECMWF workshop on GPS RO, 43–52, ECMWF publication, http://www.ecmwf.int/publications/library/do/references/list/11122008.

Wickert J, Gendt G, Beyerle G, Dick G, Heise S, Helm A, Reigber Ch, Schmidt T, Jakowski N, Jacobi Ch (2007) Ground and space based GPS atmospheric sounding: Brief overview and examples. Intl Meeting Tropical Radar Network, NARL Publication, Tirupati, India, pp. 1–10.

Wickert J, Jakowski N (2007), GNSS based sounding of the Atmosphere/Ionosphere in: National Report of the Federal Republic of Germany on the Geodetic activities in the years 2003–2007, ISBN 3 7696 8595 4, pp. 125–129.

Wickert J, Schmidt T, Beyerle G, Heise S, Reigber Ch (2006) Global atmospheric sounding with GPS radio occultation aboard CHAMP. In: Flury J, Rummel R, Reigber Ch, Rothacher M, Boedecker G, Schreiber U (eds.), Observation of the Earth System from Space, Springer, Berlin, pp. 55–77.

Wickert J, Beyerle G, König R, Heise S, Grunwaldt L, Michalak G, Reigber, C, Schmidt T (2005) GPS radio occultation with CHAMP and GRACE: A first look at a new and promising satellite configuration for global atmospheric sounding. Ann. Geophysicae 23, 653–658.

Wickert J, Schmidt T, Beyerle G, König R, Reigber C, Jakowski N (2004) The radio occultation experiment aboard CHAMP: Operational data processing and validation of atmospheric parameters. J. Meteorol. Soc. Jpn. 82, 381–395.

Near-Real Time Satellite Orbit Determination for GPS Radio Occultation with CHAMP and GRACE

Grzegorz Michalak and Rolf König

1 Introduction

One of the CHAMP and GRACE mission objectives is to perform radio occultation measurements of GPS signals propagating through Earth's atmosphere. From these measurements it is possible to derive vertical profiles of bending angles, temperature and humidity of the atmosphere on a global scale which can be used by numerical weather prediction systems (NWP). To fulfill this mission objective, rapidly available precise orbits and clock offsets both for occulting GPS satellites and the Low Earth Orbiters (LEOs) are required. Efficient occultation data assimilation in the NWP systems requires a 3 h time line for occultation products. As the orbits are needed to generate the occultation products, the latency of the orbit products is required not to exceed 0.5 h. For this purpose a Near-Real Time (NRT) orbit processing system was developed to generate precise GPS, CHAMP, GRACE-A and TerraSAR-X orbits with a mean latency of 15–30 min (Michalak et al., 2007). The orbit latency is defined here as a difference between the epoch of the orbit generation and the epoch of the last data point used in the processing. The space-borne GPS Satellite-to-Satellite Tracking data (SST) and the occultation data can be downloaded (dumped) from each LEO once per revolution, approximately every 1.5 h. Processing of the most recent dump, containing 1.5 h of occultation data, starts when the NRT orbits become available. The typical processing time of the occultation data is 0.5 h; taking into account additional 0.5 h of NRT orbit latency, the delay of occultation products generated from the recent dump is between 1 and 2.5 h (on average 1 h 45 min). This delay meets the 3 h timeline and the data can be successfully assimilated by the weather centers (Wickert et al., 2009). Dumping of the SST data in each revolution is assured for near polar satellite orbits by operating a GFZ's northern latitude receiving station in Ny Ålesund. To enhance reliability and to test different approaches of orbit generation, three independent NRT processing

G. Michalak (✉)
Helmholtz Centre Potsdam, GFZ German Research Centre for Geosciences,
Department 1: Geodesy and Remote Sensing, Telegrafenberg, 14473 Potsdam, Germany
e-mail: michalak@gfz-potsdam.de

F. Flechtner et al. (eds.), *System Earth via Geodetic-Geophysical Space Techniques*,
Advanced Technologies in Earth Sciences, DOI 10.1007/978-3-642-10228-8_39,

chains were developed delivering the orbits with different accuracies and latencies which can be used also for other applications according to their accuracy/latency requirements. Details of the different approaches are given in the following sections.

2 NRT Orbit Processing System

The Near-Real Time LEO orbit processing system is based on so-called two step approach in which the LEO orbits are estimated using fixed GPS orbits and clocks estimated before. For this reason the system consists of two separate subsystems. One is designed to generate GPS NRT orbits and clocks; the second one generates LEO NRT orbits. The estimation of the GPS orbits and clocks is performed by using data of 30–60 stations of a globally distributed GPS ground network from IGS. The modelling standards and estimated parameters are very similar to those used for the so-called Rapid Science Orbits (Michalak et al., 2003). Since the processing of the GPS ground data is the most time consuming part, for the NRT application this processing was split into a long and a short arc. The long 24 and 12 h GPS arcs (see details below) are generated on an hourly basis and parallel to this the short 3 h arcs extending the long arcs are generated every 15 min. The generation of the short arcs is fast and gives access to GPS orbits and clocks with low latencies of approximately 15 min, where waiting and downloading of the GPS data takes 10 min, and processing takes less than 5 min. Subsequent 14 h LEO NRT arcs are based on the combination of the most recent long and short GPS arcs. The LEO NRT processing starts as soon as new space-borne GPS satellite-to-satellite (SST) data become available, downloaded from the satellite or "dumped". Therefore this way of processing is called dump-related. Typical delay in access to SST dump data for CHAMP and GRACE is in the range of 5–10 min. To assure high reliability and to test possible accuracies and latencies, the NRT orbit processing system was split into three separate chains which generate LEO orbits based on different sets of GPS orbits. The description of the chains (CHAIN 1, CHAIN 2 and CHAIN 3) is given below. In addition to CHAMP and GRACE, the TerraSAR-X satellite, launched on June 15, 2007 was also included in the NRT system. The accuracy of the LEO NRT orbits is determined by independent Satellite Laser Ranging (SLR) observations. Accuracies and latencies achieved for all LEOs and for all chains are summarized in Table 1. The previously running Ultra-rapid Science Orbit (USO) system (König et al., 2005) delivering LEO orbits with latencies above 2 h was eventually shut off and replaced by the new NRT system in September 2007. The latencies for USO and NRT processing for CHAMP are given in Fig. 1.

2.1 CHAIN 1: GPS-Based Processing

In this chain, called "GPS-based", the 14 h LEO orbits are based on the combination of 24 and 3 h GPS orbits and clocks, estimated from the GPS ground station data with 5 min spacing. The 3 h arcs are predictions originating from the long 24 h arcs,

Table 1 Summary of the accuracies and latencies of the 14 h NRT LEO orbits for various NRT processing chains. For calculation of the position and velocity overlap values, the last 2 h of the LEO arcs are used. Latency is defined as the difference between the orbit generation time and the epoch of the last available SST observation used in the processing

	SLR RMS (cm)	3-D Pos. overlap (cm)	3-D Vel. overlap (mm/s)	Latency (min)
CHAMP Period 2006/08/17–2008/12/15				
CHAIN 1 (GPS-based)	6.8	11.5	0.11	31
CHAIN 2 (IGU-based)	9.6	18.8	0.18	13
CHAIN 3 (IGU-fixed-30s)	5.1	6.5	0.07	30
GRACE-A Period 2006/08/22–2008/12/15				
CHAIN 1 (GPS-based)	7.6	11.0	0.09	31
CHAIN 2 (IGU-based)	10.6	19.2	0.17	13
CHAIN 3 (IGU-fixed-30s)	6.0	7.0	0.06	30
TerraSAR-X Period 2007/08/27–2008/12/15				
CHAIN 1 (GPS-based)	–	–	–	–
CHAIN 2 (IGU-based)	9.8	17.8	0.17	30–60
CHAIN 3 (IGU-fixed-30s)	5.6	5.4	0.06	30–60

but the 5 min clocks are estimated. The latency of the 3 h GPS orbits is currently approximately 20 min, where 15 min is the waiting and data downloading time, the remaining 5 min is the data processing proper. Currently the 3-D accuracy of the short 3 h GPS arcs, when compared to the estimated part of the Ultra Rapid Orbits (IGU) of the International GNSS Service (IGS) is 19 cm (see Fig. 2). The LEO orbits are generated with an average latency of 30 min and an accuracy of 7 cm

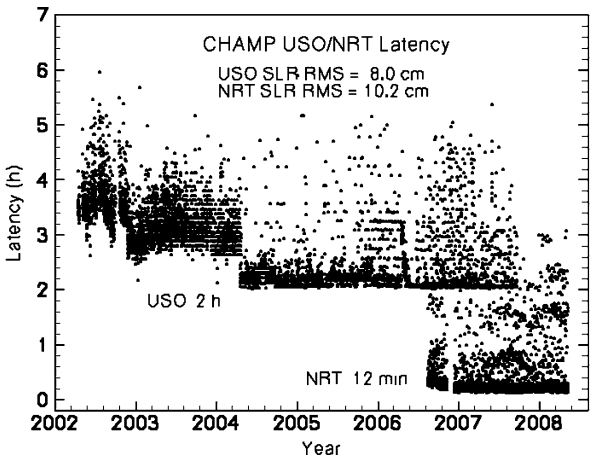

Fig. 1 The latency of the CHAMP orbit generation for two systems: USO and NRT. The NRT latency comes from the CHAIN 2

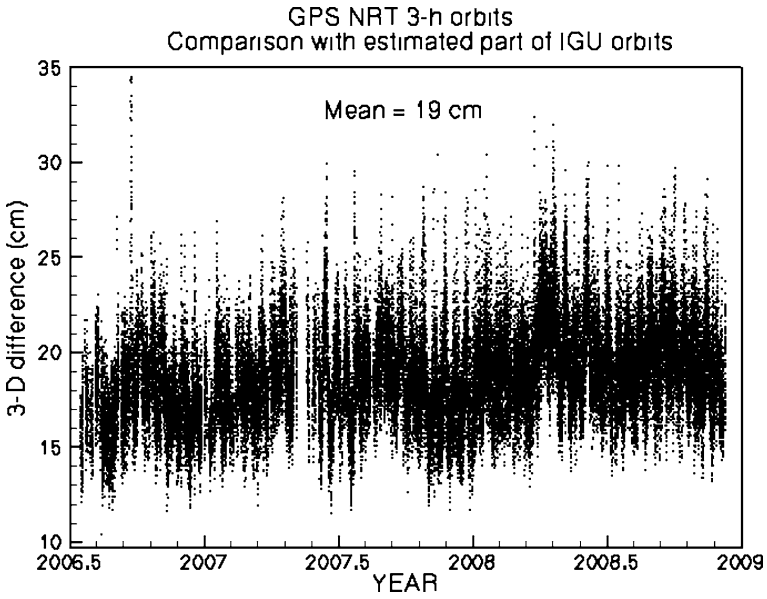

Fig. 2 Position differences between the GPS NRT orbits (3-h arc length) and the estimated part of the IGU orbits

validated by independent Satellite Laser Ranging (SLR) measurements. This chain is not active for the TerraSAR-X satellite.

2.2 CHAIN 2: IGU-Based Processing

In this chain, designated as "IGU-based", the 14 h LEO orbits are based on purely predicted IGU orbits and clocks. Since the spacing of the IGU orbits and clocks is 15 min, for processing of the 30s SST data the IGU clocks are linearly interpolated to 30s intervals. Because there is no ground GPS data processing involved, the LEO orbits can be generated very rapidly with a mean latency of 13 min, but a comparably low accuracy of 10 cm (via SLR validation). This low accuracy is mainly caused by the predicted IGU clocks used as fixed in the LEO processing. The chain is very robust because it depends solely on the availability of the IGU orbits and the SST dump data; no GPS ground data are needed. Accuracies and latencies of the NRT orbits for CHAMP, GRACE-A and TerraSAR-X satellite generated by this chain are given in the Figs. 3, 4, and 5.

2.3 CHAIN 3: IGU-Fixed-30s Processing

This chain, designated as "IGU-fixed-30s", generates LEO orbits based on fixed predicted IGU orbits, but 30s clocks estimated from GPS ground data. Since estimation

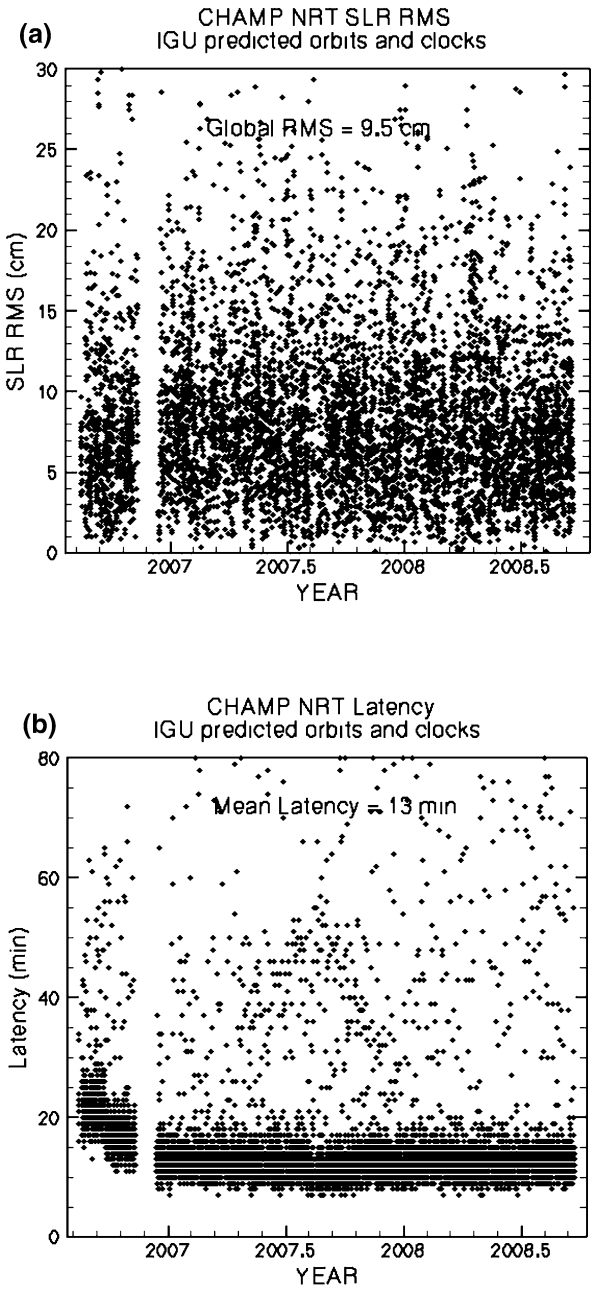

Fig. 3 (**a**) Accuracy of CHAMP NRT orbits generated by CHAIN 2. (**b**) Latency of CHAMP NRT orbits generated by CHAIN 2

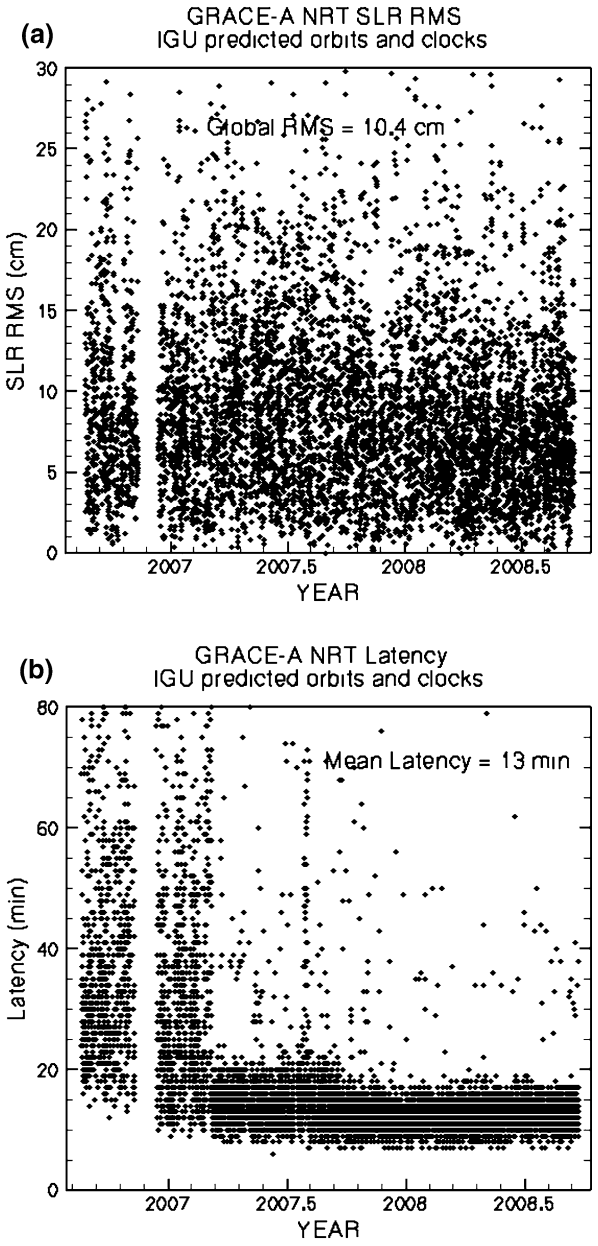

Fig. 4 (**a**) Accuracy of GRACE-A NRT orbits generated by CHAIN 2. (**b**) Latency of GRACE-A NRT orbits generated by CHAIN 2

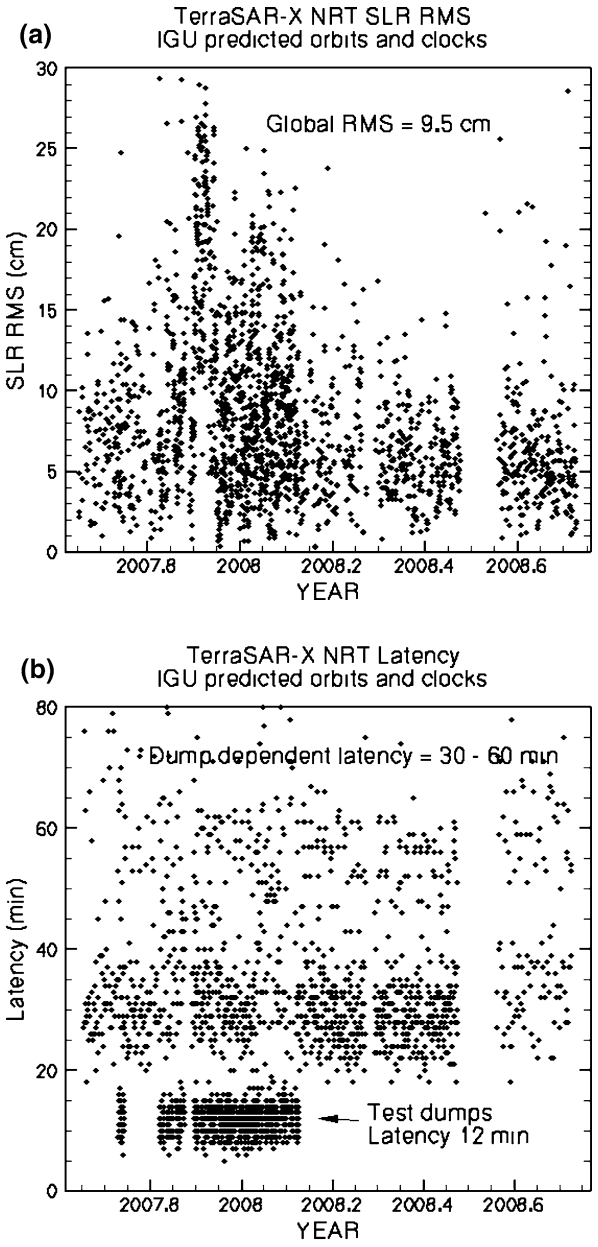

Fig. 5 (**a**) Accuracy of TerraSAR-X NRT orbits generated by CHAIN 2. (**b**) Latency of TerraSAR-X NRT orbits generated by CHAIN 2. Due to lacking of the data from polar receiving station Ny Å lesund, the data are significantly delayed. Test dumps over Ny Å lesund demonstrated very low latency also for TerraSAR-X

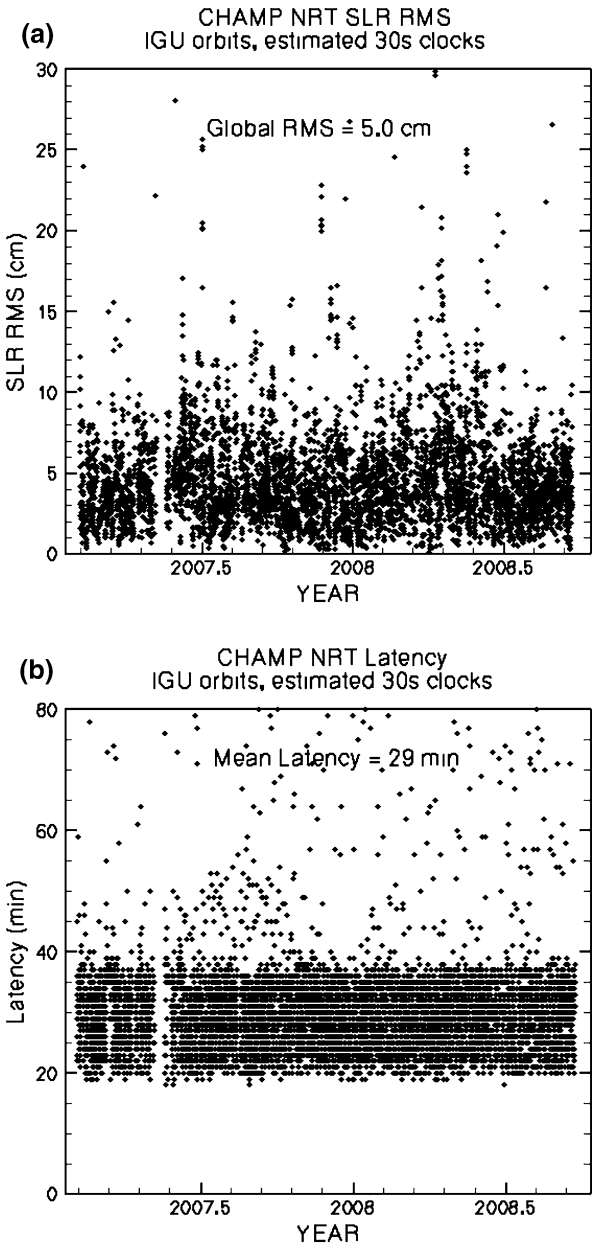

Fig. 6 (**a**) CHAMP NRT orbit accuracy generated by the CHAIN 3. (**b**) CHAMP NRT orbit latency generated by the CHAIN 3

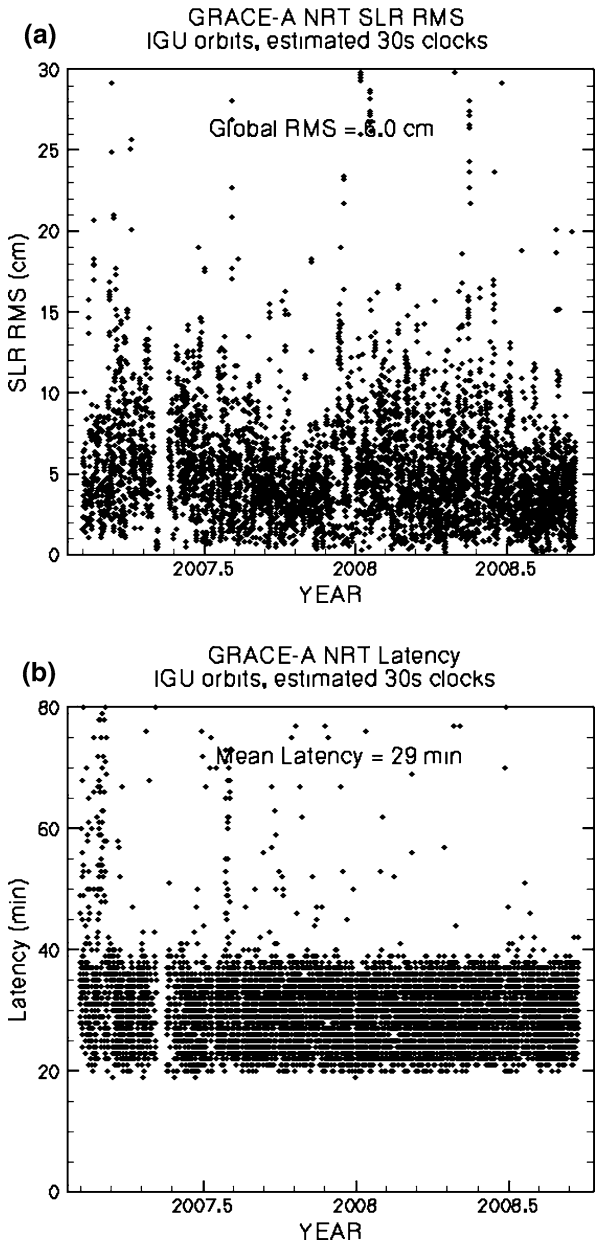

Fig. 7 (**a**) Accuracy of the GRACE-A NRT orbits generated by CHAIN 3. (**b**) Latency of the GRACE-A NRT orbits generated by CHAIN 3

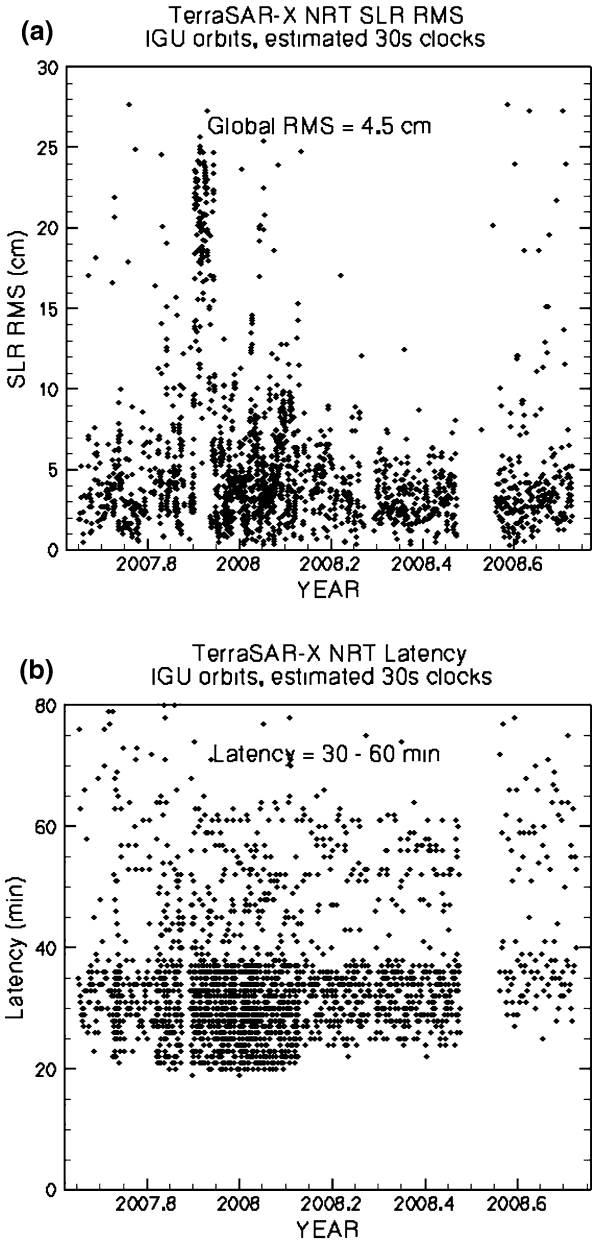

Fig. 8 (**a**) Accuracy TerraSAR-X NRT orbits generated by the CHAIN 3. (**b**) Latency of the TerraSar-X NRT orbits generated by the CHAIN 3

of the dense 30s clocks is time consuming, the length of the hourly generated long GPS arc was reduced from 24 to 12 h, the short arc remains of 3 h length. This chain is a kind of mixture of the two above chains, generates LEO orbits with an acceptable mean latency of 30 min but with the highest accuracy of 5–6 cm. For TerraSAR-X the latency (90 min) is dictated mainly by the dump data delay (see Table 1) but will be improved in the future once the data are dumped over the polar receiving station Ny Ålesund. This chain is active since February 2007. The accuracies and latencies of CHAMP, GRACE-A and TerraSAR-X orbits generated by this chain are given in Figs. 6, 7, and 8.

3 Summary

Within the German "Geotechnologien NRT-RO" project, GFZ has developed a NRT orbit processing system for GPS and LEO orbits to support NRT radio occultations. The system generates NRT LEO orbits every 1.5 h with average position accuracies of 6–10 cm validated by SLR over whole arcs. For NRT occultation products only last 2 h of arcs are used. The accuracy of these orbit parts is computed from arc overlaps. The LEO orbits of lower accuracy (20 cm for position, 0.20 mm/s for velocity) are generated with a latency of 13 min when using predicted IGU orbits and clocks. More precise orbits (6–7 cm for position, 0.06 mm/s for velocity) are generated with a latency of 30 min when using IGU predicted orbits but 30s clocks being estimated. In all processing chains the orbit latency can assure the generation of occultation products with average delay well below 3 h required for NWP systems. The NRT processing system is designed for easy extension to other LEOs delivering NRT data, what was demonstrated by inclusion of the TerraSAR-X data already 3 months after the launch of the satellite on June 15, 2007. The variety of the approaches to the NRT orbits (three independent chains for each of the LEOs) enhances the reliability of the system. The system is fully operational and automatic, requires however non-negligible human activities to account for new unexpected situations affecting the automatic processing.

Acknowledgments We thank the CHAMP, GRACE and TerraSAR-X teams for their great work to guarantee the availability of GPS SST data. The described near-real time activities at GFZ are supported by the German Ministry for Education and Research within the GEOTECHNOLOGIEN programme (Research project NRT-RO/No. 1262) and also by GFZ.

References

König R, Michalak G, Neumayer K H, Schmidt R, Zhu S Y, Meixner H, Reigber C (2005) Recent developments in CHAMP orbit determination at GFZ. In: Reigber C, Lühr H, Schwintzer P, Wickert J (eds.), Earth Observation with CHAMP. Results from Three Years in Orbit, Springer, Berlin.

Michalak G, Baustert G, König R, Reigber C (2003) CHAMP rapid science orbit determination – status and future prospects. In: Reigber C, Lühr H, Schwintzer P (eds.), First CHAMP Mission Results for Gravity, Magnetic and Atmospheric Studies, Springer, Berlin.

Michalak G., Wickert J, König R, Rothacher M (2007) Precise satellite orbit determination for GPS radio occultation in near-real time (NRT). European Geosciences Union General Assembly 2007 Vienna, Austria, 15–20 April 2007, Poster EGU2007-A-08740.

Wickert J, Michalak G, Schmidt T, Beyerle G, Cheng C Z, Healy S B, Heise S, Huang C Y, Jakowski N, Köhler W, et al. (2009) GPS radio occultation: results from CHAMP, GRACE and FORMOSAT-3/COSMIC. Terr. Atmos. Ocean. Sci. 20, doi: 10.3319/TAO.2007.12.26.01(F3C).

The Operational Processing System for GPS Radio Occultation Data from CHAMP and GRACE

Torsten Schmidt, Jens Wickert, and Grzegorz Michalak

1 Introduction

The GPS radio occultation (RO) technique has established as an excellent method for global and continuous monitoring of the Earth's atmosphere (Melbourne et al., 1994; Anthes et al., 2008). During the last 2–3 years most of the weather service centers worldwide have begun to assimilate RO data in their global and/or regional weather models (Healy et al., 2007).

The use of analysis results obtained from RO data, as e.g. atmospheric excess phases, bending angles or refractivity profiles, by weather prediction centers requires an operational data processing system generating and delivering data products automatically within a certain time limit. Such a continuous Near-Real Time (NRT) data processing system, the CHAMP (GRACE) Atmospheric Processor (in the following the acronym CAP is used for both, the CHAMP and GRACE processing system), is operating at GFZ Potsdam with RO data from the German CHAMP and the US–German GRACE satellite missions (Reigber, 1998).

Because of different user demands with respect to the availability of RO products two data processing modes were introduced: a NRT mode and a standard mode. Currently in the NRT processing mode the daily averaged time delay between occultation measurements and availability of analysis results for the weather service centres via the GTS (Global Telecommunication System) is less then 2 h for about 75% and less than 3 h for about 90% of all daily products. In the standard processing mode quality checked profiles of atmospheric parameters are available with a latency of about 2 days.

The realization of CAP follows the principle of separating the processing system into a scientific and controlling part leading to an independent and more flexible software development. The CAP is designed to be easily extendable by additional scientific modules or input data. Thus, it also allows for an extension to other single- or multi-satellite radio occultation missions, as e.g. COSMIC or TerraSAR-X.

T. Schmidt (✉)
Helmholtz Centre Potsdam, GFZ German Research Centre for Geosciences,
Department 1: Geodesy and Remote Sensing, Telegrafenberg, 14473 Potsdam, Germany
e-mail: tschmidt@gfz-potsdam.de

F. Flechtner et al. (eds.), *System Earth via Geodetic-Geophysical Space Techniques*,
Advanced Technologies in Earth Sciences, DOI 10.1007/978-3-642-10228-8_40,

This chapter is focused on the controlling components of the CAP that generate a continuous data flow between the scientific software modules and the user. Further, we concentrate on the description of the NRT part of the processing system.

2 Infrastructure and Input Data

The generation of RO products requires a complex infrastructure. It was developed with the start of RO measurements aboard CHAMP in 2001, and since then maintained and extended for, e.g., GRACE (2002) and other satellite missions (TerraSAR-X in 2007).

The main components of the infrastructure are (Fig. 1):

- the Black-Jack GPS receiver (provided by NASA/JPL) onboard CHAMP,
- three downlink stations receiving CHAMP data (Neustrelitz and Weilheim, both located in Germany, and Ny-Aalesund in Spitsbergen, Norway) in cooperation with DLR,
- the fiducial low latency and high rate GPS ground network operated in cooperation between GFZ and JPL,
- an orbit processing facility for determination of NRT orbits for the GPS satellites and CHAMP,
- the CHAMP/GRACE Atmospheric Processor generating CHAMP/GRACE radio occultation data products, e.g., atmospheric excess phases, profiles of bending angle, refractivity, temperature, and humidity (Wickert et al., 2001), and
- the CHAMP Information System and Data Center (ISDC) archiving and distributing CHAMP data and analysis results.

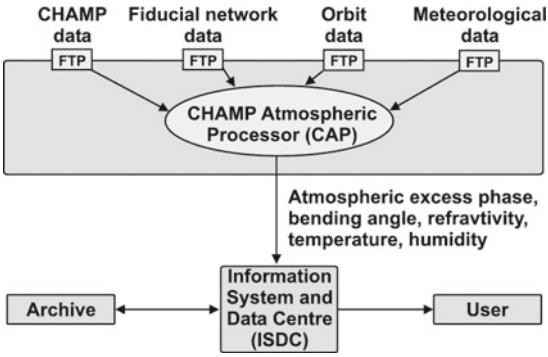

Fig. 1 Infrastructure and input data for GPS radio occultation data processing from CHAMP

3 The CHAMP/GRACE Atmospheric Processor

The goal of the CAP is to coordinate the different data streams and to start the various scientific applications automatically when all input data for an application are available. The CAP is a modular structured and dynamically configurable software

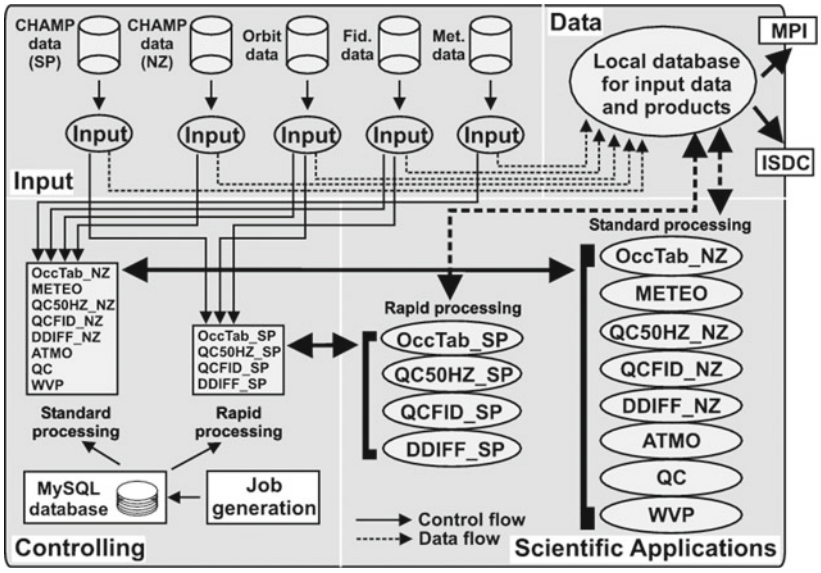

Fig. 2 Schematic view of the CHAMP atmospheric processor at GFZ Potsdam

package consisting of a scientific and controlling part (Fig. 2). Thescientific software modules (e.g. DDIFF, ATMO) calculate the atmospheric excess phases and vertical atmospheric profiles. The controlling components ensure the continuous data flow of all input data through the scientific analysis modules and provide the interface for feeding the RO products into the data center (ISDC) or directly to the German Weather Service (DWD) who puts the data to the Global Telecommunication System (GTS) since July 2007.

CAP runs on multiple UltraSparc II/III processor machines and is a combination of different subroutines and scripts written in C++, Fortran, IDL, Perl, and C-Shell.

4 Standard and NRT Processing

The processing of RO data at GFZ Potsdam is divided into two parts (Fig. 2):

- the standard processing using CHAMP/GRACE data via the dump stations Neustrelitz and Weilheim (Germany) and Rapid Science GPS and CHAMP/GRACE Orbits (RSO) (König et al., 2002),
- the NRT processing using CHAMP/GRACE data via the polar dump station at Ny-Aalesund, Spitsbergen and NRT Science Orbits (Michalak et al., 2007).

These two modes are necessary due to demands on product availability. The availability of RO data products, i.e., the time delay between measurement and delivery of products to the data center or user, depends on two factors: (1) the

moment at which all input data for the respective applications (Fig. 2) are available and (2) the duration that CAP needs to process the input data and generate products. The NRT data user (e.g., DWD) require a data availability within a time window of less than 3 h.

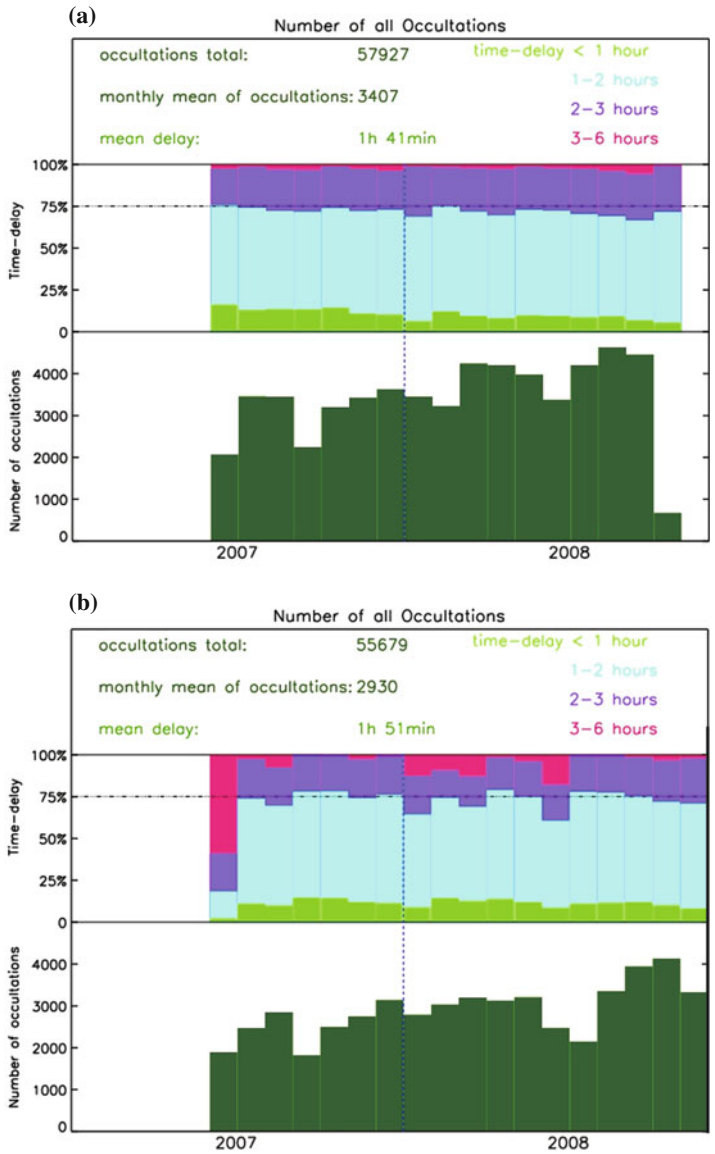

Fig. 3 Number of monthly CHAMP (**a**) and GRACE (**b**) RO data and time delay between measurement and delivering of the data to the DWD (GTS) from the NRT processing since June 2007

The first point is fulfilled due to the installation of a polar dump station. This enables a contact to CHAMP about every 90 min. Since 2006 the GPS and CHAMP/GRACE satellite orbits are available at latest 30–40 min after the according dump. These NRT orbits cover a 3 h time window.

The second point (duration of data processing) is uncritical, because the processing of one dump with about 10–20 RO events takes less than 5 min.

Figure 3 shows the number of monthly CHAMP/GRACE RO data and the time delay between measurement and delivering of the data to the DWD (GTS) from the NRT processing mode since June 2007. At this time the continuous data transfer of GPS RO products from GFZ to worldwide weather centers has started.

The averaged time delay between CHAMP or GRACE measurements and data product delivery is less than 2 h. For about 10–15% of the products a time delay less than 1 h is reached (Fig. 3).

5 Summary

The CAP enables an operational data processing and the delivery of analysis results to the data center or directly to the user. Since June 2007 (start of NRT product delivery) more than 100,000 CHAMP and GRACE RO products, as bending angles or temperature profiles have been generated (about 150 daily, as of January 2009).

Due to the modular structure CAP is suitable for easy extension to other single- or multi-satellite RO experiments.

In the standard processing mode quality checked products (refractivity and temperature profiles) are available with a latency of about 2 days. A near-polar receiving station at Spitsbergen and a dump-oriented CHAMP/GRACE and GPS orbit production cycle made it possible to implement a NRT processing at GFZ Potsdam for the first time. Since mid-2007 GPS RO products with an averaged time delay of less than 2 h between measurement and availability of the analysis results are generated and transferred continuously.

Acknowledgments This study was carried out in the Geotechnologien program under the grant of the German Federal Ministry of Education and Research.

References

Anthes RA, Bernhardt PA, Chen Y, Cucurull L, Dymond KF, Ector D, Healy SB, Ho SP, Hunt DC, Kuo YH et al. (2008) The COSMIC/FORMOSAT-3 mission: Early results. Bull. Amer. Meteor. Soc. 89, 1–21.

Healy SB, Wickert J, Michalak G, Schmidt T, Beyerle G (2007) Combined forecast impact of GRACE-A and CHAMP GPS radio occultation bending angle profiles. Atmos. Sci. Lett. 8, 43–50.

König R, Zhu SY, Reigber C, Neumayer KH, Meixner H, Galas R, Baustert G, Schwintzer P (2002) CHAMP rapid orbit determination for GPS atmospheric limb sounding. Adv. Space Res. 30(2), 289–293.

Melbourne WG, Davis ES, Hajj GA, Hardy KR, Kursinski ER, Meehan TK, Young LE (1994) The application of spaceborne GPS to atmospheric limb sounding and global change monitoring, JPL Publication, 94-18, Jet Propulsion Laboratory, Pasadena, California.

Michalak G, Wickert J, Koenig R, Rothacher M (2007) Precise satellite orbit determination for GPS radio occultation in near-real time (NRT), EGU2007-A-08740 abstract.

Reigber C (1998) GPS Atmosphere sounding: An innovative approach for the recovery of atmospheric parameters, HGF Strategy fund proposal, Potsdam, Germany.

Wickert J, Reigber C, Beyerle G, König R, Marquardt C, Schmidt T, Grunwaldt L, Galas R, Meehan TK, Melbourne WG et al. (2001) Atmosphere sounding by GPS radio occultation: First results from CHAMP. Geophys. Res. Lett. 28, 3263–3266.

Assimilation of CHAMP and GRACE-A Radio Occultation Data in the GME Global Meteorological Model of the German Weather Service

Detlef Pingel, Andreas Rhodin, Werner Wergen, Mariella Tomassini, Michael Gorbunov, and Jens Wickert

1 Introduction: Data Assimilation

Prior to a numerical weather forecast run, the state of the meteorological model has to be updated using observational information. This operation is called the assimilation step in the process of weather forecasting. Common observational data sources include in-situ data such as radiosondes, weather station measurements, data from aircrafts and buoys. In the meantime, satellite remote-sensing measurements play a major role in weather prediction. Most remote-sensing observations are radiances of a given wavelength at nadir. Radio occultation data, however, are a relatively new source of observational information. Quantities that describe an occultation process, like bending angles of the individual rays or the refractivity field, depend directly on the temperature and the humidity along the ray's path. Therefore, radio occultations can be assimilated in order to include additional information on temperature and humidity into the model. They have been proven to be a valuable source of information in atmospheric research and weather prediction (Wickert et al., 2009; Healy et al., 2007b).

The information of radio occultations about the earth's atmosphere is complementary to radiance observations in several senses: whereas temperature and humidity retrievals derived from radiances have a relatively low vertical resolution, the radio occultation observations are sensitive to vertical structures on a much smaller scale. Unlike radio occultation, radiance measurements generally fail in cloudy areas (McNally, 2002). Another beneficial property is the lack of fundamental biases, which is an advantage when taking into account the elaborate procedure of radiometer calibration, and the nearly uniform global coverage.

At the German weather service, the assimilation of radio occultation data is performed by the three-dimensional variational (3D-Var) assimilation method (Daley and Barker, 2000), which was recently introduced as the operational global assimilation scheme. The assimilation of observational data is done in a statistically optimal

D. Pingel (✉)
Deutscher Wetterdienst, DWD, Offenbach, Germany
e-mail: detlef.pingel@dwd.de

F. Flechtner et al. (eds.), *System Earth via Geodetic-Geophysical Space Techniques*, Advanced Technologies in Earth Sciences, DOI 10.1007/978-3-642-10228-8_41,

way, taking into account the observations, the preceding forecast and error characteristics of both model and observations. Therefore, a thorough specification of observational and forecast errors is of high relevance in data assimilation. Within the assimilation process, a cost function containing penalty terms for deviances of the analysis state both from the background and the observations is minimized as a function of the analysis. For the 3D-Var, this numerical minimization is performed in observation space. This has two advantages in comparison with a minimization in model space: First, it reduces the size of the numerical problem, as the number of model grid points generally outnumbers the number of observations. The second advantage is related to the necessity to apply a function to the model data, in order to obtain first guess values in the observation space. This transition from model to observation space allows to consider observations which depend on the model background data in a highly nonlinear way, such as satellite radiances and radio occultations. Therefore, the prognostic variables of the atmospheric model such as temperature and humidity fields are to be related to the radio occultation data.

The radio occultation data can be processed to a different degree in order to be compared to the model background (see Fig. 1). Raw measurements include the phase delay which the radio signal builds up on its way through the ionosphere and atmosphere, together with the corresponding amplitude. Along with the time delay of the radio signal, the direction of propagation of the signal is slightly bended towards the centre of the earth due to the vertical gradient of the atmosphere's refractivity. Numerical methods using geometrical optics or more sophisticated approaches like the canonical transform method convert the time-dependent phase information into a vertical profile of bending angles. Profiles of refractivity can be

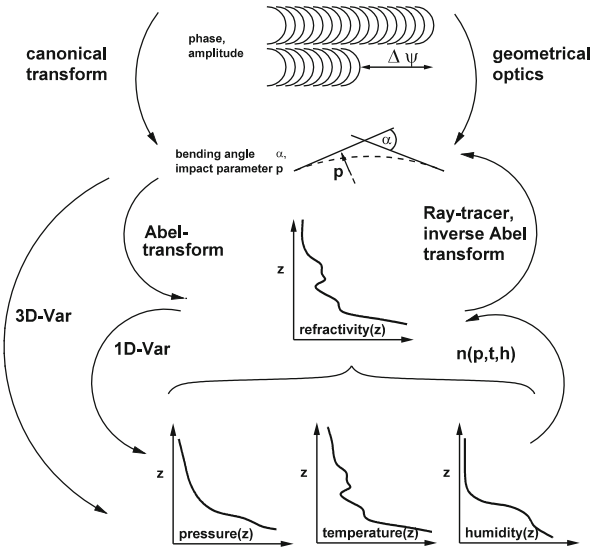

Fig. 1 Observational quantities related to GPS radio occultation data

retrieved via the so-called Abel transform. The refractivity field itself can be related to observational counterparts of the original radio signal in terms of the model variables pressure, temperature and humidity. This step can be performed by e.g. a variational method and includes, as the preceding Abel transform, carefully chosen information from the background model.

For variational assimilation schemes, model counterparts of the observational data are required. The refractivity field is derived from the atmospheric fields of pressure, temperature and humidity in a straightforward way. Based on the refractivity field, bending angles profiles can be derived by the inverse Abel transform, or, in a more refined way, by use of an optical ray-tracing propagator.

Basically, phase delay, bending angles or refractivity fields can play the role of the observations to be assimilated. At the DWD, bending angles have been chosen as observations, as they allow for a reliable specification of significant background and observational errors. Hence a forward operator is to be implemented to map the model background at the location of the observation to the corresponding first guess bending angle.

2 Activities of the DWD in the NRT-RO Project

The first objective of the DWD participation in the Near Real Time-Radio Occultation (NRT-RO) research project was to find a reasonable setup for the forward observation operator that is suitable for data assimilation under the specific terms of operational application. The assimilation setup was then put to the test in assimilation experiments, assessing the impact of the radio occultation observations on the weather forecast quality. Accompanying these experiments, a long-term monitoring of the radio occultation observations was arranged. To this end, the statistical parameters of the differences of observations and background values (O-B) were determined on a monthly basis.

3 Evaluation of Bending Angle Forward Operators

The evaluation of a possible forecast operator setup is a prerequisite for both the accomplishment of the monitoring as well as for the assimilation experiments of radio occultation observations. Two intrinsically different models have been considered to serve as forward operators: A three-dimensional ray tracing model and a one-dimensional model.

The ray-tracing model is supposed to be the best fit to the physical reality, as it takes into account the horizontal gradients of the temperature and humidity atmospheric fields as well as the drift of the ray's tangential points in the course of an occultation (Gorbunov and Kornblueh, 2003) (Fig. 2d). A certain disadvantage of the ray-tracing operator is the high demand of computing resources (both of time and memory).

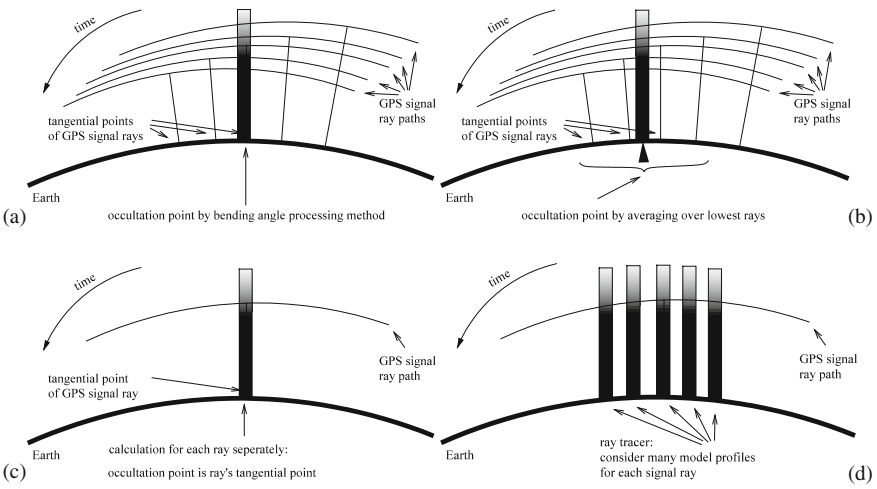

Fig. 2 Design of the bending angle forward operators (schematic), one-dimensional (**a**) H_{1d}, (**b**) H_{1dmn}, (**c**) H_{2d}), and three-dimensional ray-tracer (**d**) H_{3d}). For details see the explanations in the text

The one-dimensional forward operator is based on the assumption of spherically symmetric atmospheric fields. It applies an inverse Abel transform to the refractivity profile that is derived from the temperature and humidity profile at a single point, the occultation point. The reduction of the horizontally extended occultation event to a single point ignores the fact of the tangential point drift. Furthermore, the choice of this occultation point introduces a certain indefiniteness to the forward model. To model the drift of the tangential points at least to some extent, three modifications of the one-dimensional forward operator have been implemented for test purposes, each of them considering a differently determined occultation point:

The first modification performs the inverse Abel transform at the occultation point as given in the corresponding observation data set of bending angles (Fig. 2a). For the second modification, the occultation point is determined as the mean of the individual ray's tangential points in the lowest 20 km of the occultation profile (Fig. 2b). The third modification applies the inverse Abel transform to each ray of the occultation profile separately (Fig. 2c). This approach is expected to model the tangential point drift best compared to the two preceding modifications.

The data set to test the performance of the different forward operators is a CHAMP phase delay data set (phase delays by the GeoForschungsZentrum Potsdam GFZ). It is processed to yield bending angles with the method of canonical transform (CT2, Gorbunov and Lauritsen, 2002, 2004a, b; Gorbunov, 2004; Gorbunov et al., 2006) at the DWD. It contains bending angles and observation error estimates from the 2 months January and June 2005. The monitoring is performed, using the

DWD global meteorological model GME (Majewski et al., 2002) tree-hourly forecast fields as model background. The statistical properties of the innovations, i.e. of the differences of observation and first guess, are then taken into account to evaluate the different forward operators.

Figure 3a–c shows zonal averages (impact height vs. latitude) of the ratio of the (O-B) standard deviation of the three versions H_{1d}, H_{1dmn} and H_{2d} of the one-dimensional forward operator to the respective value of the three-dimensional ray-tracing operator H_{3d} for January 2005 (bin size: 1 km · 10° latitude). For all three one-dimensional forward operators, the values of the ratios are larger than unity for most areas and heights (they are strictly larger than unity when considering global means). This indicates the better performance of the ray-tracing forward operator in terms of standard deviation.

When comparing the different one-dimensional forward operators, the operator H_{1d}, accepting the occultation point as given by the CT2 method, performed poorest (Fig. 3a). The corresponding standard deviation exceeds the respective value for H_{3d} by up to 8%. However, the ratio is significantly smaller for the tropics compared to

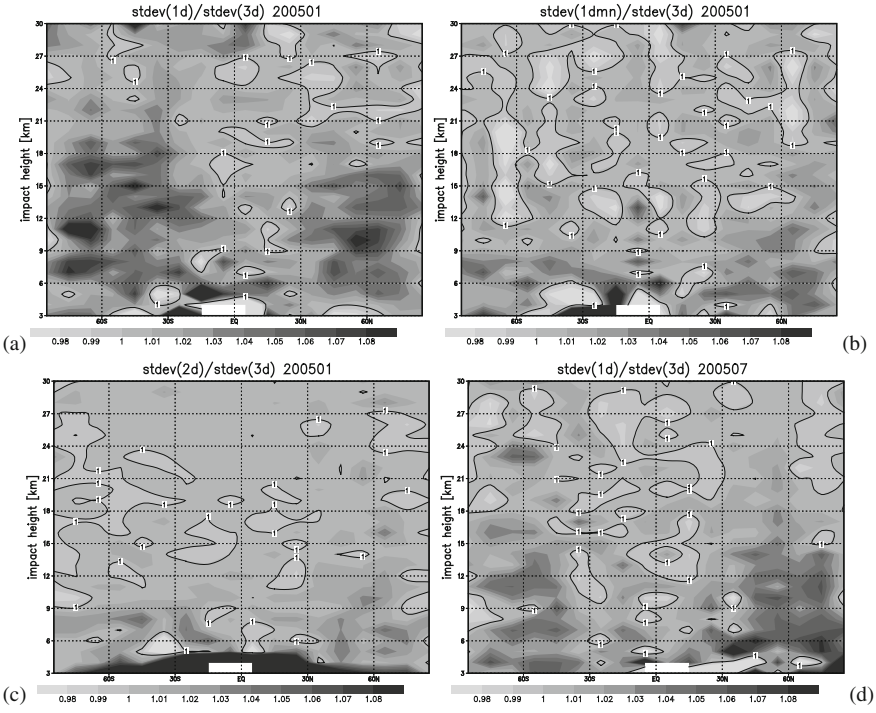

Fig. 3 Ratio of the O-B standard deviation of the three modifications of the inverse-Abel-transform bending angle forward operator to the respective value of the three-dimensional ray-tracing operator

the extra tropics. This is related to the fact that due to differences of the atmospheric dynamics horizontal gradients of temperature and humidity are less pronounced in the tropics than in the extra-tropics. As the sensitivity for these gradients is one of the characteristics of the operator H_{3d} compared to H_{1d}, the bending angle values of the one- and three-dimensional operators tend to be comparable in the tropics.

Compared to the operator H_{1d}, the operator H_{1dmn} shows a reduced standard deviation for impact heights above ca. 8 km (Fig. 3b). This indicates that the averaging process brings the occultation point closer to the tangential points of the rays in the upper troposphere and lower stratosphere.

The first guess values of the version H_{2d}, applying the inverse Abel transform to each individual ray, are closest to the ray-tracing results (Fig. 3c) as expected. Above an impact height of ca. 10 km, the difference to the operator H_{3d} is less than 1% for most areas. Additionally, the ratio of the standard deviations is more uniform for H_{2d} than for H_{1d} and H_{1dmn}.

However, for the lowermost rays especially in the tropical latitudes, the more refined version H_{2d} performs worse than the more simple versions H_{1d} and H_{1dmn}. This effect might be related to the fact that for most occultations events the positions of the tangent points of the lowest lying rays lie off the more or less straight line described by the successive tangent points of higher rays. These "kinks" might be an inappropriate choice as a location for georeferencing points when the H_{2d} forward operator is applied. A thorough investigation of this effect is necessary, though.

Below an impact height of ca. 8 km, the ray tracing forward operator H_{3d} is significantly better than any of the one-dimensional forward operators in terms of standard deviation. This may be attributed to the fact that below this height the bending angle signal contains predominantly humidity information (especially in the tropics). Water vapor is, contrary to temperature, a quantity that fluctuates significantly on a horizontal scale comparable with the extent of the occultation. These fluctuations are considered for by the operator H_{3d}, but not by the one-dimensional forward operators.

Figure 3d shows the same quantity as Fig. 3a, but for July 2005. The shift of the maxima of the ratio of the standard deviations in the lower troposphere towards the north is clearly visible, corresponding to the increase of humidity in these region in the summer of the northern hemisphere.

Although there are significant differences on the level of innovation statistics, the overall deviances of the optimized one-dimensional forward operators from the ray tracing result are only minor (1–2%) for impact heights above 8 km. As the statistical weight of GPS RO observations is small below this height (large observation errors due to humidity gradients), this suggests the usage of an appropriately optimized one-dimensional bending angle forward operator for the operational assimilation, in agreement with results of other studies (Healy et al., 2007a; Poli and Joiner, 2006). For the following monitoring and assimilation experiments, optimized one-dimensional forward operators are applied rather than the ray-tracing operator.

4 Monitoring

In a long-term monitoring process, the bending angle observations are compared with the corresponding background equivalents, derived from the forecast fields of the GME by application of the H_{1dmn} modification of the one-dimensional inverse Abel transform forward operators. Near real time bending angle data sets of CHAMP and GRACE-A by the GFZ and COSMIC by COSMIC/UCAR (University Corporation for Atmospheric Research) are considered. In addition, a third data set is generated by applying the CT2 method (at the DWD) to NRT phase delay data sets of CHAMP and GRACE-A from GFZ for selected months. The CT2 method allows to estimate values of the bending angle observational error, which are not included in the near real time bending angle data set from GFZ. Thus, additional statistical information on the occultation data is gained.

The statistical properties of the corresponding differences, the innovations, are taken into account to assess the consistency of model and observational bending angle values and corresponding error estimates. To remove outliers, a basic first-guess check is performed.

As the CHAMP and GRACE-A near real time data not yet include estimates for the observational error, a simple, partially linear functional dependence of the observation error on the impact height is assumed (Healy and Thépaut, 2006) (Fig. 4a). This observation error model is in contrast to the zonally varying observation error for CHAMP and GRACE-A, derived by the CT2 method (Gorbunov, 2002; Gorbunov et al., 2006) (Fig. 4b) and COSMIC (TACC, 2007a, b) (Fig. 4c).

Figure 5 shows zonally averaged means of statistical parameters of the (O-B) innovations of the combined CHAMP and GRACE-A near real time bending angle data set of July 2007. In general, the CHAMP and GRACE-A observed bending angles agree with the corresponding background equivalents reasonably well and within the assumptions made for the background and observation error in the assimilation system. The estimated observational errors (Fig. 4) are considerably smaller than the model background errors (Fig. 5a), especially in the upper troposphere of the extra tropics. This is probably due to an overestimation of the background

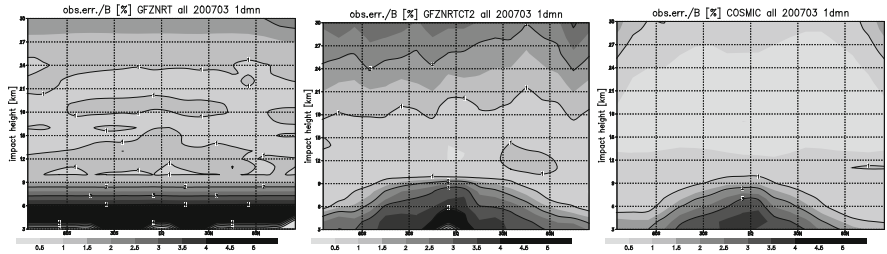

Fig. 4 Estimated bending angle observation error for (**a**) CHAMP/GRACE-A (functional approach, bending angles by GFZ), (**b**) CHAMP/GRACE-A (phase delay by GFZ, bending angles by CT2 at DWD), (**c**) COSMIC (bending angles by UCAR/CDAAC)

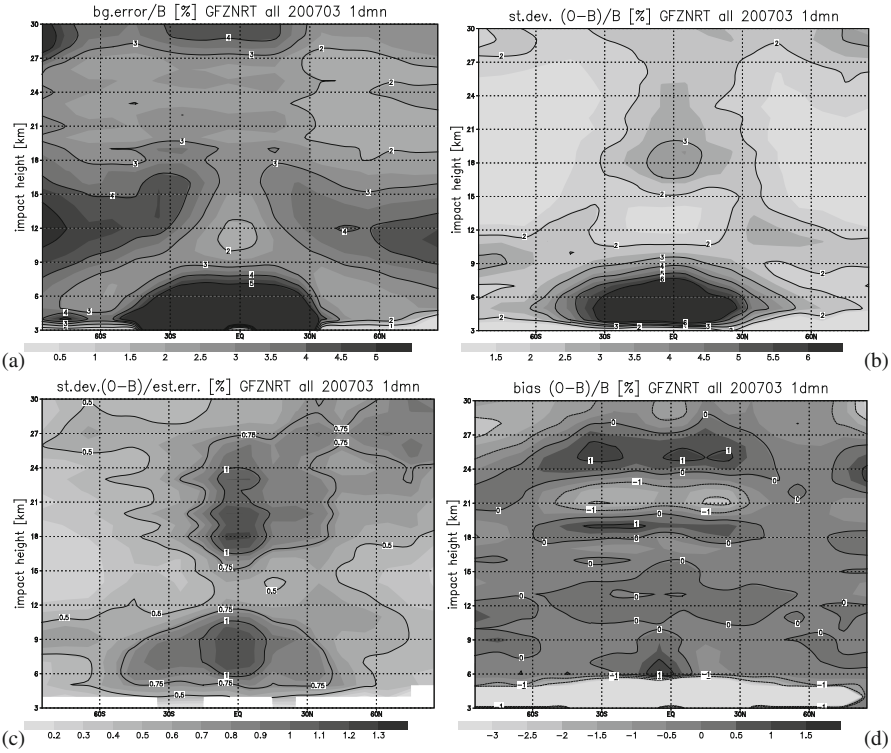

Fig. 5 (**a**) Estimated relative bending angle background error in the GME model, (**b**) standard deviation of innovations, (**c**) ratio of standard deviation of innovations (O-B) with respect to the estimated standard deviation and (**d**) bias of innovations for the CHAMP and GRACE-A data set and forward operator H_{1dmn} (percentage of first guess value in (**a**), (**b**), (**d**))

error in these regions and implies a relatively high statistical weight of the radio occultation observations in the assimilation process.

Figure 5b displays the actual (O-B) standard deviation of the observation data set. Generally higher values in the lower latitudes indicate the more pronounced influence of the tropical humidity. A maximum of the standard deviation at the impact height of ca. 18 km in the tropics is caused most certainly by the presence of gravity waves. The deviations above 25 km result from the ionospheric fluctuations which can only be partly corrected in the retrieval process.

The quadratic sum of the observation error and background error estimate is an estimate for the expected standard deviation of the O-B statistics. The ratio of the actual standard deviation with respect to the estimated error (Fig. 5c) is less than one for most areas and height levels, indicating a better agreement of observations and background values than estimated from the error specification of the assimilation system. In some regions, e.g. the upper tropical troposphere, the relatively high value of the (O-B) standard deviation might be explained by the occurrence of gravity

waves. The bias of the innovations is reasonably small, but shows a remarkable vertically oscillating pattern in the upper troposphere and stratosphere in the tropics and mid-latitudes (Fig. 5d).

5 Assimilation Experiments

The assimilation setup, including the optimized bending angle forward operator, is tested in an assimilation experiment. The experiment assesses the impact of the radio occultation observations from CHAMP, GRACE-A and the six FORMOSAT-3/COSMIC satellites on the weather forecast quality. It is carried out for the time of March 2008 with assimilation intervals of 3 h. In the experiment, the radio occultation bending angles of the above-mentioned satellites are assimilated together with conventional in-situ-data and AMSU-A radiance observation data. In the corresponding control experiment, conventional data and radiances are the only observational source. Subsequent forecast runs are performed to assess the impact on the forecast results.

The forecast quality can be quantified by the anomaly correlation coefficient (ANOC) of an atmospheric field. It measures the correlation of deviances of the forecasts with those of the coinciding analysis with respect to the model climatology. The larger the value of the ANOC is, the closer is the forecast to the analyzed value. A value of 0.6 is agreed to be the lower limit for forecasts with significant synoptic information.

Figure 6 shows the anomaly correlation coefficient for the control experiment and the experiment additionally including radio occultation observation for 18 forecasts. They are calculated for the (a) tropical region (based on the temperature field at 850 hPa) and the (b) southern hemisphere (based on the geopotential field at 500 hPa). In terms of the anomaly correlations, the assimilation of radio occultation results in a significant increase of the ANOC in the southern hemisphere. A similar

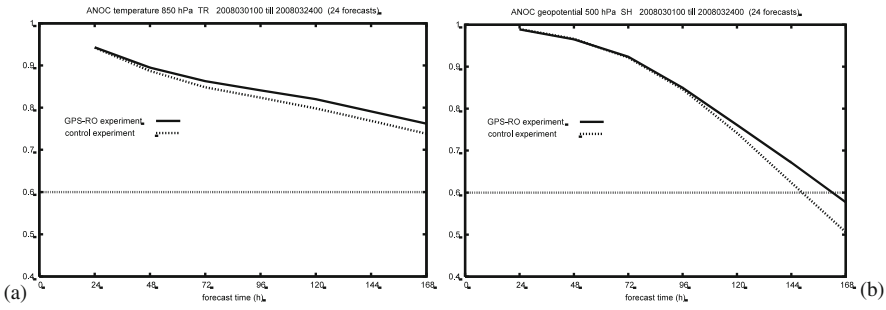

Fig. 6 Impact of radio occultation data on forecast quality: Assimilation of radio occultation data results in an increase of the anomaly correlation coefficient (ANOC) in the (**a**) tropical region and the (**b**) southern hemisphere, which indicates a significant improvement of the forecast scores (see text for details)

result holds for the temperature field. In the northern hemisphere, the assimilation of radio occultation has a smaller (but still slightly positive or neutral) impact in terms on the ANOC of geopotential and temperature. This is most probably caused by the fact that the overall weight of the radio occultation observations is less in the northern hemisphere due to good coverage and high quality of the conventional observation in this region. In addition, the verification of the assimilated temperature and humidity against corresponding measurements of radio soundings and aircraft data shows a significant reduction of the standard deviation for the experiment with assimilation of radio occultation observations.

6 Summary and Outlook

The performance of three different modifications of a one-dimensional and a three-dimensional ray-tracing bending angle forward operator is evaluated for use in a three-dimensional variational data assimilation system. The ray-tracing operator takes horizontal gradients and the ray's tangential point drift into account. The modifications of the one-dimensional operator apply the inverse Abel transform, assuming spherically symmetric atmospheric fields, and reflect the tangential point drift each to a different degree. Considering the standard deviation of the differences of first guess to observed occultation data above the impact height of 8 km, the four forward operators differ by less than 2%. Therefore, a choice of a properly optimized, numerically less expansive one-dimensional forward operator for the use in an operational data assimilation system seems legitimate.

Monitoring of near real time radio occultation bending angle data sets from CHAMP, GRACE-A, and FORMOSAT-3/COSMIC has been carried out for the time of several months. The standard deviations of the observations-first guess differences are well within the error bound estimation of the assimilation system.

An experiment assimilating bending angle observations shows a significant improvement of the forecast quality in the southern hemisphere and proved radio occultation data to be a valuable source of meteorological information.

Acknowledgements We thank the GeoForschungsZentrum Potsdam for reliably providing CHAMP and GRACE-A data sets of radio occultation data, both offline and near real time processed. We thank the FORMOSAT-3/COSMIC project for provision of radio occultation data. We thank Michael Gorbunov for making the CT2 processing method and both bending angle forward operators available to us. The German Ministry for Education and Research supported the research project NRT-RO related to the near real time provision and usage of radio occultation data within the GEOTECHNOLOGIEN research program.

References

Daley R, Barker E NAVDAS Source Book 2000: NRL Atmospheric Variational Data Assimilation System, Naval Research Laboratory, Monterey, Canada, 2000.

Gorbunov ME (2002) Ionospheric correction and statistical optimization of radio occultation data. Radio Sci. 37, RS1084, doi:10.1029/2000RS002370.

Gorbunov ME, Operational processing of CHAMP data: mathematical methods, data filtering and quality control, and software implementations, Report, German Weather Service, 2004.
Gorbunov ME, Kornblueh L: Principles of variational assimilation of GNSS radio occultation data, Report 350, Max-Planck-Institut für Meteorologie, Bundesstrasse 55, D-20146 Hamburg, 2003.
Gorbunov ME, Lauritsen KB: Canonical transform method for radio occultation data, Sci. Rep. 02-10, Dan. Meteorol. Inst. Copenhagen, available at http://www.dmi.dk/dmi/Sr02-10.pdf, 2002.
Gorbunov ME, Lauritsen KB (2004a) Analysis of wave fields by Fourier integral operators and their application for radio occultations. Radio Sci. 39, RS4010, doi: 10.1029/2003RS002971.
Gorbunov ME, Lauritsen KB (2004b) Canonical transform method for radio occultation data. In: Kirchengast G, Foelsche U and Steiner AK (eds.), Occultations for Probing Atmosphere and Climate, Vol. 39, Springer, New York, 61–68.
Gorbunov ME, Lauritsen KB, Rhodin A, Tomassini M, Kornblueh L (2006) Radio holographic filtering, error estimation, and quality control of radio occultation data. J. Geophys. Res. 111.
Healy SB, Eyre JR, Hamrud M, Thépaut J-N (2007a) Assimilating GPS radio occultation measurements with two-dimensional bending angle observation operators. Q. J. R. Meteorol. Soc. 133, 1213–1227.
Healy SB, Thépaut J-N (2006) Assimilation experiments with CHAMP GPS radio occultation measurements. Q. J. R. Meteorol. Soc. 132, 605–623.
Healy SB, Wickert J, Michalak G, Schmidt T, Beyerle G (2007b) Combined forecast impact of GRACE-A and CHAMP GPS radio occultation bending angle profiles. Atmos. Sci. Lett. 8, 43–50.
Majewski D, Liermann D, Prohl P, Ritter B, Hanisch T, Paul G, Wergen W (2002) The operational global icosahedral-hexagonal gridpoint model GME: description and high-resolution tests. Mon. Wea. Rev. 130, 319–338.
McNally AP (2002) A note on the occurrence of cloud in meteorologically sensitive areas and the implications for advanced infrared sounders. Q. J. R. Meteorol. Soc. 128, 2551–2556.
Poli P, Joiner J (2006) Effects of horizontal gradients on GPS radio occultation observation operators. II: A Fast Atmospheric Refractivity Gradient Operator (FARGO). Q. J. R. Meteorol. Soc. 130, 2807–2825.
TACC, Ionospheric data inversion (GMRION): Algorithms for inverting radio occultation signals in the ionosphere, Taiwan Analysis Centre for COSMIC, Central Weather Bureau, Taiwan, http://tacc.cwb.gov.tw/cdaac/doc/documents/gmrion.pdf, 2007a.
TACC, Atmospheric data inversion (ROAM): Algorithms for inverting radio occultation signals in the neutral atmosphere, Taiwan Analysis Centre for COSMIC, Central Weather Bureau, Taiwan, http://tacc.cwb.gov.tw/cdaac/doc/documents/roam05.doc, 2007b.
Wickert J, Michalak G, Schmidt T, Beyerle G, Cheng CZ, Healy SB, Heise S, Huang CY, Jakowski N, Köhler W et al. (2009) GPS radio occultation: results from CHAMP, GRACE and FORMOSAT-3/COSMIC. Terr. Atmos. Oceanic Sci. 20(1), 35–50, doi:10.3319/TAO.2007.12.26.01(F3C).

Part VII
MAGFIELD

The Earth's Magnetic Field at the CHAMP Satellite Epoch

Mioara Mandea, Matthias Holschneider, Vincent Lesur, and Hermann Lühr

1 Introduction

The story of geomagnetism begins centuries ago with the first ideas suggesting that the Earth's magnetic field, itself, resembles a giant magnet. Like a conventional magnet, our Planet has two magnetic poles, which do not coincide with the geographic poles. At the magnetic poles, a compass needle stands vertically pointing either directly towards or away from the magnetic centre of the Earth. A bar magnet loses its magnetic properties over time, but the Earth's magnetic field has been around for billions of years, so something is sustaining it. In reality the Earth differs from a solid magnet, and its magnetic poles are in constant motion as a result of continual fluid convections in its outer core. A century ago, Einstein stressed that the origin of the Earth's magnetic field was one of the greatest mysteries of physics. While our comprehension of the Earth's magnetic field has remarkably improved, the self-sustaining, and somehow chaotic, nature of the Earth's magnetic field remains poorly understood.

At the Earth's surface, a compass needle swings until it aligns along a magnetic North-South direction. In reality, the Earth's magnetic field has a more complex geometry than a pure North–South axial dipole. Traditionally, and for obvious reasons, magnetic observations have been made at the Earth's surface. The magnetic field is thus commonly described in a local reference frame, either using the Cartesian (*X – north*, *Y – east* and *Z – vertical downward*) components, or the angles *D, I* (*declination* and *inclination*).

Nowadays, it is well-known that the observed Earth's magnetic field is the sum of several internal and external contributions (Fig. 1). The dipole dominated core field is more than one order of magnitude stronger than the other contributions (Langel, 1987). This main part of the geomagnetic field is believed to be generated by convective motion in the Earth's iron-rich, electrically conducting, fluid outer core, by

M. Mandea (✉)
Helmholtz Centre Potsdam, GFZ German Research Centre for Geosciences,
Department 2: Physics of the Earth, Telegrafenberg, 14473 Potsdam, Germany;
Now at Universitee Paris Diderot, Institut de Physique du Globe de Paris, France
e-mail: mioara@gfz-potsdam.de

F. Flechtner et al. (eds.), *System Earth via Geodetic-Geophysical Space Techniques*,
Advanced Technologies in Earth Sciences, DOI 10.1007/978-3-642-10228-8_42,

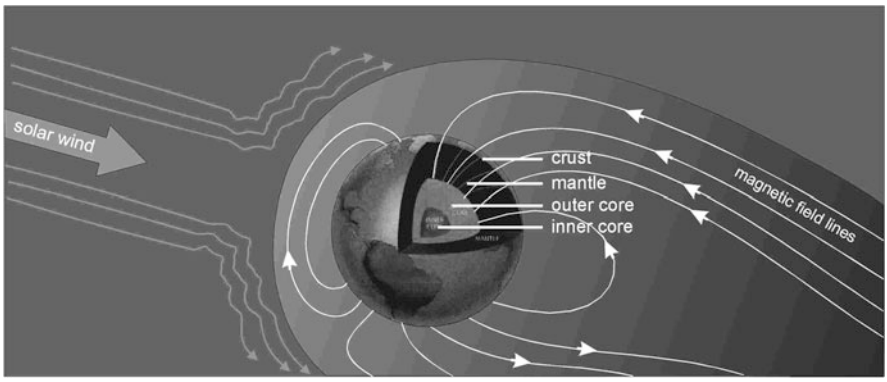

Fig. 1 Contributions in the Earth's magnetic field are internal (outer core and crust (lithosphere)) and external (ionosphere and magnetosphere) in origin

a process known as the geodynamo. This process is not fully understood, because a few indirect observations exist to constrain it, only. According to the dynamo theory, the observed magnetic field is a product of this process, and its structure within the core is very complex. This geodynamo generated field is named *core field* or *main field*, and its temporal variation, over time scales from decades to centuries, is named *secular variation*. So, one can consider that the core field morphology at the Earth's surface is relatively simple, being dominated by a dipole-like field, inclinated with respect of the Earth's rotation axis, and which accounts for some 90% of the total field.

The *lithospheric (crustal) magnetic field*, with its origin in the remanent and induced magnetization of the crust and upper mantle, is not only weaker, but also of much smaller spatial scale, when compared to the large scale core field. Its complexity goes back to geological and tectonic origins (Mandea and Purucker, 2005), and depends on magnetic minerals, mainly magnetite with varying content in titanium. The titano-magnetite constituents have a Curie temperature in order of some 600°C, above which they become essentially non-magnetic. Therefore, the lithospheric magnetization is limited to a layer of about 7–50 km in thickness, depending on the local heat flow.

The Earth's magnetic external fields stem from the interaction with the solar wind, which compresses the magnetic field lines on the sunward side and stretches them into a long tail on the night side. Generally, solar wind particles do not cross field lines and are thus primarily deflected around our planet. They may, however, enter the magnetosphere when interplanetary and geomagnetic fields merge during times of increased solar activity, or close to poles where the field-lines are nearly vertical. Their interaction with the atmosphere then causes the well-known aurora. For more information on the geomagnetic field contributions and variations the reader is referred to Gubbins and Herrero-Bervera (2007) and Glassmeier et al. (2009).

An important feature of the geomagnetic field is its variability on many different time scales, from less than a second to millions of years (Mandea and Purucker, 2005). It even changes its polarity. This knowledge relies on various data sources,

ranging from rock magnetization measurements to historic magnetic measurements, and even recent high-quality data provided by magnetic observatories and the magnetic satellites MAGSAT, Ørsted, CHAMP and SAC-C, (Lühr et al., 2009). The combination of ground and continuous satellite measurements allows the core magnetic field and its time variation to be described with a very high resolution in space and in time (Lesur et al., 2008; Olsen and Mandea, 2008). Recent dynamo simulations have contributed significantly to understand the core field geometry and its dynamics, and temporal changes, including excursions and reversals (Christensen and Wicht, 2007; Wicht et al., 2008).

Since the magnetic field changes in space and time, magnetic observations must continually be made, on ground and in space, and models are generated to accurately represent the magnetic field as it is. One of the most difficult tasks is to separate the internal contributions between the part produced in the core and the one produced by the lithosphere (Langel and Hinze, 1998). It is generally agreed that the core contributions are well described up to degree and order 13, when spherical harmonic analysis is used as modeling tool. However, as it has been pointed out many times, features of the lithospheric magnetic field with wavelengths in excess of 3,000 km (spherical harmonic degree 13) are completely obscured by the overlapping core field. Between 2,600 and 3,000 km both core and lithospheric signatures are present, hindering efforts for their separation (Mandea and Thébault, 2007). No method has been found yet to separate completely the two sources. The general practice has been to ignore the crustal contribution below degree 13, and core component above degree 16 (see below). Generally speaking, the previous efforts at their separation of the two fields have failed, and there is a strong reason to believe that the two fields are not completely separable, unless the core field is shut off or changed significantly.

However, recently large improvements have been achieved in resolving the Earth's lithospheric field with spatial scales reaching down to a few hundreds of km in the satellite component of the recently published World Digital Magnetic Anomaly Map (Korhonen et al., 2007). In the following we focus on this field component, with more details on used data (from ground and space platforms), the mathematical tools to represent them (on global and regional scales), and finally the new lithospheric field models and their contributions to a better understanding of the tectonic and geological features.

2 Ground and Space Measurements

Two types of measurements are needed to characterize the geomagnetic field: scalar and vector. The Overhauser magnetometer, a type of proton precession or resonance magnetometer, is typically installed at magnetic observatories, but is also used for some other ground observations and on the Ørsted and CHAMP magnetic satellites. In contrast, vector measurements made with a fluxgate magnetometer are subject to instrument drift. To minimize this drift contribution in the final data, different approaches are used for ground or satellite measurements.

2.1 Ground Measurements

2.1.1 Magnetic Observatories

Historically, magnetic observatories were established to monitor the secular change of the Earth's magnetic field, and this remains one of their most important functions. This generally involves *absolute measurements* that are sufficient in number to monitor instrumental drift of fluxgate magnetometers giving *variation measurements* of the three field components. Over 70 countries operate some 200 observatories worldwide.

A scalar measurement of the field intensity obtained commonly by a proton magnetometer is absolute: this means it depends only on our knowledge of a physical constant and a measurement of frequency, and can be achieved with great accuracy (in excess of 10 ppm). Scalar magnetometers make measurements of the strength of the magnetic field only, and provide no information about its direction. It is also possible to make an absolute measurement of the direction of the geomagnetic field with respect to the horizontal plane (*I – inclination*) and the angle in the horizontal plane between the magnetic North and true North (*D – declination*). This can only be performed with an instrument known as a fluxgate-theodolite (DI-flux) that requires manual operation and takes about 15 min per measurement. The DI-flux consists of a non-magnetic theodolite and a single-axis fluxgate sensor mounted on top of a telescope. The DI-flux is considered to be an absolute instrument, which means that the angles measured by the instrument do not deviate from the true values *D* and *I*. This is achieved by using an observation procedure that eliminates unknown parameters such as sensor offset, collimation angles and theodolite errors. In a land-based observatory, such absolute measurements are typically made once/twice a week and are used to monitor the drift of the fluxgate variometers.

A vector measurement made with a fluxgate magnetometer is subject to instrument drift arising from sources both within the instrument (e.g. temperature effects) and also the stability of the instrument mounting. Because these measurements are not absolute, they are referred to as variation measurements, and the instruments are known as *variometers*. One of the most widely used variometers is the FGE fluxgate manufactured by the Danish Meteorological Institute, Denmark. The sensor unit consists of three orthogonally mounted sensors on a marble cube. In order to improve long-term stability, these sensors have compensation coils wound on quartz tubes, resulting in a sensor drift of only a few nT per year. The marble cube is suspended by two strips of crossed phosphor-bronze working as a Cardans suspension to compensate for pillar tilting that might cause baseline drift. The box containing the electronics is almost magnetic free, and is placed several meters from the sensor to further minimize its effect on the readings. Measurements are made by applying an alternating magnetic field to a material of high-magnetic permeability. The voltage induced in a pickup coil is then measured, and the resulting even harmonics are proportional to the ambient magnetic field in the direction of the coil winding. The magnitude and directional response of these instruments needs to be calibrated against accurately known sources.

All modern land-based magnetic observatories use similar instrumentation to produce similar data products. For a full description, see Jankowski and Sucksdorff (1996) and also the INTERMAGNET web site.[1] The fundamental measurements recorded are averaged 1-minute values of the vector components and of scalar intensity. The 1-minute data are important for studying variations in the geomagnetic field external to the Earth, in particular the daily variation and magnetic storms. Data from a sub-network of observatories are used to produce the Kp and magnetic activity indices. From the 1-minute data, hourly, daily, monthly and annual mean values are produced. The monthly and annual mean values are used to determine the secular variation emulating from the Earth's core. Figure 2 shows the magnetic field evolution for the three components (*X, Y, Z*), and the corresponding secular variation, measured at Niemegk observatory (Germany). It is very clear that the quality of secular-variation estimates (sometimes of the order of a few nT/yr) depends critically upon the quality of the measurements at each observatory.

Installed mainly on continents, the magnetic observatories are very unevenly and sparsely distributed. This is the reason why in some regions, as for example the Pacific, the ground-data based models uncertainty is very large. One possibility for

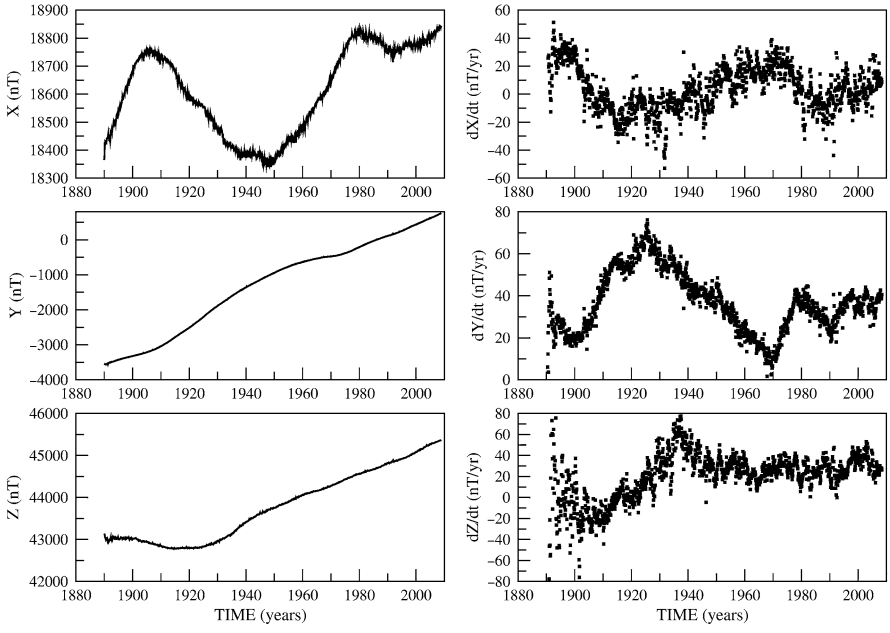

Fig. 2 Temporal evolution of the monthly means for the X, Y, Z components and the corresponding secular variation, recorded at Niemegk observatory (Germany)

[1] www.intermagnet.org

improving the geomagnetic models in such areas is to consider some other sources of data, as those provided by repeat stations or by satellites.

2.1.2 More Ground or Near-Earth Measurements

The network of repeat stations. Because of the temporal changes in magnetic field and the uneven distribution of observatories, at national level repeat station networks exists. However, this is not true everywhere: for example there is not such a network in Russia or in all Central African regions. For a repeat station survey three components of the geomagnetic field are measured (generally the two angular components and the total intensity) at several well-defined points distributed across the considered region. However, unlike at geomagnetic observatories, the field is not continuously recorded, measurements are made at best once per year, often only every 5 years. To obtain final data that is comparable to those provided by the geomagnetic observatories, specific data reduction methods have to be applied. Repeat station data offer better spatial resolution than do observatory data alone, and they are used for a better spatial resolution in global magnetic modeling, lithospheric induction, and conductivity studies, reduction of aeromagnetic surveys, and for describing the lithospheric field (although much denser station networks are needed for that task).

Aeromagnetic surveys. For studying the lithospheric field, detailed features of the magnetic field are required. They are so complicated that observatory or repeat station measurements alone are not adequate. Moreover, dense ground measurements, when existing, are generally inappropriate because of the irregular surface topography and the surface anthropogenic activity that creates artificial magnetic sources in many different places. Therefore, measurements at fixed aircraft altitude and along regular profiles are more convenient. It is extremely difficult to point a fixed direction is space, and therefore, aeromagnetic surveys usually record the strength of the magnetic field; i.e. they are scalar measurements. Aeromagnetic surveys are fast, which reduces the secular variation problem for a given survey. The external field variations are reduced using the nearest magnetic observatory or a fixed base station set up especially for the survey. Aeromagnetic surveys are usually a few kilometers to hundreds kilometers. They are carried out for a variety of purposes. Fields of research include, for instance, investigation of crystalline basement and mineral exploration, for fault and fracture zones or for imaging volcanic structure. Large aeromagnetic surveys with wider profile spacing are devoted to both regional and detailed geological investigations over landmass and continental shelves. They can provide information about the distribution of rocks occurring under thin layers of sedimentary rocks, useful when trying to understand geological and tectonic structures. However, the aeromagnetic measurements are not useful in constraining the secular variation of the core field. As this kind of data is largely used in obtaining a global view of the lithospheric field, more details about the aeromagnetic data, their processing and use are given in the following.

2.2 Satellite Measurements

Since the 1960s, with the American OGO series of satellite, the Earth's magnetic field intensity has been measured intermittently from space at altitudes varying from some 400–1,500 km. The main advantages of satellite compared to airplane are its capability to measure the magnetic field over a rather long period, at a relatively constant altitude and to provide a homogeneous data distribution. Moreover, data are obtained with the same instrument characteristics. In the following, it is illustrated that these properties are extremely valuable for the magnetic field modeling in general and, more precisely, for the lithospheric field description.

The first satellite mission that provided vector data for geomagnetic field modeling was initiated by the National Aeronautics and Space Administration (NASA). The MAGSAT satellite (Langel et al., 1980) operated over a 6-month period between 1979 and 1980, a short period that provided the first consistent, but low resolution, map of the lithospheric field. The following 20 years lacked of high-quality magnetic field missions, but the Danish Ørsted satellite,[2] launched in 1999, improved the situation. However, the primary goals of the mission have been to study the variations of the magnetic field of the Earth and its interaction with the sun particles stream. As a result, the satellite altitude is too high to provide us with a high resolution view of the lithospheric field sources.

Ørsted was followed by the German CHAMP (Challenging Minisatellite Payload) satellite[3] and the SAC-C satellite with the Ørsted-2 experiment, launched in July and November 2000, respectively. All three missions carry essentially the same instrumentation and provide magnetic field observations from space with unprecedented accuracy. Due to the somewhat different altitudes (Ørsted: 630–860 km, CHAMP: 310–450 km; SAC-C: ~700 km) and drift rates through local time, the spacecraft sense the various internal and external field contributions differently.

The most successful mission for magnetic field studies is the CHAMP satellite (Fig. 3), still fully operating in mid-2010, ten years after its launch. Its low-Earth circular orbit is particularly suitable for crustal field mapping. The initial average satellite altitude was 454 km, but the satellite is slowly descending and reaches 330 km altitude in 2009. The lithospheric maps obtained from this satellite experiment are the most robust and have an unprecedented resolution. In the following example, when dealing with satellite data, we mainly rely on the CHAMP satellite mission, and this satellite, its instruments, and data processing are discussed in more detail.

---

[2] http://www.spacecenter.dk/research/solarphysics/orsted

[3] http://www.gfz-potsdam.de/portal/-?$part=sec23

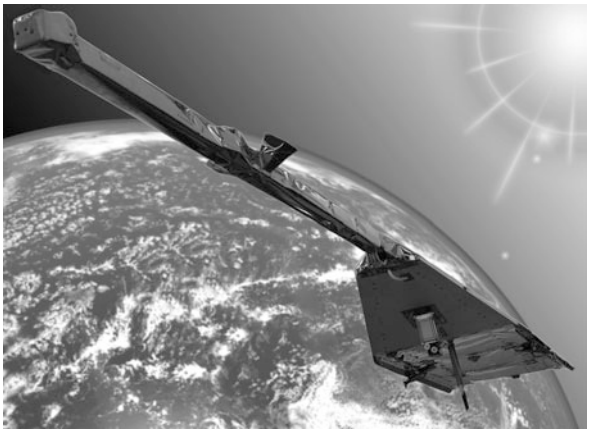

Fig. 3 The CHAMP satellite – photo of the real-size model in Helmholtz-Zentrum Potsdam Deutsches GeoForschungsZentrum, GFZ-Building H

2.3 CHAMP Data Processing

The CHAMP satellite carries a number of scientific instruments: the scalar Overhauser Magnetometer (OVM), the vector Fluxgate Magnetometer (FGM) and two dual-head star cameras (Advanced Stellar Compass, ASC), the Accelerometer (ACC), the GPS receiver, the Digital Ion Drift-Meter (DIDM). In addition, for processing the readings of the scientific instruments, auxiliary information such as temperatures, currents and the precise satellite orbit have to be derived from dedicated sensors. A data processing chain has been developed to routinely generate Level 2 data from all the aforementioned instruments. A first description of the processing approach can be found in Rother et al. (2005). The CHAMP data are made available through the Information System and Data Center (ISDC) at GFZ to the community of approved co-investigators and registered data users.

Data are available at different processing levels, defined in the "CHAMP project". Level 0 are raw data as received by the telemetry. These are densely packed or even compressed in order to allow for an efficient transmission. Level 1 products are decoded and formatted but uncalibrated data, convenient to read by standard codes. They contain the full information of measurements performed in space. Level 2 products are properly scaled and calibrated data, in physical units. Each of these products can be related to a certain instrument. It has to be noted that the definition of the processing levels in the "CHAMP project" is somewhat different from the convention for ESA missions.

In the following some details of the processing steps which are applied for generating the magnetic field Level 2 products are given. The description is ordered by instruments, starting with the raw data, and presents the major steps to achieve the Level 2 products.

2.3.1 Overhauser Magnetometer Data Processing

The CHAMP Overhauser magnetometer (OVM) is regarded as the magnetic reference instrument. Its output frequency is directly proportional, through the

gyro-magnetic ratio, to the ambient magnetic field magnitude. On this mission, it samples the magnetic field at a rate of 1 Hz with a resolution of 0.1 nT. In order to make the readings a traceable standard, the output frequency is compared to a reference oscillator.

Although the OVM readings are highly accurate, they do not simply reflect the Earth's magnetic field. There are magnetic influences from the spacecraft and the instruments which have to be taken into account. The major processing steps for correcting the data are outlined in Fig. 4.

The Level 1 data are the input for the processing. Each reading comes with a time stamp, accounting for the time of transmission from the instrument to the on-board data handling system (OBDH). For the data interpretation it is important to know precisely the epoch at which the reading is valid. Since the satellite is a fast moving platform (7.6 km/s), readings have to be time-tagged with millisecond precision. The relevant time difference has been determined in ground tests. The epoch of the OVM readings is defined as the reference time to which the Level 2 data of all the other instruments, relevant for the magnetic field products, are resampled.

During the processing step 2 the applied scale factor to the magnetic field readings is checked and corrected. For determining the actual frequency of the internal oscillator the cycles are counted within a gate of 60-GPS seconds. To convert the Larmor frequency into magnetic field strength, the gyro-magnetic ratio is applied, as recommended by the International Association of Geomagnetism and Aeronomy (IAGA), during the IUGG General Assembly in Vienna, 1991. With this convention the CHAMP scalar magnetic field readings can be traced back uniquely to the two internationally maintained standards, GPS-second and gyro-magnetic ratio.

The remaining corrections concern the disturbances produced by the satellite. In step 3, all fields adding to the true ambient are considered together. Contributions

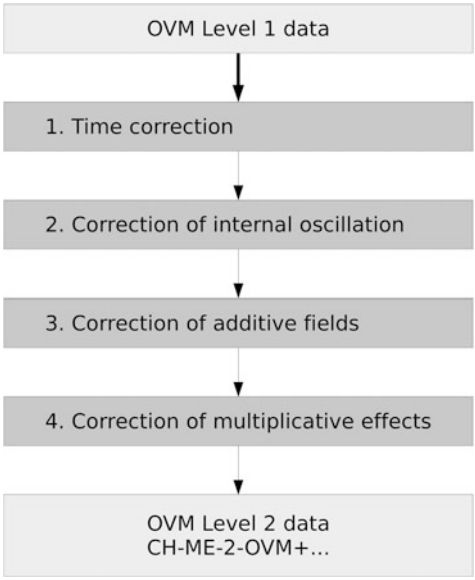

Fig. 4 Schematic flow chart for the processing of the overhauser magnetometer data. For details of the processing steps see the text

come from the remanent magnetization of the spacecraft, from electric currents in the systems, and also from the directional anisotropy of the sensor. These extra fields cannot be simply subtracted. Their influence on the field magnitude has to be determined by finding the projection of the disturbance on the total field vector. Only this projection is considered in the correction. Since the external contributions are small compared to the ambient field, the corrections can be accomplished conveniently using a scalar product between the disturbance vector **b** and the ambient magnetic field vector $\mathbf{B_{FGM}}$, measured by the FGM.

$$|\mathbf{B_{OVM}}| = B_m - \frac{b \cdot \mathbf{B_{FGM}}}{B_m}, \tag{1}$$

where $|\mathbf{B_{OVM}}|$ is the total intensity field corrected for disturbances and B_m is the reading of the OVM. The disturbance vector **b** is the sum of several contributions,

$$\mathbf{b} = \mathbf{b_{SC}} + \mathbf{b_{aniso}} + \mathbf{b_{stray}} + \mathbf{b_{torq}}. \tag{2}$$

The remanent magnetic field of the spacecraft, $\mathbf{b_{SC}}$, has been determined in a pre-flight system test. Since the OVM is mounted at the tip of a 4 m long boom, the remaining effect is only of the order of 0.5 nT. Also the dependence of the OVM reading on the direction of the field vector, $\mathbf{b_{aniso}}$, is rather small (< 0.3 nT). There are some stray fields, $\mathbf{b_{stray}}$, generated by electric currents, e.g. in the solar panels which make effects of less than 0.5 nT. Current readings from the housekeeping data are also needed for this correction. Comparably large are the contributions from the three orthogonal magneto-torquers, $\mathbf{b_{torq}}$, which are used for controlling the spacecraft attitude. These fields reach amplitudes of more than 3 nT at the position of the OVM. Fortunately, they can be predicted quite reliably when the currents through the torquer coils are measured.

$$\mathbf{b_{torq}} = \begin{pmatrix} q_{1,1} & q_{1,2} & q_{1,3} \\ q_{2,1} & q_{2,2} & q_{2,3} \\ q_{3,1} & q_{3,2} & q_{3,3} \end{pmatrix} \begin{pmatrix} I_x \\ I_y \\ I_z \end{pmatrix} \tag{3}$$

Where I_x, I_y, I_z are the currents through the three respective coils and $q_{n,m}$ are the elements of the torquer correction matrix, which have to be determined in the magnetic system test.

In step 4, corrections associated with perturbation proportional to the ambient magnetic field are considered. For CHAMP, these are the permeability of the spacecraft and the cross-talk from the FGM onto the OVM. For considering these effects, a somewhat different approach is needed. Indeed,

$$|\mathbf{B_{OVM}}| = B_m - (dxB_x^2 + dyB_y^2 + dzB_z^2)/B_m \tag{4}$$

where dx, dy, dz denote the modifications in the scaling factors in the vector directions; B_x, B_y, B_z are again the ambient field components as measured by the

FGM. The values of *dx*, *dy* and *dz* are for both effects, S/C permeability and FGM cross-talk, of order 1×10^{-5}. They have also been determined during the system magnetic tests. Fortunately, all three components of the two contributions happen to have similar amplitudes, but opposite signs. Therefore, the total disturbance caused by multiplicative effects is largely cancelled.

After applying the described corrections to the OVM data, they are considered Level 2 and transferred to the data center, ISDC. Based on the fairly small sizes of the various correction terms described above one can conclude that the field magnitudes provided in this Level 2 product are rather reliable. Finally, it is considered that an absolute accuracy of better than 0.5 nT is reached.

2.3.2 Fluxgate Magnetometer Data Processing

The fluxgate magnetometer (FGM) measures the three components of the magnetic field. These vector field measurements are performed at a rate of 50 Hz with a resolution of 0.1 nT. This higher rate is justified by the significantly larger variability of vector components compared to the fluctuations of the field magnitude. The FGM is an analogue instrument; therefore its characteristics are expected to change in response to environmental influences or with time. In order to ensure reliable readings of the vector field components from a multi-year mission, the calibration parameters have to be updated at regular intervals (for CHAMP this is done every 15 days). The in-flight calibration is based on a direct comparison between of the FGM readings with the OVM Level 2 data. Details of the calibration approach are given below.

Figure 5 shows, in a similar way as Fig. 4, the main processing steps applied to the FGM Level 1 data. It starts again with the proper dating of the readings where the delay of the time stamp with regard to the exact epoch of measurement is considered. In step 2 the raw data are converted to physical units with the help of a preliminary set of parameters. The measurements are expected to have a bias and need to be scaled. Firstly, the offset vector is subtracted from the FGM readings, measured in engineering units. Thereafter, the results are scaled into nT. For CHAMP, linear, quadratic and cubic terms are taken into account. As an example, for the x component, one can write:

$$B_{x0} = S_{1x}(E_x - O_x) + S_{2x}(E_x - O_x)^2 + S_{3x}(E_x - O_x)^3 \tag{5}$$

where B_{x0} is an estimation of the magnetic field in the x direction, S_{1x}, S_{2x}, S_{3x} are the scaling factors, E_x are the FGM readings in engineering units, and O_x is the offset in the x direction. The non-linear corrections have been determined in the laboratory before the launch. They are rather small and thus considered to be constant over the mission. Finally, the deviations of the sensor elements from the orthogonality are corrected:

$$\mathbf{B}_1 = \mathbf{C} \cdot \mathbf{B}_0 \tag{6}$$

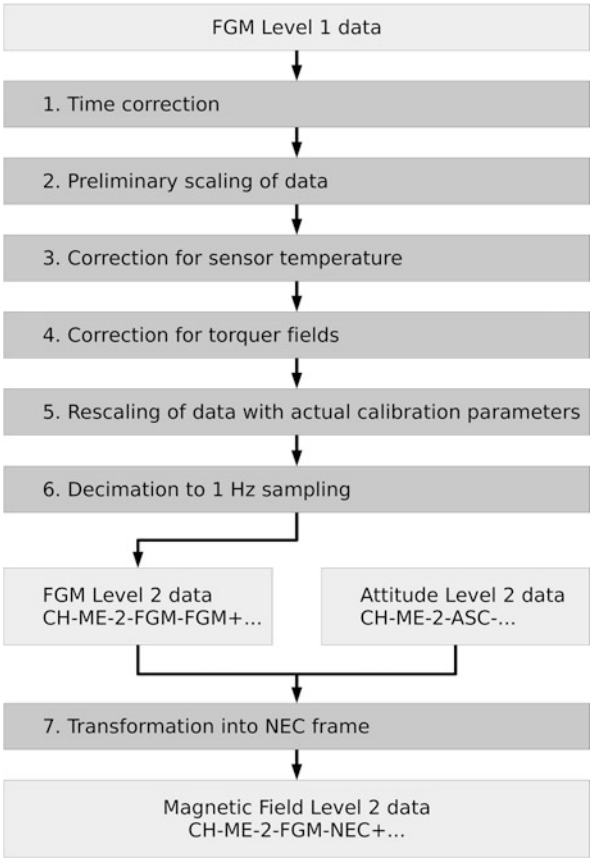

Fig. 5 Schematic flow chart for the processing of the Fluxgate magnetometer data. For details of the processing steps see the text

where **C** is the matrix correcting for the non-orthogonality. This matrix has the form

$$C = \begin{pmatrix} 1 & \cos(x,y) & cox(x,z) \\ 0 & 1 & \cos(y,z) \\ 0 & 0 & 1 \end{pmatrix} \tag{7}$$

where the elements represent the cosine of the angle between respective sensor elements.

Corrections of the environmental influences start with step 3. The sensor changes its geometry with the ambient temperature. This has an influence on the scaling factor. Other parameters, bias and sensor orientation, are not affected by the temperature. In pre-flight tests the temperature coefficients have been determined.

They amount to about 30 ppm/K for all axes. This effect is corrected using the temperature measurements at the sensor place.

During the step 4 the magnetic fields produced by the spacecraft are considered. For the FGM, there is no need to correct for constant or slowly varying influences, such as the remanent and induced magnetic field of the spacecraft: these effects are accounted for in the FGM calibration parameters. However, disturbances varying over short time have to be corrected directly. An example of that is the magnetic field, $\mathbf{B_{torq}}$, caused by the torquer coils.

$$\mathbf{B_{torq}} = \begin{pmatrix} p_{1,1} & p_{1,2} & p_{1,3} \\ p_{2,1} & p_{2,2} & p_{2,3} \\ p_{3,1} & p_{3,2} & p_{3,3} \end{pmatrix} \begin{pmatrix} I_x \\ I_y \\ I_z \end{pmatrix} \tag{8}$$

where $p_{n,m}$ are the elements of the torquer correction matrix for the FGM. As noted before, these elements have been determined during the magnetic system tests. The vector $\mathbf{B_{torq}}$ has to be subtracted from the scaled FGM readings

FGM data corrected to this level are used for the scalar calibration. This calibration against OVM data results in an improvement of the nine FGM processing parameters (3 scale factors, 3 offset values, 3 angles between sensors). The fully calibrated vector data, $\mathbf{B_{FGM}} = \mathbf{B_1} + \mathbf{dB}$, are obtained in this way

$$\mathbf{dB} = \begin{pmatrix} dS_x & \cos(d\langle x,y\rangle) & \cos(d\langle x,z\rangle) \\ 0 & dS_y & \cos(d\langle y,z\rangle) \\ 0 & 0 & dS_z \end{pmatrix} .(\mathbf{B_0} - d\mathbf{O}) \tag{9}$$

where all the quantities preceded by a d are the corrections with respect of the original values and $\mathbf{B_0}$ as it has been defined above.

So far, the processing scheme is applied to the full 50 Hz data set. Before conversion to Level 2 products the vector data are re-sampled to 1 Hz, in order to make them consistent with the scalar data (step 6). This re-sampling is not accomplished by a simple average over the FGM reading within a second. A linear fit to the 100 values centered on the target time has been preferred. The new value is then computed from the derived function at the epoch of the related OVM reading. This procedure is performed individually for all three components.

The new data set is then a Level 2 product accessible through the ISDC. These fully calibrated vector data are useful for certain applications, but they are given in the FGM sensor frame. For that reason during step 7 a transformation of the data into the commonly used NEC frame is done. NEC is a local Cartesian frame having its origin at the position of the satellite. The three components point to geographic north, east and to the centre of the Earth, respectively. A number of rotations have to be performed for this coordinate transformation:

$$\mathbf{B_{NEC}} = R_{(\mathrm{NEC}\leftarrow\mathrm{ITRF})} \cdot R_{(\mathrm{ITRF}\leftarrow\mathrm{ICRF})} \cdot R_{(\mathrm{ICRF}\leftarrow\mathrm{ASC})} \cdot R_{(\mathrm{ASC}\leftarrow\mathrm{FGM})} \cdot \mathbf{B_{FGM}} \tag{10}$$

The rotation angles from the FGM sensor system to the star camera (ASC) are determined before launch. The rotation into the celestial frame, ICRF, is based on the Level 2 attitude data. For the rotation from the ICRF into the Earth-fixed, ITRF frame, the current Earth's rotation parameters are used (as provided by the IERS service), where the satellite position is taken from the precise orbit determination. The final rotation into the NEC frame requires just the satellite position. Magnetic field vector data in the NEC frame are the prime data source for all modeling efforts and for various other applications. Therefore, this is the magnetic field Level 2 product most frequently downloaded from the ISDC.

2.3.3 In-Flight Scalar Calibration

When processing the FGM magnetic field readings for a multi-year mission, in-flight calibration plays an important role. For that reason we present the approach used for CHAMP and the results obtained over its flight-time, in some more detail.

During the calibration process the readings of the OVM are used as a reference. By comparing field magnitude values with those from FGM, the nine principle parameters of the vector instrument can be determined in a non-linear inversion. The basic idea is that the OVM and FGM should provide the same values for the magnetic field strength, and any difference can be explained by an improvement of the nine basic FGM parameters. These parameters are expected to be constant over at least 1 day. In a linear approximation, it is required that

$$\Delta\mathbf{B} = \mathbf{B}_1 \cdot \mathbf{dB} = 2\mathbf{B}_1 \cdot \begin{pmatrix} dS_x & \cos\left(d\langle x,y\rangle\right) & \cos\left(d\langle x,z\rangle\right) \\ 0 & dS_y & \cos\left(d\langle y,z\rangle\right) \\ 0 & 0 & dS_z \end{pmatrix} . \left(\mathbf{B_0} - d\mathbf{O}\right) \qquad (11)$$

where $\Delta\mathbf{B}$ is the difference in the field strength between OVM and FGM estimates.

Equation (11) represents a linear expression relating the processed OVM data to the magnetic field components from the FGM through the nine unknown. In practice, a system of equations is set up making use of all 86,400 daily measurements, from which the nine FGM parameters are determined by least squares.

With a day of data, the FGM parameters are determined. Averages over 15 days are used in the FGM processing for the final scaling of the vector data. After this last processing step the root mean square (rms) value of the difference between OVM and FGM varies from 0.1 to 0.2 nT. This can be regarded as a verification of the used calibration approach.

The CHAMP satellite has been in orbit for more than 8 years. It is thus interesting to see how the prime FGM parameters have varied over the mission period. In Figs. 6, 7, and 8 the long-term variations of the applied parameters are shown. For the convenience of interpretation, vertical lines are drawn at times when the ascending arc of the orbital plane coincides with the 6 o'clock local time sector, and mean values are subtracted in order to allow a more direct comparison of the

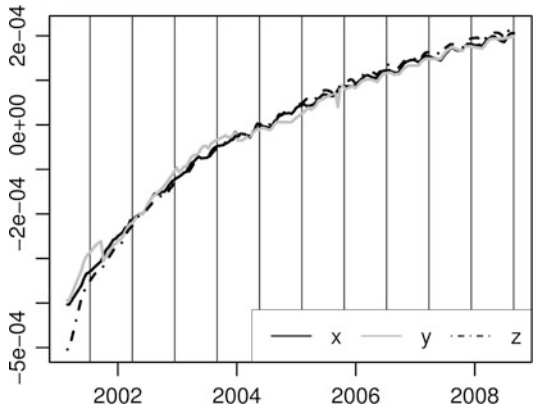

Fig. 6 Temporal changes of the Fluxgate magnetometer scale factors. Mean values have been subtracted. The *vertical lines* indicate times when the orbital plane is in the 6 o'clock local time sector

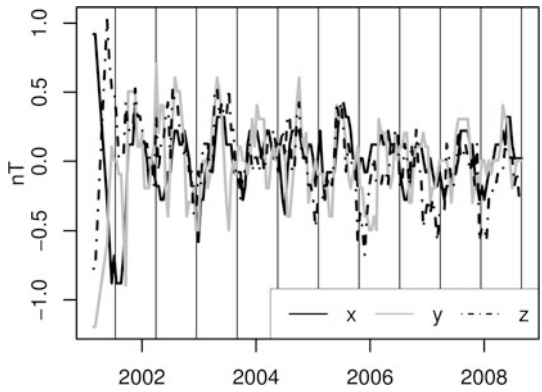

Fig. 7 Temporal changes of the Fluxgate magnetometer offset values. The vertical lines indicate times when the orbital plane is in the 6 o'clock local time sector

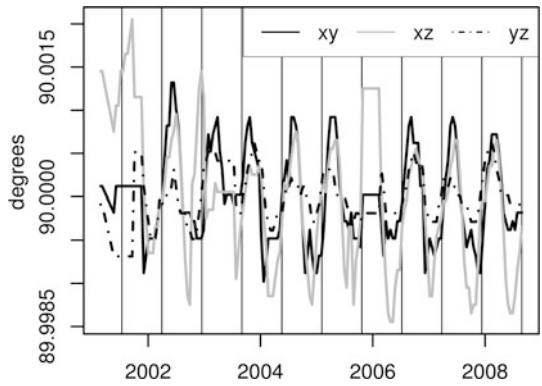

Fig. 8 Temporal changes of the angles between the Fluxgate sensor axes. The *vertical lines* indicate times when the orbital plane is in the 6 o'clock local time sector

Table 1 Mean values of the nine Fluxgate parameters, which have been substracted from the curves plotted in the Figs. 6 and 7

$b_{plot} = b - b_{offset}$		
b_{plot}	b	b_{offset}
bx_{plot}	bx	27.380
by_{plot}	by	20.695
bz_{plot}	bz	21.374
$anlge_{plot} = angle - angle_{offset}$		
$anlge_{plot}$	angle	$angle_{offset}$
α_{plot}	α	0.02588
β_{plot}	β	0.060247
γ_{plot}	γ	0.038787
$s_{plot} = s - s_{offset}$		
s_{plot}	s	s_{offset}
sx_{plot}	sx	1.002353
sy_{plot}	sy	1.003278
sz_{plot}	sz	1.003194

field components. The values subtracted are listed in Table 1. There are systematic differences between the variations of the scale factors and the other parameters. The scale values show a monotonic increase over time. The trend is the same for all three components and it can reasonably well be approximated by a logarithmic function. Over the mission lifetime, the scale factor has changed by 7 parts in 10.000, corresponding to an error in magnetic field of some 40 nT.

The other parameters show no significant long-term trend, but exhibit periodic variations in phase with the orbit local time. Amplitudes of the offset variations (Fig. 7) are generally smaller than 0.5 nT. Regarding the sensor stability (Fig. 8) variations are confined to angles of 0.001° which correspond to 3.6 arcs. For these six parameters the in-flight calibration confirms the high stability of the FGM instrument on CHAMP. It should be noted here that the stability of the six parameters may even be better than shown here. The synchronization of the deduced variations with the orbital local time suggests that other, not corrected perturbations of the measurements leak into these parameters. However, this does not affect the validity of the Level 2 data.

2.4 Advanced Stellar Compass Data Processing

For the scientific use of the vector measurements the orientation of the components has to be known with high precision. To achieve this goal CHAMP is equipped with a special optical bench, which houses the FGM and two star camera head units (CHU). The purpose of the optical bench is to provide a mechanically stable connection between magnetometer and star tracker. Figure 9 shows schematically the arrangement of the instruments on the boom and the orientation of the various coordinate systems. The viewing direction of the two cameras is separated by 102°.

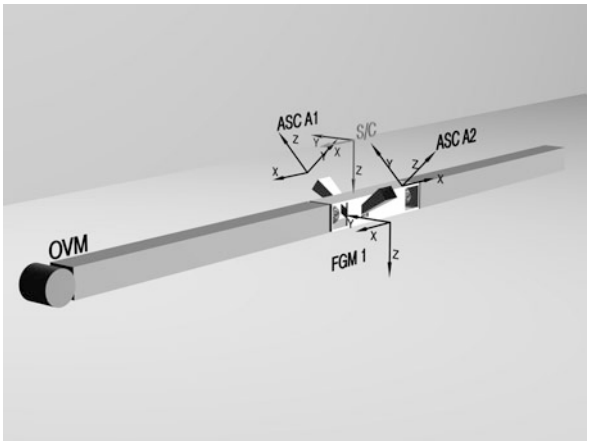

Fig. 9 Schematic drawing of the CHAMP boom and its instrument assembly. Also the orientations of the relevant coordinate systems referred to in the text are shown

Therefore, they survey two completely different regions of the sky, and the information provided by the two camera heads are combined in order to improve the attitude determination.

The Advanced Stellar Compass (ASC) is a sophisticated instrument, performing self-consistently the attitude determination on-board at a rate of 1 Hz. This includes the correction for aberration due to the finite speed of the light. The basic data processing to be performed on ground is therefore quite straightforward. Figure 10 presents a schematic flow chart of the ASC data processing steps. It starts again with the adjustment of the time stamp to the measurement time.

In step 2 the transmitted attitude readings are transformed back from the spacecraft frame into the CHU frame. Step 3 is required for removing artificial jumps in the attitude readings. Due to some hardware problems at certain times the readout of the CCD in the camera does not work properly. In those cases the first row of pixels is skipped. As a result, the internal attitude determination algorithm provides a biased output. Fortunately, the bias of about 85 arcsec is constant, and can be removed in the processing. The challenge is to identify the affected readings. An example is given in Fig. 11. The angular differences between CHU1 and CHU2 are plotted when both attitudes are given in the S/C frame. As expected, there are no jumps in the rotation around the x axis (roll). In the two other directions, jumps are evident. Four different states can exist, from both correct attitudes to both biased attitudes. The angle variations after corrections of the attitude jumps are also shown. Remaining differences between the two independent attitudes are much smaller, except for the beginning of 2005. Shortly after Christmas 2004 a strong intergalactic gamma burst (Mandea and Balasis, 2006), destroyed a number of CCD pixels. Only after uploading a new dead-pixel map a reliable attitude determination has again been possible.

Star trackers have a characteristical anisotropic direction accuracy. While one can determine the two angles perpendicular to the viewing directions very precisely, the uncertainty of the rotation angle about the bore-sight is larger by a factor of

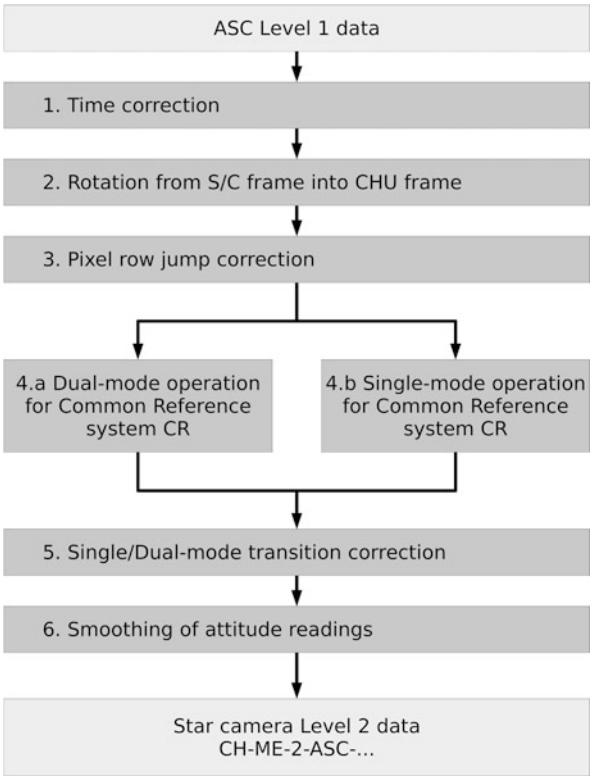

Fig. 10 Schematic flow chart for the processing of the Advanced Stellar Compass data. For details of the processing steps see the text

about 6. To overcome this limitation in step 4a the attitude readings of the two star trackers are combined, whenever both provide reliable readings. In that case the uncertainty in the rotation angles can be omitted. A common reference frame (CR) is defined using exclusively the directions given by the bore-sight of the star cameras. If these directions are for the camera 1 and 2, respectively, then the reference frame is calculated by:

$$\begin{aligned} Z_{\mathrm{CR}} &= -(Z_1 + Z_2)/|Z_1 + Z_2| \\ X_{\mathrm{CR}} &= -(Z_1 \times Z_2)/|Z_1 \times Z_2| \\ Y_{\mathrm{CR}} &= Z_{\mathrm{CR}} \times X_{\mathrm{CR}} \end{aligned} \tag{12}$$

There are time-intervals, however, when one of the cameras is blinded. In that case a pre-defined rotation is applied for obtaining the attitude in the CR frame from the useable camera. Then the quality of the attitude is reduced due to the uncertainty of the rotation angle. The attitude data are therefore affiliated with quality flags showing on which camera the result is based on. As expected, the transition from dual head to single head attitude readings is not always smooth. For that reason in

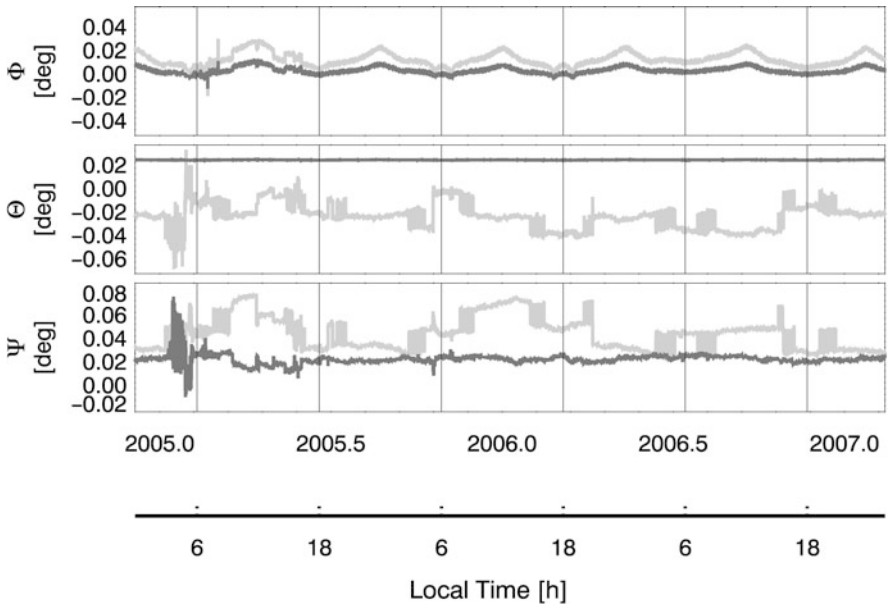

Fig. 11 Differences between attitudes derived from CHU1 and 2 (both in S/C frame) for 2005–2007. The *grey curve* shows the situation before jump correction, and the *black curve* after correction

step 5 a fitted linear trend is added to the single head values to ensure a smooth continuous data series.

A further smoothing is performed in step 6. The CHAMP spacecraft, due to its large mass, cannot change its attitude rapidly. For that reason, the attitude variations are constrained, by applying a low-pass filter. After this processing the ASC Level 2 data are transferred to the ISDC.

2.5 Magnetic Field Data in NEC Frame

An extra demanding task is to rotate the magnetic field vector data into a geophysically well-defined frame, such as North-East-Center (NEC). Data from several sources have to be considered for this transformation. Instruments involved are the OVM, FGM, ASC and GPS receiver. Only if the readings of all these instruments are resampled to the same time, given in UTC, they can be combined and transformed. A time difference of 10 ms can cause an error up to 0.6 nT. On CHAMP all measurement cycles are synchronized by the second-pulse PPS (Precise Positioning Service) of the GPS receiver, therefore the required timing accuracy of a measurement to a few milliseconds can be achieved.

A remaining uncertainty of the data in NEC frame comes from the finite stability of the optical bench. There is no direct way to check it in space. An indirect approach

is to co-estimate the Euler angles between the FGM and ASC as part of the modeling of the geomagnetic field. In an attempt to minimize the difference between magnetic field readings and model predictions the three angles are treated as free parameters. Small values for these angles can be considered in a closed loop validation of the magnetic field data in NEC frame. Figure 12 shows a time series of obtained Euler angle variations of the optical bench for 2005–2007. The three components describe rotations around the roll, pitch and yaw axis. Variations of order $\pm 0.001^\circ$ can be observed, and particularly, the α and γ angles show variations synchronized with local time. In this context it has to be noted that the estimation of Euler angles assumes a magnetic field which can entirely be described by a scalar potential. For measurements done into the ionosphere this is not strictly true. The synchronized variations may therefore indicate that the violation of the assumptions is local time dependent. There are several jumps in the bottom plot occurring just at dawn and dusk. This behavior can be explained because only night time data are used for the magnetic field modeling. When the satellite orbit passes the 06/18 local time sector the considered data set is switched from ascending to descending or vice versa. Obviously, the magnetic field data in the NEC frame are somewhat different depending on the sampling direction from North to South or South to North.

The angle β shows also some spikes and deviations. The narrow spikes could be associated with time errors. At certain intervals the GPS receiver sees only 4–5 GPS satellites. This is not sufficient to generate a reliable time signal. In those cases

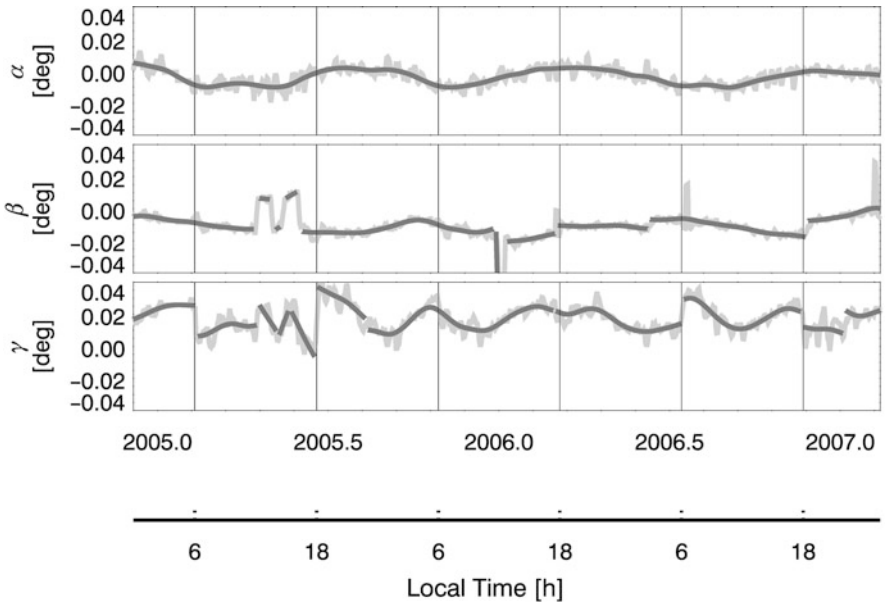

Fig. 12 Temporal variations over 2005–2007 of the co-estimated optical bench Euler angles: rotations around the roll (*top*), pitch (*middle*) and yaw (*bottom*) axes are shown. *Vertical lines* mark the crossings of the orbital plane through the 06 and 18 local time

the PPS is off by a fraction of a second. Such a time error has a similar effect as a wrong pitch angle. Therefore, these spikes appear only in the β angle values. The large negative excursion in the middle of the frame is associated with the leap second at the beginning of 2006. Some of developed codes are obviously not able to handle this situation correctly.

Figure 12 shows the result of Euler angles co-estimation when using a 3-day interval for field modeling. The dark heavy line is a smooth piecewise fitted curve. Angles derived from this later curve are used to improve the rotation from the FGM to the ASC system. With this final update a set of reliable NEC data processed is available. Finally, lets us stress that the undulations visible in Fig. 12 cannot be interpreted directly as variations of the Euler angles. They are the sum of many small imperfections of data from various instruments. Nevertheless, by applying these corrections the final NEC magnetic field data quality is greatly improved.

2.6 Complementarity of the Ground and Satellite Data

Ideally, a dataset used in a global field modeling has to fulfill the following requirements:

- samples should be taken at evenly distributed points, dense enough to cover the shortest wavelengths,
- readings at different locations should be taken simultaneously,
- measurements should be made in areas free of electric currents, i.e. free of sources of induced magnetic fields.

These three conditions could be satisfied by a dense ground-based network. In reality, as shown before, the observatory network is not dense enough and rather unevenly distributed. This weakness can be overcome by satellite measurements. Using only magnetic field observations from space has, however, also its short-comings. For example, the last two requirements can not be fulfilled by a single satellite. Satellites take measurements sequentially orbit-by-orbit, and it takes several days or even months to achieve an appropriate global coverage. In order to compensate for this weakness temporal changes of the magnetic field during the considered interval have to be corrected or co-estimated. Since satellites orbit the Earth in the ionosphere, they cross various kinds of currents. For the mitigation of this problem two procedures are possible: one is to remove the magnetic effects of these currents from the recorded data, and the second is to select time intervals when the currents, which cannot be corrected, are sufficiently weak (see below).

Spatial distribution. The distribution of magnetic observatories over the globe (Fig. 13) is highly non-uniform. A possibility to counterbalance this uneven geographical distribution is the use of an adequate weighting scheme (Langlais and Mandea, 2000). However, adequate weighting cannot make up for the lack of information in the regions sparsely covered by data. Another possibility to improve our knowledge of the secular variation is to have well-distributed global measurements

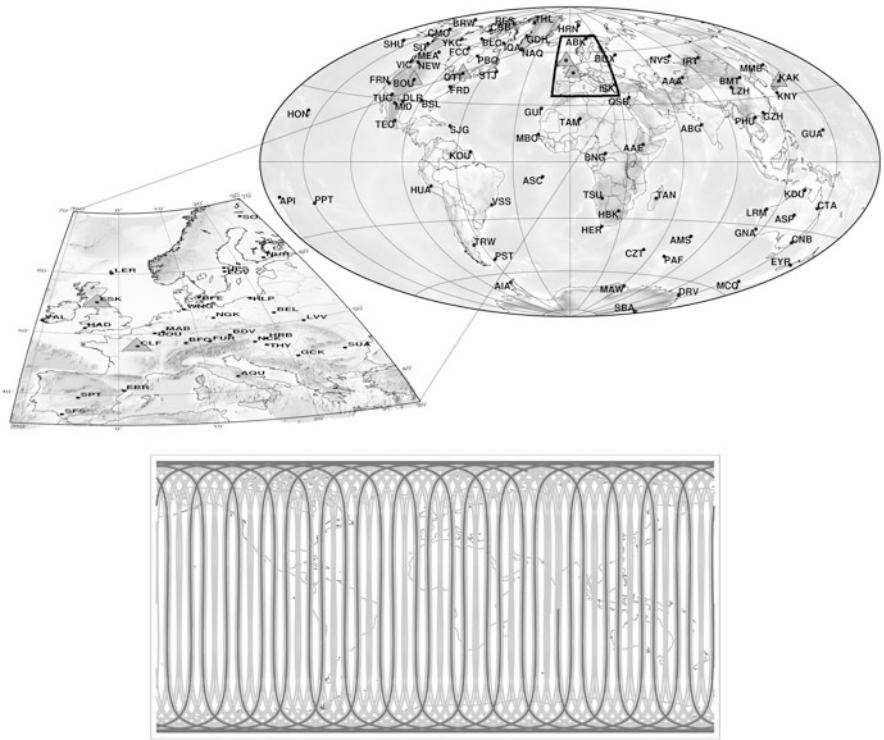

Fig. 13 Map of the INTERMAGNET magnetic observatory distribution (*top*). Coverage of the Earth with CHAMP satellite magnetic data after 1 day DOY 288 2007 (*black*) and 1 week (DOY 226-232 2007) (*grey*, *bottom*)

from satellites. The data provided by each of the three satellites currently in orbit ensure a good coverage of the Earth's surface over a 4-month period. Figure 13 shows the orbit tracks for 1 day and for 1 week, respectively, for the CHAMP satellite. The coverage over 1 week already appears sufficient for a good data distribution in space, but this coverage is not sufficient in local time. Moreover, these plots are based on all available measurements, without considering data quality and selection criteria with respect to external disturbances.

Temporal coverage. The number of observatories providing hourly means or 1-minute data (INTERMAGNET observatories) is lower than the total number of worldwide observatories. Nevertheless, they cover a large time-span when comparing with the satellite missions. Figure 14 indicates the time-span covered by the number of observatories providing different data, and also the short interval covered by satellite missions.

Magnetic field measurements obtained by various platforms have their strengths and weaknesses. By properly combining these data, information about the characteristics of the geomagnetic field can be retrieved. This is shown in the following sections.

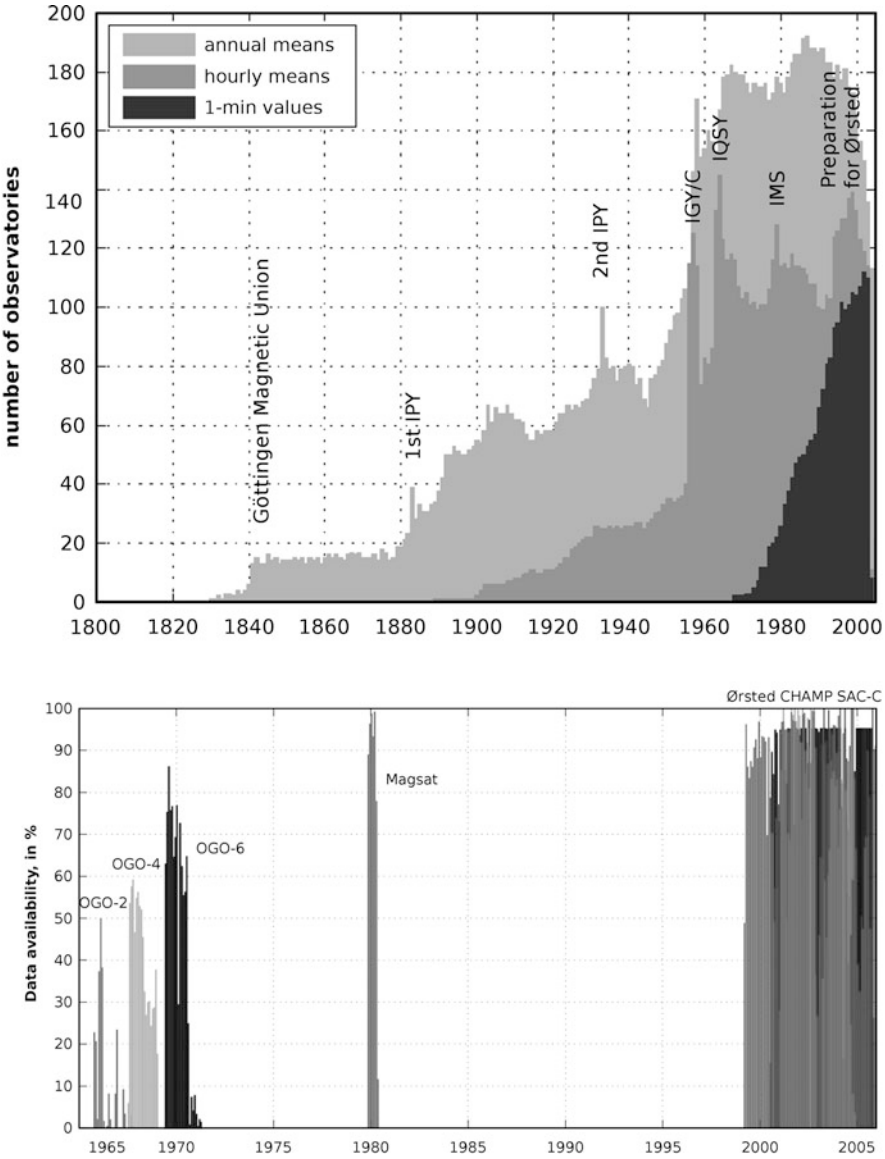

Fig. 14 Temporal distribution (in 2005) of the various kind of data provided by magnetic observatories (*top*). Temporal distribution of the satellite missions carrying a scalar magnetometer (POGO series) or a scalar and vector magnetometer (MAGSAT, Ørested, CHAMP, SAC-C)

3 Data and Field Modeling

An important prerequisite for deriving more precise and higher resolution models of the geomagnetic field is the availability of high-quality measurements. Under the assumption of suitable data the modeling task may be separated in a few crucial

steps. The first one is linked to data selection, as in each single measurement all contributions exist, and the wish is to minimize the external ones. Thereafter, the inversion of the measurements to obtain a mathematical description of the field distribution is at a global or regional scale.

Before presenting in some more details a description of the geomagnetic field produced by the lithosphere, we summarize the efforts needed in a good data selection process, as well as the basis for the global and regional modeling.

3.1 Data Selection

3.1.1 Data Selection – General Needs

Before applying different techniques to available measurements, a selection of different datasets is needed. This process is generally different from one modeler to another, however, the main idea is to minimize as much as possible the various external contributions. For example, the GRIMM model[4] (Lesur et al., 2008), mainly used in the following in magnetic field description, is built using exclusively vector magnetic data. The main motivation for this choice is the need to use satellite measurements during polar summers. Therefore, the fields generated by field aligned currents and in the ionosphere have to be modeled at high latitudes, and this can be achieved only if vector data are available at all local times.

GRIMM model covers the time span 2001–2005, when CHAMP vector data with acceptable quality flag settings are available. Using two magnetic components only lead to a robust model and it has the further advantage that there is no need to model the field generated by the ring current. The CHAMP measurements have been selected between $\pm$ 55° magnetic latitudes such that

- IMF B_z has positive values
- 20 s minimum separate two data points
- the local time (LT) is in between 23:00 and 05:00
- the sun is below the horizon up to 100 km above the Earth's reference radius
- the VMD (Thomson and Lesur, 2007) norm is no larger than 20 nT and the norm of its derivative is less than 100 nT/day.

At magnetic latitudes outside the $\pm$ 55° interval, the three components of the magnetic data vector are used. CHAMP data with acceptable quality flag settings are selected for positive IMF B_z values, with 20 s minimum between two data points, a VMD norm no larger than 20 nT and the norm of its derivative is less than 100 nT/day. The use of the full magnetic vector at all local times is necessary for separating the field generated by field aligned currents or in the ionosphere from the internal core field. Using the full vector data at high latitude also improves the

[4] www.gfz-potsdam.de/magmodels/GRIMM

robustness of the low order internal Gauss coefficients, in the same way that vector data are used at mid-latitudes to avoid the Backus effect in models built mainly from scalar magnetic data.

GRIMM model is also based on observatory hourly mean values, selected following the same criteria, as for the between $\pm$ 55° magnetic latitudes.

3.1.2 Data Selection – New Approach

The new satellite era brings us in a situation when a large number of magnetic measurements has became available, due to the three magnetic missions, Ørsted, CHAMP and SAC-C. The forthcoming ESA's Swarm constellation mission, scheduled for launch in 2011, will dramatically increase this number.

In this context, modeling the magnetic potential field of the Earth becomes a challenging task with high demands on computer memory and time. As noted before, for internal field modeling, the measurements are selected according to the quiet geomagnetic conditions (geomagnetic indices, local time, etc). Nevertheless, the number of data remains important. Often, the number of measurements, taken into account in inversions, is simply reduced by decimating them. Such a "random selection" may obviously lead to loss of information. In addition, not only the satellite data, but also surface data have been considered. High resolution field modeling, at global or regional scales, indeed requires to combine the "medium" resolution satellite measurements with very dense surface datasets comprising ground-based, airborne and marine measurements. This increases considerably the size of the datasets from which the potential field models are computed.

To overcome these possible drawbacks, it appears necessary to develop techniques to deal with these large amounts of data. Recently, two important aspects have been considered: firstly, the data have to be preprocessed in a compact and reasonable way, secondly, the design of the model and the inversion scheme have to allow fast and local computations. Thus, Minchev et al. (2009) have proposed to take advantage of: (i) the rather smooth behavior of the internal magnetic field at satellite altitude and (ii) the mathematical and geometrical properties of the wavelets frames (see below), which can be used as a modeling technique. In this context, local multipole approximations of the wavelets at satellite altitude, have been developed.

To cope with the large number of satellite measurements, and in particular with some 300 millions of measurements, from the upcoming 4-year Swarm multisatellite mission, methods have been developed to avoid the storage of large normal matrices needed for a large number of spherical harmonics. Those methods are based on the iterative approach (see for instance Kusche, 2000; Schuh, 2000; Keller, 2001). They make use of a matrix that is representative of the normal system, but easier to compute. Such matrix allows to compute an approximate solution of the normal system, that is iteratively refined. It can also be used as a pre-conditioner of the normal system, allowing to speed-up convergence rates of iterative solvers.

In Minchev et al. (2009) the space-domain is decomposed, i.e. a shell at satellite altitude is defined by the measurement positions, into a sum of geometrical 3D-bodies (triangular prisms). Each unity-volume contains a certain amount of field

measurement points. As soon as the considered unity-volume is small enough, the data are located in the vicinity of each other and the field itself appears smooth. In the inverse problem, the expansion of the related magnetic field in wavelets frames may be replaced by a power series of local multipole developments around the centre of mass of the data positions inside the defined volume. In this way, a piecewise decomposition of the magnetic field is obtained, at satellite altitude. The coefficients of each local development may then be used in global field modeling. Let us describe in more detail the space discretization at the satellite level.

The space, where the satellites revolve, is considered as a shell. Its thickness is directly defined by the range of radius of the considered data positions according to geocentric coordinate system. This shell is discretize to K number of unity-volumes P_j (with j=1,. . .,K) equivalent to the number of facets of an icosahedron centered onto the Earth (Chambodut et al., 2005).

Each unity-volume P_j is defined such that it gets property of compact geometry: its thickness is chosen to be more or less equivalent to the size of the icosahedron edges at the satellite altitude. If the thickness of the shell defined by the data is large, another layer of unity volume is added in the radial direction. The aim is to obtain unity-volumes with reasonable shapes, neither flat thin shells, nor long thin radial columns, as shown in Fig. 15.

For a given dataset, the balance should be determined between the number of unity-volume K (directly related to their size), the number of data per unity-volume M_j (with j=1,. . .,K) and the degree of multipole expansion inside a prism (Chambodut et al., 2005). For example, in case of a few data in a large unity-volume, this configuration may allow recovery of large wavelengths potential field, and thus leads to the use of low degree polynomials. At the contrary, in case of a large number of data in a small unity-volume, this configuration may allow recovery of smaller wavelengths potential field, and thus leads to the use of higher degree polynomials.

A crucial question regarding the use of the multi-polar expansion technique arises. Depending on the size of the considered dataset, how the size of the

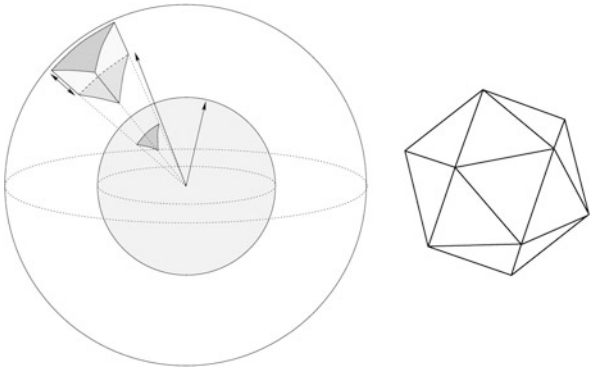

Fig. 15 A unity-volume at satellite altitude (*left*); the simplest icosahedron – 20 faces (*right*)

unity-volumes (the number of data per unity-volume) and the maximal order of the local harmonic polynomials have to be chosen. This choice has to be done to obtain optimal performances. It is clear that the higher the resolution of the space discretization is, the better the approximation will be. On the other hand, the maximal reduction of the size of the underlying problem, is obtained for the lowest possible resolution. Therefore, it is needed to find a balance between the resolution of the space discretization and the degree of the local expansion used in the model.

Figure 16, shows the maximum relative error between all spherical harmonics up to degree 30 and their corresponding local multi-polar approximations, versus the ratio (in %) between the sizes of the underlying and the approximated problems (size reduction), for a given dataset. For small and moderate size datasets, low orders local approximations, of first ($L = 4$) and second ($L = 9$) orders, are preferable. Higher order approximations would be beneficial, when a dataset is large enough, so the number of local coefficients per unity-volume can be compensated by the amount of data approximated in each cell.

In Minchev et al. (2009) two cases have been investigated, for the gravity and magnetic field. It has been shown that depending on the chosen precision of the approximation, the speed and the quality of the inversion can practically be controlled. Thus, fast quick-look solutions or highly precise models can be computed with a great deal of flexibility. The performed tests have also shown that the amount of errors introduced by approximations in models can be controlled. Distortions are small, and become negligible when the process is iterated. This new method can be applied to any kind of modeling functions like wavelets or other radial basis functions.

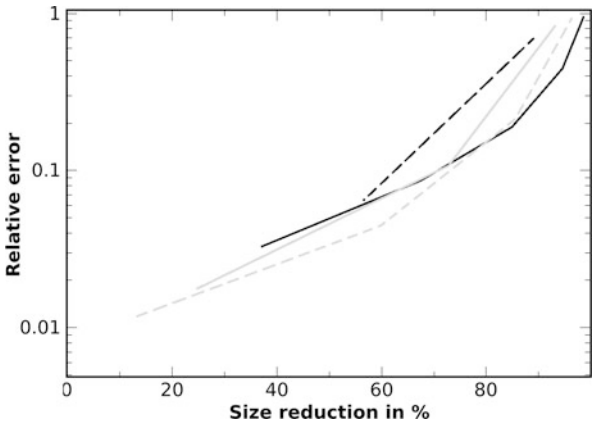

Fig. 16 Ratio in % between the sizes of the original and the approximated problems versus the approximation relative error for $L = 4$ (*black*), $L = 9$ (*dashed grey*), $L = 16$ (*grey*), $L = 25$ (*dashed black*)

3.2 Global Modeling

The most commonly employed global method to represent the geomagnetic field is the Spherical Harmonic Analysis (SHA). In a space defined by three spherical coordinates (r, θ, ϕ), the geomagnetic induction field **B** can be expressed as

$$\mathbf{B} = -\nabla V \tag{13}$$

where V is a scalar potential satisfying ΔV=0.

At the Earth's surface this potential can be expressed as the sum:

$$V = V_{\mathrm{i}} + V_{\mathrm{e}} \tag{14}$$

where V_{i} and V_{e} represent the internal and external scalar potential, respectively.

In spherical coordinates equation ΔV=0 can be written as

$$\frac{\partial}{\partial r}\left(\frac{r^2 \partial V}{\partial r}\right) + \frac{1}{r^2 \sin\theta}\frac{\partial}{\partial \theta}\left(\sin\theta \frac{\partial V}{\partial \theta}\right) + \frac{1}{r^2 \sin^2\theta}\frac{\partial^2 V}{\partial \phi^2} - 0 \tag{15}$$

and it is solved by separation of variables and then expanded into a spherical harmonic series (see below).

Harmonics are widely used in mathematics and physics to represent complex, usually natural, functions. These harmonics are periodic functions of varying amplitude and period. The more harmonics are used, the closer the approximation to reality is.

In the absence of magnetic sources, the geomagnetic field can be presented as the negative gradient of a potential: $\mathbf{B_p} = -\Delta V(\theta,\phi,\rho,\tau)$. The source of this poloidal field can be from internal or from external origin and the associated potentials, V_{i} and V_{e} respectively, are described on a spherical surface. Following (Gauss, 1839), the two potentials V_{i} and V_{e} can be developed as spherical harmonic expansions:

$$V_{\mathrm{i}}(\theta, \phi, r, t) - a\sum_{l,m}\left(\frac{a}{r}\right)^{l+1} g_l^m(t) Y_l^m(\theta, \phi) \tag{16}$$

$$V_{\mathrm{e}}(\theta, \phi, r, t) - a\sum_{l,m}\left(\frac{r}{a}\right)^{l} q_l^m(t) Y_l^m(\theta, \phi) \tag{17}$$

where θ and ϕ are the colatitude and longitude, $a = 6{,}371.2$ km is a reference radius, ${Y_l}^m(\theta,\phi)$ are the usual Schmidt normalized spherical harmonic (SH) functions and ${g_l}^m(t)$, ${q_l}^m(t)$ are the Gauss coefficients. The convention used here is that negative orders ($m < 0$) are associated with $\sin(m\phi)$ terms, whereas zero or positive orders ($m \geq 0$) are associated with $\cos(m\phi)$.

Traditionally, the North, East, Vertical down system of coordinates is used to give the expression of the gradient of the potential. Here, as for the GRIMM model, the geocentric Cartesian system of coordinates is used. The direction Z of the geocentric Cartesian system of coordinates (i.e. $\approx$ the Earth's rotation axis) is considered, first. Also, it is assumed that an optimal distribution of vector data at satellite altitude

is available, such that a magnetic field model can be robustly built. The data set is made of the Z component of the measured magnetic field. The magnetic field of external origin in this Z direction is given by:

$$\mathbf{B}^{e}_{pZ} = -\cos\theta \cdot \partial_r V_{\mathrm{e}}(\theta, \phi, r, t) + \sin\theta \cdot \frac{1}{r}\partial_\theta V_{\mathrm{e}}(\theta, \phi, r, t) \tag{18}$$

which leads to:

$$\mathbf{B}^{e}_{pZ} = -\sum_{l=1}^{L}\sum_{m=-1}^{l}\left(\frac{r}{a}\right)^{l-1} q_l^m(t)\sqrt{(l+|m|)(l-|m|)}\,Y_{l-1}^m(\theta, \phi) \tag{19}$$

The external field is generally assumed to be large scale and generated mainly in the magnetosphere which justify the use of $L = 2$ as the maximum SH degree. Considering only the first degree ($l = 1$), only the order $m = 0$ appears and therefore only the SH function ${Y_0}^0(\cos\theta)$ is involved. This function is a constant in space, so, as expected, the large scale external field along the Z direction (i.e. associated with ${q_1}^0$) is a constant in space. The field of internal origin is given by:

$$\mathbf{B}^{i}_{pZ} = -\sum_{l=1}^{L}\sum_{m=-1}^{l}\left(\frac{a}{r}\right)^{l+2} g_l^m(t)\sqrt{(l+|m|+1)(l-|m|+1)}\,Y_{l+1}^m(\theta, \phi) \tag{20}$$

In this equation for a given degree l the SH function is ${Y_{l+1}}^m(\theta, \phi)$ whereas it was ${Y_{l-1}}^m(\theta, \phi)$ in the expression 19 of the external field. If the maximum SH degree $L = 2$ is and acceptable approximation for the external field, the SH function of the highest degree in equation 19 is ${Y_1}^m(\theta)$ whereas in Eq. (20) the SH function of the minimum degree is ${Y_2}^m(\theta, \phi)$. Therefore using only the distribution of Z data described above leads to a separation of the internal and external field contributions to the magnetic field. It leads also to a unique set of Gauss coefficients. However, for a better accuracy one of the two other directions can be used. The expressions for the internal poloidal field in the X and Y directions are:

$$\begin{aligned}\mathbf{B}^{i}_{pX} = -\tfrac{1}{2}\textstyle\sum_{l=1}^{L}\left(\frac{a}{r}\right)^{l+2}\Big\{&\sqrt{(l+1)(l+2)}\,g_l^0(t)Y_{l+1}^1(\theta, \phi)\\ &+\textstyle\sum_{m=1}^{l}\sqrt{(l+m+1)(l+m+2)}\,(g_l^m(t)Y_{l+1}^{m+1}(\theta, \phi) + g_l^{-m}(t)Y_{l+1}^{-m-1}(\theta, \phi))\\ &-\textstyle\sum_{m=1}^{l}\sqrt{(l-m+1)(l-m+2)}\,(g_l^m(t)Y_{l+1}^{m-1}(\theta, \phi) + g_l^{-m}(t)Y_{l+1}^{-m+1}(\theta, \phi))\Big\}\end{aligned} \tag{21}$$

$$\begin{aligned}\mathbf{B}^{i}_{pY} = -\tfrac{1}{2}\textstyle\sum_{l=1}^{L}\left(\frac{a}{r}\right)^{l+2}\Big\{&\sqrt{(l+1)(l+2)}\,g_l^0(t)Y_{l+1}^{-1}(\theta, \phi)\\ &+\textstyle\sum_{m=1}^{l}\sqrt{(l+m+1)(l+m+2)}\,(g_l^m(t)Y_{l+1}^{-m-1}(\theta, \phi) + g_l^{-m}(t)Y_{l+1}^{m+1}(\theta, \phi))\\ &-\textstyle\sum_{m=1}^{l}\sqrt{(l-m+1)(l-m+2)}\,(g_l^m(t)Y_{l+1}^{-m+1}(\theta, \phi) + g_l^{-m}(t)Y_{l+1}^{m+1}(\theta, \phi))\Big\}\end{aligned} \tag{22}$$

Over the polar regions, the vector satellite data are strongly contaminated by the field generated by field aligned currents (FAC). At satellite altitude part of this field is toroidal and is given by: $B_t = -\eta \times \nabla_s\, \Psi(\theta,\phi,t)$ where η is the unit vector in the

radial direction and $\Psi(\theta,\phi,r,t)$ is given by:

$$\Psi(\theta,\phi,t) = r\sum_{l,m}^{L}\alpha_l^m(t)Y_l^m(\theta,\phi) \tag{23}$$

These equations, corresponding to the radial FAC, lead to a purely tangential field that contains all SH degrees up to L and therefore it cannot be separated from the internal field unless the three components of the vector data are used. The SH in Eq. (23) can be replace by a series of localized function $\mathcal{F}_i(\theta,\phi)$ (see for example Lesur, 2006) defined by:

$$\mathcal{F}_i(\theta,\phi) = \sum_{l,m}^{L} f_l Y_l^m(\theta_i,\phi_i)Y_l^m(\theta,\phi) \tag{24}$$

where the f_l are chosen such that the gradients of the function $\mathcal{F}_i(\theta,\phi)$ vanish rapidly away from its centre (θ_i,ϕ_i). If f_l for all l and if there is enough of these functions then the expression 23 is equivalent to (see Lesur, 2006 for "exact equivalence" rules):

$$\Psi(\theta,\phi,t) = r\sum_{i}\alpha_i(t)\mathcal{F}_i(\theta,\phi) \tag{25}$$

Similarly, a model of the field generated in the ionosphere may be required and, assuming the ionospheric currents are all flowing on a thin shell of radius, they are defined by: $J_{\rm io} = -\eta \times \nabla_s\Phi(\theta,\phi,t)$ where the current function $\Phi(\theta,\phi,t)$ is given by:

$$\Phi(\theta,\phi,t) = r_{io}\sum_{l,m}^{L}\beta_l^m(t)Y_l^m(\theta,\phi) \tag{26}$$

This flow of current give rise to a poloidal magnetic field that is therefore the negative gradient of a potential $V_{\rm io}(\theta,\phi,r)$. It is easy to establish that this potential is related to the current function coefficients via:

$$V_{io}(\theta,\phi,r,t) = \begin{cases} \mu_0 r_{io}\sum_{l,m}\frac{l}{2l+1}\left(\frac{r_{io}}{r}\right)^{l+1}\beta_l^m(t)Y_l^m(\theta,\phi) \text{ for } r \geq r_{io} \\ -\mu_0 r_{io}\sum_{l,m}\frac{l+1}{2l+1}\left(\frac{r}{r_{io}}\right)^{l}\beta_l^m(t)Y_l^m(\theta,\phi) \text{ for } r \leq r_{io} \end{cases} \tag{27}$$

where $\mu_0 = 4\pi 10^{-7}$ is the vacuum permeability. As above, this potential can be written in terms of localised functions:

$$\tilde{\mathcal{F}}_i(\theta,\phi,r,t) = \begin{cases} r_{io}\sum_{l,m}\frac{l}{2l+1}\left(\frac{r_{io}}{r}\right)^{l+1} f_l Y_l^m(\theta_i,\phi_i)Y_l^m(\theta,\phi) \text{ for } r \geq r_{io} \\ -r_{io}\sum_{l,m}\frac{l+1}{2l+1}\left(\frac{r}{r_{io}}\right)^{l} f_l Y_l^m(\theta_i,\phi_i)Y_l^m(\theta,\phi) \text{ for } r \leq r_{io} \end{cases} \tag{28}$$

and it is obtained:

$$V_{io}(\theta,\phi,r,t) = \mu_0\sum_{i}\beta_i(t)\tilde{\mathcal{F}}_i(\theta,\phi,r) \tag{29}$$

Separating the ionosphere contribution to the magnetic field from the field generated in the lithosphere and in the core is not easily done: the full vector data is needed and also a sampling of the field at all local time.

Using CHAMP and observatory data (selected as indicated before), one of the very high quality model available today is built, i.e. the GRIMM model (Lesur et al., 2008). Using this model, a detailed picture of the core field and its secular variation is obtained at the Earth's surface. Figure 17 shows the global distribution of the North, East and vertical downward components (X, Y, Z) of the geomagnetic core field for the epoch 2003.25.

One of the remarkable achievements of the GRIMM model is its representation of the temporal changes of the core field, i.e. its secular variation and acceleration. Figures 18 and 19 show these two quantities. Interestingly, the analyze of the secular acceleration indicates how rapidly the core field changes. This has enormous implications for the core dynamics, that we do not discuss here, but the interested reader is referred to Olsen and Mandea (2008) and Lesur et al. (2010).

Using the internal coefficients from a spherical harmonic analysis, is it possible to define the power spectra of the internal field (Lowes-Mauersberger spectra), following (Lowes, 1966):

$$W(n) = (n+1)\sum_{n=1}^{N_i^{\max}} \left((g_n^m)^2 + (h_n^m)^2\right) \tag{30}$$

For example, using the MAGSAT vector data, it was clearly shown, for the first time, that there is a major break in the power spectrum near spherical harmonic degree 13 (Langel and Estes, 1985). This break is interpreted to represent the change from dynamic core processes to quasi-static lithospheric ones. In Fig. 20 the power spectrum obtained from a recent field model, GRIMM is shown. The steep part of the spectrum ($n \leq 13$) is clear and indicates the signature of the long wavelengths of the core field, the transition degrees ($n = 13$–15) can be attributed to signals from both the core and the crustal sources, and the higher degrees ($n \geq 16$) are dominantly lithospheric in origin.

3.3 Regional Modeling

For describing of the magnetic field at regional scales, methods such as the Spherical Cap Harmonic Analysis have been proposed (Haines, 1985) and the related translated origin spherical cap harmonic analysis (De Santis, 1991), have been developed to model the field over small patches of the globe. Korte and Constable (2003) have pointed out that, the basis functions are not orthogonal, so it is not possible simultaneously to represent the potential for the vertical and horizontal field components, exactly. Thébault et al. (2004) and Thébault et al. (2006b) have re-posed SCHA as a boundary value problem within a cone extending above the reference surface, thereby allowing satellite data to be downward continued to the Earth's surface.

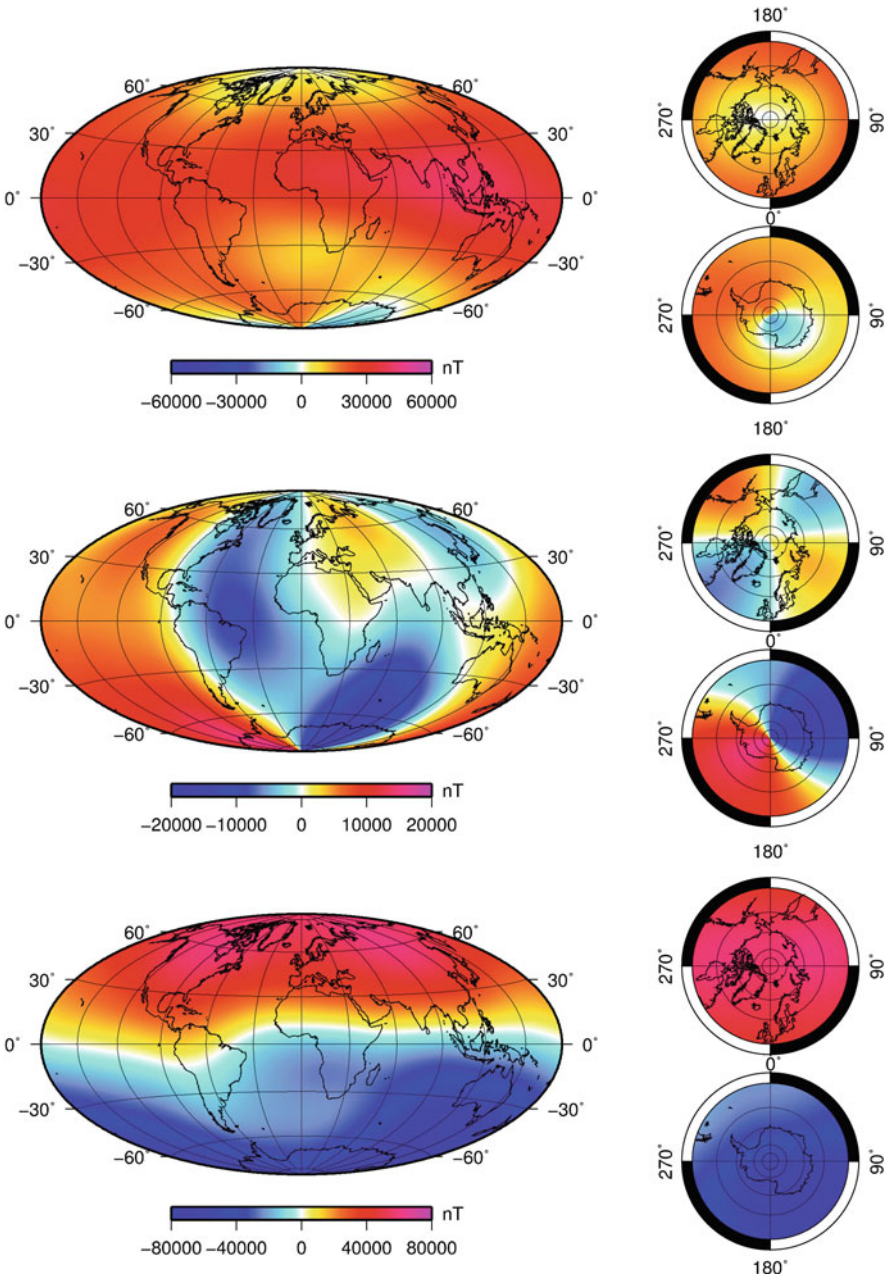

Fig. 17 Maps of the geomagnetic core field components, at the Earth's surface: north component (*top*), east component (*middle*), vertical downward component (*bottom*). Moldwide and polar projections

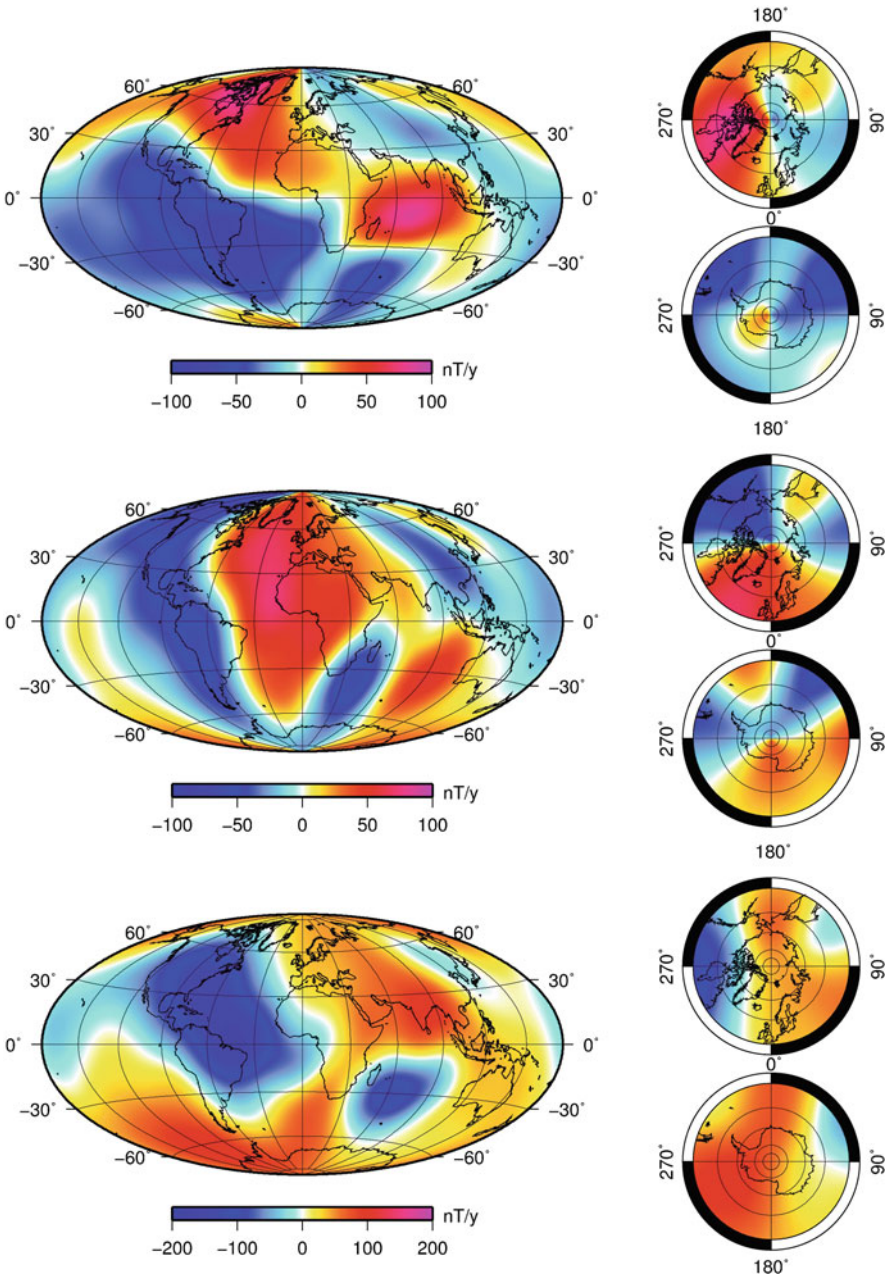

Fig. 18 Maps of the secular variation components, at the Earth's surface: north component (*top*), east component (*middle*), vertical downward component (*bottom*). Moldwide and polar projections

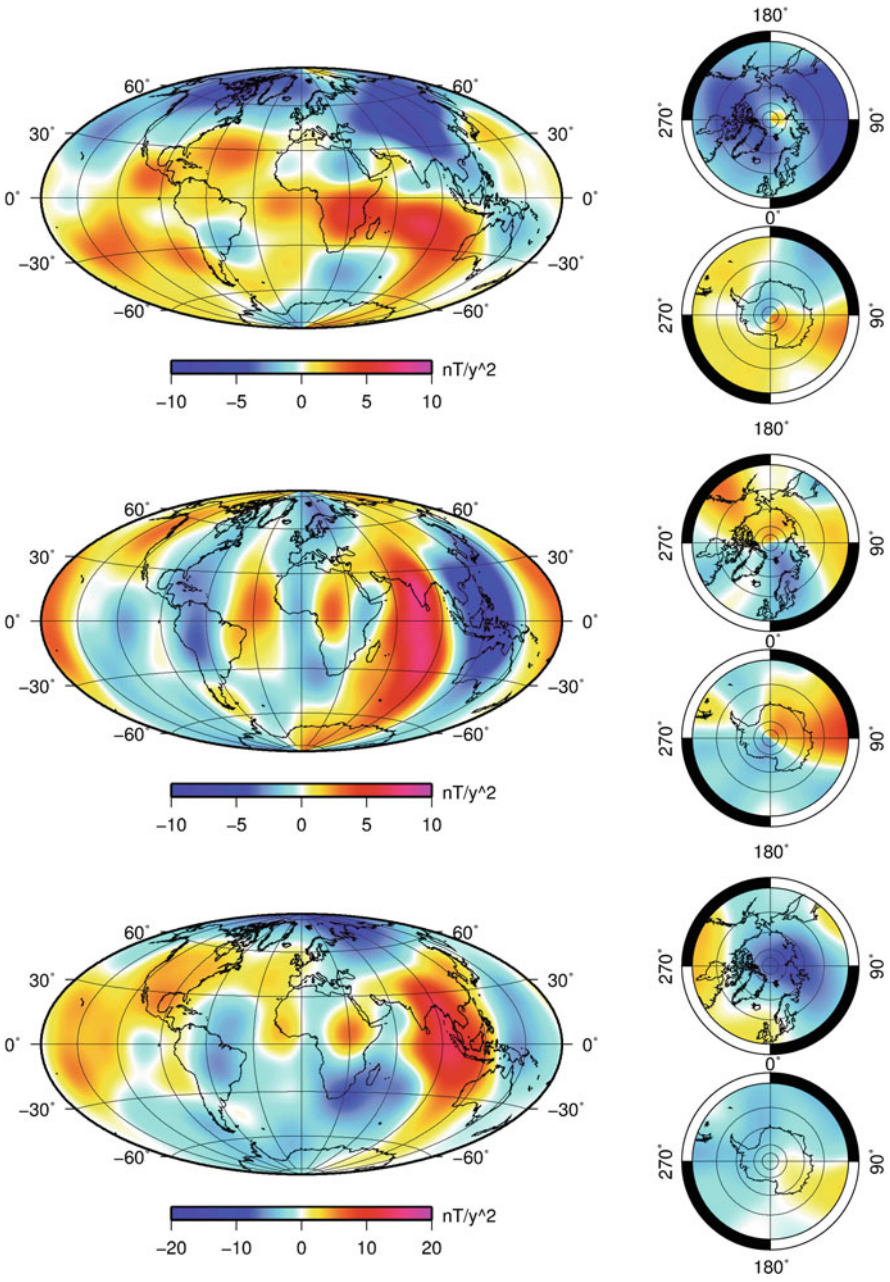

Fig. 19 Maps of the secular acceleration components, at the Earth's surface: north component (*top*), east component (*middle*), vertical downward component (*bottom*). Moldwide and polar projections

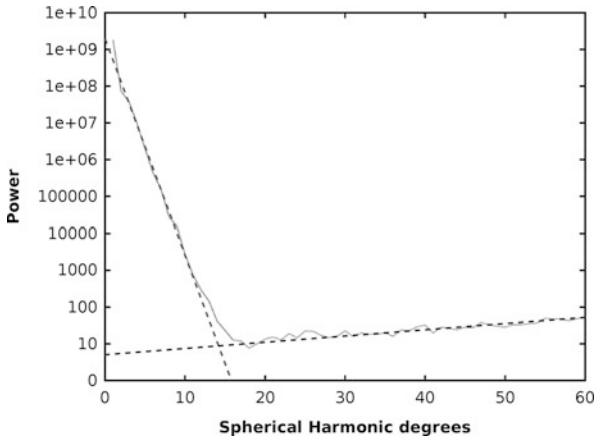

Fig. 20 The power spectrum obtained from the GRIMM model: the steep part of the spectrum ($n \leq 13$) indicates the core field contribution, the transition degrees ($n = 13$–15) can be attributed to both core and lithospheric contributions, and the higher degrees ($n \geq 16$) describe the lithospheric contribution. Units are in nT^2

This representation has been successfully applied for regions as small as the French Metropolitan territory (Thébault et al., 2006a).

Basis functions, such as harmonic splines (Shure et al., 1982), or with more local support, wavelet-like functions (Lesur, 2006) are better suited to data sets with variable resolution over the globe. Recently, lots of efforts have been made in developing new tools to describe the geomagnetic field at regional scale. They are based on the wavelet frames and the pioneering work by Holschneider et al. (2003). In the following the main aspects of this approach are described.

3.3.1 Wavelet Frames

The wavelets frames have been used to model the Earth's magnetic field, as the frame concept is more general than the basis one. The elements of a frame do not need to be linearly independent, therefore the representation into a frame is no longer unique.

The potential V of the magnetic field is expressed by the following superposition of Poisson wavelets g_i:

$$V(\vec{x}) = \sum_{i=1}^{W} \alpha_i g_i(\vec{x}), \tag{31}$$

where W is the finite number of wavelet, α_i are unknown coefficients and $\vec{x}$ is the evaluation point.

A Poisson wavelet on the sphere (Holschneider et al., 2003) is defined as:

$$g_{\vec{y}}^{(d)}(\vec{x}) = \frac{1}{\vec{x}} \sum_{l=0}^{\infty} \left(\frac{|\vec{y}|}{|\vec{x}|} \right)^{\ell} \ell^d \mathcal{Q}_l \left(\frac{\vec{x}.\vec{y}}{|\vec{x}||\vec{y}|} \right), \tag{32}$$

where $\vec{y}$ is the position of the mathematical source, d is the scale of the wavelet and $\mathcal{Q}_l = (2\,l + 1)\mathcal{P}_l$ is the reproducing kernel on the sphere, with $\mathcal{P}_\ell$ denoting the Legendre polynomials. A discretization of the mathematical sources of the wavelets is applied (Holschneider et al., 2003; Chambodut et al., 2005) to obtain a set of wavelets, which suitably covers the space and frequency domains. The sum is infinite because the developing is around the centre of the Earth. If instead, a development around the point $\vec{x}$ is used, the infinite sum becomes finite and:

$$\begin{aligned} g_{\vec{y}}^{d}(\vec{x}) &= \sum_{l=0}^{d+1} (2\alpha_l^{d+1} + \alpha_l^d) \frac{Rl!|x|^l P_l(\widehat{\vec{x}-\vec{y}}.\hat{y})}{|\vec{x}-\vec{y}|^{l+1}} \\ &= (-1)^{d+1} \sum_{l=0}^{d+1} (2\beta_l^{d+1} - \beta_l^d) \frac{Rl!|y|^l P_l(\widehat{\vec{y}-\vec{x}}.\hat{x})}{|\vec{x}-\vec{y}|^{l+1}}. \end{aligned} \tag{33}$$

The coefficients α and β have a simple recursive expression, which may be implemented efficiently, as the coefficients ${\alpha_l}^d$ are recursively defined through:

$$\begin{aligned} &\alpha_l^d = \alpha_{l-1}^{d-1} + l\alpha_l^{d-1}, \quad d \geq 1 \\ &\alpha_k^0 = \delta_{k,0}. \end{aligned} \tag{34}$$

The coefficients ${\beta_l}^d$ are recursively defined through

$$\begin{aligned} &\beta_l^d = \beta_{l-1}^{d-1} + (l+1)\beta_l^{d-1}, \quad d \geq 1 \\ &\beta_k^0 = \delta_{k,0}. \end{aligned} \tag{35}$$

3.3.2 Inverse Problem

Let us consider $\vec{b}_i$, the values of the magnetic field at some observation points $\vec{x}_i$, with i=1,. . .,M (typically at the satellite level). Usually, these values are contaminated with some errors. It is meaningful to suppose known $\sum_{i,j}$, the 2-point correlation matrix of the errors, and $\Gamma(b)$ – a quadratic form providing some a priori information about the magnetic field (for example, the quadratic form may incorporate the average decrease of spectral energy of the field).

The problem which has to be solved is to find a minimizer α of the following expression:

$$(A\alpha - b)^T \sum^{-1} (A\alpha - b) + \lambda\Gamma(b), \tag{36}$$

where A is the matrix containing the values of the wavelets at measurement points, α is the unknown vector of the wavelet coefficients and λ is a Lagrange multiplier.

3.3.3 Local Multipole Approximations

In order to take advantage of the properties of the Poisson wavelets (their localization in space and frequency and their smoothness at the satellite altitude), each wavelet can be approximated, within a given unity-volume P_j, by its local multipole expansion around the centre of mass $\vec{x}_{0,j}$ of the M_j data points inside it.

For a fixed unity-volume P_j, a Poisson wavelet is approximated by:

$$g_{\vec{y}}^{d}(\vec{x}) \approx \sum_{\ell=0}^{L} \sum_{m=-\ell}^{\ell} c_{\ell}^{m} h^{\ell} Y_{\ell}^{m}(\beta,\gamma), \tag{37}$$

where L is the degree of the multipole development, c_{ℓ}^{m} are constant coefficients, Y_{l}^{m} are again the spherical harmonics of degree l and order m, and (h,β,γ) are the spherical coordinates of the point $\left(\vec{x}-\vec{x}_{0,j}\right)$.

Using the approximation (37) the original inverse problem (36) gets the following form:

$$(\tilde{A}\tilde{\alpha}-b)^{T}\sum{}^{-1}(\tilde{A}\tilde{\alpha}-b)+\lambda\Gamma(b). \tag{38}$$

In the above formulation, the matrix $\tilde{A}$ can be represented as:

$$\tilde{A}=\Psi C, \tag{39}$$

where Ψ is a $(M \times K[(L+1)^2])$ block-diagonal matrix, containing the values of the local functions from (37) and C is a $(K[(L+1)^2] \times W)$ full matrix containing the local coefficients.

Considering this decomposition of the matrix $\tilde{A}$, the problem (38) can be rewritten in the following form:

$$\begin{aligned} &(C\tilde{\alpha}-\eta)^{T}S(C\tilde{\alpha}-\eta)+\lambda\Gamma(b),\\ &\text{where}\begin{cases} S=\Psi^{T}\sum{}^{-1}\Psi \\ \eta=S^{-1}\Psi^{T}\sum{}^{-1}b. \end{cases} \end{aligned} \tag{40}$$

The simplest possible case is when $L=0$. It is equivalent of approximating the Poisson wavelets by piecewise constant functions and replacing the data by their averaged values over each unity-volume.

This suggests that it is possible to considerably reduce the size of the original problem involving the big system matrix A, with a new one which has a smaller system matrix C. Obviously, a trend should be found between the gain of time and the computational power of the inverse problem and the accuracy of the representation of the data.

The first numerical tests, performed on CHAMP satellite magnetic data, allowed us to check the behavior of the icosahedral volume implementation and furthermore the applicability of the mathematical method.

In the two previous sections, the accent has been put on the magnetic data and tools to model them. The given details are crucial for describing the part of the geomagnetic field originating in the lithosphere. This field, at global and some regional scales is discussed in the following section. This is indeed one of the main topic of this contribution.

4 Lithospheric Field: More Details at All Scales

The lithospheric contribution of the geomagnetic field has to be modeled by combining satellite with ground-based, airborne and marine magnetic data in order to describe all resolvable wavelengths. A prior thorough analysis of the available data is necessary to detect outliers, incorrect coordinate systems or shifts in the data before merging them. Careful examination of the data suggests that near surface compilations contain long wavelengths (> 400 km) that differ significantly, both in strength and shape, from global lithospheric field models based on satellite data. In contrast, the wavelengths smaller than 400 km are naturally attenuated at the satellite altitude and the derived models of the lithospheric field are then not very accurate. The satellite models are therefore used to describe the large scale lithospheric contribution on global scale. Thus, in the following the global and regional features of the lithospheric field are separately addressed.

4.1 Lithospheric Field and Its Large Scale

The satellite missions brought significant improvements in retrieving the large-scale magnetic signatures of the Earth's crust and upper mantle. Due to the flight altitude of satellites it is impossible to resolve small-scale field structures from satellite data. Indeed, a limitation inherent to magnetic surveys from satellites is that the measurements have to be performed at a certain altitude. This implies that magnetic features smaller than the orbit height cannot be resolved well because the spatial decay of magnetic fields with distance from the source depends on spatial wavelength. Considering recent satellites, with a typical altitude in average about 800 km for Ørsted, 700 km for SAC-C and 400 km for the CHAMP mission, it is possible to compute the impact of the orbit altitude on different wavelength features. The attenuation factors are listed in Table 2 for the spherical harmonic degrees 20, 50 and 80, relative to observations at the Earth's surface. From this table it becomes clear how important measurements from low orbits are for high-degree magnetic field models. Present improvements in the lithospheric field models are therefore based entirely on CHAMP observations.

Table 2 Attenuation factors for small-scale crustal features (expressed by the SH degree) at different orbital altitudes relative to amplitudes at the Earth's surface

Altitude	deg20	deg50	deg80
Surface	1	1	1
300 km	0.36	9.1×10^{-2}	2.3×10^{-2}
400 km	0.26	4.2×10^{-2}	6.8×10^{-3}
700 km	0.10	4.4×10^{-3}	1.9×10^{-4}
800 km	0.07	2.1×10^{-3}	6.1×10^{-5}

Nevertheless, high-degree spherical harmonic models are important for a number of different purposes, like interpretation and identification of geological provinces and tectonic boundaries (Ravat and Purucker, 2003), or large wavelength leveling of aeromagnetic surveys and marine survey track lines, or also, reduction of crustal magnetic field signatures in studies of other field contributions. As mentioned before, spherical harmonic around degrees 13–15 core and lithospheric field contributions have similar amplitudes. Inverse models therefore typically start at spherical harmonic degree 16, while forward models include estimates of the longer wavelengths.

The first high-degree internal models, also called lithospheric field models, have been obtained from POGO and MAGSAT data. Due to the short MAGSAT mission duration and limitations of the only scalar data provided by the POGO series, reliable expansions only up to degrees between 45 and 60 could be achieved (Cain et al., 1989; Arkani-Hamed et al., 1994; Ravat et al., 1995). Advances came along with the low-orbit CHAMP mission. The first version of a family of high-degree models (MF), based on only one year of CHAMP scalar data, provided a magnetic anomaly map valid at an altitude of 438 km and for spherical harmonic degrees 14–65 (Maus et al., 2002). Many prominent crustal magnetic features could already be identified on this map (some of them being discussed in the following). With the following versions the vector field data were also considered, allowing for upward/downward continuations of the model. Downward continuation, however, has to be regarded with caution, as any noise in the data contributing to the model is strongly amplified by this process. The corresponding amplification factors for different altitudes can be inferred from Table 2.

The GRIMM model also has a lithospheric contribution. Figure 21 shows the GRIMM (Lesur et al., 2008), xCHAOS (Olsen and Mandea, 2008) and MF5 (Maus et al., 2007) power spectra for the spherical harmonic degrees 16–60. Even, if both the GRIMM and xCHAOS models are focused on the core field, they nonetheless present similar spectra up to SH degree 45. This is an improvement compared to the correlation between CHAOS and the BGS/G/L/0706 model (Thomson and Lesur, 2007) and it clearly confirms that not only the MF5 lacks power, but also presents spurious features at these low degrees.

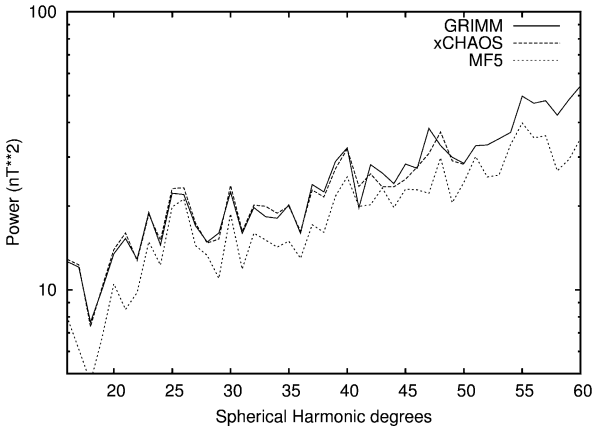

Fig. 21 Power spectra of for the GRIMM, xCHAOS and MF5 models at the Earth's reference radius for SH degrees 16–60

Figure 22 present the vertical down component of the GRIMM lithosphere field modeled at the Earth's surface for SH degree 16–45 and its differences relative to MF5. The shapes of these spurious anomalies are typical of those introduced by along track filtering.

4.2 Lithospheric Field and Its Small Scale

4.2.1 World Digital Magnetic Anomaly Map

A possibility to recover the lithospheric field with a shorter wavelength content (degrees/orders higher than 130) is to merge satellite data, aeromagnetic and marine survey data, and ground-based data (observatory and repeat stations). They have also to be processed together. A huge international effort has been done to produce such a description of the lithospheric field, in the frame of the World Digital Magnetic Anomaly Map (WDMAM).[5] The GFZ contribution to the WDMAM project (Hamoudi et al., 2007) is known as the GeoForschungsZentrum Anomaly Magnetic MAp (GAMMA).

The distribution of available magnetic datasets used to build GAMMA is shown in Fig. 23. These datasets consist in more than 50 years of aero-magnetic surveys, research vessel magnetometers crossing the seas, supplemented by anomaly values obtained from oceanic crustal ages and observations from satellites. The coverage is uneven between the continental and ocean areas, as well as between Northern and Southern hemispheres.

[5] http://projects.gtk.fi/WDMAM/

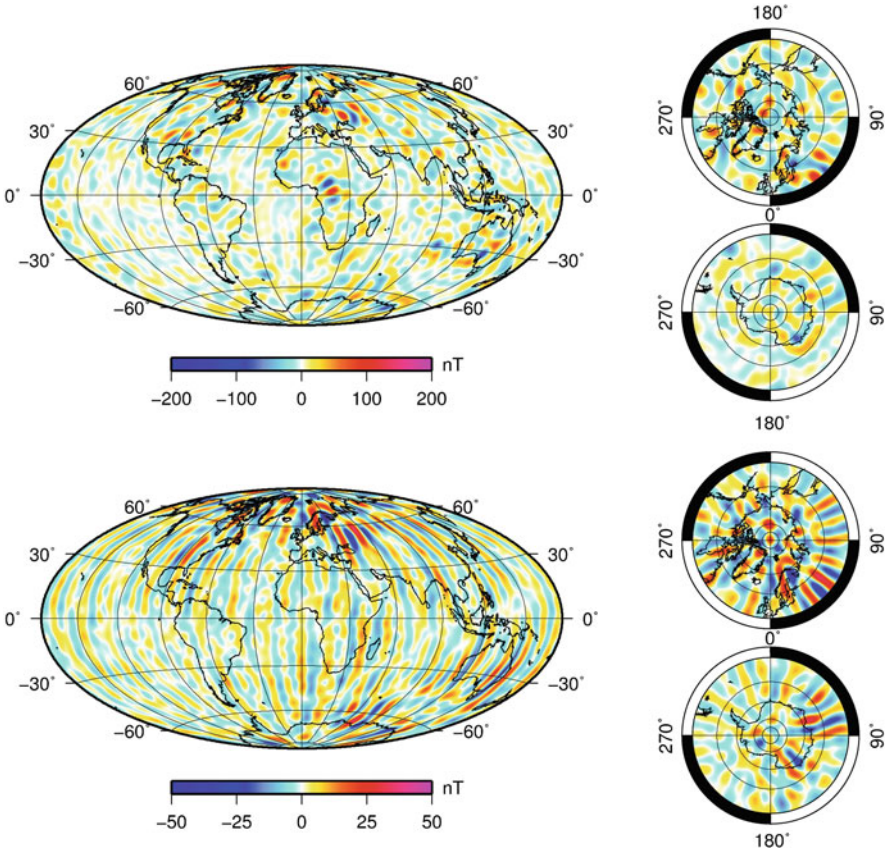

Fig. 22 Map of the vertical down component of the GRIMM lithospheric field for SH degrees 16–45 at the Earth's reference radius (*top*). Map of the vertical down component of the differences between the GRIMM and MF5 models for SH degrees 16–45, at the Earth's reference radius (*bottom*)

The available magnetic compilations are in various formats and projections. Before applying any filtering or merging procedures, all grids have to be transformed from their local reference system to a common representation on the global reference ellipsoid, WGS84. Marine data have been reprocessed to produce grids at mean sea level, when possible.

The continental-scale aeromagnetic compilations have been produced after stitching together different regional anomaly grids. These regional surveys were flown at various epochs and hence use various core field models to reduce the observed data. The patch-worked grids prone to errors, mismatch in anomaly shapes and anomalous intensity values clearly noticeable across overlapping regions, introduce fictitious anomalies. The lack of absolute reference makes it difficult to recover the long wavelength information. Despite their decimation on a regular

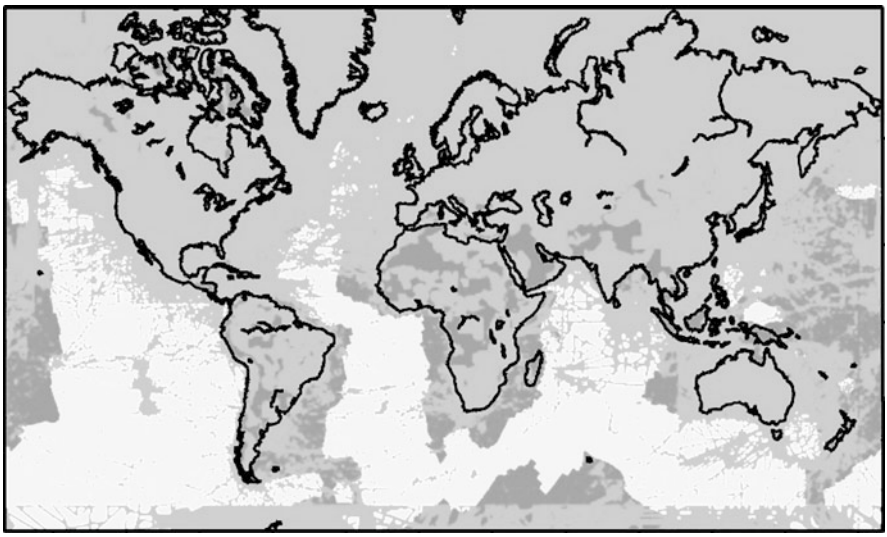

Fig. 23 Data distribution: from aeromagnetic and marine surveys (*light grey*), satellite observations (*dark grey*) and oceanic crustal ages (*white*)

grid, the final resolution may not be uniform and only a spectral analysis such as wavelet techniques could help in precisely locating the regions of varying resolution. Furthermore, not only the core field models used to reduce these regional surveys are mostly unknown, but also each individual compilation panel was often reduced using a local polynomial. This lack of information prevents us from further correcting the grids for a more homogeneous core field model. According to the WDMAM recommendations, the grids are resampled to 0.05° ($\approx 3'$ or 10 km wavelength at the equator).

As an example of the difficulties that occurred during the merging processing, detailed anomaly features are compared over overlapping regions between two adjacent grids. The example shown in Fig. 24 concerns the European (EUR) and Eurasian (ERS) grids. The EUR grid shows anomalies that are smoother than the neighboring ERS grid. Two reasons may be invoked. Firstly, the EUR grid is upward continued to 3 km altitude, while the ERS grid is produced by combining many disparate aeromagnetic surveys of smaller dimension without upward continuing the final grid. Secondly, a spectral analysis carried out on the EUR grid showed sudden power decay for wavelengths lower than 30 km and it seems that EUR grid was filtered in order to produce a homogeneous resolution map. The anomaly features across the boundary of EUR and ERS grids show partial disagreement of anomalies. For instance, the anomaly feature across the regions marked by a circle in Fig. 24 appears to continue across the grid edges but the strength of the anomaly over the EUR grid appears weaker. On the three indicated profiles (P1, P2 and P3) the strength of the total field intensities across the two grids have been investigated. All profile sections show intensity variations of the ERS grid that are consistent with

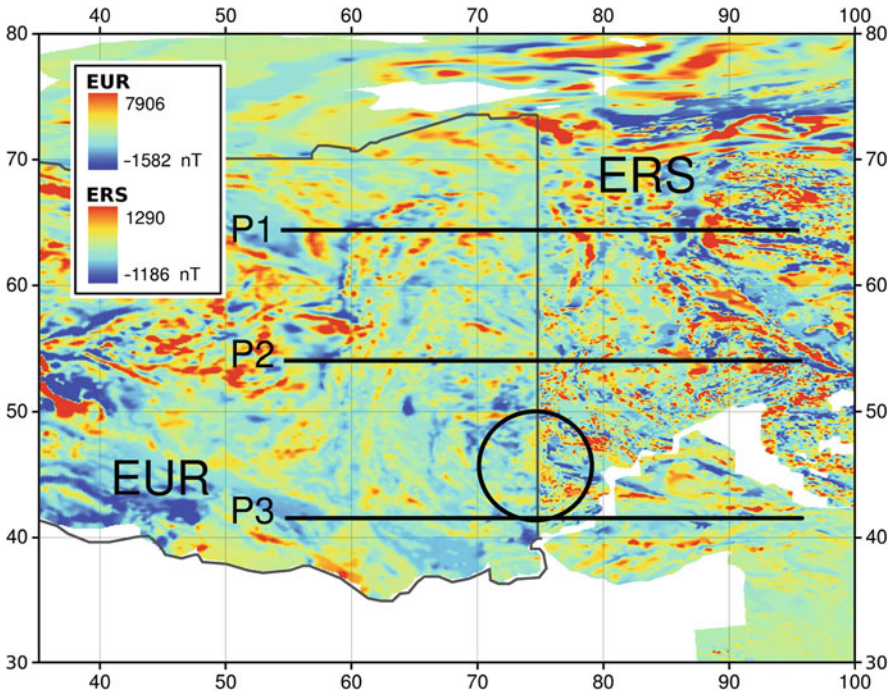

Fig. 24 Map of the two aeromagnetic compilations, European (EUR) and Eurasian (ERS) grids. The detailed anomaly features between the two grids show differences in their shape, size and strength. On the three indicated profiles (P1, P2 and P3) the strength of the total field intensities across the two grids have been investigated

anomaly patterns of the EUR grid. However, within the overlapping region total field intensities disagree in strength by 10 – 200 nT. At the grid boundary these intensities vary by 100 – 150 nT, highlighting once again the differences in the anomaly strength across the two grids. Such differences are also observed between some other grid boundaries (not shown here). To find the sources causing differences in the shape, size and strength of anomalies between various grids, as demonstrated for European and Eurasian grids, a detailed procedure was followed on to process the individual grids.

Once all surveys have been merged together, two different techniques are envisaged for filtering and smoothing the final grid. A first option consists in filtering the grid using Fourier transforms. This procedure is relatively fast but the main drawback is that it is a non-potential method, and the coefficients could not be used for predicting the three components of the magnetic field. Another method is based on the spherical harmonics analysis. The grid is interpolated on the Gauss-Legendre knots and the parameters up to spherical harmonic degree 500 are obtained by least-squares (maximum resolution of 80 km). Above degree 500, the coefficients are difficult to be obtained as the signal/noise ratio is very low. This is also due to the data gaps and heterogeneous resolution at the global scale.

A few other international teams have done the same work for processing magnetic data, producing candidates for the WDMAM. The proposed grids have been compared and merged, and the best aspect of each has been preserved for the final compilation. The resulting map was published by CCGM.

The WDMAM gives the essence of the magnetic anomalies at 5 km altitude. Its release is still too novel to illustrate its scientific outcomes. In Fig. 25, we may however recognize the remarkable magnetic features, such as Chicxulub crater, Bangui anomaly, Thromsberg anomaly, Richat structure, Atlantic ridge, Bay of Biscay, Sumatra-Java arc or Paris Basin, features discussed in details by Mandea and Thébault (2007). The WDMAM has already became an important tool for evaluating competing hypotheses and reconstructions of continental and oceanic assemblies of most regions of the world, and understanding their geologic evolution at various spatial scales.

Of course this first edition of the WDMAM is subject of improvements. One direction is to take into account data which were not available e.g. of the national or particular permission reasons, during the first compilation processing. One example is given by the large efforts to access to the Northern African surveys (Morocco and Algeria). These data are partly available, and the first map of this region is shown in Fig. 26, which is an expression of the complexity of the Maghrebides geology.

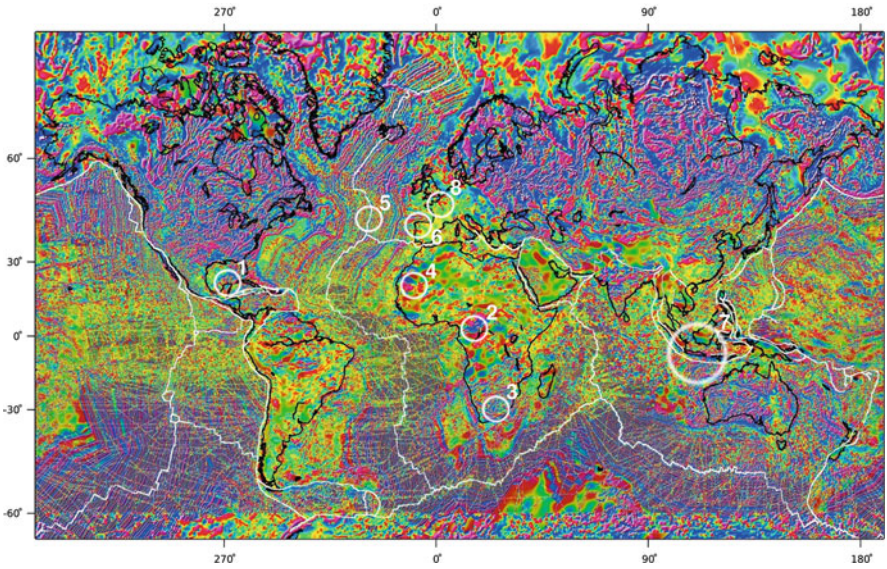

Fig. 25 Map of the GAMMA model, candidate to the first edition of the World Digital Magnetic Anomaly Map (WDMAM), giving the essence of the worldwide magnetic anomalies at 5 km altitude. The most important magnetic features are indicated: (1) Chicxulub crater; (2) Bangui anomaly; (3) Thromsberg anomaly; (4) Richat structure; (5) Atlantic ridge; (6) Bay of Biscay; (7) Sumatra-Java arc; (8) Paris Basin

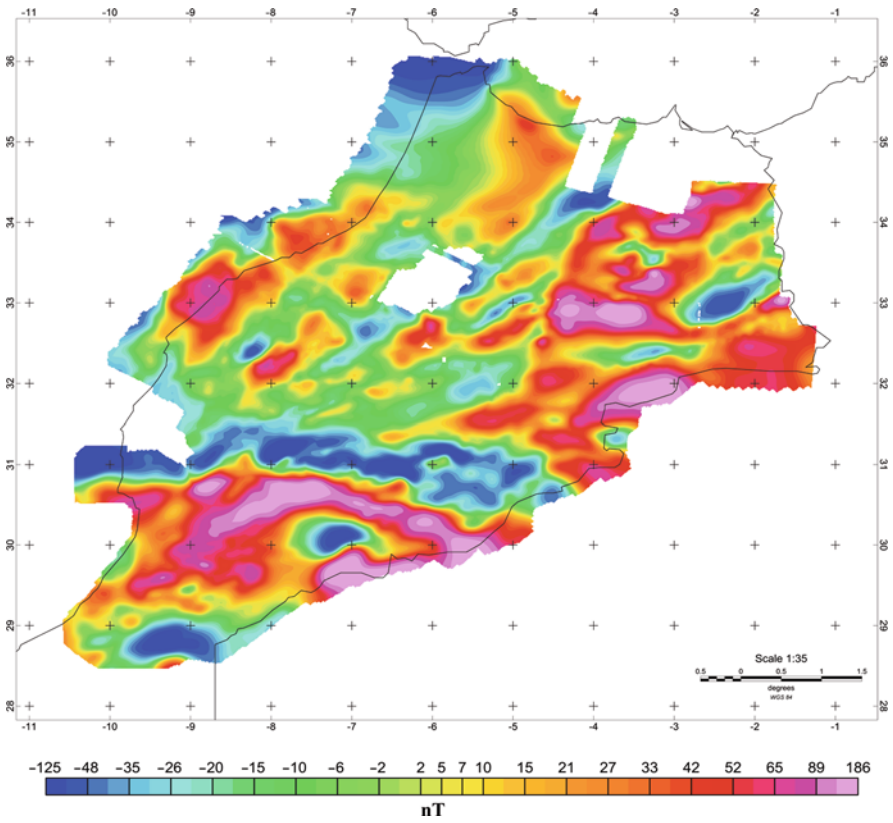

Fig. 26 The magnetic anomaly map over a part of the Northern Africa, obtained from the available Morocco data (data by courtesy of Ministry of Energy and Mine, Morocco)

Another improvement for the second edition of the WDMAM concerns the improvement of the magnetic ocean surveys. The magnetic measurements acquired over oceans and seas since more than half a century are stored by the GEOphysical DAta System (GEODAS).[6] Generally, both the original magnetic field intensity and magnetic anomaly values are stored. The magnetic anomaly values are estimated from the measured intensity data, by subtraction of the core and external magnetic fields. Recently, Quesnel et al. (2009a) used the Comprehensive Models (Sabaka et al., 2004) to properly remove the core and external magnetic fields from all original measurements. Besides, a careful analysis of each data (track by track) has been needed to correct or remove many shifted values, as well as to reduce the noise in some tracklines. Comparisons of magnetic anomaly maps before and after the indicated corrections highlight the improvement in the quality and coherence of the data. In Fig. 27 a comparison between pre-corrected and corrected data is shown.

[6] http://www.ngdc.noaa.gov/mgg/geodas/trackline.html

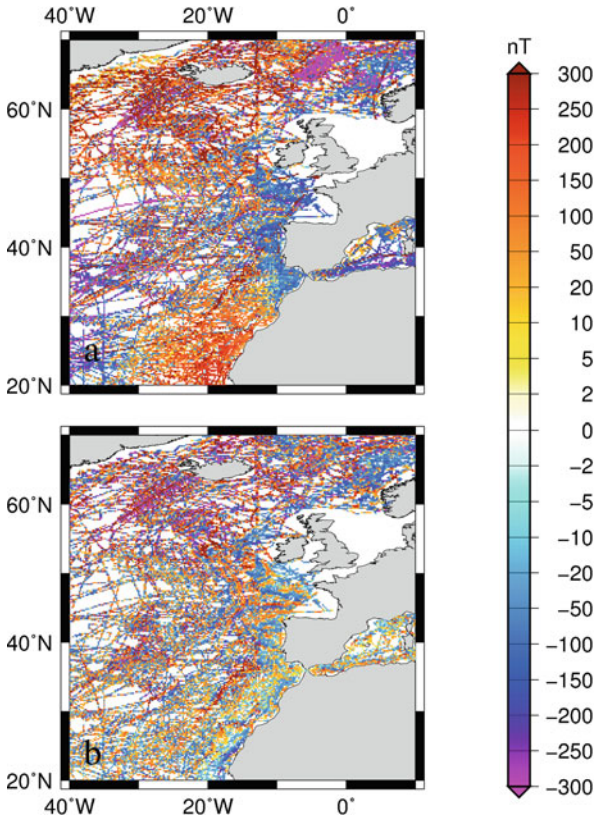

Fig. 27 Maps of the magnetic anomalies over the North Atlantic from the original anomaly values given by the GEODAS data set (*top*) and from the CM4-corrected and cleaned magnetic values (*bottom*)

4.2.2 Some Qualitative Geology

A global magnetic anomaly map is a tool for geologists to identify large-scale tectonics, especially in places where no regional geology and tectonic maps are available. A common method of interpretation consists of comparing the anomaly field with geological and tectonic maps. An exhaustive review of magnetic mapping applications is out of scope of this chapter, so only a few examples are given, which have been selected to give a flavor of magnetic anomaly applications and interpretations at various spatial scales.

The seefloor spreading. The magnetic mapping of ocean floor is an essential tool for reconstructing the history of the Earth. Oceanic linear magnetic anomalies are composed of linear segments of polarity separated by a steep gradient that were recognized since the 1950s, but were lacking a satisfactory explanation. Vine and Matthews (1963) noticed the pattern similarity between continental vertical

magnetostratigraphy and horizontal oceanic lineaments. They proposed that seafloor linear anomalies result from a combination of reversals in the Earth's magnetic field and seafloor spreading is symmetrical and parallel to ocean ridges crests. As magma ascends along the ridges it cools and solidifies. The rocks formed acquire a thermo-remanent magnetization aligned along the ambient magnetic field. As sea floor spreading continues, the magnetic field is recorded in the rocks symmetrically to the mid-ocean ridge, creating these remarkably continuous lines that are occasionally displaced by perpendicular fracture systems that reveal variations in the seafloor spreading and tectonic movements (see Fig. 25 and the North Atlantic features in Fig. 28).

The Beattie Magnetic Anomaly. The origin of the 1,000 km – long Beattie Magnetic Anomaly (Fig. 29) in South Africa remains unclear and contentious. Key issues include the width, depth and magnetization of its source. Recently, Quesnel et al. (2009b) use uniformly magnetized spheres, prisms and cylinders to provide the simplest possible models which predict the 1 km – altitude aeromagnetic measurements along a profile across this anomaly. The obtained results suggest that two similarly magnetized and adjacent sources, with a vertical offset, are more likely to explain the observed magnetic anomaly than a single source. The best model corresponds to two highly-magnetized (> 5 Am^{-1}) sheet-like prisms, extending from 9 to 12 km depth, and from 13 to 18 km depth, respectively, and with a total width reaching 80 km. Associated magnetizations seem to be mostly induced, although a weak remanent component is required to improve the fit. The aeromagnetic data and their modeling suggest that the geological sources for the Beattie Magnetic Anomaly are mostly located in the middle crust and may be displaced by a shear zone or a fault. Contrary to previous models suggesting serpentinized relics of an

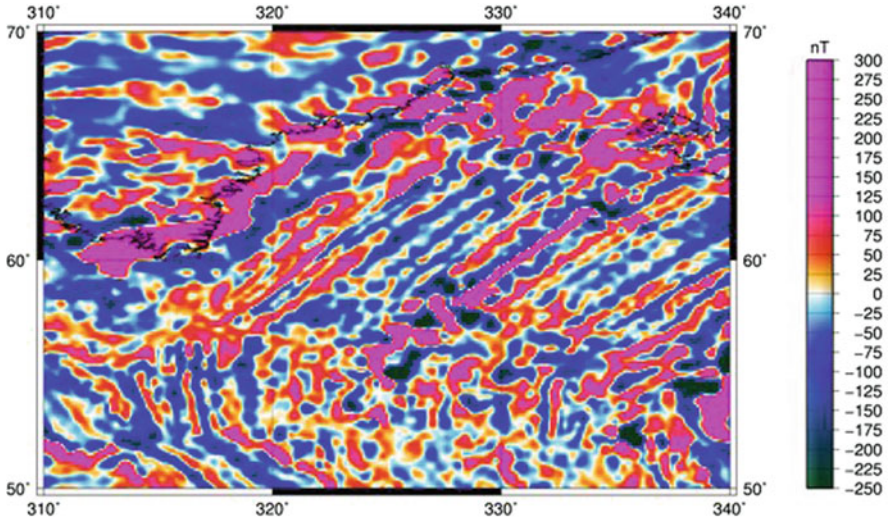

Fig. 28 Magnetic mapping of the North Atlantic ocean's floor as seen by the WDMAM

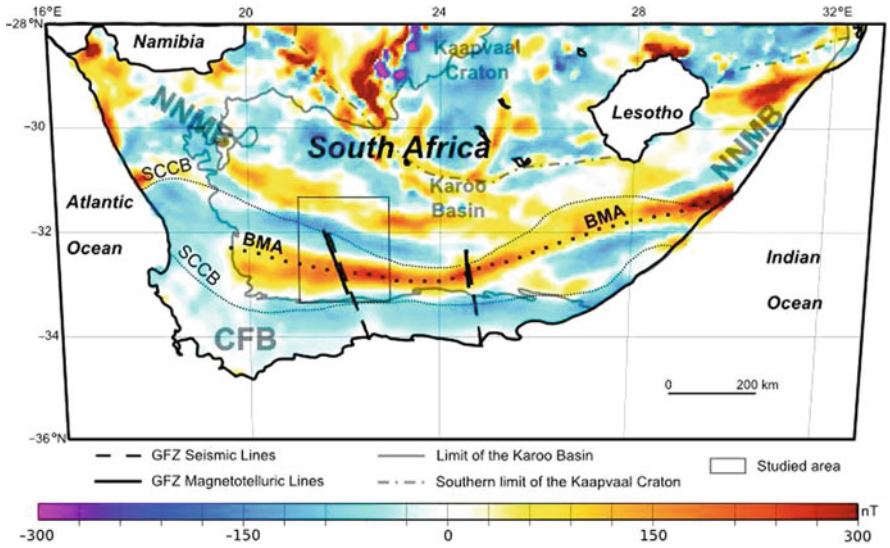

Fig. 29 Magnetic anomaly map at 5 km altitude over South Africa. The Beattie Magnetic Anomaly (BMA), the Southern Cape Conductive Belt (SCCB), Namaqua-Natal Mobile Belt (NNMB) and the Cape Fold Belt (CFB) are indicated

inferred suture zone of the Natal-Namaqua Mobile Belt, Quesnel et al. (2009b) propose that granulite-faces mid-crustal rocks within this belt may cause the Beattie Magnetic Anomaly.

The Java trench. Magnetic anomaly maps can give information about geodynamics at geological time scales. It is thus used to drive the understanding of geologic hazard but cannot be employed for hazards prediction. The aeromagnetic features of the region surrounding the Great Sumatra earthquake and tsunami of December 2004 could provide us with a current and historical view of the active subduction in the region. The subduction can be seen on the gravity anomaly map by an increase of the gravity field along the subduction zone. A lithospheric magnetic field satellite image confirms the compression boundary between the Eurasian and Indo-Australian plates. Even if this conception is oversimplified, a subduction zone near the magnetic equator, like the Sumatra trench, has a typical positive magnetic signature above the location where the "cold" magnetic ocean crust penetrates into the relatively non-magnetic mantle. To the contrary, the magnetic anomaly map realized at sea-level appears noisy and the large scales structures are hidden or distorted (see again Figs. 25 and 30). One reason is the data distribution which is not homogeneous and furthermore no data are available inland. The more geophysical reason is that a magnetic map made using shipborne and airborne data is mostly sensitive to shallow and small dimension magnetic materials. In contrast, the far-field imaging using satellite data has a better sensitivity to the deep and large magnetic anomalies. Both views are complementary and the use of each data depends on the spatial scale at which the study is realized.

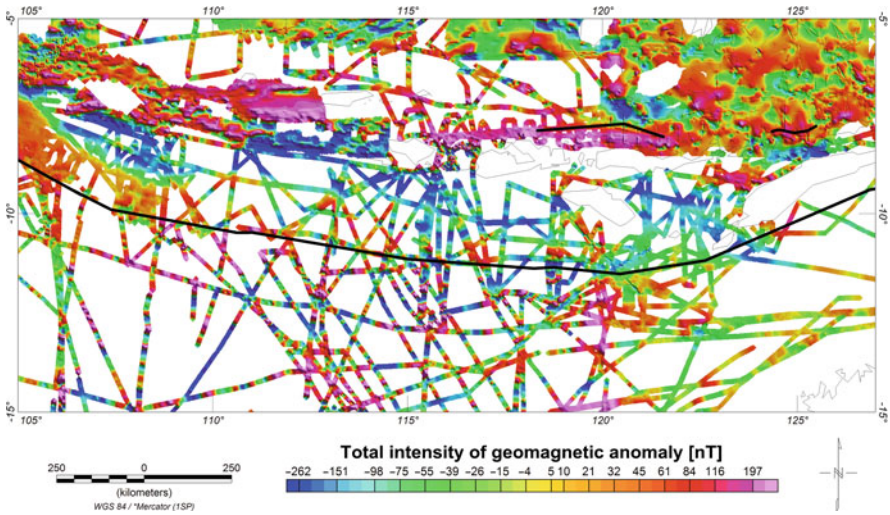

Fig. 30 Magnetic anomaly map at the Java Trench

5 Conclusions and Outlook

The different topics addressed in this chapter have in common the wish to better understand the geomagnetic field. In spite of its remarkable persistence, the Earth's magnetic field is continually changing, covering time-scales from seconds to million years, when its polarity can reverse. Considerable success has been achieved in describing the geomagnetic field, with its core, lithospheric, ionospheric and magnetospheric contributions when recent, Ørsted, CHAMP, SAC-C satellite measurements have been used together with ground-based data. For the first time, short time-scales of secular variation have been detected in satellite data. Some other interesting signatures have been found in CHAMP magnetic data, such as the SGR 1806-20 magnetar.

Although new and sometimes surprising results have been found when magnetic satellite data have been investigated, the particular combination of the long-term steadiness and short-term fluctuations of the magnetic field, still rises fundamental questions about the geodynamo, core-mantle boundary, mantle properties, and geospace environment.

Answering such questions would have both practical and scientific benefits. A full understanding of the magnetic field will emerge from improvements in measuring the field, separating its different contributions with a better spatial and temporal resolution, developing new mathematical tools to analyze available data. The upcoming ESA Swarm[7] mission will provide the best-ever survey of the geomagnetic field and its temporal evolution. This constellation will also benefit from a

[7] http://www.esa.int/esaLP/LPswarm.html

new generation of instruments, enabling measurements to be taken simultaneously over different regions of the Earth. We fully expect to obtain new insights into the interaction of the solar wind with the Earth's internally generated dynamo field. The multi-satellite approach of Swarm will especially pay off for separating internal and external field contributions. To take full advantage of the increased precision and resolution, new mathematical methods for data analysis and improved models of the external field generation will be developed. The improved knowledge of the internal field and its temporal variations should also advance our understanding of the dynamical processes in Earth's liquid iron core. Finally, new opportunities to survey the geospace environment and infer the magnetic changes will be of great interest for our Planet.

Acknowledgments Several of our colleagues involved in different aspects of this contribution participated in various steps of the work. We particularly thank Martin Rother, Ingo Michaelis, Borislav Minchev, Mohamed Hamoudi, Yoann Quesnel for providing inputs to this chapter. Alexander Jordan and Martina Krüger provided helpful support during the editorial process. We would like to acknowledge all of them for their logistic assistance.

We appreciate the dedicated work of people and institutions carrying out magnetic measurements in worldwide magnetic observatories and national repeat station networks. We also would like to acknowledge all geological surveys and group members who provided aeromagnetic and marine magnetic anomaly data for World Digital Magnetic Anomaly project. The CHAMP mission is operated and supported by Helmholtz Centre Potsdam GFZ German Research Centre for Geosciences, the German Aerospace Center (DLR) and the German Federal Ministry of Education and Research (BMBF). This work has got financial support in the frame of GEOTECHNOLOGIEN project 03F0442A.

References

Arkani-Hamed J, Langel RA, Purucker M (1994) Scalar magnetic anomaly maps of Earth derived from POGO and MAGSAT data. J. Geophys. Res. 99(B12), 24075–24090.

Cain JC, Wang Z, Kluth C, Schmitz DR (1989) Derivation of a geomagnetic model to n = 63. Geophys. J. Int. 97, 431–441.

Chambodut A, Panet I, Mandea M, Diament M, Holschneider M, Jamet O (2005) Wavelet frames: An alternative to spherical harmonic representation of potential fields. Geophys. J. Int. 163, 875–899, doi: 10.1111/j.1365-246X.2005.02754.x..

Christensen U, Wicht J (2007) Numerical dynamo simulations. In: Olson P (ed.), Treatise on Geophysics: Core Dynamics, Elsevier, Amsterdam.

De Santis A (1991) Translated origin spherical cap harmonic analysis. Geophys. J. Int. 106, 253–263.

Gauss CF (1839) Allgemeine Theorie des Erdmagnetismus. In: Gauss CF, Weber W (eds.), Resultate aus den Beobachtungen des magnetischen Vereins im Jahre 1838, Leipzig, pp. 1–57.

Glassmeier K-H, Soffel H, Negendank J (2009) Geomagnetic Field Variations, Springer, Berlin.

Gubbins D, Herrero-Bervera E (eds.) (2007) Encyclopedia of Geomagnetism and Paleomagnetism, Springer, Berlin, ISBN: 978–1–4020–3992–8.

Haines GV (1985) Spherical cap harmonic analysis of geomagnetic secular variation over Canada 1960–1983. J. Geophys. Res. 90, 2563–2574.

Hamoudi M, Thebault E, Lesur V, Mandea M (2007) GeoForschungsZentrum Anomaly Magnetic MAp (GAMMA): A candidate model for the World Digital Magnetic Anomaly Map. Geochem. Geophys. Geosys. 8, Q06023, doi: 10.1029/2007GC001638..

Holschneider M, Chambodut A, Mandea M (2003) From global to regional analysis of the magnetic field on the sphere using wavelet frames. Phys. Earth Planet In. 135(2), 107–124.
Jankowski J, Sucksdorff C (1996) IAGA guide for magnetic measurements and observatory practice, IAGA, Warsaw.
Keller W (2001) A wavelet approach for the construction of multi-grid solvers for large linear systems. AG Scientific Assembly.
Korhonen J, Fairhead J, Hamoudi M, Hemant K, Lesur V, Mandea M, Maus S, Purucker M, Ravat D, Sazonova T et al. (2007) Magnetic anomaly map of the world – carte des anomalies magnétiques du monde, scale 1:50,000,000. Commission for Geological Map of the World, UNESCO, 1st Edition.
Korte M, Constable CG (2003) Continuous global geomagnetic field models for the past 3000 years. Phys. Earth Planet In. 140, 73–89.
Kusche J (2000) Implementation of multigrid solvers for satellite gravity anomaly recovery. J. Geod., 74, 773–782.
Langel RA (1987) The main field. In: Jacobs, JA (ed.), Geomagnetism, Volume 1, Academic Press, London, pp. 249–512.
Langel RA, Estes RH (1985) The near-Earth magnetic field at 1980 determined from MAGSAT data. J. Geophys. Res. 90, 2495–2509.
Langel RA, Estes RH, Mead GD, Fabiano EB, Lancaster ER (1980) Initial geomagnetic field model from MAGSAT vector data. Geophys. Res. Lett. 7, 793–796.
Langel RA, Hinze WJ (1998) The Magnetic Field of the Earth's Lithosphere – The Satellite Perspective, Cambridge University Press, Cambridge.
Langlais B, Mandea M (2000) An IGRF candidate main geomagnetic field model for epoch 2000 and a secular variation model for 2000–2005. Earth Planets Space 52, 1137–1148.
Lesur V (2006) Introducing localized constraints in global geomagnetic field modeling. Earth Planets Space 58, 477–483.
Lesur V, Wardinski I, Asari S, Minchev B, Mandea M (2010) Modeling the earth's core magnetic field under flow constraints. Earth Planets and Space, doi: 10.5047/eps.2010.02.010, in press.
Lesur V, Wardinski I, Rother M, Mandea M (2008) GRIMM – The GFZ Reference Internal Magnetic Model based on vector satellite and observatory data. Geophys. J. Int. 173, 382–394.
Lowes FJ (1966) Mean-square values on sphere of spherical harmonic vector fields. J. Geophys. Res. 71, 2179.
Lühr H, Korte M, Mandea M (2009) The recent geomagnetic field and its variations. In: Glassmeier K, Soffel H, Negendank J (eds.), Geomagnetic Field Variations, Springer, Berlin, pp. 25–64.
Mandea M, Balasis G (2006) The SGR 1806-20 magnetar signature on the earth's magnetic field. J. Geophys. Int., doi: 10.1111/j.1365-246X.2006.03125.x.
Mandea M, Purucker M (2005) Observing, modeling, and interpreting magnetic fields of the solid earth. Surv. Geophys. 26, 415–459.
Mandea M, Thébault E (2007) The changing faces of the earth's magnetic field: A glance at the magnetic lithospheric field, from local and regional scales to a planetary view. Commission for the Geological Map of the World.
Maus S, Lühr H, Hemant K, Balasis G, Ritter P, Stolle C (2007) Fifth generation lithospheric magnetic field model from CHAMP satellite measurements. Geochem. Geophys. Geosys. 8, Q05013, doi: 10.1029/2006GC001521.
Maus S, Rother M, Holme R, Lühr H, Olsen N, Haak V (2002) First scalar magnetic anomaly map from CHAMP satellite data indicates weak lithospheric field. Geophys. Res. Lett. 29(14), doi: 10.1029/2001GL013685.
Minchev B, Chambodut A, Holschneider M, Panet I, Schöll E, Mandea M, Ramillien G (2009) Local multi-polar expansions in potential field modeling. Earth Planets Space, 61, 10, 1127–1141.
Olsen N, Mandea M (2008) Rapidly changing flows in the earth's core. Nat. Geosci. 1, 390–394.
Quesnel Y, Catalán M, Ishihara TA (2009a) A new global marine magnetic anomaly data set. J. Geophys. Res., 114, B04106, doi: 10.1029/2008JB006144.

Quesnel Y, Weckmann U, Ritter O, Stankiewicz J, Lesur V, Mandea M, Langlais B, Sotin C, Galdéano A (2009b) Simple models for the Beattie Magnetic Anomaly in South Africa. Tectonophysics, doi: 10.1016/j.tecto.2008.11.027.

Ravat D, Langel RA, Purucker M, Arkani-Hamed J, Alsdorf DE (1995) Global vector and scalar MAGSAT magnetic anomaly maps. J. Geophys. Res. 100, 20111–20136.

Ravat D, Purucker M (2003) Unraveling the magnetic mystery of the earth's lithosphere. In: Reigber C, Lühr H, Schwintzer P (eds.), First CHAMP Mission Results for Gravity, Magnetic and Atmospheric Studies, Springer, Berlin, pp. 251–260.

Rother M, Choi S, Mai W, Lühr H, Cooke D (2005) Status of the champ me data processing. In: Reigber C, Lühr H, Schwintzer P, Wickert J (eds.), Earth Observation with CHAMP, Results from Three Years in Orbit, Springer, Berlin, pp. 413–418.

Sabaka TJ, Olsen N, Purucker M (2004) Extending comprehensive models of the Earth's magnetic field with Ørsted and CHAMP data. Geophys. J. Int. 159, 521–547.

Schuh W-D (2000) Scientific data processing algorithms. In Sunkel H (ed.), From Eotvos to Milligal, Final Report, ESA Report Study.

Shure L, Parker R, Backus G (1982) Harmonic splines for geomagnetic modeling. Phys. Earth Planet In. 28, 215–229.

Thébault E, Mandea M, Schott JJ (2006a) Modeling the lithospheric magnetic field over France by means of revised spherical cap harmonic analysis (R-SCHA). J. Geophys. Res. (Solid Earth) 111, B05102.

Thébault E, Schott JJ, Mandea M (2006b) Revised spherical cap harmonic analysis (R-SCHA): Validation and properties. J. Geophys. Res., 111, B01102.

Thébault E, Schott JJ, Mandea M, Hoffbeck JP (2004) A new proposal for spherical cap harmonic modeling. Geophys. J. Int. 159, 83–103.

Thomson A, Lesur V (2007) An improved geomagnetic data selection algorithm for global geomagnetic field modeling. Geophys. J. Int. 169, 951–963, doi: 10.1111/j.1365-246X.2007.03354.x.

Vine V, Matthews D (1963) Magnetic anomalies over oceanic ridges. Nature 199, 947–949.

Wicht J, Stellmach S, Harder H (2008) Numerical models of the geodynamo: From fundamental Cartesian models to 3d simulations of field reversals. In: Glassmeier K-H, Soffel H, Negendank J (eds.), Geomagnetic Field Variations, Springer Monograph, Springer, Berlin, pp. 107–157.

Part VIII
GGOS-D

Integration of Space Geodetic Techniques as the Basis for a Global Geodetic-Geophysical Observing System (GGOS-D): An Overview

Markus Rothacher, Hermann Drewes, Axel Nothnagel, and Bernd Richter

1 Motivation

In view of the alarming global change in the Earth system and the multitude of natural hazards with huge effects on humans and economy it is of greatest importance to develop a better understanding of the processes that describe and excite these continuous as well as abrupt changes. To achieve this, the structure of all elements of the Earth system (primarily the geosphere, the oceans, the hydrosphere and the atmosphere) have to be measured and monitored exactly, and the interactions between them have to be modeled correctly, i.e., a comprehensive global Earth observing system has to be built up. The expected outcome of such a system are consistent geodetic-geophysical time series that refer to a highly accurate reference frame that is stable over decades. Based on such knowledge of the past, conclusions may be drawn for the future development of the Earth system.

On the international level, the Global Geodetic Observing System (GGOS), now a full component of the International Association of Geodesy (IAG), is the geodetic contribution to a comprehensive global observing system as it is presently set up by the Group on Earth Observation (GEO) in the form of the Global Earth Observing System of Systems (GEOSS).

The project GGOS-D fits perfectly into the framework of GGOS that has as one of its major goals the integration and combination of the various space geodetic techniques. This integration is important not only for the realization of a highly accurate and long-term stable reference frame as the basis of all Earth observation, but also for the generation of homogeneous, high-quality time series of geodetic and geophysical parameters describing the processes in the Earth system. With the project GGOS-D, that had exactly this integration of the geometric and gravimetric space-geodetic techniques as its goal, an important German contribution could be made to GGOS (and to GEOSS in the broader sense).

M. Rothacher (✉)
ETH Zürich, Photogrammetrie, HPV G 52, Schafmattstr. 34, 8093 Zürich
e-mail: markus.rothacher@ethz.ch

F. Flechtner et al. (eds.), *System Earth via Geodetic-Geophysical Space Techniques*, Advanced Technologies in Earth Sciences, DOI 10.1007/978-3-642-10228-8_43,

2 Goals of GGOS-D

The overall objective of the project GGOS-D has been the investigation of the technological, methodological and information-technological realization of a global geodetic-geophysical observing system, a system that may open up the possibility to politics and economy to reliably identify and monitor long-term environmental processes, to understand the course of natural hazards and, thus, to provide important information for disaster prevention.

The main scientific goals of the project can be summarized as follows:

- Development of a data management and information system for the exchange and the near real-time provision of data and products of a global observing system.
- Definition and implementation of standards, models and parameterizations for the consistent processing of the data of the different space geodetic techniques and for the representation of the products.
- Generation of a consistent reference frame for the computation and provision of all parameters of the global observing system.
- Development of methods for the computation of consistent time series of the most important parameters (station coordinates, Earth orientation parameters, quasar coordinates, low-degree coefficients of the gravity field, troposphere parameters, sea surface topography).
- Investigation of relationships and correlations between time series of parameters and the comparison and validation of the time series with external geophysical data.

The major improvements (compared to the status of the international community of today) that GGOS-D was aiming at are the following:

- Implementation of common standards for modelling and parameterization in all software packages involved.
- Extension of the parameter space to link for the first time geometry, Earth rotation, sea surface heights and gravity field from SLR, VLBI, GPS, altimetry and Low Earth Orbiters (LEOs). Additional parameters (not yet considered in solutions of the official services) are quasar coordinates, nutation offsets and rates, tropospheric zenith path delays and gradients and low-degree coefficients of the Earth gravity field.
- Higher resolution in time for certain parameter types: besides weekly, also daily solutions were generated and Earth rotation parameter (ERPs) were set up with a sub-daily time resolution of 1 h.
- Usage of the SINEX (Solution INdependent EXchange) format for the exchange of all time series of parameters and solutions.
- The definition of a meta data standard for the SINEX format to allow the exchange of meta data.

The goals and objectives and the list of improvements mentioned above turned out to be very challenging, but most of them could be realized during the project.

3 Structure of GGOS-D

The structure of the GGOS-D project is shown in Fig. 1. We see that the project was designed to cover the processing chain of a global geodetic observing system

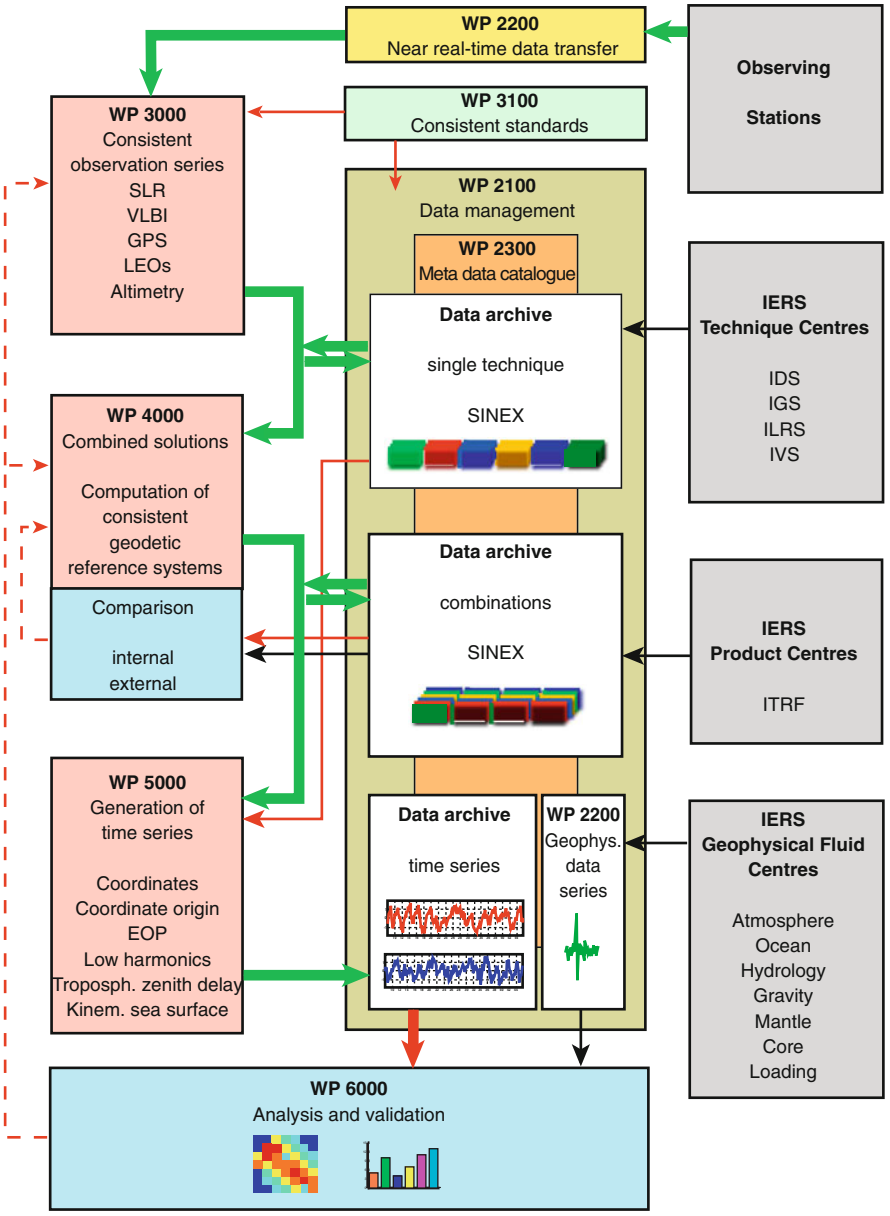

Fig. 1 Overview of the GGOS-D project

as completely and consistently as possible. This chain starts at the data collection and transfer, then goes to the processing and combination of the data and includes, finally, the validation and interpretation of the geodetic and geophysical time series. Therefore the project can be considered as a very small and reduced version of a global geodetic observing system or at least of the data management and processing part thereof. It can be seen that the data management and information system plays a central role in the GGOS-D structure as a place for the exchange of data, products and other information. It should also be noted that an iteration process is necessary to generate products of high consistency and accuracy (red dashed arrows in Fig. 1). In the time frame of the GGOS-D project two such iterations were performed.

The experiences made by the GGOS-D project in this respect are certainly very valuable for similar developments on an international level as part of the GGOS development.

4 Data Management and Information System

Figure 1 shows that the data management and information system takes a central function in the exchange and organization of data and information. All the products and time series of geodetic and geophysical parameters were exchanged between the project partners through the BKG data management system. Among others a user-friendly file browser, a discussion forum, a publication data base, and the exchange of meta data by means of SINEX files containing a meta data block were established. In addition, high-level tools to work with the data – like the data analysis tool to investigate the time series or the plot tool to visualize the data sets – have been developed.

The details of the characteristics, functionalities and options of the data management and information system realized as part of this project may be found in Schwegmann and Richter (2009, chapter “GGOS-D Data Management – From Data to Knowledge”, in this volume).

5 Common Modeling Standards and Parameterization

The consistency among the various solutions of the different techniques to be used within the GGOS-D project was considered to be an issue of high importance. Because the solutions were the basis not only for comparisons but also for a rigorous combination, the definition of common standards and a unique representation and parameterization of the relevant quantities was crucial to be able to interpret the combined solutions in the end. As seven different software packages were used to generate the solutions of the different techniques contributing to GGOS-D, all these packages had to be modified to follow the same common standards. The common models used in the various software packages were not only implemented but also validated in detail by intensive comparisons. A first set of standards was implemented during the first phase of the project (see Steigenberger et al., 2006). These

standards were then reviewed based on the experiences gathered with the initial set and a second, more demanding and complete set was agreed upon by the partners and subsequently implemented into the seven different software packages used within this project. All the modeling standards and parameter representations of this second iteration are listed in Nothnagel et al. (2009, chapter "GGOS-D Consistent and Combined Time Series of Geodetic/Geophysical Parameters", in this volume). There also the most interesting results concerning state-of-the-art modeling can be found.

6 Consistent Long-Term Time Series of the Space Geodetic Techniques

As input for the later combination of the space geodetic techniques (e.g. for a TRF or/and CRF) the global data, available from the various space techniques, were processed covering as long a period of time as possible using the standards, models and parameterizations agreed-upon within the project (see Sect. 5). A list of the time series (SINEX files) produced in the framework of the GGOS-D project is given in Table 1. Compared to the international setup of today, a considerable extension of the set of parameters estimated for each of the technique was realized and all the parameters common to more than one technique were saved in the SINEX format. As additional parameter types the quasar coordinates, nutation offsets and rates, tropospheric zenith path delays and gradients and low-degree coefficients of the Earth gravity field were set up to allow, for the first time, the linking of geometry, Earth rotation and gravity field. The decision to include as many parameters as possible and to go for a high temporal resolution for some of the parameters was also motivated by the fact, that parameters can easily be eliminated but not set up on the level of the normal equation systems and that the temporal resolution can always be reduced but not increased on the normal equation level. Therefore, daily normal equation systems were generated (daily resolution for site coordinates) and ERPs were set up on an hourly basis for VLBI and GPS.

Table 1 Consistent time series of SINEX files generated as part of the GGOS-D project

Technique	Institution	Software	Time interval	Time resolution	Status
SLR	DGFI	DOGS	1992–2007	7 d	Complete
SLR	GFZ	EPOS	1993–2006	7 d	Complete
VLBI	DGFI	OCCAM	1984–2006	1 d	Complete
VLBI	IGG/BKG	CALC/SOLVE	1984–2006	1 d	Complete
GPS	GFZ	EPOS	1994–2007	7 d	Almost complete
GPS	GFZ	Bernese	1994–2007	1 d	Complete
LEOs	GFZ	EPOS	2000–2007	1 d	Complete
Altimetry	DGFI	DGFI software	1992–2007	7 d	Complete

For each of the major techniques (i.e., VLBI, GPS and SLR) two series were produced using two different software packages. This allows the comparison and validation of results generated with different algorithms and follows the strategy used in the IAG Services to have more than one solution available for each of the techniques with a subsequent combination of the solutions. Such a combination was done for the two solution series available for VLBI and SLR. For GPS this was not possible because one of the series could only be completed towards the very end of the project.

It should be mentioned that the series generated within the GGOS-D project were not only optimized with respect to consistency, i.e., using common modeling standards and parameterizations, see Sect. 5, but also with respect to accuracy. Thus the most recent, state-of-the art modeling features were implemented as, e.g., the use of 6-hourly ECMWF grids for the computation of the hydrostatic delay and the use of the hydrostatic mapping function VMF1 by Boehm et al. (2006) for VLBI and GPS, the correction for higher-order ionospheric terms in GPS according to Fritsche et al. (2005), and the modeling of thermal deformation for the VLBI telescopes given in Nothnagel et al. (2009, chapter "GGOS-D Consistent and Combined Time Series of Geodetic/Geophysical Parameters", in this issue) and Skurikhina (2001).

To study the contribution of the data from the recent gravity field missions CHAMP and GRACE to reference frame issues (e.g., geocenter variations and principle axes of inertia of the Earth), combined daily solutions including the data of the global GPS ground station network and the data of the CHAMP and GRACE satellites (including the accelerometer and K-band measurements) were produced. In addition, time series of geocenter variations and degree 2 gravity field coefficients were also generated from altimetry data for comparison and integration studies. For this purpose all the altimetry missions present during the lifetime of Topex were calibrated against each other (see Fig. 2).

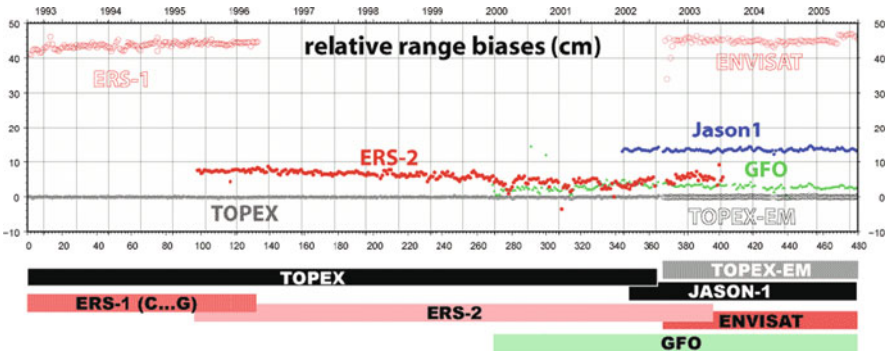

Fig. 2 Range biases resulting from the common calibration of all altimtery missions, that were measuring during the complete lifetime of Topex. The observation periods of the individual missions are given in the bar chart. The range biases may reach up to 45 cm (for ENVISAT and ERS-1) and are not stationary at all for some of the missions. Please note the obvious drifts of ERS-1 and ERS-2 that might be caused by an insufficient calibration of auxiliary sensors

7 The GGOS-D Terrestrial Reference Frame

A very accurate and stable terrestrial (and celestial) reference frame is one of the most important contributions of a global geodetic observing system to GEOSS, the Global Earth Observing System of Systems, as it provides the indispensable metrological basis for all other Earth observing systems.

Based on the homogeneous and consistent time series of SINEX files generated for the various techniques, a combined multi-year solution was produced for GGOS-D. Refined combination methods were developed and applied for a simultaneous adjustment of the terrestrial reference frame (station positions and velocities), Earth orientation parameters and the celestial reference frame (quasar coordinates). The quality of the resulting reference frames (TRF and CRF) together with the details of the non-trivial combination process (local ties, extended parameter space, ...) may be found in Angermann et al. (2009, chapter "GGOS-D Global Terrestrial Reference Frame", in this volume).

The reference frame results (TRF and CRF) also provided the basis for the subsequent generation of consistent, high-quality time series of geodetic-geophysical parameters describing the Earth System (see Sect. 8 and Nothnagel et al., 2009).

8 Comparisons and Validation of Long-Term Series of Geodetic and Geophysical Parameters

The high-accuracy terrestrial and celestial reference frames generated in the framework of the GGOS-D project (see Sect. 7) were the basis for the generation of very homogeneous and consistent time series of the geodetic and geophysical parameters that can be determined by the space geodetic techniques (site coordinates, geocenter coordinates, EOPs, troposphere zenith delays and gradients, low-degree gravity field coefficients). The time resolution of the different parameter types differ from 1 to 2 h (ERPs and troposphere zenith delays) to 1 week (SLR site coordinates, low-degree gravity field coefficients). The contributions by Nothnagel et al. (2009) and by König and König (2009, chapter "GGOS-D Integration with Low Earth Orbiters", in this volume) describe the comparisons and validation of these series in more detail. Among others the following parameters and aspects were studied:

- *Site coordinates:* The site coordinates of GPS, VLBI and SLR were compared in detail to validate the seasonal signals that are present in these time series, i.e., to find out whether amplitudes and phases were the same for the different space geodetic techniques, an indication that real geophysical phenomena and not technique-specific artifacts are involved. A considerable part of the seasonal signal in the GPS and VLBI time series seems to result from loading effects.
  The effect of the thermal expansion of the radio telescopes on the VLBI site coordinate time series was also studied and shows a systematic seasonal variation in scale of about 0.3 ppb peak to peak.

- *Earth Orientation Parameters:* x- and y-pole coordinates from a consistent combination of GPS, VLBI and SLR showed an improvement compared to the technique-specific solutions. For UT1-UTC a similar improvement could not yet be achieved due to the systematic effects in the estimates of the satellite techniques.
  Free Core Nutation (FCN) derived from VLBI and a combination of VLBI and GPS was also analysed.
- *Atmospheric Parameters:* The troposphere zenith delays and gradients from VLBI and GPS time series were compared and showed, in general, a very good agreement. Systematic differences between the techniques may point at problems in the corresponding local ties or in the GPS antenna phase center variations and are, thus, an important diagnosis tool.

It should be mentioned that interesting contributions to this project also came from the processing of the altimetry data, although this could not be fully documented in this volume because of limited space. The combination of the altimetry results with those of the geometric space techniques and the gravity missions is not trivial, because altimetry can only supply the ocean part of mass distribution and transfer in the Earth system. All the other components have to be considered as well. Only first steps in this direction could be made during the GGOS-D project, but considerable progress has since been achieved in the Research Group "Earth Rotation and Global Dynamic Processes" funded by the Deutsche Forschungsgemeinschaft (DFG) (see, e.g., Göttl and Seitz, 2008).

9 Conclusions and Outlook

The realization of a high-precision terrestrial reference frame (TRF) and the generation of very homogeneous and consistent time series of geodetic and geophysical parameters achieved in the framework of this project are very important steps for various essential research topics such as sea level change, postglacial rebound, plate tectonics and a possible increase of water vapor in the atmosphere. The accuracy of the reference frames and time series available so far was limited by inconsistencies in the modeling and parameterization and by reference frame changes. These deficiencies have been overcome by the work done within the GGOS-D project.

The processing algorithms and strategies for the integration of the space geodetic techniques that have been studied, developed and tested here can be seen as a prototype or a very reduced and small version of the data handling and processing part of a global geodetic observing system. It is to be expected that the IAG services will develop their products and services in a similar direction, establishing similar procedures and processing chains, but as an operational service also considering (near) real-time aspects.

All time series and products generated during the GGOS-D project are archived in the data management system of BKG. All these series are made available to the

scientific community. We think that, because of their consistency and accuracy, these time series are very valuable for further research, studies and comparisons. This is also true for the multi-year solutions for the Terrestrial Reference Frame (TRF) and the Celestial Reference Frame (CRF) that can be used by the IERS and the other services for comparisons and combinations.

It is clear that the time series of SINEX files and geodetic and geophysical parameters have not yet been combined and exploited to the extent that would be possible. Therefore, these time series will be the basis for further studies in the future such as the full combination of the geometric (TRF, EOPs, CRF) and gravimetric parameters (low-degree gravity field coefficients) that has not been fully achieved yet.

Acknowledgments This is publication no. GEOTECH-1287 of the programme GEOTECHNOLOGIEN of the German Ministry of Education and Research (BMBF). The work has been carried out to a large extent by the support of grants 03F0425A, 03F0425C, 03F0425D, and 03F0426A of BMBF.

References

Böhm J, Werl B, Schuh H (2006) Troposphere mapping functions for GPS and very long baseline interferometry from European Centre for Medium-Range Weather Forecasts operational analysis data. J. Geophys. Res. 111, B02406, doi: 10.1029/2005JB003629.

Fritsche M, Dietrich R, Knöfel C, Rülke A, Vey S, Rothacher M, Steigenberger P (2005) Impact of higher-order ionospheric terms on GPS estimates. Geophys. Res. Lett. 32, L23311, doi: 10.1029/2005GL02432.

Göttl F, Seitz F (2008) Contribution of non-tidal oceanic mass variations to polar motion determined from space geodesy and ocean data. In: Sideris MG (ed.) Observing our Changing Earth, IAG Symposia, vol. 133, Springer, pp. 439–445.

Skurikhina E (2001) On computation of antenna thermal deformation in vlbi data processing. In: Behrend D, Rius A (eds) Proceedings of the 15th Working Meeting on European VLBI for Geodesy and Astrometry, Institut d'Estudis Espacials de Catalunya, Consejo Superior de Investigaciones Cientificas, Barcelona, pp. 124–130.

Steigenberger P, M, Dietrich R, Fritsche M, Rülke A, Vey S (2006) Reprocessing of a global GPS network J. Geophys. Res. 111, B05402, doi: 10.1029/2005JB003747.

GGOS-D Data Management – From Data to Knowledge

Wolfgang Schwegmann and Bernd Richter

1 Contributions for a Data and Information System for GGOS-D

Inside the Joint Project the contributions for the development and implementation of a data and information system for GGOS-D serve for the exchange of data and information needed or provided by the project partners. Thus, the main task within the first project phase was to build up a data and information infrastructure to coordinate and facilitate the exchange of data as well as project related information between the project partners. These administrative tasks, supporting the work of the project partners in all work packages, are:

- Administration of a ftp server to store all data used within the joint project.
- Maintenance of a Web site to present information about the project to the public.
- Installation and administration of a project related Wiki[1] to report about and to discuss the current work of the project partners on-line.
- Implementation of a GGOS-D email exploder to distribute information between the project partners.
- Maintenance of a database to store information about meetings, talks and publications of all co-workers within GGOS-D.

As the project is moving onwards the availability of high level tools to process the data is of extreme importance. This includes general tools for the management of metadata (creation, visualization and export), for search within the available data with respect to technique, time, place, etc. and to generate time series of parameters. More specific high level tools are necessary to investigate, analyze, combine and visualize the data. Additionally, interfaces should be developed to provide geodetic-geophysical time series, which will be used for the generation, analysis, and validation of such time series.

B. Richter (✉)
Bundesamt für Kartographie und Geodäsie, 60598 Frankfurt am Main, Germany
e-mail: bernd.richter@bkg.bund.de

[1] http://en.wikipedia.org/wiki/Wiki

F. Flechtner et al. (eds.), *System Earth via Geodetic-Geophysical Space Techniques*, Advanced Technologies in Earth Sciences, DOI 10.1007/978-3-642-10228-8_44,

To implement these functionalities into a GGOS-D data and information system three main tasks, respectively Work Packages (WP), have been identified:

1. WP 2100: Data Management for a Global Geodetic-Geophysical Observing System.
2. WP 2200: Integration of External Geodetic-Geophysical Series.
3. WP 2300: Design of a Geodetic Metadata Catalogue Based on ISO Standards.

2 Data Management for a Global Geodetic-Geophysical Observing System

The GGOS-D Data and Information System and its main components are shown in Fig. 1. Thesystem is based on the IERS Data and Information System (Richter et al., 2005) and its resources developed during the previous project phase (Richter and Schwegmann, 2006). Thus, the basic functionality could be guaranteed already at the beginning of the joint project. The IERS data management system is in charge of collecting all IERS related products and data, it provides the functionality to assign metadata to all data sets and incorporates tools for the selection of data sets (with respect to technique, time, etc.) that make use of the stored metadata. The existing system has been extended in order to collect and maintain the data within GGOS-D and to assign metadata. Thus, the existing tools for the selection of specific data

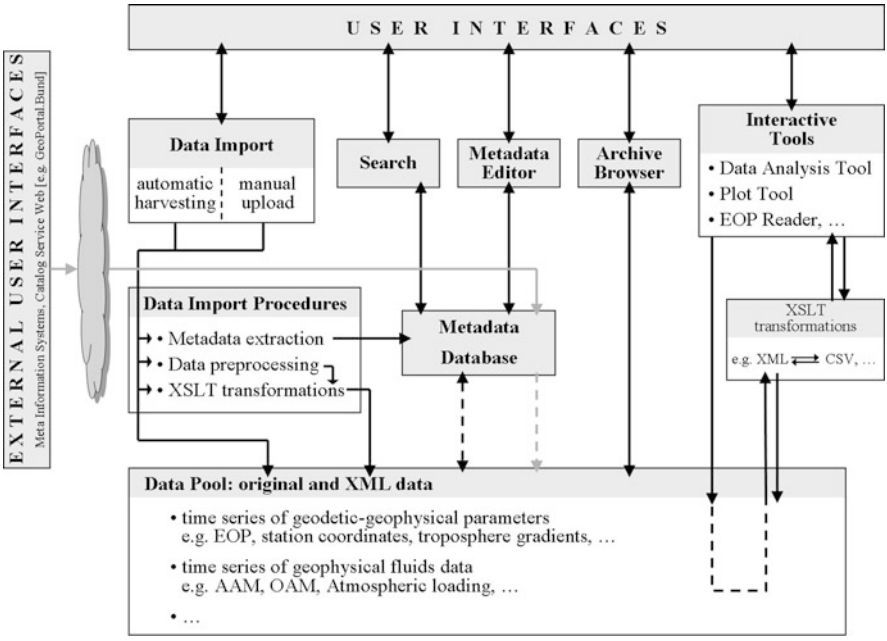

Fig. 1 GGOS-D data and information system: overview

sets can be used, too. This is important because with the growing duration of the project it becomes necessary to select data files, produced by the techniques or by combination and reaching back up to 20 years, in order to make special investigations. For the SINEX files a strategy has been developed in close cooperation with all project partners how the necessary metadata can be extracted automatically from the files, because the huge amount of files makes a manual assignment impossible. Additionally, a basic metadata editor has been developed in order to allow the project partners to enter the metadata for individual files manually. The user interfaces to search the archive as well as to edit and view metadata are shown in Fig. 2.

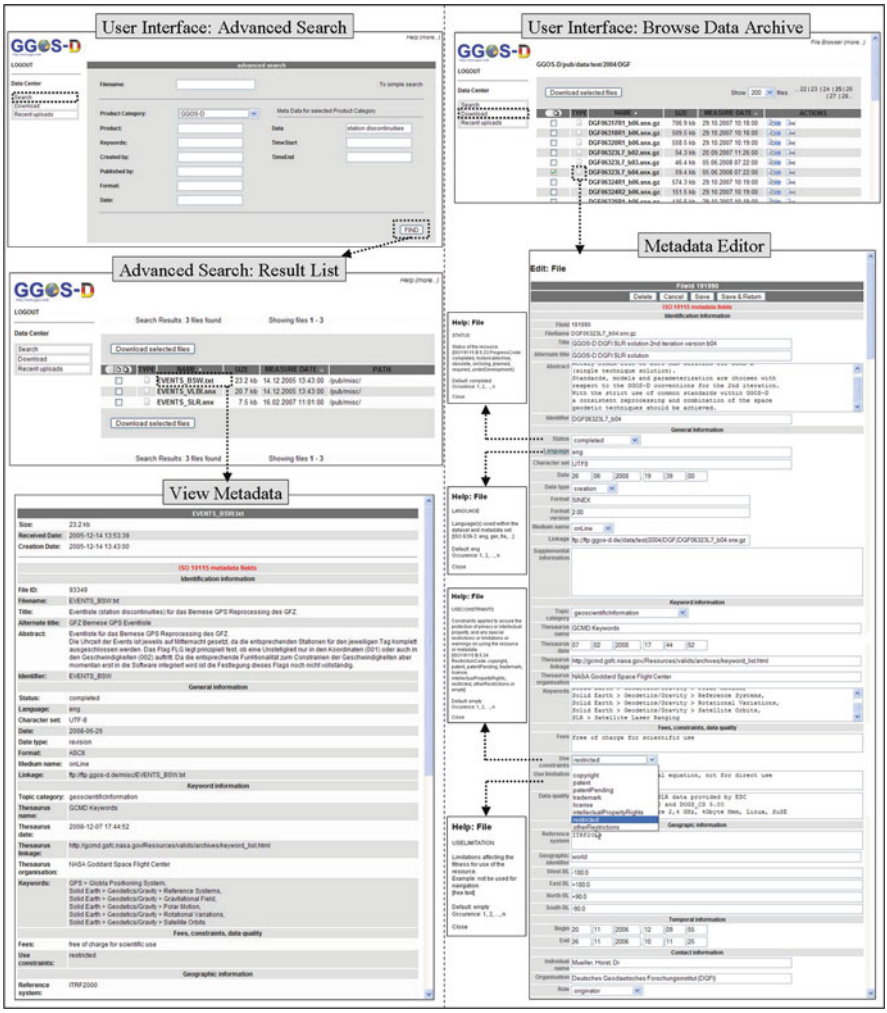

Fig. 2 GGOS-D data and information system: user interfaces for search and metadata management

The most important objective of processing the weekly SINEX files is to derive time series of geodetic-geophysical parameters. A data processing environment has been developed to allow the user to create time series of all parameters contained in the SINEX files and produce outputs in specific formats for further analyses. Besides the "standard" time series (coordinates, EOP, geocentre) it will be possible to create special time series in the parameter space of the SINEX files, which the users from the different fields of geosciences may optimize for their needs. The goal is to create the demanded time series automatically in the background. To ensure that the most up-to-date data sets are being used and to avoid multiple sets of the same data, the time series are recreated as soon as new input data are available.

Another important objective is to analyze the created time series with respect to their quality and to compare the time series between each other. For this task a generic data analysis tool is being developed at BKG within the project "Earth Rotation Information System". This project is part of the DFG sponsored Research Unit "Earth Rotation and Global Dynamic Processes".[2]

Last but not least, another emphasis should lay in the visualization of the data in order to create the basic data set by a combination of numerical input and visual selection. Thus a generic plot tool has been developed to plot the generated time series. Together with the data processing environment and the data analysis tool, three high level tools are being developed. These tools allow an integrated processing, analysis and visualization of all time series generated within the project as well as to use external datasets for validation.

3 Integration of External Geodetic-Geophysical Series

To guarantee the reliability of the generated time series of geodetic-geophysical parameters at the highest level, external geodetic-geophysical data series of the IERS Global Geophysical Fluids Centre (GGFC)[3] (Chao et al., 2000) should be integrated into the IERS Data and Information System for validation. For this, a standardization of the GGFC data in cooperation with the eight Special Bureaus of the GGFC is necessary, because the products are available in very heterogeneous formats. Unfortunately, the standardization efforts within the GGFC Special Bureaus did not succeed. Thus the project partners decided to concentrate on the most important data sets of atmospheric angular momentum (AAM) and oceanic angular momentum (OAM). These data sets have been standardized and incorporated into the IERS Data and Information System and can be further processed for the special validation tasks within the GGOS-D project.

---

[2] http://www.erdrotation.de

[3] http://www.iers.org/MainDisp.csl?pid=75-53

4 Design of a Geodetic Metadata Catalogue Based on ISO Standards

International metadata catalogues allow to search for data structures in a broader context. This makes it easier to find data sets from neighbouring fields of science, and the available data sets may get a wider group of users. Therefore, the metadata related to the data sets have been provided in a standardized form. The ISO 19115 standard (ISO, 2003) to describe metadata of geographic data is widely used by Meta Information Systems, e.g. by the German GeoPortal.Bund[4] hosted by the BKG. In order to check the adaptability of the ISO 19115 standard for Earth rotation and reference frames data, the metadata set used within the IERS Data and Information System has been extended to be conform to this international standard and the metadata of some IERS data sets have been included into the GeoPortal.Bund. Even though the 19115 standard has been developed mainly within the scope of geographic information data, it can also be applied to the data sets within GGOS-D. In particular, the SINEX format has been extended by an ISO 19115 compliant metadata block. In the future, it should be investigated which international Meta Information Systems make use of the ISO 19115 standard in order to propagate the available data sets within GGOS-D through them.

5 Summary

Within the Joint Project "Integration of Space Geodetic Techniques as the Basis for a Global Geodetic-Geophysical Observing System (GGOS-D)" the contributions for a data and information system for GGOS-D are of decisive importance and play a central role to coordinate the data and information flow between the project partners. Besides the necessary infrastructure to facilitate the exchange of data and information and to guarantee the availability of standardized data sets for all project partners, high level tools to work with the data have been provided. Such tools comprise a data processing environment to generate time series of geodetic-geophysical parameters and to prepare data sets for the usage with other tools like the data analysis tool to investigate the time series or the plot tool to visualize the data sets. Additionally, the integration of external geodetic-geophysical data series from the IERS Global Geophysical Fluid Centre (GGFC) is important for the external validation of the data series. The most important data sets for this task have been examined and prepared. Finally, a geodetic metadata catalogue based on ISO standards has been designed. The goal is to incorporate the metadata, assigned to the data series with the help of the data management system, into existing Meta Information Systems in order to find applications beyond the group of geodetic users and to stimulate new scientific investigations to derive knowledge from data. Thereby, the correct usage of the data

[4] http://geoportal.bkg.bund.de

series can be guaranteed by providing extensive metadata to describe the data and scientific investigations are supported by providing high level tools to work with the data.

Acknowledgments This is publication no.GEOTECH-1282 of the programme GEOTECHNOLOGIEN of BMBF and DGF, Grant 03F0426A.

References

Chao BF, Dehant V, Gross R et al. (2000) Space geodesy monitors mass transports in global geophysical fluids. EOS Trans. Amer. Geophys. Union 81, 247–250.

ISO (2003) ISO 19115 Geographic Information Metadata, International Organization for Standardization (ISO), Geneva.

Richter B, Schwegmann W (2006) IERS data and information system. In: Flury J, Rummel R, Reigber C, Rothacher M, Boedeker G, Schreiber U (eds.), Observation of the Earth System from Space, Springer, Berlin.

Richter B, Schwegmann W, Dick W (2005) Development of an information and database system for the IERS: Status and outlook. J. Geodyn. 40, 487–493.

GGOS-D Consistent, High-Accuracy Technique-Specific Solutions

Peter Steigenberger, Thomas Artz, Sarah Böckmann, Rainer Kelm, Rolf König, Barbara Meisel, Horst Müller, Axel Nothnagel, Sergei Rudenko, Volker Tesmer, and Daniela Thaller

1 Introduction

One of the main characteristics of the GGOS-D project is the generation of homogeneous time series of geodetic and geophysical parameters for the individual space-geodetic techniques and their combination. In order to achieve the highest accuracy possible for the geodetic and geophysical parameters, three topics are indispensable: First, all individual solution series must be generated using the most up-to-date analysis strategy as well as the best models available. Second, if parameters or models are common to more than one space-technique, the same parameterization and the same models must be applied for all techniques. And finally, the whole time series must be generated using the pre-defined analysis strategy.

Contributions of three space-geodetic techniques are considered within GGOS-D, namely GPS, SLR and VLBI. We have no single software package available that is capable to generate solution series of the highest-possible quality for all these techniques. However, there are specialists for each technique amongst the institutions cooperating within GGOS-D, so that we have two software packages for each of the space-techniques. All software packages use the classical least squares adjustment technique with the Gauss-Markov model. They are adopted to use predefined common standards so that the homogeneity of the individual contributions can be guaranteed. The availability of two contributions per technique allows to investigate the level of homogeneity achieved, and to quantify the level of the analysis noise that is left. To be able to reliably detect signals in the time series of geodetic and geophysical parameters, it is clear that the time series must be as long as possible. Therefore, all data available that allow a reasonable determination of the parameters of interest are processed within GGOS-D.

P. Steigenberger (✉)
Institute of Astronomical and Physical Geodesy, Technische Universität München, D-80333 München, Germany
e-mail: steigenberger@bv.tum.de

F. Flechtner et al. (eds.), *System Earth via Geodetic-Geophysical Space Techniques*, Advanced Technologies in Earth Sciences, DOI 10.1007/978-3-642-10228-8_45,

2 Standards, Conventions, Parameterization, Models

The consistency of the technique-specific solutions generated within the GGOS-D project is essential for a successful combination. Therefore, the definition of common standards is a prerequisite for a proper interpretation of the combined time series and the only way to avoid misinterpretations due to differences in modeling. As the solutions of the different techniques are computed with a variety of different software packages, the common standards had to be implemented in these packages as the first step of the GGOS-D project. Based on the experiences and results of the first solution, an update of the standards has been performed for a second iteration.

For a combination of different solutions on the normal equation (NEQ) level as it is done in the GGOS-D project, the parameterization of these parameters has to be identical, see Table 1. Station and quasar coordinates as well as the lower harmonics of the Earth's gravity field are represented by constant offsets per parameter interval. Parameters with high temporal resolution (e.g., troposphere zenith delays) are represented by continuous piece-wise linear functions (CPWLFs). The current value of a parameter $\mathbf{x}$ at epoch t contributes to the neighboring parameter estimates $\mathbf{x}_{t_1}$ and $\mathbf{x}_{t_2}$ at the epochs t_1 and t_2 as follows:

$$\mathbf{x}(t) = \mathbf{x}_{t_1} \frac{t_2 - t}{t_2 - t_1} + \mathbf{x}_{t_2} \frac{t - t_1}{t_2 - t_1} \tag{1}$$

This kind of parameterization has the advantage that there are no discontinuities at the interval boundaries.

Table 1 Parameterization of the 2nd GGOS-D iteration. Settings of the 1st iteration are given in parentheses. Only parameters involved in the combination are listed. CPWLF stands for continuous piece-wise linear function

Station coordinates	Constant daily/session-wise/weekly offsets for GPS/VLBI/SLR
Quasar coordinates	Constant offsets (only 2nd iteration, fixed for session solutions)
Earth rotation parameters	*Default solution:* CPWLF with a parameter interval of 24 h *Subdaily solution:* CPWLF with a parameter interval of 1 h (2 h)
Nutation parameters	CPWLF w.r.t. the a priori model IAU2000A with a parameter interval of 24 h
Troposphere parameters	CPWLF for the wet part of the troposphere zenith delay with a parameter interval of 1 h (2 h) for VLBI and 2 h for GPS Troposphere gradients are modeled according to MacMillan (1995) and represented by a CPWLF with a parameter interval of 24 h (tilting model with wet Niell (1996) mapping function for GPS, MacMillan (1995) for VLBI) Wet VMF1 mapping function (Boehm et al. 2006b) for the troposphere zenith delay (wet Niell, 1996 mapping function)
Lower harmonics of the Earth's gravity field	Spherical harmonic expansion up to degree and order 2 (only 2nd iteration)

Table 2 Common modeling standards for the second iteration of GGOS-D

Station coordinates	
Solid Earth tides	IERS Conventions 2003, McCarthy and Petit (2004)
Permanent tide	Not considered for coordinates
Pole tides	Linear trend for mean pole offsets: IERS Conventions 2003
Ocean loading	FES2004 including the center of mass correction for the motion of the Earth due to the ocean tides, http://www.oso.chalmers.se/~loading/
Atmospheric loading	Not applied
Earth orientation parameters	
A priori information	Daily values of the C04 05 series
Subdaily ERP model	IERS2003, McCarthy and Petit (2004)
Nutation model	IAU2000A, Mathews et al. (2002)
Lower harmonics of the Earth's gravity field	
A priori model	EIGEN-GL04S1 (Förste et al., 2007) including temporal variations of C_{20}, C_{30}, C_{40}
Troposphere modeling for radio techniques	
Hydrostatic delay	6-hourly ECMWF grids, http://mars.hg.tuwien.ac.at/~ecmwf1/GRID/
Hydr. mapping function	Hydrostatic VMF1 (Boehm et al., 2006b)
Wet delay	No a priori model, wet delay estimated (see Table 1)
Troposphere modeling for SLR	
Troposphere model	Mendes and Pavlis (2004)
Technique-specific effects: GPS	
Phase center model	Schmid et al. (2007), ftp://igscb.jpl.nasa.gov/igscb/station/general/igs05_1421.atx
Antenna offsets	ftp://igscb.jpl.nasa.gov/igscb/station/general/igs.snx
2nd/3rd order iono. corr.	Applied according to Fritsche et al. (2005)
Technique-specific effects: SLR	
Reflector offsets	ILRS conform
Range biases	For selected stations, ILRS conform
Arc length	7 days
Technique-specific effects: VLBI	
Thermal deformations	Applied, Nothnagel et al. (1995); Skurikhina (2001): mean value of the temperature recordings during the VLBI sessions used as station-specific reference temperature

The common standards for modeling are based on the recommendations of the IERS 2003 conventions (McCarthy and Petit 2004) and the standards of the international services International GNSS Service (IGS, Dow et al., 2005), International Laser Ranging Service (ILRS, Pearlman et al., 2002) and International VLBI Service for Geodesy and Astrometry (IVS, Schlüter et al., 2002). Table 2 lists the standards of the second GGOS-D iteration. For several modeling options more sophisticated models have been applied than those commonly used by the analysis centers of the international services. For example, tropospheric mapping functions based on numerical weather models (like the Vienna Mapping Function 1 – VMF1) provide a more realistic modeling of the atmosphere compared to the empirical models still widely used nowadays (e.g., also for the first iteration of GGOS-D).

3 Global Positioning System

The GPS plays an important role in the combination of space-geodetic techniques due to its dense and continuously observing tracking network. GPS provides access to different parameter groups relevant for a rigorous combination, namely geometric parameters (station positions, origin of the tracking network), atmospheric parameters (troposphere zenith delays and gradients) and Earth orientation parameters (polar motion, length of day and nutation rates). Two independent GPS solutions with different software packages were computed at Deutsches GeoForschungsZentrum (GFZ) Potsdam.

A modified version of the Bernese GPS Software (Dach et al 2007) was used to process GPS observations of 202 and 241 stations for the 1st and the 2nd iteration, respectively, starting with the raw RINEX (Receiver INdependent EXchange format) files. The processing scheme was deduced from an earlier GPS reprocessing effort of TU Dresden and TU München (Steigenberger et al 2006). In addition to the parameters listed in Table 1, GPS-specific parameters like ambiguities and satellite orbits have to be estimated. The satellite orbits are represented by the six Keplerian elements plus five radiation pressure (RPR) parameters (Beutler et al 1994) and pseudo-stochastic pulses at 12:00 UT. Ambiguities are fixed to integer numbers for baselines up to 6,000 km with different methods (depending on the baseline length). For the final ambiguity-fixed solution a no-net-rotation condition w.r.t. the reference frame specified in Table 3 is applied. Besides the reference frame, also the models for the antenna phase centers and the a priori RPR have been updated for the 2nd iteration (see Table 3).

Table 3 Important differences between first and second iteration of the Bernese GPS solutions

	1st iteration	2nd iteration
Number of stations	202	241
Start time	1 January 1994	
End time	24 April 2006	31 March 2007
Number of SINEX files	4,496	4,838
Reference frame	IGb00	IGS05
Phase center model	igs05_1365.atx	igs05_1421.atx
A priori RPR model	ROCK (e.g. Fliegel and Gallini, 1996)	CODE (Springer, 2000)

For the second GPS solution, observations of a global network of 403 stations have been processed using the EPOS-PV2 software (Gendt et al., 1999) improved in the recent years and following the scheme described in Zhang et al. (2007). The network consists of 216 IGS stations and 187 GPS stations located at or near tide gauge benchmarks and analyzed within the IGS Tide Gauge Benchmark Monitoring Pilot Project (TIGA). Vertical motions of TIGA GPS stations are important for correcting tide gauge records in sea level change investigations. The models used follow those in Table 2 with the following exceptions: the tropospheric modeling is based on the Global Pressure and Temperature model (Boehm et al., 2007) and the Global

Mapping Function (Boehm et al., 2006a), and no 2nd and 3rd order ionospheric corrections are applied. Initial values of geocentric coordinates and velocities of 206 stations are taken from ITRF2005 (Altamimi et al., 2007). Processing is performed at daily intervals. Daily solutions are combined into weekly ones at the level of NEQs. The solution includes weekly sets of GPS station coordinates and daily values of Earth rotation parameters and their rates in SINEX format for the time interval from January 1998 till December 2007.

4 Very Long Baseline Interferometry

The VLBI sessions between 1984 and 2007 have been analyzed independently with two different VLBI analysis packages: At the Deutsches Geodätisches Forschungsinstitut (DGFI) in Munich, a modified version of the OCCAM v6.1 software package (Titov et al., 2004) has been used, and the Calc/Solve software (Petrov 2006) at the Institut für Geodäsie und Geoinformation (IGG) of the University of Bonn. To ensure consistent processing, the two software packages have been adapted in detail according to the GGOS-D specifications as described in Sect. 2. With both software packages, the same VLBI sessions have been analyzed. Only data of non-mobile telescopes with sufficient observations during an adequate time span have been used. The GGOS-D VLBI solutions consist of 2781 sessions where group delay observations of 53 stations and 1954 radio sources have been used.

Although great care has been taken to achieve consistency, there are remaining analysis-specific differences between the two VLBI solutions. In each VLBI solution, relative offsets, linear and quadratic time derivatives of the atomic clocks at the observing sites have to be estimated, where different reference clocks and clock breaks may have been chosen. Furthermore, a slightly different set of observations may have been used due to differences in the outlier rejection. In addition, significant differences in the weighting of the observations are used in both software packages. At DGFI a refined stochastic model has been used (Tesmer and Kutterer 2004). At IGG the initial measurement weights from the correlation process have been used and modified session-wise to ensure that the χ^2 is approximately one for each baseline. NEQs have been saved in SINEX format as input for further combination efforts. These SINEX files include the whole parameter space except for the clock parameters which have been reduced from the equation systems. No additional constraints have been applied to the remaining parameters which ensures that the NEQs are completely undeformed.

Before adding both contributions to one combined VLBI solution, a number of comparisons have been carried out to detect remaining differences of both individual solutions. As an example, Fig. 1 shows the mean height differences between both individual solutions. The grey arrows illustrate the differences before the adaptation of both software packages, the black arrows after the adaptation. On average, the height differences before the adaptation reach ± 5 mm with clear systematic behavior in the quadrants. The main reason for this is the different mean pole within

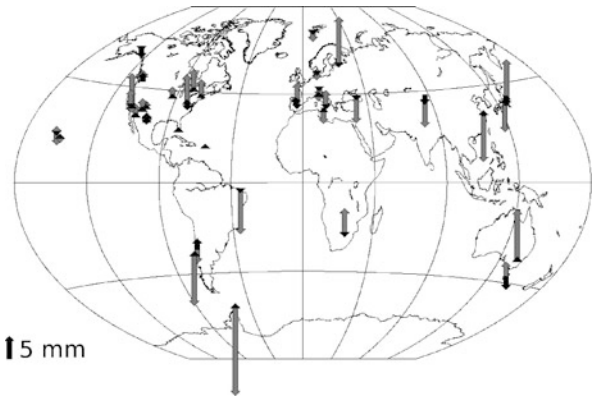

Fig. 1 Height differences between both individual solutions before adaptation of the software packages (*grey arrows*) and after the adaptation (*black arrows*)

the pole tide model. After the adaptation (black arrows) almost all offsets are smaller than ± 1 mm.

The VLBI intra-technique combination is based on datum-free NEQs. Each individual observing session has been combined separately using the software DOGS_CS (Gerstl et al., 2001).

One of the basic requirements for the combination based on NEQs is that the systems have to use the same set of a priori values. Therefore, transformations are carried out to refer all parameters to the same reference epoch, to the same reference frame (ITRF2005, Altamini et al., 2007) and an identical set of a priori EOPs.

In a second step the suitability of the individual contributions for the combination is checked. For this purpose, a solution of the station positions is calculated from each contribution. A contribution is rejected if the correction to the a priori station positions is larger than 5 cm in the horizontal components and larger than 7.5 cm in the vertical component. For each individual session, a combined datum-free NEQ system is calculated by adding the DGFI and IGG NEQs. The combined NEQ system is then saved as SINEX file for combination with the other techniques.

5 Satellite Laser Ranging

SLR is vital for the definition of a Terrestrial Reference Frame (TRF) because it is the only technique which defines the geocenter directly. SLR is also a strong contributor to the network scale and to the determination of the low degree coefficients of the spherical harmonic representation of the Earth's gravity field (hereafter shortly named "low degree harmonics"). The global SLR tracking network consists of about 30 stations with some changes, stations closing down or new stations showing up. In the GGOS-D project the global SLR tracking network is analyzed by GFZ using the EPOS (Earth Parameter and Orbit System) software package and by DGFI with the DOGS (DGFI Orbit and Geodetic parameter estimation Software) package (http://ilrsac.dgfi.badw.de/dogs/). The dynamical and measurement models

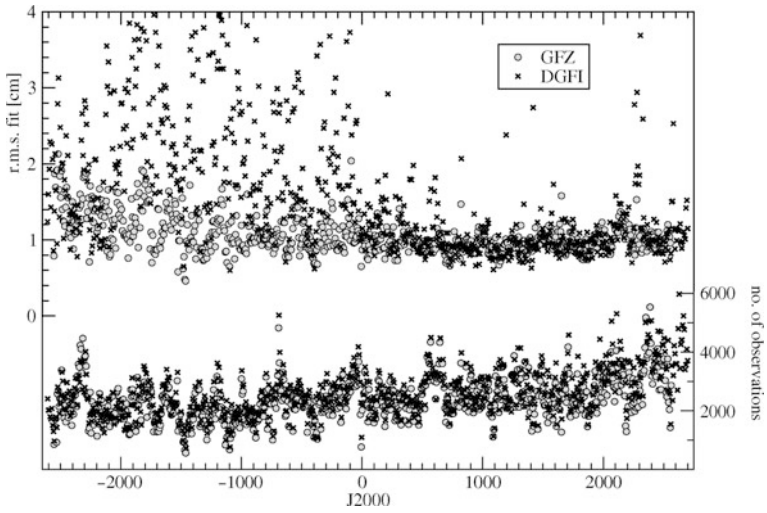

Fig. 2 Number of observations per week and RMS fit of the weekly GFZ and DGFI solutions

are adopted according to the GGOS-D standards (see Sect. 2) and harmonized in both software packages. The only difference concerns the data editing procedures which explains some of the discrepancies between the two solutions (see Fig. 2). The higher RMS values in the DGFI solutions are mainly produced from a few stations with poor tracking performance, which are often edited in the GFZ solutions.

Both centers processed weekly arcs for the period October 1992 to January 2007 (GFZ) and November 1992 to May 2007 (DGFI), respectively, solving for weekly stations coordinates and daily EOPs (polar motion and UT1). Additionally, both solutions incorporate the low degree harmonics up to degree and order 2. In order to overcome the datum defect, the coordinates, the EOPs, and the low degree harmonics are endowed with an a priori sigma of 1 m or its equivalent. The solutions are presented in form of SINEX products where GFZ delivers the NEQs regularized with the a priori sigmas plus the a priori sigmas used in a separate NEQ, DGFI provides the free (singular) NEQs directly.

In total 732 common weeks in the period from November 1992 until January 2007, are available using about 1.75 million SLR normal points to the geodetic satellites Lageos-1 and -2. The quality of the orbital fit slightly increases in the observation period from 1.5 cm in the beginning to 0.9 cm since 2000 and are comparable between the satellites and the software packages (Fig. 2).

The input of the weekly SLR combination consists of weekly solutions of DGFI and GFZ presented as datum-free NEQs for weekly station coordinates, daily polar motion and UT1 as well as for the lower harmonic coefficients of the Earth's gravity field up to degree and order 2 (C_{22}). First investigations reveal that the solution with estimated C_{22} is not stable on a weekly basis, even when the respective minimum constraints are included. Hence, the processing of weekly SLR combinations is restricted to the determination of relative weights for both solutions, the multiplication of the given NEQs with the weights and the addition of the weighted

NEQs. The relative weighting procedure is based on the hypothesis that both solutions deliver a nearly equivalent precision level for the core station coordinates. The relative weight of DGFI solution is arbitrarily set to one, whereas the weight for GFZ is determined by the sum of GFZ NEQ diagonals over the core stations divided by the respective sum of DGFI NEQ. It turns out that the GFZ weights scatter between 3 and 0.7 for 1993 to 1999 and between 2 and 0.9 for 2000 to 2006. The combination process consists of the following steps:

- Aligning the right hand sides of the NEQs to the reference values (SLRF2005 for the station coordinates, C04 05 for the EOPs, and EIGEN-GL04S1 for C_{22}).
- Minimum constraint solutions of both input NEQs with fixing C_{22} in order to find outliers mainly in the station coordinates. The minimum constraints are based on three rotational rank deficiencies for the coordinates and on the offset deficiency for UT1.
- Determination of weights, weighting the input NEQs, and combination of weighted NEQs.
- Minimum constraint solution of combined NEQs with fixing C_{22}. This solution is used for precision and comparison analysis.
- Storage of weekly combined NEQs and of weekly combined minimum constraint solutions to SINEX files.

6 Summary and Conclusions

Consistent homogeneously reprocessed long-time series of the space geodetic techniques GPS, SLR, and VLBI are the backbone of the GGOS-D project. The common standards for modeling and parameterization described in Sect. 2 are essential for a consistent combination and proper interpretation. Table 4 gives an overview of

Table 4 Technique-specific SINEX files of the 2nd GGOS-D iteration

Technique	Institution	Software	Time period	# files	Resolution
GPS	GFZ	Bernese	01/1994–03/2007	4,838	1 d
GPS	GFZ	EPOS-PV2	01/1998–12/2007	515	7 d
SLR	DGFI	DOGS OC	01/1993–05/2007	759	7 d
SLR	GFZ	EPOS	01/1993–01/2007	732	7 d
SLR combined	DGFI	DOGS CS	01/1993–12/2006	559	7 d
VLBI	DGFI	OCCAM	01/1984–12/2006	2,728	1 d
VLBI	GIB	CALC/SOLVE	01/1984–12/2006	2,707	1 d
VLBI combined	GIB	DOGS CS	01/1984–12/2006	2,536	1 d

the GPS, SLR and VLBI SINEX files available from the solutions discussed in this chapter. These solutions provide the basis for the generation of combined time series and a TRF described in the chapters GGOS-D *Consistent and Combined Time Series of Geodetic/Geophysical Parameters* and *GGOS-D Global Terrestrial Reference Frame*.

Acknowledgment The efforts of IGS (Dow et al., 2005), ILRS (Pearlman et al., 2002), IVS (Schlüter et al., 2002) are acknowledged. The authors like to thank J. Boehm for providing the ECMWF troposphere delays and coefficients of VMF1. This is publication no. GEOTECH-1283 of the programme GEOTECHNOLOGIEN of BMBF and DFG, Grants 03F0425A, 03F0425C, 03F0425D.

References

Altamimi Z, Collilieux X, Legrand J, Garayt B, Boucher C (2007) ITRF2005: a new release of the International Terrestrial Reference Frame based ontime series of station positions and Earth Orientation Parameters. J. Geophys. Res. 112:B09401, doi: 10.1029/2007JB004949.

Beutler G, Brockmann E, Gurtner W, Hugentobler U, Mervart L, Rothacher M (1994) Extended orbit modeling techniques at the CODE Processing Center of the International GPS Service (IGS): theory and initial results. Manuscr. Geod. 19:367–386.

Boehm J, Niell A, Tregoning P, Schuh H (2006a) Global Mapping Function (GMF): a new empirical mapping function based on numerical weather model data. Geophys. Res. Lett. 33:L07304, doi: 10.1029/2005GL025546.

Boehm J, Werl B, Schuh H (2006b) Troposphere mapping functions for GPS and very long baseline interferometry from European Centre for Medium-Range Weather Forecasts operational analysis data. J. Geophys. Res. 111:B02406, doi:10.1029/2005JB003629.

Boehm J, Heinkelmann R, Schuh H (2007) Short note: a global model ofpressure and temperature for geodetic applications. J. Geod. 81(10), 679–683, doi:10.1007/s00190-007-0135-3.

Dach R, Hugentobler U, Fridez P, Meindl M (eds) (2007) Bernese GPS SoftwareVersion 5.0. Astronomical Institute, University of Bern, Bern, Switzerland.

Dow J, Neilan R, Gendt G (2005) The International GPS Service: Celebrating the 10th anniversary and looking to the next decade. Adv. Space. Res. 36(3), 320–326, doi:10.1016/j.asr.2005.05.125.

Fliegel H, Gallini T (1996) Solar force modeling of Block IIR Global Positioning System satellites. J. Spacecraft Rockets 33(6), 863–866.

Förste C, Schmidt R, Stubenvoll R, Flechtner F, Meyer U, König R, Neumayer H, Biancale R, Lemoine JM, Bruinsma S, Loyer S, Barthelmes F, Esselborn S (2007) The GeoForschungsZentrum Potsdam/Groupe de Recherche de Gèodèsie Spatiale satellite-only and combined gravity field models: EIGEN-GL04S1 and EIGEN-GL04C. J. Geod. 82(6), 331–346, doi:10.1007/s00190-007-0183-8.

Fritsche M, Dietrich R, Knöfel C, Rülke A, Vey S, Rothacher M, Steigenberger P (2005) Impact of higher-order ionospheric terms on GPS estimates. Geophys. Res. Lett. 32, L23311, doi:10.1029/2005GL024342.

Gendt G, Dick G, Soehne W (1999) GFZ analysis center of IGS – Annual Report 1998. In: Gowey K, Neilan R, Moore A (eds) International GPS Service for Geodynamics 1998 Technical Reports, IGS Central Bureau, Jet PropulsionLaboratory, Pasadena, CA, pp. 79–87.

Gerstl M, Kelm R, Müller H, Ehrnsprerger W (2001) DOGSCS Kombination und Lösung großer Gleichungssysteme. DGFI Interner Bericht NrMG/01/1995/DGFI.

MacMillan D (1995) Atmospheric gradients from very long baseline interferometry observations. Geophys. Res. Lett. 22(9),1041–1044,doi:10.1029/95GL00887.

Mathews P, Herring T, Buffett B (2002) Modeling of nutation and precession: new nutation series for nonrigid earth and insights into the Earth's interior. J. Geophys. Res. 107(B4), doi: 10.1029/2001JB000390.

McCarthy D, Petit G (2004) IERS Conventions (2003). IERS Tech Note 32 Verl. Bundesa. Kart., Frankfurt.

Mendes VB, Pavlis EC (2004) High-accuracy zenith delay prediction at optical wavelengths. Geophys. Res. Lett. 31(L14602), doi:10.1029/2004GL020308.

Niell A (1996) Global mapping functions for the atmosphere delay at radio wavelengths. J. Geophys. Res. 101(B2), 3227–3246, doi:10.1029/95JB03048.

Nothnagel A, Pilhatsch M, Haas R (1995) Investigations of thermal height changes of geodetic VLBI telescopes. In: Lanotte R, Nianco G (eds.), Proceedings of the 10th Working Meeting on European VLBI for Geodesy and Astrometry, Agenzia Spatiale Italiana, Matera, pp. 121–133.

Pearlman MR, Degnan JJ, Bosworth JM (2002) The International Laser Ranging Service. Adv. Space Res. 30(2), 125–143.

Petrov L (2006) Mark V VLBI Analysis Software Calc/Solve, http://gemini.gsfc.nasa.gov/solve.

Schlüter W, Himwich E, Nothnagel A, Vandenberg N, Whitney A (2002) IVS and its important role in the maintenance of the global reference systems. Adv. Space. Res. 30(2),127–430, doi:10.1016/S0273-1177(02)00278-8.

Schmid R, Steigenberger P, Gendt G, Ge M, Rothacher M (2007) Generation of a consistent absolute phase center correction model for GPS receiver and satellite antennas. J. Geod. 81(12), 781–798, doi:10.1007/s00190-007-0148-y.

Skurikhina E (2001) On computation of antenna thermal deformation in VLBI data processing. In: Behrend D, Rius A (eds.), Proceedings of the 15th Working Meeting on European VLBI for Geodesy and Astrometry, Institut d′Estudis Espacials de Catalunya, Consejo Superior de Investi-gaciones Cientificas, Barcelona, pp. 124–130.

Springer T (2000) Modelling and validating orbits and clocks using the Global Positioning System. Geod. Geophys. Arb. in der Schweiz 60, Zürich, Switzerland.

Steigenberger P, Rothacher M, Dietrich R, Fritsche M, Rülke A, Vey S (2006) Reprocessing of a global GPS network. J. Geophys. Res. 111, B05402, doi:10.1029/2005JB003747.

Tesmer V, Kutterer H (2004) An advanced stochastic model for VLBI observations and its application to VLBI data analysis. In: Vandenberg N, Baver K (eds.), International VLBI Service for Geodesy and Astrometry 2004 General Meeting Proceedings, NASA/CP-2004-212255, NASA, Greenbelt, pp. 296–300.

Titov O, Tesmer V, Boehm J (2004) Occam v6.0 software for VLBI data analysis. In: Vandenberg NR, Baver KD (eds.), International VLBI Service for Geodesy and Astrometry 2004 General Meeting Proceedings, NASA/CP-2004-212255, NASA, Greenbelt, pp. 267–271.

Zhang F, Gendt G, Ge M (2007) GPS data processing at GFZ for monitoring thevertical motion of global tide gauge benchmarks: technical report for projects TIGA and SEAL. No. STR07/02 in GeoForschungsZentrum Potsdam Scientific Technical Report.

GGOS-D Global Terrestrial Reference Frame

Detlef Angermann, Hermann Drewes, Michael Gerstl, Barbara Meisel, Manuela Seitz, and Daniela Thaller

1 Introduction

Highly-accurate, consistent and long-term stable geodetic reference frames are a fundamental requirement for the estimation of geodetic-geophysical parameters for the Global Geodetic Observing System (GGOS). These requirements are not fully satisfied with the currently available reference frames (e.g., the International Terrestrial Reference Frame (ITRF) of the International Earth Rotation and Reference Systems Service (IERS)). The latest version, the ITRF2005, has been computed from a combination of time series of station positions and EOP's (Altamimi et al., 2007; Angermann et al., 2009). A remarkable progress has been achieved compared to past realizations which were based on the combination of multi-year solutions of the different space-techniques. However, there are still considerable deficiencies. The ITRF2005 input data are not fully consistent, the standards and models were not completely unified amongst the analysis centres, and the GPS solutions provided by the International GNSS Service (IGS) were not homogeneously reprocessed.

Within the GGOS-D project, the observation time series for the different space geodetic techniques were homogeneously processed by applying unified standards for the modelling and parameterization (see chapter "Integration of Space Geodetic Techniques as the Basis for a Global Geodetic-Geophysical Observing System (GGOS-D): An Overview" by Rothacher et al., this issue). The GGOS-D terrestrial reference frame (TRF) has been computed from a combination of long time series of VLBI, SLR and GPS observations. The station positions and velocities (TRF) have been estimated in a common adjustment with Earth Orientation Parameters (EOP) and quasar coordinates. A major focus was on the development and implementation of refined combination strategies.

The paper is structured as follows: Sect. 2 gives some information on the GGOS-D data that were used for the reference frame computation. In Sect. 3 the

D. Angermann (✉)
Deutsches Geodätisches Forschungsinstitut, D-80539, München, Germany
e-mail: angerman@dgfi.badw.de

F. Flechtner et al. (eds.), *System Earth via Geodetic-Geophysical Space Techniques*, Advanced Technologies in Earth Sciences, DOI 10.1007/978-3-642-10228-8_46,

general concept of the combination methodology is presented. Sections 4 and 5 focus on the computation of the GGOS-D global terrestrial reference frame, which is performed in two major steps: (1) The accumulation of the epoch normal equations per technique, and (2) the computation of the TRF solution by combining the accumuled VLBI, SLR and GPS normal equations. Finally, conclusions and recommendations for future realizations of the global terrestrial reference frame are provided in Sect. 6.

2 Input Data for TRF Computation

The computation of the GGOS-D terrestrial reference frame is based on homogeneously processed VLBI, SLR and GPS observation time series. Table 1 gives an overview about the input data. The time series of the different techniques are provided as unconstrained datum-free normal equations. The GGOS-D input data also comprise the local tie information, which is available at the ITRS Product Centre at http://itrf.ensg.ign.fr/local_survey.php. The geospatial distribution of co-location sites is shown in Fig. 1.

The GGOS-D input data can be characterized in comparison to ITRF2005 as follows: (1) The GGOS-D observation time series of the different space techniques were consistently reprocessed based on unified standards (see chapter "GGOS-D Consistent, High-Accuracy Technique-Specific Solutions" by Steigenberger et al., this issue); (2) in case of GPS homogeneously reprocessed observation time series were used (see Steigenberger et al., 2006; Rülke et al., 2008); (3) the modelling of the observations was improved (e.g., absolute instead of relative phase centre corrections, a bug in the implementation of the pole tide model was corrected in the VLBI software CALC/SOLVE); and (4) the type of GGOS-D input data is nearly identical to the original observation equations and is much more appropriate for the combination than, e.g., loosely constrained solutions or solutions with removable minimum constraints. If the latter are used for the combinations the constraints have to be removed, which was not possible for some of the ITRF2005 input data. A principle disadvantage is that the necessary inversion may cause loss of precision by numerical effects (Drewes and Angermann, 2003; Gerstl, 2003).

Table 1 GGOS-D input data used for the global TRF computation (NEQ = Normal equations)

Technique	Institution	Software	Data	Time period
GPS	GFZ	Bernese	Daily NEQ	1994–2007
VLBI	DGFI	OCCAM	24 h sess. NEQ	1984–2007
VLBI	IGG-Bonn	CALC/SOLVE	24 h sess. NEQ	1984–2007
SLR	DGFI	DOGS	Weekly NEQ	1993–2007
SLR	GFZ	EPOS	Weekly NEQ	1993–2007

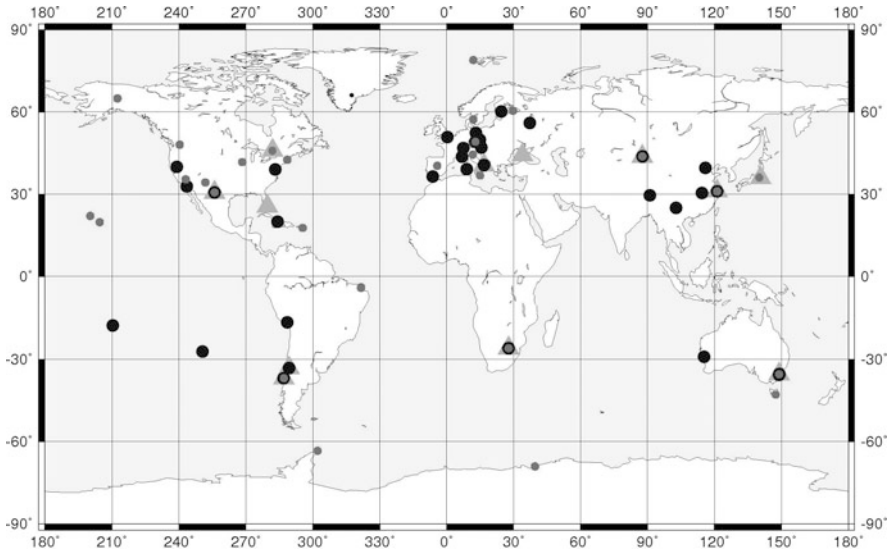

Fig. 1 Distribution of co-location sites (*triangles*: VLBI-SLR; *large circles*: GPS-SLR; *small circles*: GPS-VLBI co-locations)

3 Combination Methodology for TRF Computation

The methodology applied in the GGOS-D project is based on combining datum-free normal equations of the VLBI, SLR and GPS long observation time series. Target parameters for the combinations are the coordinates of the observing stations and their temporal variations (terrestrial reference frame), quasar coordinates (celestial reference frame), and the EOP that connect both systems. Refined combination methodologies have been developed to estimate these parameters consistently in a common adjustment. The combination has been performed with two different software packages, namely DOGS (at DGFI and IGG-Bonn) and ADDNEQ2 of the Bernese GPS software (a modified version running at GFZ). The general procedure of the combination methodology for the terrestrial reference frame computation is shown in Fig. 2.

As shown in Fig. 2, in principle two different strategies can be applied for the combination of the different space techniques and the computation of the GGOS-D terrestrial reference frame:

- (I) This approach comprises the two following major steps: (1) Accumulation of the time series normal equations per technique and analysis of the time series solutions; and (2) the inter-technique combination of the accumulated multi-year normal equations per technique and the computation of the final TRF solution.

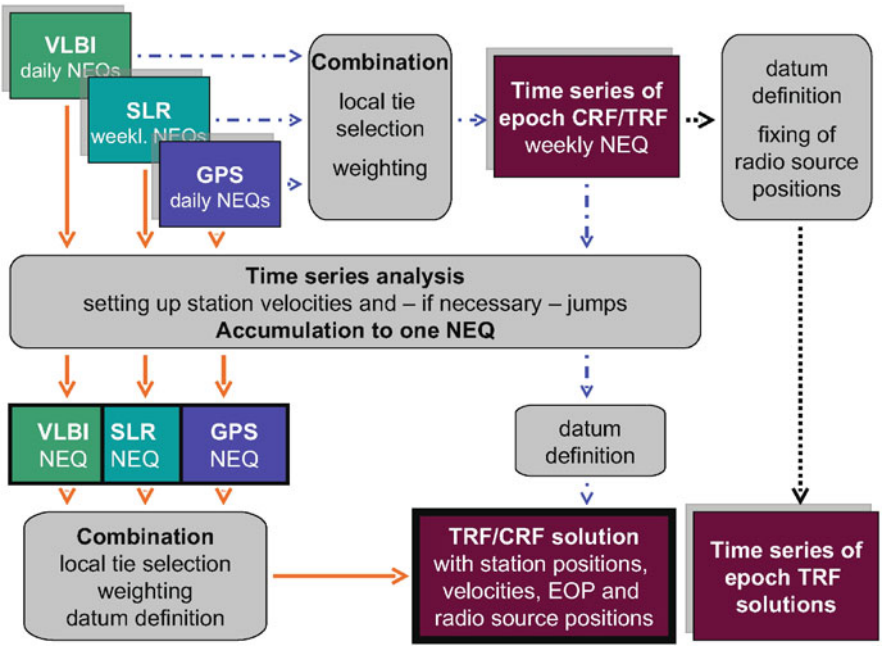

Fig. 2 Combination methodology for the terrestrial reference frame computation

- (II) The second approach can be divided in two parts: (1) The inter-technique combination of the VLBI, SLR and GPS epoch normal equations; and (2) the generation of a multi-year solution based on the weekly combined inter-technique normal equations. The first step has been applied for computing time series of the geodetic-geophysical parameters (Thaller et al., 2007; chapter by "Consistent and Combined Time Series of Geodetic/Geophysical Parameters" by Nothnagel et al., this issue).

We applied the first approach for the computation of the GGOS-D global terrestrial reference frame (see Chaps. 4 and 5). Details on the TRF combination procedure and the mathematical background are given in various publications (e.g., Angermann et al., 2004; Meisel et al., 2005; Drewes et al., 2006; Angermann et al., 2005, 2007; Krügel and Angermann, 2007; Meisel et al., 2009; Seitz, 2009).

4 Accumulation of Time Series per Space-Technique

In the first part of the terrestrial reference frame computation the time series of daily or weekly normal equations are accumulated to a multi-year normal equation for each technique. The procedure comprises two major steps: (1) The generation and analysis of station position time series to detect non-linear behaviors, and (2)

the computation of the cumulative multi-year normal equation parameterizing the individual time dependent variations of the station positions. Four different time dependent effects have to be considered: constant velocities, discontinuities, post-seismic effects and seasonal signals in station positions.

In the first iteration, constant velocity parameters were set up in the epoch normal equations to parameterize linear station motions and the epoch station positions were transformed to positions at the reference epoch 2000.0. From the analysis of position time series we identified for many stations discontinuities, which are often caused by equipment changes or large earthquakes. The discontinuities are parameterized by setting up new position and velocity parameters for the corresponding stations. Figure 3 shows as an example the position time series for the GPS station HOFN, Iceland, where an antenna and receiver change caused a jump in the height component of nearly 5 cm.

Within the GGOS-D computations, the total number of discontinuities could significantly be reduced compared to the ITRF2005 computation (Krügel et al., 2007). In ITRF2005 a large number of discontinuities had to be introduced, where many of them are due to processing and modelling changes. This was the case in particular for GPS, where 221 discontinuities had been identified for 332 stations. In the GGOS-D computations the number of discontinuities could be reduced to 124 for 240 GPS stations. This was mainly achieved due to a consistent processing of the GGOS-D data, the application of latest absolute antenna phase center corrections as well as radome calibrations.

A major focus was on investigations concerning temporal variations of station coordinates and the parameterization of non-linear motions within the TRF computations. It turned out that for many stations seasonal variations are visible, especially in the height component (see Fig. 4 as an example). A comparison with geophysical model results, computed from atmospherical, hydrological and non-tidal oceanic loading variations, shows that a large part of the annual signal may be caused by loading (e.g., Seitz and Krügel, 2009; Tesmer et al., 2008; Tesmer et al., 2009). Unfortunately, the geophysical models are not as accurate as necessary to reduce loading from the variations of the station positions. The

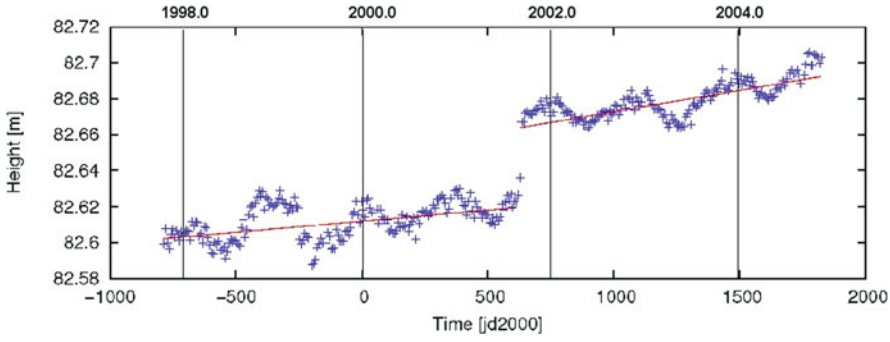

Fig. 3 Time series for the height component of the GPS station HOFN, Iceland

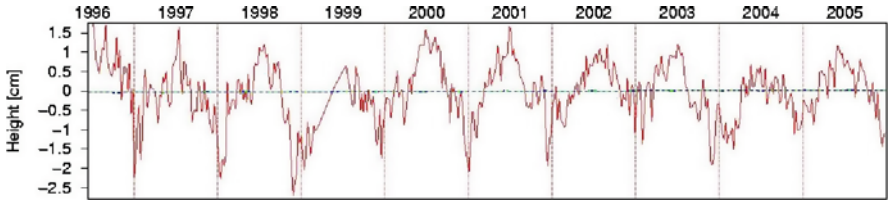

Fig. 4 Seasonal height variation for GPS station Irkutsk, Siberia

analysis of position time series has shown, that for some stations also instrumentation effects (rather than geophysical ones) are responsible for the observed signals.

One possibility to consider the annual variations of station positions is to extend the current parameterization (i.e., station positions and constant velocities), but it is necessary to find a suitable parameterization for the variations. The investigations have shown, that the shape of the annual height variations differs between the stations. Figure 5 shows two examples for the mean average shape of such annual variations.

While the Brasilia time series clearly shows a maximum and a minimum, Ankara does not have a clear minimum. The averaged annual motions of both stations can be mathematically represented rather well by sine/cosine annual and semi-annual functions. We investigated the position time series of all VLBI, SLR and GPS stations and found that for many stations such a parameterization is a good approximation for the seasonal variations. On the other hand, the procedure and parameterization is problematic if the seasonal variations are different over the observation time span. Another problem is that the additional parameters will affect the stability of the solutions. Thus, handling and parametrization of seasonal variations in station positions is a challenge for future TRF computations.

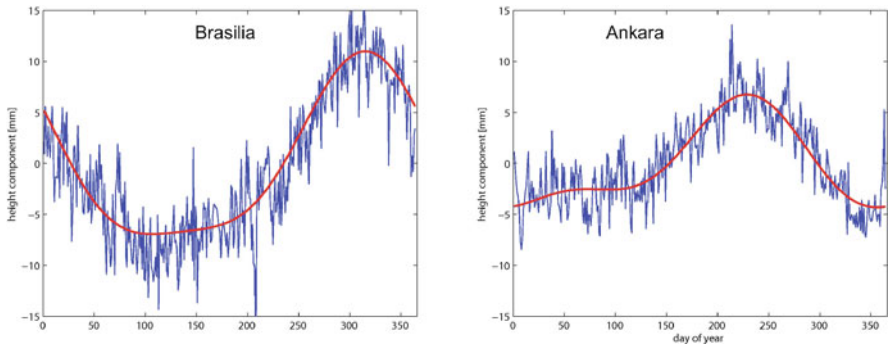

Fig. 5 Shape of the "averaged" annual height signal for two GPS stations. The *fitted curves* represent the mathematical approximation by annual and semi-annual sine/cosine functions

5 Computation of the TRF Solution

The input for the combination of different techniques are the accumulated intra-technique VLBI, SLR and GPS normal equations. The NEQs include station positions, velocities, daily EOPs, and (for VLBI) also quasar coordinates. A key issue within the inter-technique combination is the connection of the different techniques' observations given by local tie measurements between the instruments' reference points at co-location sites. As shown for example in Krügel and Angermann (2007), the selection of suitable local ties is difficult because the number and the spatial distribution of "high quality" co-location sites is not optimal. Another problem is that there are discrepancies between the coordinate difference vectors derived from the space geodetic techniques and the local ties for many co-location sites. Figure 6 shows the discrepancies for some of the VLBI and GPS co-locations. The results are given for the GGOS-D terrestrial reference frame computation in comparison with the DGFI solution ITRF2005-D. The agreement of the space geodetic solutions with the local ties is better for most stations within the GGOS-D computation, which is evidence of the progress compared to the ITRF2005.

Within the inter-technique combination the local tie selection and implementation as well as the combination of station velocities at co-location sites was done in an iterative procedure (see Krügel et al., 2007; Seitz, 2009). The quality of the selected local ties was analysed by using the following two criteria: (1) The mean offsets between the x-pole and y-pole estimates of the different techniques are a measure for the consistency of the inter-technique combination and should be minimized; (2) the deformation of the networks caused by adding local ties and equating velocities at co-location sites should be minimized. This is expressed by the RMS of position and velocity differences between the single-technique solutions and the combined solution. To identify the best set of co-location sites, different solutions were computed, varying the co-locations and the assumed accuracy of the introduced local ties. As an example, the results for VLBI and GPS co-locations are given in Table 2. It shows the mean pole offsets and the network deformation for the

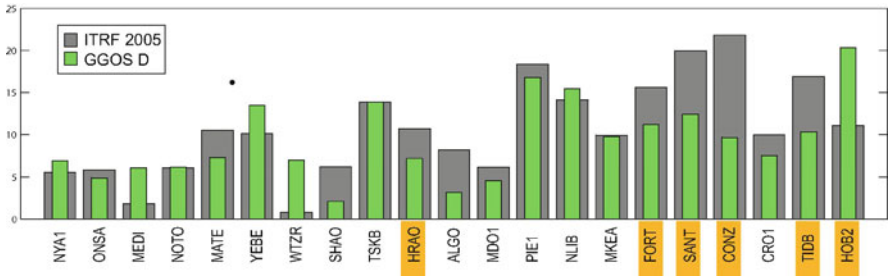

Fig. 6 Comparison of the GGOS-D results with ITRF2005-D. The 3-D difference vectors (mm) between the VLBI and GPS solutions and the terrestrial difference vectors are given for 21 co-location sites. The stations located in the southern hemisphere are *highlighted*

Table 2 Mean pole offsets and network deformation for VLBI and GPS co-locations obtained from GGOS-D inter-technique combination in comparison with DGFI solution ITRF2005-D

	Selected VLBI – GPS co-locations	Mean pole difference	Network deformation ref. epoch: 2000.0
GGOS-D	19	0.035 mas	0.3 mm
ITRF2005-D	13	0.041 mas	1.0 mm

GGOS-D inter-technique combination in comparison with the ITRF2005-D results. The number of selected co-location sites significantly increased for the GGOS-D computations, accompanied with a better agreement of the VLBI and GPS pole coordinates and a smaller network deformation.

Other tasks of the inter-technique combination include the weighting of the different techniques, the combination of station velocities of co-located instruments, the combination of the EOP, and finally the datum definition of the combined solution. The weighting is done by determining variance factors for the normal equations based on the precision of repeated (daily/weekly) station positions for the different techniques. Station velocities at co-location sites were combined only, if the differences between different techniques are not significant.

Concerning the combination of the EOP it has to be considered, that the EOP derived from VLBI observations are set up as daily offsets and drifts, whereas the EOP derived from GPS and SLR are parameterized as functional values of a piece-wise linear representation between 0 and 24 h. Thus, the VLBI EOP were transformed into values of a piece-wise linear function, too (see chapter "GGOS-D Consistent, High-Accuracy Technique-Specific Solutions" by Steigenberger et al., this issue).

The inter-technique combination is completed by pseudo-observations for the selected local ties and for the equated station velocities at co-location sites. To generate the final TRF solution, the datum conditions have to be added to the free normal equations and the complete normal equation system has to be inverted.

The geodetic datum is defined as follows: The origin is realized by SLR observations. As shown for example in Rülke et al. (2008), the network translation parameters derived from GPS are affected by orbital perturbances and thus GPS was not used for the datum definition. The scale of the TRF solution is defined by SLR, VLBI and GPS observations. This was justified, since a comparison of the scale of the technique-specific station networks showed no significant differences. The orientation of the TRF is defined by No-Net-Rotation (NNR) conditions w.r.t. ITRF2005. The kinematic datum of the final TRF solution is given by an actual plate kinematic and crustal deformation model (APKIM) derived from observed station velocities (Drewes, 2009). For the estimation of quasar coordinates NNR conditions w.r.t. ICRF-Ext.1 were applied (Tesmer et al., 2007).

The GGOS-D combination results comprise the terrestrial reference frame (station positions and velocities), daily EOP and the celestial reference frame (quasar

coordinates). For the first time, these parameters have been estimated in a common adjustment of VLBI, SLR and GPS observation time series. Thus the results ensure consistency between the TRF, the CRF and the connecting EOP. Furthermore, the reference frame results provide the basis for the generation of consistent, high-quality time series of geodetic-geophysical parameters describing the Earth system (chapter by "Consistent and Combined Time Series of Geodetic/Geophysical Parameters" by Nothnagel et al., this issue).

6 Conclusions

The GGOS-D global terrestrial reference frame (station positions and velocities) has been computed simultaneously with the quasar coordinates and daily EOP to ensure consistency of the results. The computations have been performed on the basis of homogeneously processed observation time series for the different space geodetic techniques. The results of the time series analysis have shown seasonal variations for most of the stations, which are primarily visible in the height components. A large part of the observed signals is caused by geophysical effects (e.g., hydrological and atmospheric loading), which are presently not reduced from the original observations. We investigated the position time series of all VLBI, SLR and GPS stations and found that for most of the stations the shape of the averaged seasonal signals can rather well be mathematically approximated by sine/cosine annual and semi-annual functions. However, there are still some issues that need to be further investigated regarding the parameterisation of the seasonal signals within the TRF computation. On the other hand it is clear, that deviations of the station positions from a linear model will produce errors in the estimated parameters. Furthermore, the alignment of epoch solutions to such a reference frame is also affected by these non-linear station motions. Therefore the consideration of seasonal signals in station positions is one of the most important tasks for future TRF realizations.

Acknowledgments This work was partly funded by the project GGOS-D within the GEOTECHNOLOGIEN programme of the Federal Ministry of Education and Research (BMBF: Bundesministerium für Forschung und Technologie), FKZ 03F0425.

References

Altamimi Z, Collilieux X, Legrand J, Garayt B, Boucher C (2007) ITRF2005: A new release of the International Terrestrial Reference Frame based on time series of station positions and earth orientation parameters. J. Geophys. Res. 112, B09401, doi:10.1029/2007/JB004949.

Angermann D, Drewes H, Krügel M, Meisel B, Gerstl M, Kelm R, Müller H, Seemüller W, Tesmer V (2004) ITRS Combination Center at DGFI: A terrestrial reference frame realization 2003, Deutsche Geodätische Kommission, Reihe B, Heft Nr. 313.

Angermann D, Drewes H, Gerstl M, Kelm R, Krügel M, Meisel B (2005) ITRF combination – status and recommendations for the future. In: Sanso F (ed.), A Window on the Future of Geodesy, IAG Symposia, Vol. 128, Springer, Berlin.

Angermann D, Drewes H, Krügel M, Meisel B (2007) Advances in Terrestrial Reference Frame Computations, IAG Symposia Cairns, Springer, Berlin.

Angermann D, Drewes H, Gerstl M, Krügel M, Meisel B (2009) DGFI combination methodology for ITRF2005 computation. In: Drewes H (ed.), Geodetic Reference Frames, IAG Symposia, Vol. 134, Springer, Berlin.

Drewes H, Angermann D (2003) Remarks on some problems in the combination of station coordinate and velocity solutions, IERS Technical Note 30, 89-93, Verlag des Bundesamtes für Kartographie und Geodäsie, Frankfurt am Main, 3–89888–877–0.

Drewes H, Angermann D, Gerstl M, Krügel M, Meisel B, Seemüller W (2006) Analysis and refined computations of the International Terrestrial Reference Frame. In: Flury J, Rummel R, Reigber C, Rothacher M, Boedecker G, Schreiber U (eds.), Observation of the Earth System from Space, Springer, Berlin.

Drewes H (2009) The APKIM2005 as basis for a non-rotating ITRF. In: Drewes H (ed.), Geodetic Reference Frames, IAG Symposia, Vol. 134, Springer, Berlin.

Gerstl M (2003) Numerical aspects on combination at the observation equation and normal equation level, IERS Technical Note 30, 89-93, Verlag des Bundesamtes für Kartographie und Geodäsie, Frankfurt am Main, 3–89888–877–0.

Krügel M, Angermann D (2007) Frontiers in the combination of space geodetic techniques, Proceedings of IAG Symposia Cairns, Springer, Berlin.

Krügel M, Angermann D, Drewes H, Gerstl M, Meisel B, Tesmer V, Thaller D (2007) GGOS-D Reference Frame Computations. GEOTECHNOLOGIEN Science Report, No. 11, ISSN 1619-7399.

Meisel B, Angermann D, Krügel M, Drewes H, Gerstl M, Kelm R, Müller H, Tesmer V (2005) Refined approaches for terrestrial reference frame computations. Adv. Space Res. 36, 350–357.

Meisel B, Angermann D, Krügel M (2009) Influence of time-variable effects in station positions on the terrestrial reference frame. In: Drewes H (ed.), Geodetic Reference Frames, IAG Symposia, Vol. 134, Springer, Berlin.

Rülke A, Dietrich R, Fritsche M, Rothacher M, Steigenberger P (2008) Realization of the terrestrial reference system by a reprocessed global GPS network. J. Geophys. Res., doi:10.1029/2007JB005231.

Seitz F, Krügel M (2009) Modeling vertical site displacements due to surface loads in consideration of crustal inhomogenities. In: Drewes H (ed.), Geodetic Reference Frames, IAG Symposia, Vol. 134, Springer, Berlin.

Seitz M (2009) Kombination geodätischer Raumbeobachtungsverfahren zur Realisierung eines terrestrischen Referenzsystems. Deutsche Geodätische Kommission, Reihe C, Heft Nr. 360.

Steigenberger P, Rothacher M, Dietrich R, Fritsche M, Rülke A, Vey S (2006) Reprocessing of a global GPS network. J. Geophys. Res. 111, B05402.

Tesmer V, Böhm J, Heinkelmann R, Schuh H (2007) Effect of different tropospheric mapping functions on the TRF, CRF, and position time series estimated from VLBI. In: Schuh, H., Nothnagel, A., Ma, C. (eds.), VLBI Special Issue. J. Geod., doi:10.1007/s00190-006-0127-8.

Tesmer V, Böhm J, Meisel B, Rothacher M, Steigenberger P (2008) Atmospheric loading coefficients determined from homogeneously reprocessed GPS and VLBI time series, 5th IVS General Meeting Proceedings.

Tesmer V, Steigenberger P, Rothacher M, Boehm J, Meisel B (2009) Annual deformation signals from homogeneously reprocessed VLBI and GPS height time series. J. Geod., doi:10.1007/s00190-009-0316-3.

Thaller D, Krügel M, Meisel B, Panafidina H, Steigenberger P (2007) Time series from inter-technique combinations. GEOTECHNOLOGIEN Science Report, No. 11, ISSN 1619-7399.

GGOS-D Consistent and Combined Time Series of Geodetic/Geophyical Parameters

A. Nothnagel, T. Artz, S. Böckmann, N. Panafidina, M. Rothacher, M. Seitz, P. Steigenberger, V. Tesmer, and D. Thaller

1 Introduction

Project GGOS-D, (Chapter "Integration of Space Geodetic Techniques as the Baris for a Global Geodetic - Geophysical Observing System (GGOS-D): An Overview" by Rothacher et al., 2009, this issue) and the generation of a GGOS-D terrestrial reference frame (Chapter "GGOS-D Global Terrestrial Reference Frame" by Angermann et al., 2009, this issue) provided an ideal foundation for a detailed analysis of the input data in the form of time series of parameters estimated. At the current stage, the reference frame itself has to be regarded as a global set of mean positions with a limited level of kinematic information through velocity parameters. From time series of the three dimensional coordinate components, however, a much more detailed knowledge about the kinematic behaviour of the observing sites can be inferred. In an ideal case, the results of different observing techniques located close to each other at so-called co-location sites should be very similar or even identical. Due to the specific characteristics of the techniques or of the very location of the measurement platform, this is hardly ever the case to the full extent. In addition, the accuracy of the observing techniques is still limited by small systematic effects. Therefore, a certain degree of discrepancy has still to be expected and provides invaluable information about remaining problem areas.

In addition to the site coordinates, further information can be retrieved from other elements of the parameter space and their time series like Earth orientation and atmosphere parameters. Observing techniques based on observations in the radio frequency bands are affected by the same refraction effects of the neutral atmosphere. The estimates of the atmospheric parameters should, thus, provide identical results, if the theoretical bias due to height differences between the reference points is corrected. Again, the discrepancies give important insights into remaining divergences in modelling. Another aspect beyond individual treatment of the different

A. Nothnagel (✉)
Institut für Geodäsie und Geoinformation, Universität Bonn, D-53115 Bonn, Germany
e-mail: nothnagel@uni-bonn.de

F. Flechtner et al. (eds.), *System Earth via Geodetic-Geophysical Space Techniques*, Advanced Technologies in Earth Sciences, DOI 10.1007/978-3-642-10228-8_47,

techniques is the combination and its benefit to the quality of the determination of the parameters. In this article, we describe a few selected examples of time series with their characteristics and their quality.

2 Time Series of Site Coordinates

All solutions of geometric geodetic space techniques where site positions are treated as unknown parameters require that a geometric datum is defined. When SLR, GPS and VLBI station positions are being estimated from weekly, daily and session-wise blocks of observations, respectively, the datum has to be defined for each of the weekly, daily or session-wise solutions. In order to avoid distortions of the networks, no-net-rotation (NNR) and/or no-net-translation (NNT) conditions were applied in the solutions, either on all sites or a sub-set of sites of the network. In the VLBI solutions, NNR and NNT conditions were set up for all sites of the respective networks with respect to the ITRF2005 coordinates (Altamimi et al., 2007) of the observing epochs. The GPS analyses were carried out estimating geocenter coordinates and applying NNR and NNT conditions w.r.t. IGS05 coordinates (Ferland 2006). SLR station positions were computed by applying NNR conditions with respect to ITRF2005 (rescaled), only.

2.1 Seasonal Effects in Site Positions

It has long been known that the vertical components of the positions of some GPS observing sites exhibit seasonal variations (Dong et al., 2002). The question is whether similar variations are also detectable by other techniques. If these variations are of geophysical origin, they should be rather identical at co-located sites. If not, the behaviour of the differences should give some hints on their origin.

In order to investigate common signals of the different techniques and to detect systematic and episodic differences, coordinate time series of stations where at least two techniques are co-located have been compared (see also Tesmer et al., 2009). As an example, Fig. 1 shows the median-smoothed height component time series of GPS and VLBI results of the station Wettzell (Germany, upper panel) and the median-smoothed height time series for GPS and SLR of the station Yarradagee (Australia, lower panel).

The GPS and VLBI time series of Wettzell show a very similar behaviour with clear annual variations. Both techniques exhibit approximately the same amplitude and the same phase. This is not the case for GPS and SLR at the station Yarragadee. Here, GPS shows annual variations with varying amplitudes while the SLR variations are more irregular.

Since the annual variations seem to be the strongest systematics, a more detailed investigation of the annual signal was carried out. A mean annual signal was computed from the whole time span available by averaging all values with identical

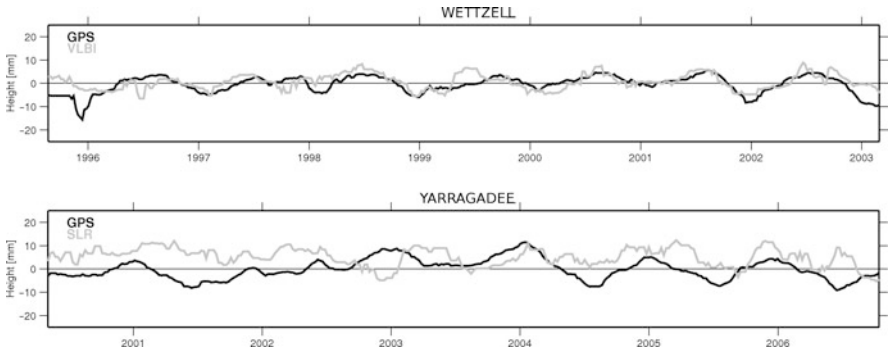

Fig. 1 Time series of the height components (daily estimates smoothed with a 70-day-median filter), *upper panel*: GPS and VLBI time series of station Wettzell (12.9° E.L., 49.1° N.L.); *lower panel*: GPS and SLR time series of station Yarragadee (115.3° E.L., -29.0° S.L.)

day-of-year (subtracting a drift first). Figure 2 illustrates the results again for the two stations Wettzell and Yarradagee. The left graph shows that the phases of the mean annual signal derived from GPS and VLBI are very similar. However, the amplitude is slightly lower from the VLBI observations. It is conceivable that this might be caused by the missing atmospheric pressure loading corrections which have a noticable effect for small VLBI networks (Boehm et al., 2009).

At Yaragadee (right graph of Fig. 2) the GPS data shows a similarly smooth behaviour which resembles a sinusoid with a slightly larger amplitude than at Wettzell and with a 180° phase shift for the southern hemisphere as to be expected. In contrast to this, the SLR data produces a lower level of variation between winter and summer, and the behaviour of the variations seems to be distorted. Together with the irregular long term variations as shown in Fig. 1, this is a clear indication that annual variations are not the main feature of the SLR site variations. In general, the SLR position time series are much more noisy than those from GPS and VLBI. In addition, they show rather irregular variations when a mean day-of-year series is

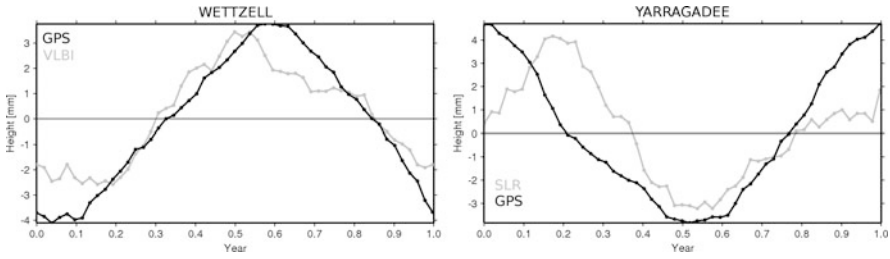

Fig. 2 Mean annual signals of the height components (daily estimates smoothed with a 70-day-median filter), *left graph*: GPS- and VLBI-derived mean annual signal of the station Wettzell, *right graph*: GPS- and SLR-derived mean annual signal of the station Yarragadee

computed as described above. One of the reasons certainly is that SLR is hampered by severe irregularities in the ability to track satellites due to overcast periods.

Wettzell and Yaragadee are just two examples which show that in some cases the techniques provide identical results while at others the variations in station positions are still technique-dependent.

2.2 Thermal Expansion Effects in VLBI

Owing to thermal expansion, the position of the VLBI reference point of a radio telescope located at the intersection of the axes depends on the temperature of the steel construction. Correcting the VLBI observations for thermal expansion effects in both VLBI software packages was one of the tasks within project GGOS-D. The validation of modelling thermal expansion effects properly is not quite straight forward. Due to the fact that the network employed in each session consists only of a small number of observatories, mostly well below 10, and due to the NNR/NNT datum definition, the correction at one site has a diluted but significant effect on all other sites. However, this effect is difficult to quantify. It depends on the network configuration and is roughly inverse proportional to the number of network stations. Nevertheless, the time series of the differences of the vertical site component between corrected and uncorrected data shows clear systematic variations with a period of 1 year. The effect itself can only be depicted if differences between corrected and uncorrected positions are computed and plotted (Fig. 3).

The example of Algonquin Park in Eastern Canada is particularly informative since the temperature difference between summer and winter is quite large (Fig. 4). A clear annual signal is obvious in the time series of the temperatures which finds a

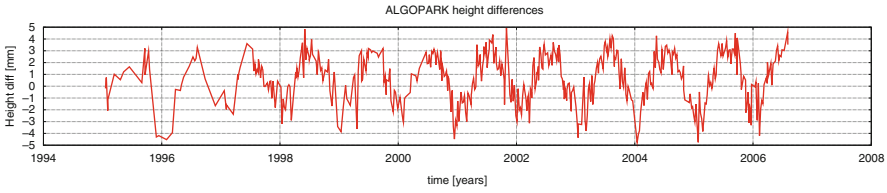

Fig. 3 Height differences between solutions without and with thermal expansion modelling of the Algonquin Park radio telescope in Canada (281.9° E.L., 45.9° N.L.)

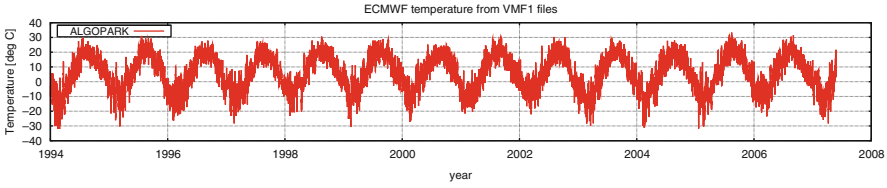

Fig. 4 Temperature variations at Algonquin Park in Canada

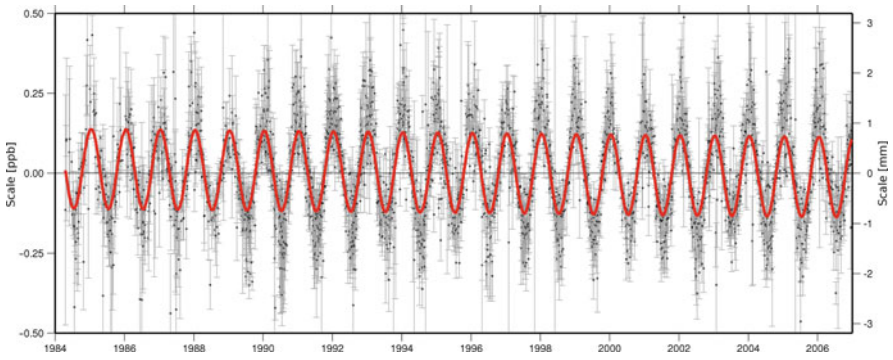

Fig. 5 Differences in scale parameters of Helmert transformations w.r.t. ITRF2005, uncorrected minus corrected for thermal expansion

direct equivalent in the estimated height variations of the VLBI telescope originating from the thermal expansion modelling. For other sites, this is not as obvious as for Algonquin, mostly due to the correlations within the estimates of station coordinates in an NNR/NNT setup.

A composite effect over all VLBI sites can be deduced if the scale components of the Helmert parameters are computed for each session solution with respect to the reference solution. The differences between the scale parameters with and without thermal expansion corrections (Fig. 5) show a clear annual sinusoid. Considering that the northern hemisphere is over-represented in number of stations and number of observing sessions, the annual period with a minimum early in the years is a necessary consequence. This would be quite different if the number of stations and the number of observations would be balanced between the two hemispheres. In such a case, the z-translation would be affected most and should also show an annual period.

The differences in scale of up to 0.4 ppb emphasize the importance of the corrections for thermal expansion effects. Within project GGOS-D, it has been shown that these corrections do improve the repeatability of baseline lengths by more than 3%.

3 Time Series of Earth Orientation Parameters

3.1 EOP Time Series Resulting from a Consistent Combination of TRF and EOP

A comparison of the combined EOP time series and the series derived from the observations of the individual techniques shows to what extent the EOPs benefit from the combination. In Fig. 6 the individual as well as the combined series are displayed, exemplarily for x-pole, y-pole and UT1-UTC (selected are 3 years of data). In order to illustrate the effect on the EOPs, the time series

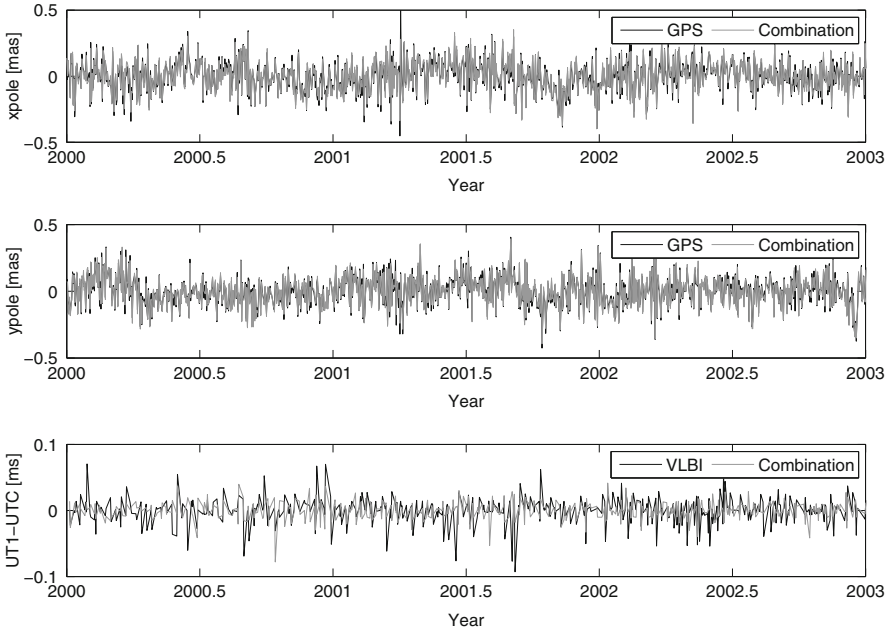

Fig. 6 Earth rotation parameters: combined solution (*grey*) is compared to the best technique-only solution (*black*). The pole coordinates and UT1-UTC are plotted w.r.t IERS EOP 05 C04 (offset removed)

are reduced by values of a reference series. As reference IERS EOP 05 C04 was chosen (http://hpiers.obspm.fr/iers/eop/eopc04_05/C04_05.guide.pdf, 10.01.2009). The corresponding RMS w.r.t. IERS EOP 05 C04 values are given in Table 1. The IERS EOP 05 C04 series does not necessarily represent the truth. However, it is reliable to be used here as a reference series to demonstrate better the effect of the combination. Considering, that the RMS value of the UT1-UTC series is reduced from 0.0193 ms (VLBI only) to 0.0124 ms (combined) the results show, that all the EOP parameters are significantly improved by the combination.

Table 1 WRMS of pole coordinates and UT1-UTC time series referenced to IERS EOP 05 C04 (offsets removed)

Technique	x-pole mas	y-pole mas	UT1-UTC ms
GPS	0.1191	0.1130	–
VLBI	0.1693	0.1627	0.0105
SLR	0.3032	0.3065	–
Combined (only common epochs)	0.1148	0.1088	0.0126

3.2 Analysis of Nutation Time Series

Similar to UT1-UTC, the two nutation angles can be determined only by VLBI in an absolute sense, whereas the satellite-techniques can contribute solely the time-derivatives, i.e., the nutation rates. Therefore, we first look at the time series derived from a VLBI-only multi-year solution. Two different types of solutions were computed: For the first solution, the temporal resolution of the nutation angles was one set for each session. For the second solution, the session-specific parameters have been transformed into a piece-wise linear polygon with an interval length of 28 days. As the major difference between the estimated nutation angles and the a priori model IAU2000 is the so-called free core nutation (FCN) with a period of about 432 days, the representation with such a long interval of 28 days is justified in order to reduce the scatter in the time series and to better determine the period of the FCN (Fig. 7). It can be seen from Fig. 7 that the amplitude of the FCN is not constant. The same applies to a combined solution from VLBI and GPS observations where the nutation was estimated as a piece-wise linear polygon of 28 days as well (not shown here).

In order to determine the time dependent amplitudes at each epoch, a fit of a sinusoid was performed with sliding time windows, each with a length of 865 days separated by 7 days. According to Roosbeek et al. (1999), the period of the FCN do not vary very much, therefore, we did the fitting by using a fixed period of 432 days. However, it should be mentioned, that there are other publications that show a varying period for the FCN (see e.g., Malkin and Miller, 2007). As it is known from theory that the FCN is a retrograde signal, the fit of the sinusoid was carried out for

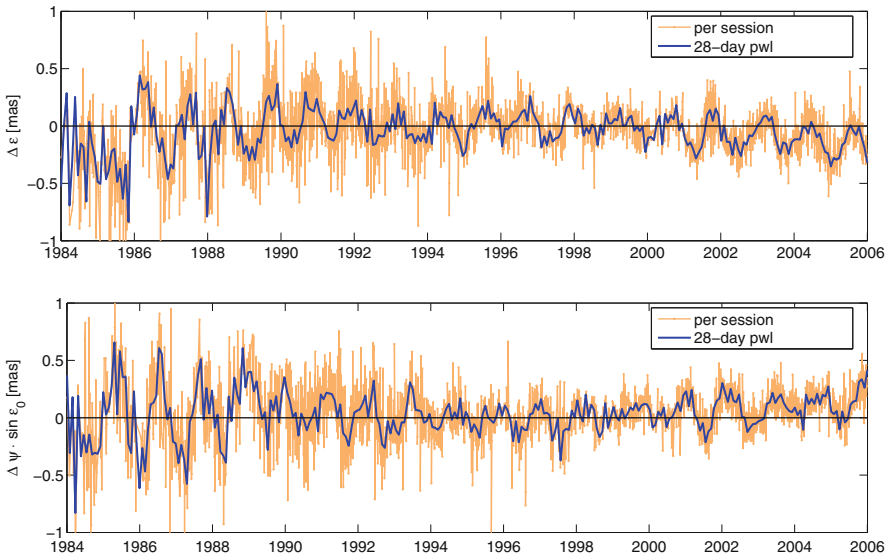

Fig. 7 Nutation in obliquity and longitude estimated from VLBI-only multi-year solutions (corrections to the IAU2000 model)

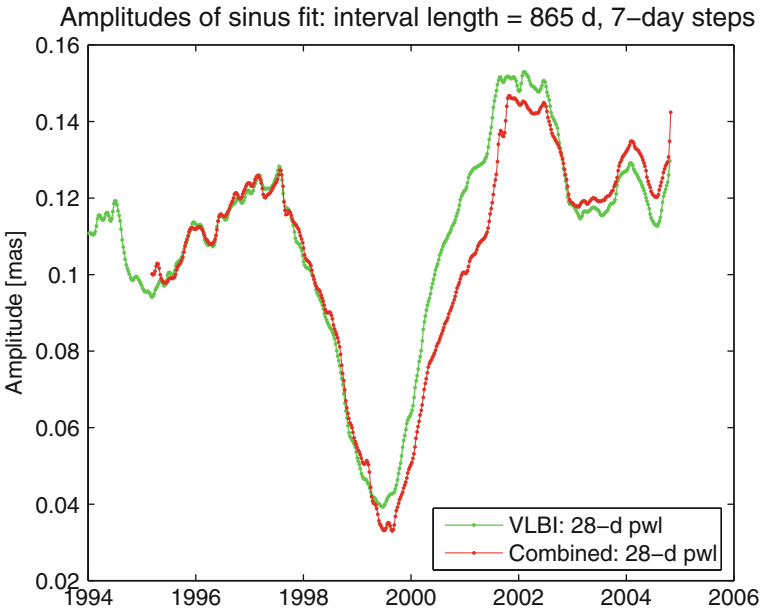

Fig. 8 Amplitude of the FCN estimated by a two-dimensional fit of a sinusoid to the multi-year solutions using sliding time windows

both nutation angles together so that a phase shift of 90° is guaranteed automatically. The estimated amplitudes are shown in Fig. 8 for the solutions with 28-day polygons. The estimated amplitudes of the FCN are around 0.12 mas, except of the time span 1997 until 2002. During these years, the amplitude rapidly decreased and increased again, with the minimum value around the middle of 1999. This result agrees well with earlier analysis, e.g. by Herring et al. (2002) who stated that there is an indication that the amplitude of the FCN increases again after 2000.

4 Time Series of Atmosphere Parameters

The tropospheric path delay ΔL is represented as a function of elevation angle ε and azimuth α of the vector between the ground station and the observed GPS satellite or quasar. The azimuth-independent part of the neutral atmosphere around a station is described as a sum of a zenith hydrostatic delay (ZHD) L_h and a zenith wet delay (ZWD) L_2 (Eq. 1). For an observation with elevation angle ε both zenith delays are mapped to the elevation angle of the observation using the Vienna Mapping Function 1 (VMF1, Boehm et al., 2006). The azimuth-dependency of the tropospheric delay of the observation is considered with coefficients for gradients in north-south (G_n) and east-west direction (G_e), mapped with the gradient mapping function m_g to the elevation of the observation.

$$\Delta L(\alpha,\varepsilon) = \Delta L_h m_h(\varepsilon) + \Delta L_w m_w(\varepsilon) + m_g(\varepsilon) \times [G_n \cos\alpha + G_e \sin\alpha] \qquad (1)$$

While for each GPS and VLBI station, the ZHD is corrected a priori (with interpolated ECMWF grid data), the ZWD is estimated in the least-squares adjustment. However, the estimated part cannot be interpreted completely as the real wet delay since it is also affected by differences in atmospheric pressure between in-situ pressure measurements and ECMWF pressure interpolations. For the gradient mapping function the simple equation by MacMillan (1995) with the wet mapping function has been used (Eq. 2)

$$m_g(\varepsilon) = m_w \cdot \cot(\varepsilon) \tag{2}$$

The troposphere zenith delay parameters are estimated as piece-wise linear functions for each station with a temporal resolution of 1 h for VLBI and of two hours for GPS, as otherwise the number of parameters in the GPS processing is too large. The GPS-derived gradients are estimated for each site once per day as a linear function. In the VLBI solutions the gradients are estimated as a linear function for each 24 h-session. A priori values for the gradients are zero. In contrast to GPS, the VLBI-derived troposphere zenith delay parameters and gradients could not be estimated completely free due to the fact that the observation geometry is poor in some of the VLBI sessions, especially the older ones. Therefore, the time derivatives of the troposphere zenith delay parameters had to be constrained to zero with a standard deviation of 1 cm/h while the troposphere gradients were constrained to zero with standard deviations of 2.5 mm and 5 mm/day. To be able to better compare the VLBI- and the GPS-derived troposphere parameters, both were always referred to intervals of full UTC hours, which is not typical for the VLBI-only solutions. The GPS troposphere parameters were estimated from weekly solutions providing continuous results over 1-week periods. The VLBI-derived parameters do not provide such continuity, as there are only about 3–4 sessions per week with changing observing networks.

The GPS and VLBI time series of the ZWD estimates for Hartebeesthoek as well as their differences are displayed in Fig. 9. The differences show an offset of 5 mm

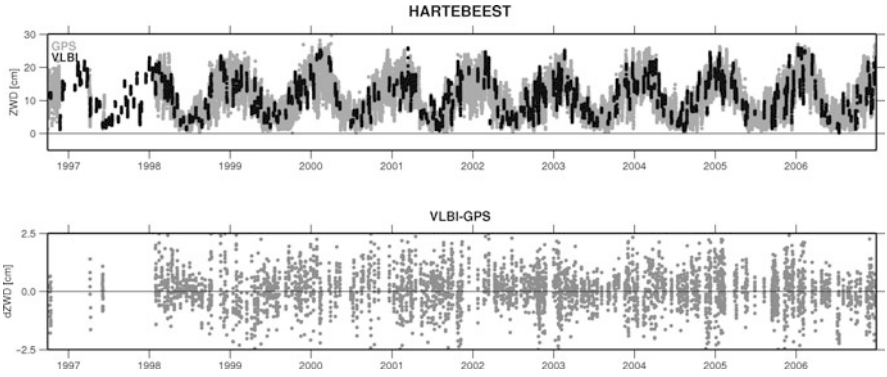

Fig. 9 Time series of zenith wet delays of the station Hartebeesthoek (27.7° E.L., −25.9° S.L.) for GPS and VLBI (*upper panel*) and differences of the series, VLBI-GPS (*lower panel*)

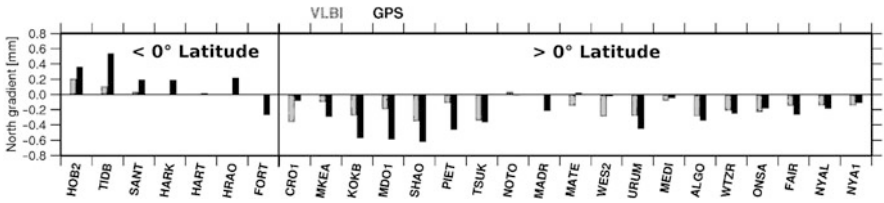

Fig. 10 Mean gradients in north–south direction of co-located VLBI and GPS stations

with a standard deviation of 1 mm and a weighted RMS of 8 mm after removing the offset. A similar result, with an offset of 4.2 ± 6.3 mm, had already been obtained by Schuh et al. (2004). In addition, a seasonal pattern is visible in the differences. In summertime, when the water content of the atmosphere as well as the variability is larger, the ZWD differences show a larger scatter (see Steigenberger et al., 2007).

Beside the zenith wet delays, the tropospheric horizontal gradients from GPS and VLBI can also be compared. Figure 10 illustrates the mean gradients in north-south direction for all GPS and VLBI co-located stations sorted from south to north. For both techniques, the gradients show the expected systematics in direction of the equator (Chen and Herring, 1997). Furthermore, this comparison shows that the mean gradients of VLBI are smaller for nearly all stations than the GPS derived mean gradients. The reason for this offset might be the constraints on the a priori values for the gradients determined by VLBI as discussed in Steigenberger et al. 2007. In addition, it might play a role that in recent years VLBI observations have been carried out as far down as 3° elevation. This strengthens the estimates of the gradients considerably.

5 Conclusions

The time series of site coordinates, Earth orientation parameters and atmosphere parameters produced within project GGOS-D provide valuable data sets for detailed studies of these geodetic/geophysical phenomena. The series combined from different observing techniques are certainly the most stable data sets since they combine the strengths of the individual techniques and mitigate their weaknesses. However, differences in the results of the individual techniques are the keys to detecting remaining deficiencies in procedures and models. For example, the divergent behaviour of station coordinates from different observing techniques, though co-located in close vicinity, indicate that systematic errors in the individual techniques still exist and that the local ties between the different sensors have to be observed more often than just once. Estimates of zenith wet delays can only be compared properly if the height difference of the GPS antenna and the reference point of the VLBI telescope is taken into account. In addition, technique specific systematics, for example, from GPS antenna phase centers and VLBI telescope structure deformations still exist and have to be addressed for further progress in accuracy and reliability.

Acknowledgments We are grateful for the use of observation data from IGS (Dow et al., 2005), ILRS (Pearlman et al., 2002), and IVS (Schlüter et al., 2002). This is publication no. GEOTECH-1258 of the programme GEOTECHNOLOGIEN of the German Ministry of Education and Research (BMBF). The work has been carried out in part with support of grants 03F0425A, 03F0425C, 03F0425D of BMBF.

References

Altamimi Z, Collilieux X, Legrand J, Garayt B, Boucher C (2007) ITRF2005: a new release of the International Terrestrial Reference Frame based on time series of station coordinates and Earth Orientation Parameters. J. Geophys. Res. 112, doi:10.1029/2007JB004949.

Boehm J, Werl B, Schuh H (2006) Troposphere mapping functions for GPS and very long baseline interferometry from European Centre for Medium-Range Weather Forecasts operational analysis data. J. Geophys. Res. 111, B02406, doi:10.1029/2005JB003629.

Boehm V, Heinkelmann R, Mendes Cerveira P, Pany A, Schuh H (2009) Atmospheric loading corrections at the observation level in VLBI analysis. J. Geod. 83(11), 1107–1113, doi: 10.1007/s00190-009-0329-y.

Chen G, Herring TA (1997) Effects of atmospheric azimuthal asymmetry on the analysis of space geodetic data. J. Geophys. Res. 102, 20489–20502, doi:10.1029/97JB01739.

Dong D, Fang P, Bock Y, Cheng MK, Miyazaki S (2002) Anatomy of apparent seasonal variations from gps-derived site position time series. J. Geophys. Res. 107(B4), 2075, doi:10.1029/2001JB000573.

Dow J, Neilan R, Gendt G (2005) The International GPS Service: Celebrating the 10th anniversary and looking to the next decade. Adv. Space Res. 36(3) 320–326, doi:10.1016/j.asr.2005.05.125.

Ferland R (2006) Proposed igs05 realization. [IGSMAIL-5447], http://igscb.jpl.nasa.gov/mail/igsmail/2006/msg00170.html

Herring T, Mathews P, Buffett B (2002) Modeling of nutation-precession: Very long baseline interferometry results. J. Geophys. Res. 107(B4), doi:10.1029/2001JB000165.

MacMillan D (1995) Atmospheric gradients from very long baseline interferometry observations. Geophys. Res. Lett. 22(9), 1041–1044, doi:10.1029/95GL00887

Malkin Z, Miller N (2007) An analysis of celestial pole offset observations in the free core nutation frequency band. In: Böhm J, Schuh H, Wresnik J (eds.), Proceedings of the 18th European VLBI for Geodesy and Astrometry Working Meeting, Institute for Geodesy and Geoinformation, TU Vienna, Vienna.

Pearlman MR, Degnan JJ, Bosworth JM (2002) The international laser ranging service. Adv. Space. Res. 30(2), 125–143.

Roosbeek F, Defraigne P, Feissel M, Dehant V (1999) The free core nutation period stays between 431 and 434 sidereal days. Geophys. Res. Lett. 26(1998GL90022550).

Schlüter W, Himwich E, Nothnagel A, Vandenberg N, Whitney A (2002) IVS and its important role in the maintenance of the global reference systems. Adv. Space. Res. 30(2), 127–430, doi:10.1016/S0273-1177(02)00278-8.

Schuh H, Snajdrova K, Boehm J, Willis P, Engelhardt G, Lanotte R, Tomasi P, Negusini M, MacMillan D, Vereshchagina I, et al. (2004) IVS tropospheric parameters – comparison with DORIS and GPS for CONT02. In: Vandenberg NR, Baver KD (eds.), International VLBI Service for Geodesy and Astrometry 2004 General Meeting Proceedings. Ottawa, Canada, February 9–11, 2004. Edited by Nancy R. Vandenberg and Karen D. Baver, NASA/CP-2004-212255, 2004. Published online at http://ivscc.gsfc.nasa.gov, p. 461, pp. 461–465.

Steigenberger P, Tesmer V, Krügel M, Thaller D, Schmid R, Vey S, Rothacher M (2007) Comparisons of homogeneously reprocessed GPS and VLBI long time-series of troposphere zenith delays and gradients. J. Geod. 81, 503–514, doi:10.1007/s00190-006-0124-y.

Tesmer V, Steigenberger P, Rothacher M, Boehm J, Meisel B (2009) Annual deformation signals from homogeneously reprocessed VLBI and GPS height time series. J. Geod. 83(10), 973–988.

GGOS-D Integration with Low Earth Orbiters

Daniel König and Rolf König

1 Introduction

The general goal is to determine consistently the dynamic and the geometric part of a terrestrial reference system. The dynamic part is defined by the Earth's gravity field, the geometric part is given by the Earth's shape and orientation in space. Determining both the dynamic and geometric part is done very efficiently by making use of a global navigation satellite system (GNSS) as well as of some Low altitude Earth Orbiters (LEOs). The dynamic part is mainly determined by the LEOs whose orbits are highly sensitive to its variations. Using the GNSS signals collected onboard the LEOs their orbits can be determined very accurately and thus the variations in the dynamic part. Processing the GNSS signals collected at the ground stations allows for deriving their positions that represent the geometric part.

Conventionally, the dynamic and geometric parts are determined separately and they are combined later on the normal equation level. These separate processings are commonly carried out following the two-step approach where firstly the orbits and clock offsets of the GPS satellites are determined and then introduced as fixed for processing the LEOs in a second step. Thus the two-step approach suffers from a loss of consistency by neglecting the correlations inherent to the parameter estimation problem.

Opposed to this processing scheme the method applied here is the integrated approach (IA) of satellite orbit determination and parameter estimation (Zhu et al., 2004) where all measurements collected by the LEOs and the ground stations are already combined on the observation level. Thus a consistent solution considering all correlations is achieved. Within this method the high-orbiting GNSS satellites provide stability to the whole configuration whereas the LEOs scan the Earth's gravity field very densely with a high temporal resolution. The GNSS used in this context is the Global Positioning System (GPS).

D. König (✉)
Helmholtz Centre Potsdam, GFZ German Research Centre for Geosciences,
Department 1: Geodesy and Remote Sensing, Telegrafenberg, 14473 Potsdam, Germany
e-mail: dkoenig@gfz-potsdam.de

F. Flechtner et al. (eds.), *System Earth via Geodetic-Geophysical Space Techniques*,
Advanced Technologies in Earth Sciences, DOI 10.1007/978-3-642-10228-8_48,

2 Characterization of the Integrated Processings

The processings following the IA are carried out by differential orbit improvement (Kaula, 1966). They are characterized by the satellites involved, the observational data used, and the parameters estimated.

The satellites involved comprise the full GPS constellation with semi-major axes of the orbits of about 26,600 km as well as the LEOs CHAMP, GRACE-A, and GRACE-B having semi-major axes of about 6,800 km.

The link between the Earth and the several types of satellites is established through the observations used. They comprise GPS phase and code measurements collected on the one hand at the ground stations of the International GNSS Service's (IGS; Dow et al., 2005) network (GPS/ground) and on the other hand collected onboard the LEOs by satellite-to-satellite tracking (GPS/SST), K-band range-rate measurements from the GRACE intersatellite link, down-weighted satellite laser ranging normal points (SLR NPs), as well as accelerations and attitude measured onboard the LEOs, see Table 1. The GPS observations are processed as L3 ionosphere-free linear combinations. About 50 globally distributed GPS ground stations are selected per day out of the IGS network. The SLR NPs are measured by the station network of the International Laser Ranging Service (ILRS; Pearlman et al., 2002) and exhibit a non-uniform and sparse distribution in space and time.

Table 1 Characterisation of the observations used

Observation type	Source	Time spacing
GPS/ground	IGS station network	30 s
GPS/SST	CHAMP, GRACE	30 s
K-band range-rate	GRACE	5 s
Accelerations	CHAMP, GRACE	5 s
Attitude	CHAMP, GRACE	5 s
SLR normal points	ILRS station network	Sporadic

The whole processing consists of orbit determination and parameter estimation "runs" each covering a single day. In case of K-band data gaps the length of a run might be reduced. The processings have been carried out using GFZ's EPOS software (Earth Parameter and Orbit System) and cover the period 2004-02-04 to 2004-12-31.

Besides a multitude of parameters set up in order to model the various non-conservative forces acting on each satellite or to precisely model observation errors only a rather small set of Earth system parameters is of interest. As listed in Table 2, this set comprises the positions of the GPS ground stations, the spherical harmonic coefficients C_{nm}, S_{nm} of the Earth's gravity field up to degree and order 2, and Earth rotation parameters (ERPs). They are all constrained to their a priori values with a sigma corresponding to 10 cm on the Earth's surface. The parameter estimation is done by least squares adjustment and is based on the GPS and K-band observations.

Table 2 Solved-for Earth system parameters

	Characteristics
Estimated parameters	
C_{nm}, S_{nm}	Up to degree and order 2
Station positions	GPS stations
ERPs	Polar motion, UT1-UTC
Offline parameters	
Parameters of Helmert transformations between estimated and a priori station positions	3 translations, global scale, 3 rotations

Entering the parameter estimation as well, the SLR NPs do not influence the solution due to their low weight.

The dynamic part of the terrestrial reference system is made up by the estimated spherical harmonic coefficients C_{nm}, S_{nm} of the Earth's gravity field. Thereby the coefficients of degree one – C_{11}, S_{11}, C_{10} – represent the position of the Earth's centre of mass, i.e. the origin of the dynamic part (dynamic origin), in x-, y-, and z-direction, respectively. The ERPs describe part of the Earth's orientation in space. In order to concisely describe the geometric part of the terrestrial reference system additionally its origin, its scale as well as its orientation with respect to the a priori station coordinates are determined offline, i.e. subsequently to each orbit adjustment run, by carrying out seven-parameter Helmert transformations between the estimated and the a priori station positions. The resulting parameters are indicated in Table 2. Notably, all Earth system parameters are determined with daily resolution.

3 Comparison with a Two-Step Processing

In order to assess the benefit of simultaneously estimating all Earth system parameters in a single step, a two-step processing has been carried out that is comparable to the processing following the IA. I.e., in a first step the GPS orbits, all GPS-related parameters like clock offsets and carrier phase ambiguities, as well as the ground station positions and the ERPs were estimated. Then, the GPS orbits and clock offsets as well as the estimated ground station positions and ERPs were introduced as fixed into the second step the orbits of the LEOs and the gravity harmonic coefficients were estimated in. The performance of both parameter estimation processes is revealed by the resulting residuals and the deviations of the estimated parameters from their expectations.

The residuals considered here are those of the GPS/SST phase measurements as well as those of the SLR NPs of the LEOs. As the SLR NPs do not influence the solutions of either processing scheme their residuals act as an absolute quality indicator. The GPS/SST phase residuals, on the other hand, are of relative nature revealing the inner quality of the adjustments.

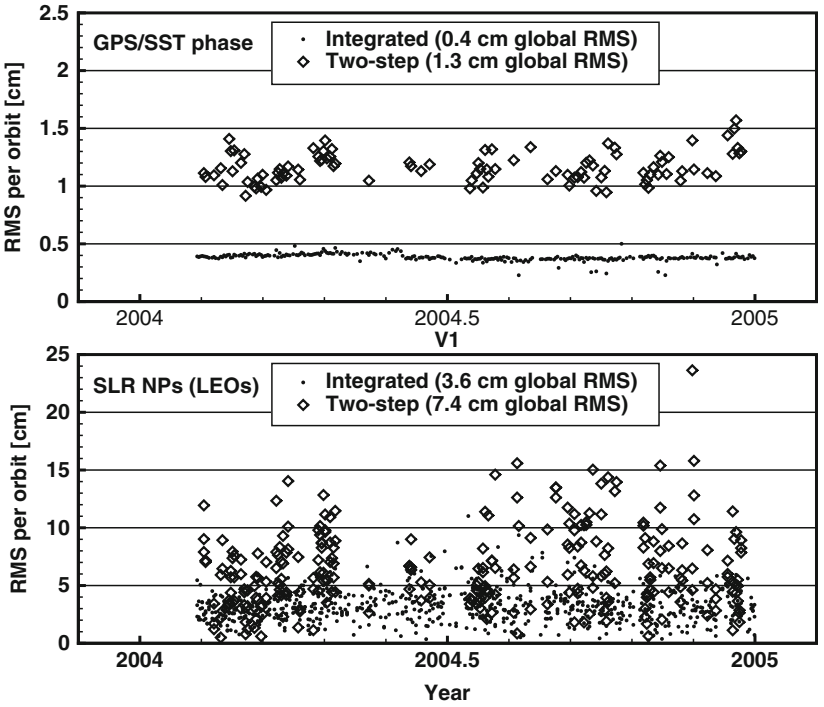

Fig. 1 Time series of orbit-wise RMS values of GPS/SST phase and LEO SLR residuals for the IA ("Integrated") and a corresponding two-step processing ("Two-step")

For both types of residuals the RMS values per run are shown in Fig. 1. As is clearly visible from the plots and indicated by the global RMS values the IA leads to much reduced residuals as well for GPS/SST phase as for SLR observations.

Concerning the estimated parameters the IA delivers more reasonable and accurate results, too. For example, this is revealed by the time series of the gravity harmonic coefficients of degree one determined by both methods as shown in Fig. 2. Especially in C_{10}, the z-component, which in general is the problematic direction in GNSS, the scatter of the time series around its expectation of zero is much smaller for the IA than for the two-step processing.

Thus it can be concluded that the IA stabilizes the GNSS geocenter considerably compared to standard solutions.

4 Time Series of the Dynamic Origin

Out of the various Earth system parameter solutions the components of the dynamic origin are presented here (Fig. 2). The unweighted standard deviations are in the range of about a centimeter revealing a stable solution despite the ambitious

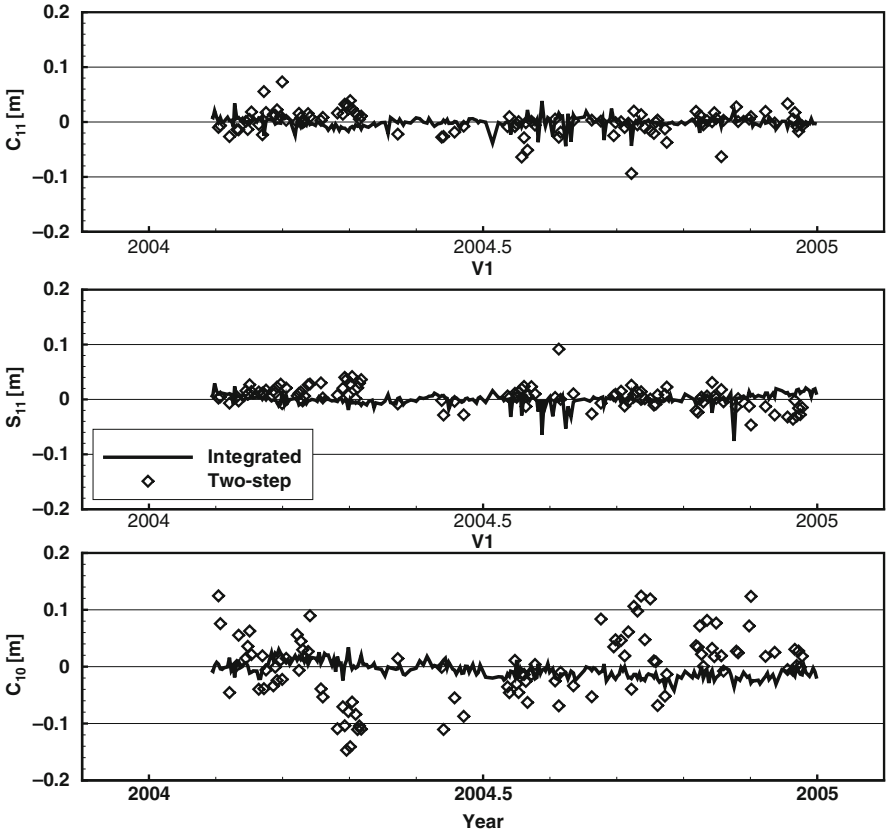

Fig. 2 Time series of the components of the dynamic origin from the IA and a corresponding two-step processing. Mean values with standard deviations of time series referring to the integrated approach: –0.8 ± 9.8 mm (C_{11}), +0.2 ± 10.8 mm (S_{11}), and –6.3 ± 13.5 mm (C_{10})

resolution of one day. A higher scatter is visible in C_{11} and S_{11} around August 2004 due to reduced lengths of the corresponding orbit runs because of K-band data gaps.

C_{11} and S_{11} exhibit no significant offsets from their expectations of zero. The comparatively high mean in C_{10} is obviously due to its strong signal with a period of approximately 1 year. Due to the restricted length of the series of less than 1 year a confirmation of the long-term presence of an annual signal is not possible. The reason for the occurrence of the signal is not yet understood.

5 Conclusions and Outlook

In the framework of determining a geodetic Earth reference frame the IA has been applied to process GPS ground, CHAMP, and GRACE data simultaneously for estimating various parameters constituting both the dynamic and the geometric part.

Corresponding time series have been determined for GPS ground station positions, gravity harmonic coefficients up to degree and order two, and ERPs covering almost the year 2004.

Evidence was given that the IA performs much better than a comparable two-step method as revealed by the SST phase and SLR residuals of the LEOs and the scatter in the components of the dynamic origin. The time series of the dynamic origin currently exhibit a precision in the range of a centimetre showing no significant offsets from their expectations.

The time series of the gravity harmonic coefficients still needs to be validated, however external solutions with daily resolution are not available on the market. For geophysical interpretation the processing period needs to be extended which is not easily achievable due to heavy computational requirements.

Acknowledgments This study was funded within the Geotechnologien program under the grant 1286 of the German Federal Ministry of Education and Research (BMBF). Data was provided by the IAG services IERS, IGS, and ILRS.

References

Dow JM, Neilan RE, Gendt G (2005) The International GPS Service (IGS): Celebrating the 10th anniversary and looking to the next decade. Adv. Space Res. 36(3), 320–326, doi: 10.1016/j.asr.2005.05.125.

Kaula WM (1966) Theory of Satellite Geodesy. Blaisdell Publication Cie., Waltham.

König D, König R, Panafidina N (2007) Combination of ground observations and LEO data. Geotechnologien Science Report No. 11, ISSN 1619–7399.

Pearlman MR, Degnan JJ, Bosworth JM (2002) The international laser ranging service. Adv. Space Res. 30(2), 135–143, doi: 10.1016/S0273–1177(02)00277–6.

Zhu S, Reigber C, König R (2004) Integrated adjustment of CHAMP, GRACE and GPS data. J. Geod., 78(1–2), 103–108.

Index

F. Flechtner et al. (eds.), *System Earth via Geodetic-Geophysical Space Techniques*, Advanced Technologies in Earth Sciences, DOI 10.1007/978-3-642-10228-8,

T